



Lecture Notes in Mechanical Engineering

Sho Itoh
Shashwat Shukla *Editors*

Advanced Surface Enhancement

Proceedings of the 1st International
Conference on Advanced Surface
Enhancement (INCASE 2019)—
Research Towards Industrialisation

 Springer

Lecture Notes in Mechanical Engineering

Lecture Notes in Mechanical Engineering (LNME) publishes the latest developments in Mechanical Engineering - quickly, informally and with high quality. Original research reported in proceedings and post-proceedings represents the core of LNME. Volumes published in LNME embrace all aspects, subfields and new challenges of mechanical engineering. Topics in the series include:

- Engineering Design
- Machinery and Machine Elements
- Mechanical Structures and Stress Analysis
- Automotive Engineering
- Engine Technology
- Aerospace Technology and Astronautics
- Nanotechnology and Microengineering
- Control, Robotics, Mechatronics
- MEMS
- Theoretical and Applied Mechanics
- Dynamical Systems, Control
- Fluid Mechanics
- Engineering Thermodynamics, Heat and Mass Transfer
- Manufacturing
- Precision Engineering, Instrumentation, Measurement
- Materials Engineering
- Tribology and Surface Technology

To submit a proposal or request further information, please contact the Springer Editor in your country:

China: Li Shen at li.shen@springer.com

India: Dr. Akash Chakraborty at akash.chakraborty@springernature.com

Rest of Asia, Australia, New Zealand: Swati Meherishi at swati.meherishi@springer.com

All other countries: Dr. Leontina Di Cecco at Leontina.dicecco@springer.com

To submit a proposal for a monograph, please check our Springer Tracts in Mechanical Engineering at <http://www.springer.com/series/11693> or contact Leontina.dicecco@springer.com

Indexed by SCOPUS. The books of the series are submitted for indexing to Web of Science.

More information about this series at <http://www.springer.com/series/11236>

Sho Itoh · Shashwat Shukla
Editors

Advanced Surface Enhancement

Proceedings of the 1st International
Conference on Advanced Surface
Enhancement (INCASE 2019)—Research
Towards Industrialisation

 Springer

Editors

Sho Itoh
Advanced Remanufacturing
and Technology Centre (ARTC)
A*STAR
Singapore, Singapore

Shashwat Shukla
Advanced Remanufacturing
and Technology Centre (ARTC)
A*STAR
Singapore, Singapore

ISSN 2195-4356

ISSN 2195-4364 (electronic)

Lecture Notes in Mechanical Engineering

ISBN 978-981-15-0053-4

ISBN 978-981-15-0054-1 (eBook)

<https://doi.org/10.1007/978-981-15-0054-1>

© Springer Nature Singapore Pte Ltd. 2020

This work is subject to copyright. All rights are reserved by the Publisher, whether the whole or part of the material is concerned, specifically the rights of translation, reprinting, reuse of illustrations, recitation, broadcasting, reproduction on microfilms or in any other physical way, and transmission or information storage and retrieval, electronic adaptation, computer software, or by similar or dissimilar methodology now known or hereafter developed.

The use of general descriptive names, registered names, trademarks, service marks, etc. in this publication does not imply, even in the absence of a specific statement, that such names are exempt from the relevant protective laws and regulations and therefore free for general use.

The publisher, the authors and the editors are safe to assume that the advice and information in this book are believed to be true and accurate at the date of publication. Neither the publisher nor the authors or the editors give a warranty, expressed or implied, with respect to the material contained herein or for any errors or omissions that may have been made. The publisher remains neutral with regard to jurisdictional claims in published maps and institutional affiliations.

This Springer imprint is published by the registered company Springer Nature Singapore Pte Ltd. The registered company address is: 152 Beach Road, #21-01/04 Gateway East, Singapore 189721, Singapore

Preface

Surface enhancement attracts a varied set of professionals with diverse backgrounds. It involves, for example, design engineers whose primary concern is functional safety and service life of the component. In development, it involves production engineers who aim to optimise process parameters to achieve high product quality. Further up the value chain, it attracts physicists and materials scientists, who explore fundamental aspects of surface modification to develop more advanced processes.

This book contains a compilation of 37 papers presented in the first International Conference on Advanced Surface Enhancement (INCASE) held in Singapore during 10–12 September 2019, which brings the experts from all these different disciplines under one umbrella and establishes a dialogue amongst the wider surface enhancement community. This confluence of academia and industry not only brings forth innovative ideas to address the challenges that the industry faces today but inspires future inventions as well.

Although the history of surface enhancement goes back several decades, it has seen rapid advances in the recent past. Practitioners and researchers belonging to different areas of this field will find these exciting developments comprehensively covered in this book. For physicists, it presents the state of the art in sensor development and integration of sensing devices with processing equipment to achieve more adaptive process control. For production engineers, it explores whether these developments can be harnessed for practical implementation to streamline their shop floor operations and make them more robust and effective.

Similarly, materials scientists will find it stimulating that the current paradigm where confirmation of process integrity is deemed to assure part quality is being challenged, and attempts to enable in-line and in-process microstructure analysis of surface-enhanced component are gaining momentum. This is a critical area of development where a strong collaboration between academic researchers and practising engineers can help to solve some long-standing problems. With more robust measurement methods in place, in future, we can not only expect improvement in quality but also gather critical data on materials properties that can help in realising closed-loop control of surface enhancement processes. This area

will also attract the interest of readers from modelling and simulation community who are working on developing predictive capabilities for materials processing.

Finally, as manufacturing moves towards higher automation and Industrie 4.0, questions are being asked on whether the surface enhancement community is prepared for this transformation. Considering the complexity of the process and the associated costs, will integrating sophisticated sensors, measurement devices, and IT infrastructure with processing equipment be practical on a large scale? Given the rapid pace at which manufacturing is changing, these questions are no longer exploratory and need to be included in strategic road maps. Focus on Industrie 4.0 being a unique feature of INCASE 2019, this book comprehensively addresses these questions by exploring potential technology gaps and the weaknesses and strengths of various alternative scenarios.

We firmly believe that this book will excite both new practitioners and experienced professionals alike. Given the comprehensive scope of this book, readers will gain a much broader perspective of how the field of surface enhancement is evolving, so that the community is better prepared to capture future opportunities and overcome near-term as well as long-term challenges that lie ahead of us.

June 2019

Sho Itoh
Shashwat Shukla

Organisation

Conference Chair

Alexander Korsunsky University of Oxford, UK

Organising Chair

Dennise Tanoko Ardi Advanced Remanufacturing and Technology Centre,
Singapore

Organising Committees

Alexander Korsunsky	University of Oxford, UK
Dennise Tanoko Ardi	Advanced Remanufacturing and Technology Centre, Singapore
Steven Baiker	Metal Finishing News, Switzerland
Michael Yap	Coventry University, UK
Sho Itoh	Advanced Remanufacturing and Technology Centre, Singapore
Shashwat Shukla	Advanced Remanufacturing and Technology Centre, Singapore
Ampara Aramcharoen	Advanced Remanufacturing and Technology Centre, Singapore
Chun Wai Kum	Advanced Remanufacturing and Technology Centre, Singapore
Shi Ying Chan	Advanced Remanufacturing and Technology Centre, Singapore

Technical Committees

Alexander Korsunsky	University of Oxford, UK
Michael Fitzpatrick	Coventry University, UK
Hitoshi Soyama	Tohoku University, Japan
Mario Guagliano	Politecnico di Milano, Italy
Chuan Hai Jiang	Shanghai Jiao Tong University, China
Lothar Wagner	Technische Universität Clausthal, Germany
David Butler	University of Strathclyde, UK
Hitoshi Omori	Institute of Physical and Chemical Research, Japan
Hirofumi Hidai	Chiba University, Japan
Minghui Hong	National University of Singapore, Singapore
John Hock Lye Pang	Nanyang Technological University, Singapore
King Ho Holden Li	Nanyang Technological University, Singapore
Seung Ki Moon	Nanyang Technological University, Singapore
Tegoeh Tjahjowidodo	Nanyang Technological University, Singapore
Shikun Zou	AVIC Beijing Aeronautical Manufacturing Technology Research Institute, China
Xu Song	Singapore Institute of Manufacturing Technology, Singapore
Chang Wei Kang	Institute of High Performance Computing, Singapore
Jacek Kaminski	Advanced Remanufacturing and Technology Centre, Singapore
Karsten Röttger	Ecoroll, Germany
Peter Beckmerhagen	Frohn, Germany
Yuji Kobayashi	Sintokogio, Japan
Michael Chen	Kunshan Carthing Precision, China
Janne Suoknuuti	Stresstech, Finland
Hali Diep	Boeing, USA
Domenico Furfari	Airbus, Germany
Thomas Haubold	Rolls-Royce, Germany
Wolfgang Hennig	Rolls-Royce, Germany
Waled Hassan	Rolls-Royce, Germany
Takashi Sato	IHI Corporation, Japan

Contents

Fatigue Life Enhancement

Optimization of Shot Peening for Titanium Alloys Ti 10-2-3 in CONDOR Project	3
Corentin Dides, Thomas Billot, and Nicolas Guillemot	
Mechanical Investigations on Composite Peened Aluminium	10
Michael Seitz and Kay André Weidenmann	
Influence of Wetblast Treatment on Fatigue Strength of Magnesium Alloy AZ31	19
Koichiro Nambu, Kenta Takashima, Isao Kumagai, and Masahiro Okumiya	
Process Model for Evaluating the Peen Velocity in Shot Peening Machine	26
Nguyen Van Bo, Ba Te, Augustine Teo, Kunal Ahluwalia, Ampara Aramcharoen, and Kang Chang Wei	
Experimental Study of Single Shot Process: Toward a Surface State Predictive Tool	36
Benjamin Levy, El Mansori Mohamed, Sabeur Mezghani, M. El Hadrouz, Julien Cabrero, and Anne-Laure Beaudonnet	
Microstructural Changes in Electroplated Chromium Coating–Substrate Interfaces Induced by Shot Peening	46
Yutaka Kameyama, Tatsuya Ohta, Keita Sasaki, Hideaki Sato, and Ryokichi Shimpo	
Investigation on Theoretical Analysis of Residual Stress Distribution Induced by Shot Peening in 2397 Aluminum-Lithium Alloy	56
Yukui Gao and Xuefei Tao	

Effect of Shakedown on the Fatigue Limit of Ultrasonic Shot Peened Steel	69
Jinta Arakawa, Yoshiichirou Hayashi, Hiroyuki Akebono, and Atsushi Sugeta	
Fundamentals and Applications of Cavitation Peening Comparing with Shot Peening and Laser Peening	76
Hitoshi Soyama	
Effect of Mechanical Properties on Fatigue Life Enhancement of Additive Manufactured Titanium Alloy Treated by Various Peening Methods	88
Yuya Okura, Hirotohi Sasaki, and Hitoshi Soyama	
Influence of Burnishing Process on Microstructure and Corrosion Properties of Mg Alloy AZ31	97
Chenyao Cao, Jiang Zhu, and Tomohisa Tanaka	
Effects of Machine Hammer Peened Surface Textures on the Tribological Behavior of Stamping Tools	108
Peter Sticht, Johannes Hohmann, and Peter Groche	
Mechanical Properties Enhancement of Additive Manufactured Ti-6Al-4V by Machine Hammer Peening	121
Leonor Neto, Stewart Williams, Jialuo Ding, Jan Hönnige, and Filomeno Martina	
An Automated Deposition Procedure for Cold Spray Additive Manufacturing Process Modeling Based on Finite Element Simulation	133
Sabeur Msolli, Zhi-Qian Zhang, Junyan Guo, Sridhar Narayanaswamy, Reddy Chilla Damodara, Zheng Zhang, Jisheng Pan, Boon Hee Tan, and Qizhong Loi	
Bonding Strength Improvement Through Numerical Simulation of Particle Impact Process During Metal Cold Spray	144
X. Song, X. Z. Jin, J. Everaerts, W. Y. Tan, W. Sun, I. Marinescu, W. Zhai, F. Li, E. J. Liu, and A. M. Korsunsky	
Product Verification and Material Characterisation	
Surface Texture Evaluation on Mirror Finish Surface Using Patterned Area Illumination Method	155
Shaowei Fu, Fang Cheng, and Tegoeh Tjahjowidodo	
Sliding Behavior of Secondary Phase SiC Embedded Alloyed Layer Doped Ti6Al4V Surfaces Ensuing Electro Discharge Machining	163
Jibin T. Philip, Deepak Kumar, Jose Mathew, and Basil Kuriachen	

Measurement of Residual Stresses on Deep Rolled Round Aluminum Samples Using Hole Drilling Strain Gage Method 173
 Mehmet Okan Görtan, Berkay Yüksel, and Bilsay Sümer

Mechanical Stress Relaxation of a Laser Peened and Shot Peened Ni-Based Superalloy 182
 Kai Siang Chin, Sridhar Idapalapati, Anna Paradowska, Mark Reid, Shashwat Shukla, and Dennise Tanoko Ardi

Incorporation of Evaluation Technology into Shot Peening Equipment 190
 Kan Aoki, Yuji Kobayashi, and Yoshiyasu Makino

Influence of the Feed Rate in the Single-Lip Deep Hole Drilling Process on the Surface Integrity of Steel Components 198
 Jan Nickel, Nikolas Baak, Frank Walther, and Dirk Biermann

Surface Finishing and Machining

Improvement of Chipping Phenomena for Crustaceous Materials Rounding by Centrifugal Barrel Finishing 215
 Hiroki Mizuno and Hiroaki Suesuga

In Situ Measurement of Granular Pressure and Velocity on Component Surfaces in Stream Finishing 226
 Sho Itoh, Jeremy Ho, Cary Turangan, and Stephen Wan

Development of Rheology and Computational Flow Model for Robotized External Finishing on Additively Manufactured Components 234
 Cary Kenny Turangan, Stephen Wan Yee Ming, Sho Itoh, and Jeremy Ho

Effects of Combined Wear Mechanisms in Internal Surface Finishing Using Controlled Hydrodynamic Cavitation Abrasive Finishing Process 244
 Arun Prasanth Nagalingam and Swee Hock Yeo

Surface Integrity Characteristics of NiTiHf High Temperature Shape Memory Alloys 254
 Yusuf Kaynak, Emre Tascioglu, and Othmane Benafan

The Effect of Finish-Milling Operation on Surface Quality and Wear Resistance of Inconel 625 Produced by Selective Laser Melting Additive Manufacturing 263
 Emre Tascioglu, Yusuf Kaynak, Özgür Poyraz, Akın Orhangül, and Soner Ören

Toolpath Generation for Robot Filletting	273
Srinivasan Lakshminarayanan, Omev Mohan Manyar, and Domenico Campolo	
Laser Processes	
Effect of Bubble Radius on Ability of Submerged Laser Peening	283
Hirotoshi Sasaki, Yuka Iga, and Hitoshi Soyama	
Crack Retardation of Damage Through Enhanced Crack Closure Effect Induced by Laser Peening	292
Yongxiang Hu and Han Cheng	
Application of Laser Peening for Cold Work Steel	298
Norihito Shibuya, Fumiaki Kumeno, Yuki Nakamura, and Ryo Yoshinouchi	
Influence of Laser Shock Peening (LSP) on the Material Properties of Additive Manufactured IN718	305
Ching Kiat Yong, Geoff D. West, Greg J. Gibbons, and Chow Cher Wong	
A Comparison of Surface and Sub-surface Features Induced by Shot Peening vs. Laser Peening on a Duplex Aged Beta Ti Alloy ...	314
S. Sudhagara Rajan, Geetha Manivasagam, Sathya Swaroop, and Nageswara Rao Muktinutalapati	
Effect of Laser-Induced Microstructure in Cavitation Erosion Performance of Martensitic Stainless Steel	321
Niroj Maharjan and Dennise Tanoko Ardi	
Effect of In-Situ Laser Remelting on the Microstructure of SS316L Fabricated by Micro Selective Laser Melting	330
Balasubramanian Nagarajan, Zhiheng Hu, Shubo Gao, Xu Song, Rui Huang, Matteo Seita, and Jun Wei	
Tailoring Surface Roughness of Micro Selective Laser Melted SS316L by In-Situ Laser Remelting	337
Zhiheng Hu, Balasubramanian Nagarajan, Xu Song, Rui Huang, Wei Zhai, and Jun Wei	
Surface Structuring of Multilayer Coated Cutting Tool Using Nd: YVO₄ Nanosecond Laser	344
Ahmed Alghamdi and Paul Mativenga	
Author Index	359

Fatigue Life Enhancement



Optimization of Shot Peening for Titanium Alloys Ti 10-2-3 in CONDOR Project

Corentin Dides¹(✉), Thomas Billot², and Nicolas Guillemot³

¹ IRT-M2P, 4 Rue Augustin Fresnel, 57000 Metz, France
corentin.dides@irt-m2p.fr

² Safran Landing Systems, 9 Rue Guynemer, 64400 Bidos, France

³ Airbus Helicopters, Aéroport International Marseille-Provence,
13725 Marignane, France

Abstract. CONDOR is an R&D project lead by IRT-M2P with different industrial partnership to increase knowledge and simulation models of shot peening. This surface hardening process aims to perform different shots with high velocity on metallic surfaces to introduce compressive stresses on it. Fatigue behavior of shot peened parts is significantly improved. During this research project a DOE has been carried out to optimize shot peening parameters on titanium alloys (surface roughness before shot peening, size and shot's hardness, covering and intensity). The DOE is composed by more than 300 fatigue specimens. All this data allows us to define specifically each shot peening parameter influence on shot peened parts efficiency. CONDOR project allows simulation development of models to simulate shot peening effect by taking into account the parameters introduced above. Those models are used to evaluate residual stress level and fatigue lifetime after shot peening and to confirm models readiness level. This study has defined optimized machining and shot peening conditions in order to increase parts fatigue lifetime.

Keywords: Shot peening · Ti 10-2-3 · Design of experiment · 4 point bending fatigue

1 Introduction

IRT M2P is a French institute of research and technology which is working on metallic materials and surfaces treatments. CONDOR project is a research and development project about shot peening. Different topics have been developed in this project; optimization of shot peening of Ti 10-2-3 alloys is one of them. Today, shot peening on titanium parts is similar to steel parts and it appears that shot peening in those conditions can lead to fatigue abatement. Very few studies are available on the impact of shot peening on fatigue life of near beta titanium alloys [1, 2]. In order to improve our understanding and to optimize shot peening of near Beta titanium alloys, a DOE has been performed with fatigue specimens (more than 300 four points fatigue bending specimens).

2 Material and Experiments

2.1 Material

The material used for this study is the Ti 10-2-3 which belongs to near beta alloys family [3].

2.2 Design of Experiments

There are many parameters in shot peening: Incidence angle, velocity, shots type, Almen intensity, coverage, projection type [2]. In addition, before shot peening, the finishing operation of machining can have an influence on final fatigue life [4], in particular roughness.

5 parameters have been chosen to define optimal conditions for shot peening and surface preparation. In order to reduce the number of tests, 3 fatigue tests levels have been defined and included as a parameters of the Matrix. The other parameters have been chosen because of industrial madders. DOE parameters are presented in Table 1.

Table 1. DOE parameters

Roughness after machining (R_a , μm)	Stress level	Shot Hardness (HRC)	Diameter (μm)	Intensity (A)	Coverage (%)
0.8	Level 1	–	–	–	–
1.6	Level 2	+	+	+	+
3.2	Level 3				

In these conditions, the DOE has 144 combinations. Considering tests' repetition to evaluate the scattering and also the additional specimens to characterize the microstructure, the amount of tests was too huge and needed to be reduced.

To do so, D-optimal methods have been used to optimize the DOE leading to a reduce plan of 325 testes.

2.3 Specimens Preparation and Testing Conditions

The specimens' geometry used for the four-points bending fatigue tests is presented on Fig. 1. Both side of specimens have been shot peened in industrial Wheelabrator machine using nozzles on a 6 axes robot. Shot peening was performed with 85° angle from the surface with a longitudinal direction displacement.

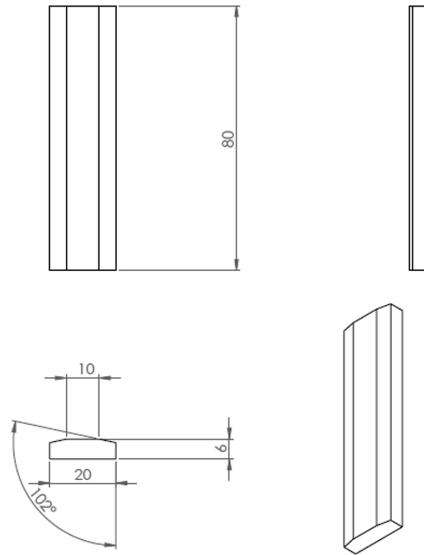


Fig. 1. Specimens shape

To start with similar microstructure, all specimens have been picked-up at mid radius of a billet. Face A corresponds to the face close to mid radius (see Fig. 2). The three roughness specified in the DOE $Ra = 0.8/1.6/3.2$ are related to different machining conditions.

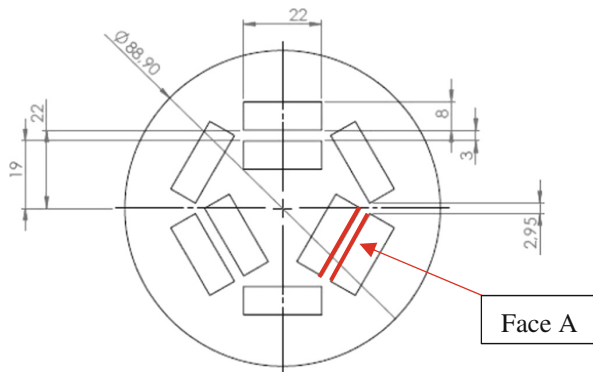


Fig. 2. Cut plan for 4 points bending fatigue

All fatigue tests have been performed with the following conditions:

- Ratio: $R = 0.1$
- Controlled in maximum stress level
- Frequency: 10 Hz

Results analysis has been performed with Minitab software.

3 Results

Prior to shot peening test plan, several fatigue tests were launched on specimens before shot peening with different surface roughness to establish the reference. These results are plotted in Fig. 3.

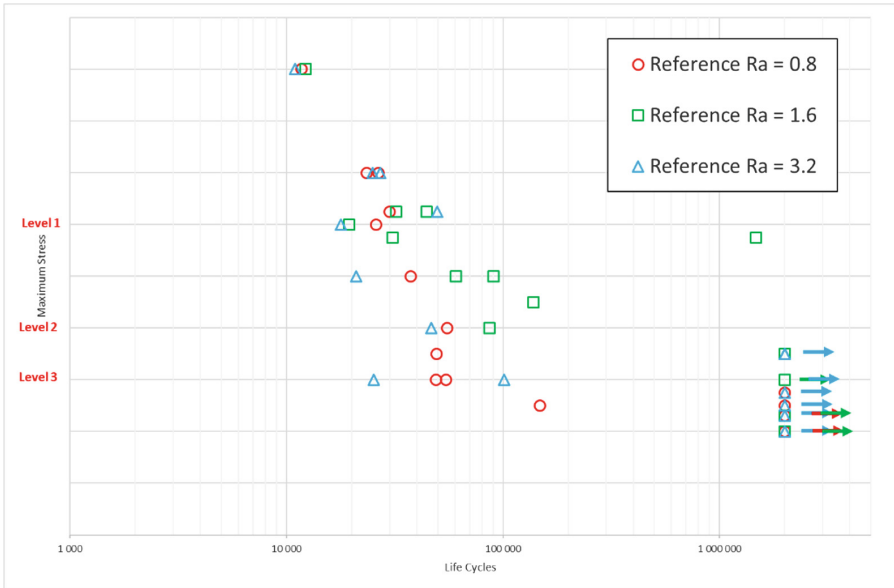


Fig. 3. Wöhler curve of Ti 10-2-3 with three different surface roughness

It can be seen that surface roughness doesn't seem to have significant effect on lifetime. Close to the endurance scattering is more important and the impact of roughness is difficult to quantify. The three stress levels used for the DOE have been defined according to the reference testes in order to represent different parts of the Wöhler curve. Stress level close to endurance is avoided to present too much non-failed specimens, which couldn't be used for the analysis.

Pareto diagram has been used to evaluate the relative impact of each of parameter, or combination of parameters, on fatigue life (Fig. 4).

This analysis shows that the parameters, or combination of parameters, which present normalized effect above 1.981 have a significant impact on fatigue life. If it turns out that surface roughness before shot peening has very low impact on fatigue, shot parameters (diameter and hardness) and Almen intensity have much more influence on fatigue life.

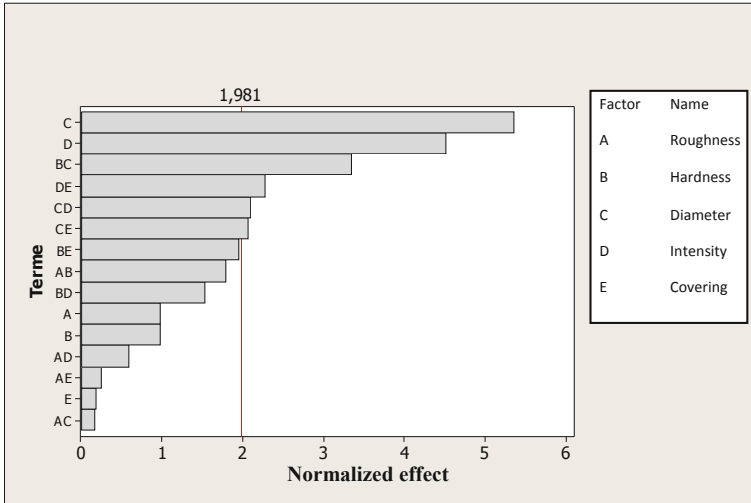


Fig. 4. Pareto diagram of normalized effect

In addition to Pareto analysis, the graphic of major effects represents the evolution of fatigue life with regard to parameters “low-high” limits (Fig. 5).

Size has a very important impact on fatigue enhancement, shots with large diameter have a beneficial effect on fatigue life time. In contrast, the intensity has to be reduce to

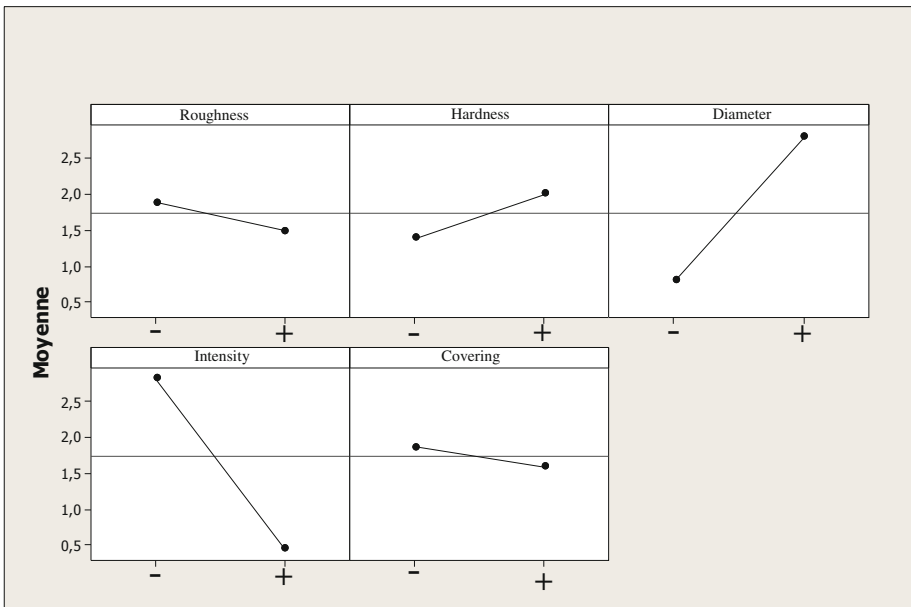


Fig. 5. Graphic of major effects on fatigue life time enhancement

improve fatigue life. As it can be seen above on Pareto diagram Covering and Roughness before shot peening doesn't have strong effect on the results observed. If Shot hardness is considering alone, it has just a few effect.

Pareto diagram shows that combinations of parameters can also have a strong impact on final results. Figure 6 is the diagram of interaction between the different parameters.

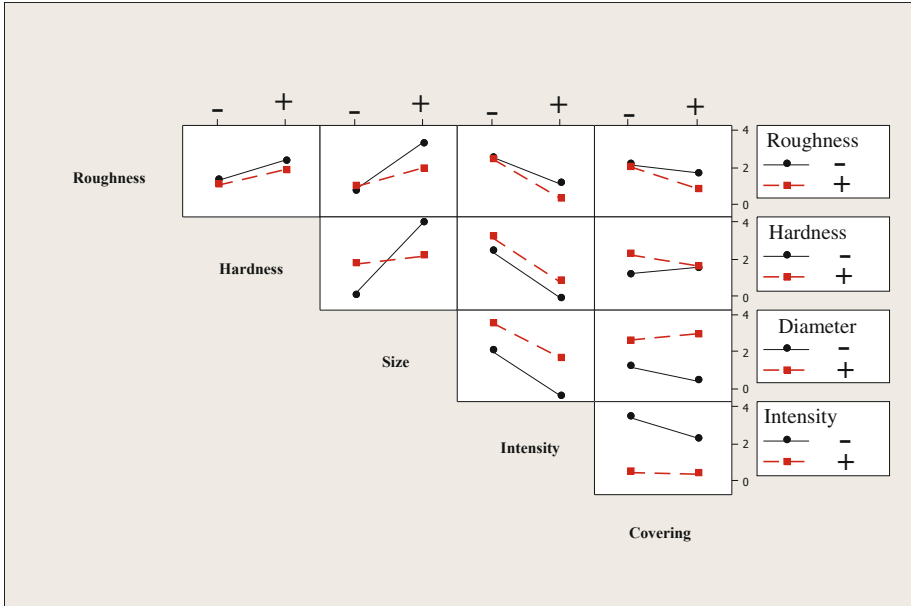


Fig. 6. Diagram of parameters interactions regarding fatigue lifetime

First observation shows that except for hardness and shots size, for each combinations, curves do not cross each other. Whatever the parameter combined with the intensity, lower value provides the best response. As for intensity, diameter seems to be more efficient with large diameters for each combination. Only the hardness is strongly affected by the diameter. Combine low hardness and high diameter shots seems to have a positive impact. Combination of covering with roughness and hardness has no impact on results. Otherwise, covering has an effect with low intensity and it seems damaging to use a too important amount of covering.

4 Conclusion

Ti 10-2-3 titanium can't be easily shot peened like most of steel. Shot peening parameters have to be chosen very carefully.

Regarding the results, a low intensity with high diameter shots seems to have the best effects on fatigue behaviour. These results can be explained by the high sensitivity

of titanium to the surface integrity (roughness, residual stresses & hardening). In addition, a low Almen intensity can introduce enough residual stress without decreasing significantly the surface roughness. Experiment results with high shots size are in the same way because the more shot diameter is high, the more surface roughness is homogenous and covering is quick. More than that, using high diameter shots can reduce creation of defect on the surface.

Covering has an impact on fatigue results only for a low intensity. This observation seems to explain that high intensities seems to generate high roughness which has a more important impact on fatigue than compressive residual stresses. Besides, a too important covering downgrade the roughness and fatigue behaviour in the same way. This conclusion is consistent with some studies in the literature on fatigue behaviour of titanium parts [5].

Because some measurements haven't been performed yet, roughness and residual stress answers are not presented in this paper but will be added in the presentation. It will allow to understand all fatigue answers and competition between roughness and residual stress on titanium alloys.

References

1. Unal, O., Cahit Karaoglanı, A., Varol, R., Kobayashi, A.: Microstructure evolution and mechanical behavior of severe shot peened commercially pure titanium. *Vacuum* **110**, 202–206 (2014)
2. Fuhr, J.P., Basha, M., Wollmann, M., Wagner, L.: Coverage and peening angle effects in shot peening on HCF performance of Ti-6Al-4V. *Procedia Eng.* **213**, 682–690 (2018)
3. Deleuze, C., Barrallier, L., Fabre, A., Esberard, C.: 19^{ème} Congrès Français de Mécanique, 24–28 août Marseille: Etude de la microstructure d'un alliage de titane biphasé de nuance Ti-10 V-2Fe-3Al et de son influence sur l'élargissement des pics de diffraction (2009)
4. Cox, A., Herbert, S., Villain-Chastre, J.-P., Turner, S., Jackson, M.: The effect of machining and induces surface deformation on the fatigue performance of a high strength metastable Beta titanium alloy. *Int. J. Fatigue* **124**, 26–33 (2019)
5. Yao, C., Wu, D., Ma, L., Tan, L., Zhou, Z., Zhang, J.: Surface integrity evolution and fatigue evaluation after milling mod shot-peening and polishing mode for TB6 titanium alloy. *Appl. Surf. Sci.* **387**, 1257–1264 (2016)



Mechanical Investigations on Composite Peened Aluminium

Michael Seitz¹(✉) and Kay André Weidenmann²

¹ Karlsruhe Institute of Technology (KIT) Institute of Applied Materials (IAM-WK), Kaiserstr. 12, 76131 Karlsruhe, Germany

Michael.Seitz@kit.edu

² Institute of Materials Resource Management, Augsburg University, Werner-von-Siemens-Straße 6, 86159 Augsburg, Germany

Abstract. Composite peening describes a novel approach based on the micro peening process. By composite peening, particles can be introduced into near-surface regions of metallic base materials. The proportion of the reinforcement phase decreases gradually with increasing distance to the surface. These so-called Functionally Graded Metal Matrix Composites (FGMMC) are characterised by a multitude of different characteristics, such as material combination, particle density, particle gradient and particle size, and a resulting broad range of properties. The composite material produced by this method promises a high application potential for lightweight, wear resistant and cyclically stressed structural components.

EN AW-1050 was selected as matrix material and alumina as abrasive respectively reinforcement material. Additional abrasives such as silicon carbide and tungsten carbide were also investigated. By varying the process parameters, such as temperature and pressure, the influence on the particle density and the particle gradient was evaluated. Penetration depths up to 30 μm could be observed at high homologous temperatures. The peening process might cause open structures near the surface, the sample were subsequently deep rolled. In addition, this process reduces the surface roughness.

Ensuing mechanical characterisation focused on bending tests. An increase in the flexural strength of the composite material compared to the base material could be observed.

Keywords: Composite peening · Metal matrix composites · Mechanical properties

1 Introduction

Metal matrix composites (MMCs) are characterised by increased specific properties compared to monolithic metals. Due to their low thermal expansion and increased creep resistance, MMCs promise superior properties even at elevated temperatures. Further applications are also conceivable in the field of fatigue and tribology. Since the highest loads often occur locally in a component, the material efficiency can be improved by reinforcing the surface layer. These so-called functionally graded metal matrix

composites (FGMMCs) have a large number of possible modifications (for instance, material combination, particle density, particle gradient) and resulting properties.

The range of manufacturing possibilities for graded MMCs is large. Therefore, a distinction is made between constitutive, homogenizing and segregating processes [1]. All processes are united by a high degree of complexity in terms of processing. In the best case, subsequent changes are associated with a huge additional effort. Exceptions are coating processes such as laser beam dispersing [2] and cold spraying [3, 4].

Shot peening is used as a standard mechanical surface treatment process. At the beginning of the 1990s, micro peening developed from conventional shot peening with significantly smaller blasting particles [5]. Compared to conventional shot peening, a lower roughness and an increased fatigue strength are achieved [6, 7].

Ando et al. has shown that it is also possible to implement blasting particles into the surface of the target material by micro peening [8]. As a result, the micro hardness could be increased. By heating the target material to high homologous temperatures, it is possible to get the blasting media much deeper into the base material, as the authors have shown with aluminium and tin [9, 10].

2 Experimental

2.1 Materials

In this study, the aluminium alloy EN AW-1050 is selected as the matrix material. The chemical composition of the alloy is listed in Table 1.

Table 1. Chemical composition of EN AW-1050

	Al	Si	Fe	Cu	Mn	Mg	Ti	Zn
EN AW-1050	99.52	0.10	0.30	<0.01	<0.01	<0.01	0.02	<0.01

Alumina, silicon carbide and tungsten carbide are selected as blasting and reinforcement material. The grain size of the blasting material is F600, which is equivalent to a weight-averaged particle size distribution of $9.0 \mu\text{m} \pm 1.0 \mu\text{m}$. However, measurements with a particle size analyser shows an average particle size of $7.94 \mu\text{m}$, $11.86 \mu\text{m}$ and $21.9 \mu\text{m}$ for alumina, silicon carbide and tungsten carbide respectively.

The hardness of alumina is 2100 HK according to the manufacturer's specifications. Young's modulus of the ceramic is approximately 400 GPa for a given purity of over 99.5% [11].

2.2 Experimental Setup

Composite Peening. The composite peening process is shown in Fig. 1. The peening process is carried out with the abrasive blasting system AccuFlo from Comco Inc., which is charged with the blasting material. The peening unit transports the blasting material with compressed air to the blasting nozzle. Preliminary studies with tin and

aluminium as matrix material showed that high homologous temperatures favour particle entry [9, 10]. For this reason, a heating device was added to the micro peening system. The temperature of the heating device is monitored by a control unit. The control unit also regulates the position and speed of the blasting nozzle. Tests are operated by ProNc software from ISEL.

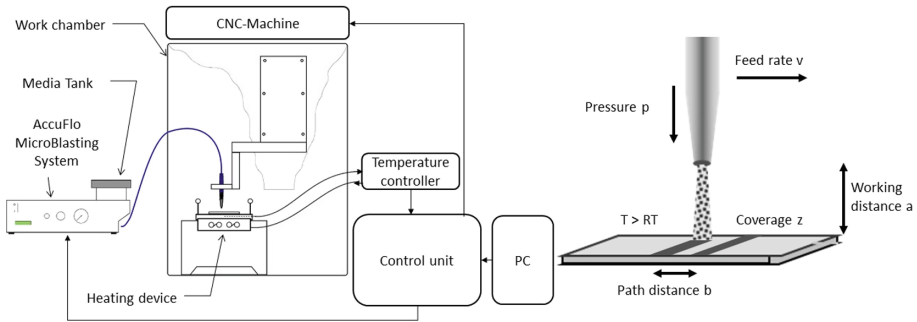


Fig. 1. Scheme of the composite peening system and process (left [10]). Selectable process parameters (right [9]).

Composite peening offers a wide range of process parameters. In addition to the control variables shown in Fig. 1 (right), the nozzle geometry and the angle of the blasting nozzle can be varied. In this work, the process-structure-property relationships of the composite peening process are investigated by varying the temperature, the blasting pressure and the number of operations. The blasting nozzle has a diameter of 0.7 mm and is orientated orthogonally to the sample surface. The working distance of the blasting nozzle is 10 mm. Peening is performed at a speed of 8 mm/s and a distance between the paths of 1 mm. Table 2 lists the investigated process parameters.

Table 2. Process parameters for composite peening

Temperature T (T/Ts)	Number of operation (-)	Pressure p (bar)
0.80; 0.90; 0.95	2; 4	4; 7

Determination of Penetration Depth. The evaluation of the penetration depth is investigated by means of light microscopy and SEM with subsequent evaluation via digital image processing (DIP). The surface roughness is determined using the μ surf confocal microscope by NanoFocus AG. The results are subsequently smoothed with a Gaussian filter of 0.8 mm.

Mechanical Characterisation. Four-point bending tests are performed on an Instron E3000 ElectropulsTM (load cell 5 kN) according to ASTM D7264, procedure B. Crosshead speed is set to 10 mm/min. The deflection of specimens is measured via

laser triangulation. Force and deflection data are recorded at 40 Hz. The rectangular samples have a width of 5 mm, a thickness of 2 mm and a 40 mm support span. The distance between the loading fins is 20 mm.

Three samples per parameter are tested. The flexural modulus and R_{p02} are determined, the former in a range of $\varepsilon_f = 0.025 - 0.075\%$.

3 Results

3.1 Microstructure

The penetration behaviour of different blasting medias is shown in cross sections in Fig. 2. The process parameters in each case are: $T/T_s = 0.9$, $p = 7$ bar, $z = 10$. The roughness of all surfaces is enhanced by composite peening.

The blasting medium in Fig. 2(a) is Al_2O_3 , which is dimpled in the surface layer of the peened sample after composite peening. In addition, porous areas are seen just below the surface. Single particle cannot be identified in the cross section. The penetration depth of SiC is significantly lower, as can be seen in Fig. 2(b). Only a thin layer of ceramic particles covers the surface. During the process, light is emitted due to triboluminescence. In the case of WC, individual ceramic particles can be seen. However, these particles are significantly smaller compared to the initial state (Fig. 2(c)). Similar to Al_2O_3 , the particles are concentrated in individual areas. In addition, pores are apparent between particles and matrix.

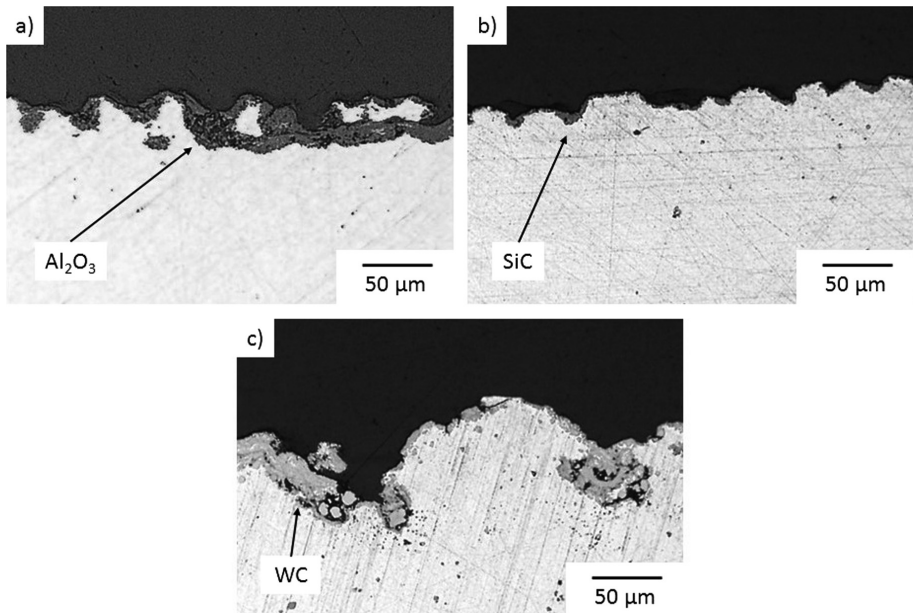


Fig. 2. Surface layer after composite peening with different blasting material. (a) Al_2O_3 , (b) SiC, (c) WC.

3.2 Surface Roughness

Figure 3 shows the surface roughness after processing with various parameters. The surface roughness is increased by composite peening, as can be seen on the left side [10]. Compared to the initial state ($R_z = 7.0 \mu\text{m}$), the roughness rises with higher coverage and pressure. The influence of the temperature is negligible. A maximum roughness of $18 \mu\text{m}$ can be measured at a pressure of 7 bar, a process temperature of $T/T_s = 0.9$ and a fourfold coverage. The results in the right figure show the roughness of the samples after composite peening and subsequent deep rolling. The roughness is considerably reduced by deep rolling in comparison to the composite peened conditions. Thus, a roughness is reached below the initial state. The most relevant influence on the roughness after deep rolling is the process temperature. Lowering the process temperature causes a roughness of $2 \mu\text{m}$ to $4 \mu\text{m}$. In this case, pressure and coverage do not influence the roughness.

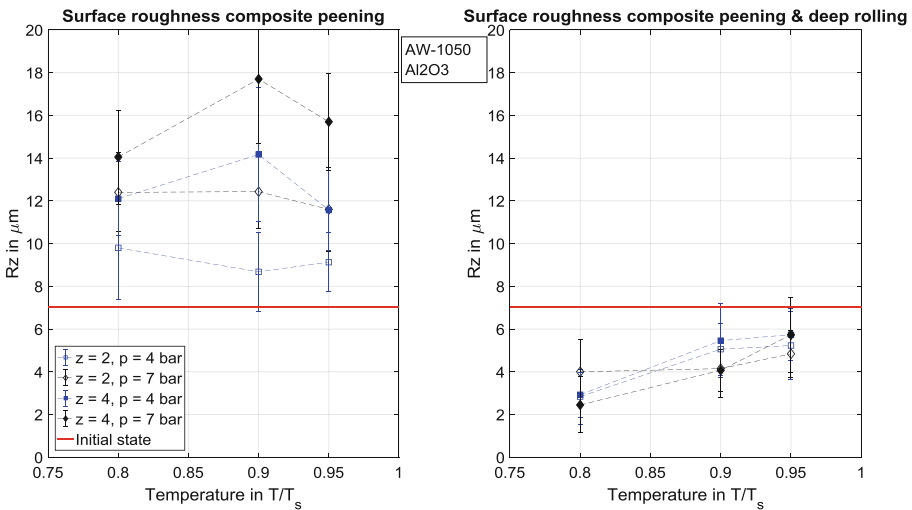


Fig. 3. Roughness R_z after composite peening (left, [10]) and composite peening with subsequent deep rolling (right).

3.3 Penetration Depth

Since the reinforcement phase is concentrated into clusters, it is difficult to determine the influence of the process parameters by the maximum penetration depth. For this reason, Fig. 4. shows the distance to the surface with a percentage of reinforcement of 10%.

Coverage and process temperature have the most prominent effect on the penetration depth of the alumina particles. For instance, at high process temperature of $T/T_s = 0.95$, the penetration depth can be increased by more than $10 \mu\text{m}$ with a fourfold coverage. The pressure has an inferior effect on the penetration depth. A minor increase was observed only in the case with a double coverage.

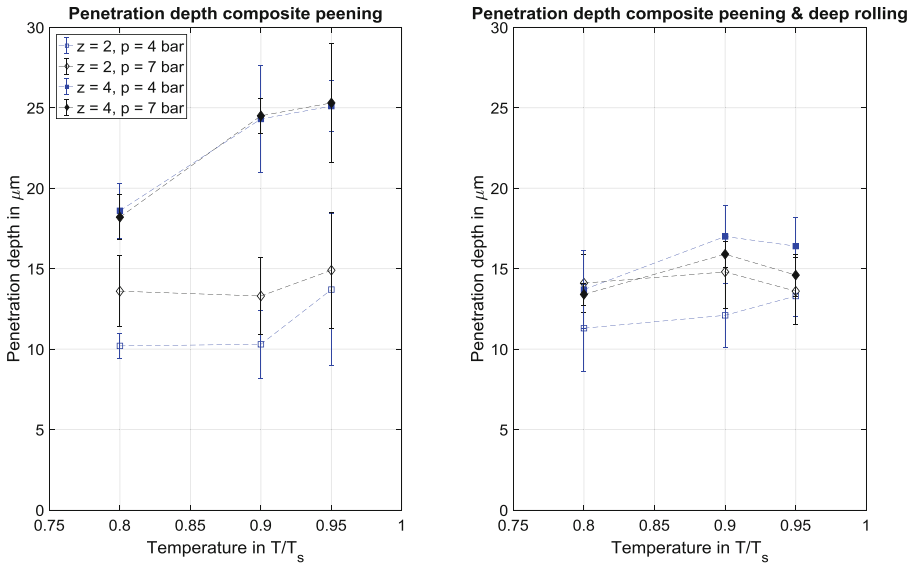


Fig. 4. Penetration depth with a 10% reinforcement ratio after composite peening (left, [10]) and composite peening with subsequent deep rolling (right).

By subsequent deep rolling, the penetration depth is reduced for almost all process parameters. In particular, the penetration depth decreases about $10 \mu\text{m}$ with fourfold coverage. In contrast, no significant effect of the penetration depth can be observed with a twofold coverage.

3.4 Mechanical Properties

Figure 5 shows the mechanical properties of the composite peened and deep rolled specimens (left: flexural modulus, right: yield strength) from the bending test. No correlation can be observed between the flexural modulus and the process parameters respectively the penetration depth. All values of the flexural modulus range from 67.3 GPa to 73.3 GPa, with almost all standard deviations overlapping.

The yield strength, in contrast, can be increased by a higher process temperature, as shown in the figure on the right. On average, an increase from 107.1 MPa to 113.5 MPa was recorded. Pressure and coverage have no significant impact.

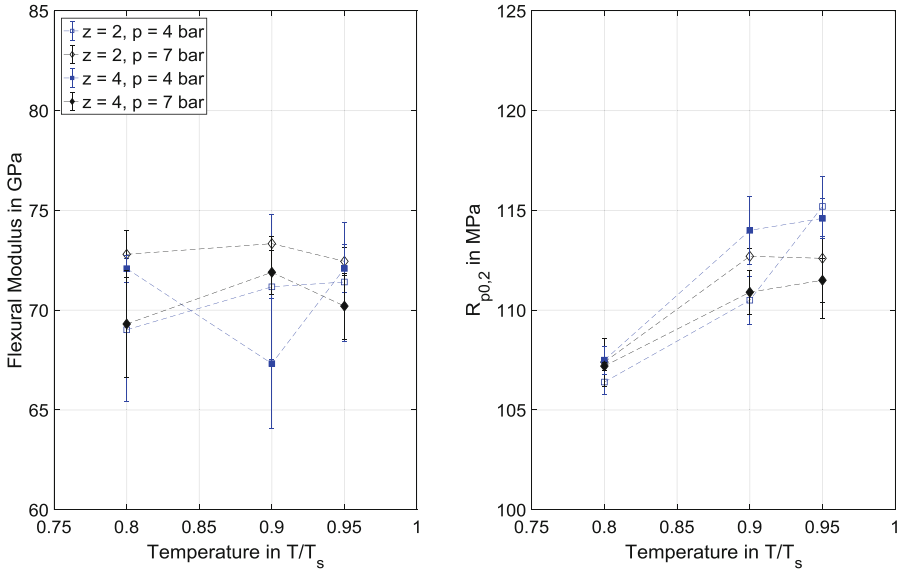


Fig. 5. Mechanical properties of the composite peened samples. Flexural modulus left and R_{p02} right.

4 Discussion

In previous studies the feasibility of introducing alumina particles into an aluminium matrix was demonstrated by composite peening at high homologous temperatures. The roughness of the composite peened surface results from the number of treatments and the peening pressure. The penetration depth is significantly influenced by the process temperature and the coverage.

By subsequent deep rolling, the roughness and the penetration depth, is reduced. There may be two different reasons for this. On the one hand, the pores and cracks that appear after composite peening are closed and on the other hand the surface is compacted and smoothed. Figures 3 and 4 indicate that a high roughness has the most significant impact on the penetration depth after subsequent deep rolling.

An enhancement in flexural modulus due to an increased penetration depth cannot be achieved. Despite the fact that alumina has a significantly higher modulus than aluminium, the thickness of the graded, reinforcing layer ($60 \mu\text{m}$) is too low compared to the thickness of the base material aluminium ($2000 \mu\text{m}$). A slight improvement in the yield strength with increasing penetration depth is observed.

The penetration characteristics of different blast media differs considerably. While Al_2O_3 reaches penetration depths of $30 \mu\text{m}$ in a heated aluminium matrix, only erosion can be observed with SiC as blasting medium. Accordingly, the penetration depth is significant lower. WC , on the other hand, penetrates much deeper compared to the other blasting media. This is probably due to the higher density and the resulting higher kinetic energy of the blasting particles. As already described in [9, 10], the reinforcing

particles in the metal matrix of all blasting media are significantly smaller than the starting material. This can be attributed to the impact of subsequently peened particles.

5 Conclusions

The following conclusions can be drawn from the above mentioned studies:

- Ceramic blasting media (Al_2O_3 and WC) can be introduced into the matrix material by composite peening. The maximum penetration depth in the case of Al_2O_3 amounts to 30 μm . SiC cannot be introduced into the aluminium matrix.
- By subsequent deep rolling the roughness can be significantly reduced. Deep rolling also serves as a compaction of the composite peened surface. This reduces the penetration depth measured optically.
- An increase in flexural modulus cannot be observed. The yield strength is increased by a higher process temperature and corresponding deeper penetration depth.

The process-structure-property-relationship for composite peened AW 1050 are shown in this paper. Future research will focus on fragmentation mechanisms of the blasting media as well as further material systems.

Acknowledgements. The authors would like to thank the German Research Foundation (DFG) for the financial support of within the project WE4273/15-1.

References

1. Kieback, B., Neubrand, A., Riedel, H.: Processing techniques for functionally graded materials. *Mater. Sci. Eng., A* **362**, 81–106 (2003)
2. Foroozmehr, E., Sarrafi, R., Hamid, S., Kovacevic, R.: Synthesizing of functionally graded surface composites by laser powder deposition process for slurry erosion applications. *Laser* **340**, 446–453 (2009)
3. Gutzmann, H., Fresse, S., Gärtner, F., Klassen, T.: Cold Gas Spraying of ceramics using the example of titanium dioxide. In: DVS Media GmbH (eds.) ITSC 2011: International Thermal Spray Conference & Exposition, p. 391. DVS Media, Düsseldorf (2011)
4. Ozdemir, I., Ogawa, K., Sato, K., Seo, D.: Iron boride coatings produced by cold spray processes. In: DVS Media GmbH (eds.) ITSC 2011: International Thermal Spray Conference & Exposition, p. 1096. DVS Media, Düsseldorf (2011)
5. Kagaya, C., Yamada, Y.: Fine particle bombarding technology and functional development of metal surface. In: The 10th International Conference on Shot Peening procedure, pp. 191–196 (2008)
6. Weingärtner, R., Hoffmeister, J., Schule, V.: Mechanische Oberflächenbearbeitung durch das Mikrostrahlen. *J. Heat Treat. Mater.* **70**(2), 59–65 (2015)
7. Kennedy, D.M., Vahey, J., Hanney, D.: Micro shot blasting of machine tools for improving surface finish and reducing cutting forces in manufacturing. *Mater. Des.* **26**(3), 203–208 (2005)
8. Ando, M., Kitano, H., Usami, H., Endo, T.: Applicability of fine particle peening on surface modification of aluminum alloy. In: The 10th International Conference on Shot Peening procedure, pp. 223–227 (2008)

9. Seitz, M., Reeb, A., Klumpp, A., Weidenmann, K.A.: Composite peening-a novel processing technology for graded reinforced aluminium matrix composites. *Key Eng. Mater.* **742**, 137–144 (2017)
10. Seitz, M., Weidenmann, K.A.: Influence of the process parameters on the penetration depth of the reinforcing phase during composite peening for the production of functionally graded metal matrix composites. *Key Eng. Mater.* **809**, 73–78 (2019)
11. Auerkari, P.: Mechanical and physical properties of engineering alumina ceramics, pp. 6–24. Technical Research Centre of Finland, Espoo (1996)



Influence of Wetblast Treatment on Fatigue Strength of Magnesium Alloy AZ31

Koichiro Nambu¹✉, Kenta Takashima¹, Isao Kumagai²,
and Masahiro Okumiya¹

¹ Toyota Technological Institute,
2-12-1 Hisakata Tenpaku-ku, Nagoya, Aichi, Japan
knambu@toyota-ti.ac.jp

² Maccho Co., Ltd., 525 Kanawa, Isurugi-machi, Nagaoka, Niigata, Japan

Abstract. From the viewpoint of weight reduction in transportation equipment such as automobiles, the use of light metals is being promoted. Magnesium alloy is the lightest in practical metals, but it has the property that its strength is low. For improvement of fatigue strength, surface modification treatment such as shot peening is generally applied. Since the magnesium alloy has high reactivity with oxygen and may ignite, surface treatment in a dry environment like shot peening is difficult. In this study, we focused on wet blasting process with low probability of ignition and examined the influence of it on fatigue strength. The fatigue strength of wet blasting AZ31 showed higher results than untreated material. As this factor, improvement of hardness near the surface and application of compressive residual stress are conceivable. Also, the particles used in the wet blasting process are smaller than the particles used in the general shot peening process. Therefore, the fact that the surface roughness did not change significantly was also considered to be one factor. From the above results, we clarified that the wet blasting treatment can safely improve the fatigue strength of the magnesium alloy.

Keywords: Fatigue strength · AZ31 · Wet blasting · Shot peening

1 Introduction

In order to reduce the weight of automobiles and the like from the viewpoint of global environmental problems, alternatives to steel materials are required. Magnesium alloy is one of the alternative materials. Magnesium alloy is the lightest metal material, but its strength is low and it has not been put to practical use as an alternative material. Surface modification treatment is an effective means to increase the strength of metallic materials [1]. There are two types of surface modification treatment: heat treatment type such as carburizing and non-heat treatment type such as shot peening [2–9]. However, because the melting point of magnesium alloys is low, it is difficult to perform heat treatment type surface modification treatment involving other elements. Furthermore, in the case of shot peening treatment, wear dust is generated due to particle collision. Since the magnesium alloy is highly reactive, wear powder may burn. From these viewpoints, we focused on blasting as a new surface modification method.

Wet blasting is a method to obtain the surface modification effect by colliding fine particles on the substrate surface as well as shot peening. Water is used as a medium to fly particles, unlike the conventional treatment method. Therefore, there is no risk of dust explosion, and a wide nozzle can be used to process a large area. Please note that the first paragraph of a section or subsection is not indented. In this study, we use wet blasting as a surface modification method for magnesium alloy AZ31, and aim to clarify its influence on fatigue strength.

2 Experimental Method

Magnesium alloy AZ31 was used as a test material. The chemical composition of the material is shown in Table 1. The test pieces were machined into the shape shown in Fig. 1. In order to remove the stress generated during specimen processing, annealing was performed at 520 °C for 1 h in an argon atmosphere. Ceramic beads mainly composed of zirconia were used for wet blasting. The composition, hardness and particle size of the particles are shown in Table 2. Wet blasting was performed at a blast pressure of 0.2 MPa and 0.3 MPa, with a treatment time of 180 s. Wet blasting can be performed for a long time than conventional shot peening. In the case of shot peening, the material softens due to the generation of heat due to the long processing time. On the other hand, wet blasting does not generate heat and can be processed for a long time. However, long-time processing may cause surface erosion. So, in this research, in order to prevent the occurrence of erosion, treatment is performed at low pressure. The treated specimens in this study were performed hardness measurement. Hardness measurement was performed using a micro Vickers hardness measurement device. The residual stress was measured using the $\text{Sin}^2 \psi$ method using V α . stylus-type surface roughness meter was used to measure the surface roughness. A rotating bending fatigue tester was used for the fatigue test. In addition, observation of crystal grains was performed using SEM-EBSD method.

Table 1. Chemical compositions

Al	Zn	Mn	Si	Fe	Cu	Mg
2.98	0.93	0.3768	0.0125	0.0013	0.0013	Bal.

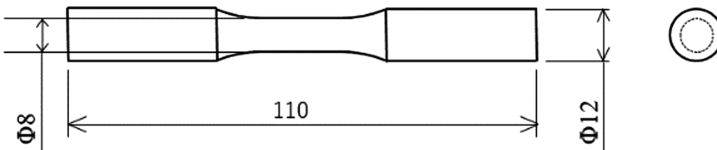


Fig. 1. Schematic view of the specimens

Table 2. Particle characteristics

Compositions	ZrO ₂	60 ~ 70%
	SiO ₂	28 ~ 33%
	Al ₂ O ₃	~ 10%
Vickers hardness		650 ~ 800 HV
Diameter		~ 63 μm

3 Result and Discussion

3.1 Experimental Result

The hardness measurement results are shown in Fig. 2. From the figure, it can be seen that the hardness of the wet blasting material is improved compared to the untreated material. The hardness increased by about 35% at the maximum. The depth of influence is about 60 μm. Next, comparing the projection pressure, it can be seen that the maximum hardness is higher when the treatment is performed at 0.3 MPa. This is considered to be due to the fact that the particle collision speed is fast, as in the conventional shot peening process. The effect depth of the wet blast is the same as the particle size, while the effect layer of hardness is shallower than the particle size in the usual shot peening treatment. It is necessary to examine the factor which such a difference appeared.

The surface roughness measurement results are shown in Table 3. From the table, it can be seen that the surface roughness increases with the increase of the projection pressure.

The residual stress measurement results are shown in Fig. 3. As can be seen from the figure, compressive residual stress is generated by wet blasting. Also, as with the conventional shot peening process, the higher the projection pressure, the larger the residual stress that is generated.

Next, Fig. 4 shows the fatigue test results. It can be seen from the figure that the fatigue limit of the wet-blasted material shows the same value as that of the untreated material. Focusing on the temporal strength, it can be seen that it is higher than the untreated material. From these results, wet blasting is considered to be effective for improving the fatigue strength on the high stress side. In addition, it is pointed out that fatigue strength reduction due to surface roughness appears notably in magnesium alloys compared to steel materials etc. [10]. From this, the influence of surface roughness can be considered as a factor that the fatigue limit did not improve.

From these results, it is thought that the wet blasting treatment is effective for the improvement of the fatigue strength because the hardness and the compressive residual stress were improved as in the conventional shot peening treatment.

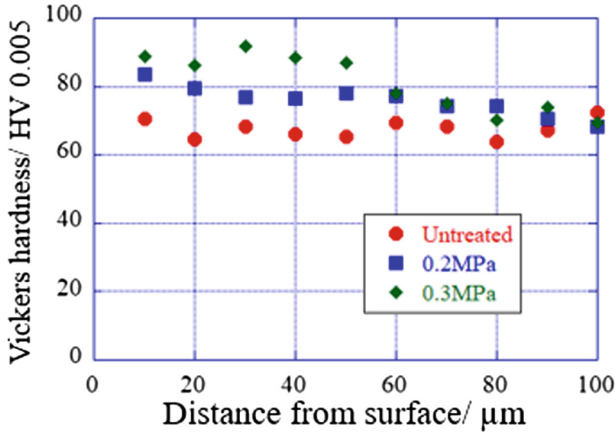


Fig. 2. Hardness distribution

Table 3. Arithmetic mean roughness Ra (μm)

Untreated	0.2 MPa	0.3 MPa
0.619	0.864	1.038

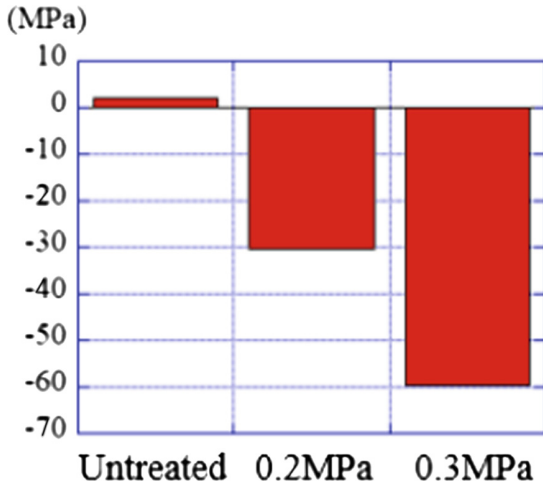


Fig. 3. Result of surface residual stress measurement

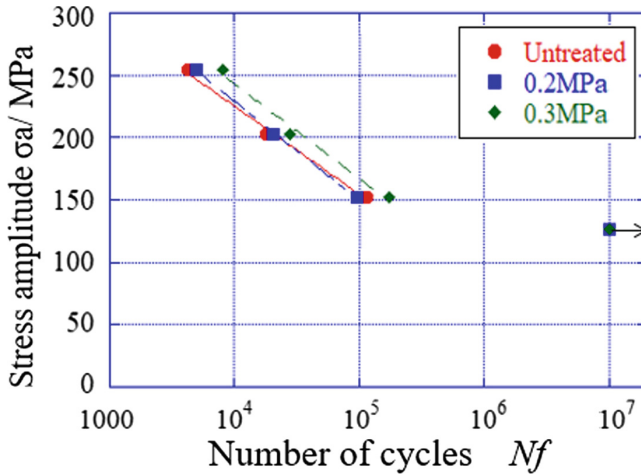


Fig. 4. Result of fatigue experiment

3.2 Grain Measurement by EBSD (Electron Backscatter Diffraction)

Magnesium alloys are characterized by having a hexagonal close-packed crystal structure and thus resisting plastic deformation. It is also known that twins occur during plastic deformation due to the small number of sliding surfaces. From these viewpoints, the influence of wet blasting on the crystal was examined. IPF (inverse pole figure) map near the surface is shown in Fig. 5. This figure shows the crystal orientation in the plane normal to the extrusion direction. It can be seen from the figure that there are few crystal grains facing the $\{0001\}$ plane in the entire analysis range of the untreated and treated materials. This is considered to be due to the formation of a strong texture due to the crystals being arranged so that the c-axis faces the center of the round bar sample by extrusion. The same results were obtained for all the specimens, which indicates that there was no dissolution of the texture in the wet blasting treatment. In addition to this, nanocrystals may be observed in the vicinity of the surface after the conventional shot peening treatment, but such a structure was not observed. Furthermore, twins generated during plastic deformation were not observed under this condition. From these results, it is considered that large strain that twins and nanocrystals are generated does not occur in wet blasting.

Next, in order to clarify the factor that the hardness improved without twin deformation, the strain in the grain was evaluated. GOS (Grain Orientation Spread) map showing the magnitude of strain in the crystal is shown in Fig. 6. This figure shows that the dark blue indicates no strain, and the strain increases as it becomes red. From the figure, it can be seen that in the case of untreated materials, almost no strain occurs due to the effect of annealing. On the other hand, it can be seen that the strain is increased in the wet blasting material. In addition, it can be seen that the strain is larger at 0.3 MPa when compared with the projection pressure. From this result, it is considered that the reason for the improvement in hardness is that the strain in the grain near the surface increased by the wet blasting treatment.

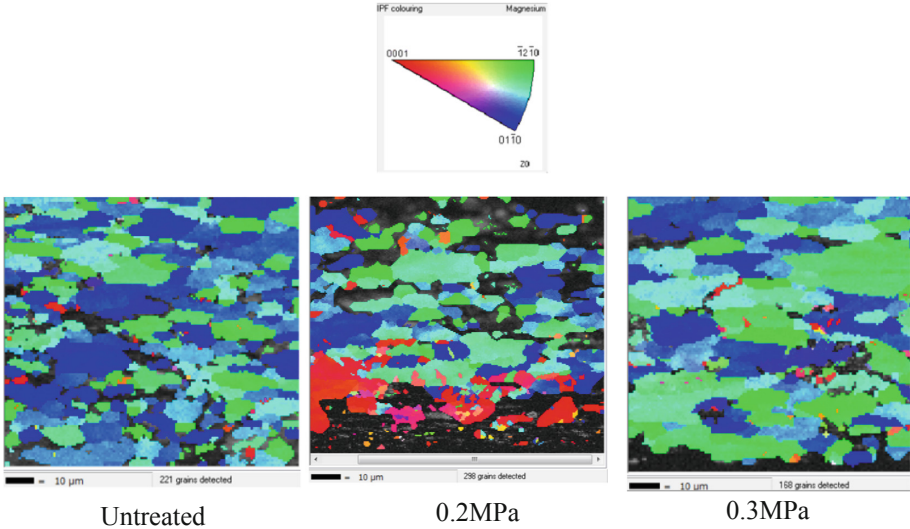


Fig. 5. IPF map.

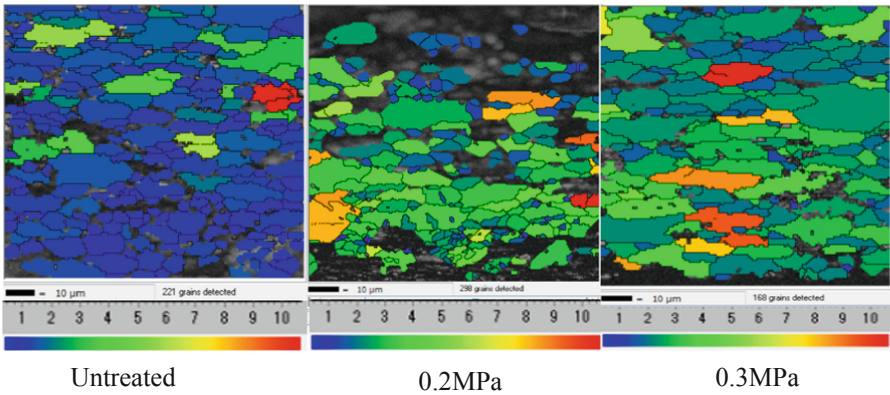


Fig. 6. IPF map.

4 Conclusions

In this study, the effects of wet blasting on the fatigue strength properties of magnesium alloy AZ31 were investigated, and the following findings were obtained.

1. It was clarified that the wet blasting treatment is effective for improving the time strength of magnesium alloy AZ31. On the other hand, no remarkable effect was obtained like shot peening treatment for steel materials. The improvement in hardness and residual stress was also obtained in the wet blasting treatment, so it is thought that the effect of improving the fatigue strength was suppressed by the influence of the surface roughness.

2. As a result of evaluating the crystal by EBSD analysis, twin formation by wet blasting was not found. However, it was clarified that the intragranular strain increased with the increase of the blast pressure.

References

1. Nakai, Y., Saka, M., Yoshida, H., Asayama, K., Kikuchi, S.: Fatigue crack initiation site and propagation paths in high-cycle fatigue of magnesium alloy AZ31. *Int. J. Fatigue* **123**, 248–254 (2019)
2. Egami, N., Kagaya, C., Inoue, N., Takeshita, H., Mizutani, H.: Hybrid surface modification of SCM415 material by vacuum carburizing and fine particle peening. *Trans. Japan Soc. Mech. Eng. A* **66**, 1936–1942 (2000)
3. Nambu, K., Okumiya, M.: Influence of soft particle peening treatment on fatigue strength of aluminum alloy a5052. In: *Lecture Note in Mechanical Engineering, Proceedings of the 7th International Conference on Fracture Fatigue and Wear*. 2018年, pp. 390–400 (2008)
4. Nambu, K., Matsuzaka, K., Egami, N.: Influence of Fine Particle Bombarding on Various Characteristics of SUP10. **76**(768), 1096–1102 (2010). (in Japanese)
5. Nambu, K., Egami, N.: Influence of vacuum carburizing treatment on fatigue crack growth characteristic in DSG2. *Fract. Struct. Integrity* **34**, 271–279 (2015)
6. Kikuchi, S., Nakamura, Y., Nambu, K., Ando, M.: Effect of shot peening using ultra-fine particles on fatigue properties of 5056 aluminum alloy under rotating bending. *Mater. Sci. Eng., A* **652**, 279–286 (2016)
7. Morita, T., Noda, S., Kagaya, C.: Influence of fine-particle bombarding and conventional shot peening on surface properties of steel. *Mater. Trans.* **55**(4), 646–652 (2014)
8. Nakamura, Y., Aoki, T., Shimizu, T., Kikuchi, S., Nambu, K., Akahori, T.: Effect of fine particle peening using hydroxyapatite shot particles and plasma sprayed hydroxyapatite coating on fatigue properties of beta titanium alloy. *WIT Trans. Eng. Sci.* **116**, 205–211 (2017)
9. Nambu, K., Toya, H., Usami, H., Takizawa, Y., Keju-Chou, Saito, M., Yamada, Y., Ando, A.: Erosive wear mechanism of metal on fatigue particle peening process. In: *The 6th International Conference on Manufacturing, Machine Design and Tribology of Proceedings*, pp. 72–73 (2015)
10. Wagner, L., Wollmann, M.: Shot peening of non – ferrous alloys to enhance fatigue performance. In: *Proceedings of ICSP10, Tokyo* (2008)



Process Model for Evaluating the Peen Velocity in Shot Peening Machine

Nguyen Van Bo¹(✉), Ba Te¹, Augustine Teo², Kunal Ahluwalia²,
Ampara Aramcharoen², and Kang Chang Wei¹

¹ Fluid Dynamics Department, Institute of High Performance Computing,
A*STAR, Singapore 138632, Singapore

nguyenvb@ihpc.a-star.edu.sg

² Data-Driven Surface Enhancement Group, Advanced Remanufacturing
and Technology Centre, A*STAR, Singapore 637143, Singapore

Abstract. Peening velocity (shot velocity) is one of the key parameters in shot peening process, which directly relates to intensity and coverage area. A desired intensity and/or coverage area can be attained by controlling the peening velocity to the right value. However, this is a challenging task as the peening velocity is the function of many different variables (peening system, nozzle design, air pressure, media (shot) flow rate, shot size, etc.). In this study, we develop a process model that links the input/operating parameters of the peening machine to the average shot stream velocity upon impact. In particular, the formulation of shot stream velocity is derived as the function of input air pressure and media flow rate, which also accounted for the peening system and nature of the flow inside (e.g., nozzle shape, pressure loss, energy transfer, and turbulence, etc.). The model is validated against the experimental data for different inlet pressure as well as the media flow rates. The calculated results are in good agreement with experimental data. Furthermore, the model validity and reliability are examined for the wide range of input parameters and the system parameter. The results also indicated that the developed process model can be applied for different peening machines with different nozzle design by defining relevant model constants. There are a few key applications for the process model; which are (1) the model can support the operators to rapidly estimate and setup the working conditions of the machine to attain the desired peening intensity and coverage area to avoid the cost and time in doing experiments based on trials and errors, and (2) The model also can be used in model predictive control (MPC) to develop the controller for the peening machine.

Keywords: Shot peening · Analytical model · Peen velocity · Peening intensity · Peening coverage

1 Introduction

Shot peening is a cold working process that is widely used in the surface enhancement process of metallic components [1]. The quality of a peening process is

relied on the intensity and coverage, which strongly depend on the direct peening parameters (such as, impinging velocity and angle, material properties, peen size and type, number of impacts, etc.). In which, the intermediate impinging velocity (or peening velocity) is one of the most important parameter that links the operational conditions (air pressure, peen flow rate, peening system, and nozzle design) to the outputs of peening process (coverage and intensity). In practical operation, to determine a set of inputs for an expected intensity and/or coverage, operators have to perform a series of experiments to build a saturation curves each time [1]. Producing these saturation curves is often very costly and time consuming. In addition, performing the computational fluid dynamics (CFD) with finite element analysis (FEA) for shot peening problem is very time consuming and expensive. Therefore, an accurate model is necessary to provide a fast and reasonable solution for analysis and control.

So far, massive of empirical models have been built to analytically evaluate (predict) important shot peening parameters (coverage and intensity) [2–8]. Among these models, the peening velocity is vitally important role as it is used as a main variable for evaluating the coverage and intensity. However, an accurate model for peening velocity is still awaited to provide a link from input parameters to output of interests. Thus, in this study, we proposed an empirical model, which is constructed using the sparse identification of nonlinear dynamics (SINDy) algorithm with limited experimental data and incorporating with the physics domain knowledge [10]. The empirical model of peening velocity can provide a fast and accurate intermediate solution value for evaluating the coverage and intensity from a particular operating conditions without the need of performing many experiments.

In addition, to improve the quality of shot peening process, controlling the impinging velocity is considered as a potential option as mentioned in [9]. However, experimentally observing the peening velocity only supports for current system control manually. It is very time consuming and requires a strong experiences of the operators. Therefore, in this study, we also proposed a new control algorithm (namely model predictive control (MPC) [11, 12]) to automatically adjust input operational conditions to attain desired peening outputs. The model-based control algorithm often requires a process model for controller development. Here, we employed the SINDy with control algorithm (proposed in [13]) to derive the process model for the shot peening process from limited experimental data. (Particularly, the empirical model of peening velocity with a proxy model will used to develop the process model for MPC controller development.) The paper is organized as: Sect. 1 is paper introduction, Sect. 2 describes the model development, Sect. 3 shows model validation for accuracy and reliability, Sect. 4 expresses the potential applications of the developed model, and Sect. 5 concludes the paper content.

2 Model Development

In this study, we assume that the peen velocity at the impact having the following form:

$$V_p = f(p, m, peentype, peendiameter, \Delta p, turbulence, etc). \quad (1)$$

where V_p is the peening velocity, p is inlet pressure, m is media (or peen) flow rate, and Δp is pressure loss along the pipeline system from the inlet to nozzle outlet. In order to determine Eq. (1) for our typical peening machine, we employed the sparse identification of nonlinear dynamical system (SINDy) algorithm (proposed by Brunton et al. [10, 13]) to extract the velocity equations from experimental data. In this study, experiments are performed for different operating conditions of inlet pressure and peen mass flow rate. Three pressure sensors are placed along the nozzle to record the pressure history of airflow. The collected history data of all input air pressure at the inlet (p_1, p_2, \dots, p_n), all pressure at three sensor location along the peening nozzle (p_{s1i}, p_{s2i} , and p_{s3i} , for $i = 1, \dots, n$), media flow rate (m_1, m_2, \dots, m_n), peening angle (θ), and peening nozzle diameter (d_{nozzle}) are stored in a state matrix \mathbf{X} as the following format:

$$\mathbf{X} = \begin{bmatrix} p_1 & m_1 & d_p & p_{s11} & p_{s21} & p_{s31} & \theta & d_{nozzel} \\ p_2 & m_2 & d_p & p_{s12} & p_{s22} & p_{s32} & \theta & d_{nozzel} \\ \dots & \dots & \dots & \dots & \dots & \dots & \dots & \dots \\ p_n & m_n & d_p & p_{s1n} & p_{s2n} & p_{s3n} & \theta & d_{nozzel} \end{bmatrix}. \quad (2)$$

And the corresponding velocity measurement for all cases is stored in a column vector \mathbf{V} as the following:

$$\mathbf{V} = [v_1, v_2, v_3, \dots, v_{n-1}, v_n]^T. \quad (3)$$

Also, we build a function library of $\Theta(\mathbf{X})$ including the candidate nonlinear functions of the column of \mathbf{X} as the followings:

$$\Theta(\mathbf{X}) = [1, \mathbf{X}, \mathbf{X}^2, \mathbf{X}^3, \dots, \exp(\mathbf{X}), \dots, \sin(\mathbf{X}), \cos(\mathbf{X}), \dots]. \quad (4)$$

In Eq. (4), each component represents a candidate function for the variable \mathbf{X} . Assume that there are few entries of the nonlinearities, which are active for each variable. Thus, we might setup a sparse regression problem to determine the sparse vectors of coefficients $\Xi = [\xi_1, \xi_2, \xi_3, \dots, \xi_n]$ that determines which nonlinear functions are active:

$$\mathbf{V} = \Theta(\mathbf{X})\Xi. \quad (5)$$

Solving for the system of equations (5), we will obtain the governing equations for peening velocity. Here, the right hand-side of the equations are the measurement peening velocity for each input variable, while the coefficients $\Theta(\mathbf{X})$ are the data matrix. The data matrix is determined from inputs parameters with function library. When the measurement contains noise that might cause a overdetermined system. So, depending on the noise level we may need to filter

the experimental data before solving for Ξ . Here, we employ sparse regression to identify a sparse Ξ corresponding to the fewest nonlinearities in our library that give good model performance with:

$$\xi_k = \underset{x}{\operatorname{argmin}} \frac{1}{2} \|\mathbf{V}_k - \hat{\xi}_k \theta^T(\mathbf{X}, \mathbf{U})\|_2^2 + \lambda \|\hat{\xi}_k\|_1. \quad (6)$$

The term $\|\cdot\|_1$ term promotes sparsity in the coefficient vector ξ . This optimization can be solved using the sequentially thresholded least squares procedures as in the following algorithm [13, 14]:

Algorithm 1. Sequentially thresholded least squares for evaluating active equation components

Input: Measurement \mathbf{V} , library candidate functions $\Theta^T(\mathbf{X}, \mathbf{U})$, and thresholding parameter λ .
Output: Matrix of sparse coefficient vector Ξ

- 1: **function** REGRESSION($\mathbf{V}, \theta^T(\mathbf{X}, \mathbf{U}), \lambda, N$)
- 2: $\hat{\Xi}^0 \leftarrow (\theta)^\dagger \mathbf{V}$ ▷ Initial guess.
- 3: **while** not converged **do**
- 4: $k \leftarrow k + 1$
- 5: $\mathbf{I}_{small} \leftarrow (\operatorname{abs}(\hat{\Xi}) < \lambda)$ ▷ Find the small entries
- 6: $\hat{\Xi}^k(\mathbf{I}_{small}) \leftarrow 0$ ▷ Find threshold
- 7: **for** all variable **do**
- 8: $\mathbf{I}_{big} \leftarrow \sim \mathbf{I}_{small}(:, ii)$ ▷ Find big entries
- 9: $\hat{\Xi}^k(\mathbf{I}_{big}, ii) \leftarrow (\theta^T(:, \mathbf{I}_{big}))^\dagger \mathbf{V}(:, ii)$ ▷ regression on those terms
- 10: **end for**
- 11: **end while**
- 12: **end function**

It should be noted that a suitable library of candidate terms is vitally important in SYNDy algorithm. If we don't have any information about physics of the problem, the strategy is to start with a basic choice, such as a polynomials, and then increase the complexity of the function library by adding other terms with higher order and more complex functions. If we have physics information, we might incorporate the physics to design the library. In this study, we used the first set of experimental data for peen type of ASR230 and different operating conditions of inlet air pressures and peen flow rates, while all other parameters are fixed. The inlet air pressure is ranging from 20 *psi* to 65 *psi*, while the peen media flow rate is from 1 kg/min to 5 kg/min. The following formulation is obtained for peening velocity:

$$V_p = \frac{1}{\sqrt{S}} * A * (1 - \exp(\frac{-p_{in}}{B + C * m + D * m^2})). \quad (7)$$

In this expression, p_{in} is the inlet air pressure (in bar). m is the peen media flow rate (in *kg/min*). $S = 230$, is assumed to be the peen type. $A = 1.125 \times 10^3$, is

assumed to be related to the peen size and peening machine. $B = \Delta p$ is related to the pressure loss along the way to nozzle exit. $C = 0.075$ assumed to account for the effect of pressure and velocity gradient, while $D = 0.00125$ considers for the effect of the viscosity and turbulence. The results are shown in Fig. 1 as follows:

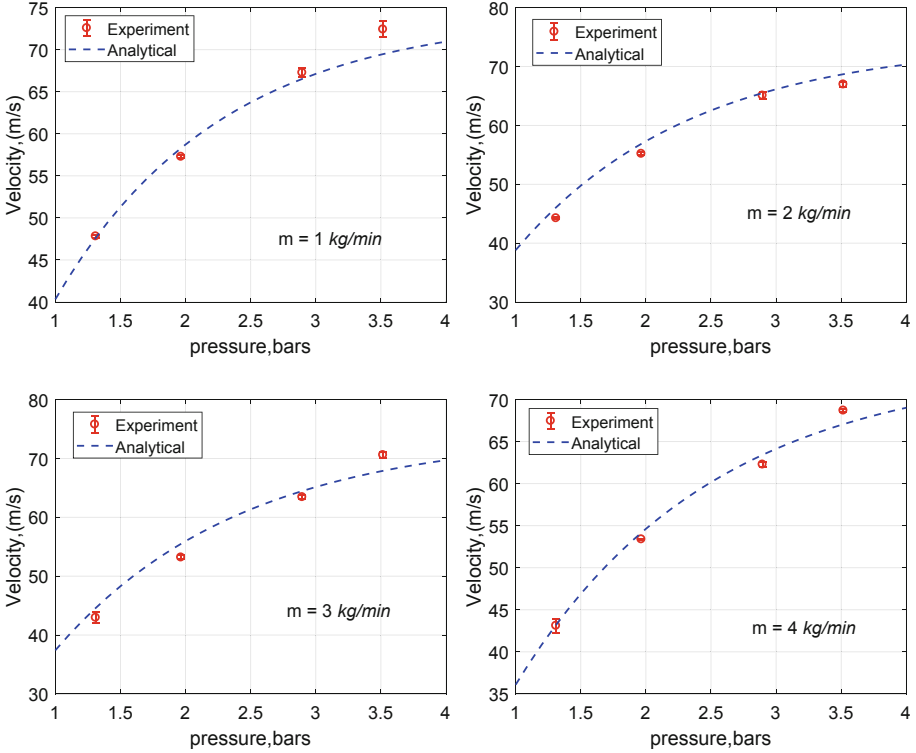


Fig. 1. Comparison between the empirical model and the experimental data for peen type of ASR230.

Figure 1 shows the comparisons of experimental data and obtained empirical model for different peen media flow rate (top-left (1 kg/min), top-right (2 kg/min), bottom-left (3 kg/min), and bottom-right (4 kg/min)). It shows that the model can accurately reproduce the experimental data for different setting of operational conditions. For further exploration, the empirical model will be benchmark against other operating conditions for accuracy and reliability.

3 Model Validation

In this section, a set of other experiments, which is not included in the model development process, is used to benchmark for the developed model for the

validity and reliability. Here, we use the same settings for all input operating conditions (air pressure and peen media flow rate) and all other setups of the same peening machine. The only difference is to change peen type from ASR230 to ASR70, which is a smaller peen. As such, in the empirical model, we only change the coefficient $S = 230$ to $S = 70$. Figure 2 shows the comparisons of the empirical model and experimental data for different peening media flow rate. Top-left figure is for the case of peen flow rate of 1 kg/min, top-right is 2 kg/min, bottom-left is 3 kg/min, and bottom-right is 4 kg/min for varying inlet air pressure. It can be seen that the model is in good agreement with the experimental data. It implies that the developed empirical model can be used to predict for the peen velocity for different operating conditions of the defined shot peening machine. In addition, we also can use this results to analytically estimate the peening coverage [2,3] and/or intensity [4]. Also, this may help the operator with a faster setup of the machine for an expecting peening outputs (coverage and intensity).

4 Applications

As mentioned in previous section, the peening velocity is a vitally important peening parameter, which can link the inputs of operation setting (e.g., air pressure, media flow rate, and other settings) to the outputs of peening coverage and intensity. Thus, the empirical model of peening velocity can be used for controlling or predicting the outputs of the peening operation with the setting inputs.

For predicting peening coverage and/or intensity, peening velocity at the impact have been used to evaluate the coverage [2,3] and intensity [4] for a defined peen type and certain operating conditions. In study [2], David utilizes the peen velocity at the impact to calculate the particle work potential ($W_p = \pi D^3 \rho v^2 / (12 \times 10^6)$) for indent diameter evaluation, which is used to evaluate the peening coverage factor (K), then coverage with $C = 100(1 - \exp(-K * t))$. While Nguyen et al. [3] used impact velocity to evaluate single dimple area as $a = \frac{E_c * d_p^2 * \sqrt{\rho} * V_p / \sin(\theta)}{\sqrt{B}}$ that can be used for different peen types and target materials. In the coverage prediction model, the multiple impaction and overlapping indentations are accounted as $C(\%) = 100(1 - \exp(-\sum_{i=1}^N \frac{a_i}{A}))$. Similarly, David [4] evaluated the peening intensity using analytical formulation of peen type and impact velocity with $I = S * 0.00366591(1 - \exp(-0.010482 * V))$. Thus, our prediction model of peening velocity can be utilized as an input for coverage prediction in both [2,3], and intensity for different operating conditions and peen types. Take for example, if we use inlet air pressure at 4 bar and media flow rate of 3 kg/min for the current shot peening machine and ASR70 peen type, using Eq. 7 we get average peening velocity at about 107.4 m/s. So that the predicting intensity is about 0.1734.

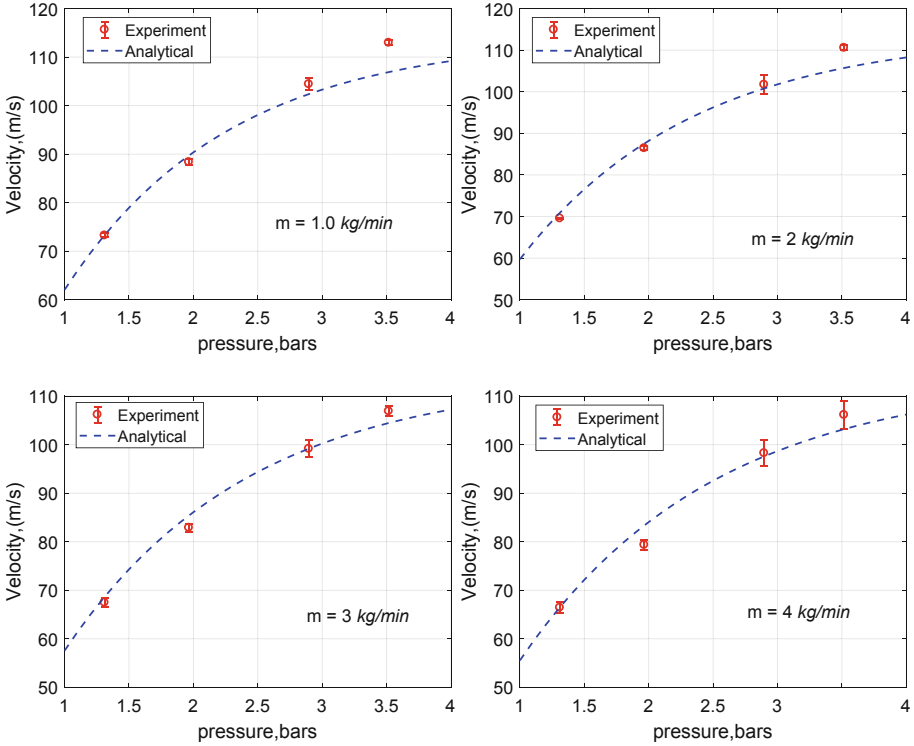


Fig. 2. Comparison between the empirical model and the experimental data for peen type of ASR70.

For system controlling, this empirical model with a proxy model can be employed to develop a control-based algorithm for peening machine. This model-based controller (or model predictive control (MPC)) [13] is an advanced control technology that uses the model to preview the future of dynamical system to adjust the control input(s) to achieve the set objective function. With the developed empirical model of peening velocity and proxy model, we can build a process plant model for MPC controller of the peening machine (See Fig. 3). Here, we assume that the inlet air pressure and peen media flow rate are manipulated variables, which are controlled to attain the peening intensity. We used our empirical model with proxy model in ([4]) $I = S * A_1(1 - \exp(-B_1 * V))$ to link control inputs (p, m) with control outputs (I) . We assume that these function is also function of time, so we take the derivatives of both functions in time and get the following process model for peening velocity.

$$\frac{dI}{dt} = F_1 \left\{ \frac{S * A}{B + Cm + Dm^2} \exp\left(\frac{-p}{B + Cm + Dm^2}\right) \left(\frac{dp}{dt} + \frac{p * C}{B + Cm + Dm^2} \frac{dm}{dt} \right) \right\} \quad (8)$$

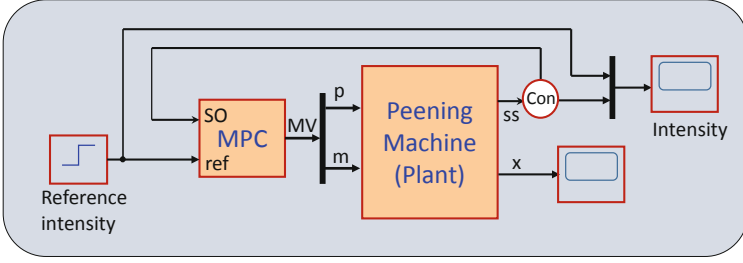


Fig. 3. Control diagram of a shot peening machine.

with

$$F_1 = S * A_1 B_1 * \exp(-B_1 * V_p) = S * A_1 B_1 * \exp(-B_1 * \frac{1}{\sqrt{S}} * A * (1 - \exp(\frac{-p_{in}}{B + C * m + D * m^2}))) \quad (9)$$

Then the control problem becomes

$$\underset{p \in [p_{min}, p_{max}], m \in [m_{min}, m_{max}]}{\text{minimize}} \quad J(X(t), y(t), p, m), \quad (10)$$

s.t.

$$\dot{I} = f(p, m) \quad (\text{Equations (8) and (9)}), \quad (11)$$

$$p_{min} \leq p(t) \leq p_{max}, \quad (12)$$

$$m_{min} \leq m(t) \leq m_{max}. \quad (13)$$

In this control problem, $J(X(t), y(t), p, m)$ is the objective function of the control problem, which is often expressed as $J(X(t), y(t), p, m) = \text{Min}(\sum_{i=1}^N (\hat{y} - y_s)Q(\hat{y} - y_s)^T + \sum_{k=1}^M \Delta u R \Delta u^T)$. p_{min} and p_{max} are the pressure constraints of the peening system (with minimum and maximum pressure, respectively), while m_{min} and m_{max} are the minimum and maximum peen flow rate of the peening system, respectively. \hat{y} and y_s are the measurement and set point intensity (or designed intensity).

To demonstrate for control application, a control soft-launch has been performed to attain three different values of intensity, which are $I = 0.325$ for $t \in [0, 10]$ s, $I = 0.525$ for $t \in [0, 80]$ s, and $I = 0.175$ for $t \in [80, 120]$ s. The delay time is set at about 5 s for peen velocity responding at the impact region. The peening media flow rate is fixed at 3 kg/min, while the inlet air pressure is controlled to attain the set intensity. Figure 4 shows the results of soft-launch control with designed MPC controller. Solid red line is designed set point for intensity, while solid black line is output measurement intensity. The blue line is adjusting value of pressure at the inlet (Δp) in (bar) to achieve the set-points. The dashed black line is prediction intensity, while dotted green line is prediction pressure. The process control is quite stable, accurate, and reliable. The simulation time of this nonlinear MPC met well with real-time control requirement. It implies that the proposed control approach is quite promising for real-time controller development of automated shot peening machine.

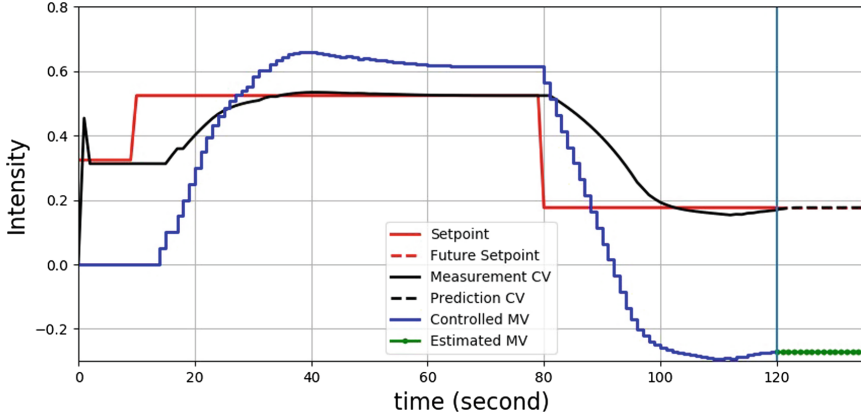


Fig. 4. Results of soft-launch control with developed MPC controller for peening machine.

5 Concluding and Future Works

In this study, the sparse identification of nonlinear dynamics (SINDy) algorithm is employed to construct the empirical model for peening velocity from limited data resources. It also can incorporate with physics domain knowledge to build the function library. The obtained model is developed for particular shot peening machine with known nozzle design and peening type information. In this study, the model is developed from an experimental data set for fixed peen type (ASR230), and different inlet air pressure and peen flow rate. For the current peening system, the model can accurately predict the impinging velocity for different peen types and operating conditions.

For practical operations, the developed empirical model can be employed to predict the impinging velocity for different conditions, which can provide information to reasonably estimate the peening coverage and/or intensity. The obtained results may provide great information for practical setup of the real peening operation. It can help to reduce the cost and time to perform a lot of experimental work to build saturation curve for practical operations.

For system controlling, the empirical model of peening velocity with proxy model can be used to develop a process model for model-based controller development. A fundamental closed-loop optimal model predictive control (MPC) framework has been developed for shot peening machine based on the developed peening velocity model and proxy model. A soft-launch control has been performed to achieve some set different intensities by automatically controlling the inlet air pressure, while the peening mass flow rate is fixed at 3 kg/min . The preliminary results show that the control process is fast, stable, accurate, and reliable. It is suitable for real-time control.

For future plant, this work needs further developments to establish a practical and reliable feedback control system. Such as, the process model needs to be

developed further for more accurate and incorporating with reliable sensor data. Data driven technique also needs to be implemented for improve process model and feedback control. Depending on the received data from sensor, a filter model will be integrated into control system.

Acknowledgment. This work is supported by the project entitled: “Machine Learning Assisted Control of Shot Peening Process” under Grant number A1894a0032, which is lead by Dr. Kang Chang Wei (IHPC, A*STAR) and Dr. Ampara (ARTC, A*STAR).

References

1. Harrison, J.: Controlled shot-peening: cold working to improve fatigue strength. *Heat Treat.* **19**, 16–18 (1987)
2. David, K.: Quantification of shot peening coverage. *The Shot Peener*, Fall (2014). <https://www.electronics-inc.com/wp-content/uploads/QuantificationOfShotPeeningCoverage.pdf>
3. Nguyen, V.B., Poh, H.J., Zhang, Y.W.: Predicting shot peening coverage using multi-phase computational fluid dynamics simulations. *Powder Technol.* **256**, 100–112 (2014). <https://doi.org/10.1016/j.powtec.2014.01.097>
4. David, K.: Variability of a shot stream’s measured peening intensity. *The Shot Peener*, Summer (2011). <https://www.shotpeener.com/library/pdf/2011120.pdf>
5. David, K.: Peening intensity: true meaning and measurement Strategy. *The Shot Peener*, Summer (2016). <https://www.shotpeener.com/library/detail.php?anc=2016030>
6. David, K.: Curve fitting for shot peening data analysis. *The Shot Peener*, 6. Spring (2002). <https://www.shotpeener.com/library/pdf/2002091.pdf>
7. David, K., Abyaneh, M.Y.: Theoretical basis of shot peening coverage control. *Shot Peener*, vol. 13, no. 3, pp. 5–70 (1999). <https://www.shotpeener.com/library/pdf/1995043.pdf>
8. David, K.: Theoretical principal of shot peening coverage. *Shot Peener*, vol. 19, no. 2, pp. 24–26 (2005). <https://www.shotpeener.com/library/detail.php?anc=2005145>
9. Bill, B., Kevin, Y.: Particle velocity sensor for improving shot peening process control. *Shot Peener*, Technological aspects (2005). <https://www.shotpeener.com/library/pdf/2005114.pdf>
10. Brunton, S.L., Joshua, L.P., Kutz J.N.: Discovering governing equations from data by sparse identification of nonlinear dynamical systems. In: *Proceedings of the National Academy of Sciences of the United States of America*, vol. 113, no. 15, pp. 3932–3937 (2016). <https://doi.org/10.1073/pnas.1517384113>
11. Tobias, G.: *Model Predictive Control of High Power Converters and Industrial Drives*. Wiley, London (2016). ISBN 978-1-119-01090-6
12. Wang, L.: *Model Predictive Control System Design and Implementation Using MATLAB®*, p. xii. Springer Science & Business Media, London (2009)
13. Kaiser, E., Kutz, J.N., Brunton, S.L.: Sparse identification of nonlinear dynamics for model predictive control in the low-data limit, 474. In: *Proceedings of the Royal Society A: Mathematical, Physical and Engineering Sciences*. <https://doi.org/10.1098/rspa.2018.0335>
14. Zhang, L., Schaeffer H.: On the convergence of the SINDy algorithm. *Journal CoRR* (2018). <http://arxiv.org/abs/1805.06445>



Experimental Study of Single Shot Process: Toward a Surface State Predictive Tool

Benjamin Levy¹(✉), El Mansori Mohamed^{2,4}, Sabeur Mezghani³,
M. El Hadrouz³, Julien Cabrero¹, and Anne-Laure Beaudonnet¹

¹ Saint-Gobain Research Provence,
550 Avenue Alphonse Jauffret, 84300 Cavaillon, France
benjamin.levy@ensam.eu,

Anne-Laure.Beaudonnet@saint-gobain.com

² Laboratory of Mechanics, Surface and Materials Processing (MSMP-EA7350),
Arts et Métiers ParisTech d'Aix-En-Provence, 2 cours des Arts et Métiers,
13617 Aix-en-Provence, France

Mohamed.ELMANSORI@ensam.eu

³ Laboratory of Mechanics, Surface and Materials Processing (MSMP-EA7350),
Arts et Métiers ParisTech de Châlons-En-Champagne, Rue Saint-Dominique,
51000 Châlons-en-Champagne, France

⁴ Texas A&M Engineering Experiment Station,
College Station, TX 77843, USA

Abstract. The present study aims at enhancing the comprehension of the interactions between shot and target during shot-peening process, with focus on the energy transmitted and roughness generation. A single impact approach was developed in order to establish relations between the process parameters, media and target properties, and the generated surface state.

Al-6061-T6 plates were peened with only one shot made of different materials (ceramic, metals) under controlled process conditions (pressure, distance and angle). Process parameters such as incident and rebound velocities were determined by coupled fast-cam.

This approach allows identifying key criteria combining media properties and shot peening process parameters, initial step, to monitor and optimize the surface topography of the peened sample.

Keywords: Shot peening · Ceramic shot · Surface topography optimization

1 Introduction

Surface finish impact many functionalities of products such as fatigue (cracking), wear (pullout); corrosion (pitting corrosion) [1], bacterial adhesion [2], cosmetic [3]. To improve surface properties and hence the marketing of products, shot penning is one of the most processes involved at industrial scale. Shot peening is defined as a cold working process that induces plastic deformation in the peened part, which in turns generates residual stresses. Residual stresses level is related to process parameters like peening time, pressure or coverage [4]. This is the better-known application and one of the most studied [5, 6] applications both from the scientific (open literature) and technical (case studies) purposes.

However, there are applications for which surface topography plays a crucial role in obtaining the desired cosmetic and mechanical properties [7]. Roughness generation [8] could be a major problem for certain applications, particularly in aeronautics and automobile.

In the field of telecom, roughness generation by shot peening changes cosmetic finishing of casing, anti-fouling [9] or aesthetics' aspects of packaging's allowing to increase products attractiveness. Surprisingly, roughness generation in shot peening process remains poorly understood.

Increase current roughness knowledge is one of the largest assets to build a strong physical model to improve the understanding of blasting process. The definition of a representative surface element, the number of impacting beads, the dynamic a geometric of bead presence (shape, diameter, speed...), should pave the way for increasing roughness understanding. In this way, we think that the first step is to better observe the phenomenon by projecting only one shot on target and make a fine description of its impact on surface modification. In what follows we shall deal with collision between spherical ball and flat aluminum surface, and then consider the process signature transfer between them.

2 Objectives

A single impact approach was developed in order to establish relations between the process parameters, the media properties, the target properties, and the generated surface state (indent shape and roughness).

3 Methodology

In order to generate experimental data, several researchers have simulated the impact of one bead on target through using a mechanical press (like Brinell test), drop test or using a blasting system with very low coverage rate [Saint-Gobain internal report]. Blasting system with low coverage is the most realistic but it is difficult to associate a bead [10], along with its trajectory or speed, with an indentation. Although this method is probably the most rigorous, the tracking of a single bead can sharpen the comprehension of the interaction between key parameters.

3.1 Specimen and Shot Preparation

As a first step, we treated Al 6061-T6 non-polished plate of dimension $50 \times 50 \times 1$. Mechanical properties are given in Table 1.

Table 1. Target's properties

Properties	Yield strength (MPa)	Poisson's ratio	Density (kg.m^{-3})	Young's Modulus (GPa)	Vickers hardness
	270	0,33	2700	69	107

All shots were requalified to have a weak diameter scatter, using 850 μm test sieves, which is in accordance with NF ISO 3301-2 standards.

For each commercial batches of shot, 200 g were sieved. After 5 min in sieve shaker (Retsch AS200 Tap), only shot which had been blocked in sieve's metal cloth were kept. In this study, 5 batches of shots are compared: Z850 (ZirShot[®] Saint-Gobain), ZC850 (ZirShot HDC[®] Saint-Gobain), APTZ, S330 and G3. Mechanical properties are summarized in Table 2.

Table 2. Shot's properties

Shots	B/L	SPCT	Diameter (μm)	Young's Modulus (GPa)	Poisson's ratio	Density (kg. m^{-3})	Vickers hardness
Z850	0,95	0,99	850	220	0,29	3880	698
ZC850	0,94	0,99		198	0,32	6220	1185
APTZ	0,93	0,99		198	0,32	5400	1350
S330	0,92	0,99		200	0,33	7400	540
G3SPH	0,87	0,98		200	0,33	7400	700

G3 beads are made with spheroidize wire cut, and they may obtain particular shape during process. G3 beads were cycled (270 min at 27A) into little blast system for the purpose of increase beads sphericity.

3.2 Experimental Data

To generate experimental data, shots were projected one by one via an isolated Venturi nozzle [Arena Blast CN4 et BU8] on Al 6061-T6 Target. To get reliable results, each experiment was repeated ten times under identical conditions. During this process, two synchronized fast cams (of Photron brand) allowed us to record shot flight information. Mono-impact experiments were performed under the machining condition given in Table 3.

Table 3. Experimental condition

Nozzle	Distance	Angle	Pressure	Target
Venturi - $\varnothing 8$ mm	20 cm	90°	4 Bar	Al 6061-T6

To carry out this project, we developed a laboratory-peening machine with an industrial nozzle. The purpose is to reproduce at full scale the forces and deformations occurring at the regions of contact when dealing with spherical beads and flat surfaces in collision as involved at shot peening. Peening box is fully instrumented by two fast Cam, one pressure reducing valve and one industrial Venturi nozzle. A fast cam recorded from the top of the box (XY plane) and the other one from the front of the box (XZ plane) as noted in the sketch (see Fig. 1) given below.

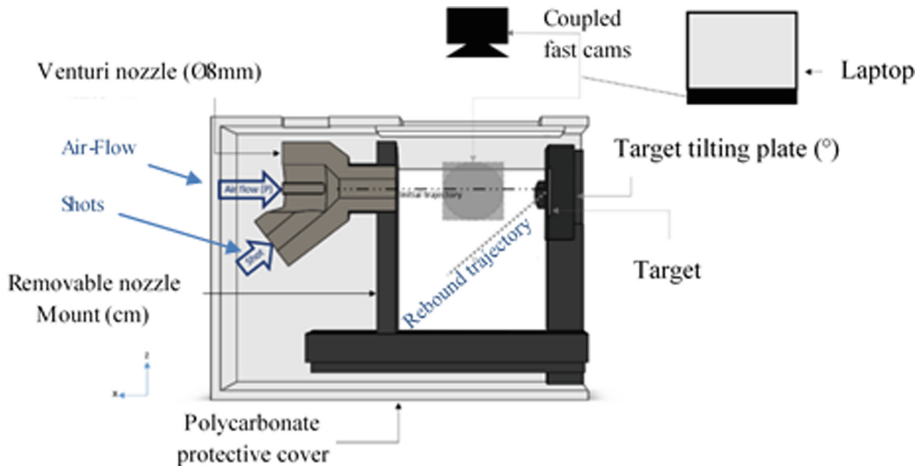


Fig. 1. Sketch of the installation: industrial Venturi nozzle.

The first step in data analysis was to do video analysis to extract from the two videos spatial coordinates, XYZ speeds and accelerations. For this we used free software named Tracker 5.0.5¹, which allows to follow evolution of shot during trajectory with only one element of scale and the Frame/Second reference.

4 Results and Discussions

In this section, we consider the impact of beads nature on indent morphology and process signature. All results are based on the average of the 10 measured values by sample.

4.1 Velocities and Kinetic Energies

Using results of coupled fast cam, velocities of beads can be expressed. According to two components: incident (trajectory between nozzle and target) and return (after impact) (see Fig. 2).

- Z850 is the product with the lowest density (3440 kg.m^{-3}) and it is the fastest one. On the other hand, G3SPH is the heaviest bead (7400 kg.m^{-3}) and the slowest. So increasing of density leads to decreasing beads velocity.

The work was steered by Venturi nozzle air pressure (Table 3). We have shown that beads velocity is inversely related to beads density. Then, in order to make rebound velocities of beads comparable, we have calculated the rate of change of velocities, according to the equation below:

¹ Tracker 5.0.5 12 May 2018 Copyright © 2018 Douglas Brown [<https://physlets.org/tracker>].

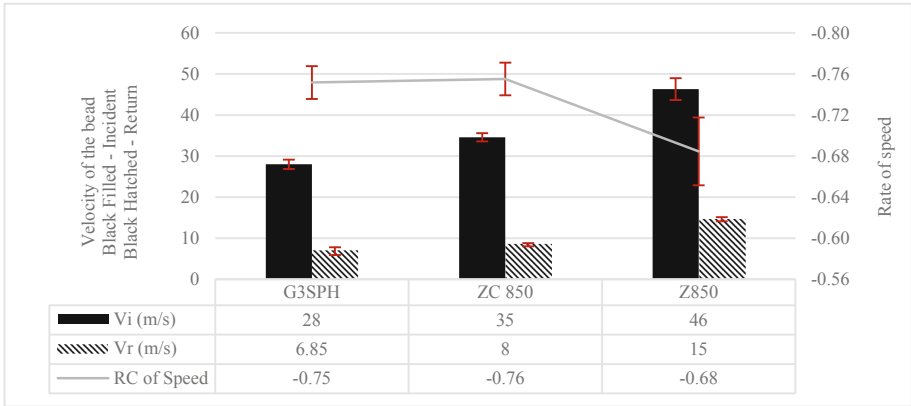


Fig. 2. Histogram showing average incident and rebound velocities of each kind of beads and the rate of change between the two previous velocities.

$$Rv = \frac{(V_r - V_i)}{V_i} \tag{1}$$

When we observe the rebound of beads (Fig. 2), it is possible to see that G3SPH and ZC850 have the same variation of speed while it is higher for Z850, which means that the first two products are losing more speed than the last one. Z850 is indeed a low hardness rigid ceramic bead and it is the bead that preserved the highest velocity during the impact phase. At the same time, G3SPH is a ductile steel bead with same hardness than Z850 and which loses as much velocity than ZC850, which is a high hardness rigid ceramic bead. These variations must be linked to the plastic flow occurring and the energy lost between the bead and the target during the collision. There is a close link between incident velocity and beads density on one side and hardness dynamic hardness of beads and rebound velocity on the other side.

Based on beads velocities above, it's possible to calculate the Kinetic Energy (KE) of each bead by using this formula:

$$KE = \frac{4\pi}{6} \times \rho \times R^3 \times v^2 \tag{2}$$

Where ρ , R and v are respectively the bead density, bead radius and bead velocity.

Due to his speed, Z850 is the product with the higher kinetic energy despite is lower density. In the other hand, due to his density (double than Z850 one) ZC 850 has almost the same kinetic energy (about 1250 μ J) while his velocity is 10 m/s lower. From the industrial point of view, this is quite interesting. This means that there is an ideal trade-off in term of density effect: beyond a density threshold, velocity becomes insufficient.

And it would seem that capacity to transmit energy is proportional to bead hardness and the higher the ratio between target hardness and bead hardness is, the more efficient the process is.

4.2 Indent Profile

One way to better understand interactions between beads and target is to characterize the indent imbedded by the bead on the target. Figure 3 shows surfaces of studied beads before collision and indentation left on surface target after collision with a scanning electron microscopy (SEM).

SEM observations allow to observe roughness on beads surface. G3SPH surface indicates clearly facets due to repeated shock, allowing to obtain sphere from cut wire while S330 has a shell made of steel oxide. On its part, Z850 has dendritic texture on his surface, which creates pyramidal structure. APTZ show fine roughness on surface, and it seems that ZC 850 is the smoothed one.

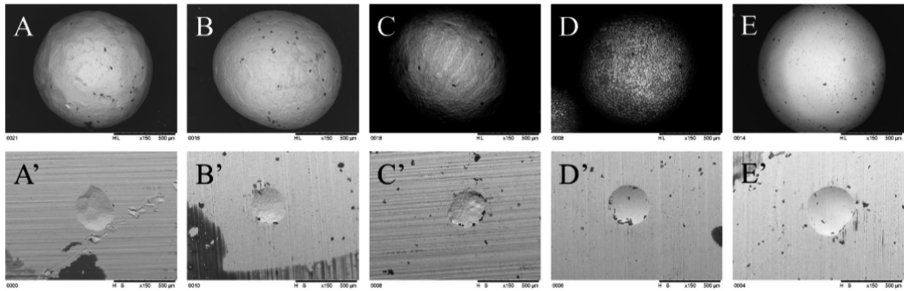


Fig. 3. Top-down: SEM pictures (x150) of beads before impact on target; ‘SEM pictures (x150) of indentation left on surface target. Left-Right: A_S330; B_G3SPH; C_APTZ; D_Z850; E_ZC 850.

Second, observations of indents under SEM show that it is possible to find the same shape of roughness into the indent than on beads surface. In addition, Indents observations with LEXT 5000 allow to fine characterize shapes (depth, diameter and roughness) of indent. It is also possible to compare average diameters of indent with the ratio (R) as calculated below:

$$R = \left(\frac{Hardness_{Bead} \times Density_{Bead}}{Hardness_{Target} \times Density_{Target}} \right) \tag{3}$$

Histogram reported on Fig. 4, shows three different behaviors:

- Z850 indent is the smaller (about Ø300 µm) and Z850 beads have the smaller hardness and density ratio. It’s interesting to note that Z850 beads are also ones that are the fastest and deploy the highest incident kinetic energy. So, material property of beads could be more significant than process parameters in indent creation.

- G3SPH has the smallest incident kinetic energy and create 10% higher diameter indent than Z850. S330 and G3SPH are both steel product with the same density [7400 kg.m⁻³], different Vickers's hardness [540 & 700] and diameters of indents are the same for both products. It's seemed that indent diameter is linked to bead density.
- Finally, high density and high hardness ceramic products inlay a largest indent while they have a density much lower than ductile steel beads. And ZC 850 has the same kinetic energy than Z850 but his indents diameter is bigger than Z850 one. In view of these results, it's seemed that indent diameter is linked to bead hardness.

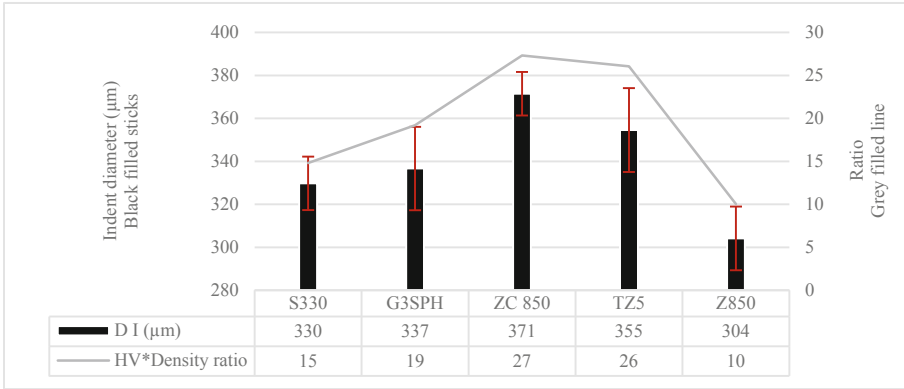


Fig. 4. Histogram showing average diameter of indent embedded by each products Al 6061-T6 target, at 4 bar, 20 cm and 90°. Histogram also included ratio calculate according to (3).

In this way, indent diameter could be tuned by modification of the R ratio, observed on grey curve, see upward. Thus, it would appear that density and hardness of the bead played a role in diameter of the indent and both are proportional to indent diameter.

Similarly, the indent depth seems to have no direct link with beads hardness but we can observe a trend which link proportionally density and indent depth, see Fig. 5.

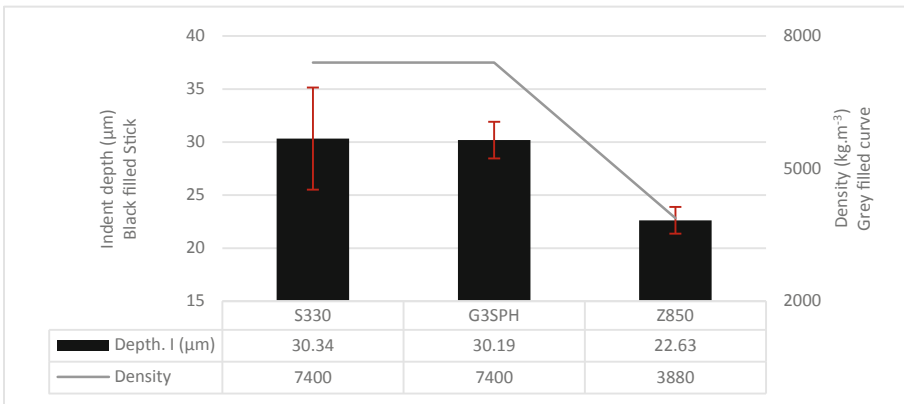


Fig. 5. Histogram showing average depth (μm) of indent embedded by S330, G3SPH and Z850 bead on AL 6061-T6 target at 4 bar, 20 cm and 90°. Histogram also showing beads' density.

Under the same variation of kinetic energy and the same hardness, Z850 and G3SPH show that diameter of indent is bigger for higher density [From 3400 to 7400 kg.m⁻³, about 30% deeper]. At the same time, G3SPH and S330 show that, under the same variation of kinetic energy and the same density, diameter of indent is the same for different hardness (hardness variation about 160 HV).

Therefore, according to Eq. (2), upward, indent of all beads have an equivalent sphericity, diameter indent is link to hardness and density while depth of indent is linked to density of beads. Beyond the impact on indents' shape we have observed the impact of surface roughness of beads into the surface roughness of the indent.

4.3 Process Signature Transfer

It is possible to see, using a SEM, that the same patterns are observable on beads and into indents, see Fig. 6.

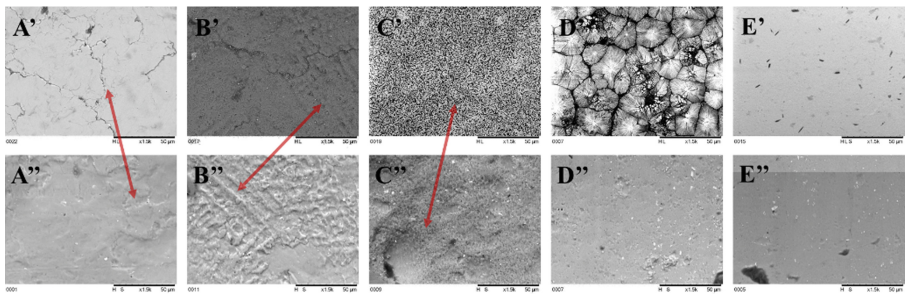


Fig. 6. Top-down: [A' to E'] SEM pictures of Surface of beads before impact on target (x1.5k); [A'' to E''] SEM pictures (x1.5k) Indentation left by previous beads on surface target. Left-Right: A_S330; B_G3SPH; C_APTZ; D_Z850; E_ZC 850

We calculate the Sa parameter that represents the arithmetic mean of the absolute ordinate Z (x, y) within the evaluation area, with the following equation:

$$Sa = \frac{1}{A} \iint_A |Z_{(x,y)}| dx dy \tag{4}$$

Figure 7 show all the results obtained thanks to measurement and calculation.

Steel beads have the highest surface roughness (Sa value about 30 μm) while ceramic beads have Sa value below to 20 μm. All beads, except ZC850, increase the surface roughness of target after impact. ZC850 has smoothest surface of beads and decrease the surface roughness of target. So during shot peening process, beads printed on the surface target two kind of roughness (scale effect). This means that in the case of industrial shot peening process, there are two permanent roughness impressions leave by bead after rebounding, one at macro-scale due to coverage of beads and one inside the indent scale (micro or meso-scale) left on target surface.

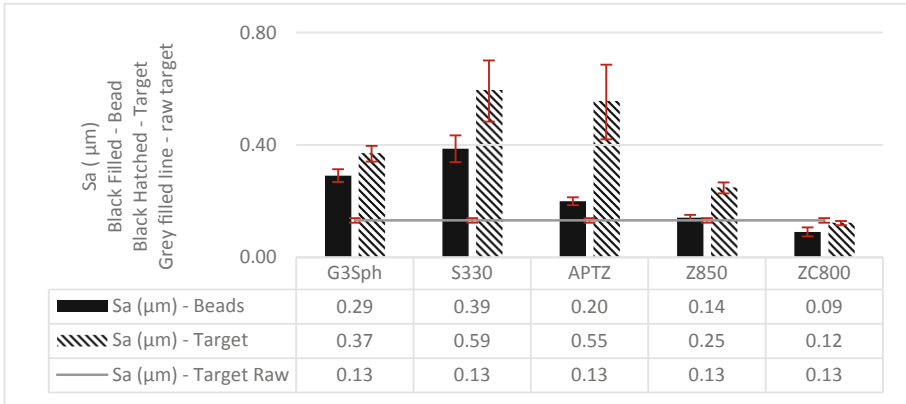


Fig. 7. Histogram showing average Sa, calculate thanks to (4), of the surface of beads and the indent surface. Grey line represented the untreated surface of target.

Target surface roughness played an important role on surface functionalization like capability to deviating light. Thanks to Nano roughness functionalization, it is possible to modify the design [10] and texture [11] of the target and develop new casing. In conclusion, it would be interesting to control the surface roughness of bead to increase the capability of surface functionalization.

5 Conclusion

In this study, we have examined energies transmitted and roughness generation during blasting process, through a single impact approach. In that respect, a test bench was developed which allows to acquire beads incident and rebound velocities thanks to coupled fast cams. This study shows that bead velocity is linked to its density. At the same time, indent diameter and depth is proportional to beads density. To that extent, there is a precise optimum for beads density to maximize treatment capability by maximizing kinetic energy.

In this way, efficiency of blasting process is closely linked to the ratio between beads and target hardness, as well as to transmitted energies. The indent diameter is also proportional to beads hardness. As a consequence, signature impact of the blasting process is strongly correlated to dynamic hardness of beads. Finally, beads could impact surface roughness at multiple scales and change orientation and pattern of target surface.

Thanks to the present study, it is now possible to have a good understanding of both mechanical and textural signatures of beads onto blasted target. It is critical to scale up the process and observe indent shape modification due to overlapping, in real blasting process. However, the transfer of surface beads roughness to target it is the same.

Indeed, experimental data allowed to build a strong mono-impact model (not described here). These learnings added solid guidelines to convert mono-impact simulation to multi-impact simulation, in way to create a predictive model for surface properties of blasted object.

References

1. Karaoglanli, A.C., et al.: Effect of shot peening on the oxidation behavior of thermal barrier coatings. *Appl. Surf. Sci.* **354**, 314–322 (2015)
2. Bagherifard, S., et al.: The influence of nanostructured features on bacterial adhesion and bone cell functions on severely shot peened 316L Stainless steel. *Biomaterials* **73**, 185–197 (2015)
3. Beaudonnet, A.L., Cabrero, J., Lambert, T.: Method for modifying the appearance of a surface (2016)
4. Cabrero, J., et al.: High density ceramic shot for peening application. In: ICSP-13, Montreal (2017)
5. Abadie, F.X., et al.: Application of ceramic shot for peening of automotive suspension coil springs. In: ICSP-10, Japan, Tokyo (2008)
6. Abadie, F.-X., Marconi, G.P., Morgano, E.: Enhancement of high strength steel endurance, application to automotive transmission components. In: ICSP-11, IN, USA (2011)
7. Clausen, R., Stangenberg, J.: Roughness of shot-peened surfaces - definition and measurement. In: The 7th International Conference on Shot Peening, Hamburg-Harburg (1999)
8. Raphet, B.: Etat de surface: Caractérisation. Annecy: technique de l'ingénieur, vol. R1230 (2008)
9. Coniglio, N., et al.: Effect of nano-peening surface texturing on self-cleaning function (2018)
10. Ferwerda, J.A., Pellacini, F., Greenberg, D.P.: A psychophysically-based model of surface gloss perception, p. 14853. Program of Computer Graphics, Ithaca
11. Turbil, C., Simonsen, I.: Light scattering from complex rough surfaces, Paris s.n. (2018)



Microstructural Changes in Electroplated Chromium Coating–Substrate Interfaces Induced by Shot Peening

Yutaka Kameyama¹(✉), Tatsuya Ohta², Keita Sasaki², Hideaki Sato¹, and Ryokichi Shimpo¹

¹ Tokyo City University, Tokyo 158-8557, Japan
ykameya@tcu.ac.jp

² Tokyo City University Graduate Division, Tokyo 158-8557, Japan

Abstract. Shot peening has been widely used for industrial field because of its attractive effects to increase strength of treated material. In addition, microstructural changes induced by shot peening have been recent interest since they possibly promise adding surface functions and enhancing the surface characteristics. In this study, shot peening was conducted on electroplated chromium coatings deposited on carbon steel substrate in order to create mechanically-mixed microstructure which was composed of iron and chromium. Microstructural changes induced by shot peening was carefully analyzed under ranging peening time. Results indicated that shot peening using steel grit particles created specific microstructure where fragments of chromium plating were dispersed into steel matrix whereas shot peening using spherical shot insufficiently induced the microstructural changes. It was implied that fragments of chromium plating were transported from top surface to steel substrate interior and simultaneously pulverized due to continuous impact of the particles during shot peening process. Severe plastic deformation induced at the shot-peened surface played as a driving force to induce material transportation and resulting “composite” microstructure formation.

Keywords: Shot peening · Electroplating · Mechanical alloying · Severe plastic deformation

1 Introduction

Shot peening (SP) has been a potential surface enhancement process which brings increased fatigue strength for machine components. In addition, interests on SP has been rapidly expanding because various reports indicated alternative effects of SP. For example, it has reported that SP under oblique nozzle angle could create periodical surface texture which reduced friction coefficient of the surface [1].

Material transfer [2] from the particles to the peened surface would be one of new potential effects of SP. This effect has been attempted to apply for enhancing thin film adhesion [3], adding solid lubricants onto the surface [4], creating bioactive surface for medical devices [5, 6], and forming intermetallic coatings [7]. It should be noted that some reports indicated that transferred material was embedded into the substrate when

shot particles much harder than the substrate were employed for SP. Nanocrystallization caused by SP has been also reported by many researchers [8–10]. It was considered that severe plastic deformation of peened material gave driving force of dynamic recrystallization [9]. Takagi et al. [9] proposed “folding deformation” model which occurred in substrates relatively softer than shot particles. “Folding deformation” resulted in formation of thick nanocrystal layer.

Considering the fact that SP induced embedment of the transferred materials as well as nanocrystallization due to “folding deformation”, it can be suggested that material should be mechanically-mixed when it is treated with SP. Although the detail of the mixing mechanism has not been clarified, it is expected that the microstructural changes resulted from the mixing process would be adopted as a new approach of a novel surface modification.

This study aims to investigate the changes in microstructure which occurred in a steel substrate coated with chromium plating. It is supposed that coating elements and substrate would be likely mixed in mechanical manner by conducting SP. Microstructure was analyzed after conducting SP on coated workpieces to elucidate how the mixing process progressed.

2 Experimental Procedure

Figure 1 summarized flowchart of specimen preparation. By conducting electrodeposition followed by SP, four types of specimens, which varied in substrate roughness as well as particle used for shot peening, were prepared: SS(Steel Shot)-Cr/S_S(Steel substrate with Smaller roughness), SG(Steel Grit)-Cr/S_S, SS-Cr/S_L(Steel substrate with Larger roughness), and SG-Cr/S_L. The detailed procedure of the preparation is described as below.

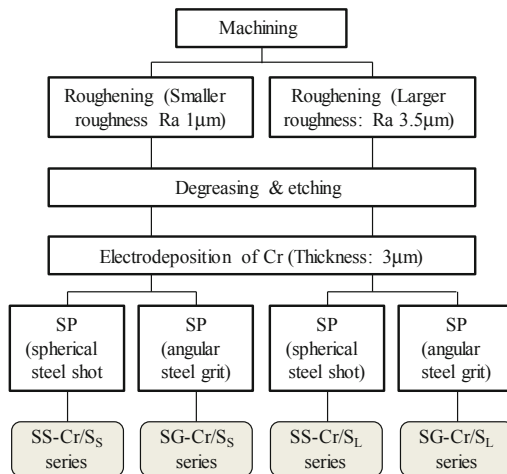


Fig. 1. Flowchart of specimen preparation.

First AISI1045 carbon steel rods of 15 mm in a diameter and a 30 mm in a length were machined. A end of the rod, to be coated with Cr plating, were roughened by conducting SP using two different conditions as listed in Table 1. This aimed to range the interfacial roughness between the coating and the substrate. Approximate mean roughness (R_a) values achieved by the primal roughening process were 1 μm for a tool steel fine particle, and 3.5 μm for a cast steel grit. M10 internal screw was tapped on another end of the rods to connect workpiece holder in electrodeposition process. The machined and SP-finished rods were then coated with hard chromium plating. After degreasing and acid etching to clean the surface, Cr plating was electrodeposited from a Sargent bath on the SP-finished end of the rod. The bath contained 250 g/L of chromic acid and 2.5 g/L of sulfuric acid. Electrodeposition was conducted under current density set at 8 A/dm² for initial 5 min, followed by increased to 40 A/dm². A current density of 40 A/dm² is a typical setting for electrodeposition process using a Sargent bath. Deposition was conducted for 2 min under this condition. The bath temperature was maintained at 323 K during electrodeposition. Cr plating of 3 μm in a thickness was obtained by the above described electrodeposition process. Finally, the rod end with Cr plating was cut into a disk of 4 mm thickness.

Table 1. Shot peening conditions for roughening of the substrate prior to electrodeposition

Peening apparatus	Air suction type, nozzle diameter: $\phi 6$ mm
Nozzle distance	100 mm
Shot particles	Tool steel fine particle ($\phi 50$ μm), resulting $R_a = 1.0$ μm Steel grit (approx. size 1000 μm), resulting $R_a = 3.5$ μm
Peening angle	90°
Peening pressure	0.3 MPa
Particle supply rate	1 g/s
Peening time	60 s for tool steel particle 120 s for steel grit

Then SP was conducted on two types of Cr-coated substrates, which were varied in the interfacial roughness, to induce microstructural changes around the coating-substrate interface. To elucidate the effect of particle shape on the SP-induced microstructural changes, two shot particles were chosen to be employed for SP: angular steel grits of approximately 1000 μm in size and spherical steel shots of 1000 μm in average diameter (Fig. 2). For angular grits, curvature radius at the sharpest corner in each grit was less than 100 μm . Peening time was ranged from 210–630 s to clarify how the microstructural changes occurred and progressed as a function of a peening time. Here peening time of 210 s corresponded to the time to reach the area coverage of 90% for Cr-plated workpieces. Table 2 lists detailed conditions of SP.

Four types of Shot-peened Cr-coated specimens were then examined by using electron probe micro analyzer (EPMA) to obtain elemental maps of Cr elements and Fe elements. EPMA observation was conducted on cross section of the specimens. Prior to the observation specimen were cut embedded into Wood's alloy and polished.

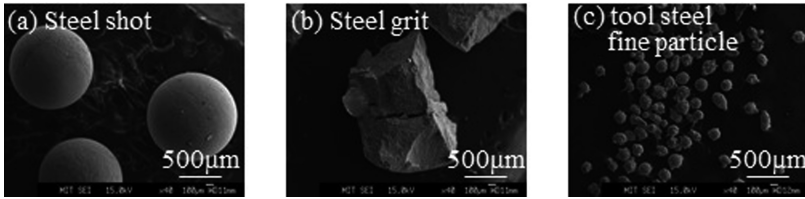


Fig. 2. Typical feature of particles used for SP. Note that tool steel fine particle was used for roughening step prior to electrodeposition.

Table 2. Conditions applied for SP on Cr-coated steel substrate

Peening apparatus	Air suction type, nozzle diameter: $\phi 6$ mm
Nozzle distance	100 mm
Shot particles	Steel shot ($\phi 1000$ μm), Steel grit (approx. size 1000 μm)
Peening angle	90°
Peening pressure	0.3 MPa
Particle supply rate	1 g/s
Peening time	210 s, 420 s, 630 s

3 Results and Discussions

3.1 Changes in Cr-Coated Steel Specimens Caused by SP

Figure 3 shows cross sectional elemental maps of Cr-coated specimens with ranged interfacial roughness. Note that SP as the final step had not conducted for these specimen. Results revealed that Cr-coatings were successfully deposited. The coatings completely followed along the roughened substrates.

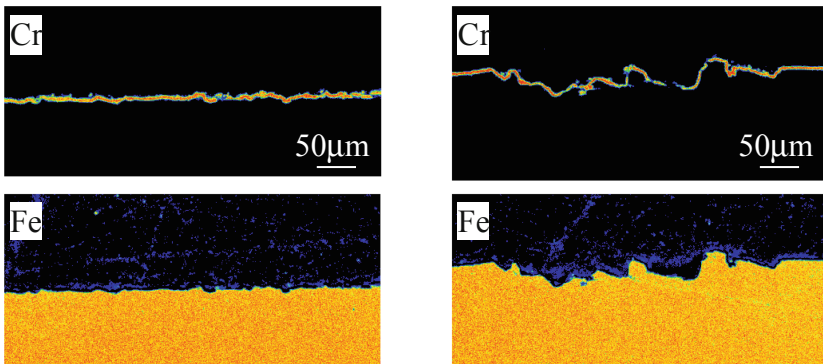


Fig. 3. EPMA elemental maps obtained from cross section of as-electrodeposited specimen. Left: interfacial roughness $R_a = 1.0$ μm , and right: interfacial roughness $R_a = 3.5$ μm

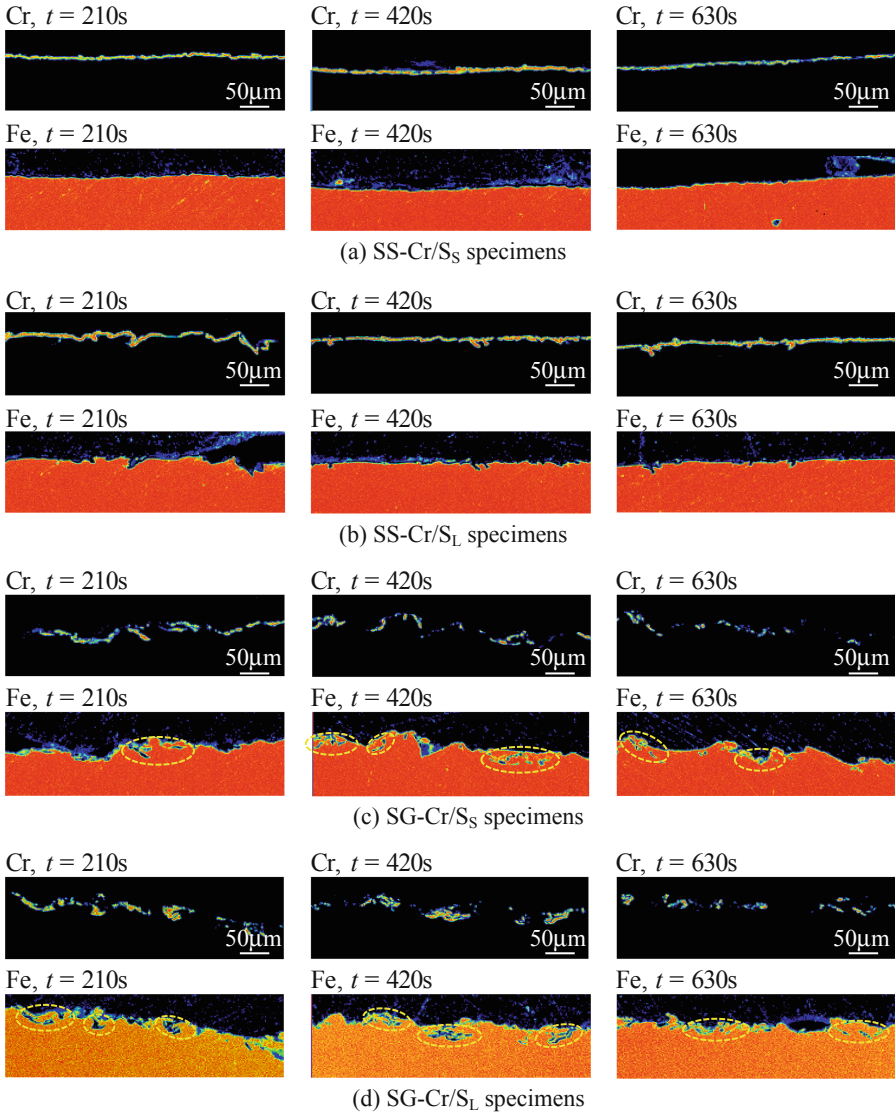


Fig. 4. EPMA elemental maps corresponding to Cr and Fe obtained from specimens treated with SP under ranged peening time t . For SG-Cr/S_s and SG-Cr/S_L specimens, yellow marks indicate the existence of embedded Cr fragments.

Figure 4 compared the elemental maps obtained from a variety of specimens which were prepared by the four sequences mentioned in Fig. 1 and under ranged peening time t for the final step of SP. For SG-Cr/S_s and SG-Cr/S_L specimens, it should be noted that fragments of Cr plating divided into small pieces owing to SP were embedded in the steel matrix. The embedded fragments were more clearly observed as

peening time increased. The fragments distributed approximately 15 μm in depth from the surface after 630 s. Results mentioned above proved mechanical mixing of Cr plating and steel substrate occurred when the Cr-coated surface was bombarded by angular steel grit. Resulting microstructure comprised of steel matrix and dispersed Cr fragments. This microstructure was created regardless of the interfacial roughness. Elemental maps corresponding to Fe and Cr indicated that both elements existed separately in the mixed structure. Thus it was considered mechanical alloying did not occur in case of this experiment although it has been reported mechanical alloying occurred due to severe plastic deformation.

In contrast, Cr plating was maintained on the substrate surface for the SS-Cr/S_L and SS-Cr/S_S specimens: shot-peened ones using spherical steel shot. Embedment of Cr fragments was not clearly observed for these specimens. This meant that collision of spherical particle did not provide enough driving force for mechanical mixing. Angular grit with sharp corner indented the surface with high contact pressure when it collided with the surface [11]. This feature should possibly accelerate the mechanical mixing process.

3.2 Quantitative Evaluation of Material Transport

As described above, SP using angular grit induced the mixing process, creating specific “composite” microstructure. Necessary nature to form such microstructure was to transport Cr fragments from top surface to material interior. To discuss more details, image processing of cross sectional EPMA elemental maps was attempted. The goal of the analysis was to realize how the Cr fragments moved during SP process. Thus, the maps (500 μm length \times 250 μm depth) which showed Cr elements distribution obtained from the specimens under ranged peening time were analyzed to determine the area of Cr plating appearing on the cross section.

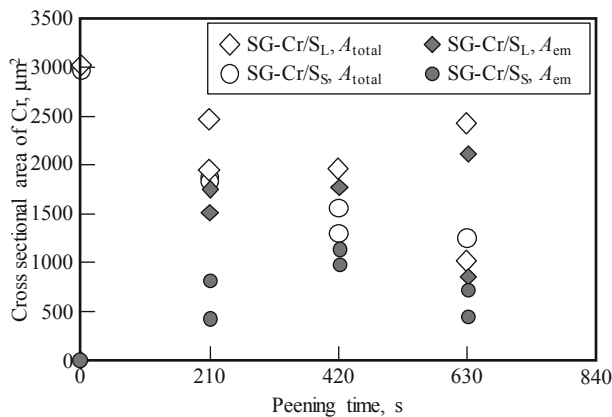


Fig. 5. Cross sectional area corresponding to Cr plating measured on the EPMA elemental maps. A_{total} : Total area of Cr plating, and A_{em} : area corresponding to embedded Cr fragments. Note that each individual plot corresponds to the result obtained from each examined point.

Figure 5 shows the cross sectional area corresponding to Cr plating measured on the cross sections as a function of peening time of final-step SP. Two points were examined for each specimen under ranged peening time. Results obtained from each point were plotted in the figure. Two classification of the cross sectional areas were compared in this figure: A_{total} and A_{em} . A_{em} was defined as the cross sectional area of the Cr fragments which located inside the substrate while A_{total} showed the area of Cr plating both of existing on the surface and being embedded. Result indicated that A_{total} declined with increasing peening time. This was resulted from erosive effect caused by SP. In contrast, A_{em} , corresponding to embedded Cr fragments increased with peening time increased and then turned into slight decrease. The rise in the earlier stage could be attributed to embedment of Cr fragments, and the following slight decrease was due to erosion. Thus, the erosion of Cr plating simultaneously occurred as mixing behavior progressed. The measurement conducted on one of the SG-Cr/S_L specimen revealed that A_{em} increased even after 630 s of SP while another one showed decreased value of A_{em} . This should be because mixing behavior was more dominant than erosive effect for the specimen. As SG-Cr/S_L specimens showed larger A_{em} than SG-Cr/S_S ones, larger roughness of the substrate possibly assisted to occur mixing effect.

For further investigation, each embedded fragments were carefully analyzed to characterize in terms of the cross sectional area and the position from the substrate surface. Figure 6 shows the relationship between the cross sectional area and the position for each individual fragment.

Results showed that the cross sectional areas of individual fragments were reduced with increasing peening time. Distribution of the fragments became deeper as peening time increased. Those results demonstrated that Cr fragments were pulverized and simultaneously transported as particles repeatedly collided with the Cr-coated surface. As discussed above, the driving force of this behavior should be severe plastic deformation of the substrate; materials flow of the substrate likely buried the prior surface accompanied with Cr plating. After peening time of 630 s, coarse fragments which were larger than $100 \mu\text{m}^2$ were no longer existed inside the steel matrix.

Consequently, the mechanism of the mixing process could be summarized as follows:

- (1) Cr plating which adhered on the substrate surface was divided into coarse pieces by particle collision.
- (2) Cr fragments were overlaid by deformed substrate, resulting in being embedded.
- (3) As particles collided with the surface, embedded fragments were pulverized into much finer pieces. The pieces were simultaneously transported into substrate interior. This was also resulted from overlaying by the deformed material.

In this process, the larger roughness at the coating/substrate interface accelerated the embedment of Cr fragment in the earlier stage of the SP; embedded fragments larger in size were observed in SG-Cr/S_L specimen than in SG-Cr/S_S one. This should be because intricate geometry of roughened interface assisted the substrate material to deform onto the coatings.

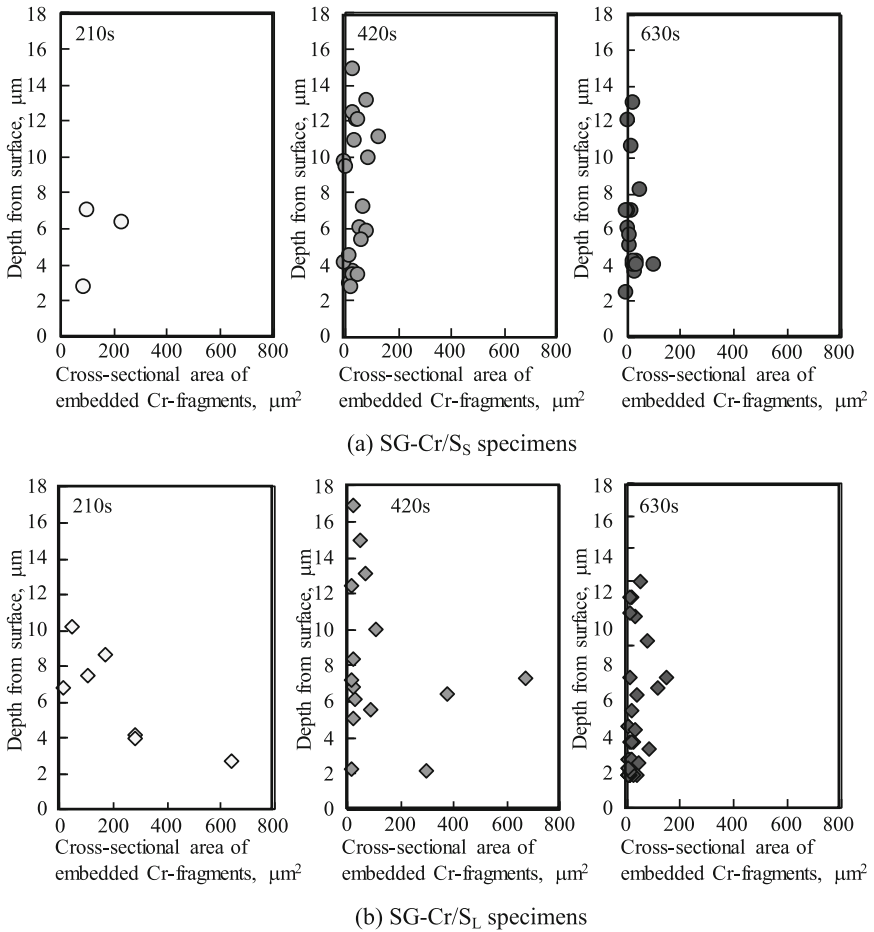


Fig. 6. Comparison in embedded Cr fragments depending on peening time. Each plot indicates the position and size of each individual fragments.

It was suggested that the findings in this study should be also applicable for peening process conducted on “uncoated” materials. It has reported that fine particle peening using relatively hard shot particle created lamellar microstructure in which elements transferred from the shot particle were concentrated below the surface [2]. In this case, elements transferred from the particle were embedded deeper as the peening progressed. This phenomenon could be attributed to the same mechanism found in this study: pulverization and simultaneous transportation due to deformation of the substrate.

4 Conclusions

As a new benefit induced by shot peening (SP), this paper focused on microstructural changes in shot-peened surface. SP was conducted on chromium-coated steel substrate to investigate SP-induced mechanical mixing behavior at the coating-substrate interface. This study concluded as follows:

- (1) Specific microstructure which consisted of chromium fragments and steel matrix was created by SP conducted on chromium-coated steel substrate.
- (2) The mixing effect was enhanced by employing angular-shaped shot particles for SP, and accelerated by roughening the steel substrate surface prior to deposition of chromium coating.
- (3) Formation of the mixed structure progressed because chromium coating was pulverized and simultaneously transported into steel substrate during SP process. The driving force of those behaviors should be mechanical impact and severe plastic deformation of the substrate caused by particle collision.

References

1. Kameyama, Y., Ohmori, H., Kasuga, H., Kato, T.: Fabrication of micro-textured and plateau-processed functional surface by angled fine particle peening followed by precision grinding. *CIRP Annals* **64**(1), 549–552 (2015)
2. Kameyama, Y., Komotori, J.: Effect of micro ploughing during fine particle peening process on the microstructure of metallic materials. *J. Mater. Process. Technol.* **209**(20), 6146–6155 (2009)
3. Kameyama, Y., Komotori, J.: Tribological properties of structural steel modified by fine particle bombardment (FPB) and diamond-like carbon hybrid surface treatment. *Wear* **263**(263), 1354–1363 (2007)
4. Kameyama, Y., Nishimura, K., Sato, H., Shimpo, R.: Effect of fine particle peening using carbon-black/steel hybridized particles on tribological properties of stainless steel. *Tribol. Int.* **78**, 115–124 (2014)
5. Kikuchi, S., Yoshida, S., Nakamura, Y., Nambu, K., Akahori, T.: Characterization of the hydroxyapatite layer formed by fine hydroxyapatite particle peening and its effect on the fatigue properties of commercially pure titanium under four-point bending. *Surf. Coat. Technol.* **288**, 196–202 (2016)
6. Kikuchi, S., Nakamura, Y., Nambu, K., Akahori, T.: Formation of hydroxyapatite layer on Ti–6Al–4 V ELI alloy by fine particle peening. *Int. J. Autom. Technol.* **11**(6), 915–924 (2017)
7. Takesue, S., Saito, S., Komotori, J., Misaka, Y., Kawasaki, K.: Surface properties of intermetallic compound layer formed on titanium alloy by AIH-FPP (atmospheric controlled induction heating fine particle peening) treatment. *Mater. Trans.* **59**(9), 1452–1457 (2018)
8. Liu, G., Wang, S.C., Lou, X.F., Lu, K.: Low carbon steel with nanostructured surface layer induced by high-energy shot peening. *Scripta Mater.* **8**, 1791–1795 (2001)
9. Takagi, S., Kumagai, M., Ito, Y., Konuma, S., Shimodaira, E.: Surface Nanocrystallization of Carburized Steel JIS-SCr420 by Fine Particle Peening. *Tetsu-to-Hagane* **92**(5), 318–326 (2006). (in Japanese)

10. Nakamura, N., Takagi, S.: Near-surface nanocomposite structure on commercial purity aluminum induced by fine particle bombardment. *Mater. Trans.* **52**(3), 380–385 (2011)
11. Kitamura, T., Terasaki, T., Akiyama, T.: Effect of grain shapes on residual stress distribution due to shot peening. *J. Soc. Mater. Sci. Japan* **49**(6), 651–654 (2000)



Investigation on Theoretical Analysis of Residual Stress Distribution Induced by Shot Peening in 2397 Aluminum-Lithium Alloy

Yukui Gao^(✉) and Xuefei Tao

School of Aerospace Engineering and Applied Mechanics, Tongji University,
100 Zhangwu Road, Shanghai 200092, China
ykgaol2088@126.com, 1710849@tongji.edu.cn

Abstract. In order to investigate the effect of shot peening (SP) on residual stress distribution, an amendatory theoretical model considering the effects of friction between shots and treated component has been proposed based on Hertz contact theory. The residual stress field induced by shot peening in 2397 Aluminum-Lithium alloy was considered as an example. To verify the theory, the residual stresses field along the depth in 2397 Aluminum-Lithium alloy was measured by means of X-ray diffraction method, accompanied by layer removal technique. The distributions of residual stresses derived from experimental results were in good accordance with theoretical model, while the minor errors still existed among them. The slight errors are mainly ascribed to surface roughness, ideal elastoplastic constitutive model and crystallographic textures. As a result, the theoretical model and corresponding algorithm can be applied to predict residual stresses fields under various shot peening conditions for Aluminum-Lithium alloys and other metallic materials, as well.

Keywords: Shot peening · Residual stress field · Hertz theory · Aluminum-Lithium alloy

1 Introduction

Over the past decades, shot peening, a surface modification technique, has long been extensively employed in aviation industry to improve the fatigue life of metallic materials through introducing compressive residual stress field and work hardening, etc. [1]. Many researches have shown that compressive residual stress plays a vital role in postponing the initiation and propagation of cracks, thus enhancing the fatigue resistance [2]. Consequently, how to exactly determine and subsequently design the residual stress field is of great significance. In most cases, it could be measured by various experimental approaches, such as hole-drilling method [3], X-ray diffraction [4] and neutron diffraction [5], etc. However, most of them are destructive and time-consuming especially when the intention is to obtain the in-depth residual stress field, preventing further in-service employment of the measured components. Therefore, finite element method (FEM) has been operated. Prof. Guagliano [6] proposed a

numerical approach to relate Almen intensity to residual stress field induced by shot peening. Prof. Meguid [7] proposed a 3D finite element model with randomly distributed shots considering strain rate dependent plasticity, which has been proven to be a powerful tool in investigating the mechanisms of peening treatment. But to a large extent, the accuracy of numerical results mostly depends on the mesh size, boundary condition and convergence [8, 9]. FEM models are rather time and resources consuming as well.

To break through the dilemma, there is a growing body of literature using theoretical and empirical methods to ascertain residual stress fields [10, 11]. Their empirical and analytical equations do have some scientific significance, but up to date, researchers have not treated friction in much detail. However, in shot peening, especially in conventional shot peening without water, the effect of friction must be paid enough attention since the frictional heat will certainly expend some of the kinetic energy of shots, thus affecting the distribution of residual stresses. In addition, the plastic deformation combined with the heat induced by shot peening may also bring about phase transformation and dynamic recovery or dynamic recrystallization, which can act as contributors to the change of residual stresses. This phenomenon has been researched by Chen *et al.* [8], and they presented a qualitative description that temperature rise resulted from friction would decrease the value of compressive residual stress. Nevertheless, a quantitative model is still lacking.

In this work, in line with the Hertz contact theory, we proposed a new methodology for assessing the residual stress distribution introduced by shot peening theoretically by considering the effects of friction between shots and specimen. The theoretical data was corroborated by comparison with experimental results of residual stress field induced by shot peening in 2397 Al-Li alloy. Hence, the convenience and veracity enable the ameliorative model and its corresponding algorithm to a wider application in determining and designing residual stresses distributions not only in Al-Li alloys but also in other metallic components. What's more, it can also pave a way towards a better design of shot peening parameters with respect to the mechanical properties of target materials.

2 Theoretical Analysis

2.1 Hertz Contact Theory Between Elastic Shot and Semi-infinite Elastic Specimen

The impact of shots on specimen has been developed by Johnson *et al.* [12]. The schematic diagram of Hertz contact between two spheres can be viewed in Fig. 1.

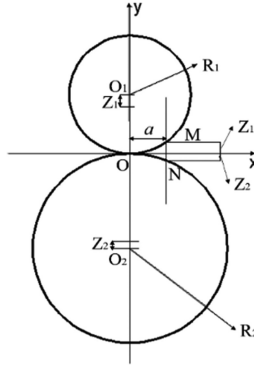


Fig. 1. Schematic diagram of Hertz contacts between two spheres.

The total load P applied on the specimen can be obtained by integrating pressure distribution in elastic contact area [12]:

$$P = \left(\frac{4E_H}{3}\right)R^{1/2}\delta^{3/2} \tag{1}$$

The energy transformation can be utilized to illustrate the characteristics of contact between shot and specimen. Considering the effects of friction between shots and specimen, the initial kinetic energy of an impacting shot can be converted into two parts, i.e. elastic work and friction work:

$$\frac{1}{2} \left(\frac{\pi\rho D^3}{6}\right)(V\sin\theta)^2 = \int_0^{\delta^*} Pd\delta + \int_0^{S_{max}} F_t ds \tag{2}$$

In which D , ρ and V correspond to the diameter, density and velocity component of shot, respectively; θ is the incident angle; δ^* is the maximum relative displacement between shot and specimen, S_{max} denotes the maximum relative tangential displacement between shot and specimen.

According to reference [12], the tangential displacement of an impact is:

$$s = F_t \cdot \frac{(2 - \nu_t)(1 + \nu_t)}{a_e E_t} \tag{3}$$

$$ds = \mu \left(\frac{4E_H}{3}\right)(2 - \nu_t)(1 + \nu_t)d\delta$$

and the force of friction can be expressed as:

$$F_t = \mu P = \mu \left(\frac{4E_H}{3}\right)R^{1/2}\delta^{3/2} \tag{4}$$

Then Eq. 2 can be resolved as:

$$\frac{1}{2} \left(\frac{\pi \rho D^3}{6} \right) (V \sin \theta)^2 = \int_0^{\delta^*} \left(\frac{4E_H}{3} \right) R^{1/2} \delta^{3/2} d\delta + \int_0^{\delta^*} \mu \left(\frac{4E_H}{3} \right) \left(\frac{D}{2} \right)^{1/2} \delta^{3/2} \cdot \mu \left(\frac{4E_H}{3E_t} \right) (2 - \nu_t)(1 + \nu_t) \cdot d\delta = \mu^2 \left(\frac{16E_H^2}{9E_t} \right) R^{1/2} (2 - \nu_t)(1 + \nu_t) \frac{2}{5} \delta^{*2/5} \quad (5)$$

Therefore, the maximum relative displacement δ^* can be derived as:

$$\delta^* = \left\{ \frac{\frac{1}{2} \cdot \frac{\pi \rho D^3}{6} \cdot (V \sin \theta)^2}{\frac{2}{5R^{1/2}} \cdot \frac{4E_H}{3} \cdot \left[1 + \mu^2 \left(\frac{4E_H}{3E_t} \right) (2 - \nu_t)(1 + \nu_t) \right]} \right\}^{2/5} \quad (6)$$

Then the radius of the maximum elastic contact area a_e^* is:

$$a_e^* = R \cdot \left\{ \frac{5}{4} \cdot \frac{\pi \rho (V \sin \theta)^2}{E_H \left[1 + \mu^2 \left(\frac{4E_H}{3E_t} \right) (2 - \nu_t)(1 + \nu_t) \right]} \right\}^{1/5} \quad (7)$$

The maximum elastic force p_0^* can be determined as:

$$p_0^* = \frac{1}{\pi} \cdot \left[\frac{40 \pi \rho E_H^4 (V \sin \theta)^2}{1 + \mu^2 \left(\frac{4E_H}{3E_t} \right) (2 - \nu_t)(1 + \nu_t)} \right]^{1/5} \quad (8)$$

2.2 Elastic-Plastic Analysis of Loading Process

The three principle stresses and the corresponding equivalent stress and strain based on Von Mises criteria can be stated as:

$$\sigma_{xe} = \sigma_{ye} = -P_0 \cdot \left[-\frac{1}{2}M + (1 + \nu)T \right] \quad (9)$$

$$\sigma_{ze} = -P_0 \cdot M \quad (10)$$

where

$$M = \left[1 + \left(\frac{z}{a_e^*} \right)^2 \right]^{-1} \quad (11)$$

$$T = 1 - \frac{z}{a_e^*} \arctan \left(\frac{a_e^*}{z} \right) \quad (12)$$

$$\sigma_{ie} = \frac{\left[(\sigma_{xe} - \sigma_{ye})^2 + (\sigma_{ye} - \sigma_{ze})^2 + (\sigma_{ze} - \sigma_{xe})^2 \right]^{1/2}}{\sqrt{2}} \quad (13)$$

$$\varepsilon_{ie} = \frac{\sigma_{ie}}{E_t} \quad (14)$$

During the process of elastic-plastic deformation, the plastic strain can be deduced from a simplified ideal elastoplastic constitutive model:

$$\varepsilon_p = \begin{cases} \varepsilon_e & \text{for } \varepsilon_e < \varepsilon_s \\ \varepsilon_s + \alpha(\varepsilon_e - \varepsilon_s) & \text{for } \varepsilon_e > \varepsilon_s \end{cases} \quad (15)$$

In Eq. 15, α is the ratio between the radius of the maximum plastic contact area a_p^* and the radius of the maximum elastic contact area a_e^* , while ε_s is the strain corresponding to the yield strength σ_s :

$$\varepsilon_s = \frac{\sigma_s}{E_t} \quad (16)$$

The maximum radius of plastic contact area a_p^* can be calculated based on the assumption that the incident angle of an impacting shot is 90° , making a perfect dent on the surface of specimen, as is shown in Fig. 2.

$$\frac{4\pi}{3} \rho R^3 \frac{dV}{dt} = \pi a_p^2 \bar{p} \quad (17)$$

where \bar{p} is the average pressure applied by shot on the dent, V is the initial velocity of shot, and δ_p is the relative plastic displacement between the centers of two objects. Since $V = d\delta_p/dt$ and $\frac{dV}{dt} = V \frac{dV}{d\delta_p}$, then Eq. 17 can be interpreted as:

$$\frac{4\pi}{3} \rho R^3 V \frac{dV}{d\delta_p} = \pi a_p^2 \bar{p} \quad (18)$$

In accordance with the Pythagorean theorem, the geometrical relationship for the plastic dent, as shown in Fig. 2, can be expounded as:

$$R^2 = a_p^2 + (R - \delta_p)^2 \quad (19)$$

Since δ_p is much smaller than R , δ_p^2 can be omitted and Eq. 19 can be switched to:

$$a_p = \sqrt{2\delta_p R} \quad (20)$$

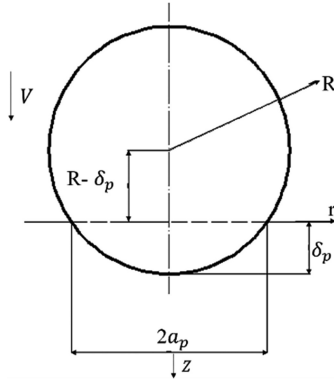


Fig. 2. Schematic diagram of plastic contact [10].

Substitute Eq. 20 into Eq. 18 and integrate Eq. 18, the maximum plastic depth of a dent can be made clear:

$$\delta_p^* = \sqrt{\frac{2\rho R^2 V^2}{9\sigma_s}} \quad (21)$$

In which \bar{p} is a constant and it is supposed to be $9\sigma_s$. Then the maximum radius of plastic contact area can be calculated as:

$$a_p^* = R \left(\frac{8\rho V^2}{9\sigma_s} \right)^{1/4} \quad (22)$$

If the incident angle is not 90° , Eq. 22 can be replaced as:

$$a_p^* = R \left(\frac{8\rho (V \sin\theta)^2}{9\sigma_s} \right)^{1/4} \quad (23)$$

The plastic stress can thus be derived from elastic-plastic stress-strain curve:

$$\sigma_p = \begin{cases} \sigma_e & \text{for } \varepsilon_p < \varepsilon_e \\ \sigma_s + H(\varepsilon_p - \varepsilon_s) & \text{for } \varepsilon_s \leq \varepsilon_p \leq \varepsilon_b \\ \sigma_b & \text{for } \varepsilon_p > \varepsilon_b \end{cases} \quad (24)$$

where H is a linear strain-hardening parameter and σ_b is the tensile strength of specimen, while ε_s and ε_b are strain corresponding to the yield strength and tensile strength of specimen, respectively.

2.3 Analysis of Rebounding Process

Following the peening is the process of rebounding. The analysis of this process is conducted with the following assumptions: (1) the specimen is isotropic even when work hardening happens; (2) the deformation induced by shot peening is rather small as compared with the bulk of specimen; (3) the process of rebounding is elastic unless there is reverse yielding; (4) the hydrostatic stress will not lead to plastic deformation.

Accordingly, when the coverage is below 100%, the induced stress can be calculated as:

$$\sigma_{ij}^1 = \begin{cases} 0 & \text{for } \sigma_e < \sigma_s \\ s_{ij}^p - s_{ij}^e & \text{for } \sigma_s \leq \sigma_e \leq 2\sigma_p \end{cases} \quad (25)$$

The three stresses in x , y and z directions respectively are:

$$\begin{aligned} \sigma_x^t &= \sigma_y^t = \frac{1}{3}(\sigma_p - \sigma_e) \\ \sigma_z^t &= -2\sigma_x^t \end{aligned} \quad (26)$$

If $\sigma_e > 2\sigma_p$, reverse yielding and work hardening will happen. Firstly, the $2\sigma_p$ can be unloaded and then yielding come into emergence. However, some residual stresses cannot be fully released:

$$\Delta\sigma_e = \sigma_e - 2\sigma_p \quad (27)$$

The elastic strain corresponding to $\Delta\sigma_e$ is:

$$\Delta\varepsilon_e = \frac{\Delta\sigma_e}{E_t} \quad (28)$$

The plastic strain can be determined as:

$$\Delta\varepsilon_p = \alpha \cdot \Delta\varepsilon_e \quad (29)$$

And the plastic stress is:

$$\Delta\sigma_p = H\Delta\varepsilon_p \quad (30)$$

In this case, the three principal stresses in x , y and z directions respectively are:

$$\begin{aligned} \sigma_x^t &= \sigma_y^t = \frac{1}{3(-\sigma_p - \Delta\sigma_p)} \\ \sigma_z^t &= -2\sigma_x^t \end{aligned} \quad (31)$$

When the coverage reaches 100%, the induced stress can be obtained as:

$$\begin{aligned} \sigma_x^{ind} &= \sigma_y^{ind} = \frac{1+\nu}{1-\nu}\sigma_x^t \\ \sigma_z^{ind} &= 0 \end{aligned} \quad (32)$$

2.4 Residual Stress Distribution in the Thin Plate

The residual stress distribution calculated previously is with the hypothesis of semi-infinite body. But the real specimens, especially those thin plates, will have finite thickness so that the boundary condition provided by semi-infinite model ought to be released. As a consequence, an extra axial force (F_x) and bending moment (M_x) should be superimposed to the previously calculated σ^{ind} so that a balance is reached.

$$\int_0^h \sigma_x^{ind} b dz + F_x = 0 \quad (33)$$

$$\int_0^h \sigma_x^{ind} \left(\frac{h}{2} - z \right) b dz + M_x = 0 \quad (34)$$

where b is the width of specimen while h is the thickness of it. Finally, the residual stress distribution induced by shot peening can be deciphered as follows:

$$\sigma_x^{res} = \sigma_x^{ind} + \sigma_x^s + \sigma_x^b = \sigma_x^{ind} + \frac{F_x}{A} + \frac{M_x \left(\frac{h}{2} - z \right)}{I} \quad (35)$$

where A is cross-sectional area of specimen, σ_x^s is the axial stress derived from F_x , σ_x^b is the bending stress derived from M_x and $I = 1/12 \cdot b \cdot h^3$.

2.5 The Algorithm Corresponding to the Theoretical Model

Taken as an example, the residual stress field of 2397 Al-Li alloy produced by S110 cast steel shots with an intensity of 0.3 mmA was analyzed. Basic mechanical properties of S110 cast steel shot and 2397 Al-Li alloy are listed in Table 1.

Table 1. Mechanical properties of S110 cast steel shot and 2397 Al-Li alloy.

	Young's modulus (GPa)	Poisson's ratio	Density (kg/m ³)	Yield strength (MPa)	Tensile strength (MPa)	Elongation (%)
S110	210	0.31	7800	1693	/	/
2397 Al-Li	69.31	0.341	2650	423	473	7

With reference to [13], the height of Almen strip after being shoot can be determined as:

$$h' = \frac{3M_x l^2}{2Ebt^3} \quad (36)$$

And regarding A-type strip: $E = 200$ Gpa, $l = 31.75$ mm (l is the distance for measuring Almen intensity), $b = 18.95$ mm and $h = 1.295$ mm.

After calculation and fitting through Matlab 2016R, the relationship between intensity of A-type strip and velocity of shot can be predicted by Eq. 37. In this fitting formula, the variance $R^2 = 1$ while the fitting curve is depicted in Fig. 3.

$$\text{Intensity} = 0.08189 \cdot V^{0.4991} - 0.04947 \tag{37}$$

where V is the initial velocity of shot.

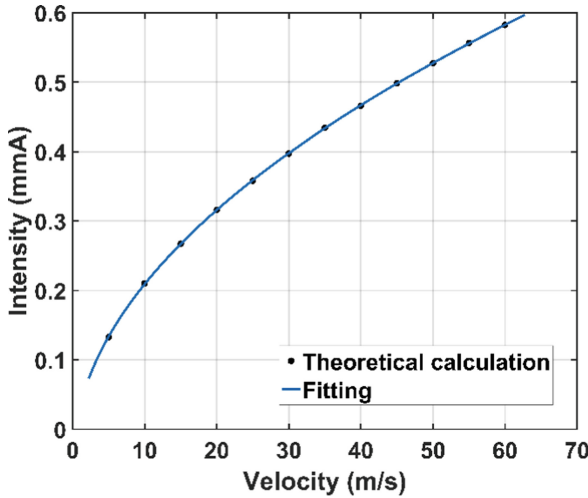


Fig. 3. The fitting curve of relationship between velocity of shot and intensity of A-type strip.

On the basis of the intercorrelation between velocity and intensity derived above, the velocity of shot corresponding to the intensity of 0.3 mmA is approximately 18.5 m/s. Then the procedure can be displayed as follows:

Step 1: Input parameters (The mechanical properties are shown in Table 1.)

1. Cast steel shot: $D_s = 0.36$ mm, $R = D/2 = 0.18$ mm, $V = 18.5$ m/s, coulomb friction coefficient $\mu = 0.2$, $\theta = 90^\circ$, $E_H = \frac{1}{\frac{1-\nu_s^2}{E_s} + \frac{1-\nu_t^2}{E_t}}$
2. AA2397 Al-Li alloy: $h = 4$ mm, $b = 40$ mm, $\varepsilon_s = \sigma_y/E_t$, $H = (\sigma_b - \sigma_y)/(\varepsilon_b - \varepsilon_s)$

Step 2: Analysis

3. Calculate a_e^* and p_0^* through Eq. 7 and Eq. 8 respectively.
4. $a_p^* = R \times \left(8 \times \rho_s \times (V \sin \theta)^2 / (9 \times \sigma_y) \right)^{1/4}$
5. Calculate $\alpha = a_p^* / a_e^*$.
6. For each depth along z -direction from surface of specimen through the whole depth with an increment of $1e^{-5}$, calculate the following parameters:

- Calculate M , T , σ_{xe} , σ_{ye} , σ_{ze} , σ_{ie} , ε_{ie} with the help of Eq. 11 ~ Eq. 14.
 - Calculate ε_p , σ_p and σ_x^t , σ_y^t , σ_z^t with the help of Eqs. 15, 24 and 31.
 - Calculate σ_x^{ind} with Eq. 32.
 - Integrate F_x and M_x with the help of Eq. 33 and Eq. 34, respectively.
7. Finally, calculate residual stress with Eq. 35.

The calculated residual stress field of 2397 Al-Li alloy induced by shot peening is set out in Fig. 5 in the next section. Compressive residual stresses are introduced in the surface layer of specimen and the maximum compressive residual stress locates in subsurface due to the stress relaxation caused by severe plastic deformation on the surface. Beneath the compressive residual stresses, tensile residual stresses exist to balance it and along the thickness of specimen, the integration of residual stress is zero.

3 Experimental Procedure

To illuminate the reliability of theoretical model, the measurements of in-depth residual stresses were performed by means of XRD using PROTO LXR D X-ray diffractometer (Radiation Co-K α , irradiated area 1 mm², $\sin^2\varphi$ method, 9 diffraction angles (2θ) from -40° to 40°). Experimental facilities and specimen are shown in Fig. 4.

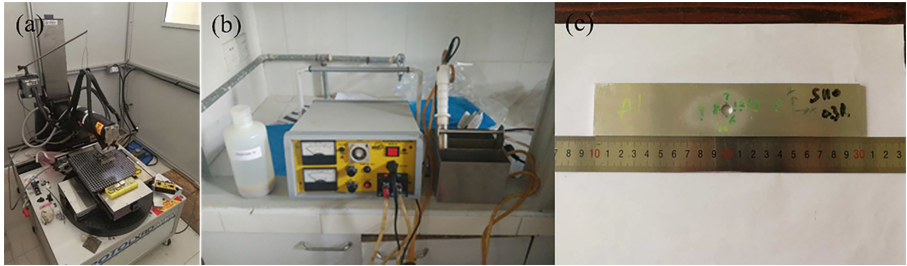


Fig. 4. Experimental setup (a) PROTO LXR D X-ray diffractometer (b) electrochemical polishing instrument and (c) specimen.

In order to gain the in-depth residual stress, the thin surface layer was successively removed by electro-polishing method. For the reason of stress relaxation, the experimental results need to be corrected by the Eq. 38 [14].

$$\sigma_c(z) = \sigma_m(z) - 4\sigma_m(h) \left(\frac{h-z}{h} \right) \quad (38)$$

In Eq. 38, z is the depth from the lower surface to the point we are interested in, σ_m is the measured residual stress, σ_c is the residual stress after correction and h is the initial thickness of whole specimen.

Figure 5 reveals the measured residual stresses and those after correction as well as the theoretical one. It is clear that stresses after correction are slightly smaller than those

uncorrected owing to stress relaxation during electro-polishing removal. Though slightly different, the whole trend fits well with those acquired from theoretical model.

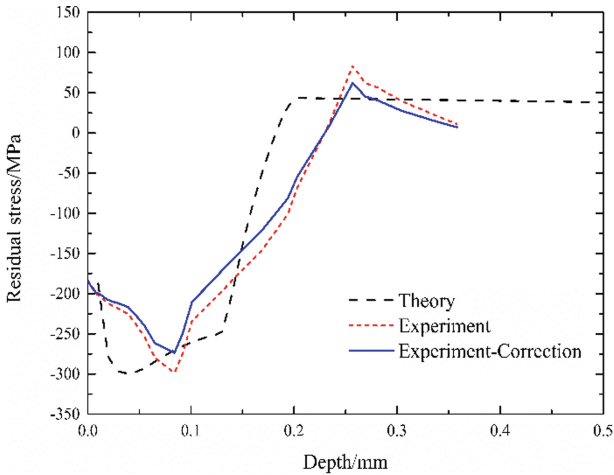


Fig. 5. Residual stress field derived by theoretical model and experiments.

The residual stress fields gotten from foregoing two methods and the four critical parameters [10] (with their relative errors) determining the profile of residual stress distribution are listed in Table 2.

Table 2. Four critical parameters of residual stress field and their respective relative errors.

	Theoretical	Experiment	Experiment-correction
σ_{srs}	-187.388	-183.88 (1.87%)	-183.88 (1.87%)
σ_{mcrs}	-299.713	-273.646 (8.76%)	-273.645 (8.7%)
σ_{mtrs}	43.43	62.155 (43%)	62.15 (43.1%)
Z_0	0.19	0.234 (23.16%)	0.234 (23.16%)

This study is exploratory and interpretative in nature. From the above results, the residual stress distribution acquired by two methods all imply that a considerable depth of specimen is characterized with significant compressive residual stresses and tensile residual stresses beneath them. The overall trends are similar. It is reasonable to predict, determine and design the residual stress distribution by means of the modified theoretical model along with its relevant algorithm though some slight differences still exist. The deviations are mainly attributed to the following reasons:

1. In theoretical analysis, ideal elastoplastic model is welded to calculate the plastic stress and strain, which is a little deviant from real material. The effects of work hardening or work softening are overlooked.
2. The residual stress obtained from theoretical model is distributed throughout the whole depth of specimen. In practical measurements, however, the depth of affected layer is rather limited. It can be explained by the fact that, in this theory, the plate is supposed to be rather thin so that the effects of axial force F_x and bending moment M_x can not be neglected. But the specimen is relatively thick, weakening the effects of axial force and bending moment.
3. The increased surface roughness neglected in theoretical analysis is another factor resulting in the difference. During experimental measurements, the high points in the rough surface contribute more to the X-ray diffraction which may bring in deviances to experimental results especially at topmost surface. Composite shot peening can be utilized to reduced surface roughness.
4. In addition, there exist some rolling textures in the specimen, especially in the subsurface beneath the modified layer produced by shot peening, which make X-ray diffraction peaks rather diffused, leading to experimental errors. To get rid of this problem, residual stresses can be measured by hole-drilling method in the future investigation.
5. Finally, the difference between single point of impact in theoretical analysis and multiple impacts in practical experiment is another factor influencing the relative error. The methodology is just an approximation of the real process. In practical experiment, the residual stress is the result of plastic deformation produced by multiple shots overlapping on one another, which is a little deviant from ideal distributions of residual stresses.

4 Conclusion

This paper proposed a modified theoretical model considering the effect of friction between shots and specimen on the basis of Hertz contact theory. From the perspective of energy transformation, the kinetic energy of shot transforms into plastic work and friction work, so that the effect of friction ought to be well investigated. The optimized model together with relevant algorithm are more accurate than those that simply represent the contribution of friction by a factor. Moreover, experiments are conducted to validate the credibility of the theoretical model. The residual stress distributions derived from experiment are consistent with that of theory while slight differences are primarily put down to the differences between constitutive model, surface roughness, crystallographic textures and the difference between single point of impact in theoretical analysis and multiple impacts in practical experiment. All in all, the present model as well as its relevant algorithm can act as a useful tool to determine and design residual stress distributions by applying appropriate shot peening parameters.

References

1. Mahmoudi, A.H., Ghasemi, A., Farrahi, G.H., Sherafatnia, K.: A comprehensive experimental and numerical study on redistribution of residual stresses by shot peening. *Mater. Des.* **90**, 478–487 (2016). <https://doi.org/10.1016/j.matdes.2015.10.162>
2. Gao, Y.K., Wu, X.R.: Experimental investigation and fatigue life prediction for 7475-T7351 aluminum alloy with and without shot peening-induced residual stresses. *Acta Mater.* **59**, 3737–3747 (2011). <https://doi.org/10.1016/j.actamat.2011.03.013>
3. Kim, C.H.: Investigation on the hole-producing techniques of residual-stress measurement by incremental hole-drilling method in injection molded part. *Fiber Polym.* **19**, 1776–1780 (2018). <https://doi.org/10.1007/s12221-018-8332-7>
4. Wu, L.H., Jiang, C.H.: Effect of shot peening on residual stress and microstructure in the deformed layer of Inconel 625. *Mater. Trans.* **58**, 164–166 (2017). <https://doi.org/10.2320/matertrans.M2016298>
5. Farajian, M., Hardenacke, V., Pfeiffer, W., Manuela, K., Joana, R.K.: Numerical and experimental investigations on shot-peened high-strength steel by means of hole drilling, X-ray, synchrotron and neutron diffraction analysis. *Mater. Test.* **59**, 161–165 (2017). <https://doi.org/10.3139/120.110978>
6. Guagliano, M.: Relating Almen intensity to residual stresses induced by shot peening: a numerical approach. *J. Mater. Process. Tech.* **110**, 277–286 (2010). [https://doi.org/10.1016/S0924-0136\(00\)00893-1](https://doi.org/10.1016/S0924-0136(00)00893-1)
7. Chen, Z., Yang, F., Meguid, S.A.: Realistic finite element simulations of arc-height development in shot-peened Almen strips. *J. Eng. Mater. Technol.* **136**, 041002 (2014). <https://doi.org/10.1115/1.4028006>
8. Chen, J.S., Desai, D.A., Heyns, S.P., Pietra, F.: Literature review of numerical simulation and optimization of the shot peening process. *Adv. Mech. Eng.* **11**, 1–19 (2019). <https://doi.org/10.1177/1687814018818277>
9. Kim, T., Lee, J.H., Lee, H., Cheong, S.K.: An area-average displacement to peening residual stress under multi-impacts using a three-dimensional symmetry-cell finite element model with plastic shots. *Mater. Des.* **31**, 50–59 (2010). <https://doi.org/10.1016/j.matdes.2009.07.032>
10. Gao, Y.K., Yao, M., Li, J.K.: An analysis of residual stress fields caused by shot peening. *Metall. Mater. Trans. A* **33**, 1775–1778 (2002). <https://doi.org/10.1007/s11661-002-0186-2>
11. Miao, H.Y., Larose, S., Perron, C., Levesque, M.: An analytical approach to relate shot peening parameters to Almen intensity. *Surf. Coat. Tech.* **205**, 2055–2066 (2010). <https://doi.org/10.1016/j.surfcoat.2010.08.105>
12. Johnson, K.L.: *Contact Mechanics*. Cambridge University Press, Cambridge (1987)
13. Guagliano, M.: Relating Almen intensity to residual stresses induced by shot peening: a numerical displacement. *J. Mater. Process. Tech.* **110**, 277–286 (2001). [https://doi.org/10.1016/S0924-0136\(00\)00893-1](https://doi.org/10.1016/S0924-0136(00)00893-1)
14. Shepard, M.J.: Laser shock processing induced residual compression: impact on predicted crack growth threshold performance. *J. Mater. Eng. Perform.* **14**, 495–502 (2005). <https://doi.org/10.1361/105994905X56214>



Effect of Shakedown on the Fatigue Limit of Ultrasonic Shot Peened Steel

Jinta Arakawa¹, Yoshiichirou Hayashi², Hiroyuki Akebono¹ (✉),
and Atsushi Sugeta¹

¹ Hiroshima University, 1-4-1 Kagamiyama,
Higashi-Hiroshima, Hiroshima, Japan
akebono@hiroshima-u.ac.jp

² Electric Power Development Co., Ltd., Chigasaki, Kanagawa, Japan

Abstract. We performed in-plane bending fatigue tests under controlled load conditions on ASTM 309 stainless steel specimens with surface compressive residual stress. The results provide a fatigue limit of 415 MPa, which agrees with the value of 404 MPa calculated based on a modified Goodman line considering shakedown. Therefore, the surface layer was clearly restricted by the internal bulk and was relieved under controlled displacement, after which shakedown occurred. Then, the fatigue limit of the metal material with surface compressive residual stress should be estimated by using a modified Goodman line considering shakedown to avoid unexpected fractures that could occur by following a modified Goodman line that does not consider shakedown.

Keywords: Shakedown · Modified Goodman line · Compressive residual stress

1 Introduction

Quenching and heat treatment, which are applied to the entire body of a metal component, enhance the fatigue resistance of metals subjected to tension-compression [1–3]. Microstructure modifications, such as carburizing and nitriding, and various peening methods can improve the fatigue resistance of non-welded metal components and welded connections [4–10]. It is clear that shot peening introduces a high hardness and a high compressive residual stress on the material surface, which enhances the fatigue strength of the material [11–14]. A variety of peening techniques exist; furthermore, a variety of reports have discussed the fatigue strengths of peened metals and have shown that peening enhances fatigue strength. Authors also investigated in previous studies, the effect of USP on the fatigue strength of ASTM CA6NM cast stainless steel, which is used in hydroelectric turbine runners [15]. According to the fatigue tests, the shot-peened specimens had higher fatigue strengths than untreated specimens, and the fatigue limit of the peened material was 60% greater than that of the untreated material. Furthermore, the authors reported that the effect of USP treatment on the fatigue strength of a metal can be quantitatively evaluated by using the values of Vickers hardness and compressive residual stress introduced by USP treatment on the surface layer. Therefore, the surface compressive residual stresses generated by surface

treatments are effective factors for improving the fatigue strengths of metals. However, it can be thought that the material with surface compressive residual stress may cause shakedown phenomenon in the surface layer even if the material is subjected to controlled load conditions, because the surface layer is under controlled displacement conditions during fatigue tests due to the restriction of the internal bulk area. Therefore, according to this idea, it can be implied that a large compressive residual stress does not dramatically improve the fatigue strength of a material, because the surface compressive residual stress layer reaches the yield stress point during cyclic fatigue tests, which generates the shakedown phenomenon. However, there are few reports about the fatigue limit behaviors related to the shakedown phenomenon of a material with surface compressive residual stress. Furthermore, the authors evaluated the fatigue limit based on assuming the occurrence of shakedown behavior by using a modified Goodman line in previous study [15]; however, the authors could not define the existence of the shakedown behavior perfectly. Therefore, in our study, objective is to determine whether the shakedown behavior should be taken into account for the evaluation of the fatigue limit of a metal with surface compressive residual stress, after considering the specimen geometry, USP treatment conditions and applied stress gradient in detail to clearly examine the shakedown effect.

2 Specimen and Experimental Procedure

2.1 Specimen

Shakedown tests were conducted on welded ASTM 309 stainless steel specimens with the following mechanical properties; 0.2% proof stress of 536 MPa and tensile strength of 689 MPa. The geometry of the test specimens is provided in Fig. 1. The calculated stress concentration factor of the notch root obtained using the finite element method is 4.03, and this value is considered for estimating the hot spot stress. Furthermore, the notched area was treated by USP under the conditions given in Table 1.

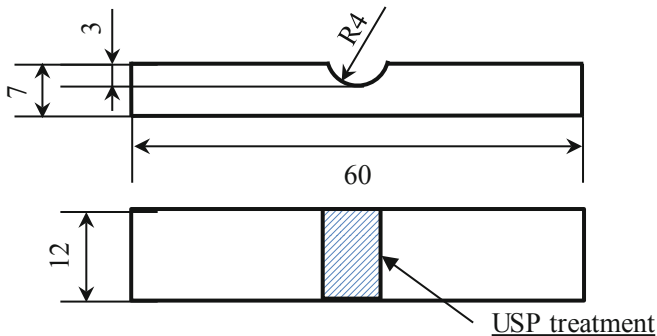


Fig. 1. Schematic diagram showing dimensions of tests specimens used to evaluate shakedown.

Table 1. Ultrasonic shot peening conditions.

Materials	AISI 52100 $\phi 2.0$
Amplitude	50 μm
Distance	20 mm
Peening time	20 s
Coverage	100%

2.2 Experimental Procedure

The fatigue tests under the conditions of the cantilever in-plane bending were conducted for 6 specimens by applying a stress ratio, R , of -1 at a frequency, f , of 15 Hz, and the fatigue limit was set at $N_f = 10^7$ cycles. A hardness testing device was used to determine the micro-Vickers hardness of the specimen in conjunction with an indentation load of 1.96 N and a hold time of 10 s. The extent of the compressive residual stress was determined by radiographic measurement using an X-ray apparatus based on the $\cos(\alpha)$ method, and the distribution in the depth direction was acquired by using the same apparatus, with step-by-step removal of a very thin layer (25–50 μm). Furthermore, residual stress measurements were repeated three times at each point, and an average value was calculated and recorded.

3 Experimental Results

3.1 Hardness and Compressive Residual Stress Distribution

Figures 2 and 3 show the measured hardness and residual stress distribution, respectively, in the depth direction of the USP-treated specimen presented in Fig. 1. Figure 2 shows that the surface Vickers hardness of the peened specimen is 346 HV, which is 1.19 times that of an untreated sample (291 HV). Furthermore, according to Fig. 3, the peening treatment imparts a high compressive residual stress of -500 MPa at the metal surface. These data also demonstrate that the deformation layer resulting from USP is approximately 0.5–0.7 mm deep. Furthermore, the Vickers hardness of the USP-treated specimen in the depth direction is fitted with straight line, $HV(x) = -0.12x + 346$ (for the depth of $x \leq 472$ μm) and $HV(x) = 291$ (for the depth of $x > 472$ μm), to calculate the fatigue limits in the depth direction.

3.2 S-N Curve and Fracture Mechanism

Figure 4 shows the S - N data obtained for USP-treated ASTM 309 stainless steel, and the fatigue limit of this material is close to 415 MPa. Furthermore, according to a typical scanning electron microscope (SEM) image of the fracture surface in Fig. 5, the crack initiation sites were at the surface of the specimen by a surface slip due to intrusion and extrusion. This fracture mechanism is very important for evaluating the fatigue limit of the material with surface compressive residual stress because this fracture mechanism implies that the evaluation of the fatigue limit should be carried out in just surface layer. Additionally, the entire specimen fractured via the same fracture mechanism as discussed above, i.e. from cracks initiated at the surface of the specimen.

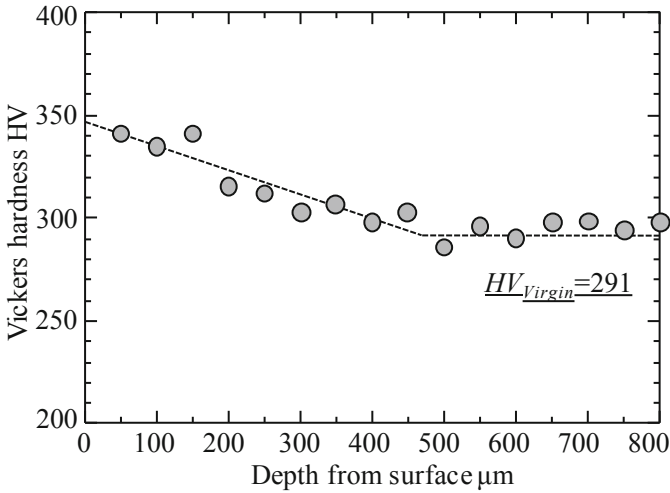


Fig. 2. Vickers hardness distribution.

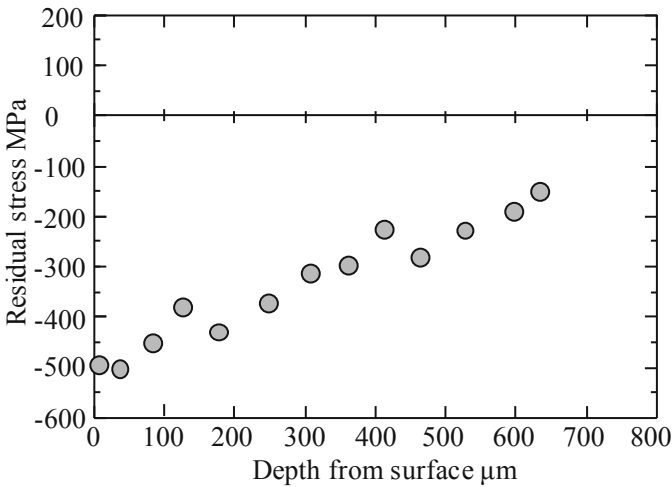


Fig. 3. Residual stress distribution.

3.3 Fatigue Limit Evaluation of USP Treated ASTM 309 Stainless Steel

The fatigue limit for USP-treated ASTM 309 stainless steel was evaluated based on the modified Goodman line considering shakedown. Calculated fatigue limit was 404 MPa at the surface including shakedown, and 440 MPa without shakedown. Then applied stress of 420 MPa and this is the fracture condition mentioned in Fig. 4. Furthermore, the fatigue limit of USP treated ASTM 309 stainless steel is 415 MPa in Fig. 4. Figure 6 shows the modified Goodman line of USP treated ASTM 309 stainless steel

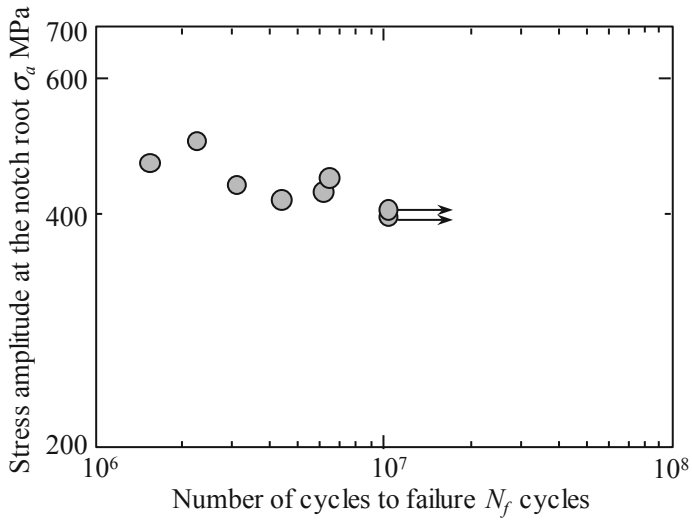


Fig. 4. *S-N* data for USP-treated ASTM 309 stainless steel.

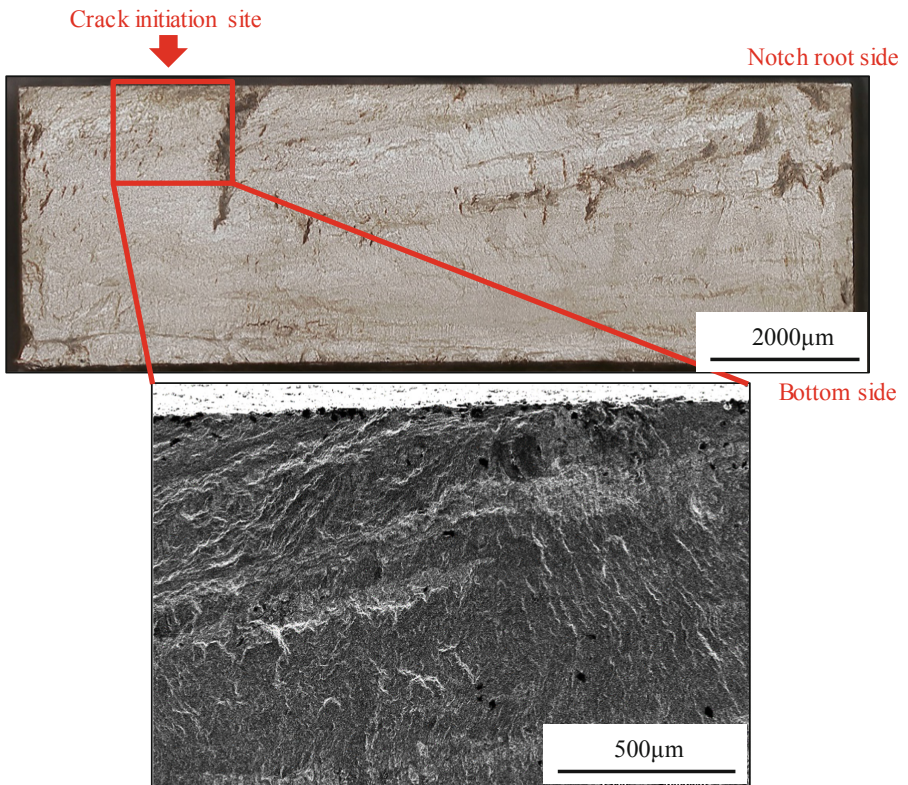


Fig. 5. Images showing the crack initiation site at $\sigma_a = 420$ MPa on fracture surface of USP ASTM 309 stainless steel.

considering shakedown phenomenon, and clearly implies that estimated fatigue limit of 404 MPa agrees with experimental results of 415 MPa. This result implies that shakedown behavior occurs during cyclic fatigue tests. In addition, the occurrence of shakedown, even under controlled load conditions, is attributed to the restriction of the surface USP layer by the internal bulk. Therefore, based on these results, the fatigue limit for a metal with compressive residual stress should clearly be estimated based on a modified Goodman line considering shakedown to avoid the unexpected fracture of the metal material that could occur by following the modified Goodman line not considering shakedown.

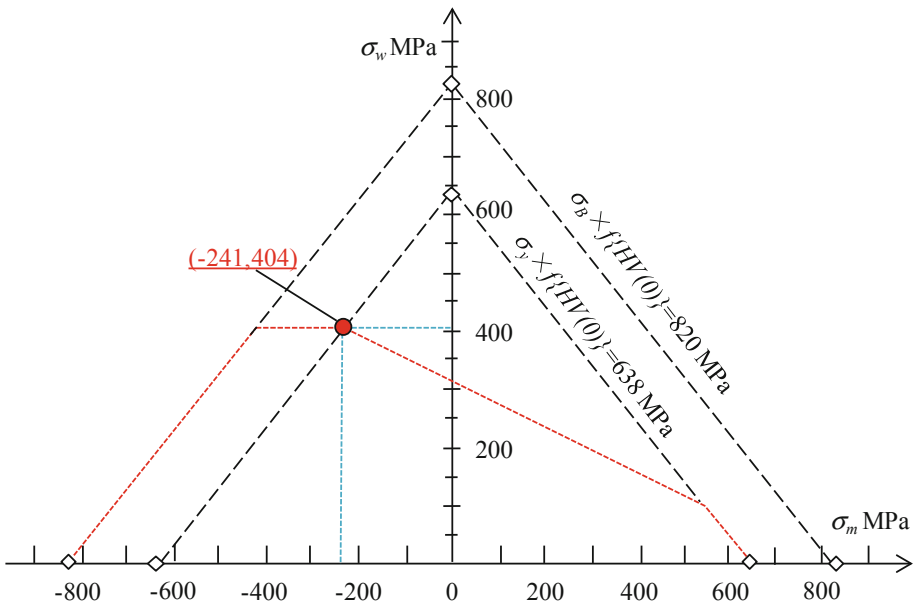


Fig. 6. Fatigue limit diagram considering $f\{HV(x)\}$ at the surface for ASTM 309 stainless steel specimen.

4 Conclusions

1. The fatigue limit of a metallic material with surface compressive residual stress obtained by using plane bending fatigue tests is approximately equal to the fatigue limit acquired by the modified Goodman line considering shakedown effects. Therefore, this result implies that the surface compressive residual stress layer is under controlled displacement conditions despite the entire specimen being subjected to controlled load conditions.
2. The fatigue limit of a metallic material with surface compressive residual stress should be estimated by using a modified Goodman line considering shakedown to avoid unexpected fractures that could occur by following a modified Goodman line that does not consider shakedown.

References

1. Davari, N., Rostami, A., Abbasi, S.M.: Effects of annealing temperature and quenching medium on microstructure, mechanical properties as well as fatigue behavior of Ti-6Al-4V alloy. *Mater. Sci. Eng. A*. **683**, 1–8 (2017)
2. Zhang, J., Wu, B., Zhang, L., Pyoun, Y., Murakami, R.: Effect of ultrasonic nanocrystal surface modification on surface and fatigue properties of quenching and tempering S45C steel. *Appl. Surf. Sci.* **321**, 318–330 (2014)
3. Morita, T., Tanaka, S., Ninomiya, S.: Improvement in fatigue strength of notched Ti-6Al-4V alloy by short-time heat treatment. *Mater. Sci. Eng. A* **669**, 127–133 (2016)
4. Farokhzadeh, K., Edrisy, A.: Fatigue improvement in low temperature plasma nitride Ti-6Al-4V alloy. *Mater. Sci. Eng. A* **620**, 435–444 (2015)
5. Winck, L.B., Ferreria, J.L.A., Araujo, J.A., Manfrinato, M.D., da Silva, C.R.M.: Surface nitriding influence on the fatigue life behavior of ASTM A743 steel type CA6NM. *Surf. Coat. Technol.* **232**, 844–850 (2013)
6. Berg, J., Stranghöner, N.: Fatigue behavior of high frequency hammer peened ultra high strength steels. *Int. J. Fatigue* **82**, 35–48 (2016)
7. Fernández-Pariente, I., Bagherifard, S., Guagliano, M., Ghelichi, R.: Fatigue behavior of nitride and shot peened steel with artificial small surface defects. *Eng. Fract. Mech.* **103**, 2–9 (2013)
8. Conrado, E., Gorla, C., Davoli, P., Boniardi, M.: A comparison of bending fatigue strength of carburized and nitride gears for industrial applications. *Eng. Fail. Anal.* **78**, 41–54 (2017)
9. Achintha, M., Nowell, D., Fufari, D., Sackett, E.E., Bache, M.R.: Fatigue behavior of geometric features subjected to laser shock peening: experiments and modelling. *Int. J. Fatigue*. **62**, 171–179 (2014)
10. Shimamura, Y., Narita, K., Ishii, H., Tohgo, K., Fujii, T., Yagasaki, T., Harada, M.: Fatigue properties of carburized alloy steel in very cycle regime under torsional loading. *Int. J. Fatigue* **60**, 57–62 (2014)
11. He, B.Y., Bache, K.A., Mellor, B.G., Gary, H., Reed, P.A.S.: Fatigue crack growth behavior in the LCF regime in a shot peened steam turbine blade material. *Int. J. Fatigue*. **82**, 280–291 (2016)
12. Zhou, J.Z., Huang, S., Zuo, L.D., Meng, X.K., Sheng, J., Tian, Q., Han, Y.H., Zhu, W.L.: Effects of laser peening on residual stress and fatigue crack growth properties of Ti-6Al-4V titanium alloy. *Opt. Lasers Eng.* **52**, 189–194 (2014)
13. Zhu, L., Guan, Y., Wang, Y., Xie, Z., Lin, J., Zhai, J.: Influence of process parameters of ultrasonic shot peening on surface roughness and hydrophilicity of pure titanium. *Surf. Coat. Technol.* **317**, 38–53 (2017)
14. Dalaei, K., Karlsson, B.: Influence of shot peening on fatigue durability of normalized steel subjected to variable amplitude loading. *Int. J. Fatigue* **38**, 75–83 (2012)
15. Arakawa, J., Kakuta, M., Hayashi, Y., Tanegashima, R., Akebono, H., Kato, M., Sugeta, A.: Fatigue strength of USP treated ASTM CA6NM for hydraulic turbine runner. *Surf. Eng.* **30**, 662–669 (2014)



Fundamentals and Applications of Cavitation Peening Comparing with Shot Peening and Laser Peening

Hitoshi Soyama  

Tohoku University, 6-6-01 Aoba-ku, Sendai 980-8579, Japan
soyama@mm.mech.tohoku.ac.jp

Abstract. Although impact induced by cavitation bubble collapse causes severe damage in hydraulic machineries, the impact can be utilized for the mechanical surface treatment of metallic materials in the same way as shot peening. The peening using cavitation impact is named as “cavitation peening”. In the paper, the concepts and key factors on cavitation peening are presented including mechanism of generation of cavitation by using a submerged water jet. The difference between cavitation peening and water jet peening was also demonstrated by measuring peening intensity such as arc height of metallic plate. In order to discuss the difference between improvement of fatigue strength of stainless steel by cavitation peening, water jet peening, shot peening and submerged laser peening, a plane bending fatigue test was carried out. The specimens were treated at various processing time by each peening method, and the optimum processing time at each peening methods was revealed, then the fatigue strength of stainless steel treated at the optimum processing time was evaluated. It was concluded that the fatigue strength at $N = 10^7$ of cavitation peening was highest followed by shot peening, submerged laser peening and finally water jet peening.

Keywords: Cavitation peening · Laser shock peening · Shot peening · Water jet peening · Fatigue strength · Residual stress

1 Introduction

Cavitation bubble collapse causes severe impact which can deform metallic materials and it is harmful for hydraulic machineries such as pumps and valves [1, 2]. However, the cavitation impact can be utilized for mechanical surface treatment in the same way as shot peening [3, 4]. The peening technique using cavitation impact is called as “cavitation peening” [3] or “cavitation shotless peening” [5], as shots are not used.

At the initial stage of cavitation peening, in order to mitigate stress corrosion cracking of stainless steel in nuclear power plants, introduction of compressive residual stress into stainless steel using cavitation impacts around a submerged high speed water jet was demonstrated [6], and it was confirmed [7], then it was applied to nuclear power plants [8]. Epling and Youman also reported that cavitation peening using a submerged water jet at relatively higher injection pressure was applied for nuclear power plants in order to mitigate stress corrosion cracking [9]. In one of the pioneering works in this

field, as Enomoto et al. tried to introduce compressive residual stress into stainless steel by water column impact caused by a submerged water jet [10], they called as water jet peening and some researchers and engineers are still calling water jet peening. As mentioned above, although cavitation peening using the submerged high speed water jet, the bubble collapse impact is utilized during cavitation peening. The name of water jet peening evokes water column impact which is increasing with the injection pressure of the jet. On the other hand, during cavitation peening, too high injection pressure of the jet causes the decrease of peening intensity. Namely, the term of water jet peening causes confusing of cavitation peening and water jet peening [11].

More recently, peening intensity of cavitation peening was enhanced by controlling environmental condition at bubble collapse region [12, 13] and optimizing nozzle geometry [14–16]. Then the improvements of fatigue properties of mechanical components such as gears were demonstrated [17–20]. Han et al. also revealed that the fatigue strength of SAE1045 steel was improved by the cavitating jet. Ju and Han indicated that the improvement of the strength of titanium was caused by interaction of twinning [21]. Hutli et al. revealed that a cavitating jet could be useful for the surface modification of mechanical and electrical properties by observing aluminum alloy in nano-and micro level [22]. Balamurugan et al. reported that cavitation peening could introduced compressive residual stress into gear tooth of bevel gears. Takahashi et al. investigated the effects of cavitation peening on the bending fatigue strength of aluminum alloy with a crack-like surface defect comparing with shot peening [23].

There are many advantages of cavitation peening. As there are no solid collisions, the surface is smoother than that of conventional shot peening, thus the improvement of fatigue strength of light metals, which is commonly soft, by cavitation peening is larger than that of conventional shot peening [24]. During cavitation peening, impacts at cavitation bubble collapses are utilized. Thus, a water jet at relatively low injection pressure with large nozzle produces large peening effects comparing with high injection pressure with small nozzle [25]. Furthermore, an expensive plunger pump is not required. Note that peening intensity produced by a water jet at too high injection pressure is much smaller than that at relatively low injection pressure [11, 25]. Although a submerge water jet has been used in conventional cavitation peening, a cavitating jet in air without a water filled chamber was realized by injecting a high speed water jet into a low speed water jet which was injected into air using a concentric nozzle [26–28]. The research of the cavitating jet in air was followed by Marcon et al. [29], and they reported that the same materials should be used for the measurement of the arc height [30]. Thus, cavitation peening can be applied for the treatment of outer surface of pipelines and tanks as well. Furthermore, cavitation peening using ultrasonic cavitation was also investigated [31, 32].

Even though submerged laser peening, a bubble, which is developed after laser ablation, can produced large impact at bubble collapse [3, 33], as bubble behavior is similar to cavitation bubble. Sasoh et al. reported the amplitude of pressure induced laser ablation was larger than that of bubble collapse, when the amplitude of pressure wave in the water was measured by a submerged shock wave sensor [34]. However, it was reported that the impact induced by the bubble collapse was larger than that of laser ablation, when the impact passing through the metallic material was measured by a PVDF sensor [3, 33]. Glaser and Polese also reported that the first bubble collapse

was effective during submerged laser peening [35]. Namely, the submerged laser peening is a kind of cavitation peening using a submerged pulse laser [36]. Ren et al. reported that the introduction of compressive residual stress and work hardening of aluminum alloy by cavitation peening using submerged pulse laser [37]. Furthermore, when mechanism of cavitation peening is clearly understood, peening effect of submerged laser peening can be enhanced.

In the present paper, in order to treat metallic materials by cavitation peening at optimum condition, fundamental of cavitation peening was described with visualization of cavitation bubble. The difference between cavitation peening and water jet peening was also explained to avoid misunderstanding the mechanism of cavitation peening. The difference of peening methods was also described with a result of improvement of fatigue strength of stainless steel treated by cavitation peening, shot peening, submerged laser peening and water jet peening.

2 Fundamental of Cavitation Peening

2.1 Cavitation and Cavitating Jet

Cavitation is a phase change phenomenon from liquid phase to gas phase by increasing flow velocity [38]. When the pressure reaches to vapor pressure of the liquid, liquid becomes vapor, i.e., gas phase, the vapor bubble is called as cavitation bubble or simply cavitation. When the flow velocity is decreased, the cavitation bubble shrinks and becomes liquid. At this stage, i.e., bubble collapsing stage, the bubble surface opposite to the solid surface produces micro jet [39, 40], and it causes severe impact. After the shrinkage, the diameter of the bubble increases, it is called as rebound. At the rebound, the shock wave is generated. The micro jet and the shock wave are two major reasons why cavitation bubble collapse generates severe impact which can make plastic deformation of metallic surface.

In order to visualize the impact at the bubble collapse, Fig. 1 shows the aspect of bubble which was generated by pulse laser [4]. As shown in Fig. 1(a), the diameter of the bubble was increased up to 0.35 ms and then shrink. The metallic plate was used in Fig. 1(a) and the acrylic resin was used in Fig. 1(b) for the target. The black and white pattern due to photo elasticity was observed in Fig. 1 (b). Namely, the impact was generated at bubble collapse.

In order to reveal generation mechanism of cavitation at cavitation peening, Fig. 2 shows cavitation through Venturi tube [4]. At expanding region after narrow part, cavitation bubbles were observed. As mentioned above, the cavitation was generated at narrow part where the pressure decreased, as flow velocity increased at narrow region. At expanding region where the pressure increased due to the decrease of flow velocity, the cavitation bubble collapsed. When the expanding region was cut, the cavitation bubbles were shed into the water as shown in Fig. 3(a) [4]. The step-shape narrow geometry, i.e., nozzle, can also generate the cavitation bubble as shown in Fig. 3(b), as the cavitation was generated in the vortex core of the shear layer around the water jet [4]. Moreover, a submerged water jet through a nozzle and/or an orifice can generate the cavitation bubbles. Note that aggressive intensity of the cavitation impacts was

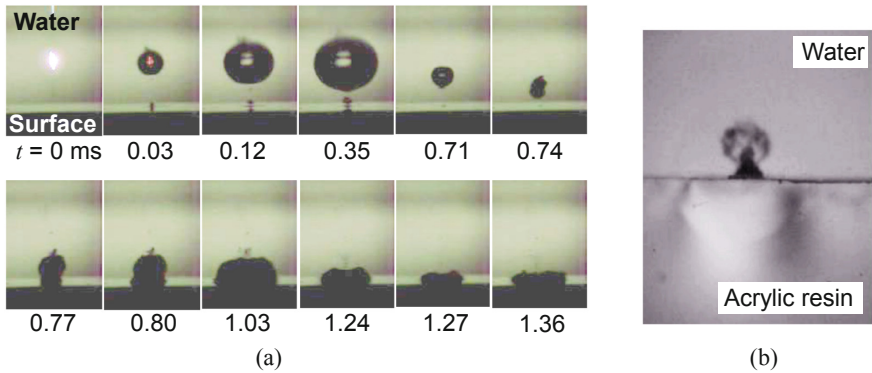


Fig. 1. Visualization of impact at bubble collapse by observing aspect of bubble which was generated by pulse laser. The bubble behavior near solid surface was shown in (a). The stress distribution at bubble collapse was shown by photo elasticity as black and white pattern of the acrylic resin in (b).

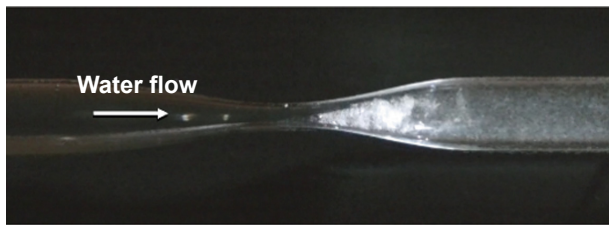
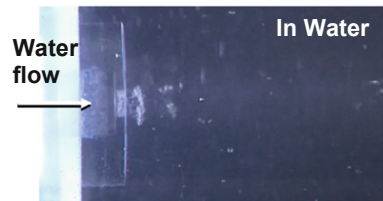


Fig. 2. Aspect of cavitation in Venturi tube. The water flowed from left to right. The white bubbles in narrow region were cavitation bubbles. The dim white bubbles in the straight part of the tube were residual bubbles after cavitation bubble collapse.



(a) Venturi type nozzle



(b) Step type nozzle

Fig. 3. Aspect cavitation through (a) Venturi type nozzle and (b) Step type nozzle. (a) Cavitation in narrow region was shed into water. (b) Cavitation was generated in vortex core of shear layer around the jet.

strongly affected by the nozzle geometry especially the shape of the downstream part of the orifice [14–16]. Figure 4 reveals typical aspect of cavitating jet in water and in air for cavitation peening. For both cases, the step type nozzle was used for the high speed water jet. When the injection pressure was increased the vortex cavitation near nozzle (see Fig. 3(b)) were combined together and produced cloud cavitation which was clearly shown in Fig. 4(a). The shedding of the cloud cavitation is periodical phenomenon and the similarity law of the shedding frequency was obtained from experimental observation of the jet [41]. In the case of the cavitating jet in air, the aggressive intensity of the jet depended on the injection pressure of the high and low speed water jet [26, 27], and the nozzle geometry [28]. The frequency of the wavy pattern of the low speed water jet was the same frequency of the cloud shedding of the high speed water jet. Note that the cavitating jet in water can introduce compressive residual stress in deeper region and the cavitating jet in air can introduce large compressive residual stress near surface [3].

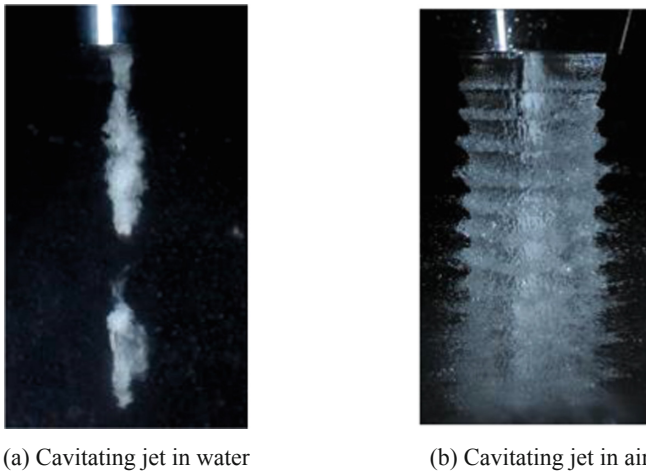


Fig. 4. Aspect of cavitating jet in water (a) and in air (b). A high speed water jet was injected into a water filled chamber in (a), and a high speed water jet was injected into a low speed water jet which was injected into air without a water filled chamber in (b).

2.2 Comparison Between Water Jet Peening and Cavitation Peening

Although a high speed water jet is used for both water jet peening and cavitation peening, peening mechanisms of water jet peening and that of cavitation peening are different. During water jet peening, water column impacts are used for producing plastic deformations. On the other hand, cavitation impacts are used for making the plastic deformation pits during cavitation peening. Even though the water jet is submerged in water jet peening, the water column impact can generate the pits.

In order to classify the water jet peening and cavitation peening, Soyama proposed a classification map using cavitation number σ and the standoff distance s [10]. In the

case of cavitating flow, the cavitation number σ is the most important parameter. The cavitation number σ through an orifice is defined by the upstream pressure of the orifice p_1 , the downstream pressure of the orifice p_2 and vapor pressure p_v , as follows [38].

$$\sigma = \frac{p_2 - p_v}{p_1 - p_2} \approx \frac{p_2}{p_1} \tag{1}$$

Note that the pressures in Eq. (1) are absolute pressures. When the relationships between p_1 , p_2 and p_v are $p_1 \gg p_2 \gg p_v$, such as a cavitating jet, σ can be simplified as in Eq. (1).

In the case of cavitation peening, cavitation cloud is developed and collapsed, thus a certain distance is required to utilize cavitation impacts. Soyama collected over 150 data and then proposed the distinguished line to classify between cavitation peening and water jet peening. When the treatment is carried out at the distance s which is larger than the following line, it is cavitation peening [11]. If the distance s is smaller than the following value, it is water jet peening [11]. Here, d is nozzle throat diameter.

$$\frac{s}{d} = 1.8 \sigma^{-0.6} \tag{2}$$

In order to demonstrate the difference between cavitation peening and water jet peening, Fig. 5 reveals peening intensity as a function of standoff distance s which was distance from the nozzle to the target [25]. The peening intensity was shown by the inverse of curvature $1/\rho$ which was obtained from arc height of treated band steel 1 mm in thickness. As the treated area was narrow near the nozzle and it was wide at far from the nozzle, the band steel width 5 mm was used at $s \leq 100$ mm and that of 50 mm was used at $s \geq 100$ mm [25]. Namely, the width of the main treatment area at $s \leq 100$ mm was about 5 mm due to water column impact, and that of 50 mm caused by cavitation impacts was about 50 mm at $s \geq 100$ mm [25]. As shown in Fig. 5, two

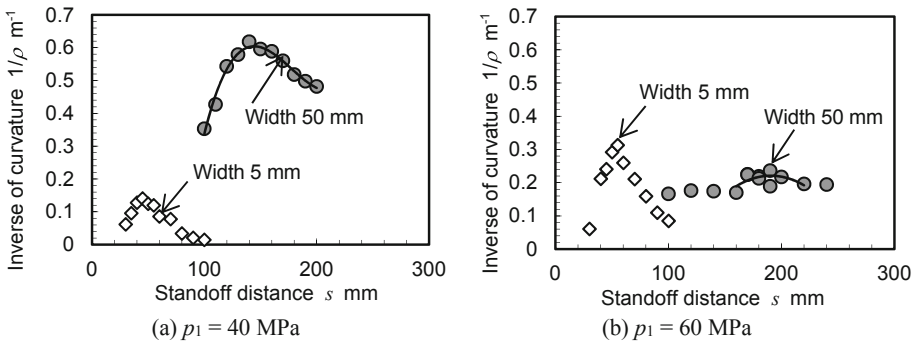


Fig. 5. Peening intensity as a function of standoff distance at $p_1 = 40$ and 60 MPa. The peening intensity was revealed by inverse of curvature obtained from the arc height of band steel.

peaks are shown. The peak near nozzle, i.e., 1st peak, was produced by water column impact, i.e., water jet peening [11]. On the other hand, there are peaks at $s = 140$ mm in Fig. 5(a) and $s = 200$ mm in Fig. 5(b). These peaks were generated by cavitation peening, as cavitation bubbles developed and then collapsed far from nozzle.

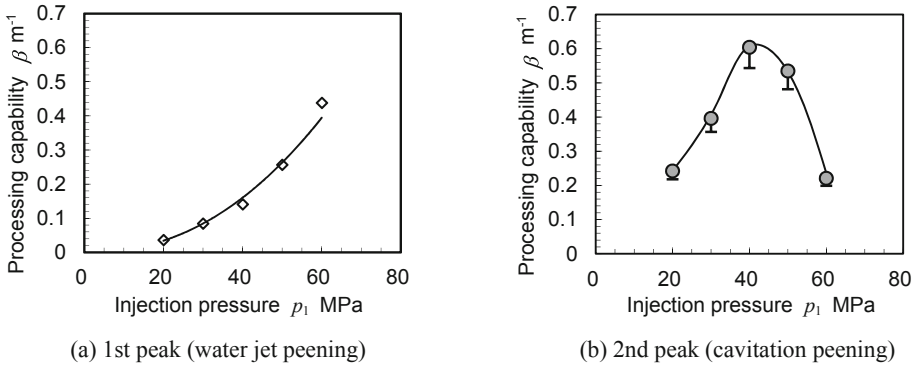


Fig. 6. Processing capability of water jet peening and cavitation peening. The processing capability was obtained from the inverse of curvature considering the treated area and the width of the specimen.

Figure 6 shows the processing capability of the jet at various injection pressure for water jet peening (see Fig. 6(a)) and cavitation peening (see Fig. 6(b)). The processing capability was calculated from the peak value of the inverse of curvature at each injection pressure considering the width of the band steel and the treatment area [25]. As shown in Fig. 6(a), the processing capability of water jet peening increased with the injection pressure, as water column speed increased with the injection pressure. On the other hand, the processing capability of cavitation peening had a maximum at $p_1 = 40$ MPa at the present condition. This result shows that the peening intensity of cavitation peening decreases at high injection pressure. Note that the processing capability of cavitation peening at $p_1 = 40$ MPa was 1.4 times larger than that of water jet peening $p_1 = 60$ MPa, although the jet power at $p_1 = 40$ MPa was nearly half of that at $p_1 = 60$ MPa.

3 Experimental Facilities and Procedures

In order to investigate the comparison between the improvements of the fatigue strength by cavitation peening, water jet peening, shot peening and laser peening, stainless steel was treated and fatigue properties were examined by a displacement controlled plane bending fatigue tester. The tested stainless steel was austenitic stainless steel Japanese Industrial Standard JIS SUS316L. The thickness of the specimen was 2 mm. The specimen was treated by cavitation peening, water jet peening, shot peening and submerged laser peening. Figure 7 illustrates schematic diagram of

submerged water jet system which was used for water jet peening and cavitation peening. For both case, the injection pressure was 30 MPa and nozzle throat diameter was 2 mm. At water jet peening, the standoff distance was chosen as 70 mm and it was 222 mm for cavitation peening by measuring the arc height of band steel of 1 mm in thickness changing with the distance s [33]. Namely, 70 mm and 222 mm are the optimum distance for water jet peening and cavitation peening, respectively.

In the case of shot peening, recirculating shots accelerated by a water jet was used [42]. The used shot was made of stainless steel JIS SUS440C, and the diameter and number of shot were 3.2 mm and 500, respectively. The conditions were optimized by measuring the arc height of the plate changing with the number of shots [42]. The injection pressure of the water jet was 12 MPa. Note that the water jet without shot at the same conditions did not introduce compressive residual stress into the stainless steel.

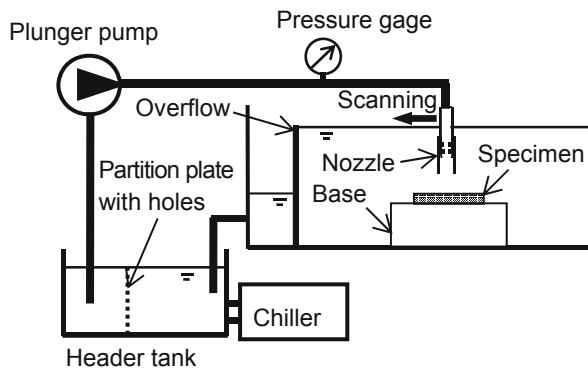


Fig. 7. Schematic diagram of submerged water jet system for water jet peening and cavitation peening.

For the submerged laser peening, Nd:YAG laser with Q-switch was used. The wave length, the maximum energy, the beam diameter, the pulse width and the repetition frequency of the laser pulse were 1,064 nm, 0.35 J, 6 mm, 6 ns and 10 Hz, respectively. Although at conventional submerged laser peening without the tape, the wave length and the maximum energy of the laser pulse were 532 nm and 0.2 J at second harmonic of Nd: YAG laser was used, at the present submerged laser peening, the fundamental harmonic, i.e., 1,064 nm and 0.35 J were chosen to use bubble impact after laser ablation.

4 Results

In order to find optimum coverage, Fig. 8 shows the fatigue life of stainless steel at $\sigma_a = 400$ MPa as a function of coverage for shot peening SP, cavitation peening CP, laser peening LP and water jet peening WJP. For each case, the coverage was described

by normalized coverage. It was obtained by normalized processing time per unit length or pulse density, which had a maximum fatigue life at $\sigma_a = 400$ MPa. It was 8 s/mm for cavitation peening, 8 s/mm for water jet peening, 0.88 s/mm for shot peening and 4 pulse/mm² for laser peening. In the case of the fatigue life at $\sigma_a = 400$ MPa, shot peening had a maximum.

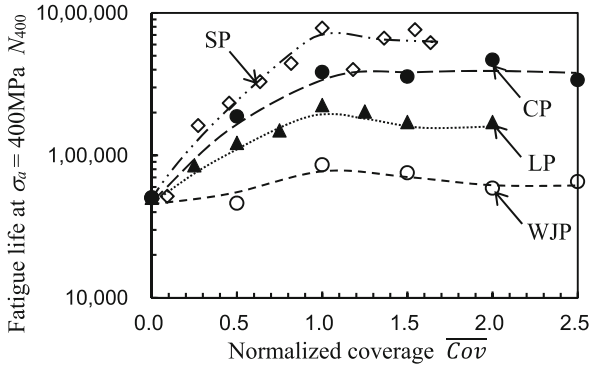


Fig. 8. Fatigue life of stainless steel JIS SUS316L as a function of coverage for shot peening SP, cavitation peening CP, laser peening LP and water jet peening WJP.

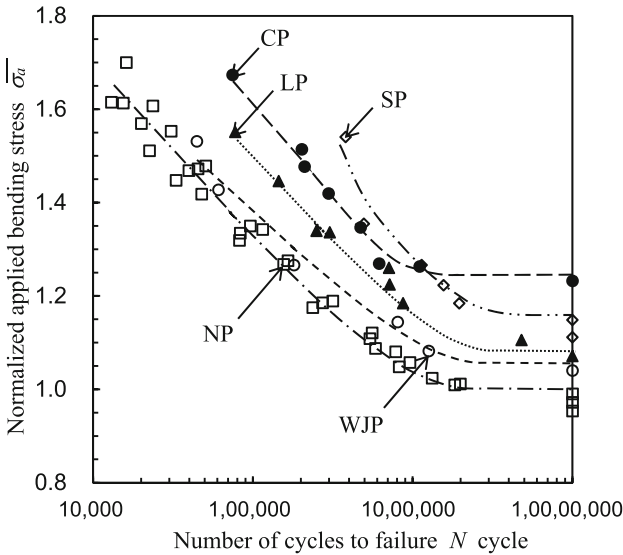


Fig. 9. Improvement of fatigue strength of stainless steel JIS SUS316L by shot peening SP, cavitation peening CP, laser peening LP and water jet peening WJP.

In order to investigate the fatigue strength, the specimen was treated by each peening methods at optimum coverage, and tested by a plane bending fatigue test. Figure 9 reveals *S-N* curve. In Fig. 9, the applied stress was normalized by the fatigue strength of non-peened specimen. When the fatigue strength at $N = 10^7$ was calculated by Little's method [43], it was 279 MPa for the non-peened specimen, 296 MPa for water jet peening, 303 MPa for laser peening, 325 MPa for shot peening and 348 MPa for cavitation peening. Therefore, it was found that cavitation peening can improve fatigue strength of stainless steel by about 25%.

5 Conclusions

In order to treat the metallic materials by cavitation peening at optimum condition, the fundamental of cavitation peening was explained comparing with water jet peening. The correlation on the improvement of fatigue strength of stainless by cavitation peening, shot peening, laser peening and water jet peening was investigated by using a plane bending fatigue test using specimens made of stainless steel JIS SUS316L.

It was revealed that the improvements in fatigue strength at $N = 10^7$ compared with the non-peened specimen were 25% by cavitation peening, 6% by water jet peening, 9% by laser peening and 16% by shot peening.

In the future work of cavitation peening, the research work will be concentrated into the aluminum alloy and/or titanium alloy. Because the great advantage of cavitation peening is realized by treatments of rather soft metallic materials such as aluminum alloy and titanium alloy, although cavitation peening can improve mechanical properties of hard materials such as carbonized steel and tool steel alloy.

Acknowledgements. This work was partly supported by JSPS KAKENHI Grant Number 17H03138 and 18KK0103.

References

1. Soyama, H., Oba, R., Kato, H.: Cavitation observations of severely erosive vortex cavitation arising in a centrifugal pump. In: Proceedings of 3rd International Conference on Cavitation Institution of Mechanical Engineers, pp. 103–110 (1992)
2. Soyama, H., Ohba, K., Takeda, S., et al.: High-speed observations of highly erosive vortex cavitation around butterfly valve. Trans. JSME **60B**, 1133–1138 (1994)
3. Soyama, H.: Key factors and applications of cavitation peening. Int. J. Peen Sci. Technol. **1**, 3–60 (2017)
4. Soyama, H.: <https://youtu.be/BurRGrmOGQY>. Accessed 18 Apr 2019
5. Soyama, H., Saito, K., Saka, M.: Improvement of fatigue strength of aluminum alloy by cavitation shotless peening. J. Eng. Mater. Technol. **124**, 135–139 (2002)
6. Soyama, H., Yamauchi, Y., Ikohagi, T., et al.: Marked peening effects by highspeed submerged-water-jets - residual stress change on SUS304. Jet Flow Engineering **13**(1), 25–32 (1996)
7. Hirano, K., Enomoto, K., Hayashi, E., et al.: Effect of water jet peening on corrosion resistance and fatigue strength of type 304 stainless steel. J. Soc. Mater. Soc. Jpn. **45**, 740–745 (1996)

8. Saitou, N., Enomoto, K., Kurosawa, K., et al.: Development of water jet peening technique for reactor internal components of nuclear power plant. *Jet Flow Eng.* **20**(1), 4–12 (2003)
9. Epling, M., Youman, B.: Ultra-high-pressure cavitation peening offers new way to maintain components in operational nuclear reactors. *Power* **160**, 46–49 (2016)
10. Enomoto, K., Hirano, K., Mochizuki, M., et al.: Improvement of residual stress on material surface by water jet peening. *J. Soc. Mater. Soc. Jpn.* **45**, 734–739 (1996)
11. Soyama, H.: Surface mechanics design of metallic materials on mechanical surface treatments. *Mech. Eng. Rev.* **2**, 1–20 (2015). Paper No. 14-00192
12. Soyama, H.: Improvement in fatigue strength of silicon manganese steel SUP7 by using a cavitating jet. *JSME Int. J. Ser. Solid Mech. Mater. Eng.* **43**, 173–178 (2000)
13. Soyama, H., Park, J.D., Saka, M.: Use of cavitating jet for introducing compressive residual stress. *J. Manuf. Sci. Eng.-Trans. ASME* **122**, 83–89 (2000)
14. Soyama, H.: Enhancing the aggressive intensity of a cavitating jet by means of the nozzle outlet geometry. *J. Fluids Eng.* **133**, 1–11 (2011). Paper No. 101301
15. Soyama, H.: Effect of nozzle geometry on a standard cavitation erosion test using a cavitating jet. *Wear* **297**, 895–902 (2013)
16. Soyama, H.: Enhancing the aggressive intensity of a cavitating jet by introducing a cavitator and a guide pipe. *J. Fluid Sci. Technol.* **9**, 1–12 (2014). Paper No. 13-00238
17. Soyama, H., Shimizu, M., Hattori, Y., et al.: Improving the fatigue strength of the elements of a steel belt for CVT by cavitation shotless peening. *J. Mater. Sci.* **43**, 5028–5030 (2008)
18. Lee, H., Mall, S., Soyama, H.: Fretting fatigue behavior of cavitation shotless peened Ti-6AL-4V. *Tribol. Lett.* **36**, 89–94 (2009)
19. Soyama, H., Sekine, Y.: Sustainable surface modification using cavitation impact for enhancing fatigue strength demonstrated by a power circulating-type gear tester. *Int. J. Sustain. Eng.* **3**, 25–32 (2010)
20. Seki, M., Nishie, N., Kozai, S., et al.: Fatigue strength of steel rollers and gears treated by cavitation peening with short processing time. *J. Adv. Mech. Design Syst. Manuf.* **6**, 33–43 (2012)
21. Ju, D.Y., Han, B.: Investigation of water cavitation peening-induced microstructures in the near-surface layer of pure titanium. *J. Mater. Process. Technol.* **209**, 4789–4794 (2009)
22. Hutli, E., Bonyar, A., Osztetzky, D., et al.: Plastic deformation and modification of surface characteristics in nano-and micro-levels and enhancement of electric field of FCC materials using cavitation phenomenon. *Mech. Mater.* **92**, 289–298 (2016)
23. Takahashi, K., Osedo, H., Suzuki, T., et al.: Fatigue strength improvement of an aluminum alloy with a crack-like surface defect using shot peening and cavitation peening. *Eng. Fract. Mech.* **193**, 151–161 (2018)
24. Soyama, H.: Improvement of fatigue strength of metallic materials by cavitation shotless peening. *Metal Finish. News* **7**, 48–51 (2006)
25. Kamisaka, H., Soyama, H.: Effect of injection pressure on mechanical surface treatment using a submerged water jet. *J. Jet Flow Eng.* **33**, 4–10 (2018)
26. Soyama, H.: Introduction of compressive residual stress using a cavitating jet in air. *J. Eng. Mater. Technol.* **126**, 123–128 (2004)
27. Soyama, H.: High-speed observation of a cavitating jet in air. *J. Fluids Eng.* **127**, 1095–1108 (2005)
28. Soyama, H., Kikuchi, T., Nishikawa, M., et al.: Introduction of compressive residual stress into stainless steel by employing a cavitating jet in air. *Surf. Coat. Technol.* **205**, 3167–3174 (2011)
29. Marcon, A., Melkote, S.N., Castle, J., et al.: Effect of jet velocity in co-flow water cavitation jet peening. *Wear* **360**, 38–50 (2016)

30. Marcon, A., Melkote, S.N., Yoda, M.: Effect of nozzle size scaling in co-flow water cavitation jet peening. *J. Manuf. Process.* **31**, 372–381 (2018)
31. Sasaki, T., Yoshida, K., Nakagawa, M., et al.: Effect of horn tip geometry on ultrasonic cavitation peening. *Residual Stress Thermomech. Infrared Imaging Hybrid Tech. Inverse Probl.* **9**, 139–146 (2016)
32. Bai, F., Long, Y.Y., Saalbach, K.A., et al.: Theoretical and experimental investigations of ultrasonic sound fields in thin bubbly liquid layers for ultrasonic cavitation peening. *Ultrasonics* **93**, 130–138 (2019)
33. Soyama, H.: Comparison between the improvements made to the fatigue strength of stainless steel by cavitation peening, water jet peening, shot peening and laser peening. *J. Mater. Process. Technol.* **269**, 65–78 (2019)
34. Sasoh, A., Watanabe, K., Sano, Y., et al.: Behavior of bubbles induced by the interaction of a laser pulse with a metal plate in water. *Appl. Phys. A* **80**, 1497–1500 (2005)
35. Glaser, D., Polese, C.: Cavitation bubble oscillation period as a process diagnostic during the laser shock peening process. *Appl. Phys. A-Mater. Sci. Process.* **123**, 10 (2017)
36. Soyama, H.: Surface mechanics design by cavitation peening using submerged pulse laser. In: *Abstracts of 7th International Conference on Laser Peening and Related Phenomena*, vol. 57 (2018)
37. Ren, X.D., Wang, J., Yuan, S.Q., et al.: Mechanical effect of laser-induced cavitation bubble of 2A02 alloy. *Opt. Laser Technol.* **105**, 180–184 (2018)
38. Brennen, C.E.: *Cavitation and Bubble Dynamics*. Oxford University Press, Oxford (1995)
39. Plesset, M.S., Chapman, R.B.: Collapse of an initially spherical vapour cavity in neighbourhood of a solid boundary. *J. Fluid Mech.* **47**, 283–290 (1971)
40. Lauterborn, W., Bolle, H.: Experimental investigations of cavitation-bubble collapse in neighborhood of a solid boundary. *J. Fluid Mech.* **72**, 391–399 (1975)
41. Nishimura, S., Takakuwa, O., Soyama, H.: Similarity law on shedding frequency of cavitation cloud induced by a cavitating jet. *J. Fluid Sci. Technol.* **7**, 405–420 (2012)
42. Naito, A., Takakuwa, O., Soyama, H.: Development of peening technique using recirculating shot accelerated by water jet. *Mater. Sci. Technol.* **28**, 234–239 (2012)
43. Little, R.E.: Estimating the median fatigue limit for very small up-and-down quantal response tests and for *S-N* data with runouts. *ASTM STP* **511**, 29–42 (1972)



Effect of Mechanical Properties on Fatigue Life Enhancement of Additive Manufactured Titanium Alloy Treated by Various Peening Methods

Yuya Okura^(✉), Hirotooshi Sasaki, and Hitoshi Soyama^{ID}

Tohoku University, 6-6-01 Aoba-ku, Sendai 980-8579, Japan
yuya.okura.rl@dc.tohoku.ac.jp

Abstract. Additive manufacturing (AM) of metallic materials is attractive processing for biomedical implants and aviation components. However, fatigue life of AM parts are remarkably weak. Mechanical surface treatment such as cavitation peening, shot peening and laser peening can improve the fatigue life of AM parts. In the present paper, in order to demonstrate the fatigue life enhancement of AM parts by various peening methods, titanium alloy Ti6Al4V manufactured by electron beam melting EBM was treated by cavitation peening, shot peening and laser peening, and then tested by a plane bending fatigue test. And also, in order to make clear mechanism on the fatigue life enhancement of AM parts, mechanical properties such as residual stress, yield stress and hardness were evaluated, and the correlation between the mechanical properties and the fatigue life was investigated. Note that the yield stress was evaluated by an inverse analysis using an indentation test. It was concluded that the fatigue life of Ti6Al4V manufactured by EBM was proportional to a parameter defined by residual stress, yield stress, surface roughness and hardness.

Keywords: Cavitation peening · Laser shock peening · Shot peening · Additive manufacturing · Fatigue strength · Residual stress

1 Introduction

Additive manufactured AM metallic materials are attractive materials for biomedical implants and aviation components, as complex shapes are directly produced from computer aided design system. Unfortunately, fatigue strength of AM parts are remarkably weak comparing with bulk materials [1]. Mechanical surface treatment such as shot peening (SP) is one of methods to improve fatigue strength of AM parts [1–3].

Most popular mechanical surface treatment is SP. In these days, novel mechanical surface treatments such as laser peening (LP) [4–7] and cavitation peening (CP) [8, 9], in which shots are not required, have been developed. As well known, the surface of AM parts are very rough because of particles of metallic materials. The peening mechanism of LP and CP is a kind of shock wave process, and the shock wave might reach the valleys of surface asperities, then it can introduce work hardening and compressive residual stress.

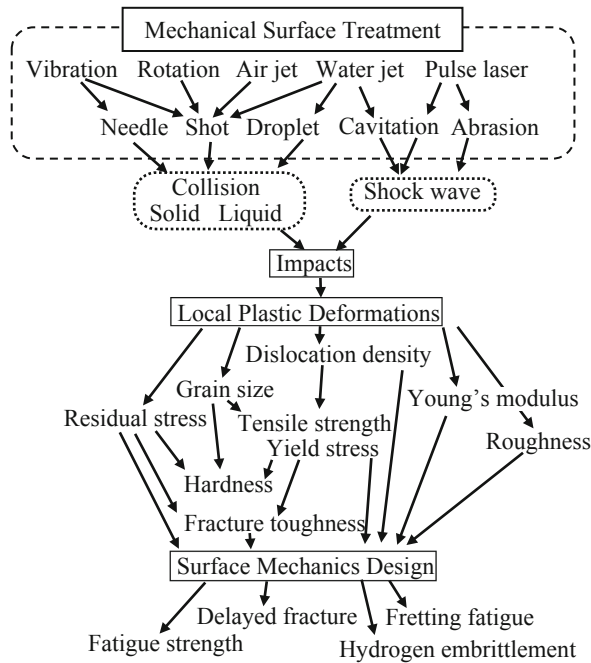


Fig. 1. Surface mechanics design for the improvement of fatigue strength by using mechanical surface treatment.

The mechanical surface treatments such as SP, LP and CP produce local plastic deformations on the metallic surface by impacts due to solid/liquid collision and/or shock wave (see Fig. 1). These plastic deformations affects mechanical properties such as roughness, residual stress, hardness, yield stress etc. and micro structures. In most cases, the mechanical surface treatment and its conditions are decided by trial and error. Thus, surface mechanics design considering individual mechanical properties has been proposed [10]. In few cases, the relation between fatigue life and mechanical properties was revealed [11, 12], but it is insufficient to understand the effect of fatigue life on AM parts.

In the present paper, in order to establish mechanical surface treatment to enhance fatigue strength of AM metallic materials, the improvement of fatigue strength of titanium alloy Ti6Al4V manufactured by electron beam melting EBM was demonstrated by using CP, SP and LP. And also, in order to understand the effects of influential factors on the improvement of fatigue life by mechanical surface treatments, the mechanical properties such as surface residual stress, surface hardness, surface roughness and yield stress were evaluated, and the relation between the fatigue life and mechanical properties was investigated. Note that the yield stress of samples was evaluated by an inverse analysis using an indentation test [13, 14], as conventional tensile test cannot show the yield stress of surface modified layer.

2 Experimental Facilities and Procedures

In order to demonstrate the improvement of fatigue properties of Ti6Al4V manufactured by EBM by using mechanical surface treatments, the specimen was treated by CP, SP and LP, and then tested by a displacement controlled plane bending fatigue test.

Figure 2 illustrates the CP system. A high speed water jet whose injection pressure was 30 MPa was injected through a nozzle of 2 mm in diameter. The distance from the nozzle to the target was 222 mm [15]. The processing time per unit length by CP was 10 s/mm.

Figure 3 shows the used SP system [16]. In the system, shots were accelerated by a water jet whose injection pressure was 12 MPa. The material of shot was stainless steel JIS SUS440C, and the diameter and number of shot were 3.2 mm and 500, respectively. The processing time per unite length was 1 s/mm.

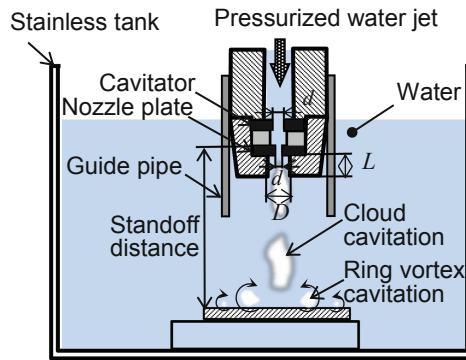


Fig. 2. Schematic diagram of CP system. The injection pressure was 30 MPa, the nozzle throat diameter was 2 mm, and the standoff distance was 222 mm.

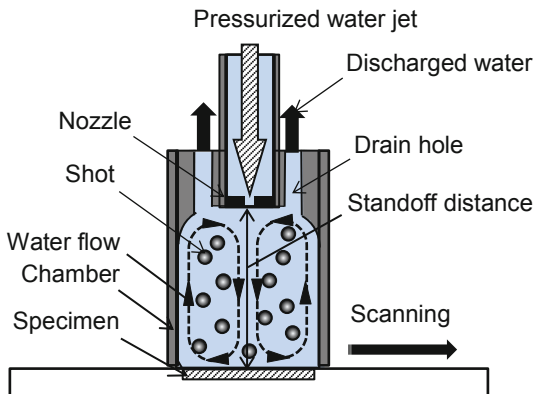


Fig. 3. Schematic diagram of recirculating SP system. The shots were accelerated by a water jet whose injection pressure was 12 MPa.

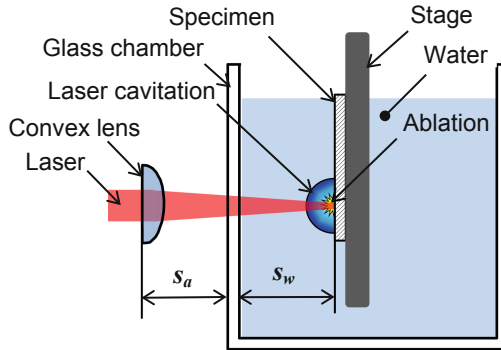


Fig. 4. Schematic diagram of submerged LP system. The pulse laser was focused on the surface of the specimen.

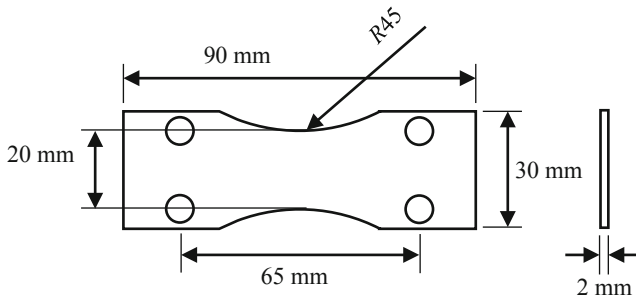


Fig. 5. Geometry of a plane bending fatigue specimen. The thickness was 2 mm.

Figure 4 illustrates schematic diagram of submerged LP system. The standoff distances in air s_a and in water s_w were optimized by measuring arc height of metallic plate. The used pulse laser was a Q-switched Nd:YAG of fundamental harmonic, i.e., 1064 nm. The maximum energy, the beam diameter, the pulse width and the repetition frequency of the laser pulse were 0.35 J, 6 mm, 6 ns and 10 Hz, respectively. The pulse density was 5 pulse/mm².

Figure 5 shows the geometry of a specimen for a plane bending fatigue test. The specimen was manufactured by EBM. The averaged diameter of used Ti6Al4V powder was about 75 μ m. The spot size of electron beam for selectively melting was 0.2 mm in diameter, and stacking pitch was 90 μ m. The stacking direction of EBM was width direction. The solution heat treatment was carried out at 1,208 K at vacuum condition for 105 min then argon gas cooling. After that, aging treatment was done at 978 K at vacuum condition for 2 h then argon gas cooling. In order to avoid initiation of crack at the edges, the edges of all the specimens were polished using rubber whetstone of #80 and #180 by hand. The stress ratio at the fatigue test was $R = -1$.

The yield stress was evaluated by the inverse analysis using an indentation test. The grid for the numerical simulation was shown in Fig. 6. The surface hardness was measured by Vickers hardness tester with applied force of 1.96 N. The surface

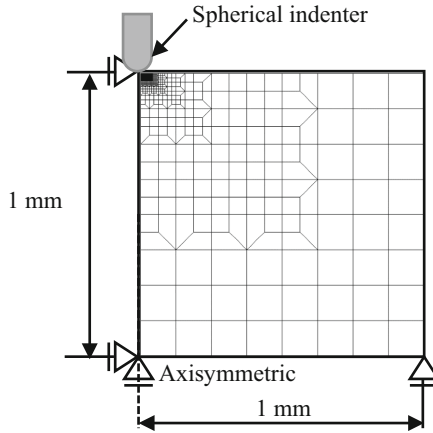


Fig. 6. Schematic diagram of recirculating shot peening system. The shots were accelerated by a water jet whose injection pressure was 12 MPa.

roughness was measured by a needle contact type profilometer. The residual stress of the surface was evaluated by a two-dimensional XRD (2D-XRD) method. The used X-ray was Cu K α X-rays from a tube operated at 35 kV and 40 mA through a 0.8 mm diameter collimator. Diffractive X-ray from the Ti (2 1 3) lattice plane was detected by a two-dimensional position sensitive proportional counter.

In order to make clear the factors on fatigue life, the following equation to estimate fatigue life $N_{f\ est}$ at $\sigma_a = 400$ MPa was proposed from residual stress σ_R , yield stress σ_y , surface Vickers hardness H_V and surface roughness R_a [17]. The residual stress σ_R , yield stress σ_y , surface Vickers hardness H_V and surface roughness R_a were normalized by those of non-peened values, and these were revealed by σ'_R , σ'_y , H'_V and R'_a , respectively. Then, the constants a , b , c and d were obtained by optimizing by a least square method.

$$N_{f\ est} = 10^{\frac{c1 - (400 + a \cdot \sigma'_R)}{c2}} \cdot \frac{\sigma'_y{}^b \cdot H'_V{}^c}{R'_a{}^d} \tag{1}$$

Here, $c1$ and $c2$ were obtained by s - N curve of non-peened specimens. The experimental fatigue life $N_{f\ exp}$ at $\sigma_a = 400$ MPa was calculated from experimental data of $\sigma_a \approx 400$ MPa, as the displacement controlled fatigue tester was used at the present experiment.

3 Results

Table 1 shows the experimental data of surface residuals stress σ_R , yield stress σ_y , surface Vickers hardness H_V , surface roughness R_a and fatigue life of experiment $N_{f\ exp}$ at $\sigma_a = 400$ MPa for non-peened (NP), CP, SP and LP. Table 2 reveals obtained data of surface residuals stress σ'_R , yield stress σ'_y , surface Vickers hardness H'_V , surface

roughness R'_a for the calculation of estimated fatigue life $N_{f\ est}$ at $\sigma_a = 400$ MPa. The calculated $N_{f\ est}$ at $\sigma_a = 400$ MPa was also revealed in Table 2 from using Eq. (1) by optimizing the constants a , b , c and d . The constants were shown in Table 3.

By CP, SP and LP, surface compressive residuals stress was increased comparing with NP surface. The surface compressive residual stress was increased about 430 MPa by CP, 230 MPa by LP and 130 MPa by SP. At the present study, in the case of surface residual stress, yield stress and surface Vickers hardness, the values of as built specimens were used those of as machined specimens, as the surface roughness of as built specimens were too large to obtain the values. As shown in Table 1, the surface roughness of as built specimen was drastically decreased by SP from 19 μm to 5 μm , as shots deformed the un-melted particles on the surface. On the other hand, the surface roughness of as built specimen was scarcely decreased by CP and LP. In the case of as machined specimen, the surface roughness was increased by CP and SP. The yield stress was increased from 196 MPa to 967 MPa by SP, namely, the SP increased the yield stress about 5 times. As shown in Table 1, in the case of as machined specimen, the fatigue strength at 400 MPa became about 3 times larger by CP and 2 times by SP. In the case of as built specimen, the fatigue life was enhanced by 2 times by CP, 4 times by SP and 3 times by LP. Namely, the fatigue life of titanium alloy Ti6Al4V manufactured by EBM was drastically improved by the peening techniques.

Table 1. Experimental data of mechanical properties and fatigue life

Process	Peening	σ_R MPa	σ_y MPa	H_V	R_a μm	$N_{f\ exp}$
As machined	NP	-220	196	344	0.220	106,444
	CP	-648	418	367	0.530	295,423
	SP	-348	967	386	0.320	191,179
As built	NP	-220	196	344	19.274	41,783
	CP	-648	418	367	17.819	96,895
	SP	-348	967	386	4.658	163,912
	LP	-450	592	338	19.102	124,707

Table 2. Obtained mechanical properties and estimated fatigue life

Process	Peening	σ'_R	σ'_y	H'_V	R'_a	$N_{f\ est}$
As machined	NP	0	1	1	1	105,899
	CP	428	2.13	1.07	2.41	280,588
	SP	128	4.93	1.12	1.45	215,785
As built	NP	0	1	1	87.6	39,447
	CP	428	2.13	1.07	81.0	129,129
	SP	128	4.93	1.12	21.2	119,467
	LP	230	1.72	1.72	86.8	84,205

Table 3. Obtained constants by optimization

<i>a</i>	<i>b</i>	<i>c</i>	<i>d</i>
0.224	0.955	0.221	0.258

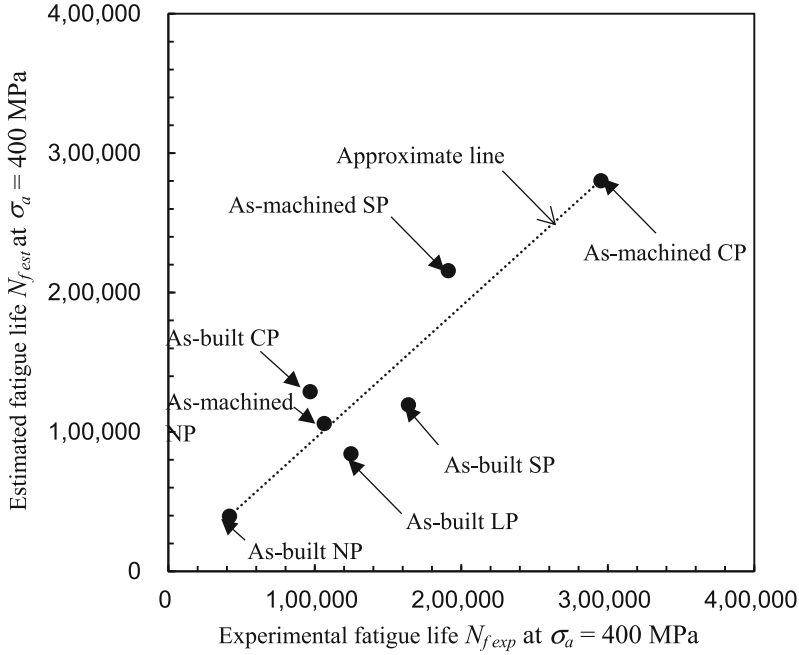


Fig. 7. Relation between experimental- and estimated fatigue life at $\sigma_a = 400$ MPa

In order to demonstrate the proposed estimation method of fatigue life by mechanical properties, Fig. 7 shows the relation between the experimental fatigue life and the estimated fatigue life. The estimated fatigue life was roughly proportional to that of experimental fatigue life. The correlation coefficient r was 0.935. From the correlation coefficient for these 7 points, the probability of non-correlation is less than 0.2%. Namely, it can be concluded that the relation between the experimental fatigue life and the estimated fatigue life is highly significant. This result reveals that the fatigue life of titanium alloy specimen manufactured by EBM can be estimated by Eq. (1) using the surface residual stress, the surface roughness, the surface Vickers hardness and yield stress.

4 Conclusions

In order to demonstrate the improvement of additive manufactured metallic by mechanical surface treatment and to make clear the important factors on the enhancement, the titanium alloy Ti6Al4V manufactured by electron beam melting EBM was treated by cavitation peening, shot peening and laser peening. The results obtained can be summarized as follows.

- (1) The fatigue life was improved by cavitation peening, shot peening and laser peening.
- (2) As the fatigue life of as machined specimen was larger than that of as built specimen, the surface roughness was an important factor of the fatigue life of Ti6Al4V manufactured by EBM.
- (3) The fatigue life of tested Ti6Al4V can be estimated by considering the surface residual stress, the surface Vickers hardness, yield stress and the surface roughness. Thus, it can be concluded that these are important factors of the enhancement of fatigue strength by the mechanical surface treatments.

Acknowledgements. This work was partly supported by JSPS KAKENHI Grant Number 17H03138 and 18KK0103.

References

1. Edwards, P., O'Conner, A., Ramulu, M.: Electron beam additive manufacturing of titanium components: properties and performance. *J. Manuf. Sci. Eng-Trans ASME* **135**, 1–7 (2013)
2. Sato, M., Takakuwa, O., Nakai, M., et al.: Using cavitation peening to improve the fatigue life of titanium alloy Ti-6Al-4V manufactured by electron beam melting. *Mater. Sci. Appl.* **7**, 181–191 (2016)
3. Soyama, H., Okura, Y.: The use of various peening methods to improve the fatigue strength of titanium alloy Ti-6Al4V manufactured by electron beam melting. *AIMS Mater. Sci.* **5**, 1000–1015 (2018)
4. Peyre, P., Fabbro, R., Merrien, P., et al.: Laser shock processing of aluminium alloys. Application to high cycle fatigue behaviour. *Mater. Sci. Eng. A-Struct. Mater. Prop. Microstruct. Process.* **210**, 102–113 (1996)
5. Sano, Y., Obata, M., Kubo, T., et al.: Retardation of crack initiation and growth in austenitic stainless steels by laser peening without protective coating. *Mater. Sci. Eng. A* **417**, 334–340 (2006)
6. Hatamleh, O., Lyons, J., Forman, R.: Laser and shot peening effects on fatigue crack growth in friction stir welded 7075-t7351 aluminum alloy joints. *Int. J. Fatigue* **29**, 421–434 (2007)
7. Gill, A., Telang, A., Mannava, S.R., et al.: Comparison of mechanisms of advanced mechanical surface treatments in nickel-based superalloy. *Mater. Sci. Eng. A* **576**, 346–355 (2013)
8. Soyama, H., Saito, K., Saka, M.: Improvement of fatigue strength of aluminum alloy by cavitation shotless peening. *J. Eng. Mater. Technol.* **124**, 135–139 (2002)
9. Soyama, H.: Key factors and applications of cavitation peening. *Int. J. Peen Sci. Technol.* **1**, 3–60 (2017)

10. Soyama, H.: Surface mechanics design of metallic materials on mechanical surface treatments. *Mech. Eng. Rev.* **2**, 1–20 (2015). Paper No. 14-00192
11. Kokubun, T., Soyama, H.: Evaluation of fatigue crack propagation in surface modification layer of duralumin treated by various peening. *Trans. JSME* **83**, 1–15 (2017)
12. Kokubun, T., Soyama, H.: Suppression of fatigue crack propagation of duralumin by hybrid peening. *Trans. JSME* **84**, 18-00161-00161-00114 (2018)
13. Nishikawa, M., Kawaragi, Y., Soyama, H.: A method to identify the yield stress of metals using micro-indentation tests with a spherical indenter. *Trans. JSME* **76A**, 1781–1788 (2010)
14. Nishikawa, M., Takakuwa, O., Soyama, H.: Evaluation of yield stress distribution in the surface layer and fatigue properties of the stainless steel modified by cavitation peening. *Trans. JSME* **76A**, 1367–1372 (2010)
15. Soyama, H.: Comparison between the improvements made to the fatigue strength of stainless steel by cavitation peening, water jet peening, shot peening and laser peening. *J. Mater. Process. Technol.* **269**, 65–78 (2019)
16. Naito, A., Takakuwa, O., Soyama, H.: Development of peening technique using recirculating shot accelerated by water jet. *Mater. Sci. Technol.* **28**, 234–239 (2012)
17. Soyama, H.: Improvement of fatigue strength of additive manufactured metals by solid-liquid-gas interfacial phenomena induced by pulse laser. In: 2019 International Conference on Advanced Material Research and Processing Technology (2019, in print)



Influence of Burnishing Process on Microstructure and Corrosion Properties of Mg Alloy AZ31

Chenyao Cao, Jiang Zhu^(✉) , and Tomohisa Tanaka

Tokyo Institute of Technology, 2-12-1, O-okayama, Meguro, Tokyo, Japan
zhuji@mep.titech.ac.jp

Abstract. Magnesium (Mg) alloy is an attractive biodegradable implant material in orthopedic fixation applications. Compared with the permanent metallic implant material, such as titanium alloy and stainless, the Young's modulus of Mg alloys is close to human bone, and it can be gradually absorbed in the human organism. The problems such as stress shielding and secondary surgery operation can be avoided by using Mg alloy. However, the corrosion speed of Mg alloys is too fast for actual medical application. In order to solve this problem burnishing process, which is a kind of surface finishing process, was tried to improve corrosion resistance of Mg alloys in this research. Burnishing experiments were done using a newly developed ball burnishing tool on annealed Mg-Al-Zn alloy AZ31 plates. In order to determine how the parameters of burnishing process affect the microstructure and corrosion properties, the experiments were designed based on Taguchi orthogonal array L9, in which three parameters (burnishing force, tool path interval, and feed speed) are varied at three different levels. For each processing condition, the microstructure near the surface and thickness of layer affected by burnishing process were evaluated by microscope. The experimental results indicated that after the burnishing process the grain size is refined. In addition, corrosion test was carried out and the mass loss of each sample was evaluated. The result shows that burnishing process is effective to improve the corrosion resistance.

Keywords: Magnesium · Burnishing · Corrosion property · Microstructure

1 Introduction

In the treatment of bone fractures, implant such as bone plates and bone screws are used to fix the broken bones. Usually the implants are made of Titanium alloys and stainless for their high stability and biocompatibility. However, such material can hardly dissolve in human body due to the high corrosion resistance, so a secondary surgery is necessary to remove the bone plates after healing. Another problem is stress shielding may occur due to the high stiffness of the permanent implant material. For example, the Young's modulus of titanium alloy is about five times higher than the human bones. During the treatment, fractured bones need proper stimulation to get strong. If stress shielding occurs, bones cannot receive enough stimulation. As a result, even after healing, the healed bones are still weak and would break again easily.

Recently, magnesium alloys received increasing attention in the application of orthopedic fixation. Because magnesium alloys can be gradually absorbed in the human body, and it has similar Young's modulus to human bone, the problems of titanium alloys and stainless can be avoided if magnesium alloy can be used to make implant [1]. However, due to the poor corrosion resistance of magnesium alloys, they may dissolve and disappear before bone recovers completely.

In industrial application, there are many methods to improve the corrosion resistance of magnesium alloys, such as alloys contained with REE (rare earth element), surface coating, and mechanical surface enhancement. In the above methods, REE and surface coating introduce other elements rather than magnesium, and such elements may be poisonous to human body. Therefore, in this research the approach of mechanical processing is tried to improve corrosion resistance of magnesium alloys.

Burnishing process is a kind of surface finishing process to improve the surface property. As shown in Fig. 1, a rigid ball or roller is used to deform and draw material from the peaks of the surface into valleys due to elastic-plastic contact. After this process, the change of surface roughness, grain size and crystal orientation will lead to the improvement of corrosion resistance. Generally, after burnishing grains will become small, and small grain may increase corrosion resistance [2, 3]. In this research, Mg-Al-Zn alloy AZ31 was chosen as the test material, and burnishing experiments were carried out. The grain size, the thickness of work-hardened layer and corrosion properties of the processed sample were evaluated and discussed.

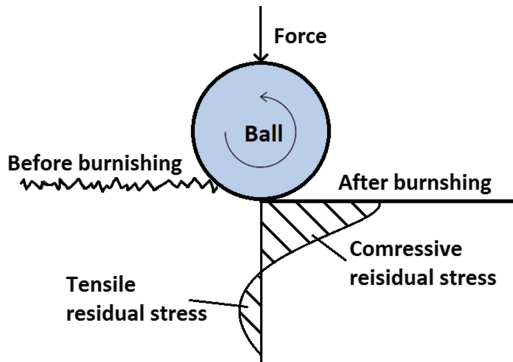


Fig. 1. Schematic of ball burnishing process

2 Methodology

2.1 Burnishing Experiment

The raw materials in this research are AZ31 sheets made by hot rolling. In order to eliminate the influence of hot rolling on the surface of sheets, the top surface of the sheets was removed by a milling process, surface roughness R_a after milling process is $0.23 \mu\text{m}$. After that, the sheets were annealed in vacuum at $500 \text{ }^\circ\text{C}$ for 1 h to release the residual stresses, induce grain growth and induce crystal orientation to random distribution.

In the previous research, a new ball burnishing tool, which could precisely control the burnishing force was designed and fabricated [4]. A tungsten carbide (WC) ball with a diameter of 5 mm, is used as the burnishing ball to contact and press the workpieces. In the burnishing experiments, this tool was fixed on a 3-axis CNC milling machine, the trajectory of the burnishing tool is scan line as shown in Fig. 2. No lubrication fluid is used in this experiment to prevent the reaction of the material and the lubrication fluid.

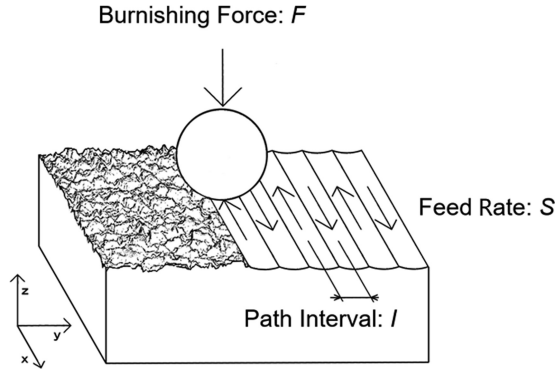


Fig. 2. Diagram of burnishing process and burnishing parameters.

In order to evaluate the influence of each parameter on surface properties and corrosion resistance of Mg alloy AZ31, the experiment was designed using Taguchi method [5]. Taguchi method is usually used to find the most influential parameter for optimizing process condition by calculating S/N ratio (Signal/Noise ratio) of each parameter. S/N ratio is calculated by Eq. 1.

$$S/N = 10 \log \left(\frac{1}{n} \sum_{i=1}^n y_i^2 \right) \quad (1)$$

Here y is measured value such as grain size under different levels, n is number of experiments. In this equation, larger S/N ratio means larger value.

In this research, using orthogonal table a L9 experiment was designed with three main parameters of burnishing process: burnishing force F , tool path interval I , and feed rate S which were varied at three different levels. The sample number and processing condition are shown in Table 1, in which sample No. 0 is the sample without burnishing.

Table 1. Number of samples and processing conditions.

No.	Burnishing force (N)	Path interval (mm)	Feed rate (mm/min)
0	–	–	–
1	100	0.1	100
2	200	0.1	200
3	50	0.1	50
4	100	0.05	50
5	50	0.05	200
6	200	0.05	100
7	100	0.15	200
8	200	0.15	50
9	50	0.15	100

2.2 Microstructure Observation

After burnishing experiment, the processed areas and an area without burnishing process were cut off and then cut from middle in order to let cross-sections expose. Cross-sections were polished until no scratch remains using a polishing disk with 2- μm abrasive grains. The polished sample were etched by etching solution, which is made of 4.2 g picric acid, 10 ml acetic acid, 10 ml distilled water and 70 ml 95% ethanol, for 6 s to make grain boundaries visible. Finally, these samples were observed by microscope to evaluate the work-hardened layer thickness and grain size.

2.3 Corrosion Test

In this research, immersion test was carried out to evaluate how burnishing process influences the corrosion resistance of Mg alloy AZ31. The samples after immersion were evaluated by mass loss and surface observation.

The samples were carefully prepared in order to guarantee that in each sample only the processed surface contacts the solution, and the contact areas in each sample are same. As shown in Fig. 3, firstly the top surface was cut by milling machine with an area of 10 mm \times 10 mm left. Then the samples were embedded in cold-setting embedding resin EpoFix, with top surface covered by pieces of tape to avoid it is stained by resin. After the resin is cured, samples were polished until the tape is exposed. After peeling the tape, samples with only 10 mm \times 10 mm area exposed were finished.

Before the immersion test, the samples were marked and weighed by a precision electronic balance with the resolution of 0.1 mg for three times, and the average value was taken as the original weight of each sample. Then each sample was put into a little bottle which was filled with 5 wt% NaCl solution. In order to keep solution at a certain temperature, 10 bottles were put into water bath, whose temperature was kept at 37 $^{\circ}\text{C}$. The samples were taken out and dried after 7 days immersion.

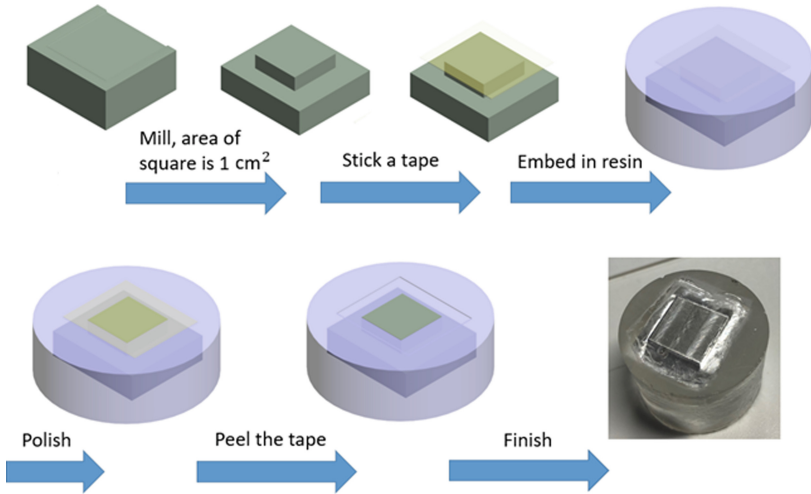


Fig. 3. Preparation for corrosion test.

In this corrosion test, the main corrosion products are $\text{Mg}(\text{OH})_2$, MgO and MgCl_2 . Among these corrosion products, $\text{Mg}(\text{OH})_2$ rarely dissolves in water, and it clings to the surface of samples tightly [7]. In order to measure the mass loss and observe the surface correctly, $\text{Mg}(\text{OH})_2$ was removed by putting the samples in etching solution for 15 min. The constituent of the etching solution is 4.2 g picric acid, 10 ml acetic acid, 10 ml distilled water and 70 ml ethanol (95%), this solution can only dissolve $\text{Mg}(\text{OH})_2$ without reacting with Mg. Finally, the samples are carefully washed and dried. The weight of samples was measured again, and surfaces of samples were observed.

3 Result and Discussion

3.1 Work-Hardened Layer Thickness

The micrographs of the cross section of sample No. 0 and No. 9 are shown in Fig. 4. In Fig. 4, left side of each micrograph shows the surface of the sample, right side is the interior of the sample. Comparing two micrographs, it can be found that the grains of the sample after burnishing are smaller than the sample without burnishing. On micrograph of sample No. 9, it can be observed that the left side is dark, and grains are hard to be seen. This is because samples were sank into etching solution entirely for same time and the area close to the surface was influenced more by burnishing so it has different properties compared with the area beneath, as a result, left side is hard to be seen.

In the case of sample No. 9, because the material received more influence from burnishing process, the grains near surface is smaller than the grains beneath the surface. Theoretically, the smaller the grains are, the higher corrosion resistance would be achieved because of less intermetallic compounds [6]. In addition, the higher the

work-hardened layer thickness are, the longer lifespan of bone plate would be. Therefore, in order to control the absorption rate of bone plate, the size of grains and work-hardened layer thickness should be controlled.

Work-hardened layer thickness is estimated by the change of grain size. As shown in Fig. 4, the grains beneath the surface have bigger size. When the depth reaches a specific value, the sizes of grains do not change much. Therefore, where the grain size stops changing is considered as the bottom of work-hardened layer. Using this method, work-hardened layer thickness of the processed samples were measured, and the results are shown in Table 2.

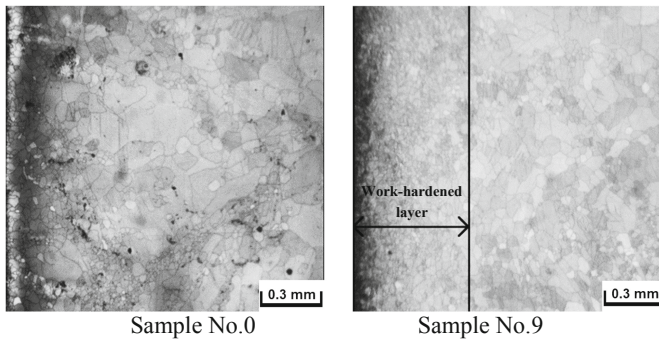


Fig. 4. Micrographs of cross-section of sample No. 0 and sample No. 9.

Table 2. Work-hardened layer thickness.

No.	1	2	3	4	5	6	7	8	9
Thickness (mm)	0.81	0.94	0.81	1.34	0.60	0.94	0.93	1.07	0.59

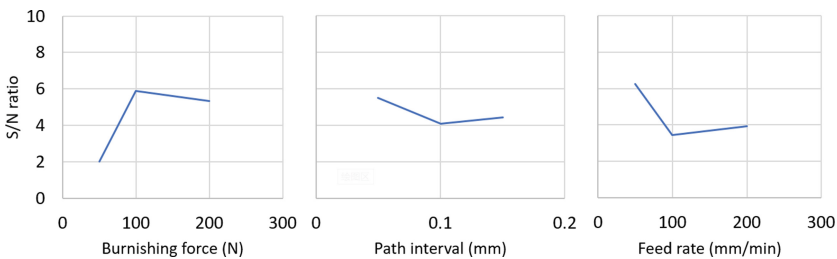


Fig. 5. S/N ratio of work-hardened layer thickness.

In order to find out the most influential parameter and the influence of each parameter, S/N ratio of each parameters was calculated.

Calculated average S/N ratios for each factor are shown in Fig. 5. It can be detected that burnishing force is the most influential factor, stronger burnishing force leads to thicker work-hardened layer.

3.2 Grain Size

Because grains near surface are hard to be observed according to Fig. 4, to evaluate the grain size of each sample, the average size of grains at where the depth is 0.5 mm beneath the surface were measured by drawing a vertical line at where depth is 0.5 mm, as shown in Fig. 6, then grain size was calculated by Eq. 2.

$$d = \frac{l}{n} \quad (2)$$

Here d represents grain size, l represents length of draw line and n represents the number of grains contact draw line. The results are shown in Table 3. S/N ratio was calculated by Eq. 1 as well. The result is shown in Fig. 7. The small value means small grain size. It can be found that just like work-hardened layer thickness, burnishing force is the most influential factor as well. Grains became smaller with stronger burnishing force.

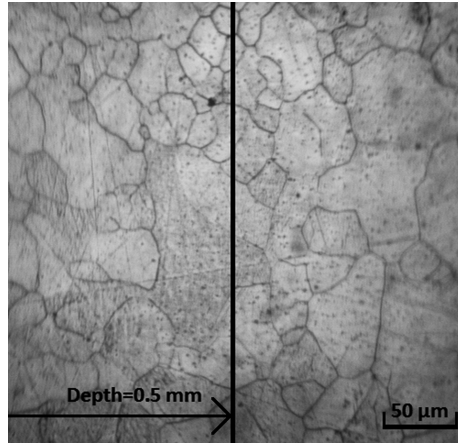


Fig. 6. Micrograph of sample No. 9 at depth of 0.5 mm.

Table 3. Grain size at where depth is 0.5 mm.

No.	0	1	2	3	4	5	6	7	8	9
Grain size (μm)	56.3	19.4	13.2	28.7	26.4	41.3	17.4	27.5	16.5	33.0

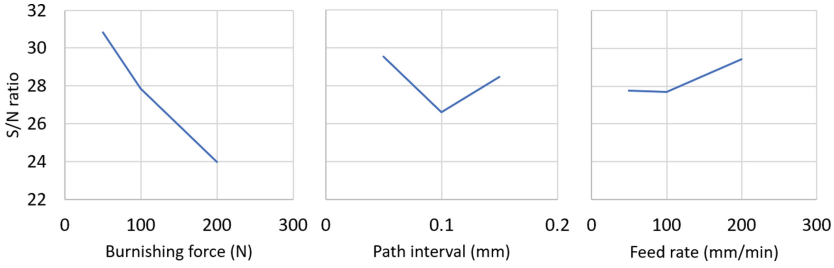


Fig. 7. S/N ratio of grain size.

3.3 Corrosion Test

Mass loss of each sample is measured three times and the average value is shown in Table 4. Mass loss of the sample without burnishing is 24.2 mg and it is higher than samples after burnishing except No. 8, whose mass loss is 25.6 mg. Sample No. 6 has the least mass loss, which is 8.8 mg. From this result, it can be considered that corrosion resistance of Mg alloy AZ31 is increased after burnishing process. S/N ratio of mass loss was calculated as well, the results are shown in Fig. 8. It can be found that path interval has the biggest influence on entire corrosion resistance.

Table 4. Mass loss of each sample.

No.	0	1	2	3	4	5	6	7	8	9
Mass loss (mg)	24.2	23.9	19.2	18.1	16.5	17.7	8.8	18.3	25.6	22.4

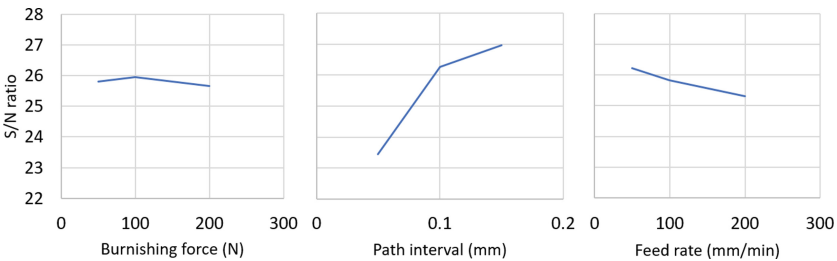


Fig. 8. S/N ratio of mass loss.

The surface pictures of sample No. 0, No. 6 and No. 8 before and after immersion test are shown in Fig. 9. From these results, it can be found that the surface of sample No. 0 after immersion was corroded entirely and uniformly. On the contrary, corrosion of other processed samples is not uniformly distributed. It can be noticed that some areas were not corroded, especially in the case of sample No. 6, the marked areas are still very flat. However, the surface of processed samples had some big pits which were extremely damaged due to corrosion.

Because AZ31 is the alloy of Mg, Al and other components, intermetallic compounds are distributed everywhere. For the different corrosion potential of intermetallic compounds and pure Mg, if the alloy is put into electrolytic solution, primary battery will form and lead to local corrosion which can accelerate the corrosion process. As a result, a lot of small pits can be found on the surface of sample No. 0.

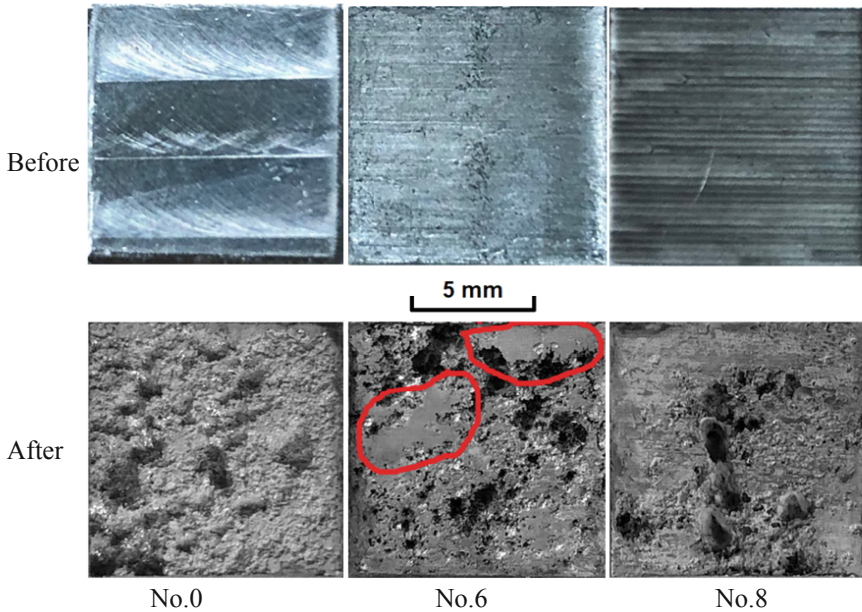


Fig. 9. Surface of sample before and after corrosion test.

However, in the case of the samples which were processed by burnishing process, surfaces show a different pattern. In burnishing process, surfaces were pressed by burnishing ball, as a result grains on the surfaces became smaller and higher amount of lattice defects formed at the same time. Intermetallic compounds can dissolve into the lattice defect so local corrosion could be suppressed [8]. Therefore, some areas of processed samples stay flat.

On the other hand, some big pits can be found on the processed samples, while there is no big pit on sample No. 0. This phenomenon is considered as the result of unevenness of corrosion resistance which was caused by the friction changing between tool and samples during the burnishing process. The areas have bigger grain show lower corrosion resistance. Just like local corrosion caused by intermetallic compounds, area with lower corrosion resistance would be corroded early than other areas, as a result, big and shallow pits form. As surfaces were corroded, metal below surface was less influenced by burnishing process so it has furthermore low corrosion resistance. Therefore, pits acted as anode so became bigger and deeper, which can be found in both sample No. 6 and sample No. 8.

Theoretically, small grain size can lead to high corrosion resistance. While in this research crack and flaking caused by burnishing may occur and cause some areas have lower corrosion resistance than surrounding. And some other factors may influence corrosion resistance as well, therefore, S/N ratio of mass loss does not show a similar trend to S/N ratio of grain size.

4 Conclusions

In this research, the microstructure and corrosion properties of Mg alloy AZ31 processed by ball burnishing process is studied. The Taguchi's orthogonal array method is used to design the experiment. The grain size, work-hardened layer thickness were measured and evaluated. The corrosion properties were investigated by immersion test and evaluated by mass loss and surface observation. The main findings are summarized as below.

1. After burnishing process, the grains close to the surface are refined. The work-hardened layer can be achieved up to about 1 mm. Burnishing force is found to be the most influential factor to grain size and work-hardened layer thickness.
2. An immersion experiment process to quantitatively evaluate the mass loss of the burnished samples was designed. The experimental results show that burnishing process is effective to increase the corrosion resistance of Mg alloy AZ31.

Acknowledgements. This work is supported by JSPS KAKENHI Grant Number JP18K03868, and AMADA Foundation Grant Number AF-201711. The authors are grateful for the materials analysis division, technical department, and Equo Kobayashi laboratory of Tokyo Institute of Technology for their support to achieve the experiment results.

References

1. Dua, H., Wei, Z., Liu, X., Zhang, E.: Effects of Zn on the microstructure, mechanical property and bio-corrosion property of Mg–3Ca alloys for biomedical application. *Mater. Chem. Phys.* **125**(3), 568–575 (2011). <https://doi.org/10.1016/j.matchemphys.2010.10.015>
2. Pu, Z., Song, G.L., Yang, S., Outeiro, J.C., Dillon, O.W., Puleo, D.A., Jawahir, I.S.: Grain refined and basal textured surface produced by burnishing for improved corrosion performance of AZ31B Mg alloy. *Corros. Sci.* **57**, 192–201 (2012). <https://doi.org/10.1016/j.corsci.2011.12.018>
3. Song, G.L., Xu, Z.Q.: The surface, microstructure and corrosion of magnesium alloy AZ31 sheet. *Electrochim. Acta* **55**(13), 4148–4161 (2010). <https://doi.org/10.1016/j.electacta.2010.02.068>
4. Sawada, S., Zhu, J., Shiou, F.-J., Yoshioka, H.: Study on ball burnishing tool enabling constant force control. In: *Proceeding of Spring Annual Meeting of the Japan Society for Precision Engineering*, Paper ID: M16, Tokyo, Japan (2017). (in Japanese)
5. Shiou, F.-J., Huang, S.-J., Shih, A.J., Zhu, J., Yoshino, M.: Fine surface finish of a hardened stainless steel using a new burnishing tool. *Proc. Manuf.* **10**, 208–217 (2017). <https://doi.org/10.1016/j.promfg.2017.07.048>

6. Song, G.-L.: The effect of texture on the corrosion behavior of AZ31 Mg alloy. *JOM* **64**(6), 671–679 (2012). <https://doi.org/10.1007/s11837-012-0341-1>
7. Virtanen, S.: Biodegradable Mg and Mg alloys: corrosion and biocompatibility. *Mater. Sci. Eng. B* **176**(20), 1600–1608 (2011). <https://doi.org/10.1016/j.mseb.2011.05.028>
8. Raman, R.K.S.: The role of microstructure in localized corrosion of magnesium alloys. *Metall. Mater. Trans. A* **35**(8), 2525–2531 (2004). <https://doi.org/10.1007/s11661-006-0233-5>



Effects of Machine Hammer Peened Surface Textures on the Tribological Behavior of Stamping Tools

Peter Sticht^(✉), Johannes Hohmann, and Peter Groche

Institute for Production Engineering and Forming Machines, Technische Universität Darmstadt, Otto-Berndt-Str. 2, 64287 Darmstadt, Germany
sticht@ptu.tu-darmstadt.de

Abstract. Machine hammer peening (MHP) is a dynamic process to smoothen tool surfaces, increase hardness and introduce residual compressive stresses into the surface layer. Additionally, MHP can be used to apply surface textures that act as lubricant pockets onto tools with specifically shaped hammer heads. These surface textures have proven to minimize friction and decrease wear and tear of sheet metal forming tools. As of now, the wear behavior of these surface textures has not yet been investigated sufficiently in stamping processes.

This paper focuses on the application of surface textures by MHP onto stamping tools used for shear cutting operations on a mechanical press. Within the experimental investigations, different textures are applied on the shell area of the stamping tools. During the cutting process, the resulting cutting force is monitored. Based on the force monitoring of the tools the forces are compared after 10000 and 20000 strokes and a correlation analysis between the stroke count as well as wear of the stamping tool, characterized by their functional volumes is conducted.

It is shown that MHP induced surface textures are not only capable of reducing wear and tear, but also that the process condition can be monitored by characteristic process values and inline measurements. This allows for an improved tool construction with adapted surface textures and, taking the correlation of the process monitoring data and the wear of the tools into consideration, longer and more plannable maintenance intervals and higher process reliability can be achieved.

Keywords: Surface texture · Machine hammer peening · Shear cutting

Nomenclature

d	(hammer) head diameter
a	distance of indentation
f	MHP frequency
I	MHP intensity
s	step over distance
v	feed rate
h	stroke
FTI	force-time integral
V _{mp}	peak material volume
V _{vv}	dale void volume

1 Introduction

Forming processes and their reliability are heavily affected by the surface integrity of the tools used. Therefore, high effort is put into the finishing of tool surfaces [1]. Machine hammer peening (MHP) is commonly used for smoothing technical surfaces [2] and introducing residual compressive stresses [3] as well as causing strain hardening in the surface layer of the components treated [4]. By using specially shaped hammer heads, surface textures, which serve as lubricant pockets, can be applied onto the surface in the same process step [5]. The aforementioned effects are caused by an oscillating hammerhead that is deterministically guided over the surface by an industrial robot or a machining center [6].

Within the modern industrial environment, mainly electro-magnetic [7] or pneumatic [8] systems are used, whereas piezo-electric [9] actuators are used in current research applications. Primarily, MHP is used in the tool and mold making industry to ensure the surface integrity of the tools that will be put in production processes such as deep drawing. It has been shown that micro textures can lower the friction coefficients by about 30% compared to manually polished surfaces [5]. Also, wear phenomena and locations change, as particles that would be able to move in process direction are being caught by the micro textures and prevented from causing further abrasive wear on the tool [10].

Not only forming processes, but also cutting processes benefit from textured surfaces. Kitamura et al. show that micro dimples applied on a fine blanking stamp by a laser can improve the tribological conditions [11]. Therefore, an additional process step is necessary, compared to the use of mechanical surface finishing and simultaneous texturing by MHP.

In order to provide guidelines for the application of micro textures on cutting stamps by MHP, the general behavior of the micro textures during cutting processes will be investigated. Following the investigations of [12] and [13], it can be seen that the wear occurrence is significantly higher on the stamp, or more precisely, on the shell surface of the stamp, than on the die. Therefore, this paper focuses on the wear phenomena of the shell surface of the stamp influenced by the MHP process.

Due to the fact that sensors integrated in stamping tools have reached increased capability in recent years, the opportunity rises to expand the monitoring systems and differentiate between sufficient or insufficient process conditions [14]. The improvements achieved in the monitoring systems lead to a benefit in productivity [15]. Using those further developed monitoring systems, the tribological behavior of the tools can be assessed during the process. Based on the investigations performed within the scope of this paper, correlations between several process parameters during both the MHP process affecting the surface integrity of the stamping tools as well as the stamping process itself are deduced. This leads to further process understanding and reduces wear related maintenance delays.

2 Approach

To investigate the characteristic behavior of micro textured cutting stamps, the parameters for the mechanical surface treatment of the tools have to be determined first. Based on previous investigations within the area of surface textured drawing tools

[5, 10], four different surface states will be investigated in this paper: One stamp treated by MHP without any surface texture, and three stamps with either a low, medium or high density of micro textures on the surface. All tools are treated with the same hammering parameters, only the step over distance and the feed rate is varied to reach different percentage areas of the textures on the surface. One stamping tool without any additional surface treatment serves as a reference and is, like all of the above, a state of the art cutting stamp. In the following, the initial surface characteristics of the stamps are measured by means of confocal white light microscopy and the cutting tools are put into test. The test setup is a mechanical press that is equipped with several load sensors, as presented in Fig. 1. The tools and workpieces are evaluated regarding their process characteristics by means of an analysis of the process data gathered from the different sensors and optical measurements after 0, 100, 1000, 5000, 10000 and 20000 strokes. The workpiece material used is a cold rolled low carbon steel for cold forming with a thickness of 2 mm (DC03, material number 1.0347, SAE CS3). This sheet metal is used with an initial lubrication from the previous rolling process of 1.07 g/m^2 .

3 Experimental Setup

The experiments are performed on a high speed press Bruderer BSTA 810. The tool setup is depicted in Fig. 1. For measuring the process force in the top tool, a load washer Kistler 9051A is integrated (a). Additionally, the forces are measured by three symmetrically arranged force washers (Kistler 9047C) beneath the bottom tool plate (d). Four Kistler 5073A charge amplifiers are applied for the force measurements. A National Instruments CompactRio is used as measuring amplifier. The sampling rate is set to 100 kHz. All signals are processed by Matlab 2016b. Furthermore, the optical measurements are performed with a confocal white light microscope (nanofocus μSurf)

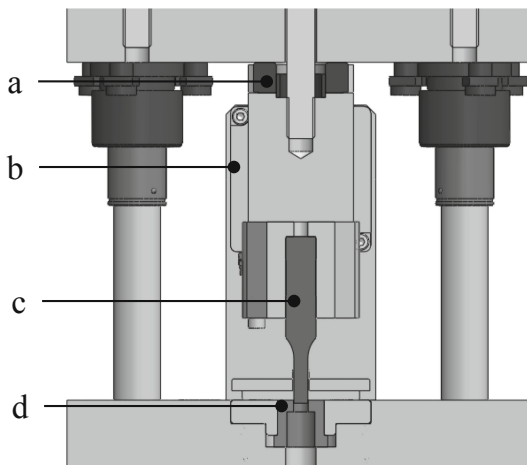


Fig. 1. Setup of the stamping tool: (a) force measuring ring Kistler 9051A, (b) Keyence laser sensor LK-H027, (c) stamp, (d) die

to investigate the wear mechanisms on the shell surface of the stamps. The local displacement measurement is realized by a Keyence laser sensor LK-H027 between the bottom and top tool plate.

The stamping process is commonly monitored by the resulting process parameters as it is shown in [16–18]. The observed parameters can be examined for the stamp-, push- and withdraw-phase.

The cutting stamps and dies are made of M2 high speed tool steel (material number 1.3343, SAE SKH9) and hardened to 55 HRC (Dayton Progress Type BPX 13 1971 P6.0). The composition of the material allows for a good combination of toughness, wear resistance, and hardness. The stamp diameter is 6 mm and the clearance is 0.15 mm. The test series are performed with a stroke rate of 300 spm and a stroke of 35 mm. After a distance of 0.5 mm from the cutting edge, the MHP treatment starts, so the cutting edge is not blunted accidentally. The original surface of the tool is shown as a topography measurement with the confocal white light microscope (nanofocus μ Surf) in Fig. 2.

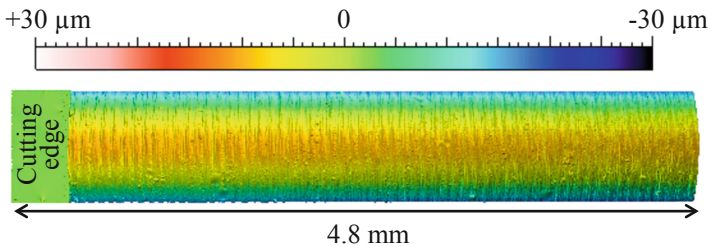


Fig. 2. Original surface of the cutting tools as delivered

The original surface of the tools has a roughness R_z of $2.68 \mu\text{m}$. The surface is turned and the resulting grooves are clearly visible. All measurements are taken with a magnification factor of 20 if not indicated differently. The color range reaches from $-30 \mu\text{m}$ to $+30 \mu\text{m}$.

An electro-magnetic hammering system (Accurapuls) is used for the MHP treatment of the tools. Using this hammering system, the hammering frequency f and the intensity I are controllable during the process. A spherical hammerhead with a diameter of 20 mm as primary hammerhead geometry is used for all hammering operations. The hammering frequency is constantly held at 180 Hz, the stroke is set to 0.4 mm and the stroke intensity I remains constant at 90%. In order to obtain micro textures on the surface after the hammering process, a hammerhead with a micro tip (Fig. 3) as secondary geometrical feature is used for the MHP treatment of the textured tools.

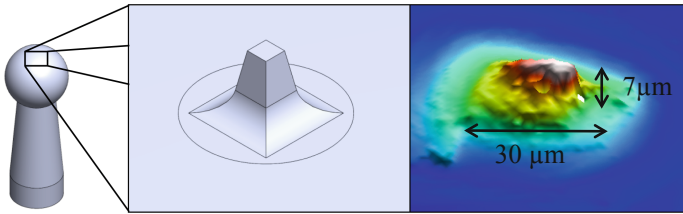


Fig. 3. Micro tip on the hammer head to apply surface textures

To reach a variation in the percentage area of the secondary geometrical structures, the feed rate v , which results from the turning speed of the cylindrical stamp and its diameter, and the step over distance s , is changed. Thus, four different surface topologies with no, low, medium, and high share of textures are created. In Fig. 4(a), the hammered tool surface with no textures is shown. All MHP-treated surfaces have approximately the same roughness as the hammerhead diameter is comparatively large (20 mm) in contrast to the micro tip (30 μm).

The MHP-treated area has a roughness R_z of 1.82 μm (stamp 1), hence it is 32% smoother than the initial surface. The feed rate v is set to 716 mm/min or 38 rpm, accordingly. This leads to a theoretical distance of the indentations of 67 μm . The same parameter setup is used for the MHP process of the stamping tool with a medium percentage area of the secondary geometrical textures (stamp 3) leading to the same roughness. The textured surface is presented in Fig. 4(b). Caused by deviations of the turning speed of the stamping tools during the MHP-process, the resulting distance of the indentations is measured at 60 μm . The textures have a dimension of 30 μm in process direction.

As a result of the distance of indentation not being a whole-number multiple of the circumference of the cutting stamp, the textures do not line up straight and cover the whole lateral surface of the tool in the direction of the stamping process. In order to detect whether or not the percentage area of the textures has an influence on the tribological behavior of the tool surface during the experiments, two more texture patterns are created and described in the following.

A lower percentage area of the textures can be achieved by increasing the feed rate to 829 mm/min or 44 rpm. The calculated distance of the indentations at 180 Hz is 77 μm , whereas the measured distance is 70 μm .

To reach a higher density of the secondary geometric textures on the surface, the feed rate is lowered to 641 mm/min or 34 rpm respectively. The theoretic distance of indentations thus is 60 μm . The surface textures depicted in Fig. 4(d) show a vertically measured distance of 53 μm .

The geometry of the textures with the high and medium percentage areas of textures does not appear in even rectangles on the surface which is caused by the indentation of the hammerhead of the next impact and creates crescentic textures. Due to the larger distances of the indentations, the pockets on the surface (Fig. 4(c)) remain near their original shape. Thus, material in the surface layer is plasticized and shifted in radial direction from the center of the impact towards the existing textures. This effect can be observed when the impact energy of the hammerhead causes an indentation with a

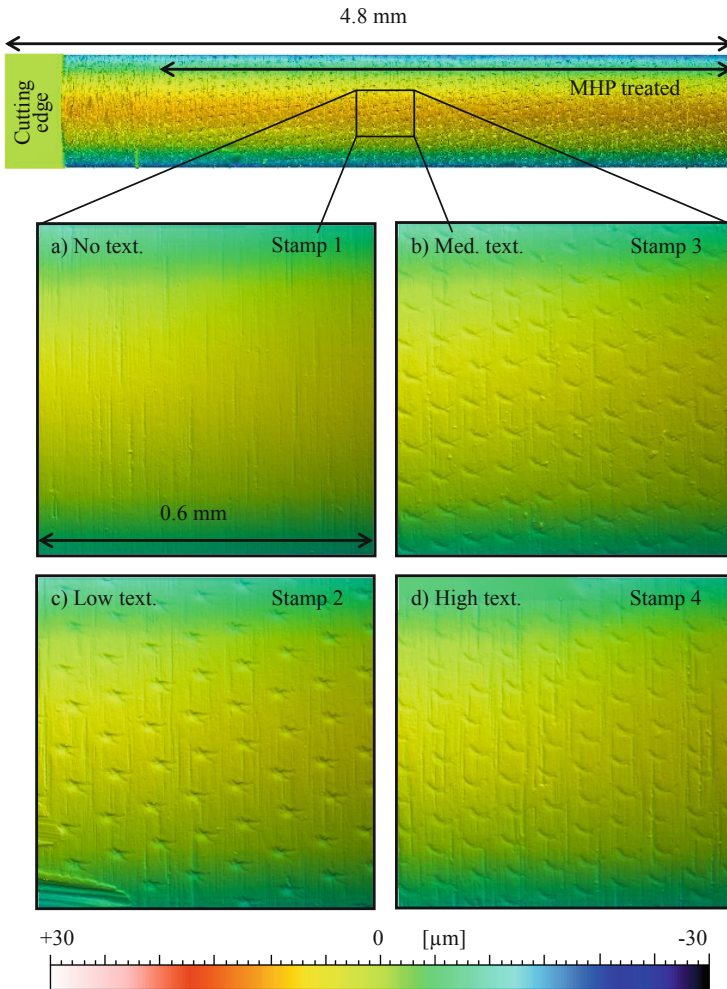


Fig. 4. MHP-treated surface of the cutting tools with (a) no textures, (b) medium textures, (c) low textures and (d) high textures (percentage area)

larger radius than the distance of two following indentations. The dependency of the diameter of indentation and impact energy is shown in [19]. The area percentage of the micro textures projected in process direction is 13% (stamp 2), 19% (stamp 3) and 24% (stamp 4). Taking the surfaces shown as a basis, the experimental matrix can be arranged. Each stamp is put into operation after the MHP process and located in the tooling system as presented in Fig. 1. The characteristic process forces are monitored using the setup described above.

4 Results and Discussion

In this section, the results of the force measurements and the confocal surface measurements after distinct stroke numbers are presented and discussed. The force signals can be divided into three main sections: The stamp section (a), the push section (b) and the withdraw phase (c). Depicted in Fig. 5, one can clearly determine these sections and their different behavior, as initial wear of the stamping tools occurs. Figure 4 illustrates the force signals after 10,000 strokes, the displacement is measured in mm and the force is measured in kN.

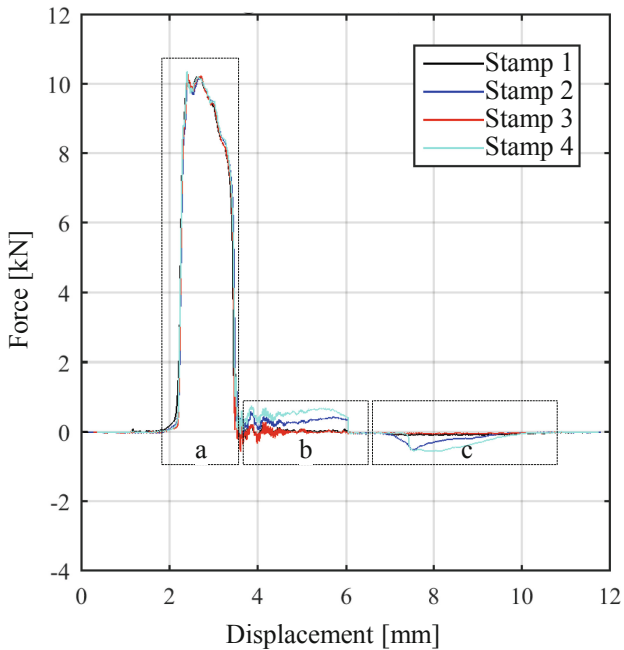


Fig. 5. Force signals of the investigated tools after 10,000 strokes

It can be stated that there is no variation in the maximum stamp force of the four different tool surfaces. During the push and withdraw section, a difference in the forces can be seen. Stamp 4 (high texture density) shows the highest push and withdraw forces, followed by stamp 2 (low texture density) and stamp 3 (medium texture density). Stamp 1 (no textures) shows almost no change in the force signals compared to the initial condition. These force signals are correlated with characteristic surface values by means of their functional volume according to standard ISO 25178. For each stamp, the peak material volume (V_{mp}) and the dale void volume (V_{vv}) are evaluated. These values describe the function of a surface based on the excess (V_{mp}) or missing (V_{vv}) volume of material. As the wear phenomena are not evenly partitioned around the circumference of the stamp, four sides are measured (Fig. 6).

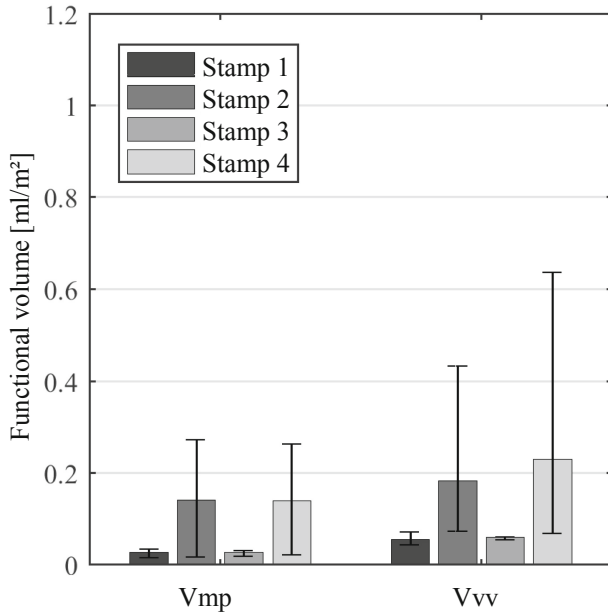


Fig. 6. Functional volumes of the cutting stamp surface after 10,000 strokes

The characteristic functional volume parameters confirm the assumption that can be derived from the force signal measurements. Adhesive as well as abrasive wear phenomena can be correlated with the characteristic process data. The wear mostly occurs on the side of the cutting stamp that is heading towards the intake direction of the sheet metal (see Fig. 9). This can be seen looking at the error bars in the diagram (Fig. 8), where the maximum and minimum values of the functional volumes are in evidence.

The stamp has to overcome a distance of 2 mm until it initially touches the sheet metal. After 20,000 strokes, the characteristic values are evaluated again (Figs. 7 and 8).

Furthermore, the force signals after 20,000 strokes can be correlated with the functional volumes again. The force signals after 20,000 strokes are shown in Fig. 7.

Taking the force-displacement values into consideration, it can be noticed that the cutting tools show different wear behavior, depending on their initial surface texture. Stamp 2 (low texture density) clearly shows the highest push and withdraw forces while the force values of stamp 1 and 4 can be located in the midrange. Stamp 3 (medium texture density) shows almost no change in its force signal. This is also confirmed by the functional volume parameters and can be seen in Fig. 8. Here, the increase in the parameters V_{mp} and V_{vv} and the irregularity of the wear phenomena become evident.

It can be stated that there is a good correlation between the force signals (see Fig. 7) and the functional volumes (Fig. 8). The reasons for the detected effects can be seen in the differing surface power density that is caused by the different feed rates of the MHP process needed to create different texture densities. It can be realized that the hammered shell surface (stamp 1) and the medium textured surface of stamp 3 show an advantage

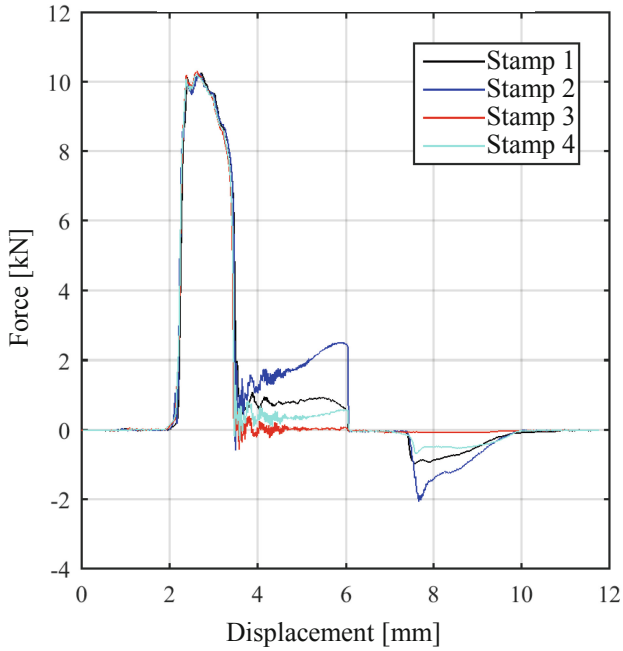


Fig. 7. Force signals of the investigated tools after 20,000 strokes

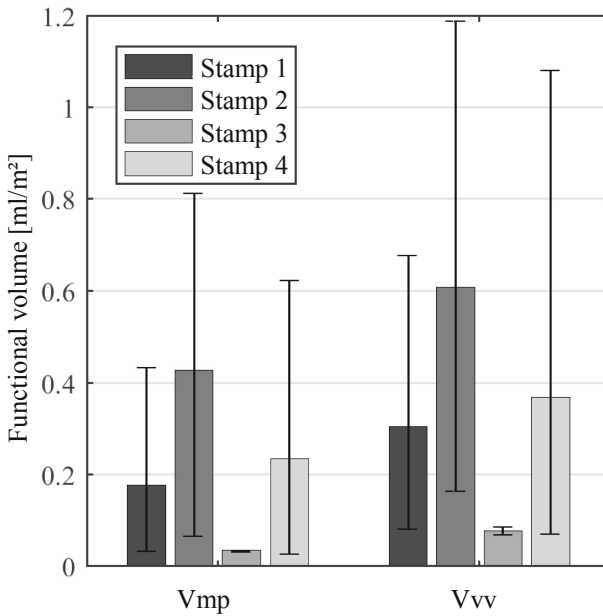


Fig. 8. Functional volumes of the cutting stamp surface after 20,000 strokes

regarding stamps 2 and 4. The advantage in wear comparing stamp 1 and stamp 3 can only be a result of the micro textures applied, as the stamps are treated with the exact same MHP parameters regarding the stroke, frequency, stepover distance and feed rate.

This phenomenon also confirms the findings in [5], where surfaces with texture coverage of 20% result in the lowest friction coefficients compared to 15% and 25% area percentage. Furthermore, there is an optimum in the coverage of surfaces with micro textures where two different effects occur. Firstly, the capability of providing lubrication in the contact zone increases when the percentage area of the textures is rising. Secondly, due to the decreasing contact area at high texture densities, the contact normal pressure is increasing, causing higher friction coefficients and thereby higher wear. This effect occurs when the contact normal pressure reaches a critical amount resulting in excessive wear and tear. For non-critical contact normal stresses, the friction coefficient could also decrease with less contact area.

To give an example for highly abrasive and adhesive wear, the four shell surface sections of stamp 2 are displayed in Fig. 9.

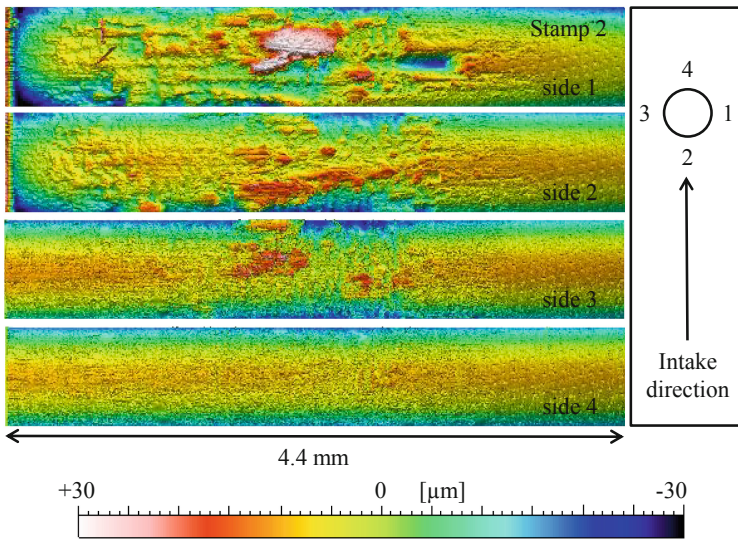


Fig. 9. Wear locations on stamp number 2 after 20,000 strokes and sheet metal intake direction (cutting edge on the left side)

The asymmetry of the wear phenomena can be explained by slight deviations in the stamp position by the press superimposed by wear caused by the relative movement of the sheet metal due to strip tension. Taking all stamping tools as a reference, side 3 and 4 always show the least wear and tear. Therefore, side 3 and 4 represent the lower edges of the error bars in the Figs. 6 and 8, whereas sides 1 and 2 represent the upper edges of the error bars.

As the wear of the stamps obviously does not have an influence on the maximum stamp force, a change in the maximum stamp work cannot be detected, which confirms

the findings in [14]. The push and withdraw section show a clear differentiation in their characteristic values. The push work and the withdraw work as force-time integrals (FTI) are therefore identified as decisive factors and presented in the following figures (Fig. 10).

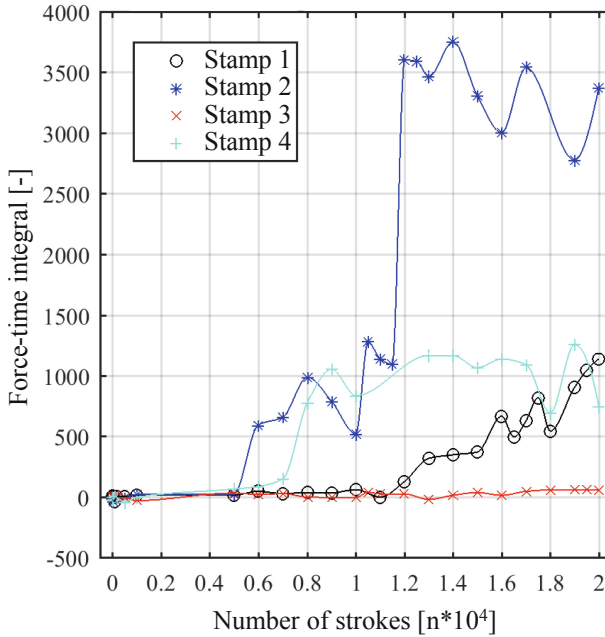


Fig. 10. Force-time integrals of the push work over the number of strokes

The first increase in the push work can be detected at 5,000 strokes for the stamp with a low percentage area of micro textures on the surface (stamp 2). The FTI then rises until 8,000 strokes are reached, after which it declines to 500 (FTI) at 10,000 strokes. Most probably this effect is caused by a material built up by adhesive wear on the stamp shell, which breaks off the surface. This effect can repeatedly be noticed for all FTI-curves showing wear.

The push work values can be correlated with the functional volumes at 10,000 and 20,000 strokes with stamp 1 showing the most distinct wear, stamp 1 and 4 at similar levels and stamp 3 with the best wear resistance over all 20,000 strokes. This finding corresponds well with the results of [5], where the best surface integrity is achieved with a similar surface texture. The same behavior regarding the tribological effects of the MHP surface treatment can be seen for the withdraw work (Fig. 11). Here, however, the effects are not as pronounced.

The data presented allows for the assumption that the medium texture density of the machine hammer peened surface leads to an optimized wear behavior under the boundary conditions in the case at hand.

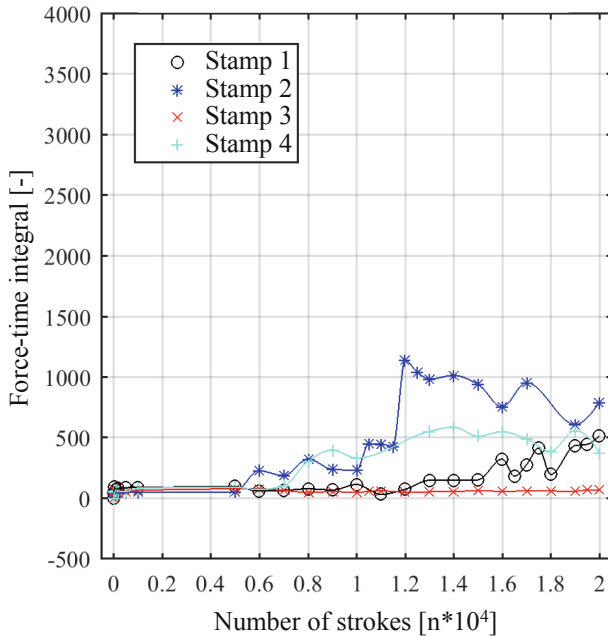


Fig. 11. Force-time integrals of the withdraw work over the number of strokes

5 Conclusion and Outlook

It is shown in the paper presented, that it is possible to monitor the process condition of a stamping process with state of the art monitoring systems. At the same time machine hammer peened surface textures can be applied on stamping tools, leading to an increased wear resistance. Thus, not only more plannable maintenance intervals but also tribological optimized tool surfaces can be achieved.

To gain further insights regarding the application and functional principle of MHP induced surface textures under different boundary conditions, more experiments will be performed.

As the wear phenomena occur unevenly on the shell surface of the stamp, not only the vertical loads, but also the horizontal loads on the cutting tool will be considered in future works. As a result, an even more precise evaluation of the process condition is feasible. Also, the effects of tool wear on the produced goods will be evaluated and a wear threshold considering the quality of the sheet metal products will be defined.

Acknowledgements. The authors would like to thank their industrial partners for the support and the ongoing collaboration within the field of production technology and research on forming machines at PtU.

References

1. Schulze, V., Bleicher, F., Groche, P., Guo, Y.B., Pyun, Y.S.: Surface modification by machine hammer peening and burnishing: CIRP Ann. Manuf. Technol. **65**, 809–832 (2016)
2. Wied, J.: Oberflächenbehandlung von Umformwerkzeugen durch Festklopfen: Ph.D.-Thesis, Darmstadt (2011)
3. Hacini, L., van Le, N.: Effect of impact energy on residual stresses induced by hammer peening of 304L plates. J. Mater. Process. Technol. **208**, 542–548 (2008)
4. Groche, P., Engels, M., Müller, C.: Wear behavior of sheet metal forming tools made from nodular cast iron after mechanical surface treatments. Trans. NAMRI SME **38**, 531–538 (2010)
5. Steitz, M., Stein, P., Groche, P.: Influence of hammer-peened surface textures on friction behavior. Tribol. Lett. **58**, 24 (2015)
6. Steitz, M., Scheil, J., Müller, C., Groche, P.: Effect of process parameters on surface roughness in hammer peening and deep rolling. Key Eng. Mat. **554–557**, 1887–1901 (2013)
7. Patent DE 10 2006 033 004 A1: Klopfvorrichtung- und Verfahren, Deutsches Patent- und Markenamt, Germany (2006)
8. Patent 10 2010 019 547 A1: Kaltschmiedevorrichtung und Kaltschmiede-verfahren, Deutsches Patent- und Markenamt, Germany (2010)
9. Lienert, F., Hoffmeister, J., Schulze, V.: Residual Stress Depth Distribution after Piezo Peening of Quenched and Tempered AISI 4140. In: Materials Science Forum, vol. 768–769, pp. 526–533 (2014)
10. Steitz, M., Klasen, P., Groche, P.: Wear behavior of hammer peened surface textures during strip drawing test. In: IDDRG 2015 Conference, Shanghai, China (2015)
11. Kitamura, K., Makino, T., Nawa, M., Miyata, S.: Tribological effects of stamp with micro-dimples in blanking under hydrostatic pressure. CIRP Ann. Manuf. Technol. **65**, 249–252 (2016)
12. Borchert, P.: Einflüsse der Werkzeuggeometrie und der Maschine beim Schneiden von kaltgewalztem Elektrolech, Dissertation, TU Hannover (1976)
13. Hoffmann, H., Golle, R., Demmel, P., Mair, J., Nürnberg, G., Hörmann, F.: Extension of blanking applications through innovation: tagungsband feintool. University Colloquium, Zürich (2009)
14. Hohmann, J., Schatz, T., Groche, P.: Intelligent wear identification based on sensory inline information for a stamping process. In: Proceedings of 5th International Conference on Advanced Manufacturing Engineering and Technologies (NEWTECH), pp. 285–296. Springer, Heidelberg (2017)
15. Klocke, F.: Prozessüberwachung, Editorial, wt Werkstattstechnik 91, vol. 5, pp. 255–258 (2001)
16. Tan, Y., Hahn, O., Du, F.: Process monitoring method with window technique for clinch joining. ISIJ Int. **45**, 723–729 (2005)
17. Khrebtov, P.: Neuartiges Verfahren zur Online-Prozessüberwachung und –Fehlerklassifizierung beim Durchsetzfügeverbinden von Blechen. Dissertation, Technische Universität Clausthal (2011)
18. Roskam, R.: In-Prozess-Überwachung von Pressen der Blechverarbeitung. Dissertation, Technische Universität Hannover (1999)
19. Sticht, P., Steitz, M., Groche, P.: Prediction and experimental validation of an impact energy threshold for mechanical surface smoothing. Proc. CIRP **45**, 159–162 (2016). 3rd CIRP Conference on Surface Integrity



Mechanical Properties Enhancement of Additive Manufactured Ti-6Al-4V by Machine Hammer Peening

Leonor Neto^(✉), Stewart Williams, Jialuo Ding, Jan Hönnige, and Filomeno Martina

Cranfield University, Cranfield MK43 0AL, UK
l.neto@cranfield.ac.uk

Abstract. Wire + Arc Additive Manufacturing (WAAM) is a technology potentially offering reduction of material wastage, costs and shorter lead-times. It is being considered as a technology that could replace conventional manufacturing processes of Ti-6Al-4V, such as machining from wrought or forged materials. However, WAAM Ti-6Al-4V is characterized by coarse β -grains, which can extend through several deposited layers resulting in strong texture and anisotropy. As a solution, inter-pass cold rolling has been proven to promote grain refinement, texture modification and improvement of material strength by plastically deforming the material between each deposited layer. Nevertheless, with the increased interest in the WAAM technology, the complexity and size of the deposited parts has increased, and its application can be hindered by the low speed and complex/costly equipment required to perform rolling at this scale. Therefore, Machine Hammer Peening (MHP) has been studied as an alternative cold work process. MHP can be used robotically, offering greater flexibility and speed, and it can be applied easily to any large-scale geometry. Similarly to rolling, MHP is applied between each deposited layer with the new ECOROLL peening machine and, consequently, it is possible to eliminate texturing and reduce the β -grains size from centimeters long to approximately 1 to 2 mm. This effect is studied for thin and thick walls and no considerable change in grain size is observed, proving the applicability of MHP to large components. The yield strength and ultimate tensile strength increases to 907 MPa and 993 MPa, respectively, while still having excellent ductility. This grain refinement may also improve fatigue life and induce a decrease in crack propagation rate. In this study, it has been shown that MHP is a suitable process for WAAM Ti-6Al-4V applications, can be applied robotically and the grain refinement induced by very small plastic deformations can increase mechanical properties.

Keywords: Wire plus arc additive manufacturing · Machine hammer peening · Titanium · Grain refinement · Mechanical properties

1 Introduction

Wire + Arc Additive Manufacturing (WAAM) is a process suitable for production of medium to large components with medium complexity. It promises a reduction of production time, material wastage and overall cost of equipment and manufacturing [1]. For these reasons, industrial sectors have been showing an increasing interest in this technology. Particularly the aerospace industry sees the potential of applying WAAM to high strength materials, such as Ti-6Al-4V, which are difficult and costly to manufacture when using conventional manufacturing processes [2]. WAAM technology has been widely reported for the deposition of Ti-6Al-4V alloy [2–4], but its industrial application is limited by the lower and anisotropic mechanical properties in the as-deposited condition, which while being above the Additive AMS 4999 specification are lower than wrought alloys. This is a result of the typical macrostructure of WAAM Ti-6Al-4V that is characterized by coarse columnar prior- β grains, which can extend several centimeters in the building direction (vertical direction). The preferential growth of prior- β grains results in a higher yield and ultimate tensile strength and lower elongation in the horizontal direction when compared with the vertical direction [2]. Also, the microstructure of Ti-6Al-4V WAAM is a crucial factor, affecting the fatigue life of the components. In the last deposited layer of a WAAM built wall, the microstructure is predominantly composed of fine Widmanstätten α , while the remaining wall shows coarser Widmanstätten α . This coarse lamellar microstructure of as deposited WAAM Ti-6Al-4V has been reported as beneficial for a decrease in the fatigue crack growth [5, 6]. It is also shown that the decrease of the lamellae size increases the strength of the material [7].

Martina et al. [7] shows that the application of inter-pass cold rolling induces microstructural changes to Ti-6Al-4V WAAM material. This process consists of applying a defined load on the top surface of each layer through a roller and re-depositing a subsequent layer. This procedure is repeated until the desired geometry is obtained. The combination of the applied plastic strain and heating the material above the recrystallization temperature induces grain refinement of the initially columnar prior- β grains into very small equiaxed grains. The grain size varies according to the load applied and roller design but ranges from approximately 139 to 6 μm for loads of 50 and 75 kN, respectively. This is compared to the unrolled grain size of a few to tens of mm. In the same study, it was also observed that there was a decrease of α lamellae thickness with an increase of applied load. Both changes in the microstructure resulted in isotropic properties and increased strength. Qiu [8] also does a preliminary study of the fatigue crack propagation rate of inter-pass rolled samples and concludes that there is an improvement of fatigue crack growth properties when compared with unrolled WAAM and wrought materials. Isotropic properties are also achieved.

With the development of the WAAM technology, there is an increasing demand for more complex and larger components which precludes the use of a rolling process. For inter-pass rolling, a stiff gantry is required in order to apply loads of up to 100 kN, which is costly and limits the design freedom of WAAM applications [9, 10]. Also, the rolling speed reported ranges from 3 to 7 mm/s [7, 11], which may increase significantly the production time of the WAAM components. Machine Hammer Peening

(MHP) has been previously studied as an alternative to this technology [11–13]. It is shown that MHP has the capability of refining the previously columnar β grains and that it can be applied robotically, guaranteeing the flexibility and repeatability required to employ this technology to WAAM components. The MHP speed is also 18 mm/s [11], which is much greater than rolling, although the transformed area is not as wide as with rolling. In another study [13], it is also reported that an increase in tensile properties and grain refinement is achieved, but the methodology used for MHP and deposition is unclear.

This paper aims to further understand the capability of MHP as an alternative or aid to the already established cold rolling process. The microstructure changes are studied for thin and thick walls and linked with an observed increase of tensile properties and prediction of fatigue behavior.

2 Experimental Work

2.1 Manufacturing and Setup of WAAM Samples

The as-deposited and inter-pass MHP samples are built using a robotic arm, with an integrated plasma transferred arc torch with wire feeder and an MHP ECOpeen-C tool, as shown in Fig. 1. After each deposited layer, the robotic arm is rotated 90° to obtain a vertical position for the ECOpeen-C tool. This rotation is repeated every layer to perform inter-pass MHP and inverted again for deposition.

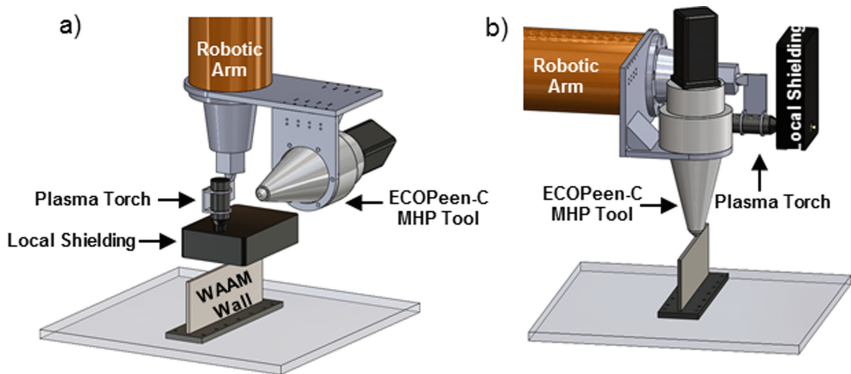


Fig. 1. Experimental set-up (a) ready for deposition and (b) after a 90° rotation to vertically position the ECOpeen-C tool and apply MHP

To deposit Ti-6Al-4V wire, an EWM T552 Tetrax Plasma power source is used. The wire is supplied by Perryman and its composition is shown in Table 1. For all samples, the substrates of the same alloy are cut to a dimension of 90 × 350 × 8 mm. To prevent oxidation of the deposited material, a local shielding device is employed with a gas flow rate of 70 l/min of pure-shield argon (99.99%) [14]. Two different wall geometries are produced – thin and thick walls. For thin walls (<10 mm), single bead

tracks are deposited for a length of 315 mm up to a height of 130 mm which consisted of 110 layers. The thick walls are deposited using an oscillation strategy, which consists of moving the torch in a squared zig zag pattern with the oscillation width determining the width of the wall (~ 20 mm) and a step advancement in the direction of the length of the wall of 4 mm. 10 layers are deposited for this condition giving a wall height of approximately 25 mm. A dwelling temperature of 140 °C is kept for as deposited and inter-pass MHP samples. This control is carried out with a touch probe sensor applied between each layer in the center of the wall. Further deposition parameters are in Table 2.

Table 1. Wire composition [WT%]

Ti	Al	V	Fe	O	C	N	Others
Balance	6.14–6.15	3.91–3.94	0.17–0.18	0.15	0.021	0.007–0.008	0.0172

Table 2. Welding parameters for thin and thick (oscillated) walls

Deposition parameter of:	Thin walls	Thick walls
Current [A]	145	170
Wire feed speed [m/min]	2.4	3
Travel speed [mm/s]	5	6.2
Wire diameter [mm]	1.2	1.2
Work piece distance [mm]	8	8
Dwelling temperature [°C]	140 ± 10	140 ± 10
Plasma gas flow [l/min]	0.8	0.8
Shielding gas flow [l/min]	8	8

The ECOpeen-C is an electro-driven MHP tool developed by ECOROLL AG, which allows a variable impact energy range from 50 to 700 mJ and has the capability of adapting to uneven surfaces up to 4 mm (stroke). In this initial study, an energy of 700 mJ is used and this tool has proven to be able to adapt to the slight uneven WAAM top layers both in thin and thick geometries, providing a consistent MHP pattern. For this energy level, the tool frequency of 225 Hz is used to obtain an indentation distance of 0.5 mm (distance between each impact of the tool into the material – Fig. 2), the travel speed of the robotic arm is set at 112.5 mm/s. The diameter of the tool insert has a radius of 10 mm. For thin walls, a single peening line is employed, as shown in Fig. 2(a) and (b) and highlighted in blue. For thick walls, a MHP squared pattern is used for a length of 5 mm (Fig. 2(c)).

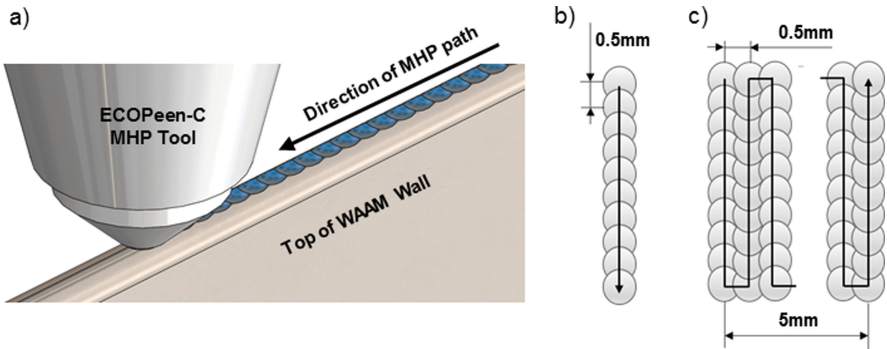


Fig. 2. Thin wall with (a) top layer MHP with a peening line (blue colored) and tool paths for (b) peening line of thin walls and peening square of oscillated thick walls. A 0.5 mm indentation distance is kept for all directions.

2.2 Material Characterization and Testing

For each condition tested, a cross section is cut in the perpendicular direction to the MHP path (vertical cut), hot mounted in conductive resin, grinded and polished. For optical microscopy and Scanning Electron Microscope (SEM) analysis, etching with a diluted solution of hydrofluoric acid is applied. Eight SEM images are captured using a backscatter detector for higher contrast imaging of α lamellae size. To measure the size of the prior β -grains, a contour is drawn to outline the shape and size of each grain, which was after measured in both the vertical and horizontal directions. Only grains under the MHP paths are measured in three different locations.

To obtain a microhardness profile, a Zwick/Roell ZHV hardness machine is used with a load of 1 kg and a dwell time of 15 s. For thick walls, 10 parallel lines spaced 0.2 mm from each other are measured from the top peened layer until the substrate. The spacing between each measurement in the same line was also 0.2 mm. For thin walls, the same spacing is used but only 5 parallel lines are measured, due to the width of impact of the single path of MHP applied.

Tensile testing is carried out for both as deposited and inter-pass MHP conditions of thin walls. The orientation of testing is shown in Fig. 3(a), where five coupons in the vertical (build direction) and horizontal (deposition direction) directions are extracted following the dimensions in Fig. 3(b).

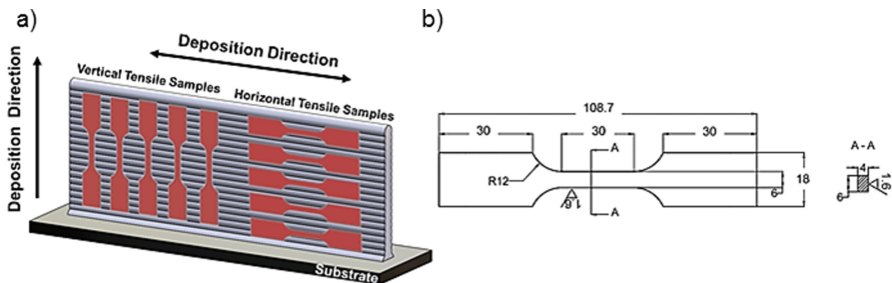


Fig. 3. Tensile specimens (a) position and (b) dimensions of the coupons (all in mm)

3 Results and Discussion

3.1 Effect of MHP on Grain Refinement

The β grain refinement achieved by applying inter-pass MHP is shown in Fig. 4. Figure 4(a) shows the contrast between the long columnar grains of the as deposited condition and the refined grains after applying inter-pass MHP in thin walls. This effect is explained by Donoghue et al. [15] in which it is suggested that exposing the plastically deformed material to temperatures above β transus activates grain refinement. The average β -grain size is approximately 1 mm but with a large variation of size, ranging from 200 μm to more than 2 mm long, as is evidenced in Fig. 4(b). Interestingly, similar grain sizes are achieved in a study by Hönnige et al. [11], even though a much lower energy impact tool is used. The grain size is still larger than the one achieved by inter-pass cold rolling [7]. However, the ideal beta grain size for industrial applications is still unknown and the grain size achieved by MHP could be enough. Figure 4(c) shows the grain refinement from as deposited to inter-pass MHP samples of an oscillated thick wall. The MHP pattern is only applied at the center of the deposited material so the grains in the center are refined but there are still columnar beta grains at the edges of the wall. Figure 4(d) shows a magnified image of the central area for both as deposited and MHP conditions of oscillation strategy. An average grain size of approximately 1.4 mm is measured for the MHP condition, with a similar variation of size for the thin wall. Although for oscillated deposition the material is exposed to higher temperatures for a longer period, no considerable changes of grain size are observed when comparing with thin walls. Similarly to what is reported in Hönnige et al. [12], grain refinement is observed where there was no strain measured. Nevertheless, in general, the beta grain size is in the order of the layer height. Thus, to obtain grain refinement, the magnitude of MHP or the deposition strategy are not controlling parameters.

3.2 Effect of MHP on Mechanical Properties

Microhardness

The measurements of microhardness show a visible increase of hardness for the inter-pass MHP samples when compared with the as deposited condition. Near the top surface, the hardness magnitude is similar for the thin and thick inter-pass MHP samples, but it is detected a change of depth of work hardening effect by the drop of magnitude in the hardness profiles between the thin and thick walls of inter-pass MHP. For the thick inter-pass MHP sample, an impact of approximately 2 mm is detected while for thin inter-pass MHP it is approximately 1 mm (Fig. 5). This is possibly achieved by the combination of two factors. Firstly, by applying a peening pattern to the thick walls instead of only one peening line of the thin walls, the magnitude of cold work increased and, as a result, there is a visible increase of the depth of the MHP impact. Also, due to the increased thickness of the material of the thick walls, the deformation into the material is more laterally constrained and is acting mainly downwards into the material [15]. Further testing of the plastic strain induced should be carried out with different methods to complement the microhardness profile presented.

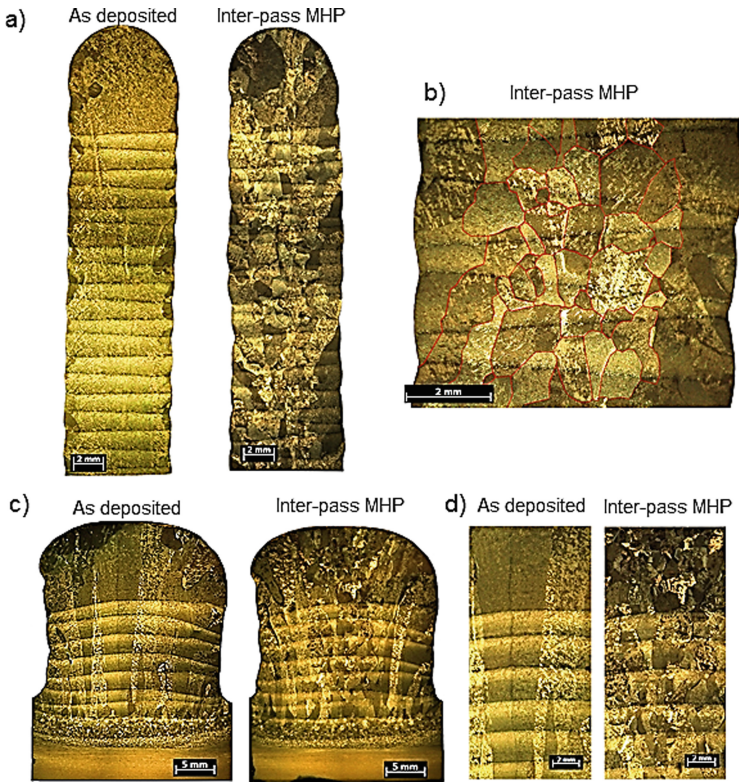


Fig. 4. Macrostructure of (a) thin walls as deposited and after inter-pass MHP, (b) an amplified grain size of the MHP sample, (c) oscillated thick walls as deposited and inter-pass MHP and (d) amplified macrostructure for grain size inspection.

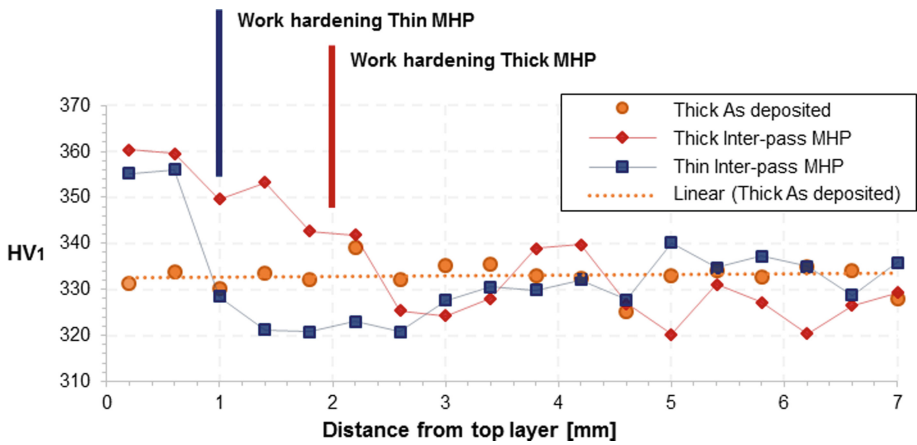


Fig. 5. Micro-hardness profile of MHP and as deposited thick and thin walls

Tensile Properties

For the as deposited samples, anisotropic properties are obtained. In the horizontal direction, higher strength and lower elongation are observed, when compared to the vertical direction. This is explained by the preferential vertical growth of the prior- β grains and agrees with the literature [2, 9, 16]. For both directions of the inter-pass MHP, there is an increase of ultimate tensile and yield strength with a corresponding decrease in elongation of 9% in the vertical direction, but it is not critical as the elongation is still above 10% (Fig. 6). The preferential direction of elongation for the vertical direction with a decrease in strength is eliminated and isotropic properties are achieved through the grain refinement induced by inter-pass MHP. Similar properties have been reported in Byun et al. [13].

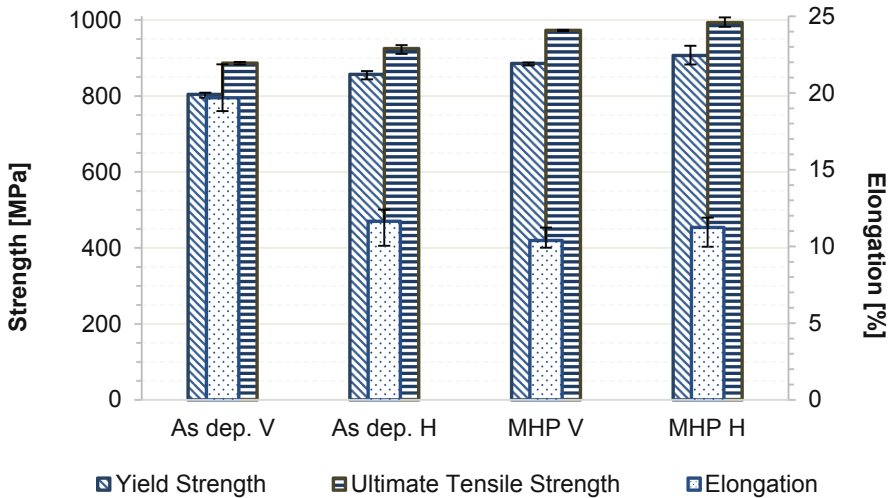


Fig. 6. Tensile properties of as deposited and inter-pass MHP of thin walls

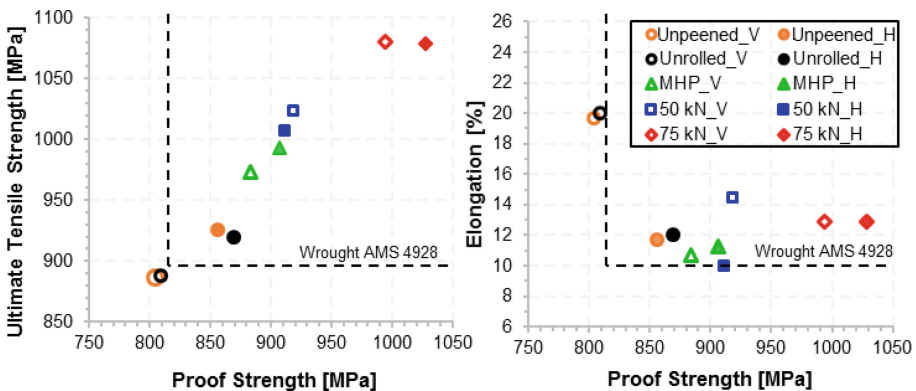


Fig. 7. Comparison of horizontal and vertical tensile properties of inter-pass MHP obtained in the current study and reported inter-pass cold rolling properties [16].

To compare the properties of MHP in this work with the published inter-pass cold rolling from Martina [16], Fig. 7 is plotted. The properties obtained with MHP are lower when compared to cold rolling loads of 75 kN and similar to 50 kN. Slightly lower elongation is obtained compared to rolling but it is still above 10%, which is the reference value of the Wrought AMS 4928 standard.

3.3 Strength and Fatigue from α Lamellae Size and Prior-Beta Refinement

Similar α lamellae thickness is observed for both as deposited and inter-pass MHP thin wall samples, as shown in Fig. 8. This is observed not only in these SEM images but in all acquired images. Martina et al. [4] reported a decrease of α lamellae thickness as the load of cold rolling increased. It is expected that the size of the inter-pass MHP samples showed a lower effect but still a decrease in thickness. It is possible that this divergent result from [4] is due to the different procedure of applying cold work. In [4], rolling is only applied when the component is at room temperature, while the as deposited condition is continuously deposited until the desired geometry is achieved. In the present study a stabilized dwelling temperature at 140 °C is used for both the MHP and as deposited samples. The different starting temperatures of subsequent deposition, for as deposited and cold rolled specimens, changes the cooling rate for each condition and can promote α lamellae size growth for the lower cooling rate of the as deposited condition [17]. However, in [4] it is possible to observe also a decrease in α lamellae thickness between 50 and 75 kN, which suggests that cold work still had an important role in the thickness of the α lamellae. It is possible that the MHP process does not apply deformation with enough magnitude and/or depth to promote a finer α lamellae [5], but further studies are required to achieve a firm conclusion. As the α lamellae microstructure is similar for both as deposited and inter-pass MHP samples, it is likely that the microstructure transformation that leads to the strength increase of MHP samples was the prior- β refinement.

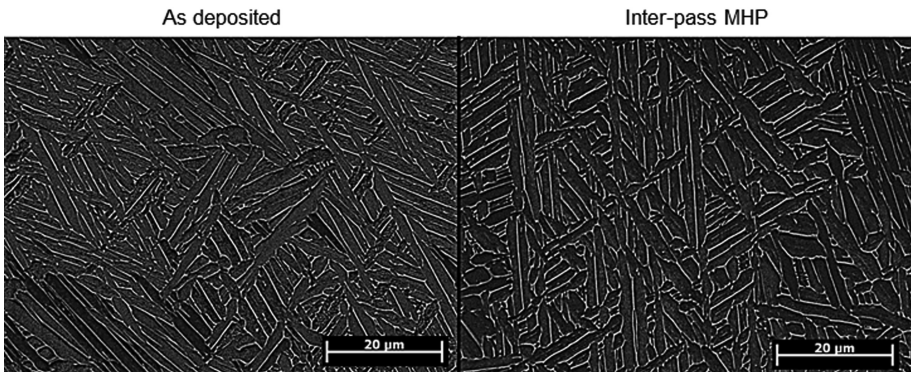


Fig. 8. SEM images of as deposited and inter-pass MHP of thin walls

It is possible that the fatigue properties of the as deposited and inter-pass MHP samples will be similar, once there is no significant change of α lamellae size. The fatigue properties for as deposited Ti-6Al-4V WAAM walls when compared with wrought material are widely reported in the literature [2, 18–21]. The fracture toughness proved to be similar for the WAAM material compared to the wrought material but still has anisotropy [18], while the fatigue crack growth rate of the WAAM material is lower than the wrought material due to the propagation through a tortuous path along its lamellar structure [19, 20]. Fatigue life is also improved for WAAM Ti-6Al-4V [2].

Lorant [21] shows the importance of avoiding large columnar beta grains for crack propagation. It was shown that when the crack is aligned with a columnar β grain, the path followed the prior- β grain boundary. Qiu [8] studied the effect of inter-layer cold rolling on the fatigue crack growth rate and achieved improved and isotropic properties. However, the cause of such improvements is not conclusively correlated with the microstructural changes of the cold rolled material, due to the small sample size tested.

4 Conclusions

The main conclusions redrawn from this study are:

1. Similar grain refinement is achieved by inter-pass MHP of thin walls and oscillated thick walls. This is achieved by the activation of grain refinement of the prior beta grains.
2. An increase of tensile properties and isotropy was achieved by inter-pass MHP. These properties are close to the ones reported for inter-pass cold rolling with 50 kN.
3. Similar α lamellae thickness was obtained for as deposited and inter-pass MHP samples.

The present study has proven that MHP can be used as an aid or replacement for cold rolling for WAAM components. Although the properties of as deposited WAAM can be already used for some industrial applications, by applying inter-pass MHP the improvement in flexibility and properties increases the application scope of this novel technology.

Acknowledgments. The authors would like to thank Alfred Ostertag, Marco Nischkowsky, Karsten Roettger and Stefan Zenk of ECOROLL AG for providing the ECOpeen-C MHP tool and for the operational support, as well as, to Flemming Nielsen, Nisar Shah and Steve Pope for the technical support throughout the experiments carried at the WELPC, Cranfield University. The authors gratefully acknowledge the funding received from the European Union's Horizon 2020 research and innovation program in the project LASIMM (Large Additive Subtractive Integrated Modular Machine) under the grant agreement No 723600. The authors are also grateful for the funding of the Engineering and Physical Sciences Research Council (EPSRC) through New Wire Additive Manufacturing (grant number EP/R027218/1) and Open Architecture Additive Manufacturing (grant number 113164) research program.

References

1. Williams, S.W., Martina, F., Addison, A.C., Ding, J., Pardal, G., Colegrove, P.: Wire + Arc additive manufacturing. *Mater. Sci. Technol.* **32**(7), 641–647 (2016)
2. Wang, F., Williams, S., Colegrove, P., Antonysamy, A.A.: Microstructure and mechanical properties of wire and arc additive manufactured Ti-6Al-4V. *Metall. Mater. Trans. A* **44**(2), 968–977 (2013)
3. Wang, F., Williams, S., Rush, M.: Morphology investigation on direct current pulsed gas tungsten arc welded additive layer manufactured Ti6Al4V alloy. *Int. J. Adv. Manuf. Technol.* **57**, 597–603 (2010)
4. Martina, F., Mehnen, J., Williams, S.W., Colegrove, P., Wang, F.: Investigation of the benefits of plasma deposition for the additive layer manufacture of Ti-6Al-4V. *J. Mater. Process. Technol.* **212**, 1377–1386 (2012)
5. Lütjering, G.: Influence of processing on microstructure and mechanical properties of (α + β) titanium alloys. *Mater. Sci. Eng. A* **243**(1–2), 32–45 (1998)
6. Schroeder, G., Albrecht, J., Luetjering, G.: Fatigue crack propagation in titanium alloys with lamellar and bi-lamellar microstructures. *Mater. Sci. Eng., A* **319**, 602–606 (2001)
7. Martina, F., Colegrove, P.A., Williams, S.W., Meyer, J.: Microstructure of interpass rolled wire + arc additive manufacturing Ti-6Al-4V components. *Metall. Mater. Trans. A* **46**(12), 6103–6118 (2015)
8. Qiu, X.: Effect of rolling on fatigue crack growth rate of wire and arc additive manufacture (WAAM) processed Titanium. MSc Thesis, Cranfield University (2013)
9. Colegrove, P.A., Donoghue, J., Martina, F., Gu, J., Prangnell, P., Hönnige, J.: Application of bulk deformation methods for microstructural and material property improvement and residual stress and distortion control in additively manufactured components. *Scripta Mater.* **135**, 111–118 (2017)
10. McAndrew, A.R., et al.: Interpass rolling of Ti-6Al-4V wire + arc additively manufactured features for microstructural refinement. *Addit. Manuf.* **21**, 340–349 (2018)
11. Hönnige, J.R., Colegrove, P., Williams, S.: Improvement of microstructure and mechanical properties of wire + arc Additively Manufactured Ti-6Al-4V with Machine Hammer Peening. *Proc. Eng.* **216**, 8–17 (2017)
12. Hönnige, J., Colegrove, P., Prangnell, P., Ho, A., Williams, S.: The effect of thermal history on microstructural evolution, cold-work refinement and α/β growth in Ti-6Al-4V wire + arc AM. Ph.D. thesis, Cranfield University (2018). Chapter
13. Byun, J.G., Yi, H.J., Cho, S.M.: The effect of interpass peening on mechanical properties in additive manufacturing of Ti-6Al-4V. *J. Weld. Join.* **35**(2), 6–12 (2017)
14. Ding, J., Colegrove, P., Martina, F., Williams, S., Wiktorowicz, R., Palt, M.R.: Development of a laminar flow local shielding device for wire + arc additive manufacture. *J. Mater. Process. Technol.* **226**, 99–105 (2015)
15. Donoghue, J., Antonysamy, A.A., Martina, F., Colegrove, P.A., Williams, S.W., Prangnell, P.B.: The effectiveness of combining rolling deformation with wire-arc additive manufacture on β -grain refinement and texture modification in Ti-6Al-4V. *Mater. Charact.* **114**, 103–114 (2016)
16. Martina, F.: Investigation of methods to manipulate geometry, microstructure and mechanical properties in titanium large scale Wire + Arc Additive Manufacturing. Ph.D. thesis, Cranfield University (2014)
17. Donachie Jr., M.: Titanium: A Technical Guide, 2nd edn. ASM International, Materials Park (2000)

18. Zhang, X., Martina, F., Ding, J., Wang, X., Williams, S.W.: Fracture toughness and fatigue crack growth rate properties in wire + arc additive manufactured Ti-6Al-4V. *Fatigue Fract. Eng. Mater. Struct.* **40**(5), 790–803 (2017)
19. Zhang, J., Wang, X., Paddea, S., Zhang, X.: Fatigue crack propagation behaviour in wire + arc additive manufactured Ti-6Al-4V: effects of microstructure and residual stress. *Mater. Design* **90**, 551–561 (2016)
20. Nalla, R.K., Ritchie, R.O., Boyce, B.L., Campbell, J.P., Peters, J.O.: Influence of microstructure on high-cycle fatigue of Ti-6Al-4V: bimodal vs. lamellar structures. *Metall. Mater. Trans. A* **33**(3), 899–918 (2002)
21. Lorant, E.: Effect of Microstructure on Mechanical Properties of Ti-6Si-4V Structures Made by Additive Layer Manufacturing. MSc thesis, Cranfield University (2010)



An Automated Deposition Procedure for Cold Spray Additive Manufacturing Process Modeling Based on Finite Element Simulation

Sabeur Msolli¹(✉), Zhi-Qian Zhang¹, Junyan Guo¹,
Sridhar Narayanaswamy¹, Reddy Chilla Damodara¹, Zheng Zhang²,
Jisheng Pan², Boon Hee Tan³, and Qizhong Loi³

¹ Institute of High Performance Computing,
A*STAR, Singapore 138632, Singapore
msollis@ihpc.a-star.edu.sg

² Institute of Materials Research and Engineering,
A*STAR, Singapore 138634, Singapore

³ Advanced Remanufacturing and Technology Centre,
A*STAR, Singapore 637143, Singapore

Abstract. The present paper presents modeling of the Cold Spraying Process using a progressive build-up technique. This technique is based on the modeling features dedicated to the Additive Manufacturing Process. It has the major advantage in saving computational cost while maintaining reasonable numerical accuracy compared to other finite element solutions that involve realistic impact simulations for thousands of particles. The new approach uses the database obtained from one-time finite element simulations performed with the Eulerian scheme by computing the corresponding thermomechanical fields averaged over a gauge length. This is inserted into the progressive build-up model with a pair of subroutines for the definition of initial stresses and equivalent plastic strains. The material addition has been performed in the finite element analysis by progressively activating the elements that take the values of the averaged thermomechanical fields at the moment of activation. To undergo element activation, another pair of subroutines are used to locate the elements that are within a sphere of a fixed radius and belonging to the deposition toolpath or segment. The deposition segments considered in the modeling are an event series presenting the element status with respect to the tool coordinates and time. The deposition input parameters have been specified using a table collection. The progressive build-up procedure has been used to determine the thermomechanical fields such as temperature in the coating and residual stress in the structure.

Keywords: Cold spray · Additive manufacturing · Elements activation

1 Introduction

Cold spraying process is an emerging manufacturing technique for depositing coatings in different kinds of substrate and repairing damaged parts. It consists on impinging high velocity metallic or non-metallic particles upon the target material to achieve a

strong bonding between the deposit and the substrate. Contrary to thermal spraying process where deposition is performed at high temperature [1, 2], cold spraying does not require increased heating of particles or substrate to achieve material adhesion. Nevertheless, the mechanical properties of the coating and its adhesion to the substrate are strongly dependent on several process parameters such as deposition velocity, impact angle, material combination, particle diameter, roughness of the substrate surface, etc. [3–5]. Importantly, the particle reaching a critical velocity is key for achieving strong bonding between the substrate and the deposition material [6, 7]. This critical velocity leads to large plastic deformations and shear instability at the particle/substrate interface where the materials melt selectively and promote a kind of mechanical scouring of the surfaces, favorable to their adhesion [8, 9]. The residual stress generated after cold spraying also is a considerable concern that should be precisely evaluated using simulations.

The numerical simulations of cold spray are usually based on dynamic analysis using nonlinear finite element modeling for collision of a single particle or a few particles using the Eulerian method, that has proved simulate experimental observations [10]. Nevertheless, finite element modeling of cold spraying is challenging, because it is computationally expensive, especially for thick coating involving thousands of particles impacting a substrate. Arising from this need, we have in this paper, identified strategies previously adopted for simulation of fusion and extrusion deposition additive manufacturing to simulate the cold spraying process. Element activation is among used techniques to simulate 3D printing in additive manufacturing process and appears as a realistic way to describe progressive layer build-up. By fully or partially activating elements, it is possible to control the initial and computed thermomechanical fields from predefined ones. The automated model is presented to show the application of the modeling tools and the effect of the partial element activation on the distribution of the residual stress.

2 Progressive Build-Up Technique

2.1 FE Simulation of Cold Spraying Process Using Eulerian Method

The Eulerian simulations presented hereafter are based on a 3D configuration of the cold spraying process. The finite element model consists of 150 Aluminium Alloy 6061-T6 particles of 60 microns diameter and moving with an initial velocity of 600 mm/s, impacting a large Aluminium Alloy 6061-T6 substrate of 1.8 mm × 2.4 mm at an angle of 90° with respect to surface plane. Both the substrate and the particles are considered as deformable bodies. 8-node thermally coupled linear brick, multi-material, reduced integration elements with hourglass control have been adopted for the Eulerian mesh. The volume fraction of the elements has been set to 1. To produce periodic conditions on the substrate sides, non-reflecting Eulerian boundary conditions have been applied to the impact-free surfaces of the substrate. The total time of the simulation is 5×10^{-3} s including spraying and relaxation (load-free) time. The simulations are adiabatic, so there is no thermal energy dissipation outside the system. To represent adequately the viscoplastic behavior of the constitutive materials involved

in the cold spraying process, the Johnson-Cook viscoplastic law has been adopted as it permits to describe accurately the strain rate and temperature dependent effects. The Johnson-Cook law is expressed as follows

$$\sigma = \left[A + B\varepsilon_p^n \right] \left[1 + C \ln \left(\frac{\dot{\varepsilon}_p}{\dot{\varepsilon}_0} \right) \right] \left[1 - \left(\frac{T - T_0}{T_m - T_0} \right)^m \right] \quad (1)$$

where σ , ε_p , and T are the equivalent stress, the plastic strain and the temperature, respectively. $\dot{\varepsilon}_p$ is the equivalent plastic strain rate. A , B , C , n , and m are material parameters. T_m is the melting temperature and T_0 is the reference temperature.

The material parameters of the Johnson-Cook model are chosen depending on the couple of materials composing the substrate and the coating. In these simulations, aluminium Alloy 6061-T6 grade has been chosen as the material for the model parts. The material parameters for Al6061-T6 are given in Table 1. The purpose of these simulations is to compute the thermomechanical fields of stress, strain and temperature required for the equivalent model. As shown in Fig. 1, the particles are initially randomly distributed on the space and projected toward the substrate with an initial velocity of 600 mm/s. After the impact, the particles are severely deformed and stacked on the substrate surface forming a coating layer of about 0.4 microns. The database obtained from these Eulerian simulations has been stored to be used as input in the 3D equivalent coating model.

Table 1. Material parameters used for Johnson-Cook model [11].

A (MPa)	B (MPa)	C	n	m	$\dot{\varepsilon}_0$ (s ⁻¹)	E (GPa)
324	114	0.002	0.42	1.34	0.001	68
T _m (K)	T ₀ (K)	ρ (kg m ⁻³)	ν	C _p (J Kg ⁻¹ K ⁻¹)	λ (W m ⁻¹ .K ⁻¹)	α
880	298	2700	0.3	896	0.0071	16×10^{-6}

The obtained mapping of the stress, equivalent plastic strain and temperature are presented in the Fig. 1. It clearly shows the high amount of plastic strain in the coating compared to that in the substrate. The deposited particles were severely flattened and their interfaces particularly present higher plastic deformation as a localized shear mechanism is occurring during high velocity impact. This plastic deformation is mainly related to the kinetic energy of the particles and therefore, to the initial velocity explaining the effect of the input process parameters on the produced deformation. Since the cold spraying process has been considered as adiabatic in these simulations, all the plastic work was totally dissipated into heat, leading to a high temperature in the coating layer. The temperature at the particle/substrate interface is higher as the surfaces involved in the impact was subjected to heat transfer that diffuses almost uniformly towards the entire surface of the substrate and the surrounding particles.

2.2 Variable Extraction and Averaging

The progressive build-up procedure for coating deposition has been developed based on the previous results of the Eulerian simulations. This 3D automated implicit model has been conceived to reduce the computational cost, by using the element activation technique.

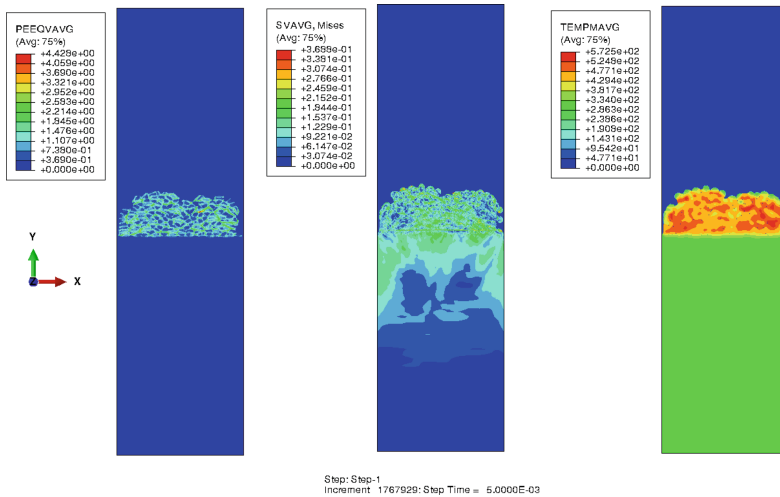


Fig. 1. The distribution of stress (left), equivalent plastic strain (middle) and temperature (right) at the end of the deposition process.

The extracted numerical database from the Eulerian simulations, serving as input in the automated model, is composed of the stress components, the equivalent plastic strain, and the temperature distribution in the substrate and the coating. These variables have been volume averaged before being implemented. The variable averaging has been performed according to the following strategy: all the thermomechanical fields including stress, plastic strain and temperature has been extracted for both the substrate and the particles in some specific paths. For the substrate, four paths have been chosen along the deposition direction, so the variables are averaged over these paths at a fixed time point corresponding to the end of the spraying process. At the end of the averaging operation, a mean profile of the relevant variable as a function of the substrate depth is obtained assuming that the variable is uniform along the substrate width. The latter assumption is justifiable as the particles are uniformly impacting the substrate leading to evenly distributed fields along the substrate width.

As for the coating, the thermomechanical fields averaging has been performed using different sizes of a square unit cell as shown in Fig. 2(a). The unit cells include the lowest elements of the first particles impacting the substrate to capture the variation of the variables at the end of the spraying process. No relaxation step was taken into account since the considered state represents the immediate end of the spraying

process. The extraction and the variable averaging have been carried out using a Python script. The averaged values have been stored in a separate file for the upcoming automated build-up simulations.

Figure 2(b) shows the dependence of the average temperature on the unit cell size. It can be seen that the temperature is almost constant over the coating thickness at around an average value of 465 K, and thus the effect of the unit cell size is not distinguishable. Figure 2(c) shows the variation of the average Von Mises stress against the unit cell size. The stress decreases about half when the unit cell size is equal to the coating thickness. The decrease of stress is related to the temperature changes in the coating. As previously shown, the adjacent particle layers close to the substrate surface are subjected to the first impact wave. They were impacting substrate with a flat surface at room temperature. Plastic deformation is severe in this area leading to more heating followed by a progressive cooling. As the cooling begins to occur, compressive stresses increase in these layers leading to a more prestressed particles/substrate interface. On the other hand, the particles coming from the second wave and above and freshly deposited on the top of the coating have higher temperature and therefore, present lower stress. In fact, the particle/particle impact seems quite different from the particle/substrate impact. Since less stress generates for the particle/particle impact due to high temperature, the average stress value is decreasing with increased unit cell size, and then becoming unchangeable at about 130 MPa from a unit cell size of 100 μm . It comes to the conclusion that beyond 100 μm of unit cell size, the average stress value of 130 MPa represents well the homogenized behavior of the coating. For coating thickness below 100 μm , it is better to consider a certain dependence of the stress to the

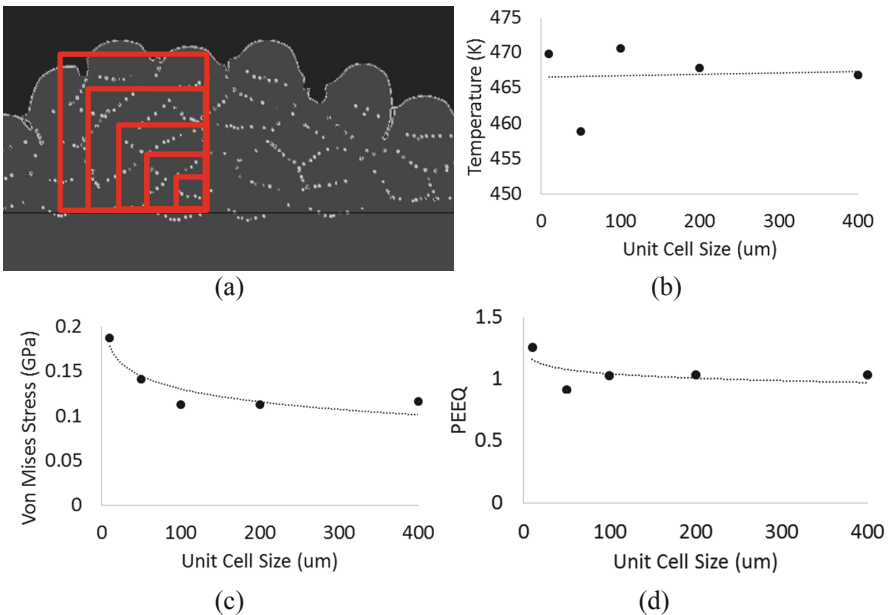


Fig. 2. Averaged values of stress, equivalent plastic strain and temperature and their dependence to the size and location of the unit cell chosen for the averaging operation. (a) unit cell definition in the coating, (b, c, d) temperature, stress and equivalent plastic strain.

deposited coating thickness rather than an averaged stress computed from a representative volume element (RVE), as the value of the stress is strongly dependent on the particle location. Finally, the average equivalent plastic strain has been extracted and illustrated in Fig. 2(d).

The particles deform severely when impacting the substrate at room temperature generating a domain with high strain localization. The particle/particle impact is slightly different as the shear mechanism combined to particles sliding generate smaller amount of plastic deformation compared to the first layer of particles. The average plastic strain becomes almost constant from a unit cell size of 100 μm .

2.3 Heat Transfer Analysis

The geometric model for the finite element model consists of AA 6061-T6 coupon which has the dimensions of 76 mm \times 19 mm \times 3 mm coated with AA 6061-T6 layer of 0.365 mm thickness. Both the coupon and the coating have been meshed using structured 8-node linear heat transfer bricks DC3D8. The coating thickness is composed of 8 mesh layers. The coupon is tied to the coating using a tie mesh constraint. The average temperature of the particles has been imported from the Eulerian simulations into the coating layer as an initial predefined temperature. The toolpath deposition pattern has been provided by the cold spraying device from the history of the nozzle movement. The cold spraying process has been described by activating elements which are supposed to represent the homogenized behavior of a coating block. The element and material activation process has been monitored using a couple of sub-routines. The first utility routine calls the segment in which the element should be activated. The second subroutine activates the element belonging to the segment and included in a cylinder of radius R and height H. The activation of the elements can be either fully or partially performed. Full activation of the element is automatically released when the element centroid belongs to the scanning domain. The number of coating mesh layers is equal to the number of spraying scans performed to obtain the final coating thickness. Therefore, each scan activates its associated element layer. Contrarily to the full activation, partial activation is possible with intermediate value of the element volume fraction ranging between 0 and 1. We have considered partial activation technique hereafter to model the deposition process. In order to fully exploit the capability of the partial element activation, a single coating mesh layer has been considered whose size is equal to the coating thickness. The partial activation enables the volume fraction of the element to increase progressively until reaching a maximal value of 1 in certain locations at the end of the entire cold spraying process. The volume fraction of the elements has been computed using a continuous function of space coordinate of the deposition spot. Therefore, elements located far from the scanning geometry would have no volume fraction. To match experimental observation, nonlinear profile of the element volume fraction has been described by a normal distribution which assumes that for a fixed time domain, the volume fraction is maximal in the centerline of the scanning area and nonlinearly decreases into the edges. Therefore, the volume fraction added in each time increment, is simply determined knowing the scanning orientation and the shape of the particles distribution (normal distribution for the case of partial activation, for instance).

The nozzle patterns have been formatted as event series representing the location of the nozzle with respect to time and space coordinates. The width and height of the deposited coating, the number of passes, and the nozzle velocity have been entirely introduced using a table collection that permits to extract these input data if needed. It represents also a convenient way to remotely control these parameters and evaluate their effect on the deposition process. The input process parameters as defined experimentally are summarized in Table 2.

Table 2. Experimental input parameters for the cold spraying process.

Coating width w (mm)	Coating height H/pass (mm)	Number of passes	Spray time (s)	Coating velocity (mm/s)	Total path length (mm)
1	0.091	4	63	400	25200

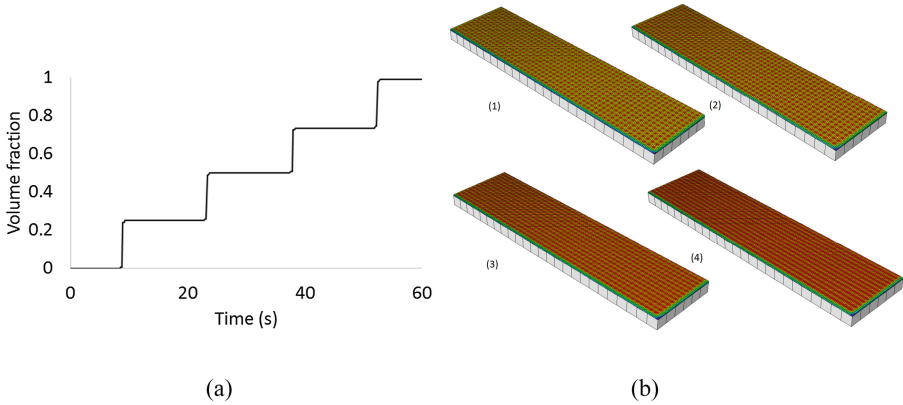


Fig. 3. (a) Volume fraction cumulated during spraying (partial activation) process in element located on the scanning trajectory. (b) Volume fraction map over different spraying passes for partially activated elements.

For partial activation, the volume fraction of the element increases nonlinearly for every pass. Figure 3(a) illustrates cumulated volume fraction obtained for each pass, followed by a quiet period where there is no volume fraction cumulated. As the volume fraction is nonlinear over space, it has been found to be heterogeneous on the coupon surface and tends to form straight and periodic lines of high volume fraction elements, see Fig. 3(b). At the end of the spraying operation, the entire volume fraction has been recovered for the elements crossing the nozzle centerline.

Temperature distribution has been also extracted in Fig. 4. It is shown that several peaks of temperature have been reached for each performed scan. Temperature rise has been observed at the moment of element activation as initial temperature has been assigned to the elements. It can be seen that the transient regime is short and rapid cooling occurred in the element as high conductivity material has been selected. The computed average temperature in the coating showed steady state temperature that

increases continuously in stairs. Transient regime lasts longer in the case of partial element activation. Initially, temperature of the element after partial activation is slightly higher than that of a fully activated element. This is related to the scaling of the material properties of a partial activated element by its volume fraction leading to higher temperature in the transient regime. In addition, an important aspect is the trend of the steady state temperature which is similar to that of the full activation case. It has to be noticed that a mixture law is used to compute thermomechanical fields in a partially activated element. This constitutes a major difference compared to the full activation.

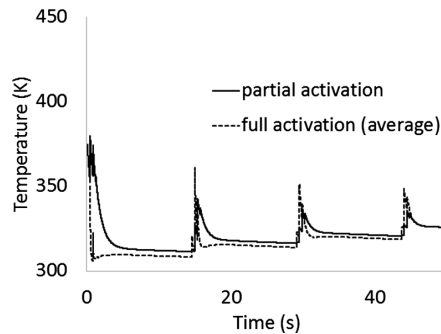


Fig. 4. Temperature evolution during in the coating during the cold spraying process. Temperature in the element partially activated and located in the same area as the fully activated elements.

2.4 Structural Analysis

Stress distribution in the coupon and the coating is among the needed outcomes of the thermomechanical simulations. Residual stress is related to the part deflection and therefore monitors the final shape of the coated part and constitutes a major precursor for crack initiation and part failure. Initial stress fields in the coating and the coupon have been considered based on the original particle impact model. They have been accounted for using a couple of subroutines for stress and equivalent plastic strain initialization. These subroutines permit a better control of the initial stress and plastic strain mapping over the whole part volume. Contrary to the thermal analysis, not all the entire coupon has been coated but only a band of 3 mm width in the center has been coated. In addition, the cold spraying operation has been reduced to 4 passes in order to save computational time. Element activation has been applied for both coupon and coating. Initial state of stress is present in a thin layer of the coupon. Consequently, only that thin layer has been partially activated. Figure 5(a) shows the stress and displacement distribution in the whole part at the end of the coating process. Residual stress has been generated on the coupon leading to the plate bending (Fig. 5(a)). Large values of residual stress observed in this area are due to a fast cooling rate generating thermal gradient and leading to part deflection. Largest deflection values are located along Z-axis and situated at the middle of the coated part of the coupon (Fig. 5(b)).

Figure 6(a) shows the progressive increase of the element volume fraction over time. The increase of the volume fraction is due to both the number of scan undergone by the element during the spraying process and the number of overspraying time which slightly contributes to the increase. The accumulation of the volume fraction is linked to the increase of the stress as demonstrated in Fig. 6(b).

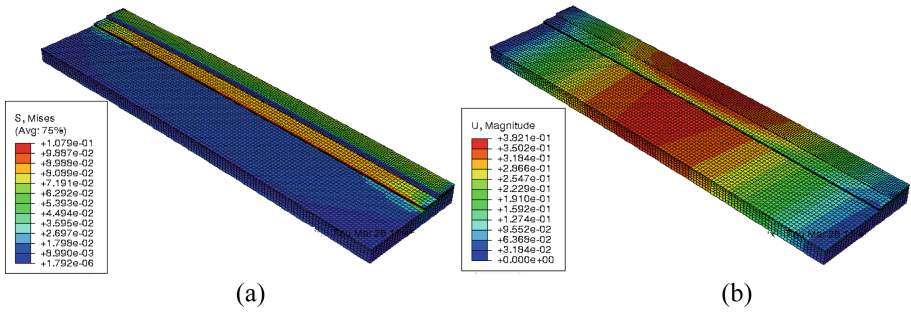


Fig. 5. (a) Stress and (b) displacement maps in the structure using partial activation.

The stress exhibits jump every time the element volume fraction is updated. The initial value of stress recorded from the original particle model is scaled by the volume fraction in the partially activated element which explains the relatively small value of stress at the beginning of the element activation compared to the imposed initial stress. As for the temperature, the stress is updated in the activated elements following a mixture rule to ensure smoothness of the solution in the element.

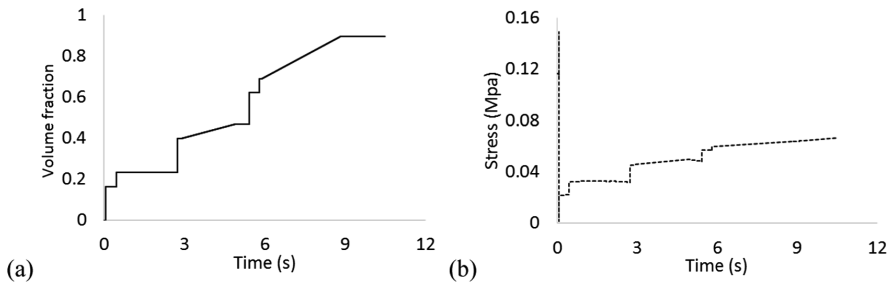


Fig. 6. Partial activation of elements. (a) volume fraction increase with the number of scans over the element. (b) Associated stress evolution in the element.

Profile of the residual stress after the deposition process along the structure depth is shown in Fig. 7. The stress trend is similar to the one observed in some other additive manufacturing processes such as extrusion and fusion deposition.

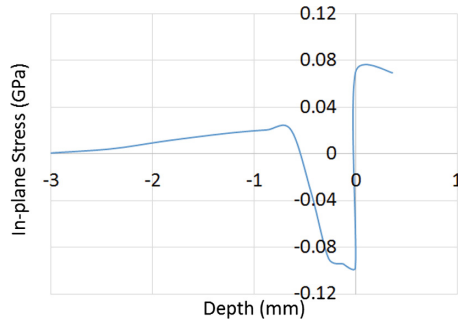


Fig. 7. Residual stress profile in the coupon and coating after the deposition process using partial element activation.

Compressive values of the stress (100 MPa) are predominant in the top thin layer of the coupon as this part is subjected to a fast cooling while tension stress exists in the hot coating layer (80 MPa).

3 Conclusion

A progressive build-up technique is developed to model the cold spray process thereby addressing the limiting aspects of high computational cost and excessive model size. Based on the element activation technique, the model describes the temperature changes, the residual stress profile and the amount of deflection in the structure. Partial element activation further improves computational time by choosing a bigger element size at full activation but at the same time maintaining reasonable accuracy in the results. Further investigations are needed to compare and correlate the experimental results for stress and deflection with that numerically determined.


References

1. Gärtner, F., Stoltenhoff, T., Voyer, J., Kreye, H., Riekehr, S., Koçak, M.: Mechanical properties of cold-sprayed and thermally sprayed copper coatings. *Surf. Coat. Technol.* **24**(200), 6770–6782 (2006)
2. Pathak, S., Saha, C.G.: Development of sustainable cold spray coatings and 3D additive manufacturing components for repair/manufacturing applications: a critical review. *Coatings* **7**(8), 122 (2017)
3. Assadi, H., Gärtner, F., Stoltenhoff, T., Kreye, H.: Bonding mechanism in cold gas spraying. *Acta Mater.* **51**(15), 4379–4394 (2003)
4. Chen, C., et al.: Evaluation of the interfacial bonding between particles and substrate in angular cold spray. *Mater. Lett.* **173**, 76–79 (2016)
5. Yu, M., Li, W.-Y., Wang, F.F., Suo, X.K., Liao, H.L.: Effect of particle and substrate preheating on particle deformation behavior in cold spraying. *Surf. Coat. Technol.* **220**, 174–178 (2013)

6. Henao, J., et al.: Deposition behavior of cold-sprayed metallic glass particles onto different substrates. *Surf. Coat. Technol.* **349**, 13–23 (2018)
7. Li, Y., Wang, X., Yin, S., Xu, S.: Influence of particle initial temperature on high velocity impact process in cold spraying. *Proc. Environ. Sci.* **12**, 298–304 (2012)
8. Grujicic, M., Zhao, C., DeRosset, W., Helfrich, D.: Adiabatic shear instability based mechanism for particles/substrate bonding in the cold-gas dynamic-spray process. *Mater. Design* **25**(8), 681–688 (2004)
9. Meng, F., Yue, S., Song, J.: Quantitative prediction of critical velocity and deposition efficiency in cold-spray: a finite-element study. *Scripta Mater.* **107**, 83–87 (2015)
10. Guetta, S., et al.: Influence of particle velocity on adhesion of cold-sprayed splats. *J. Therm. Spray Technol.* **18**(3), 331–342 (2009)
11. Akram, S., Jaffery, S.H.I., Khan, M., Fahad, M., Mubashar, A., Ali, L.: Numerical and experimental investigation of Johnson-Cook material models for aluminum Al 6061–T6 alloy using orthogonal machining approach. *Adv. Mech. Eng.* **10**, 9 (2018)



Bonding Strength Improvement Through Numerical Simulation of Particle Impact Process During Metal Cold Spray

X. Song^{1,5}, X. Z. Jin², J. Everaerts³, W. Y. Tan², W. Sun², I. Marinescu⁴, W. Zhai⁵, F. Li⁴, E. J. Liu², and A. M. Korsunsky³

¹ School of Mechanical and Automation Engineering, Chinese University of Hong Kong, William M.W. Mong Engineering Building, Shatin, Hong Kong
xsong@simtech.a-star.edu.sg, songx02@gmail.com

² School of Mechanical and Aerospace Engineering, Nanyang Technological University, 50 Nanyang Avenue, Singapore 639798, Singapore

³ Department of Engineering Science, University of Oxford, Oxford OX1 3PJ, UK

⁴ Rolls-Royce Singapore Pte Ltd, 1 Seletar Aerospace Crescent, Singapore 797565, Singapore

⁵ Singapore Institute of Manufacturing Technology, Agency for Science, Technology and Research (A*STAR), Singapore 637662, Singapore

Abstract. Cold spray is an emerging additive manufacturing technique with potential applications in surface functionalization, bulk component production and restoration/repair. During the cold spray process, metallic powders are accelerated to supersonic velocities by the carrier gas of high pressure and temperature and impact on the substrate to form layers of coating through deformation-induced bonding. However, the coating fabricated by this process suffers from low cohesive strength and weak interfacial bonding. Therefore, process optimization through numerical simulation is much needed. Here we employ finite element simulation with Johnson-Cook plasticity and dynamic failure model to numerically predict the temperature distribution within single particle, and they show good agreement with experimental observation using SEM. This provides a validated description of microscopic phenomena using numerical simulation, hence it can be employed further to study the bonding strength of the metal cold spray coating. Through microstructural analysis, we propose a semi-empirical relationship between the nodal temperature profile and local bonding strength, hence identified that the increase of the localized bonding area in a single splat is the determining factor for the increase of the bonding strength.

Keywords: Metal cold spray · Finite element simulation · Interfacial bonding strength

1 Introduction

Metal Cold Spray (MCS) is an emerging additive manufacturing technology with great potential in coating and repair. The solid powders are accelerated to supersonic velocities by the carrier gas of high pressure and temperature created from the

convergent-divergent nozzle, and hit on the prepared substrate to form layers of coating through intensive plastic deformation. One advantage of the cold spray technique is to keep the powder and substrate temperatures below the melting point so that the initial physical and chemical properties of the material can be retained. The metallic bonding formed at the particle/substrate interface in cold spraying process is attributed to “adiabatic shear instability”, which was proposed by Assadi et al. [1]. Furthermore, when the particle is impacting on the substrate at a velocity above the critical velocity, the contact process is so quick that the heat generated by the plastic deformation greatly increases the local temperature and softens the material. As a result of the thermal softening, the rate of strain hardening is reduced while the strain and the temperature are abruptly increased at that region. This secondary jump in temperature and strain (as compared with the initial temperature jump due to particle’s first contact with the substrate, which is universal across all particle contact areas) can be obtained using finite element analysis, and it is one of the unique features of the metal cold spray process. In this work, we attempt to quantitatively link this characteristics with the interfacial bonding strength, which provides a valuable predictive tool for the process engineers to carry out virtual parametric study.

2 Methodology

2.1 Finite Element Simulation

The method of constructing the finite element (FE) model used in this paper has been described in detail in previous work [2]. It is provided briefly here again for completeness.

Taking into account the experimental configuration, a three dimensional FE model has been developed with ABAQUS/Explicit to simulate the impact between a single sprayed power particle and the substrate (Fig. 1). Accordingly, 8-node hexahedral elements with reduced integration and stiffness hourglass control (C3D8R) were employed with meshing size gradually increases from 0.3 μm at the impact center to 1.0 μm at rest of the part. The diameter of the spherical particle is set to be 30 μm which is taken from the average diameter of the powder particle used in the experiments. The Johnson – Cook plasticity and dynamic failure model is applied to simulate the plastic deformation, strain hardening and progressive damage of both the particle and substrate. The material properties and the parameters of the Johnson – Cook model for Ti-6Al-4V are applied to both the particle and the substrate in the FE model according to previous literature [3].

Up to this point, the bonding at the contact surface has not been well defined in the model. The particle is still allowed to bounce back which makes the simulation results invalid after the separation. Therefore, the normal behaviour of the interaction property has to be set in a way that there is no separation or penetration allowed at the interface during the whole impact process. The more precise but complicated and laborious way to define the bonding is to employ the user-defined subroutine. At this stage of study, a much more simplified but robust way can be found in ABAQUS/Explicit, which uses the over-closure dependent pressure to tie the two contact surfaces together. The details of the numerical settings are provided in the literature [2] as well.

Although using animation of the impact process can show no separation or penetration at the contact surface. The effect of using “softened” contact has to be evaluated quantitatively to validate this new model. We employ the velocity of the top node on the particle as an indicator and plot it against time in Fig. 2 for two different contact models. The two velocity trends share the same path before decreasing to 0. After the particle tends to bounce back, the non-separation constraint in “softened” contact model “pulls” the particle back and the node velocity returns and stays at 0, as shown in Fig. 2.

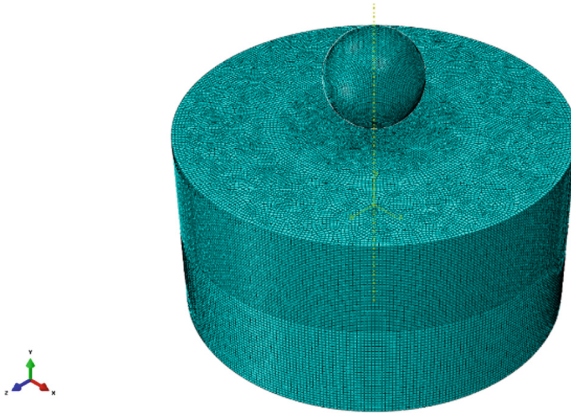


Fig. 1. 3D model for metal cold spray single particle impact (normal).

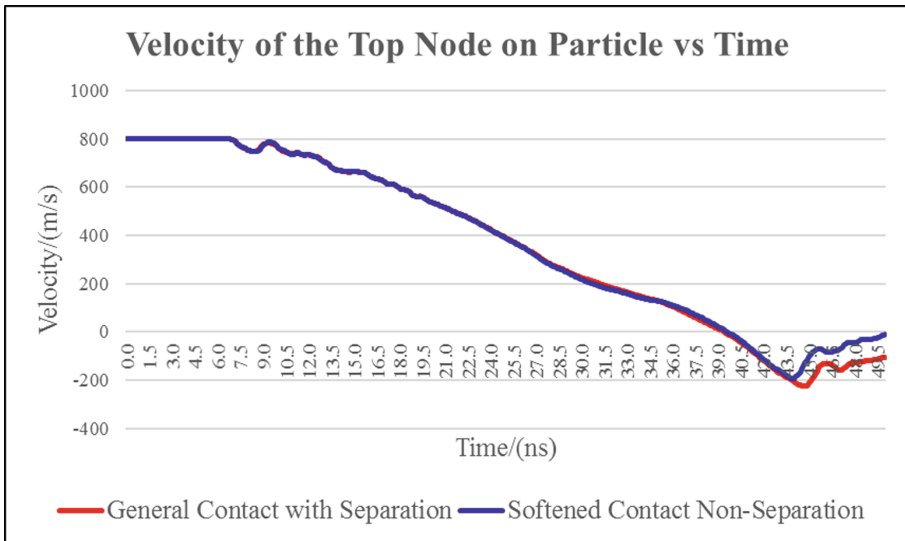


Fig. 2. Velocity trends of the top node on particle for models for two different contact models.

2.2 Experimental Setup

Ti-6Al-4V Grade 23 powder with average particle size of 30 μm was employed as the feedstock and the substrate was Ti-6Al-4V Grade 5 block with mirror-like top surface finish. The experimental setup follows previous work [4] with powder feed rate 30 g/min and transverse scan speed 500 mm/s. After the spray, mini-tensile test coupons were cut out from the block, which is illustrated in Fig. 3. Following the work of Tan WY [5], mini-tensile tests were carried out by pulling the samples with in-house designed jig until sudden rupture occurred at the interface. The UTS (Ultimate Tensile Strength) can be obtained from this exercise by dividing the maximum load with the nominal cross section (as for this brittle interface). The fracture surfaces were further examined by SEM (JSM-IT300, JEOL Ltd., Tokyo, Japan) to identify the particles of interest.

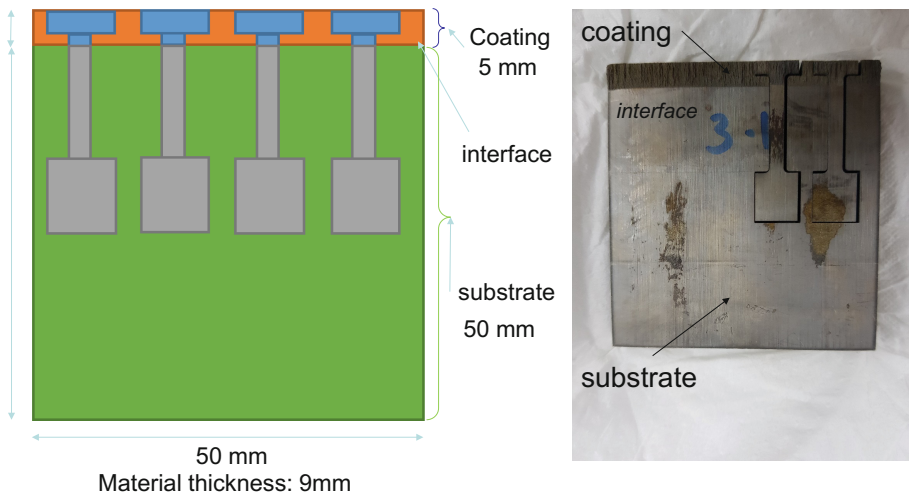


Fig. 3. Mini-tensile test dog-bone samples preparation

3 Results and Discussion

3.1 Single Particle Impact Model Validation

Since the fraction of the bonding nodes for the two different contact models are distinct from each other, it is necessary to compare the results with the surface morphology of the single particle splat in the coating. As compared in Fig. 4, the temperature contours of the bottom surface on the deformed particle shows high similarity with the surface morphology of the single particle in the coating fracture surface. The large outer ring area of the particle is identified as the bonding region, which corresponds to the high temperature region in the simulation. Conversely, the center region of the particle bottom is very smooth, showing no sign of bonding. This corresponds to the low temperature region in the simulation, which is of the same size as in the SEM. This comparison further reinforces the validity of the model using the Johnson – Cook plasticity and damage model and non-separation constraints to bond the particle and substrate together.

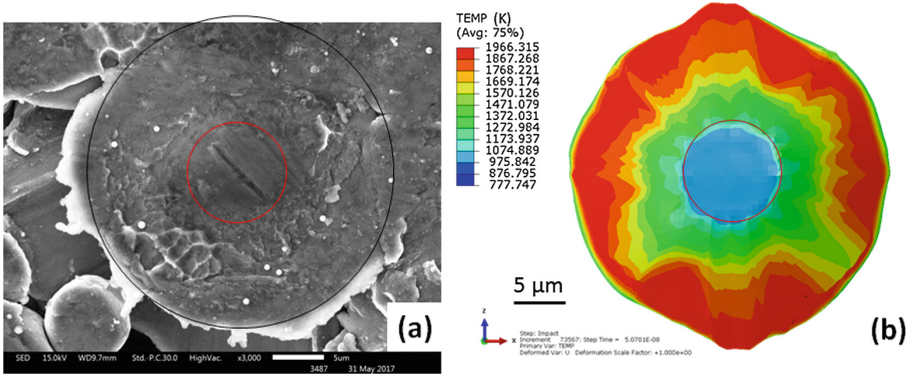


Fig. 4. Comparison between simulated temperature contour and surface morphology at the bottom of the deformed particle.

3.2 Derivation of the Bonding Stress from the Nodal Temperature Profile

The additional/second temperature jump which indicates the onset of adiabatic shear instabilities and bonding is termed as “secondary jump”, as there will always be a temperature jump at the initial stage when the particle land on the substrate at the beginning of the impact process. In a temperature history plot, “secondary jump” is characterized by the second obvious increase of the slope of the temperature history line, which is circled in red in Fig. 5. Figure 5 provides an example of the temperature profiles of individual bonding nodes due to adiabatic shear instability. Although many previous studies have suggested the link between the phenomenon of temperature secondary jump and the surface bonding in cold spray [1, 6, 7], none of them have actually provided this correlation numerically. In this work, a numerical model is developed below with a few assumptions.

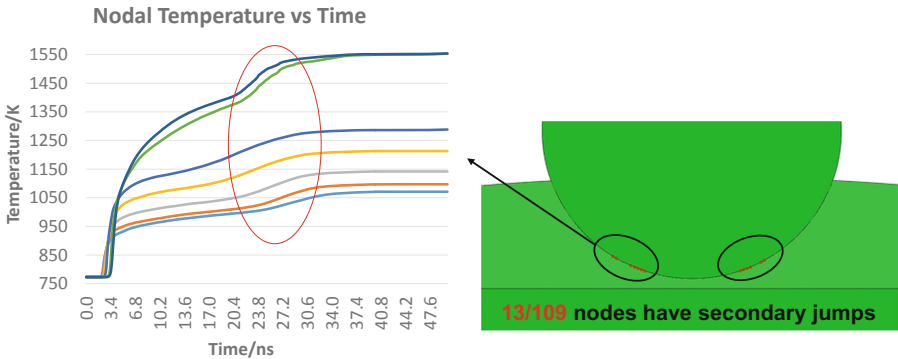


Fig. 5. Temperature profiles of the individual nodes with adiabatic shear instability and highlight of their locations in the particle.

First, the rate of temperature change T' is the local slope of the temperature history plot. The onset of the “jump” phenomenon corresponds to the change of the local slope, which can be expressed as derivative of the slope $(T')'$, and it is equal to the second derivative of temperature over time T'' . Therefore, with this approach, the “secondary jump”, which is the sudden increase of temperature rising rate, should be sensed automatically by detecting a big value of T'' . This is to identify the nodes that have bonding in the model automatically using one single value. Moreover, we can indirect validate the proposed criterion by running the model at different impact speeds and plot the T'' contour, as shown in Fig. 6. It can be seen that with increasing speed, the bonding area within one particle increases accordingly. It can be validated by the SEM analysis of the fracture surface of the residual of a single particle splat on the substrate. Figure 7 highlights different bonding areas in single particle splat with different impact speeds. The donut rings cover the bonding area of a single particle splat with characteristic rough fracture surface. The area percentage increases with the increasing speed as well. The center of the particle is still smooth, indicating no bonding at that area, also same as in the Fig. 6. In this way, we can state that the increase of the localized bonding area is the determining factor for the increase of the bonding strength.

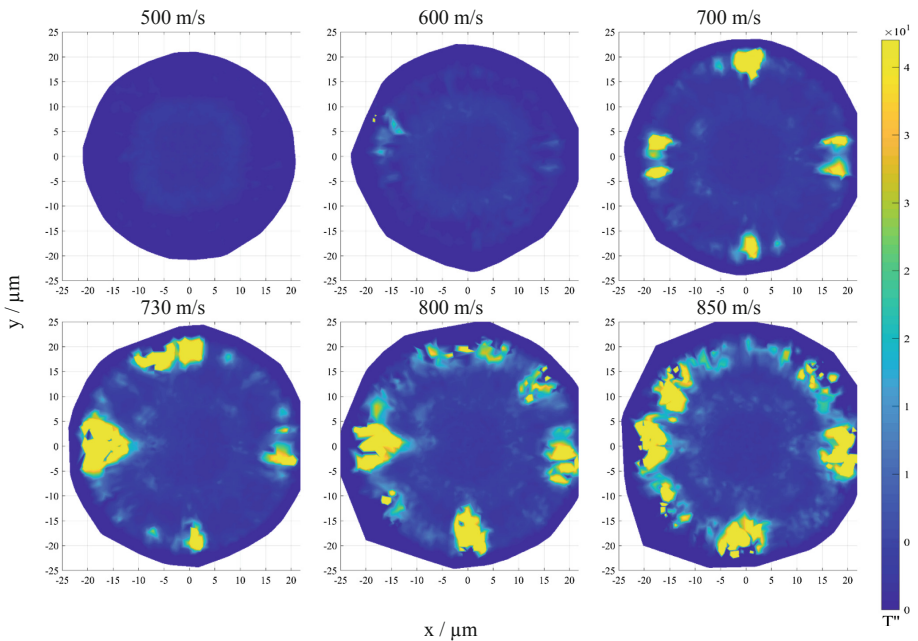


Fig. 6. Contour plots of the simulated T'' values in the contact surface at different speeds

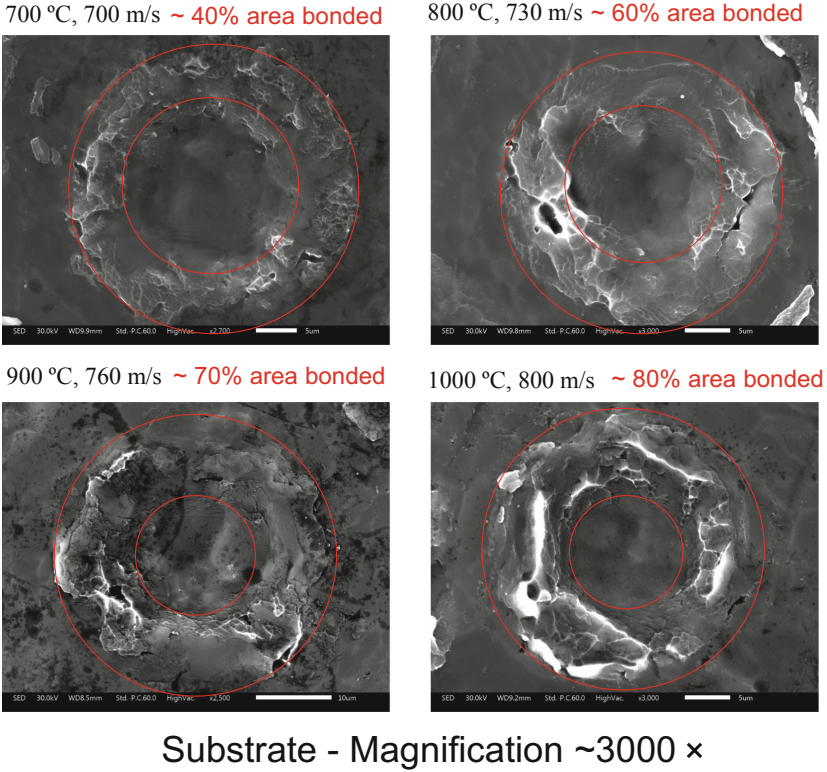


Fig. 7. The SEM images of fracture surfaces of a single particle at different impact speeds

Furthermore, for those bonded nodes, the bonding strength should, naturally, be determined by T'' as well. According to the literature, the bonding between the particles and the substrate only happens when the impact velocity exceeds some critical values [6, 7]. The deposition efficiency can increase dramatically with the increasing the impact velocity after the critical value is reached. However, the deposition efficiency is observed to be saturated once the impact velocity reaches certain ceiling value [7]. According to this, it is assumed in this paper that bonding will only happen when T'' is higher than some critical value and the bonding stress (σ) will reach maximum value (σ_{max}) after reaching ceiling impact speed. To model this assumption mathematically, the following function is proposed:

$$\sigma = 188 \times \frac{1}{1 + e^{-1.0 \times 10^{-17} \times (T'' - 8.3 \times 10^{18})}} \quad (1)$$

In this equation, 188.0 MPa is σ_{max} . 1.0×10^{-17} and 8.3×10^{18} are some constants which best fit the Ti-6Al-4V data. The fitting can be done automatically using a series of Matlab-driven ABAQUS simulations, where least square fitting was carried out in the Matlab to match experimental data. Table 1 provides the best fitted simulation results with the experimental data.

Table 1. Best-fitted simulation results in comparison with the mini-tensile test data.

Impact speed (m/s)	Simulation result (MPa)	Mini-tensile test (MPa)
650	0	0
700	14	18
710	34.2	28
730	65	68
760	81	86
800	89	90
850	103	115

Therefore, the local bonding stress can be calculated as a function of its T'' value using the equation above and the total bonding force of a single particle can be calculated by integrating the bonding stress over the bonded area. Then the interfacial bonding strength can be obtained by dividing the total force by the average footprint of a single particle in the experiment. Using this equation, we can running single particle impact model at different conditions to predict their bonding strength at the interface.

4 Conclusion

In this study, finite element simulation of single particle normal impact process has been carried out to predict the macroscopic coating bonding strength. Temperature secondary jump, which has direct association with the adiabatic shear instability and bonding, has been represented by the value of second order derivative of the temperature history curve. Such value is also associated with the interfacial bonding strength through a Sigmoid function. Such function provides a valuable tool for the metal cold spray community to link the manufacturing process with the coating property directly, which makes the numerical prediction of the bonding strength possible.

References




1. Assadi, H., Gartner, F., Stoltenhoff, T., Kreye, H.: Bonding mechanism in cold gas spraying. *Acta Mater.* **51**(15), 4379–4394 (2003)
2. Song, X., Everaerts, J., Zhai, W., Zheng, H., Tan, W.Y., Sun, W., Li, F., Marinescu, I., Liu, E. J., Korsunsky, A.M.: Residual stresses in single particle splat of metal cold spray process – Numerical simulation and direct measurement. *Mater. Lett.* **230**, 152–156 (2018)
3. Lesuer, D.: Experimental investigation of material models for Ti-6Al-4V and 2024-T3, pp. 1–36. Livermore Univ. California, Lawrence Livermore National Laboratory (1999)
4. Tan, W.Y., Sun, W., Phang, Y.P., Dai, M.H., Marinescu, I., Dong, Z.L., Liu, E.J.: Effects of traverse scanning speed of spray nozzle on the microstructure and mechanical properties of cold-sprayed Ti6Al4 V coatings. *J. Therm. Spray Technol.* **26**(7), 1484–1497 (2017)
5. Tan, W.Y., Sun, W., Bhowmik, A., Lek, J.Y., Marinescu, I., Li, F., Khun, N.W., Dong, Z.L., Liu, E.J.: Effect of coating thickness on microstructure, mechanical properties and fracture behaviour of cold sprayed Ti6Al4 V coatings on Ti6Al4 V substrates. *Surf. Coat. Technol.* **349**, 303–317 (2018)

6. Schmidt, T., Gärtner, F., Assadi, H., Kreye, H.: Development of a generalized parameter window for cold spray deposition. *Acta Mater.* **54**(3), 729–742 (2006)
7. Schmidt, T., Assadi, H., Gärtner, F., Richter, H., Stoltenhoff, T., Kreye, H., Klassen, T.: From particle acceleration to impact and bonding in cold spraying. *J. Therm. Spray Technol.* **18**, 794–808 (2009)

Product Verification and Material Characterisation



Surface Texture Evaluation on Mirror Finish Surface Using Patterned Area Illumination Method

Shaowei Fu^{1,2} , Fang Cheng¹ , and Tegoeh Tjahjowidodo^{1,2} 

- ¹ Advanced Remanufacturing and Technology Centre (Agency for Science, Technology and Research), Singapore 637143, Singapore
{fu_shaowei, chengf}@artc.a-star.edu.sg
- ² School of Mechanical and Aerospace Engineering, Nanyang Technological University, Singapore 639798, Singapore
ttegoeh@ntu.edu.sg

Abstract. Mirror finish surface products are widely used in many industries such as aerospace, optics, semiconductor and biomedical device manufacturing. The surface texture of mirror finish products is usually measured by off-line instruments such as coherence scanning or phase shifting interferometers. However, most commercial interferometers are expensive and must be operated in a clean and vibration-free laboratory environment. In order to achieve both in-situ surface quality control and automated tool changing for the polishing process, fast and non-contact surface texture measurement are required. To address these in-situ measurement challenges, a surface texture measuring system based on fringe pattern illumination method is proposed in this paper. By analyzing the luminance contrast ratio of the fringe pattern reflection image and comparing to the measurement results from the referenced coherence scanning interferometer, the experimental results showed that the proposed system was able to measure different mirror finish surfaces with Sa and Sq values in the range of 15 nm to 120 nm and 30 nm to 160 nm respectively. In addition, the luminance contrast ratio was also correlated with directions of the machining marks and the projected fringes at different measurement angles. The surface texture aspect ratio parameter Str which provides information about the strength of the machining marks was experimentally evaluated and compared with luminance contrast change. In conclusion, the proposed measuring system was able to measure surface texture with a relative error less than 10% at measurement angle between 20° to 160°, and indicate machining pattern effects on the mirror finish surface.

Keywords: Surface texture · In-situ measurement · Fringe pattern illumination · Luminance contrast evaluation

1 Introduction

According to ASTM standard A480 [1], mirror finish is a highly reflective, smooth finish typically produced by polishing with successively finer grit abrasives and finally with buff polishing. In recent years, mirror finish surface products have become more widely used in industries such as optical, semiconductor and medical device manufacturing resulting in new measurement challenges [2, 3]. Consequently, research and development work has been undertaken to measure the surface roughness of mirror finish surface products in order to achieve in-situ surface quality control and automated tool changing for the polishing process [4, 5]. Contact based techniques (i.e. stylus profilometer) are not suitable for mirror finish surface measurement because the stylus tip may scratch the surface [6]. For mirror finish surface measurement, optical techniques such as confocal microscope [7], coherence scanning interferometer [8] and phase shifting interferometer [9] have great potential due to their non-contact mechanism to avoid both surface damage and contamination. However, they typically suffer from relatively low measurement speed and are difficult to integrate into the surface polishing process [10]. Recently, patterned area illumination method [11] was developed to evaluate the specular reflection and study the relationship between the surface roughness and gloss evaluation. It can be a potential solution to achieve fast and non-contact inspection and send measurement results in situ to the polishing operator to make decision for further processing.

In this paper, the developed patterned area illumination system and the referenced coherence scanning interferometer were used to measure the surface roughness of sixteen samples and the measurement results were compared and analysed. The experimental results showed the developed patterned area illumination system was able to do in-situ measurement of the mirror surface finish surface and also indicate machining pattern effects.

2 Materials and Method

2.1 Test Samples

For roughness measurement, a set of sixteen stainless steel samples labelled from 1 to 16 as shown in Fig. 1, were ground and polished using EcoMet 300 Pro (BUEHLER, Illinois, USA) to achieve surface roughness Sa in the range of 15 nm to 120 nm.

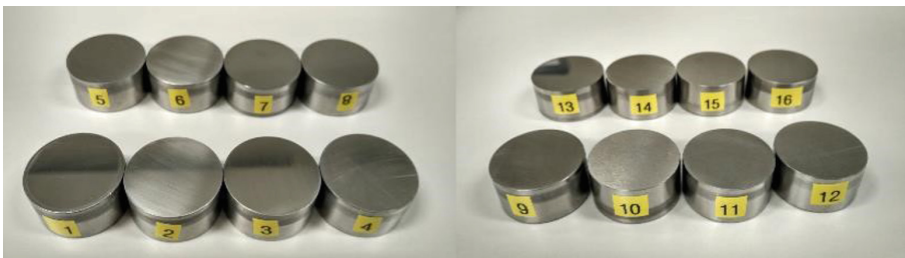


Fig. 1. Test samples for roughness measurement

2.2 Coherence Correlation Interferometer

Areal surface roughness values of the test samples were accurately measured by using a coherence correlation interferometer (Talysurf CCI HD, AMETEK Inc, Berwyn, PA, USA) with 20x objective lens as shown in Fig. 2(a). It employs coherence scanning interferometry to measure the surface texture and was able to provide a lateral resolution of 1 μm and vertical resolution of 0.1 nm. Each sample was also measured five times with a measurement area of 2 mm \times 2 mm. As an illustration, Fig. 2(b) shows surface topography measurement results of four samples with different roughness level. After form removal by third order polynomials, the arithmetical mean roughness S_a , root mean square roughness S_q and texture aspect ratio Str defined in ISO 25178-2 [12] were computed using the TalyMap software. The S_a and S_q parameters are the most widely accepted parameters to characterise surface topography in both academic and engineering industry. Str is one of the more suitable parameters to characterise the areal surface texture as it measures uniformity of the surface texture [13].

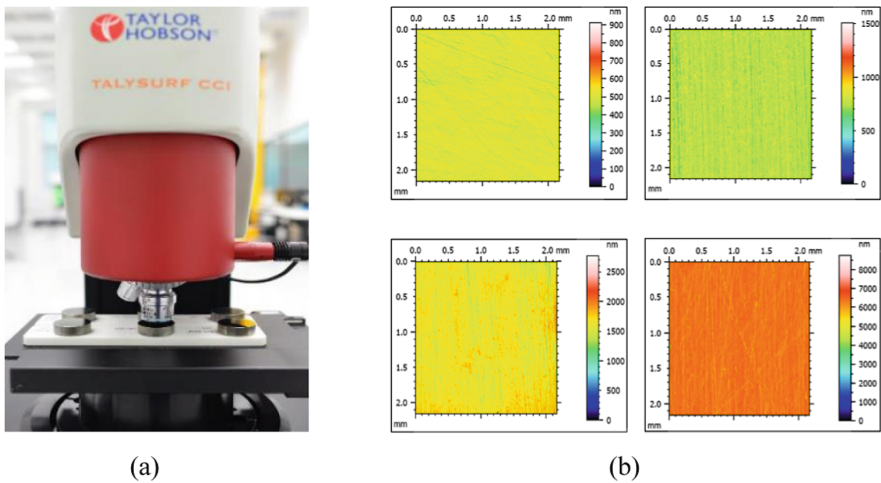


Fig. 2. (a) Talysurf CCI HD; (b) Sample surface roughness measured using Talysurf CCI

2.3 Patterned Area Illumination System

A patterned area illumination system was developed using a programmable illumination source and a monochrome machine vision camera. Figure 3(a) shows the system configuration. Figure 3(b) shows the configuration of whole inspection unit integrated on an industrial robot (IRB 140, ABB Group, Zurich, Switzerland) to achieve in-situ surface roughness measurement. A black and white fringe pattern was generated by the illumination source (Ipad mini 3, Apple Inc, Cupertino, CA, USA). In specular reflection, the incidence angle equals to the reflection angle. Hence, while the fringe patterns are projected on the mirror finish surface, a mirror-like reflected image of the fringe patterns can be captured by the machine vision camera (TXG50, Baumer Holding AG, Frauenfeld, Switzerland) and ultra-low distortion lens (M1620-MPW2, Computar, Cary, NC, USA).

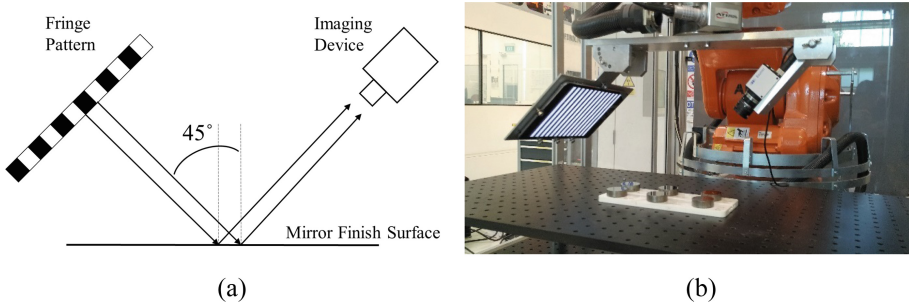


Fig. 3. (a) Model illustration of the patterned area illumination system; (b) System configuration for automated surface roughness measurement

The sharpness of the fringe patterns in the image provides information related to specular reflection on the surface and surface roughness [11]. Luminance contrast [14] of the fringe patterns can be used to evaluate the specular reflection on mirror finish surface. Michelson contrast is widely used for simple periodic patterns where both bright and dark features are equivalent [15]. The Michelson contrast is defined as:

$$C = \frac{L_{max} - L_{min}}{L_{max} + L_{min}} \quad (1)$$

where L_{max} and L_{min} are the maximum and minimum luminance in the image. However, the Michelson contrast is often affected by the ambient lighting changes and optical noises in the image. In order to reduce the influence of noise, the luminance contrast C in the developed imaging processing algorithm was defined as:

$$C = \frac{AW - AB}{AW + AB} \quad (2)$$

where AW and AB are the average intensity of the white fringes and black fringes respectively. After analysing the luminance contrast value of the fringe pattern image and the areal surface roughness parameters (Sa and Sq), a mathematical correlation can be determined. In addition, the test samples were rotated from 0° to 180° in increment of 10° . The luminance contrast difference caused by changing the measurement angles was compared and analysed with texture aspect ratio parameter Str .

3 Results and Discussion

3.1 Luminance Contrast Measurement

Sixteen test samples with different surface roughness were used for measurement. The luminance contrast (C) measured by patterned area illumination system and the surface roughness (Sa and Sq) measured by Talysurf CCI HD are presented as correlation curve in Figs. 4 and 5.

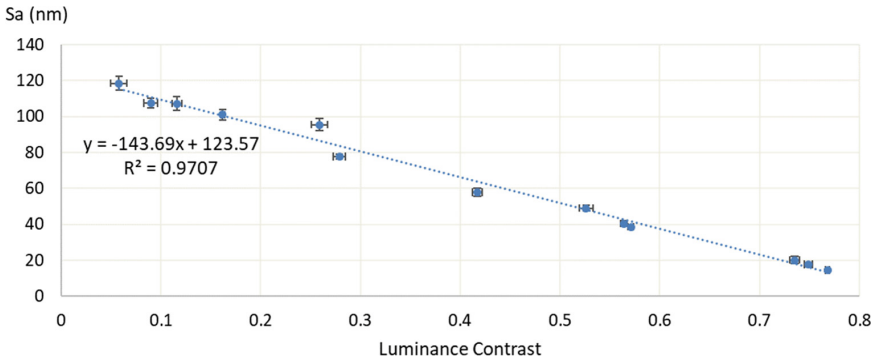


Fig. 4. S_a -Contrast curve

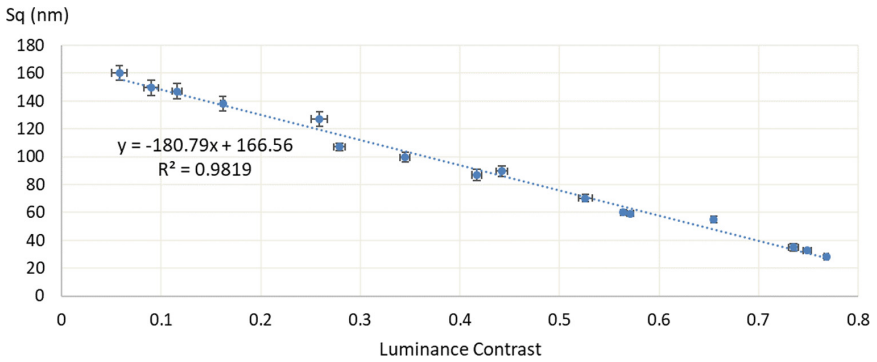


Fig. 5. S_q -Contrast curve

The S_a -contrast curve in Fig. 4 and S_q -contrast curve in Fig. 5 show good feasibility of the proposed system for areal surface roughness measurement. As widely accepted, the coefficient of determination R^2 value demonstrates how well the regression line fits the measured data points. The closer the R^2 value is to one, the better the linear relationship between two sets of data points. The high R^2 value of 0.9707 in S_a -contrast curve and value of 0.9819 in S_q -contrast curve indicate that linear regression of the data set is reliable.

Based on the S_a (S_q) and contrast values in Figs. 4 and 5, a linear relation can be modelled by Eqs. (3) and (4) as shown below. These empirical equations are based on the preliminary measurement results of the sixteen samples. More samples need to be measured to get additional data points to validate the proposed empirical equations.

$$S_a = -143.69C + 123.57 \quad (3)$$

$$S_q = -180.79C + 166.56 \quad (4)$$

3.2 Surface Uniformity Measurement

According to ISO 25178-2 [12], Str is defined as the ratio of the fastest to slowest decay to correlation length of the surface autocorrelation function. For evaluating the surface texture, Str is the most suitable parameter to characterize the surface uniformity.

Sample 2 and sample 8 shown in Fig. 6 were chosen to study the effect of machining pattern on mirror surface isotropy. These two samples represent two typical mirror finish surface with unidirectional machining pattern (sample 2) and multi-directional machining pattern (sample 8). The surface texture parameters (Sa , Sq and Str) of the two samples are presented in Table 1. They have very close Sa and Sq values, but the Str value of sample 2 and sample 8 has significant differences. In principle, Str has a value between 0 and 1. Larger values, say $Str > 0.5$, indicates uniform texture in all directions. Smaller values, say $Str < 0.3$, indicates an increasingly strong directional structure or machining pattern.

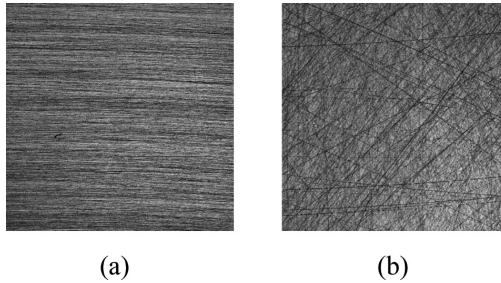


Fig. 6. Machining pattern on (a) Sample 2 and (b) Sample 8

Table 1. Surface texture parameters of sample 2 and sample 8

	Sa (nm)	Sq (nm)	Str
Sample 2	38.6 ± 1.0	59.4 ± 1.5	0.072 ± 0.006
Sample 8	40.4 ± 1.4	60.1 ± 1.8	0.426 ± 0.013

Sample 2 and sample 8 are typical examples of surfaces with similar Sq values but having different surface uniformity. The luminance contrast values at different measurement angles for sample 2 and sample 8 were plotted in Fig. 7. For sample 2, the luminance contrast value at 0° and 180° is much larger than those at the other measurement angles. As a comparison, sample 8 has random and same luminance contrast value from 0° to 180° . Other samples will be investigated whether they have a similar trend of Str value close to zero with much higher values at 0° and 180° .

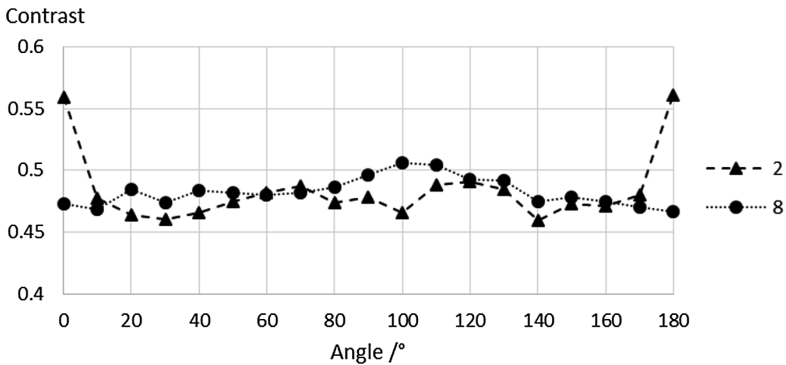


Fig. 7. Contrast value in different measurement angles

Based on above observations, the luminance contrast ratio has correlation with directions of the machining marks and the projected fringes at different measurement angles. The surface texture aspect ratio parameter Str which provides information about the strength of the machining marks was experimentally evaluated and compared with luminance contrast change.

4 Conclusion and Future Work

In this study, a surface roughness measurement system using the fringe pattern illumination method is developed to address in-situ roughness measurement on mirror finish surface. By analyzing the luminance contrast ratio of the fringe pattern reflection image and comparing to the measurement results from the referenced coherence scanning interferometer, the experimental results showed that the developed system can measure different mirror finish surfaces with Sa and Sq values in the range of 15 nm to 120 nm and 30 nm to 160 nm respectively. The experimental results demonstrated a good correlation between the luminance contrast value and the surface roughness parameters (Sa and Sq). In addition, the luminance contrast ratio was also correlated with directions of the machining marks and the projected fringes at different measurement angles. The surface texture aspect ratio parameter Str which provides information about the strength of the machining marks was experimentally evaluated and compared with luminance contrast change.




Future work is focus on the development of new fringe pattern to study the two directional gray-scale contrast change and the surface texture aspect ratio parameter Str . In addition, more samples with different surface roughness will be fabricated to validate the proposed patterned area illumination method.

References

1. ASTM (2014) A480/A480 M 14b: Standard Specification for General Requirements for Flat-Rolled Stainless and Heat-Resisting Steel Plate, Sheet, and Strip
2. Hattori, T., Okamoto, A., Kuniyasu, H.: Challenges of Finer Particle Detection on Bulk-Silicon and SOI Wafers. *Solid State Phenom.* **103–104**, 121–128 (2005). <https://doi.org/10.4028/www.scientific.net/SSP.103-104.121>
3. Ponsonnet, L., Comte, V., Othmane, A., Lagneau, C., Charbonnier, M., Lissac, M., Jaffrezic, N.: Effect of surface topography and chemistry on adhesion, orientation and growth of fibroblasts on nickel–titanium substrates. *Mater. Sci. Eng., C* **21**, 157–165 (2002). [https://doi.org/10.1016/S0928-4931\(02\)00097-8](https://doi.org/10.1016/S0928-4931(02)00097-8)
4. Miranda-Medina, M.L., Somkuti, P., Bianchi, D., Cihak-Bayr, U., Bader, D., Jech, M., Vernes, A.: Characterisation of orange peel on highly polished steel surfaces. *Surf. Eng.* **31**, 519–525 (2015). <https://doi.org/10.1179/1743294414Y.0000000407>
5. Gao, W.: Development of an optical probe for profile measurement of mirror surfaces. *Opt. Eng.* **36**, 3360–3366 (1997). <https://doi.org/10.1117/1.601563>
6. Leach, R.K.: *Fundamental Principles of Engineering Nanometrology*. Elsevier, Amsterdam (2010)
7. Fu, S., Cheng, F., Tjahjowidodo, T., Zhou, Y., Butler, D.: A non-contact measuring system for in-situ surface characterization based on laser confocal microscopy. *Sensors* **18**, 2657 (2018). <https://doi.org/10.3390/s18082657>
8. de Groot, P.: Coherence scanning interferometry. In: *Optical Measurement of Surface Topography*, pp. 187–208. Springer, Heidelberg (2011)
9. Vorburger, T.V., Rhee, H.G., Renegar, T.B., Song, J.F., Zheng, A.: Comparison of optical and stylus methods for measurement of surface texture. *Int. J. Adv. Manuf. Technol.* **33**, 110–118 (2007). <https://doi.org/10.1007/s00170-007-0953-8>
10. Fang, F.Z., Zhang, X.D., Weckenmann, A., Zhang, G.X., Evans, C.: Manufacturing and measurement of freeform optics. *CIRP Ann. Manuf. Technol.* **62**, 823–846 (2013). <https://doi.org/10.1016/j.cirp.2013.05.003>
11. Sugino, T., Tashiro, Y., Yamane, Y.: Gloss evaluation of hairline-finished metal surface using patterned area illumination method: relationship between gloss evaluation and surface roughness for the estimation of surface roughness. *Key Eng. Mater.* **749**, 251–256 (2017). <https://doi.org/10.4028/www.scientific.net/KEM.749.251>
12. British Standards Institution: BS EN ISO 25178-2 Terms, definitions and surface texture parameters (2012)
13. Leach, R.: *Characterisation of Areal Surface Texture*. Springer, Berlin (2013)
14. Pelli, D.G., Bex, P.: Measuring contrast sensitivity. *Vision. Res.* **90**, 10–14 (2013). <https://doi.org/10.1016/j.visres.2013.04.015>
15. Kukkonen, H., Rovamo, J., Tiippana, K., Näsänen, R.: Michelson contrast, RMS contrast and energy of various spatial stimuli at threshold. *Vision. Res.* **33**, 1431–1436 (1993). [https://doi.org/10.1016/0042-6989\(93\)90049-3](https://doi.org/10.1016/0042-6989(93)90049-3)



Sliding Behavior of Secondary Phase SiC Embedded Alloyed Layer Doped Ti6Al4V Surfaces Ensuing Electro Discharge Machining

Jibin T. Philip¹ , Deepak Kumar², Jose Mathew³ ,
and Basil Kuriachen¹ 

¹ Department of Mechanical Engineering,
National Institute of Technology Mizoram, Aizawl 796012, Mizoram, India
basilkuriachen@gmail.com

² Department of Mechanical Engineering, Indian Institute of Technology Delhi,
New Delhi 110016, Delhi, India

³ Department of Mechanical Engineering,
National Institute of Technology Calicut, Calicut 673601, Kerala, India

Abstract. The enhancement in process efficiency achievable by additive mixed electrical discharge machining during the processing of metal/alloy surfaces is a known facet. Nonetheless, its influence on the surface characteristics of the material remains scarcely evaluated. Hence, the evolution in tribological behavior of electrical discharge machined Ti6Al4V surfaces become the focal point of the present investigation. The process got assisted by silicon carbide powder (SiC, green, 1–10 μm) dispersed dielectric (de-ionized water) used as an insulator and the discharge medium. A computerized pin-on-disk tribometer (PoDT) was used to quantify the wear behavior of the developed surfaces. The experimentations varied based on distinction in the chosen speed (1.256 ms^{-1} (V1) and 1.884 ms^{-1} (V2)) and load (50 N and 100 N) conditions, respectively. The results depict that the tribological characteristics of the base material were enhanced by the surface doped heavily alloyed recast layer with secondary hard phases (SiC). At increased load (100 N), a catastrophic shift in wear mechanism caused by galling, led to the resultant delamination. The aftermath situation of implementing hard abrasives for surface modification is that at severe conditions (load/speed), the spalling of layers can have destructive effects on the mating surfaces.

Keywords: EDM · Tribo-behavior · Secondary phases · SiC

1 Introduction

The application base of the titanium (Ti) and its alloys are extensive, encapsulating the fields of aerospace, biomedical, and sporting equipment application domains [1]. The excellent properties of the material such as low weight to density ratio, biocompatibility, and corrosion resistance gave it a cutting-edge advantage over the other light-weight alloys based on aluminium (Al) and magnesium (Mg) [2, 3]. Among the Ti alloy series, the Ti6Al4V (Ti64) remains the heavily utilized material covering 50%

(approx.) of the world production [4]. Nevertheless, the inconsistent tribo-behavior of the Ti64 led to itself getting sidelined from material to counter-body interactive applications [5–9].

During EDM, a re-solidified layer (recast layer) develops on the workpiece surface consisting of materials from the tool, dielectric and the reaction byproducts of the dielectric breakdown. The appendage layer can also contain fragments of particles dispersed in the dielectric fluid added as additives to enhance the machining efficiency. Moreover, the operating and process parametric conditions govern the structure and thickness of the recast layer. High carbon diffusion is associated with the utilization of hydrocarbon-based dielectrics compared to the deionized water dielectrics [10]. The development of secondary discharges during additive mixed electrical discharge machining (AMEDM) assisted by SiC dispersed water dielectric has been reported to produce discrete topographical characteristics on the material surfaces [11]. The suspended particles can rush through the developed molten material ensuing discharge pulses to get integrated within the recast layer. The SiC is commonly used as an abrasive phase to increase the hardness of the materials. Further, the utilization of SiC as an additive for ED machining can as well improve the hardness of the subsurface layers. Consequently, AMEDM can result in an enhancement in the characteristics of the surface and subsurface zones of the materials. During the surface modification of Ti64 using ED machining process with SiC as an additive, the increment in powder concentration and discharge current resulted in the improvement and depletion in SiC transfer, respectively [12]. The formation of TiC and TiS₂ phases resulted in the enhanced microhardness of the functional material surfaces [13].

An appreciable amount of work has already been carried out using AMEDM for surface modification of distinct materials. Nonetheless, the utilization of the approach to enhance the tribo-behavior of the material surfaces are scarce to be found. Moreover, the low tribo-characteristics of Ti64 pose a great need to formulate advanced methods for its improvement. Subsequently, in the present work, the influence of AMEDM assisted by dispersed SiC on Ti64 surfaces has been evaluated. The experiments were repeated at different load (50 N and 100 N) and sliding speed (1.256 ms⁻¹ (V1) and 1.884 ms⁻¹ (V2)) process conditions. The tribo-behavior of the bare Ti64 (BTi64) and the electrical discharge machined Ti64 (ETi64) got compared for efficiency testing. The shift in wear mechanisms was elucidated using field emission scanning electron microscopy (FESEM) analysis of the worn-pin surfaces.

2 Experimental Methodology

2.1 Materials

The workpiece material used in the present work is Ti64, procured in the form of thin rods (length = 20 mm, dia. (\emptyset) = 6 mm). The material possesses a wide range of applicability, and its improvement in tribo-behavior can remove the constraints for being used in interactive environs. For ED machining, the tool material and the dielectric fluid were chosen as copper and deionized water, respectively. The selection of the former was due to its high electrical conductivity whereas, the latter for it does

not favor high carbon deposition. The silicon carbide powder (SiC, green, 1–10 μm) was dispersed in the dielectric for AMEDM, presuming its capability to impart hardness for the surface and subsurface regions of the functional material. For tribo-testing, the counter-body surface was chosen as EN 31 steel disk (60 HRC, size: 165 \times 8 mm), for it demonstrates higher hardness than the test material.

2.2 Sample Preparation

The Ti64 rods were hand cut to required dimensions to form two sets of samples (Set-I) and (Set-II). The Set-I samples were prepared to evaluate the wear characteristic of the Ti64 in its bare form (length = 33 mm, dia. (\emptyset) = 6 mm). A tolerance of 1 mm was left to grind and polish the surfaces using emery paper (grit size: P1200 and P1500) fastened onto a polishing machine. Whereas, the Set-II samples were given a tolerance of 2 mm, chosen as the depth for ED machining to achieve final dimensions of length = 32 mm and dia. (\emptyset) = 6 mm.

2.3 Development of ETi64 Sample Surfaces

The external setup for AMEDM fabricated using acrylic sheet consisting of pumps and valves were properly arranged inside the EDM machine as shown in Fig. 1. The samples got accurately fastened on the vice; positioned and fixed to the base of the machining tank using a magnetic chuck. The tool and the workpiece were vertically aligned so that during machining, their surfaces interact along the horizontal plane. The dielectric fluid (de-ionized water) dispersed with SiC particles (additive) was supplied to the tank, and the pump system provided at the base was used to agitate the solution to prevent settling. The machining of the Set-II samples was carried out up to a maximum depth of 2 mm at peak process parametric conditions (current (I) = 10 A, pulse on time (T_{on}) = 100 μs and servo voltage = 60 V).

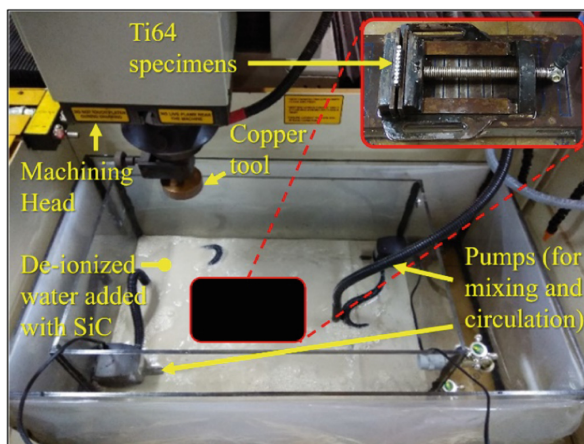


Fig. 1. Experimental setup for AMEDM, with external tank fabricated and placed inside the EDM machine consisting of pumps and valves to maintain dispersibility of the additive in the dielectric fluid and drainage.

2.4 Tribo-Test

The Set-I and Set-II samples were subjected to the tribo-characteristic evaluation at distinct sliding speed (V1 and V2) and load (50 N and 100 N) conditions, respectively. The experimentation was performed on a sophisticated computerized pin-on-disk tribometer (PoDT) at ambient and dry sliding interactions with the counter-body surface. The sliding distance was kept constant at 1000 m. An external load cell and linear variable transducer (LVDT, model: SI-708, non-linearity: $\pm 0.5\%$ of the range or better, repeatability: $\pm 0.5\%$ of the range or better, resolution: ± 0.001 mm, measurement range: ± 2 mm) was used to monitor, measure and record the real-time values of the frictional force and wear experienced by the pin material. The disk and the pins were washed and dried using acetone prior to each test. Each experimentation was repeated thrice and the plots represented are developed using the average values to avoid ambiguity. The photograph of PoDT testing of the Ti64 sample is as shown in Fig. 2.

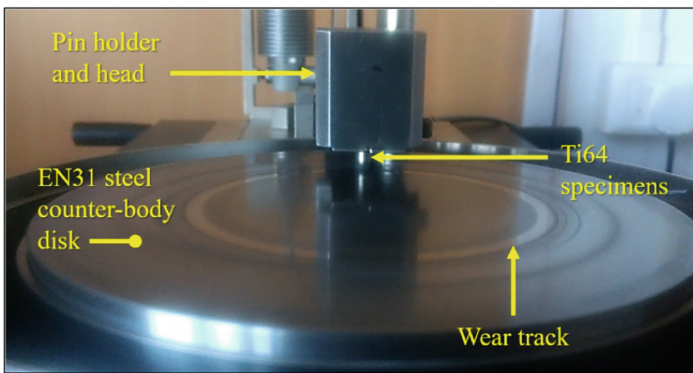


Fig. 2. PoDT testing of Ti64 samples

3 Results and Discussion

The tribo-behavior of the BTi64 and ETi64 samples tested at distinct experimental conditions on the PoDT has been quantified in terms of variation in friction and wear behavior with sliding distance and the morphology analyses of the worn pin surfaces.

3.1 Friction and Wear Behavior

The characteristic plots showing the variation in wear (μm) and coefficient of friction (CoF) of the BTi64 and ETi64 test samples at variable speed conditions are as shown in Figs. 3 and 4, respectively. At both sliding speeds, the ETi64 samples demonstrated better wear characteristics whereas it possessed high CoF values. This can be attributed to as due to the influence of the SiC particles and the re-cast layer formed on the functional material ensuing EDM processing. For BTi64, a uniform increment in wear was observed at sliding speeds of V1 and V2 ms^{-1} , respectively. The high wear observed with rise in speed can be due to the reduction in yield strength of the alloy due

to rise in temperature by frictional heating (FH) [4]. Whereas, for ETi64 the wear behavior follows an intervening trend at both sliding speeds. Precisely, at $V2 \text{ ms}^{-1}$, observable fluctuations are identified with the wear curve, probably due to the formation and removal of oxide layers. Since the high temperature conditions achieved due to high speed counter-body interactions will ease the reactions of the debris particles with the environ leading to oxidation. Conversely, at $V1$, a stabilizing trend was identified with progressive sliding since the debris emanating from the functional material will have more tendency to remain within the wear track regions. The comparatively low centrifugal force favors such a phenomenon resulting in debris perforation into the functional material, resulting in improved hardness. The argument is supported by the high CoF trend observed for ETi64 surfaces at peak sliding speeds. Since the oxide appendage layers are developed over the substrate surface, the larger area of contact is achieved during counter-body interaction leading to high friction. But the material removed due to wear will be the oxide layers, in the form of fine particles. The stability and protective action of such layers will depend on its propensity to recover once removed. Nevertheless, the low influence of oxidation at sliding of $V1$ resulted in low CoF as the SiC hard phases will create a separation between the mating surfaces. For BTi64 samples, the CoF maintained a considerably low value of 0.1 and below at varied sliding speeds.

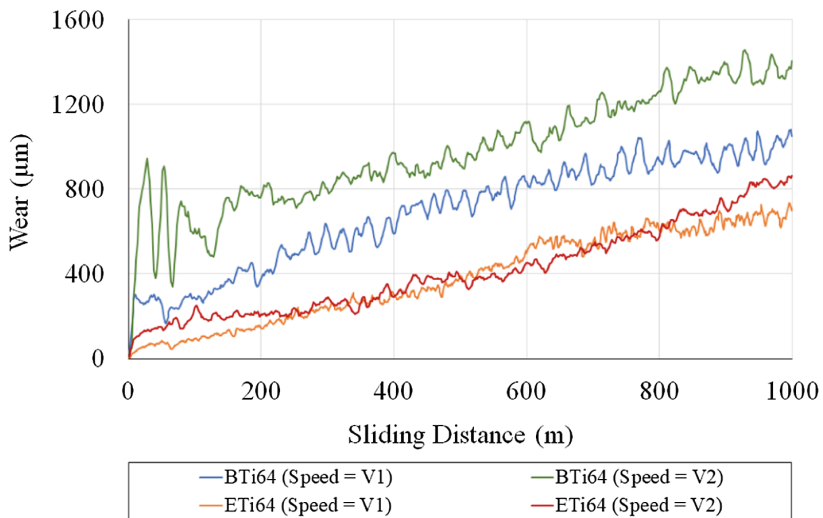


Fig. 3. Variation in wear with sliding distance of the BTi64 and ETi64 samples slid at distinct sliding speeds and constant load (50 N) conditions.

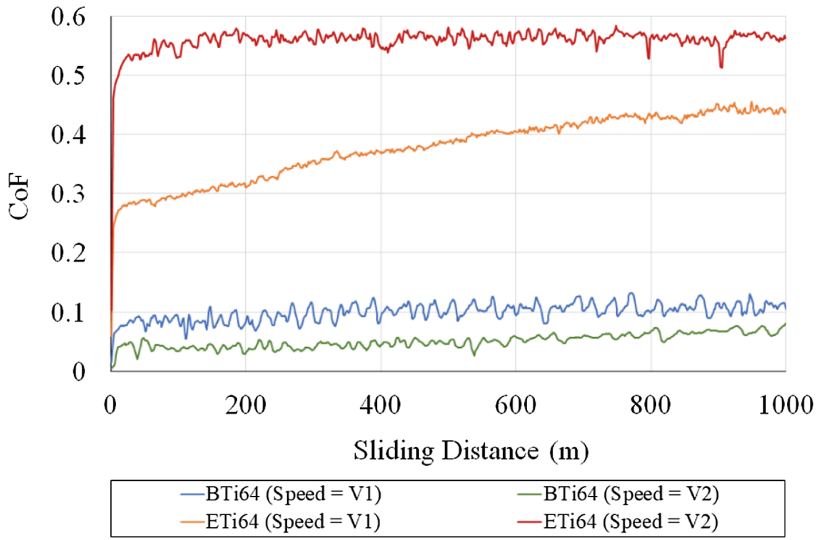


Fig. 4. Variation in CoF with sliding distance of the BTi64 and ETi64 samples slid at distinct sliding speeds and constant load (50 N) conditions.

The characteristic curves showing the variation in wear and CoF of the BTi64 and ETi64 at varied load conditions are as shown in Figs. 5 and 6, respectively. At both conditions (50 N and 100 N), the BTi64 samples were identified to undergo the maximum wear but with low CoF. Although so, it is significant to note that during sliding at 100 N load condition, the curve stabilizes after a sliding distance of 400 m and follow a steady path with an average wear of 1400 μm (approx.). Whereas, for all other samples, the wear curve followed an incremental trend. For ETi64, the sample slid at loads of 50 N and 100 N demonstrated the least wear trend in comparison to the BTi64. A fluctuating trend is identified at 100 N sliding. It can be due to the high pressure and temperature build-up at the interface forcing the hard phase debris into the functional material to drag it along the sliding direction, leading to two body/three body abrasion. The dip in wear curve observed beyond a sliding distance of 500 m can be due to the influence of oxide layer formation or the effect of the hard phases, imparting hardness to the functional material surface. Such effects can lead to shift in wear mechanisms from material removal caused by abrasion to delamination and fracture. Besides, all these negative inclinations, the recast layer formed with SiC abrasives is identified to provide better protective action. For BTi64, the low CoF can be due to the catastrophic removal of material from the surface, as observable from the wear trend curves. Unlike the characteristics observed at incremental sliding speeds, the varied load conditions led to distinctive trends, since the effect of rise in temperature favoring oxidation will be more in case of high-speed sliding. Moreover, the high pressure developed at high loads will force the hard phase debris to penetrate the functional material, if not cleared from the wear track by centrifugal action. This coupled with the sliding action will lead to ploughing action leading to severe damage.

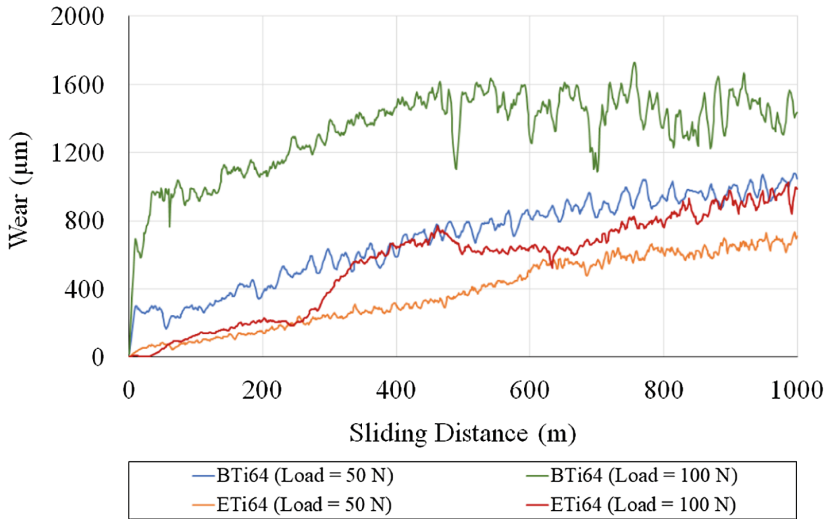


Fig. 5. Variation in wear with sliding distance of the BTi64 and ETi64 samples slid at distinct loads and constant sliding speed (V1) conditions.

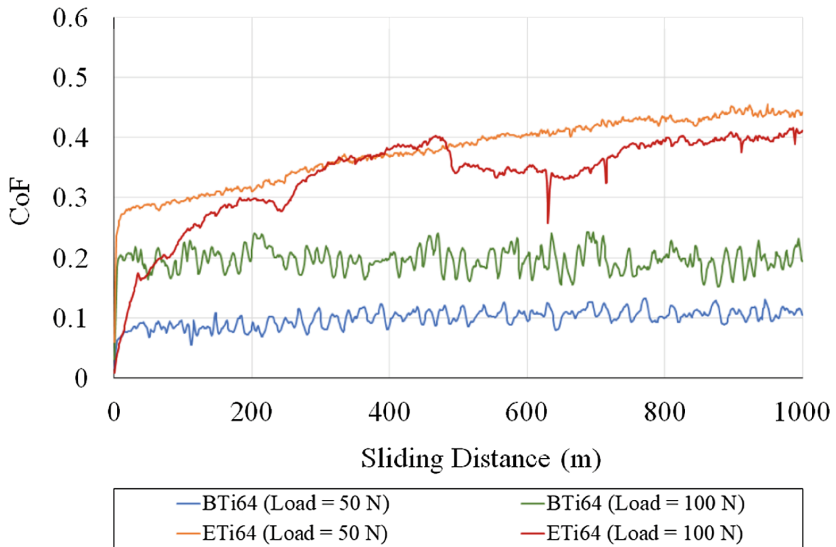


Fig. 6. Variation in CoF with sliding distance of the BTi64 and ETi64 samples slid at distinct loads and constant sliding speed (V1) conditions.

3.2 Surface Morphology Analyses

The morphology of the ETi64 worn-pin surfaces has been investigated to elucidate the occurrence and shift in wear mechanisms at various states of sliding contact (Fig. 7). It can be observed that the arguments made based on the variational plots of friction and wear at distinct sliding conditions can be validated from the SEM metallographic images of the worn-pin surfaces. The ETi64 pin surface slid at speed = V1, load = 50 N is observed to possess pierced hard phases stuck on the functional material. The influence and formation of the oxide layer is minimal. At increased speed = V2 and load = 50 N, the effect of oxidation takes over due to the increment in temperature and rigorous interaction of the surface and the debris with the environ activated by FH. The damaged oxide layers in the form of fine fragments can be observed from the FESEM images. If the recovery of the removed oxide particles does not happen timely, the hard abrasives/asperities can impinge onto the soft surface. This combined with sliding motion can lead to abrasion. The resultantly formed abrasive grooves can be observed at random positions on the surface. At increased load condition, the enforced pressure and temperature conditions can cause debris penetration and ploughing. This can lead

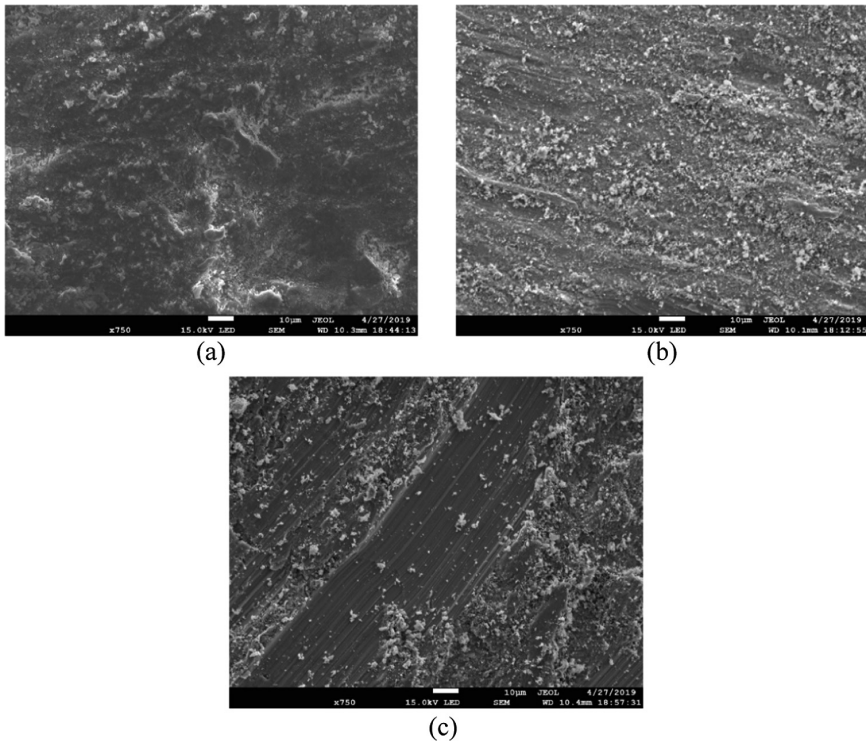


Fig. 7. The FESEM metallographic images (scale: 10 μm , magnification: $\times 750$, electron beam voltage: 15 kV) of the ETi64 worn-pin surfaces slid against the EN 31 steel counter-body surface at distinct sliding conditions (a) speed = V1 and load = 50 N; (b) speed = V2 and load = 50 N; (c) speed = V1 and load = 100 N.

to severe wear and catastrophic damage. As observable from Fig. 7 (c), the worn-pin surfaces of ETi64 developed ensuing sliding at speed = V1 and load = 100 N, the surface is covered with abrasive grooves and various modes of delamination fracture. It can also be identified that the material has also got removed in the form of plate-like structures. The surface oxides also play a considerable role in such a state of sliding due to rise in temperature.

4 Conclusions

Based on the tribo-behavioral evaluation of the BTi64 and ETi64 samples at distinct sliding speed and load conditions, the following inferences are derived.

- The ETi64 surfaces impart better wear behavior in comparison to BTi64, at all states of sliding considered under the present study. Nevertheless, compromise has been made in the case of frictional characteristics.
- The SiC hard phase particles played a significant role in wear reduction by improving the hardness and thereby stability of the functional material surfaces at a sliding speed = V1 and load = 50 N.
- The formation of oxides, governed the wear behavior at a sliding speed = V2 and load = 50 N. Based on the stability and recovery of the oxide layers, abrasive grooves were identified to be formed at random positions on the functional material surface.
- The sliding at increased load condition of 100 N, led to the material removal by abrasion resulting in the formation of grooves and shift in wear mechanism to delamination and fracture. Consequently, formation of plate-like debris was identified at distinct positions.

Finally, the energy dispersive spectroscopy (EDAX) and X-ray diffractogram (XRD) analyses carried out on the worn-pin surfaces can give a detailed insight into the various oxides formed and the composition of the various elements.

Acknowledgement. The authors extend their humble obligations to the Science and Engineering Research Board (SERB), Department of Science and Technology (DST), Government of India for the research grant sanctioned for the project (Ref. No. ECR/2016/001929) through the aid of which this initiative was undertaken.




References

1. Li, Y., Yang, C., Zhao, H., Qu, S., Li, X., Li, Y.: New developments of Ti-based alloys for biomedical applications. *Materials* 7(3), 1709–1800 (2014). <https://doi.org/10.3390/ma7031709>
2. Mao, Y.S., Wang, L., Chen, K.M., Wang, S.Q., Cui, X.H.: Tribo-layer and its role in dry sliding wear of Ti–6Al–4V alloy. *Wear* 297(1–2), 1032–1039 (2013). <https://doi.org/10.1016/j.wear.2012.11.063>

3. Geetha, M., Singh, A.K., Asokamani, R., Gogia, A.K.: Ti based biomaterials, the ultimate choice for orthopaedic implants—a review. *Prog. Mater. Sci.* **54**(3), 397–425 (2009). <https://doi.org/10.1016/j.pmatsci.2008.06.004>
4. Collings, E.W.: *The Physical Metallurgy of Titanium Alloys*, vol. 3. Metals Park Ohio (1984)
5. Budinski, K.G.: Tribological properties of titanium alloys. *Wear* **151**(2), 203–217 (1991). [https://doi.org/10.1016/0043-1648\(91\)90249-T](https://doi.org/10.1016/0043-1648(91)90249-T)
6. Yerramareddy, S., Bahadur, S.: The effect of laser surface treatments on the tribological behavior of Ti-6Al-4V. *Wear* **157**(2), 245–262 (1992). [https://doi.org/10.1016/0043-1648\(92\)90065-G](https://doi.org/10.1016/0043-1648(92)90065-G)
7. Hadke, S., Khatirkar, R.K., Shekhawat, S.K., Jain, S., Sapate, S.G.: Microstructure evolution and abrasive wear behavior of Ti-6Al-4V alloy. *J. Mater. Eng. Perform.* **24**(10), 3969–3981 (2015). <https://doi.org/10.1007/s11665-015-1667-y>
8. Wiklund, U., Hutchings, I.M.: Investigation of surface treatments for galling protection of titanium alloys. *Wear* **251**(1–12), 1034–1041 (2001). [https://doi.org/10.1016/S0043-1648\(01\)00730-X](https://doi.org/10.1016/S0043-1648(01)00730-X)
9. Straffelini, G., Molinari, A.: Dry sliding wear of Ti-6Al-4V alloy as influenced by the counter-face and sliding conditions. *Wear* **236**(1–2), 328–338 (1999). [https://doi.org/10.1016/S0043-1648\(99\)00292-6](https://doi.org/10.1016/S0043-1648(99)00292-6)
10. Lim, L.C., Lee, L.C., Wong, Y.S., Lu, H.H.: Solidification microstructure of electrodischarge machined surfaces of tool steels. *Mater. Sci. Technol.* **7**(3), 239–248 (1991). <https://doi.org/10.1179/mst.1991.7.3.239>
11. Ekmekci, B., Yaşar, H., Ekmekci, N.: A discharge separation model for powder mixed electrical discharge machining. *J. Manuf. Sci. Eng.* **138**(8), 081006 (2016). <https://doi.org/10.1115/1.4033042>
12. Öpöz, T.T., Yaşar, H., Ekmekci, N., Ekmekci, B.: Particle migration and surface modification on Ti6Al4 V in SiC powder mixed electrical discharge machining. *J. Manuf. Process.* **31**, 744–758 (2018). <https://doi.org/10.1016/j.jmapro.2018.01.002>
13. Li, L., Zhao, L., Li, Z.Y., Feng, L., Bai, X.: Surface characteristics of Ti-6Al-4V by SiC abrasive-mixed EDM with magnetic stirring. *Mater. Manuf. Processes* **32**(1), 83–86 (2017). <https://doi.org/10.1080/10426914.2016.1151043>



Measurement of Residual Stresses on Deep Rolled Round Aluminum Samples Using Hole Drilling Strain Gage Method

Mehmet Okan Görtan^(✉) , Berkay Yüksel , and Bilsay Sümer 

Hacettepe University, 06800 Ankara, Turkey
okangortan@hacettepe.edu.tr

Abstract. Deep rolling is an established process to induce plastic deformation on the surface of engineering parts. As a result, a cold worked surface and a compressive layer of residual stresses are generated in subsurface regions. Thus, strength can be increased. Although deep rolling is mostly applied to axisymmetric parts with comparatively low diameters, effect of process parameters on induced stresses are usually investigated on flat surfaces. However, different residual stress profiles are expected in depth direction in flat and cylindrical parts. In the current study, residual stresses induced in deep rolled round EN AW-6082 aluminum samples with a diameter of 14 mm were measured using hole-drilling strain-gage method. Hole drilling calibration matrices were derived using finite element simulations. These matrices were compared with the ones used for flat specimens. Evaluated residual stress profiles by using these matrices were compared for both a flat workpiece and cylindrical workpiece.

Keywords: Residual stress · Deep rolling · Cylindrical workpiece

1 Introduction

Deep rolling is a mechanical surface treatment process to enhance surface properties of workpieces and induce compressive residual stresses in subsurface regions. Depending on the compressive residual stress level, fatigue strength of workpieces can be improved. Therefore, subsurface residual stress distribution measurement is an important aspect for industrial applications [1].

There are several residual stress measurement techniques such as, hole-drilling, X-ray diffraction or neutron diffraction methods. Among these methods, hole-drilling is widely used in industry due to its ease of application and low investment requirements. It is also subject of this study [2, 3].

Determination of the residual stress distribution using hole-drilling method requires calibration matrices which are formed from strain relaxation coefficients for different depth increment and loading increment combinations. These coefficients are calculated using finite element method [2–6]. Calibration matrices in the current ASTM E837-08 standard are determined for flat workpieces. However, most of the parts used in the industry includes radiused or curved surfaces. Therefore, evaluation of the residual stress distribution data becomes erroneous as the radius of curvature decreases. As a result, newly formed calibration matrices are required for each specific case.

Calibration matrices in the ASTM E837-08 standard is based on the early works of Schajer [4, 5]. Since then, computers become more powerful. Therefore, calibration matrices for flat pieces are derived again in this study by using finer meshed finite element models and compared with the ASTM coefficients. Calibration matrices for a cylindrical part are derived and compared with ASTM coefficients as well. These newly formed coefficients are used to evaluate the subsurface residual stress distribution of two different workpieces: a deep-rolled flat specimen and a deep-rolled cylindrical specimen.

2 Derivation of Calibration Matrices

Derivation of calibration matrices is elaborated in multiple previous studies [4, 5, 7–9]. Finite element simulations should be used in these derivation activities. Strain relaxation coefficients should be evaluated by applying a known stress fields to periphery of the hole to be drilled. For every combination of the depth increment and loading increment, simulations should be performed to obtain strain relaxation coefficients A_{ij} and B_{ij} . Subscripts i and j refers to depth increment and loading increment, respectively.

Following the work of Niku-Lari et al. [7], for a material with Young's Modulus of E and Poisson's Ratio of ν , calibration matrix \mathbf{A} can be obtained by applying unit pressure (1 Mpa) to the each loading layer of the hole. Matrix \mathbf{A} consists of the calibration coefficients which are derived from the strain relaxation coefficients A_{ij} due to hole drilling into an equal-biaxial stress field. Strain relaxation coefficient A_{ij} can be calculated using following equation:

$$A_{ij} = \frac{\varepsilon(0^\circ) + \varepsilon(90^\circ)}{2(1\text{MPa})} \cdot \frac{E}{1 + \nu} \quad (1)$$

where $\varepsilon(0^\circ)$ and $\varepsilon(90^\circ)$ strains calculated on the locations of strain gages 1 and 3 for type A strain gage rosette, respectively. Calibration matrix \mathbf{B} can be calculated by applying a normal stress $+1\cos(2\theta)$ and a shear stress $-1\sin(2\theta)$ to the loading layer of the hole. Matrix \mathbf{B} consists of the calibration coefficients which are derived from the strain relaxation coefficients B_{ij} due to hole drilling into a pure shear stress field. Strain relaxation coefficient B_{ij} can be calculated using following equation:

$$B_{ij} = \frac{\varepsilon(0^\circ) + \varepsilon(90^\circ)}{2(1\text{MPa})} \cdot E \quad (2)$$

After A_{ij} and B_{ij} terms are calculated, calibration coefficients for each increment combination can be calculated as;

$$a_{ij} = A_{i,j} - A_{i,j-1} \quad (3)$$

$$b_{ij} = B_{i,j} - B_{i,j-1} \quad (4)$$

For a and b values, subscripts i and j corresponds to the row and column number of calibration matrices **A** and **B**, respectively. Then the calibration matrices which are to be used in the evaluation of residual stress distribution can be formed. Those matrices are then used to transform measured strain values to residual stresses. In this study, type A 031-RE size strain gage rosette [6] with a hole diameter of 1 mm was used and calibration matrices are formed for this type of strain gage rosette.

2.1 Finite Element Models

Finite element models were established in order to derive strain relaxation coefficients and calibration matrices. Finite element simulations were performed using the commercially available Marc.Mentat 2016.0 software. All analyses performed under the assumption of linear-elastic analysis. Elastic modulus of 69 GPa and Poisson's ratio of 0.3 were used. For every depth and loading increment combination, a separate finite element model was generated.

Flat Pieces. For flat pieces, in order to calculate the coefficients A_{ij} , an axisymmetric model with axisymmetric loading described above was established. Model consists of around 11000 (changes as the depth increment changes) 4-noded elements with full integration. This model can be seen in Fig. 1. For the calculation of the coefficients B_{ij} , an axisymmetric part with non-axisymmetric loading described above was established. 3-D model consists of around 67000 8-noded elements with full integration. This model can be seen in Fig. 2. Hole and loading increments of 0.05 mm, 0.1 mm, 0.15 mm, 0.2 mm, 0.25 mm, 0.30 mm, 0.35 mm and 0.40 mm were used in the calculations.

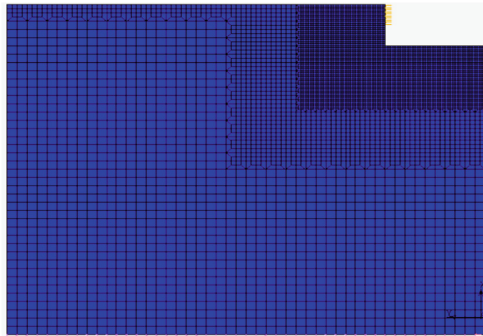


Fig. 1. Axisymmetric model with axisymmetric loading for flat piece

Cylindrical Pieces. For cylindrical pieces, calculation of the coefficients A_{ij} is not a case of axisymmetric model anymore. Therefore; for both A_{ij} and B_{ij} , 3-D models were used with around 215000 8-noded elements with full integration. Model can be seen in Fig. 3. In this study, a cylindrical part with a diameter of 14 mm (7 mm radius of curvature) was considered. Loadings described above was applied. For a cylindrical

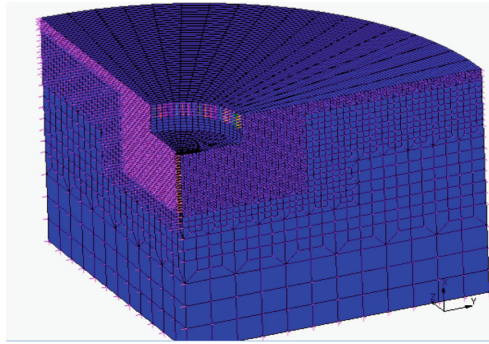


Fig. 2. Axisymmetric model with non-axisymmetric loading for flat piece

piece, determination of hole depth or loading involves ambiguity, since the hole reaches to its maximum diameter (in this case 1 mm) later than the first contact of drill and part. Luo et al. [10] considered the effective depth after the hole reaches its maximum diameter and accepted this point as ‘zero’ position in their study. This approach was not used in the current study and the position of first contact of drill with surface was considered as ‘zero’ depth. Because the curved segment of the drilled hole contributes to the strain data gathered during the testing as the hole depth increases. For 7 mm radius of curvature, hole reaches its maximum diameter at ~ 0.018 mm depth. For the evaluation of calibration constants, hole and loading increments of 0.068 mm, 0.118 mm, 0.168 mm, 0.218 mm, 0.268 mm, 0.318 mm and 0.418 mm were used in the calculations.

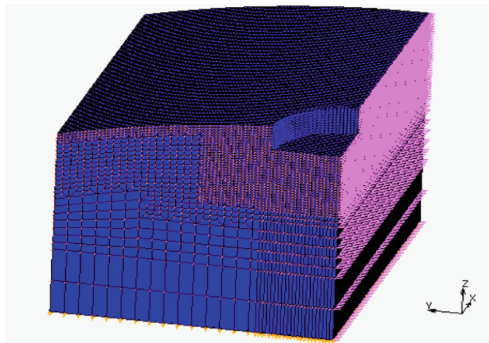


Fig. 3. Model with radius of curvature of 7 mm

2.2 Derived Calibration Matrices

In this section, derived **A** and **B** matrices for flat and cylindrical specimens were compared with the ASTM matrices. Bivariate interpolation scheme described by Schajer [5] was used to evaluate strain relaxation coefficients at different depth and loading increment combinations (i.e. 0.068 mm depth and loading increment). In the tables, each row corresponds to a certain hole depth for different loading depths and each column corresponds to a certain loading depth for different hole depths. **H** represents the loading depth, **h** represents the hole depth and both are in mm.

Table 1. Comparison of derived matrix A with ASTM values for flat specimen (in %)

h	H	.050	.100	.150	.200	.250	.300	.350	.400
.050		2.2							
.100		1.5	2.7						
.150		0.7	1.7	1.1					
.200		0.8	0.1	1.3	0.4				
.250		0.9	0.7	0.0	0.2	-0.9			
.300		0.8	0.4	0.2	-0.9	-1.2	-3.2		
.350		0.6	0.3	0.0	-0.9	-2.2	-2.8	-3.2	
.400		0.7	0.2	0.0	-1.1	-2.2	-3.8	-1.7	-0.3

Table 2. Comparison of derived matrix B with ASTM values for flat specimen (in %)

h	H	.050	.100	.150	.200	.250	.300	.350	.400
.050		-0.68							
.100		0.10	0.51						
.150		0.67	1.34	0.06					
.200		1.74	0.98	1.65	0.06				
.250		2.33	2.25	1.24	0.85	-0.65			
.300		2.74	2.52	2.38	0.91	0.11	-2.10		
.350		3.15	2.90	2.77	1.77	0.02	-0.96	-3.89	
.400		3.46	3.13	2.99	2.04	0.75	-1.12	-2.80	-6.14

As seen from Table 1, difference between derived **A** matrix and ASTM **A** matrix is not significant and around 4 percent for the extreme case. Difference for **B** matrix is more apparent and around 6 percent for the extreme case. This is expected because determination of strain relaxation coefficients B_{ij} are more sensitive to numerical calculation [5] (Table 2).

Table 3. Comparison of derived matrix A with ASTM values for cylindrical specimen (in %)

h	H	.068	.118	.168	.218	.268	.318	.418
.068		-12.0						
.118		-10.2	6.1					
.168		-9.4	7.0	8.1				
.218		-8.1	6.8	9.3	9.8			
.268		-7.2	8.4	8.9	10.6	10.6		
.318		-6.6	9.1	9.7	10.2	11.3	10.4	
.418		-5.7	10.2	11.0	11.4	12.7	15.7	10.2

Table 4. Comparison of derived matrix B with ASTM values for cylindrical specimen (in %)

h	H	.068	.118	.168	.218	.268	.318	.418
.068		-11.2						
.118		-9.1	5.5					
.168		-7.8	7.4	7.2				
.218		-6.3	8.0	9.4	8.7			
.268		-5.2	9.9	9.7	10.4	9.7		
.318		-4.3	11.1	11.5	11.1	11.3	10.1	
.418		-3.1	12.6	13.2	13.4	13.3	11.9	9.8

As seen from Tables 3 and 4, for cylindrical part, both **A** and **B** matrices shows significant difference when compared to ASTM matrices.

3 Residual Stress Measurements

Residual stress measurements were performed on a flat and a cylindrical part. Both of them were subjected to deep-rolling process with rolling force of 500 N and feed rate of 0.1 mm/rev or 0.1 mm/step. Material was EN-AW-6082 aluminum alloy. Results obtained by using ASTM coefficients and using derived coefficients were compared. Measurements was done in CNC-milling machine with a precision of 1 μm . Rotational speed of 15000 rev/min and feed rate of 1 μm /second was used to prevent inducing of additional residual stresses due to drilling operation. Centering of the hole on strain-gage rosette was done with the help of 2 cameras which were directed in perpendicular directions. Experimental setup can be seen in Fig. 4. In Fig. 5, optical microscope image of the drilled hole on strain-gage rosette can be seen. It can be seen that the hole was centered successfully.

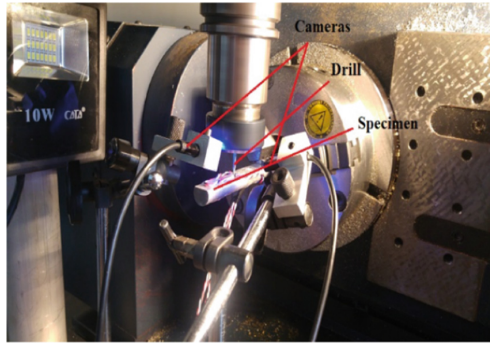


Fig. 4. Experimental setup for hole-drilling measurement

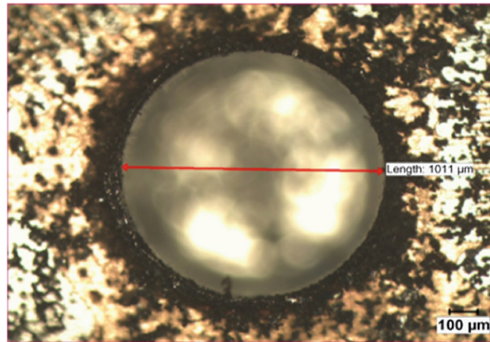


Fig. 5. Drilled hole through strain-gage rosette

3.1 Measurement of Flat Workpiece

Evaluated residual stress distributions using both the ASTM matrices and derived matrices was shown in the Fig. 6. As seen from the Fig. 6, use of derived matrices reduced the oscillations in the residual stresses as the depth increases. For the region close to the surface, there is no significant difference between ASTM and derived matrices.

3.2 Measurement of Cylindrical Workpiece

Evaluated residual stress distributions using ASTM, derived flat and derived cylindrical matrices were shown in Fig. 7. As seen from the Fig. 7, using derived matrices for flat part yielded approximately same results with the ASTM matrices and difference between them is negligible. But use of the derived matrices for cylindrical part yielded observable difference in the results compared to ASTM matrices. After the depth of 0.093 mm, there is a difference margin of ~ 60 MPa between the cylindrical-derived matrix results and ASTM matrix results for σ_x and a difference margin of ~ 30 MPa for σ_y .

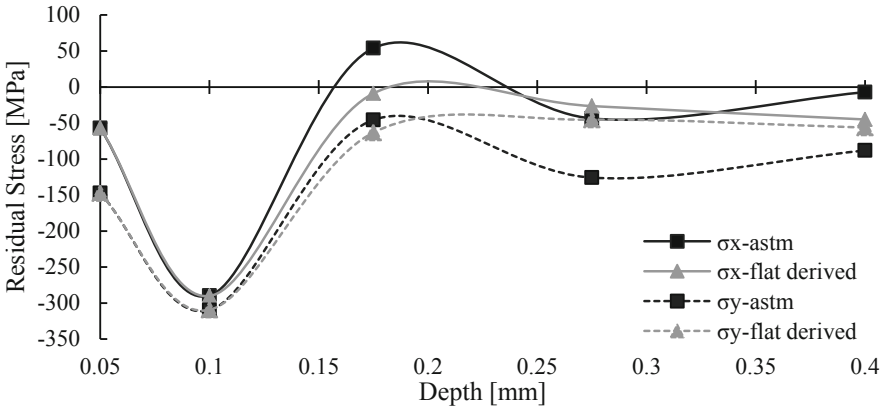


Fig. 6. Evaluated residual stress distributions for flat workpiece

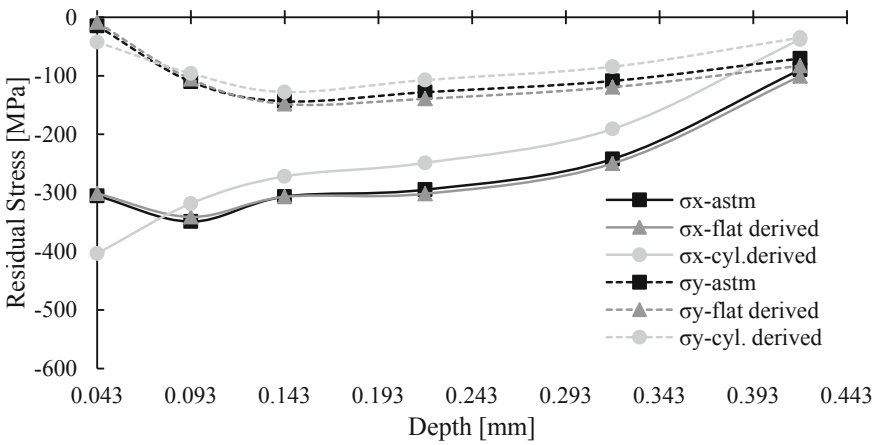


Fig. 7. Evaluated residual stress distributions for cylindrical workpiece

Difference between results is important because in a design stage of a structure, safety can be achieved by more accurate results obtained from the specific cylindrical model matrices.

4 Summary

It has been shown that calibration matrices for specific geometries can be formed with the use of finite element procedures. These calibration matrices has a significant effect on the evaluated residual stress distributions.

For flat parts, matrices were formed again, compared with ASTM matrices; and results obtained from these matrices showed that there can be improvement in the evaluated residual stress distributions by using newly formed matrices.

For cylindrical parts, it was demonstrated that specific matrices formed for the cylindrical structure has significantly changed the evaluated residual stress distributions. This feature is important because safer structures and systems can be built by using the more accurate results obtained from the evaluations with newly formed specific matrices.

Acknowledgement. The authors thank the Scientific and Technological Research Council of Turkey – TUBITAK which supported this study financially (Project Number: 217M962).

References

1. Schulze, V.: *Modern Mechanical Surface Treatment*, 1st edn. Wiley-VCH Verlag GmbH Co. KGaA, Weinheim (2006)
2. Lu, J.: *Handbook of Measurement of Residual Stresses*, 1st edn. Fairmont Press Inc., Lilburn (1996)
3. Schajer, G.S.: *Practical Residual Stress Measurement Methods*, 1st edn. Wiley, West Sussex (2013)
4. Schajer, G.S.: Applications of finite element calculations to residual stress measurements. *J. Eng. Mater. Technol.* **103**, 157–163 (1981)
5. Schajer, G.S.: Measurement of non-uniform residual stresses using the hole-drilling method. Part II. *J. Eng. Mater. Technol.* **1988**, 344–349 (1988)
6. ASTM E837-08: Standard test method for determining residual stresses by the hole-drilling strain-gage method
7. Niku-Lari, A., Lu, J., Flavenot, J.F.: Measurement of residual stress distribution by the incremental hole drilling method. *J. Mech. Work. Technol.* **11**, 167–188 (1985)
8. Flaman, M.T., Manning, B.H.: Determination of residual stress variation with depth by the hole-drilling method. *Exp. Mech.* **25**, 205–207 (1985)
9. Rendler, N.J., Vigness, I.: Determination of residual stress variation with depth by the hole-drilling method. *Exp. Mech.* **25**, 577–586 (1966)
10. Luo, J., Montay, G., Lu, J.: An advanced residual stress determination for 3D cylinder structure. *Mater. Sci. Forum* **490–491**, 62–66 (2005)



Mechanical Stress Relaxation of a Laser Peened and Shot Peened Ni-Based Superalloy

Kai Siang Chin^{1,3}(✉), Sridhar Idapalapati¹, Anna Paradowska²,
Mark Reid², Shashwat Shukla³, and Dennise Tanoko Ardi³

¹ School of Mechanical and Aerospace Engineering,
Nanyang Technological University,
50 Nanyang Avenue, Singapore 639798, Singapore
chin0211@e.ntu.edu.sg

² Australian Nuclear and Science and Technology Organisation,
Australian Centre for Neutron Scattering, New Illawarra Road,
Lucas Heights, NSW 2234, Australia

³ Advanced Remanufacturing and Technology Centre, 3 CleanTech Loop,
CleanTech Two, #01/01, Singapore 637143, Singapore

Abstract. Nickel based superalloy IN718 specimens were subjected to laser peening and shot peening. The residual stress and work hardening introduced by laser peening and shot peening were characterized using neutron diffraction method and electron backscattered diffraction (EBSD). A modified set up in reflective mode was utilized during neutron diffraction to optimize the spatial and temporal resolution to perform in-situ residual stress measurements at pre-determined cycle. Residual stress relaxation was only observed in the direction of loading while the residual stress in the transverse direction remained at a similar magnitude. Residual stress relaxation was observed to be most prominent in the first cycle of fatigue at R ratio = 0.1 with little stress relaxation in subsequent fatigue load cycles. Under tensile-tensile loading, stress relaxation occurs when the superposition of tensile residual stress and applied loading exceeds the localized yield strength of the material. Stress relaxation was found to be well correlated with the magnitude of work hardening. Residual stress relaxation as a function of depth and number of cycles were also recorded to illustrate the changes in residual stress during the cyclic loading.

Keywords: Surface treatment · Residual stress · Work hardening · Cyclic loading

1 Introduction

Fatigue is one of the common failures in engineering components. Fatigue life enhancement could be achieved with the use of compressive residual stress and work hardening at the surface. Surface treatments such as laser peening and shot peening which introduces compressive residual stress and work hardening simultaneously are commonly used to enhance the fatigue life [1–3]. Slower crack propagation rate has been observed with the presence of compressive residual stress [3–5]. On the other hand, work hardening has been linked to the increase in fatigue crack resistance and crack growth retardation [6–8].

Residual stress relaxation or redistribution is an occurrence which could reduce achievable benefits of compressive residual stress. Under the first few cycles of cyclic loading, stress relaxation occurs when the difference in plasticity between the plastically deformed layers and the bulk of the material arises [9]. The difference in plasticity occurs when the sum of the applied stress and the residual stress exceeds the material yield strength. This causes inhomogeneous yielding where the bulk is deformed plastically while the work-hardened layer remains elastic [10].

The strengthening of metals in surface treatments is achieved by the increase of dislocation generations due to the plastic deformation. Nonetheless, such mechanism increases the propensity of residual stress relaxation by dislocations recovery, especially at thermal condition. A higher work hardening could lead to accelerated stress relaxation due to the high level of stored energy [11, 12]. The higher work hardening could also indicate a greater extent of Bauschinger effect where the compressive yield strength is depreciated due to the increase of the tensile yield strength. The Bauschinger effect influences the stress relaxation where the reduced compressive yield strength could be exceeded by the superposition of applied compressive loading and compressive residual stress [13].

In this study, residual stress relaxation of laser shock peened and shot peened surfaces of a Ni-based superalloy was investigated. While Bauschinger effect has been mentioned in many studies under compressive loading [13], it is of interest of this study to determine the stress relaxation behavior under tensile-tensile loading. The residual stress of the laser peened and shot peened specimens were measured at the predetermined cycle. The residual stress measurement was conducted at a neutron facility, ANSTO, KOWARI beamline. An alternative set up of reflective method was utilized to optimize the temporal and spatial resolution of the measurement. Neutron diffraction allows a more consistent acquisition of residual stress in a non-destructive manner and eliminates random artefacts due to the use of multiple specimens.

2 Materials and Methods

2.1 Materials and Specimen Preparation

Flat bars of IN718 produced via vacuum induction melted were used in this study. See Table 1 for the chemical composition determined via X-ray fluorescence method. The material was solution annealed at 954 °C for 2 h, precipitation heat treated at 718 °C for 8 h and furnace cooled to 621 °C followed by air cooling for 8 h.

Table 1. Inconel 718 composition

C	Mn	Fe	S	Si	Cu	Ni	Cr
.03	.05	18.35	.001	.06	.03	53.46	18.46
Al	Ti	Co	Mo	Ta	B	Nb	P
.51	.98	.13	3.03	.003	.004	5.33	.007

The flat bars were then machined into fatigue specimens according to the standard ASTM E466. For the shot peening process, cast steel shots of 0.6 mm diameter at a

flow rate 3 kg/min was used, resulting in Almen intensity of 0.200 mmA. For the laser peening process, Nd:YAG laser with wavelength 1064 nm at a frequency of 5 Hz was utilized. 2 mm beam spot size and 5 J of beam energy was used for the process.

2.2 Work Hardening Characterization

A JEOL JSM 7600F Field Emission Scanning Electron Microscope equipped with Oxford Instruments' backscattered electron detector was used. The EBSD tool (Aztec Software) was employed to assess the extent of work hardening by analyzing the grain orientation spread (GOS).

2.3 Residual Stress Measurement

The diffraction measurements were conducted at ANSTO using KOWARI strain scanner. Prior to the in-situ experiment, the measurement was conducted on a reference specimen without surface treatment to determine the d_0 spacing of the material. Using the d_0 spacing obtained, ex-situ residual stress mapping was performed on 5 specimens, which included the pristine, shot peened, laser peened, shot peened fatigued at 10,000 cycles and laser peened fatigued at 10,000 cycles. The gauge volume used was $0.2 \text{ mm} \times 0.2 \text{ mm} \times 10 \text{ mm}$, see Fig. 1. This dimension of gauge volume was selected to achieve a spatial resolution up to 90 microstrain to capture the steep residual stress gradient of a typical surface treated materials while not sacrificing great amount of time for measurement. The depth penetration per gauge volume is 0.282 mm and 25 overlapping gauge volume steps were conducted across the thickness of the specimens for the determination of d_0 .

A modified reflective mode setup was used for the measurement to optimize the temporal and spatial resolution, see Fig. 1. High spatial resolution is required for the measurement procedure to resolve the steep residual stress gradient near surface. In this setup, the spatial resolution is directly determined by the gauge volume as the gauge volume was designed to be parallel with the top and bottom surface (the x_2 x_3 plane). Also, the high penetration ability of neutron beam offers a better representation of the subsurface residual stress gradient at a reasonable time scale in a non-destructive manner. Usual laboratory X-ray diffraction with limited penetration depth would normally require material removal via electropolishing to measure the subsurface residual stress.

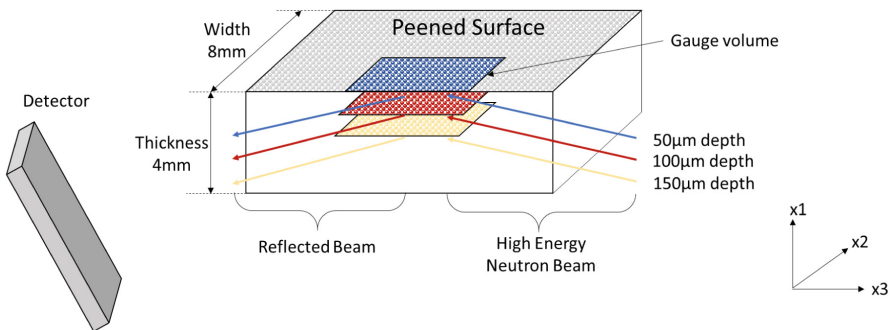


Fig. 1. Schematics of alternative reflective method set-up for in-situ diffraction measurement.

The fatigue cycling was conducted on an INSTRON stress rig at 10 Hz using R ratio = 0.1. For the in-situ experimentation, the fatigue cycling was interrupted at the 0th, 1st, 10th, 10000th and 50,000th cycles for the diffraction measurement. The measurements were done at specific steps of depth using gauge volume of 3 mm × 3 mm 0.2 mm for residual stress depth profiling. The first in-situ measurement was targeted on the surface and each subsequent depth-specific data is shifted by steps of depth from the surface. This dimension of gauge volume was used for optimum temporal and spatial resolution of the measurement at each predetermined cycle. Measurements were taken across the thickness of the specimen to obtain a full residual stress depth profiling.

3 Results

3.1 Work Hardening

GOS is a parameter in EBSD defined by the average deviation in orientation between each point in a grain and the average orientation of the grain. It is used in this study as an indication of work hardening as it could be correlated to dislocation density. When dislocations are formed in the material, the residual or plastic strain is manifested as local variations in lattice orientation [14]. In area subjected to work hardening or work hardening, local orientation differences are observed within deformed grains where individual grains with zero strain will largely display a constant orientation.

Laser peened specimen possessed a greater depth of work hardening as observed from the higher value GOS that are still scattered around 2° even at the depth of 500 μm, see Fig. 2. For shot peening specimen, depth of work hardening is only evident up to 50 μm. However, at 50 μm from the surface, shot peened specimen has a higher value of GOS at 0.80° as opposed to 0.44° possessed by laser peened specimen. The higher value of GOS observed in shot peened specimen near surface could be attributed to the repeated impact of a high volume of shots that generates a greater amount of dislocation when compared to the laser peening process with considerable lesser number of impacts by the laser shock waves.

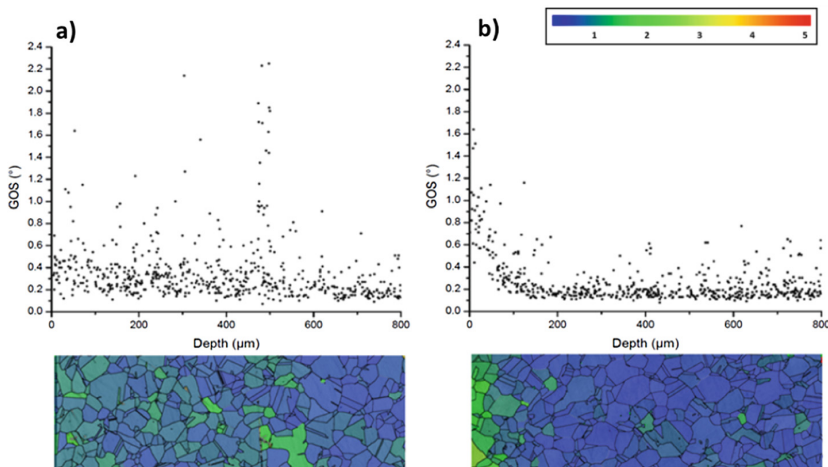


Fig. 2. GOS graph and illustration, (a) - laser peening, (b) - shot peening.

3.2 Stress Profiles and Relaxation

From Fig. 3, it could be seen that laser peened specimen has a higher magnitude of compressive residual stress at -700 MPa and tensile residual stress at 400 MPa. Laser peened specimen also has greater depth of compressive residual stress up to 1000 μm subsurface. On the other hand, shot peened specimen has a relatively lower magnitude and shallower depth of influence of compressive residual stress. The maximum compressive residual stress of shot peened specimen is observed to be at -400 MPa and the depth of compressive residual stress is approximately 500 μm beneath the surface.

Figure 4 illustrates the individual ex-situ measurement of fatigued laser peened and shot peened specimens at 10,000 cycles. It is observed that relaxation only occurs in the direction of the loading, which is the transverse direction. At the 50 μm near surface, laser peened specimen experiences lesser stress relaxation of around 100 MPa when compared to 200 MPa in the shot peened specimen. Significant stress relaxation was observed to occur at shot peened specimen up to a depth of 800 μm in contrast to laser peened specimen with relaxation only up to 400 μm . For the in-situ measurement, stress relaxation is significant but is only limited in the first cycle, see Fig. 5. Further cycling observed minimal relaxation as the residual stress remained at similar magnitude up to 50,000 cycles, see Fig. 6.

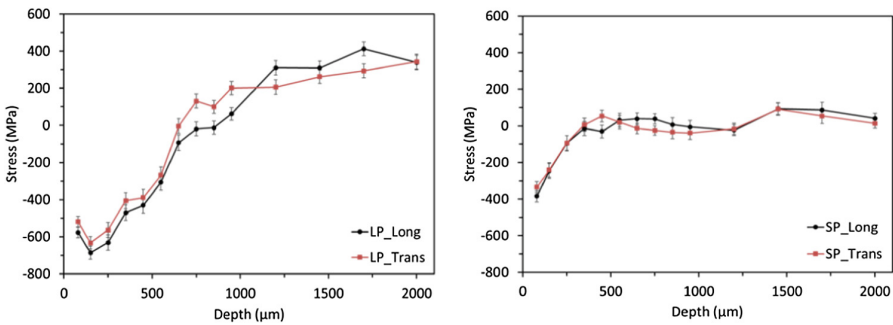


Fig. 3. Ex-situ residual stress profiles, (a) - laser peening, (b) - shot peening.

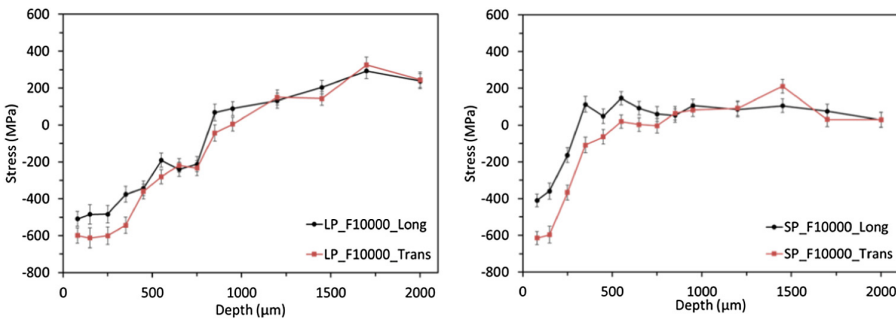


Fig. 4. Ex-situ residual stress profiles at 10000 cycles, (a) - laser peening, (b) - shot peening.

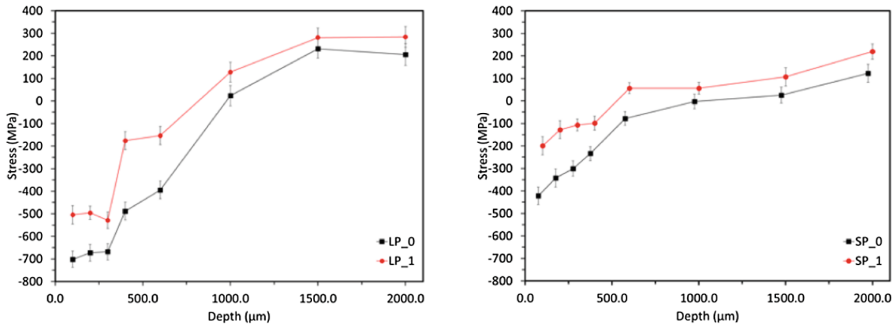


Fig. 5. In-situ residual stress profile at 0th and 1st cycle, (a) - laser peening, (b) - shot peening.

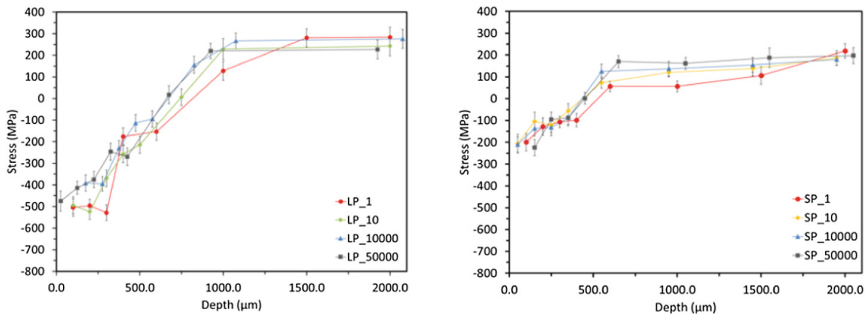


Fig. 6. In-situ residual stress profile at 1st, 10th, 10000th, and 50000th cycles, (a) - laser peening, (b) - shot peening.

4 Discussion

In contrast to stress relaxation described by Bauschinger effect (often observed in negative R ratio fatigue cycling due to the reduction of compressive yield strength caused by tensile work hardening), the stress relaxation in this study was attributed to the superposition of tensile applied and residual stresses resulting in local plastic yielding. The mechanical stress relaxation is better explained in terms of the need for the material to reduce the misfit between the deformed layer and the elastic bulk [13]. The stress relaxation is the most prominent in the first cycle as the need for the material to reduce the misfit is the greatest. Further cycling shows only minimal relaxation as the misfit has already been greatly reduced by the relaxation during the first cycle.

In spite of the greater depth and magnitude of compressive residual stresses, laser peened specimens retain compressive residual stresses better than shot peened specimens. It is suggested that stress relaxation correlates better with the magnitude of work hardening rather than depth of work hardening. For example, the narrow (50 μm) and highly work hardened shot peened surface signifies the steeper misfit between the deformed layer and the bulk. This large misfit which occurs over a narrow plastically deformed layer will increase the propensity for mechanical stress relaxation. As a result

of the large misfit, the highly work hardened layer and the elastic bulk will undergo different magnitude of yielding [13]. Thus, the elastic bulk layer will be affected and result in a greater stress relaxation even at a depth where the effect of the work hardening is not observed.

5 Conclusion

The deep penetration ability and non-destructive nature of neutron diffraction allow the acquisition of stress relaxation data from one specimen. The use of a single specimen eliminates the random artefacts and inconsistencies due to the use of multiple coupons and relatively small probing area by other conventional methods. A modified reflective mode setup was used for the neutron diffraction measurement to achieve a balance between spatial and temporal resolution.

It is postulated that magnitude of work hardening plays a bigger role in mechanical relaxation rather than the depth of work hardening. Greater stress relaxation will occur when the difference in the misfit between the deformed layer and the bulk is larger. The stress relaxation is most significant in the first cycle and occurs in the direction of the loading only. The Bauschinger effect is deemed insignificant under positive R ratio circumstances. The stress relaxation under tensile-tensile loading could be attributed to the superposition of applied tensile loading and tensile residual stress.

Future work can be expanded to thermo-mechanical loading to investigate how the role of work hardening affects the stress relaxation mechanism. It would be crucial to understand the interaction between work hardening and residual stress under the combined effects of thermal exposure and mechanical loading.

Acknowledgment. The author thanks Australian Nuclear Science and Technology Organisation, Australian Centre for Neutron Scattering for the support provided during the experimentation on KOWARI beamline. The author also gratefully acknowledges the support provided by Nanyang Technological University and the additional support and assistance from Advanced Remanufacturing and Technology Centre (ARTC), Singapore.

References

1. Withers, P.J.: Residual stress and its role in failure. *Rep. Prog. Phys.* **70**(12), 2211 (2007)
2. Altenberger, I., Nalla, R.K., Sano, Y., Wagner, L., Ritchie, R.O.: On the effect of deep-rolling and laser-peening on the stress-controlled low- and high-cycle fatigue behavior of Ti-6Al-4V at elevated temperatures up to 550 °C. *Int. J. Fatigue* **44**, 292–302 (2012)
3. Kattoura, M., Mannava, S.R., Qian, D., Vasudevan, V.K.: Effect of laser shock peening on residual stress, microstructure and fatigue behavior of ATI 718Plus alloy. *Int. J. Fatigue* **102**, 121–134 (2017)
4. Doremus, L., Cormier, J., Villechaise, P., Henaff, G., Nadot, Y., Pierret, S.: Influence of residual stresses on the fatigue crack growth from surface anomalies in a nickel-based superalloy. *Mater. Sci. Eng. A* **2015**(644), 234–246 (2015)
5. Zhu, X.Y., Shaw, W.J.D.: Correlation of fatigue crack growth behaviour with crack closure in peened specimens. *Fatigue Fract. Eng. Mater. Struct.* **18**(7–8), 811–820 (1995)

6. Altenberger, I.: Deep rolling—the past, the present and the future, In: Proceedings of the 9th International Conference on Shot Peening, pp. 144–155 (2005)
7. Dalaei, K., Karlsson, B., Svensson, L.E.: Stability of shot peening induced residual stresses and their influence on fatigue lifetime. *Mater. Sci. Eng. A* **528**(3), 1008–1015 (2011)
8. Guechichi, H., Castex, L.: Fatigue limits prediction of surface treated materials. *J. Mater. Process. Technol.* **172**(3), 381–387 (2006)
9. Zhuang, W.Z., Halford, G.R.: Investigation of residual stress relaxation under cyclic load. *Int. J. Fatigue* **23**(Supple), 31–37 (2001)
10. John, R., Buchanan, D.J., Caton, M.J., Jha, S.K.: Stability of shot peen residual stresses in IN100 subjected to creep and fatigue loading. *Procedia Eng.* **2**(1), 1887–1893 (2010)
11. Foss, B.J., Gray, S., Hardy, M.C., Stekovic, S., McPhail, D.S., Shollock, B.A.: Analysis of shot-peening and residual stress relaxation in the nickel-based superalloy RR1000. *Acta Mater.* **61**(7), 2548–2559 (2013)
12. Prév y, P.S.: The effect of cold work on the thermal stability of residual compression in surface enhanced IN718, DTIC Document (2000)
13. Zhuang, W.Z., Halford, G.R.: Investigation of residual stress relaxation under cyclic load. *Int. J. Fatigue* **23**, 31–37 (2001)
14. Wright, S.I., Nowell, M.M., Field, D.P.: A review of strain analysis using electron backscatter diffraction. *Microsc. Microanal.* **17**(3), 316–329 (2011)



Incorporation of Evaluation Technology into Shot Peening Equipment

Kan Aoki^(✉), Yuji Kobayashi, and Yoshiyasu Makino

SINTOKOGIO, LTD, 180-1, Komaki, Ohgi-cho, Toyokowa, Aichi, Japan
ka-aoki@sinto.co.jp

Abstract. Shot peening is one of surface enhance method and is used in the automotive industries and aerospace industries. The compressive residual stress induced by shot peening greatly improves the fatigue strength. Also, it is been important to induce compressive residual stress from the surface to the inside in order to improve the fatigue strength. Therefore, it is important to understand the residual stress distribution of the products. In general, product evaluation in the shot peening process is destructive inspection by sampling.

From the viewpoint of quality control, product evaluation of shot peened products should be 100% inspection. Furthermore, it is best to be able to evaluate from the surface to the inside. Therefore, we propose the inspection system for shot peening in production site. We report the features of inspection method in this system and the examination results assuming inspection of production line.

Keywords: Shot peening · Quality control · X-ray · Eddy current

1 Introduction

Shot peening is applied to improve fatigue strength of metal parts such as gears and springs. The compressive residual stress induced by shot peening greatly improves the fatigue strength [1]. In general, maximum compressive residual stress and deep residual stress distribution are necessary to increase the fatigue strength of the product. Therefore, it is important to understand the residual stress distribution of the product.

In general, in the case of measuring residual stress induced by shot peening, X-ray diffraction method is used to measure the residual stress. In this method, penetration depth of X-ray is 10 μm from the surface. Therefore, residual stress distribution is inspected destructively by electro polishing to remove the surface. For this reason, In the case of quality control of shot peening, process control of shot peening conditions and product control by sampling inspection are performed, and all of shipping product cannot check quality of product. The quality control for shot peening is desirable to do 100% inspection in actual products. The ideal production process can be established by inspecting the products at production site with adjusting to the cycle time.

We propose the inspection system of shot peening at production site. We report the features of each inspection method in this system and the examination results which simulated inspection of production line.

2 Quality Control of Shot Peening

2.1 Conventional Quality Control Method for Shot Peening

The quality of shot peening is determined by the processing conditions such as media diameter and air pressure. In addition, process control is performed by measuring the intensity of the shot peening by the Almen arc height for confirming the actual processing capability in JAPANESE automotive industry [2]. However, process control using Almen arc height is the method to confirm the process capability of shot peening machine. Therefore, quality control of actual products has been performing by measuring the residual stress for sampling products.

2.2 Subject and Countermeasure of Quality Control

The $\sin^2\psi$ method using the X-ray diffraction method is widely used in order to measure the residual stress. In the case of $\sin^2\psi$ method, X-ray is irradiated from several angle (see Fig. 1) [3–5]. The residual stress is calculated from the change in the peak shift of X-ray diffraction curve detected by the 0D or 1D sensor. Therefore the sensor which detects the X-ray diffraction is necessary to move precisely. This method cannot apply to ideal inspection process which adjusts to the cycle time of production. Because, measurement time is very long.

On the other hand, in the case of $\cos\alpha$ method, X-ray is irradiated from single angle only (see Fig. 2) [6, 7]. Residual stress is calculated by detecting many information of the entire X-ray diffraction. Therefore, the measurement time is fast. Moreover, faster X-ray measurement device were developed to apply for actual production site. This device can calculate the residual stress by using only the points A and B of X-ray diffraction ring shown in the Fig. 2.

Schematic of the device is shown Fig. 3. The collimator was used to limit the irradiation range to 1.5 mm. The specimen is irradiated with characteristic X-rays from a Cr target through a collimator, and diffracted X-rays from αFe (211) are acquired. In this case, the diffracted X-ray of Cr-K α ray is obtained around $\theta = 156.4^\circ$. In order to obtain diffracted X-rays within the usable range of the sensor, the distance from the sample to the sensor was set to $D = 25$ mm and the X-ray irradiation angle to $\psi = 35^\circ$.

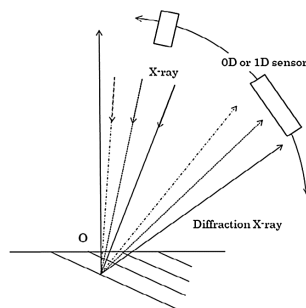


Fig. 1. $\sin^2\psi$ method

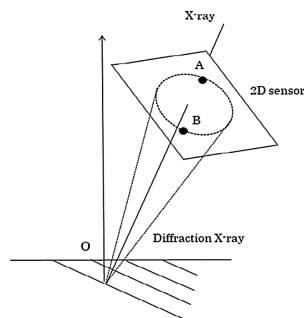


Fig. 2. $\cos\alpha$ method

In case of the X-ray diffraction method, penetration depth of X-ray is approximately 10 μm from the surface. The depth of compressive residual stress induced by shot peening is approximately 200 μm at maximum. Therefore, 100% inspection of shot peening products to understand the residual stress distribution is impossible with X-ray diffraction method only. For this reason, we have developed nondestructive inspection for shot peening products using eddy current measurement. Schematic diagram of eddy current is shown in Fig. 4. Eddy current is a current generated in a conductor by a time-varying magnetic field. The penetration depth of the eddy current can be changed by changing the frequency of the eddy current. In addition, ferromagnetic materials such as steels is changed their magnetic properties due to changing in the metallographic structure by the application of stress and plastic strain.

In the next chapter, X-ray and eddy current methods by measurement were examined.

High-speed X-ray stress measurement method is evaluated the repeatability in comparison with the $\sin^2\psi$ method. And we examined whether incorrect product had error on the surface can be detected.

The eddy current measurement method examined the internal evaluation of the shot peened specimen which varied internal quality by varying shot peening conditions.

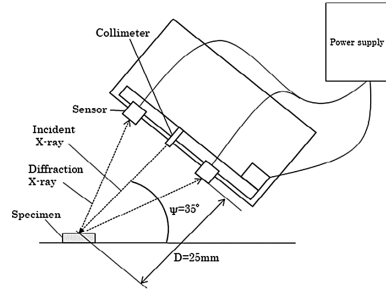


Fig. 3. Experimental setup

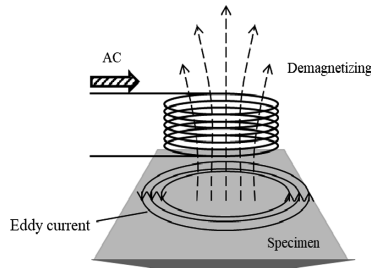


Fig. 4. Schematic diagram of eddy current

3 Experiment for the Application of Inspection of SP Products

3.1 High-Speed X-ray Stress Measurement Method

Repeatability. In order to incorporate the X-ray residual stress measurement device at production site, the repeatability of the measurement value is important. Therefore, this measurement method is evaluated the repeatability in comparison with the $\sin^2\psi$

method. The detail of specimen is shown in Table 1. The specimen was measured 20 times continuously without moving the measurement point. The measurement conditions are shown in Table 2. The result of repeatability is shown in Fig. 5. The repeatability of the device is almost equivalent to the $\sin^2\psi$ method device.

Table 1. Specimen states

Symbol	Material	Heat treatment	SP
IRON	Iron powder	–	–
SCM	JIS SCM420	Carburizing	○

Table 2. Measurement condition

	Development device	$\sin^2\psi$ method device
Tube voltage [kV]	30	40
Tube current [kA]	1.6	40
X-ray	Cr-K α	Cr-K α
Diffraction plane	α Fe (211)	α Fe (211)
Irradiation diameter [mm]	Φ 1.0	Φ 1.0
The diffraction angle 2θ [deg]	156.4	156.4
Measurement time [sec]	10	900

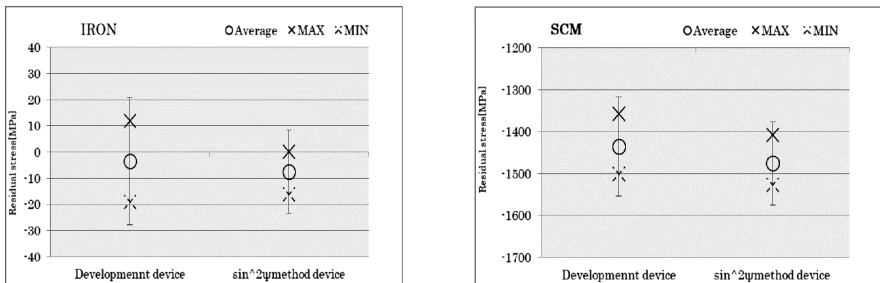


Fig. 5. The result of repeatability

Detection of Incorrect Product by Surface Residual Stress. When the same shot peening condition was performed the specimen have different hardness, development device was confirmed whether it can evaluate the difference surface residual stress. The specimen is SK85. One of the specimens was heat treated normally, and the other specimen was decarburized to vary the surface hardness. Table 3 shows the detail of the specimen. The specimens were shot peened under the same conditions. The surface residual stress on specimen was measured 20 times continuously without moving the measurement point in development device. Measurement result is shown in Fig. 6. Development device can detect the difference in residual stress on the surface. As a this result, we confirmed that it is possible to detect difference in the surface residual stress between the correct product and incorrect product.

Table 3. Specimen states

Symbol	Material	Heat treat	SP	Hardness [HV]	Notes
Correct product	JIS SK85	QT	○	460–490	–
Incorrect product	JIS SK85	○	360–400	Decarburizing	

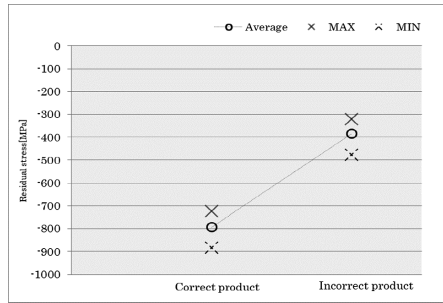


Fig. 6. Residual stress of surface that is measured

3.2 Eddy Current Measurement Method

Experimental Method

Specimen. The specimen is JIS SCM420 of chromium-molybdenum steel. And the material was machined to the specimen shown in Fig. 7. Chemical composition of the material is shown in Table 4. The heat treatment for the specimen is vacuum carburizing, quenching and tempering. The effective case depth of the carburizing is 0.5 mm, and the surface hardness is 760 HV. The shot peening conditions were adopted conditions which vary the media diameter to vary the peak depth of maximum compressive residual stress and the value of it. Shot peening conditions are shown in Table 5.

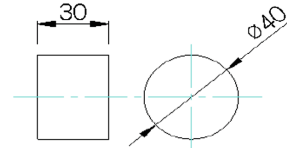


Fig. 7. Shape and dimension of specimen

Residual stress was measured by X-ray diffraction method. Specimen surface is removed by electro polishing after each measurement to measure the depth direction of residual stress distribution.

Table 4. Chemical composition of used materials [mass %]

C	Si	Mn	P	S	Ni	Cr	Mo	Cu
0.2	0.33	0.83	0.015	0.011	0.11	1.01	0.15	0.08

Table 5. Conditions of shot peening

	SP①	SP②	SP③
Shot method	Direct pressure		
Diameter [mm]	0.05	0.3	0.6
Hardness [HV]	700	700	700
Air pressure [MPa]	0.3	0.3	0.3
Coverage [%]	300	300	300
Arc height	0.275 [mm N]	0.240 [mm A]	0.497 [mm A]

Measurement Method of Eddy Current and the Evaluation. In this experiment, a coil was manufactured in accordance with the shape and size of the specimen. Schematic of the experimental device shown Fig. 8.

The eddy current detection method is used the single system of penetration type self-induction coil, and the measurement was performed using a commercially available impedance analyzer. The test frequency was decided so that the penetration depth of eddy currents becomes 5 μm–150 μm. Test specimen were placed in the coil under these measurement conditions. Then the impedance of the coil was recorded. The impedance of the coil changes with the relative permeability of the specimen to be placed. Therefore, in order to obtain the change in relative permeability of the shot peened specimen, the ratio of the impedance before and after shot processing was taken. And, the reaction of the eddy current according to the shot peening processing state inside the specimen was evaluated.

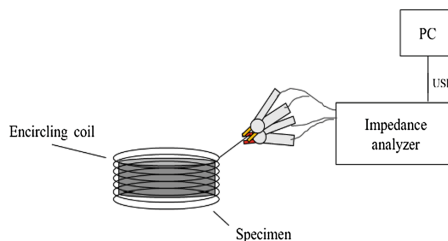


Fig. 8. Experimental setup

Measurement Result and Discussion. The residual stress distributions are shown in the Fig. 9. The maximum compressive residual stress of shot peening conditions with a media diameter of 0.05 mm is -1715 MPa. And maximum compressive residual stress of the other shot peening conditions is -1300 MPa. The depth of compressive residual stress induced by shot peening were deep with increasing the media diameter. The results of eddy current measurement

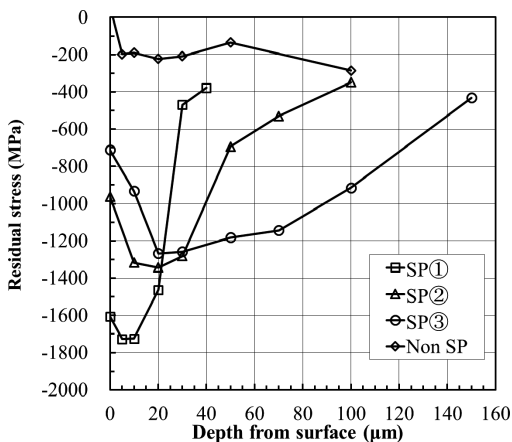


Fig. 9. Residual stress distribution

are shown in the Fig. 10. The vertical axis shows the ratio of impedance change from the untreated material to the shot peened material (hereinafter referred to as $Z1/Z0$). The horizontal axis shows the penetration depth. $Z1/Z0$ of all specimen is higher than 1 in all penetration depth of 0–150 μm (see Fig. 10). Therefore, the inductive reactance component increased. The peak value of $Z1/Z0$ increased with increasing media diameter. And peak depth of $Z1/Z0$ is 5 μm in SP①, 20 μm in SP②, 30 μm in SP③. The range from the surface to the depth where $Z1/Z0$ becomes 1 has a tendency to spread deep as the shot particle size increases. This device repeatability is ± 0.002 or less in impedance change ratio. Therefore, the change of $Z1/Z0$ in Fig. 10 is indicated as the change by each SP condition.

As a result, this eddy current system can inspect the difference in internal quality for shot peened parts. However, the reaction strength of the eddy current cannot inspect the relative relationship with the maximum residual stress. For the reason, we considered to be that the relative permeability increased by the process-induced martensitic transformation by shot peening of retained austenite contained in the carburized material, and the eddy current reacted.

From these things, it is possible to inspect the processing condition inside the test piece SP by the eddy current measurement method. Therefore, processing status inside the shot peened specimen can inspect in eddy current measurement method. However, the reaction strength of the eddy current affects the metallographic structure changed by shot peening. Therefore, Eddy current measurement methods cannot measure the residual stress inside all materials. However, in the case of inspection of shot peening in a production process, the actual product is inspected at fixed process processing conditions. Therefore, Eddy current measurement is considered to be effective enough for inspection application to evaluate the inside of shot peened products.

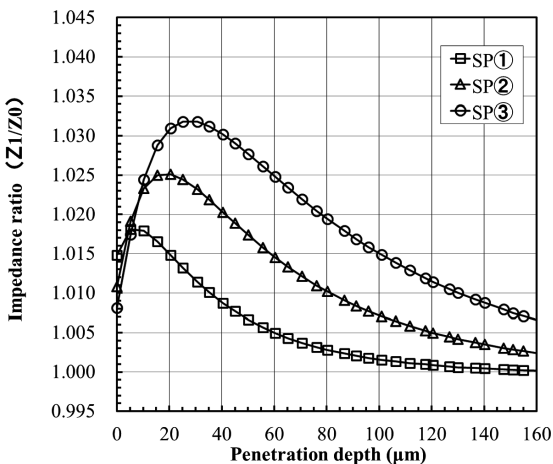


Fig. 10. Inductive reactance ratio of penetration depth

4 Conclusion

In this paper, two inspection methods are examined as inspection of shot peening at the production site. As a result of examination, we found that the two methods can be applied to the inspection of the surface and inside of shot peened products at the production site. Based on this result, we have developed an inspection device using this method. We assume that the ideal manufacturing process could be realized by combining 100% inspection of actual products at the manufacturing site and process control.

References

1. JSSP: Metal Fatigue and Shot Peening, edited by Gendaikougakusya (2004)
2. Almen, J.O.: United States Patent Office (OS patent 23450440) (1944)
3. Noyan, C., Cohen, J.B.: Residual Stress–Measurement by Diffraction and Interpretation. Springer-verlag, Heidelberg (1987)
4. JSMS-SD-5–02: Standard for X-ray stress measurement (2002) - iron and steel. J. Soc. Mater. Sci. Jpn. (2002)
5. Tanaka, K., Suzuki, K., Akiniwa, Y.: Evaluation of residual stresses by X-ray diffraction. Yokeido Ltd., Tokyo, Japan (2006)
6. Taira, S., Tanaka, K., Yamasaki, T.: A method of X-ray micro beam measurement of local stress and its application to fatigue crack growth problems. J. Soc. Mater. Sci. Jpn. **27**, 251 (1978)
7. Maruyama, Y., Miyazaki, T., Sasaki, T.: Development and validation of an X-ray stress measurement device using an Image plate suitable for the $\cos \alpha$ method. Zairyo **64**, 560–566 (2015)



Influence of the Feed Rate in the Single-Lip Deep Hole Drilling Process on the Surface Integrity of Steel Components

Jan Nickel¹(✉), Nikolas Baak², Frank Walther², and Dirk Biermann¹

¹ Institute of Machining Technology (ISF), TU Dortmund University,
Baroper Str. 303, 44227 Dortmund, Germany

{jan.nickel, dirk.biermann}@tu-dortmund.de

² Department of Materials Test Engineering (WPT), TU Dortmund University,
Baroper Str. 303, 44227 Dortmund, Germany

{nikolas.baak, frank.walther}@tu-dortmund.de

Abstract. High strength steels like AISI 4140 are commonly used in many technical areas in which the mechanical properties of materials have to meet special requirements, for example, in the case of dynamically loaded parts. In the automotive industry increasing requirements due to lightweight design or energy efficiency lead to increasing demands on the mechanical and dynamic material strength. In response to this development, optimized machining processes are capable of improving the mechanical properties like fatigue performance by influencing the surface integrity of the machined components. In this paper, the influence of the single-lip deep hole drilling process on the surface integrity of quenched and tempered AISI 4140 specimens is analyzed in detail. Under variation of one of the main process parameters, the feed rate, the process output parameters such as cutting forces and the resulting condition of the machined surface and subsurface are determined. In combination with the analysis of the resulting hardness, microstructure and surface conditions of the machined surface, a magnetic Barkhausen noise (MBN) analysis with a custom-built sensor is applied and further developed. With this non-destructive technique, the surface integrity of the bore wall and the fatigue damage over the lifecycle of the part can be analyzed. The correlation of the surface integrity produced by the single-lip deep hole drilling process with the results from the micro-magnetic measurements are used to improve the possibility of predicting a components fatigue performance.

Keywords: Fatigue life enhancement · Single-lip deep hole drilling · Residual stress

1 Introduction

The determination and prediction of the fatigue strength of components have become increasingly important in recent years. As a result, the requirements for the technical production of reproducibly high fatigue performance and for the methods of non-destructive testing of the dynamic strength of components have also increased. In the

case of dynamically loaded components, a number of influencing variables on the fatigue strength must be taken into account, such as geometry and size, mean stress, type of stress, multi-axiality, surface layer conditions (surface topography, residual stresses, microstructure and hardness), temperature, corrosive media, etc. The influence of these variables is complex and can only be described very roughly by multiplying influencing factors [1]. Some of these properties are set by the manufacturing process of the components. The functional properties of machined parts are influenced in particular by the quality of the surface and subsurface produced. Modern manufacturing processes and tools often allow an increase in productivity through higher achievable maximum cutting speeds and feed rates while complying with the set quality requirements. This development also results in an increased influence on the surface integrity of the manufactured components [1]. Single-lip deep hole drilling is a manufacturing process with a particularly large influence on the properties of the machined surface. As a result of the asymmetrical design of the tools, the cutting forces are transferred to the bore wall via the tool's guide pads. The guide pads are used to guide the tool in the bore and thus ensure that a relatively low straightness deviation of the bore can be achieved. At the same time, the pressure of the guide pads mechanically influences the bore wall and smoothens the surface, resulting in enhanced surface quality. An increase in the forces transmitted via the guide pads result in a stronger influence on the surface and subsurface of the bore. This area of the part is decisive for the dynamic strength of machined components since crack formation and propagation under dynamic loading of the components are known to be initiated from the machined surface [2, 3]. Residual compressive stresses introduced into the bore wall by a machining process can counteract loads in the later application of the components and prevent or decelerate crack formation and propagation.

Particularly in the case of components that are exposed to dynamic loads from internal pressure during their component life cycle, such as pipes and pumps in hydraulic systems, post-treatment processes such as autofrettage are used to increase the fatigue performance. Autofrettage is a local surface strengthening procedure, where a single hydraulic pressure overload, which is much higher than the subsequent operating pressure, is applied to the component to induce compressive residual stresses. This pressure causes plastic deformations in the highly stressed regions of the surface. After releasing the autofrettage pressure, compressive residual stresses remain in the surface which counteract the tensile stresses caused by the subsequent operating pressures [4]. As described above, single-lip deep hole drilling also causes a mechanical load on the bore wall. By a systematic analysis and adaptation of the drilling process parameters, this mechanical influence is to be increased to the extent that, similar to autofrettage, the microstructure is plastically deformed and compressive residual stresses are induced into the bore wall (see Fig. 1). For this purpose, the main parameters of the single-lip deep hole drilling process are varied in this study and the influence on the surface and subsurface is investigated. The main focus is on the output factors that have an influence on the fatigue strength of the components: the surface roughness, the microstructure and the residual stress condition of the bore wall. These criteria can be summarized under the term surface integrity [5].

Recent investigations on the influence of drilling operations on the surface integrity were carried out by Girinon et al. [6, 7]. Their work focused on the influence of the lubrication mode on the residual stress state when twist drilling the materials AISI 316L, Inconel 718 and 15-5HP [6]. They also published a numerical strategy to simulate the residual stresses that are induced into the bore wall by the twist drilling process. The influence of different drilling strategies conventional (twist) drilling, conventional (twist) drilling plus pre-drilling and helical milling was investigated by Rasti et al. [3]. Since the influence of the single-lip deep hole drilling process on the surface integrity and the corresponding fatigue strength is still unexplored, it is the focus of this research project. Due to the process characteristics, the high drilling quality that can be achieved and the transmission of the forces into the bore wall, single-lip deep hole drilling offers a special potential to positively influence the surface integrity of the bores.

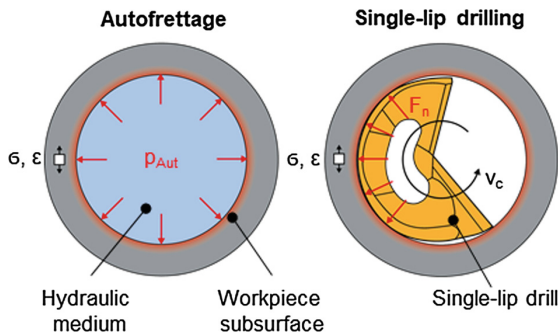


Fig. 1. Schematic sketch of the autofrettage [8] and single-lip drilling process.

The influencing process parameters on the surface integrity and their impact on the resulting fatigue strength of deep drilled components are analyzed in this research project. In the first project phase, the influence of the tool design was investigated. For this purpose eight different tool variants were used, which differed in the arrangement of the guide pads, the grinding of the cutting edge and the coating. It was shown that a radius cutting edge geometry with a large external cutting edge leads to an increase in the forces transmitted into the bore wall via the guide pads. By selecting a circumferential shape with a reduced contact zone between the tool and the bore wall, the surface pressure can be increased, which in turn results in a higher mechanical impact on the drilled surface. The selection of the reference tool was based not only on the drilling quality produced (straightness deviation, surface roughness and roundness of the bore) but also on the maximum increase in hardness achieved in combination with a refinement of the microstructure in the bore edge zone. In the second project phase, the influence of the cutting speed on the bore edge zone was investigated [9]. In addition to productivity, the cutting speed has a particular influence on the temperature generated in the machining process. If the thermal energy transferred into the bore wall during the drilling process is too high, the residual stress state in the bore surface may be

negatively affected as the formation of tensile residual stresses may be promoted [6, 10]. The results obtained from these first two work packages were used to select a tool design and a reference cutting speed from which the greatest possible positive influence on the bore edge zone is expected. For the following drilling tests these parameters were kept constant. The results presented in this publication concentrate in particular on the influence of the feed rate during single-lip deep hole drilling process on the surface integrity. In addition, the further development of the non-destructive analysis of the condition of the bores subsurface microstructure using the magnetic Barkhausen noise (MBN) analysis is presented.

2 Experimental Setup

The single-lip deep hole drilling tests were carried out on an Ixion TLF 1004 deep drilling machine. As lubricant, the drilling oil Petrofer Isocut T 404 with a viscosity of $\nu = 10 \text{ mm}^2/\text{s}$ was supplied at a pressure of $p_{\text{lub}} = 100 \text{ bar}$ via the internal cooling channel of the tool. For the drilling tests, the cutting velocity was kept constant at $v_c = 65 \text{ m/min}$. Specimens of the quenched and tempered steel 42CrMo4+QT (AISI 4140, 1.7225) with a diameter of $d = 48.5 \text{ mm}$ and a length of $l = 140 \text{ mm}$ were clamped using a fixture with prism jaws (see Fig. 2). The material has a tensile strength of $R_m = 960 \text{ MPa}$ and a hardness of 316 HV10. The sulphur content of the material, $S = 0.011 \text{ wt.}\%$, is relatively low compared to conventional 42CrMo4. A lower Sulphur content reduces the number and size of manganese sulphide inclusions in the steel, which has a positive effect on the fatigue strength of the material. The materials chemical composition can be found in the Table 1. After piloting, a through bore hole was drilled into the center of the sample with the single-lip deep drill with a diameter of $d = 5 \text{ mm}$. The feed force F_f and drilling torque M_d generated during the single-lip deep hole drilling process were measured at a frequency of 2000 Hz using a piezo-electric dynamometer from Kistler.

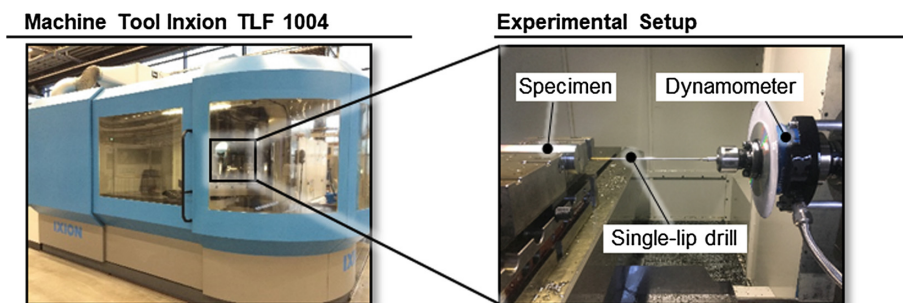


Fig. 2. Machine tool and experimental setup.

The analysis of the surface integrity is focused on the surface roughness, the hardening in the bore surface and the subsurface microstructure. The roughness was

measured tactilely with a MarSurf XR20 roughness measurement station including a GD120 feed unit from Mahr. As the Rz values take strong defects, which can promote the crack formation and propagation under dynamic loading, more into account as the Ra values, the Rz values were used to evaluate the surface quality [11]. For the digitalization of the drilled surfaces, a confocal white-light microscope Nanofocus μ surf was used.

Table 1. Chemical composition of the workpiece material 42CrMo4+QT S110 (wt-%).

Melt	C	Si	Mn	P	S	Cr	Mo	Fe
S110	0.41	0.18	0.85	0.011	0.011	1.01	0.18	bal.

The micro-magnetic characterization was carried out using a “FracDim” measuring system provided by Fraunhofer IKTS. To measure the micro-magnetic parameter at the crucial inside of the bore, a custom-built inner surface sensor was used. The sensor excites the alternating magnetic field from the outside and detects the resulting Barkhausen noise on the important inside. The micro-magnetic parameters are strongly correlated to the microstructure, grain size, phase content, hardness and the residual stresses display the influence of a change in hardness and residual stresses influences the magnetic hysteresis and the correlated parameters remanence (B_R) and coercive field strength (Φ_{cm}). The higher coercive field strength for hardened materials and for higher compressive stresses can be explained by harder magnetization processes and therefore can be correlated with residual stresses, hardness and hardness depth. It has to be mentioned, that the micro-magnetic parameters are influenced by a wide range of factors and therefore a clear separation of the effects has to be done (Fig. 3).

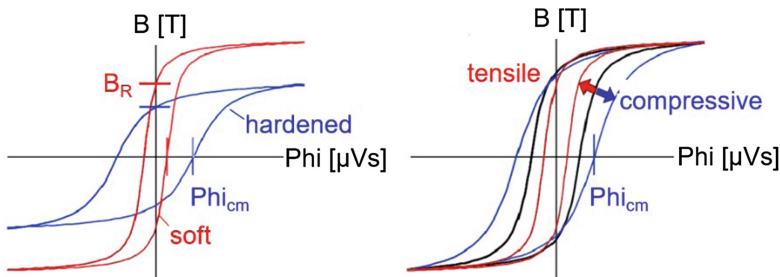


Fig. 3. Magnetic hysteresis under the influence of changes in (a) hardness and (b) residual stresses [12].

The micro-hardness measurement in the bore subsurface was carried out with a Shimadzu HMV-G21 FA hardness tester. For these measurements, specimens were cut out from the bore wall, embedded and polished. For the micro-hardness measurement in x-y-plane, three Vickers indentations were measured and averaged for each distance interval to the bore wall. To analyze and visualize the micro-hardness gradients in the

feed direction each measurement contains 252 indentation points divided in two rows that are positioned directly at the surface layer and are oriented in feed direction. These impression points were placed with a distance of $d_{surf} = 2 \mu\text{m}$, respectively $d_{surf} = 10 \mu\text{m}$. In order to be able to assess the quality of the hardening of the subsurface area close to the surface, which according to findings from previous investigations can be measured in a distance of up to max. $30 \mu\text{m}$ from the bore surface, the DIN EN ISO 6507-1 for Vickers hardness measurements was deviated from (Fig. 4).

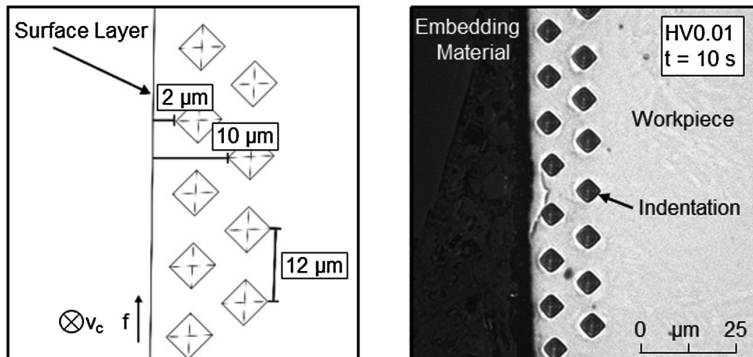


Fig. 4. Sketch of micro-hardness mapping (left), microscope image of indentations in the subsurface zone (right).

To investigate a potential feed rate dependent deviation of the micro-hardness in the surface layer, a measuring length of $l_m = 1.5 \text{ mm}$ was set in the feed direction (z-axis) of the specimens. All micro-hardness measurements were performed with a test force of HV0.01, which is equivalent to $F = 98.07 \text{ N}$, and were held for 10 s. A Zeiss Axio Imager M1 m light microscope as well as a Mira3 scanning electron microscope were used as for microstructure analysis. The analysis of the subsurface zone was performed on longitudinal section in the y-z-plane and transversal sections in the x-y-plane as sketched in Fig. 5, to differ between the mechanical impact on the microstructure in feed and cutting speed direction.

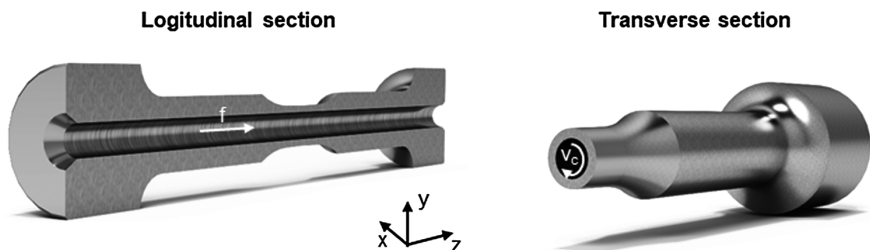


Fig. 5. Sketch of the longitudinal and transverse section of a single-lip deep hole drilled fatigue specimen.

3 Results and Discussion

3.1 Analysis of the Feed Force F_f and Drilling Torque M_d

The results for the feed force and drilling torque measured during the drilling process are visualized in Fig. 6. It shows a correlation between the tool load measured during the process and the set feed rate. The feed force is approximately doubled as it increases from $F_f = 314$ N at a feed rate of $f = 0.05$ mm to $F_f = 645$ N at $f = 0.15$ mm. For these feed rates the drilling torque even increases by a factor of 2.5 from $M_d = 1.1$ Nm to $M_d = 2.6$ Nm. Since, as described above, forces acting on the tool are in some extent transmitted into the bore wall, the height of the mechanical influence on the bore surface increases with higher feed rate as well.

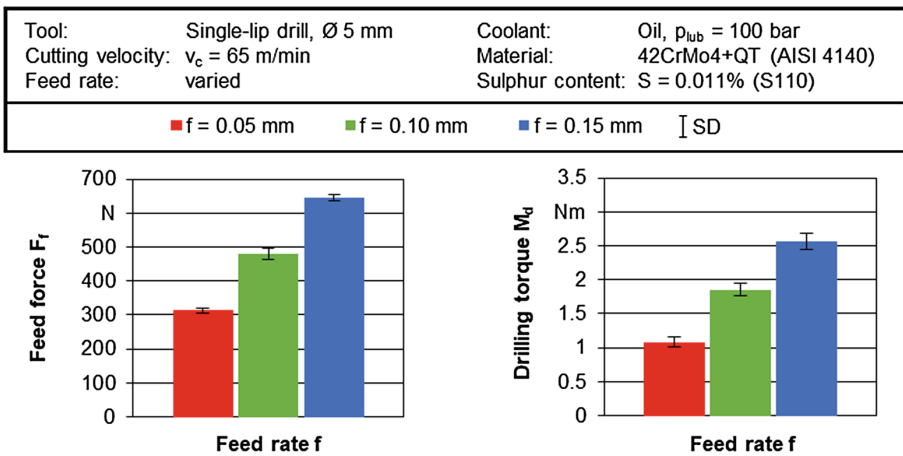


Fig. 6. Force F_f and torque M_d measurements for different feed rates.

The influence of the tool geometry on the level of the mechanical tool load has already been shown in [9]. In order to maximize the mechanical influence on the bore wall and thus, similar to the autofrettage process, insert residual compressive stresses into the surface zone, a cutting edge geometry was selected in the previous work package, which has an outer cutting edge which is much larger in relation to the inner cutting edge. It was shown that the normal forces transmitted to the bore wall could be significantly increased by this tool variant compared to the tools with a standard cutting edge grinding, producing a higher hardening in the subsurface.

3.2 Influence on the Surface Roughness

The influence of the feed rate on the surface roughness is given in Fig. 7. With the lowest feed rate of $f = 0.05$ mm, the best surface qualities were achieved with a value of $R_z = 0.93$ μ m. With $R_z = 1.26$ μ m, the value for $f = 0.1$ mm was only slightly higher and is in a range in which a negative influence on the fatigue performance of

machined components is to be considered as low [11]. For the highest tested feed rate of $f = 0.15$, a significant increase in R_z values to $2.08 \mu\text{m}$ was measured, which corresponds to an increase of 124% compared to the lowest feed rate.

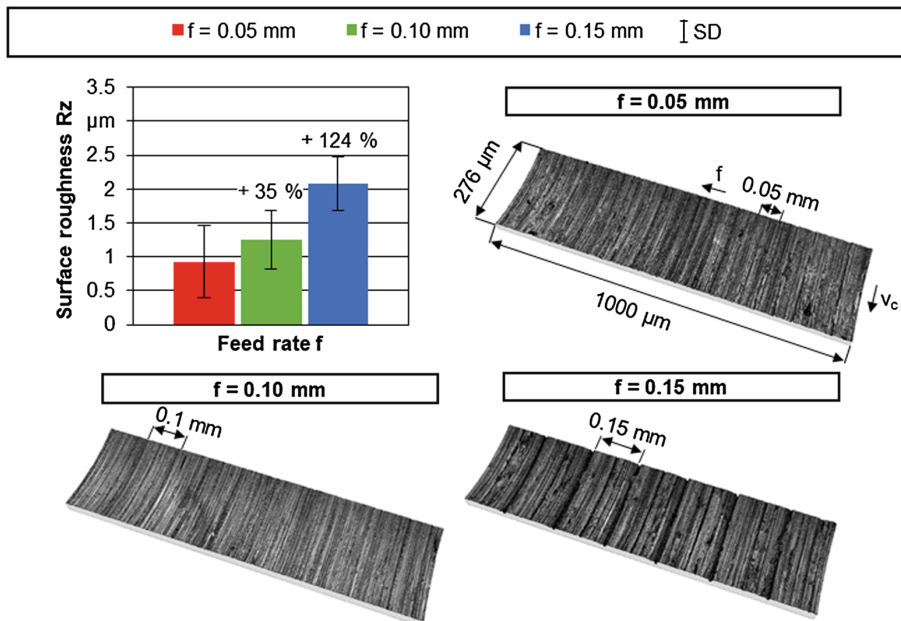


Fig. 7. Surface roughness measurements and confocal white-light microscope images of the drilled surface.

The produced bore surfaces topographies for the three feed rates are visualized by the white-light microscopic images in Fig. 7. In contrast to the lower feed rates, feed marks that reduce the surface quality are clearly visible at a feed rate of $f = 0.15$ mm. Studies have shown that from a value for the maximal high of surface profile R_t larger than $1\text{--}2 \mu\text{m}$ the reduction of the fatigue life of quenched and tempered steels is proportional to $\log R_t$ [11]. In this context, a feed rate of $f = 0.05\text{--}0.10$ mm should be used in order to produce a low surface roughness and respectively achieve a high fatigue performance of the deep-drilled components.

3.3 Influence on the Micro-hardness and Microstructure

The used feed rate significantly influences the mechanical force applied to the bore wall according to Fig. 6. To determine how the variation of the feed rate and the corresponding changes in the mechanical load on the bore wall affect the surface integrity, the changes in the microstructure were analyzed on light microscopic images of

transverse and longitudinal sections of the bore hole. In addition, micro-hardness measurements were carried out to investigate the mechanical hardening of the subsurface. The measured values of the micro-hardness at a distance of $d_{\text{surf}} = 2.5 \dots 40 \mu\text{m}$ to the bore surface at different feed rates are shown in Fig. 8. At all three feed rates, it can be observed that the hardness in the subsurface area of the bore was significantly increased. At a distance of $d_{\text{surf}} = 40 \mu\text{m}$ to the surface, approximately the initial hardness of the material is measured. To a depth of $d_{\text{surf}} = 25 \mu\text{m}$ the lowest hardening was produced at the feed of $f = 0.15 \text{ mm}$. Thus, the highest increase in hardness was achieved with the lowest feed rate, although the lowest feed forces and drilling torques were measured for these cutting parameters.

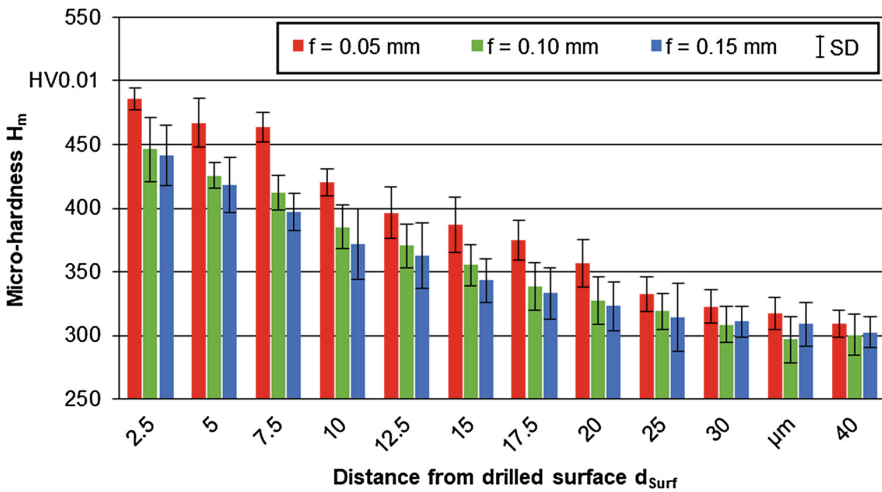


Fig. 8. Micro-hardness in the subsurface for different feed rates.

In order to illustrate the mechanical effects acting in the subsurface, the refinements in the microstructure are visualized by light and scanning electron microscopic images. Figure 9 shows images of cross sections in x-y-plane (cf. Fig. 5). In the area close to the bore surface, the material is deformed and refined by the forces occurring during the cutting process, which is particularly evident in the light microscopic images. The depth of the refinement of the microstructure due to the mechanical impact of the single-lip deep hole drilling process can be determined from the scanning electron microscope images. This depth is higher at the low feed rates of $f = 0.05$ and 0.10 mm compared to the feed rate of $f = 0.15 \text{ mm}$.

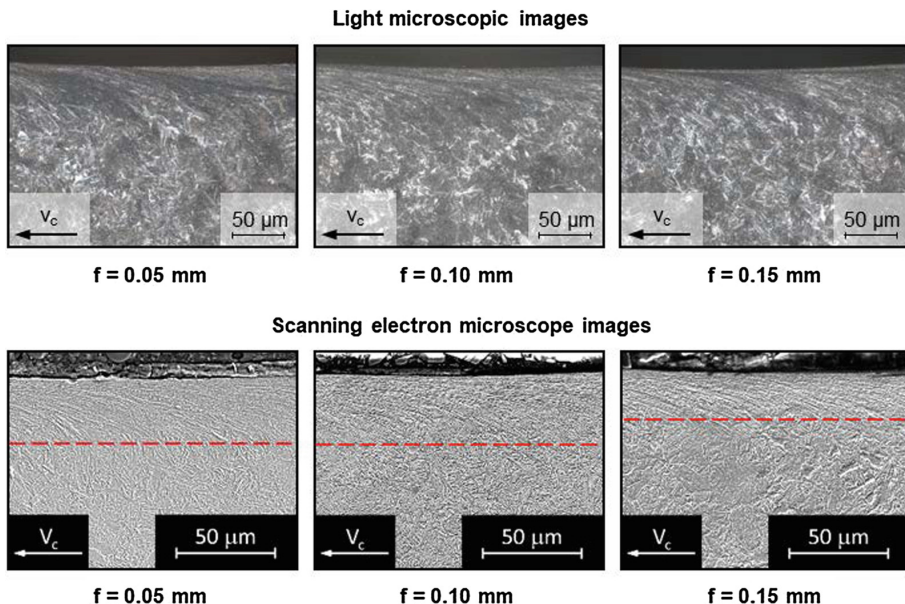


Fig. 9. Light microscope and scanning electron microscope analysis of the bore subsurface in x-y-plane.

The higher increase in hardness and greater penetration depth in the form of microstructure refinement at the lower feed rates can be explained by taking the distance of the contact areas between the tool and the bore wall into account. In addition to the height of the mechanical impact, the distance between the contacts of the guide pads with the bore wall during drilling has a decisive influence on the resulting subsurface microstructure. As sketched in Fig. 10, a higher feed rate increases the gap between the areas in which the highest force is applied to the bore surface. At a feed rate of $f = 0.15$ mm, areas with less mechanical influence may occur between the areas where the guide pads transmit the peak of force. A lower feed rate, on the other hand, results in a higher number of contacts with the guide pads for a specific segment of the bore wall.

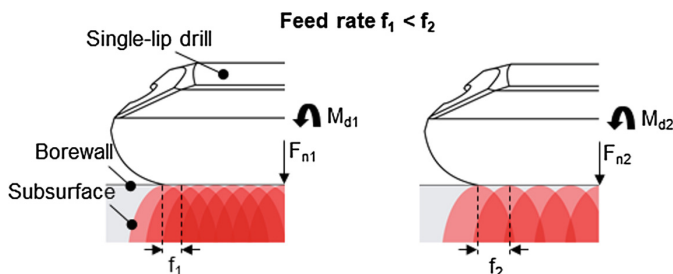


Fig. 10. Influence of feed rate on the contact area distance between guide rails and bore wall.

In order to further analyze this effect on the surface integrity, a mapping of the micro-hardness along the bore wall in feed direction was conducted as described in Sect. 2. The results of these measurements at a length of $l_m = 1.5$ mm along the bore wall are visualized in Fig. 11 for each of the three feed rates. Since the measurement was carried out at a shorter distance to the bore wall than permitted by the norm for hardness tests according to Vickers, the results only show a qualitative distribution of the hardness values along the bore. Depending on the selected feed rate, differences in the deviation of the hardness amplitudes along the bore can be observed. The fluctuations in the measured hardness values shown in this way correlate with the distance of the contacts of the guide pads with the bore wall. To illustrate this effect, the distance between the scale marks in the feed direction was adjusted according to the respective feed per revolution. Particularly at a feed rate of $f = 0.1$ mm, the scale marks correspond to the areas of higher hardness amplitudes so that a clear correlation between the hardness amplitude and the feed rate can be observed. This illustration of the hardness distribution along the bore wall shows that a lower feed rate, due to the higher number of contacts of the guide pads with a specific bore segment, leads to a more homogeneous hardening of the bore wall.

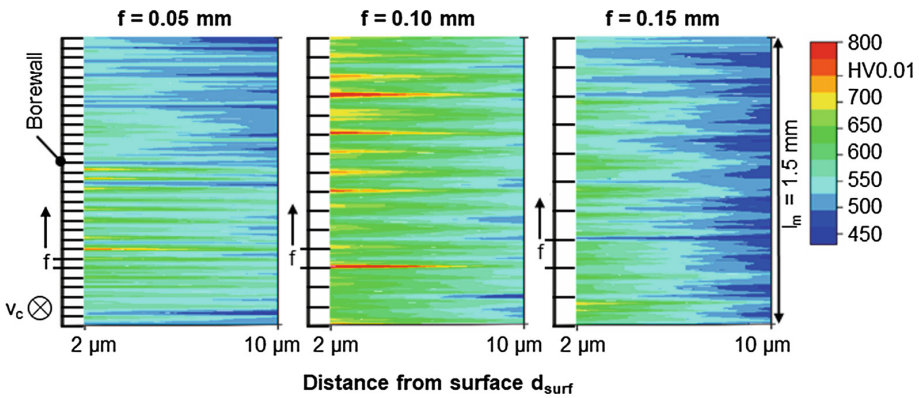


Fig. 11. Micro-hardness-mappings for varied feed rates.

The light microscopic images in the y - z -plane in Fig. 12 show a microstructure refinement for all three feed rates, as it was found in Fig. 9. In comparison to the cross sections in the x - y -plane, no deformation of the microstructure can be seen in the longitudinal section, as this mechanical deformation of the subsurface microstructure was mainly produced in direction of the cutting speed. However, differences in the depth of the microstructure refinement as a result of the different feed rates can also be seen in the longitudinal section. The marked areas, in which the microstructure was refined confirm the results shown in Fig. 9, that for the feed rate of $f = 0.15$ mm a lower penetration depth of the mechanical subsurface influence was achieved. By the shape of the bore wall at the transition to the embedding material, the feed marks generated by the tool can be found on the scanning electron microscopic images, as they were also observed in Fig. 7.

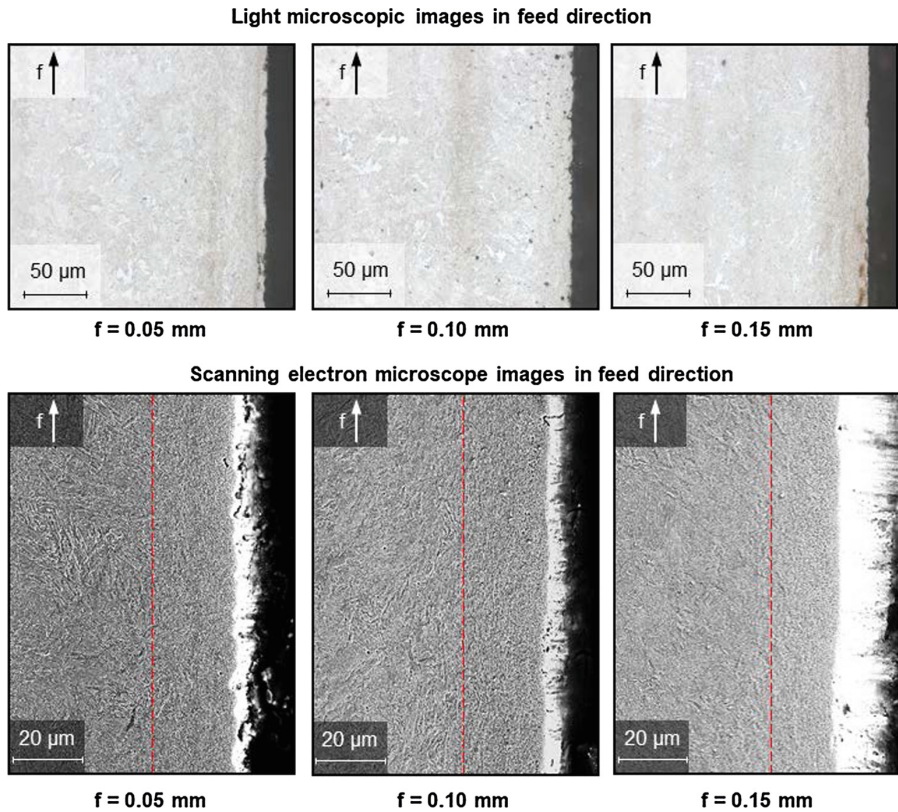


Fig. 12. Light microscope and scanning electron microscope analysis of the bore subsurface in y-z-plane.

3.4 Analysis of the Micro-magnetic Barkhausen Noise

The coercive field strength based on the micro-magnetic Barkhausen noise (MBN) measurements Φ_{cm} (Fig. 13) shows similar numbers for feed rates of $f = 0.05$ mm and 0.10 mm, whereas for $f = 0.15$ mm a significant drop was detected. Baak et al. [13] showed that there are no significant differences in residual stresses for the investigated feed rates; therefore, the drop can be explained by the hardness and hardness depth of the specimens.

The results from the MBN measurements correlate with the previously presented results for the analysis of the subsurface condition. The lower coercive field strength at a feed rate of $f = 0.15$ mm can be correlated to the lower penetration depth of the mechanical boundary zone influence, which was visualized by the microstructural analysis in form of longitudinal and transverse sections. The greater penetration depth and more homogeneous influence on the produced subsurface microstructure at low feed rates $f = 0.05$ mm and $f = 0.10$ mm can thus be detected by this non-destructive micro-magnetic analysis in the form of higher values of the coercive field strength. In

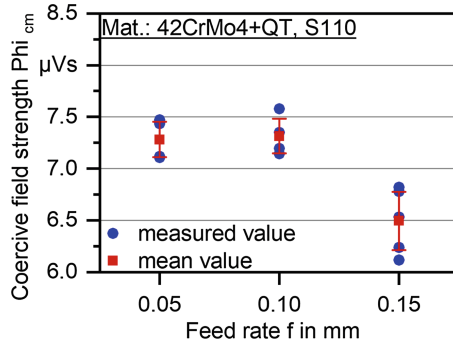


Fig. 13. Coercive field strength Φ_{cm} versus feed rate f .

contrast, the measured Φ_{cm} values decrease as well as the depth of the mechanically induced microstructure refinement at the highest feed rate.

4 Conclusions and Outlook

The results show that the surface integrity is significantly affected by the single-lip deep hole drilling process. Properties that have a decisive influence on the dynamic strength of the components, such as surface roughness as well as the microstructure or hardness in the subsurface zone, have to be taken into account when selecting process parameters. For the design of single-lip deep hole drilling processes which aim to have an influence on the bore edge zone in order to increase the dynamic strength, the level of mechanical load on the surface should be determined by the adapting of the tool geometry. Suitable adaptations with influence on the mechanical load transmitted into the bore wall are for example the variation of the shape of the cutting edge to increase the normal forces or selecting narrower guide pads to increase the surface pressure between the guide pads and the bore surface. An increase in the feed rate is only of limited suitability for increasing the mechanical surface influence with the aim of achieving positive effects on the surface integrity and the associated fatigue strength. Increasing the feed rate to $f = 0.15$ mm leads to a significant deterioration of the surface roughness and an increase of the R_z values by 124% compared to the lowest feed rate $f = 0.05$ mm. Although the level of the measured mechanical tool load in the form of the feed force and the drilling torque increases for the higher feed rate, this effect does not result in a higher hardness of the subsurface zone under the present process conditions. A higher feed rate leads to a greater distance between the contact areas with maximum pressure between the guide pads and the bore wall. This effect was detected and visualized by mapping the micro-hardness along the bore wall in the feed direction. For the purpose of influencing the surface integrity to produce an increased fatigue strength of the deep drilled components, with a feed rate of $f = 0.05 \dots 0.10$ mm the most promising results were achieved.

The results from the MBN analysis show a correlation between the measured coercive field strength and the state of the subsurface microstructure. The higher and

more homogeneous hardness as well as greater penetration depth at the lower feed rates is reflected in the level of the measured Φ_{cm} values. This analytical technique thus offers the possibility of non-destructive evaluation of the subsurface zone properties generated by the machining process. Changes in the subsurface microstructure during the components life cycle due to applied dynamic loads can as well be detected using this method. With the use of a customized sensor geometry, the MBN analysis could be applied for measurements on the inside of boreholes.

In future research, in addition to the mechanical influence on surface integrity, the thermal influence is planned to also be analyzed within the project. By designing an experimental setup for in-process measurements in the bore subsurface, information on the temperatures acting on the subsurface microstructure during the single-lip deep hole drilling process shall be gained. The combination of these results with the results obtained so far should provide a holistic assessment of the thermomechanical influence of single-lip deep hole drilling on the surface integrity. By correlation with data of the MBN analysis and from results of fatigue tests, the possibility to increase the fatigue strength of components by the drilling process is further investigated.

Acknowledgments. The project “Investigations on the influence of machining and sulphur content on the fatigue strength of the quenched and tempered steel 42CrMo4+QT” was funded by the Deutsche Forschungsgemeinschaft (DFG, German Research Foundation) – project number 320296624. All authors would like to thank the DFG for their support.

References

1. Kleemann, U., Zenner, H.: Bauteiloberfläche und Schwingfestigkeit – Untersuchungen zum Einfluss der Randschicht auf die Dauerschwingfestigkeit von Bauteilen aus Stahl. *Mat.-wiss. u. Werkstofftech* **5**(37), 349–373 (2006). <https://doi.org/10.1002/mawe.200600995>
2. Koster, W.P., Field, M., Kahles, J.F., Fritz, L.J., Gatto, L.R.: Surface integrity of machined structural components. Technical report AFML-TR-70-11, Metcut Research Associates Inc., Cininnati (1970)
3. Rasti, A., Sadeghi, M.H., Farshi, S.S.: An investigation into the effect of surface integrity on the fatigue failure of AISI 4340 steel in different drilling strategies. *Eng. Fail. Anal.* **95**, 66–81 (2019). <https://doi.org/10.1016/j.engfailanal.2018.08.022>
4. Vormwald, M., Schlitzer, T., Panic, D., Beier, H.T.: Fatigue strength of autofrettaged Diesel injection system components under elevated temperature. *Int. J. Fatigue* **113**, 428–437 (2018). <https://doi.org/10.1016/j.ijfatigue.2018.01.031>
5. Rech, J., Hamdi, H., Valette, S.: Workpiece surface integrity. In: Davim, J.P. (ed.) *Machining*, vol. 133, pp. 59–96. Springer, London (2008)
6. Girinon, M., Dumont, F., Valiorgue, F., Rech, J., Feulvarch, E., Karaoui, H., Jourden, E.: Influence of lubrication modes on residual stresses generation in drilling of 316L, 15-5PH and Inconel 718 alloys. *Procedia CIRP* **71**, 41–46 (2018). <https://doi.org/10.1016/j.procir.2018.05.020>
7. Girinon, M., Valiorgue, F., Karaoui, H., Feulvarch, É.: 3D numerical simulation of drilling residual stresses. *C. R. Méc.* **8**(346), 701–711 (2018). <https://doi.org/10.1016/j.crme.2018.06.003>
8. Greuling, S., Seeger, T., Vormwald, M.: Autofrettage innendruckbelasteter Bauteile. *Mat.-wiss. u. Werkstofftech* **3**(37), 233–239 (2006). <https://doi.org/10.1002/mawe.200500994>

9. Nickel, J., Baak, N., Biermann, D., Walther, F.: Influence of the deep hole drilling process and sulphur content on the fatigue strength of AISI 4140 steel components. *Procedia CIRP* **71**, 209–214 (2018). <https://doi.org/10.1016/j.procir.2018.05.069>
10. Jawahir, I.S., Brinksmeier, E., M'Saoubi, R., Aspinwall, D.K., Outeiro, J.C., Meyer, D., Umbrello, D., Jayal, A.D.: Surface integrity in material removal processes. *Recent Adv. CIRP Ann.* **2**(60), 603–626 (2011). <https://doi.org/10.1016/j.cirp.2011.05.002>
11. Novovic, D., Dewes, R.C., Aspinwall, D.K., Voice, W., Bowen, P.: The effect of machined topography and integrity on fatigue life. *Int. J. Mach. Tools Manuf.* **2–3**(44), 125–134 (2004). <https://doi.org/10.1016/j.ijmachtools.2003.10.018>
12. Altpeter, I., Boller, C., Fernath, R., Hiringer, B., Kopp, M., Werner, S., Wolter, B.: Zerstörungsfreie Detektion von Schleifbrand mittels elektromagnetischer Prüftechniken. In: *Proceedings of the DGZfP-Jahrestagung*, 30 May–01 June 2011, Bremen (2011)
13. Baak, N., Schaldach, F., Nickel, J., Biermann, D., Walther, F.: Barkhausen noise assessment of the surface conditions due to deep hole drilling and their influence on the fatigue behaviour of AISI 4140. *Metals* **8**(9), 720 (2018)

Surface Finishing and Machining



Improvement of Chipping Phenomena for Crustaceous Materials Rounding by Centrifugal Barrel Finishing

Hiroki Mizuno^(✉) and Hiroaki Suesuga

SINTO KOGIO, LTD., 71-2 Tsukeda, Nisijo,
Amagun, Oharu-cho, Aichi 490-1144, Japan
h-mizuno@sinto.co.jp

Abstract. Barrel finishing is a surface finishing treatment method used for various parts. In particular, the centrifugal barrel finishing is used for rounding electronic components made of crustaceous materials such as MLCC, because it is high productivity and small-volume production in great varieties. However, because the finishing method has the highest finishing power among barrel finishing, a chipping occurs at the ridges of MLCC made of crustaceous materials. The chipping causes product defects. In this study, in order to reduce the chipping, we investigated the causes of the chipping by observing the contents's (Mass) behavior in the finishing tank by using a high-speed camera. From the observation result, we found that the phenomena which the Mass was thrown out and collided against finishing walls in the processing. For this reason, the chipping occurred. In order to prevent from the phenomena, we considered flowing the Mass is always touching some wall surfaces of the tank by changing the angle of the tank rotation axis. Commonly, the angle of the tank rotation axis is $\theta = 0^\circ$. However, the Mass did not be thrown out by changing the angle of $\theta = 45^\circ$. This reason is the Mass always touching some wall surfaces of the tank. As a result of this test, it is possible to reduce chipping's volume by 80% in comparison with the conventional method.

Keywords: Mass finishing · Barrel finishing · Centrifugal barrel · Chipping · Crustaceous materials

1 Introduction

In recent years, the global production value of the electronic information industry is expanding because of the progress of the Internet of Things (IoT). The worldwide spread of the Smartphones and the Electric Vehicles (EV) has made the electronic components market active [1]. Especially, the multilayer ceramic capacitor (MLCC) is rapidly increasing in the EV field because of a large capacitance and a compact size. However, the MLCC may be damaged by the impact to the corners on handling in the manufacturing process because of crustaceous materials. As a countermeasure for this problem, barrel finishing is used for rounding to corners of the MLCC.

Barrel finishing is a finishing method which processing is performed by friction between works and media. A container called a barrel is put works and media (abrasive

stone or abrasive), and optionally water and compounds (abrasive aid) in this method [2]. After that, the contents (Mass) in the tank are processed by rotational or vibrating movement. Barrel finishing can be applied to all kinds of parts such as machined products, pressed products, sintered products, die-cast products and be applied to all finishing purposes such as deburring, de-scaling, rounding, smooth finishing [3].

There are four typical barrel finishing methods: Rotary, Vibrating, Flow and Centrifugal. Table 1 shows the characteristics of four barrel finishing method [3].

Table 1. Characteristics of four finishing method.

Finishing type	Characteristics
Rotary	The tank rotates. Simple operation but finishing time is long
Vibrating	The tank vibrates. Large and long products can be finishing but the noise is loud
Flow	The rotating disc at the bottom of the tank rotates. Excellent in workability, but not suitable for finishing thin products
Centrifugal	Several finishing tanks revolve and rotate at high speed. Suitable for small products, but most likely to be deformed due to the most finishing power

The centrifugal barrel finishing is used for rounding electronic components of crustaceous materials such as MLCC, because it is high productivity and small-volume production in great varieties. However, MLCC’s chipping occurs at a part of corners because the centrifugal barrel generates a large energy in the processing. The chipping causes deterioration of electrical characteristics. A total inspection is difficult because the size of electronic components is often 1 mm or less. There are some cases if there is even one defect in a production lot, all the lots will be defective.

Therefore, the processing of electronic components such as MLCC is required to have high productivity and high quality finishing without chipping. However, a centrifugal barrel finishing is generally used to process metal parts, and a horizontal/vertical centrifugal barrel machine is standard because of high productivity and ease of design. The application of centrifugal barrel finishing for crustaceous materials has not been adopted because the brittle fracture causes occurrence of chipping, but it is considered for using a centrifugal barrel finishing because of high productivity and it is required the reduction of the chipping.

In order to reduce the chipping, we propose that improvement of a centrifugal barrel finishing method by elucidating the chipping phenomena.

2 Conventional Method

Figure 1 shows a conventional horizontal centrifugal barrel machine, and Fig. 2 shows a schematic diagram of the movement. Four tanks are attached at equal intervals on the concentric circles of the horizontally rotating turret. When the tanks are rotating at high speed through the planetary mechanism, strong centrifugal force is generated. The

Mass flows in the direction of revolution while being pressed against inner walls of the tank, works and media as the Mass are processed by a pressure and relative movement.



Fig. 1. Conventional centrifugal barrel machine.

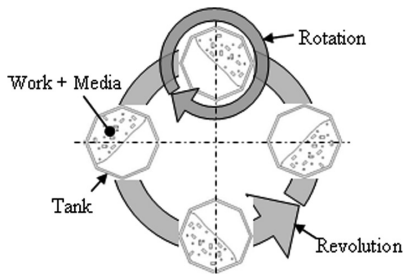


Fig. 2. Movement schematic diagram of conventional centrifugal barrel machine.

3 Investigation About Causes of the Chipping by Behavior Observation in Tank

We tried to identify causes and mechanisms of the chipping through observing the Mass's behavior in the centrifugal barrel tank by using a high-speed camera (VW-9000, KEYENCE Corporation, Japan). In order to look inside the tank, the lid of the tank was made of plastic. The camera was placed outside the machine to observe the phenomena inside the tank.

From the observation result, this phenomena were observed that the Mass was thrown out against the tank's walls, when a rotational speed is changing between 0 min^{-1} to 140 min^{-1} in the case of our machine. Figure 3 shows the photograph in that time. If a relative centrifugal acceleration is calculated from the equation shown in Fig. 4, when it is $1G$ ($1 \times 9.8 \text{ m/s}^2$) and a position of the tank is top, the Mass is momentarily $0G$ (weightlessness) in the tank. After that, the Mass collides with inner walls of the tank. The collision force is F_c at that time. In this case, the equation of motion is given as (1), where m is the mass, a is the acceleration.

$$F_c = ma \quad (1)$$

The collision force is considered to be about 10 times each single weight of the Mass.

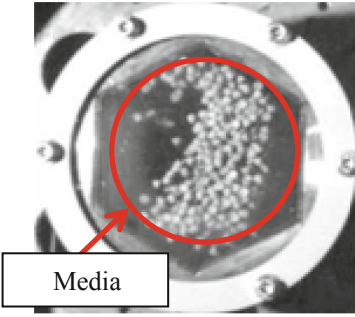


Fig. 3. 0G state.

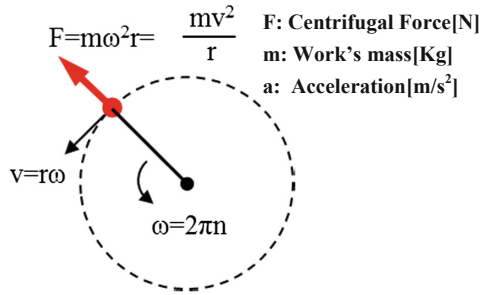


Fig. 4. Centrifugal force.

The state of 0G occurred at the rotational speed of about 70 min^{-1} . Moreover the relative centrifugal acceleration obtained from the equation also coincided with the point of 1time. Figure 5 shows a relationship between the rotational speed and the relative centrifugal acceleration. Conventionally, a chipping improvement method has been corresponded by changing factors and conditions (work materials, shape, size, type of media/compounds, type of machine, rotational speed, etc.). However, the effect of chipping was less and was not good solutions.

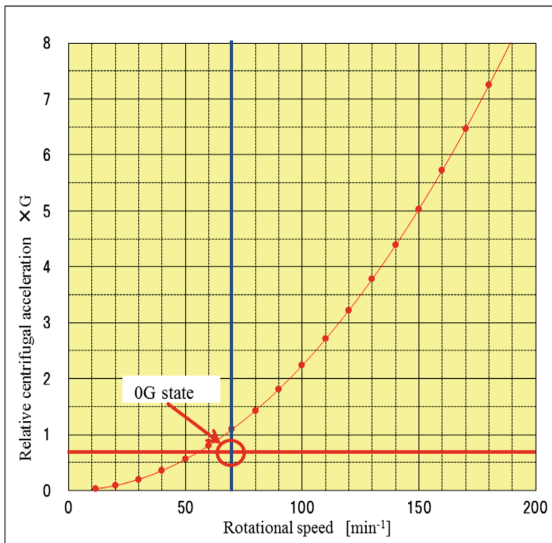


Fig. 5. Relationship between rotational speed and acceleration.

4 Examination of a New Chipping Reduction Method

4.1 Hypothesis and Observation of the Chipping Reduction Method

As a result of observing the Mass's behavior, we found that the inside of the tank was OG state for a moment in the processing. Therefore, a big collision occurs because the Mass was thrown out of walls into the air.

In other words, we considered that the chipping can be reduced by changing the angle of the tank rotation axis and flowing the Mass is always touching some wall's surfaces of the tank. Figure 6 shows a schematic diagram of flowing the Mass's state by changing the angle of the tank rotation axis.

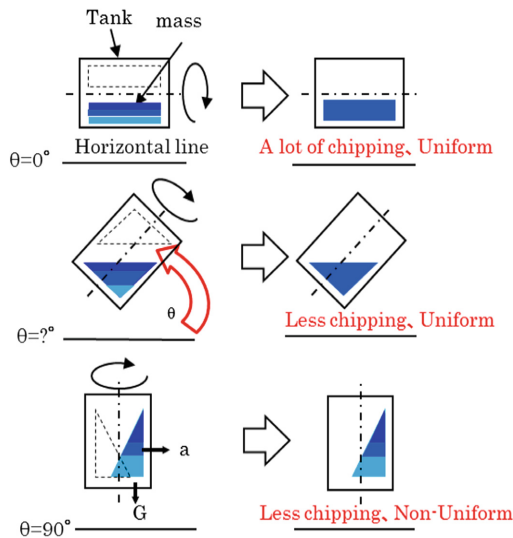


Fig. 6. The angle of the tank rotation axis and the Mass's state.

The angle of the tank rotation axis was decided $\theta = 0^\circ$ in the horizontal direction with respect to the ground. The angle of the tank rotation axis was changed $\theta = 45^\circ$ and $\theta = 90^\circ$. Figure 7 shows the Mass's behavior was observed by using a high-speed camera in that state. As a result, the phenomena that the Mass was thrown out can be suppressed by changing the angle of the tank rotation axis. Accordingly, it is presumed that the chipping can be reduced as the angle of the tank rotation axis approaches $\theta = 90^\circ$ (perpendicular to the horizontal) from $\theta = 0^\circ$ in the horizontal direction with the ground.

However, a finishing variation is occurred as the angle of the tank rotation axis approaches $\theta = 90^\circ$. As a reason for that the Mass doesn't deposit uniformly in the rotation direction (the Mass of the upper is smaller and the lower is larger) as the angle of the tank rotation axis approaches $\theta = 90^\circ$.

Conversely, when the angle of the tank rotation axis is horizontal $\theta = 0^\circ$ with respect to the ground, the Mass is deposited almost uniformly in the rotation direction. Since, chipping increases from $\theta = 90^\circ$ to $\theta = 0^\circ$.

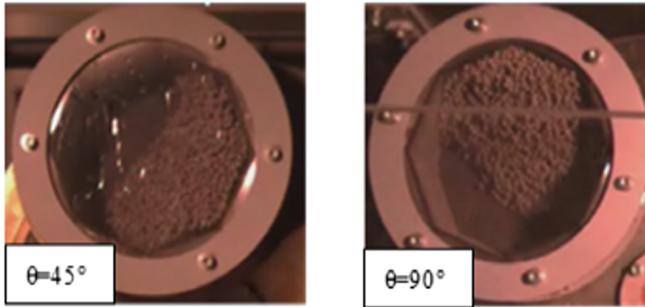


Fig. 7. Observation with a high speed camera.

4.2 Confirming the Effect of Chipping Reduction Method Through Tests

The chipping's volume is evaluated by changing the angle of the tank rotation axis between $\theta = 0$ and 90° . In order to evaluate the chipping's volume generated by processing and the chipping reduction effect, we inserted 2 L of media and five test pieces for evaluation into the 8 L of tank. Figure 8 shows the test piece made of ceramic materials in the tests.

The tests were conducted two patterns. The one was a Dry method with media and evaluation test pieces only. The other was Wet method with media, evaluation test pieces, compounds and water. The amount of water charged is slightly higher than the top of the Mass in Wet method.

The test pieces were prepared for hardness HV 220 for Dry method and HV 1200 for Wet method. The chipping's volume was evaluated by measuring the length \times width \times depth of the maximum volume with a laser microscope (VK-X200, KEYENCE Corporation, Japan).

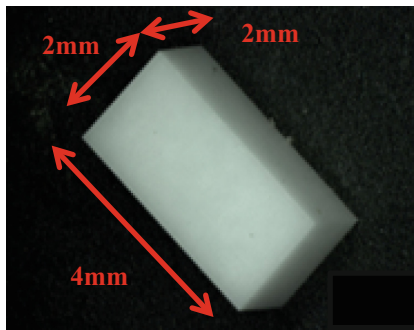


Fig. 8. Photograph of the test piece.

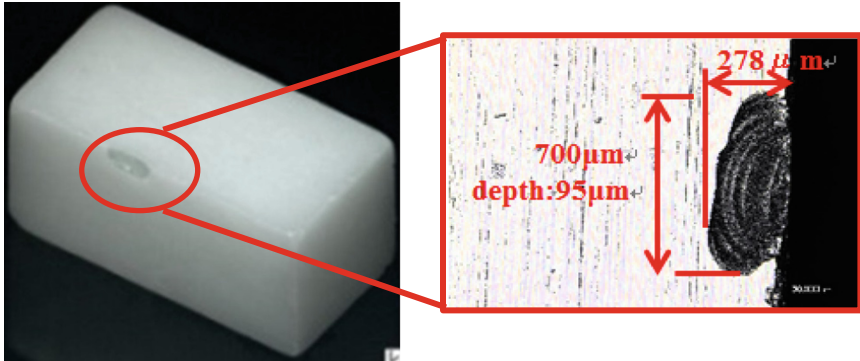


Fig. 9. Example of the chipping.

Figure 9 shows an example of chipping. Figure 10 shows the relationship of the force applied to a test machine (finishing tank). The variable conditions of the test machine is the following two.

- (1) The angle of the tank rotation axis.
- (2) Rotational speed at which the component force A becomes $1 \times 9.8 \text{ m/s}^2$.

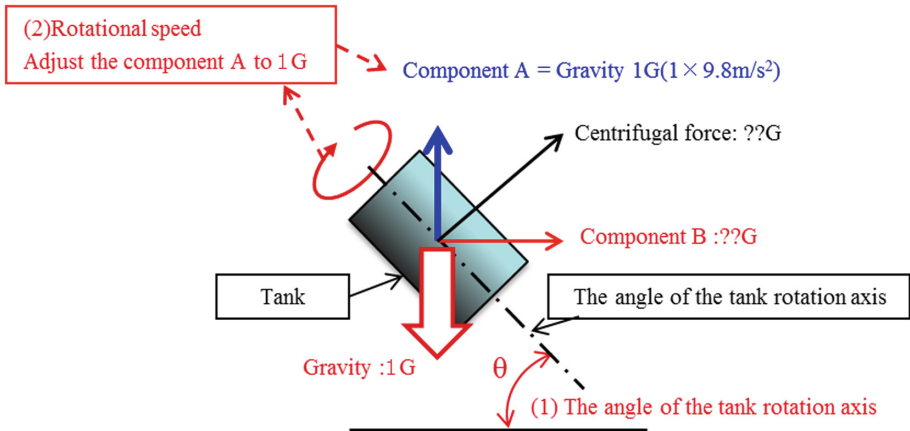


Fig. 10. Component of the centrifugal force.

In order to compare with results of changing each the angle of the tank rotation axis, the rotational speed was intentionally adjusted to the speed at which chipping occurs.

Also, the direction perpendicular to the bottom surface (the opposite direction of gravity) is defined as the force component A, and the horizontal direction is defined as the force component B. The centrifugal force applied to the tank is combined the force A and B.

5 Results and Discussions

Figures 11 and 12 show the relationship between the angle of the tank rotation axis and the chipping’s volume. When the angle of the tank rotation axis is at an angle of $\theta = 45^\circ$, the centrifugal component forces A and B are balance in both Dry and Wet method. For this reason, the chipping’s volume was reduced because the phenomena that the Mass was thrown out into the air were suppressed.

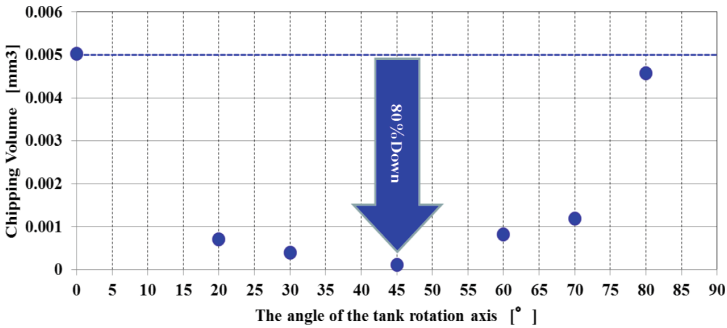


Fig. 11. Relationship between the angle of the tank rotation axis and chipping volume (Wet).

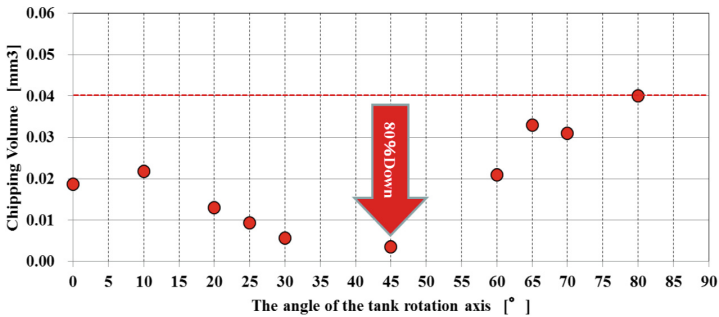


Fig. 12. Relationship between the angle of the tank rotation axis and chipping volume (Dry).

Moreover, an edge (R) was measured and evaluated when the angle of the tank rotation axis was changed between $\theta = 0$ to 90° in the same manner as in the chipping evaluation test for the finishing variation. Using a stylus shape measuring instrument (CONTOURECOAD 2600E, TOKYO SEIMITSU CO., LTD, Japan), a total of $N = 20$ was measured for the R shape of 4 sides of the ridge line under one condition. Figure 13 shows the measurement points and Figs. 14 and 15 show the measurement results.

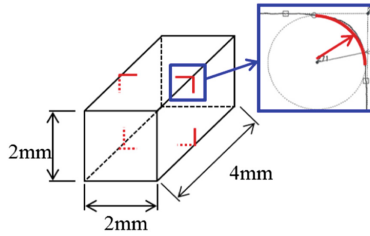


Fig. 13. Measured points of R shape.

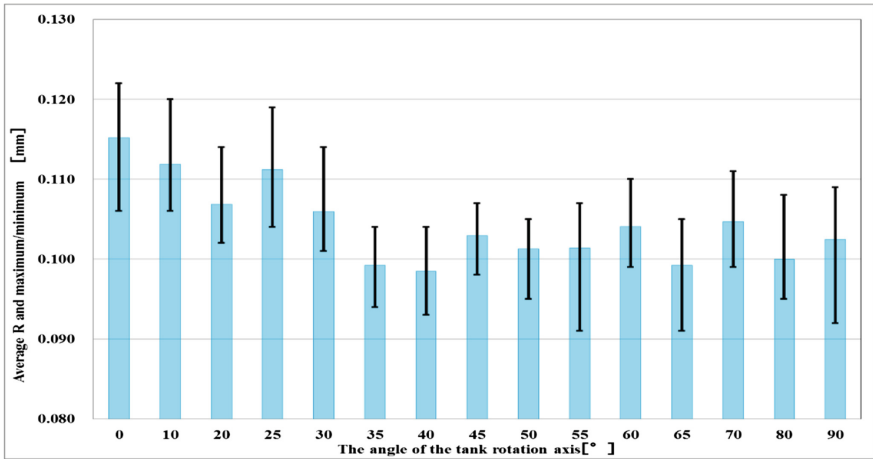


Fig. 14. Measurement results of the angle of the tank rotation axis and R shape (Wet).

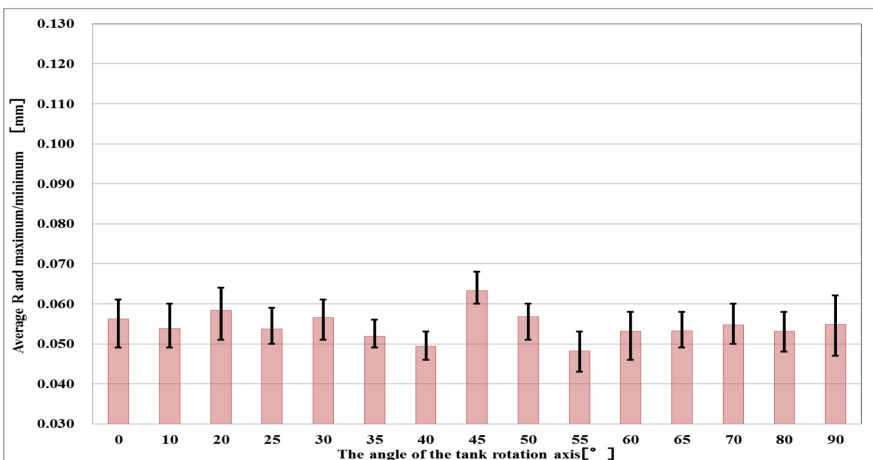


Fig. 15. Measurement results of the angle of the tank rotation axis and R shape (Dry).

The finishing variation (standard deviation) was determined from the measurement results of the edge R. Figure 16 shows the relationship with the angle of the tank rotation axis. From Fig. 16, the finishing variation is the smallest around $\theta = 45^\circ$ in both Dry and Wet methods.

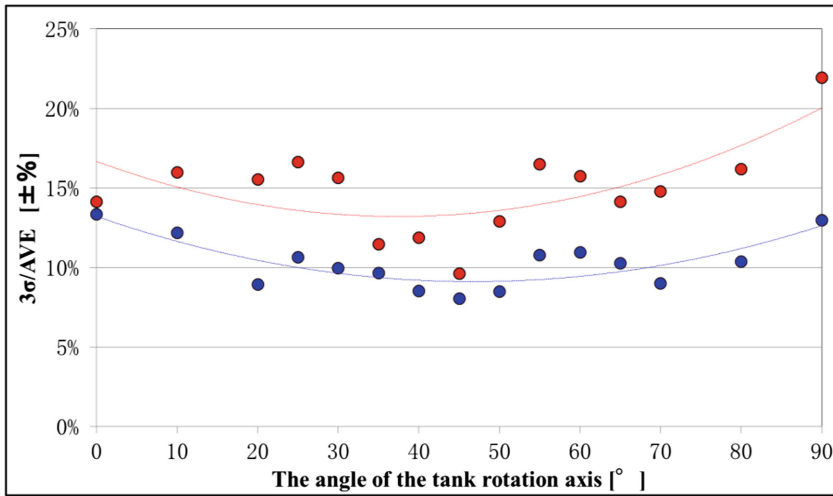


Fig. 16. Relationship between the angle of the tank rotation axis and the finishing variation.

Even in the same horizontal conditions, the angle of the tank rotation axis $\theta = 90^\circ$ has more the finishing variation than $\theta = 0^\circ$. This is because, the Mass is considered to not to deposit uniformly in the rotation direction as the angle of the tank rotation axis approaches $\theta = 90^\circ$.

6 Conclusions

When rounding crustaceous materials using a centrifugal barrel, the tests were performed to improve the chipping phenomena and the following conclusions were obtained.

- (1) The Mass is momentarily 0G in the tank, when changing a rotational speed between 0 min^{-1} to 140 min^{-1} in the case of our conventional centrifugal barrel machine. The chipping phenomena occur because the Mass was thrown out against the tank's walls.
- (2) The chipping's volume has reduced about 80% in comparison with the conventional centrifugal barrel finishing method by changing the angle of the tank rotation axis. The centrifugal component forces A and B are conceivable to be balanced at the angle of the tank rotation axis $\theta = 45^\circ$ and the balance between the forces applied to the Mass was maintained. As a result, we considered chipping is reduced because the phenomena that the Mass was thrown out is suppressed.



- (3) The chipping's volume was the least when the angle of the tank rotation axis is $\theta = 45^\circ$. When the angle of the tank rotation axis is $\theta = 45^\circ$, the stirring effect is considered to become high because two forces of the centrifugal component forces A and B added to the gravity. Therefore the finishing variation seems to be reduced.

References

1. Electronic parts and mounting technology committee. J. Jpn. Inst. Electron. Packag. **22**(1), p. 28 (2019)
2. Sinto Brator Ltd.: Barrel Finishing Machine and Process. Nikkan Kogyo Sinbun, Tokyo (1975)
3. Best-Japan Study Group: Baritekunorozi nyumon (Introduction to Burr technology), pp. 113–115. Sakurakikaku, Tokyo (2002)



In Situ Measurement of Granular Pressure and Velocity on Component Surfaces in Stream Finishing

Sho Itoh¹ , Jeremy Ho¹, Cary Turangan² , and Stephen Wan²

¹ Advanced Remanufacturing and Technology Centre (ARTC), Agency for Science, Technology and Research (A*STAR), 3 Cleantech Loop, #01-01, CleanTech Two, Singapore 637143, Singapore
sho_itoth@artc.a-star.edu.sg

² Institute of High Performance Computing (IHPC), Agency for Science, Technology and Research (A*STAR), 1 Fusionopolis Way, #16-16 Connexis (North), Singapore 138632, Singapore

Abstract. Stream finishing, one of the fast mass finishing processes that enables a material removal rate up to 500 $\mu\text{m}/\text{h}$, is a candidate for the post processing method for external surfaces of additively manufactured (AM) components. The problem here is non-uniform material removal (MR), which is probably caused by a conventional method of rotating target components 360° in a stream finishing bowl. Our plan is to control the component orientations and toolpath depending on each geometry. In order to consider the optimized toolpath, MR simulation is a promising tool. This study focuses on in situ measurement of process values around the target components, which are essential for modelling the granular flow. We measured the pressure and velocity on components surfaces using prototyped tools submerged in the stream finishing media. As a result, the measured pressure increased with the submersion depth, and reached 0.05 MPa at a depth of 250 mm. Regarding the contact angle, the pressure reached maximum in the normal direction toward media flow. The media motion on the surface was successfully tracked using a transparent container. The measured velocity reached maximum when the surface is parallel to media flow. Using these acquired pressure and velocity, a simple estimation of MR was conducted using Preston's law, and agreed with the experimental result. The measured values will enable the calibration and validation of the simulation model, which can be used for the future toolpath prediction.

Keywords: Stream finishing · Robotic finishing · Granular flow · Tribometer · Additive manufacturing

1 Introduction

1.1 Post Processing of Additively Manufactured (AM) Components

Additive manufacturing (AM) technology has provided a new approach to manufacture metal components [1]. Industries are trying to adopt AM technology to automotive,

aerospace, medical fields, and have demonstrated its application for prototypes such as a fuel nozzle, engine and heat exchanger [2]. One of the challenges on AM technology is post processing method to finish its surfaces including internal and external structures, as as-formed surface roughness is 3–30 $\mu\text{m Ra}$. Regarding finishing method for external surfaces, several methods can be applied such as machining, blasting, vibratory finishing, stream finishing, and chemical polishing. We consider that stream finishing is a candidate for industrial use of the external finishing of the AM components, because of the high material removal (MR) rate up to 500 $\mu\text{m/h}$. In a conventional way, the stream finishing bowl and component have been rotated 360° during the process, respectively. However, as shown in Fig. 1, the defect appears if polishing parameter is not controlled. Therefore, we are considering that it is beneficial to control orientations and toolpath for improving the MR uniformity.

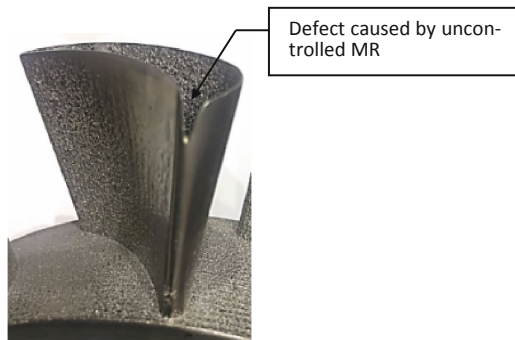


Fig. 1. Photograph of an example of the polished AM component without toolpath control.

For controlling the toolpath, one possible approach is to create MR simulation model, then to predict MR distribution using the model without a physical trial and error. The example is: (1) to calculate MR in each component orientation toward the media flow direction, (2) to combine the orientations so that the summation of MR becomes uniform, and (3) to polish the component using the predicted toolpath plan. To simulate the dense particle flow, Jop et al. [3] proposed granular flow model. The merit of this idea is to enable us to simulate granular flows by considering continuum based fluid dynamics by introducing granular viscosity. In order to apply the model to the stream finishing, in turn, it is necessary to calibrate, that is, identify parameter values in the model, using measured granular velocity and pressure. However, up to the authors knowledge, there is no available tool to measure granular pressure and velocity on components surfaces in a stream finishing bowl [4–6].

1.2 Objectives

The objective of this study is to measure granular pressure and velocity for stream finishing by prototyping new measurement tools. In this study, the measurement tools for the granular pressure and velocity were separately prepared. Then, the influences of

component submersion depth and component angle toward media flow were elucidated, which influences the amount of MR and surface roughness according to our experience.

2 Experimental

2.1 Stream Finishing System

As shown in Fig. 2, stream finishing system (SF-105-A-W, OTEC) with a robotic arm (IRB4400/60, ABB) was set-up. A tool changer at the tip of the robotic arm enables to change each measurement tool described in Sect. 2.2. Media flow speed was controlled by changing the rotational speed of the stream finishing bowl. Polymer type media (KM6, OTEC) and ceramic type media (DBS4/4, OTEC) were used in the pressure and velocity measurement and MR measurement described in Sect. 3.3, respectively. The process parameters used is summarized in Table 1.

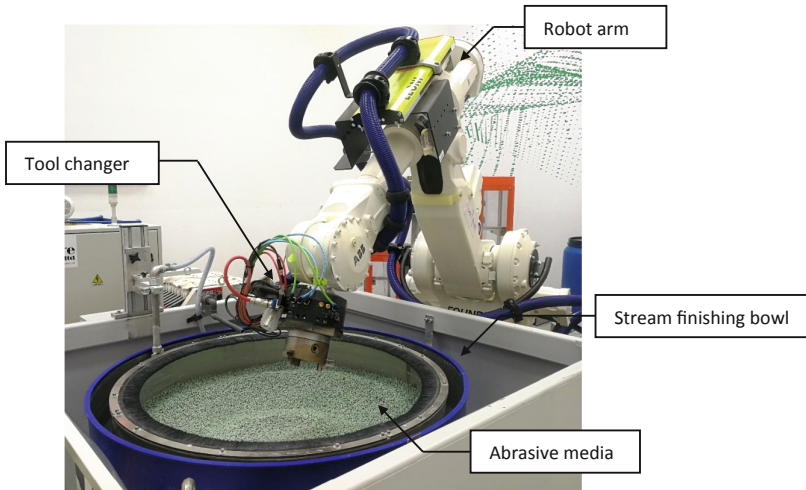


Fig. 2. Photograph of the stream finishing system.

Table 1. Process conditions of the stream finishing.

Media	Polymer type (KM6, OTEC) Ceramic type (DBS4/4, OTEC)
Rotational speed	30, 60 rpm
Location	
Radius r	250 mm
Depth z	100, 200, 250 mm
Angle θ	0°, 30°, 60°, 90°
Liquids, compounds	Dry (without water and compounds)

2.2 Measurement Tools

Pressure Measurement. A force transducer (U93, HBM) was mounted in a stainless steel casing with a cubic size of ~ 50 mm. A circular button part with a diameter of 16 mm, which contacts with abrasive media, was prepared, and connected to the force transducer. Figure 3(a) shows the schematic of the top view of the coordinates.

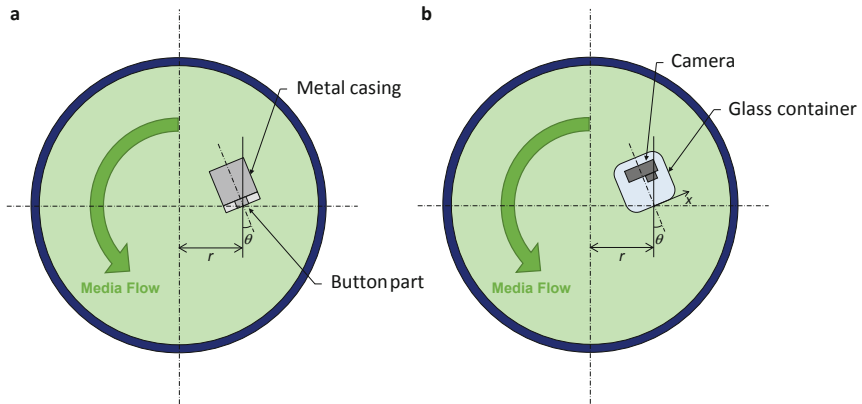


Fig. 3. Schematic of the top view of the used coordinates for (a) pressure and (b) velocity measurement.

Velocity Measurement. A transparent glass container with a size of $78 \times 78 \times 70$ mm in which a digital camera was installed, was used to monitor media movement. Although the corner part of the container was rounded, the shape was considered to be square. Firstly, the media movement was captured with a frame rate of 120 frame/sec. Then, the velocity was calculated by dividing the tracked media traveling distance by its time. Figure 3(b) shows the schematic of the top view of the coordinates.

3 Results and Discussions

3.1 Pressures

Figure 4 shows an example of the transitional detected force until 30 s at a rotational speed of 30 rpm and location (r, z, θ) of $(250 \text{ mm}, 200 \text{ mm}, 0^\circ)$. The data fluctuation was observed, which was probably caused by the vibration of the casing bombarded by the plastic media. Then, the averaged value (as shown in a broken line) was used for evaluation. The acquired averaged force was divided by a contacted area size to transform the data into pressure. Figure 5 shows the acquired pressure at a rotational speed of 30, 60 rpm, and location (r, θ) of $(250 \text{ mm}, 0^\circ)$. The graph showed that the

recorded pressure increased with the submersion depth, and reached 0.05 MPa at a depth of 250 mm when 30 rpm. Unexpectedly, the value in 60 rpm was lower than that of 30 rpm. It is considered that the phenomenon was caused by centrifugal force applied to the media during polishing, which is leading to the media height distribution change. Figure 6 shows acquired pressure with a rotational speed of 30 rpm, and location (r, z) of (250 mm, 200 mm). The value decreased from 0.03 MPa at 0° , then, the value was slightly more than 0 MPa at 90° . This result shows media is still contacting the surface at 90° .

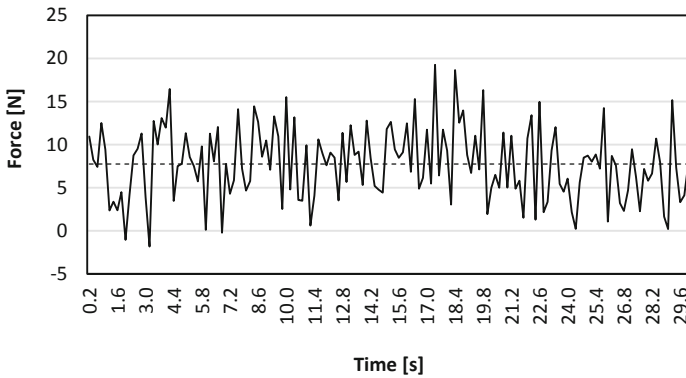


Fig. 4. The transitional acquired force using the tribometer at a rotational speed of 30 rpm and location (r, z, θ) of (250 mm, 200 mm, 0°). The duration of the data acquisition was 30 s.

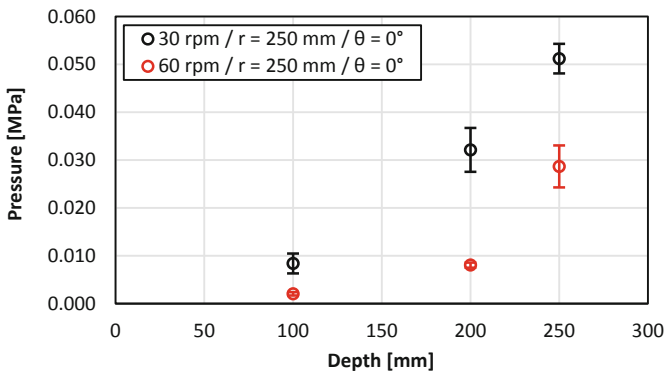


Fig. 5. Pressure data with a rotational speed of 30 rpm and 60 rpm, and location (r, θ) of (250 mm, 0°).

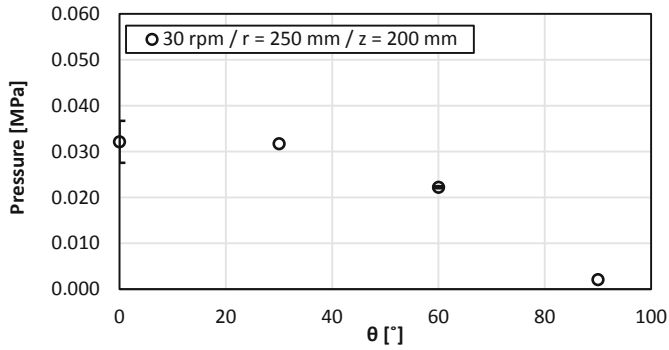


Fig. 6. Pressure data with a rotational speed of 30 rpm, and location (r, z) of (250 mm, 200 mm).

3.2 Velocities

By using the transparent container, the media motion was successfully recorded. Figure 7 shows an example of the captured image. By using the sequenced image, selected media was tracked to measure the velocity in two directions, V_x and V_z . Figure 8 shows the measured result of two directions of velocities at a bowl rotational speed of 30 rpm, and location (r, z) of (250 mm, 200 mm). V_x value reached the maximum, 582.4 mm/s at 90°. On the other hand, V_z value reached the maximum, 157.4 mm/s at 60°. The reason for the media moving upward is considered that the upper side is having lower granular pressure, which is leading to easier flowing than the deeper side of the bowl. Also, the similar velocity values were acquired at a location (r, z) of (250 mm, 100 mm).

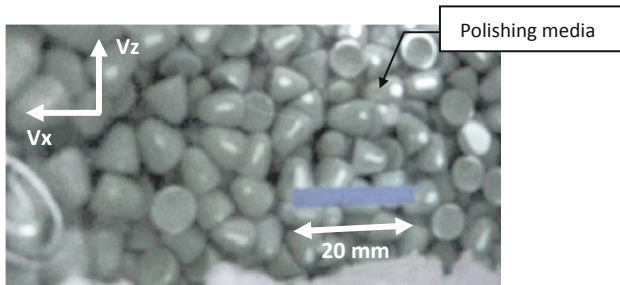


Fig. 7. Photograph of a captured image using the transparent container. The white tape shows a scale with a length of 20 mm.

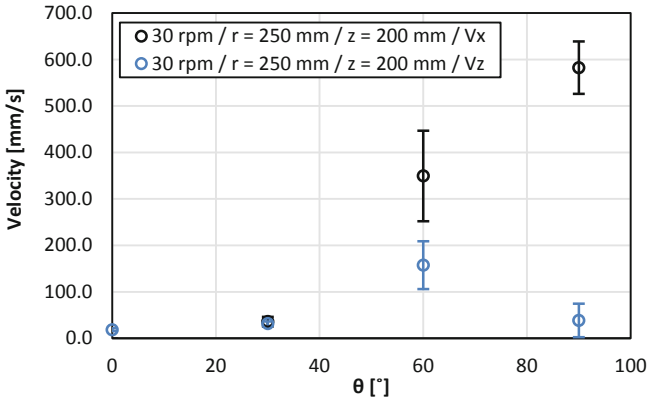


Fig. 8. Flow data with a rotational speed of 30 rpm, and location $(r, z) = (250 \text{ mm}, 200 \text{ mm})$.

3.3 Discussions

Regarding MR model, the following Preston's law [7] has been widely used:

$$MR = kPVt \quad (1)$$

Here, k represents a coefficient including media hardness, P pressure, V velocity, and t processing time. By considering a constant value of k and t , PV values will influence the MR in this model. Using the values acquired in Figs. 6 and 8, PV becomes 0.8, 1.4, 8.4, 1.2 when θ is 0° , 30° , 60° , 90° as shown in Table 2. To confirm the model, MR was measured experimentally. The titanium components printed using an electron beam, was polished by stream finishing for 45 min using ceramic media. The result also showed that MR value reached the maximum when θ is 60° . Therefore, the experimental result was agreed with the Preston's law. Further calibration is necessary to estimate MR precisely.

Table 2. Comparison of the calculated PV and measured MR (45 min).

Angle θ	PV using Figs. 6 and 8	Measured MR
0°	0.8	39.8 μm
30°	1.4	43.7 μm
60°	8.4	221.1 μm
90°	1.2	21.4 μm

4 Conclusions

In this study, the granular pressure and velocity were measured using the prototyped tools. As a result, the recorded pressure increased with the submersion depth in the bowl. When changing the angle, the value became the maximum when θ is 0° . The

media motion was successfully monitored by using a transparent container. The velocity became the maximum when θ is 90° . The influence of the submersion depth was not observed. By using these data values, a simple estimation using the Preston's law was conducted, then, showed the agreement with experimental result using ceramic media.



For the future work, the following activities have been planned: (1) simulating the media flow and subsequently upgrading it to MR model, and (2) predicting the toolpath using the MR model.

References

1. Frazier, W.E.: Metal additive manufacturing: a review. *J. Mater. Eng. Perform.* **23**, 1917–1928 (2014). <https://doi.org/10.1007/s11665-014-0958-z>
2. GE Additive. <https://www.ge.com/additive/industry-overview>. Accessed 2 Apr 2019
3. Jop, P., Forterre, Y., Pouliquen, O.: A constitutive law for dense granular flows. *Nature* **441**, 727–730 (2006). <https://doi.org/10.1038/nature04801>
4. Cariapa, V., Park, H., Kim, J., Cheng, C., Evaristo, A.: Development of a metal removal model using spherical ceramic media in a centrifugal disk mass finishing machine. *Int. J. Adv. Manuf. Technol.* **39**, 92–106 (2008). <https://doi.org/10.1007/s00170-007-1195-5>
5. Fleischhauer, E., Azimi, F., Tkacik, P., Keanini, R., Mullany, B.: Application of particle image velocimetry (PIV) to vibrational finishing. *J. Mater. Process. Technol.* **229**, 322–328 (2016). <https://doi.org/10.1016/j.jmatprotec.2015.09.017>
6. Hashimoto, F., Johnson, S.P., Chaudhari, R.G.: Modeling of material removal mechanism in vibratory finishing process. *CIRP Ann. Manuf. Technol.* **65**, 325–328 (2016). <https://doi.org/10.1016/j.cirp.2016.04.011>
7. Preston, F.W.: The theory and design of plate glass polishing machines. *J. Soc. Glass Technol.* **11**, 214–256 (1927)



Development of Rheology and Computational Flow Model for Robotized External Finishing on Additively Manufactured Components

Cary Kenny Turangan¹(✉) , Stephen Wan Yee Ming¹, Sho Itoh² ,
and Jeremy Ho²

¹ Institute of High Performance Computing,
A*STAR, Singapore 138632, Singapore
cary@ihpc.a-star.edu.sg

² Advanced Remanufacturing and Technology Centre,
A*STAR, Singapore 637143, Singapore

Abstract. Stream finishing is accepted as one of the post processing operations. It is not only capable of grinding but also offers polishing of additive manufactured components, having advantages of larger material removal rates and controllable toolpath. We have developed a stream finishing model through semi quantitative prediction via computational fluid dynamics (CFD) simulations. The scheme couples the granular flow field with the material removal scheme by solving the granular flow using a continuum-based method. For the rheology, the media viscosity is determined to resolve the flow field so the pressure induced by the media and the material removal rate can be predicted. The model calibration involves developing a tribometer and using it to measure the media pressure for several scenarios based on the rotational speed of the drum (30 rpm), radial distances of the tribometer (100, 250, 400 mm), submerged depths (100, 200, 250 mm) and its glancing angles (0, 15°, 30°, 45°, 60°, 75°, 90°). The work is extended to study the media flow for a simplified square work piece. The results indicate that the particle velocities on the surface of the work piece predicted by simulations are comparable to those of experiments. They show similar patterns and magnitudes for the parameters tested, which demonstrate the capability of the model to correctly predict the granular flow field.

Keywords: Stream finishing · Rheology model · CFD

1 Introduction

Additive manufacturing technology produces metallic components with a variety of geometries. The components fabricated by additive manufacturing often have rough surfaces that seriously limit the potential of manufacturing technique. Such components including those having the complex geometries require to be post proceeded before putting them into the service.

Loose abrasive mass finishing techniques have been known to be capable of volume polishing of engineering components. However, the goal of uniform polishing remains a difficult challenge. Stream finishing is considered to be a candidate for

external finishing of additive manufacturing parts because it can induce larger material removal rate compared to other finishing process such as the vibratory finishing. Stream finishing can control the toolpath by introducing a robot arm, leading to more increased freedom. The primary challenge is how to design the toolpath to finish the components with complex geometry.

One solution is to create a simulation model of media flow and material removal. By using them, the material removal can be predicted. This solution will reduce the trial and errors of polishing the components. Several parameters need to be identified by performing sensitivity analysis to develop models that can predict the desired output. For example, if the flow is considered to be of granular, the continuum and Navier-Stokes equations can be employed. To create the simulation model, the physical parameters (e.g. pressure, velocity) should be obtained. Therefore, appropriate devices must be prepared. However, there is no established method and apparatus to measure pressure and velocity in stream finishing [1–3].

The main objective of our work is to develop capabilities in process modelling and simulation for external finishing of additive manufactured components. This will give semi quantitative predictions and/or insights into local stock removal distribution to help experiments having more uniform polishing. Consequently, it will reduce the number of trials and errors of experiments. The fundamental idea of the modelling methodology is to couple the granular flow field [4, 5], in which the work piece is immersed, with a material removal model [6, 7]. The granular flow-field is then solved using a continuum-based rheology model [8, 9]. The main reason why this approach is employed is because the discrete element method (DEM) that accounts for all granular particles as individual entities is simply not feasible on industrial scales.

2 Rheology Model, Methodology and Experimental Set-up

2.1 Rheology Model and Simulation Methodology

The rheology model adopted in our work is based on the one presented by Jop *et al.* [8]. The inertial number I is given by

$$I = \frac{|\dot{\gamma}_{ij}|d}{\sqrt{P/\rho_p}} \quad (1)$$

where $|\dot{\gamma}_{ij}|$ is the strain rate, d is particle size, P is isotropic pressure and ρ_p is particle density. The coefficient of friction $\mu(I)$ that is a function of inertial number I can be calculated from

$$\mu(I) = \mu_1 + \frac{\mu_2 - \mu_1}{\frac{I_0}{I} + 1} \quad (2)$$

where μ_1 , μ_2 and I_0 are constants. The media viscosity η that is responsible for the wear on the work piece or component can be determined from

$$\eta = \frac{\mu(I)P}{|\dot{\gamma}_{ij}|}. \quad (3)$$

The implementation of this rheology model in the CFD solvers (e.g. ANSYS Fluent and CFX) is via a user-defined function (UDF) that is incorporated into the solvers as these rheology equations are not standard functions in those solvers. The UDF contains the steps described in the flowchart in Fig. 1. This granular viscosity η is the variable that must be determined by the solvers as it is used to resolve the granular flow field.

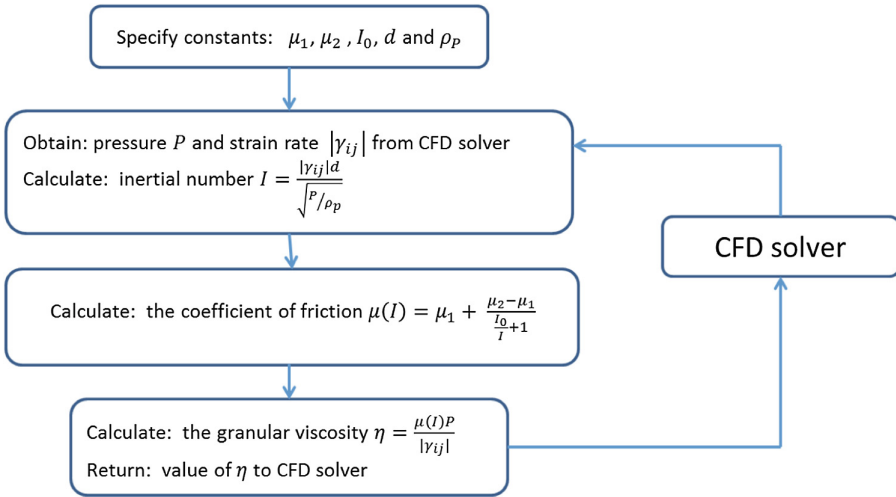


Fig. 1. The flowchart describing the steps in the UDF that is incorporated in the CFD solver to determine the granular viscosity η .

For the purpose of the model calibration against the experiment, a tribometer has been developed. This device was used in the experiments to measure the force (and hence pressure loading) imposed by the granular flow on its surface. With the appropriate constants parameters, the model can predict the flow field and material removal rate of any work piece in a given granular flow.

2.2 Experimental Set-up

The stream finishing equipment for the experiment at ARTC (Advanced Remanufacturing Technology Centre) consists of a 1070 mm-dia drum (SF-105-A-W, OTEC) that has 330 mm maximum depth to contain media particles (see Fig. 2(d)). It has a 0–100 rpm rotational speed range. It is also equipped with a robotic arm (IRB 4400/60, ABB) that holds the component or work piece. The media particles (KM6, OTEC) are made of polymer and have blunt conical shape with size of 6 mm base diameter and 6 mm height. For the work presented here, the calibration is done by means of pressure measurements. A tribometer has, therefore, been designed with a load cell (U93, HBM)

enclosed in a steel casing and with a 16 mm-dia button on which the media force is measured (for the pressure to be determined). The tribometer is to be attached to a 25 mm-dia steel rod held by the robotic arm, and to be submerged in the rotating drum. In the experiments, the drum was set to rotate with 30 rpm speed. The experimental technique employed here is described in detail by Itoh et al. [10].

3 Calibration of the Rheology Model

The CFD simulations for the calibration of the rheology model were performed using ANSYS Fluent. Additionally, ANSYS CFX was used for comparison. Figure 2 illustrates the representation of the stream finishing drum in the computational model, which contains the granular media and the tribometer. Steady state simulations were carried out and the media flow inside the drum was assumed to be laminar. For the flow to be of single phase, only the media that is treated as a continuum fluid was considered. Therefore, the evolution of the free surface of the media (which results from the drum rotation and its centrifugal force that would tend to move the particles towards the side of the drum wall) was not modelled. Note that although both ANSYS Fluent and CFX are capable of resolving the free surface evolution using the volume of fluid (VOF) scheme, this type of simulation is not in our current scope.

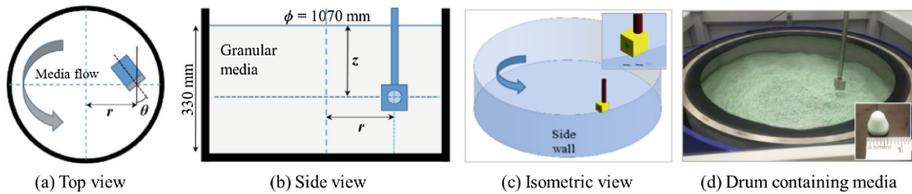


Fig. 2. The schematic of the domain for CFD simulations shows the tribometer model as a work piece submerged inside a rotating drum filled with granular media. The drum has a diameter of 1070 mm and maximum depth of 330 mm. The parameters used are as follows: r is the radial distance of the tribometer button from the centre, z is the depth of the tribometer button from the free surface and θ is the glancing angle with respect to the normal direction. The drum containing the media used in the experiment at ARTC is also shown (inset: media particle sample).

For the calibration purpose, we consider the cases whereby the drum was rotated at 30 rpm speed. Three parametric studies with varying radial distance r , depth z and glancing angle θ carried out were:

- $r = (100, 150, 200, 250, 300, 350, 400)$ mm, $z = 200$ mm (constant), $\theta = 0$;
- $r = 250$ mm (constant), $z = (100, 150, 200, 225, 250)$ mm, $\theta = 0$;
- $r = 250$ mm (constant), $z = 200$ mm, $\theta = (0, 15^\circ, 30^\circ, 45^\circ, 60^\circ, 75^\circ, 90^\circ)$.

The boundary conditions (BC) of the computational model are as follows. The top surface was set with pressure outlet BC. The side and bottom surfaces were set as rotating walls with 30 rpm speed with respect to the positive y -axis so the flow was in the anti-clockwise direction. The tribometer and its holder were set with stationary wall BC.

The calibration aims to obtain the suitable values of constants μ_1 , μ_2 and I_0 of the rheology model that is incorporated in the solvers (via the UDF). For this, a simple iteration method has been adopted in which initial values of the constants are first used in the UDF. The CFD simulation is then run with given operating parameters to calculate the granular viscosity η . The pressure reading on the surface of the tribometer from the simulation is compared with the one measured in the experiment. If the pressures match, the constants and setting in the simulation are retained and the simulation is completed. Otherwise, the values of the UDF constants are adjusted and the simulation is rerun. From this process, we estimated the constants to be $\mu_1 = 0.35$, $\mu_2 = 0.65$ and $I_0 = 0.3$. For the present work, this simple approach is deemed sufficient. However, future studies may be performed to better determine these constants and their accuracy.

Three different mesh resolutions were tested (coarse, medium and fine mesh, see Fig. 3) for the case with distance $r = 0.250$ mm, depth $z = 0.200$ mm and $\theta = 0$. The mesh counts were 46,600, 86,511 and 261,541 for the coarse, medium and fine mesh, respectively, in polyhedral form. In the rheology model, 6 mm particle diameter d and estimated density ρ_p of 2918 kg/m³ (obtained from the experiment) were used. The pressure loading imposed by the media flow on the tribometer for the coarse, medium and fine mesh were 36.5 kPa, 36.7 kPa and 36.9 kPa. The medium mesh resolution was, therefore, used for the subsequent simulations, which gave sufficient accuracy and yet economical computational time.

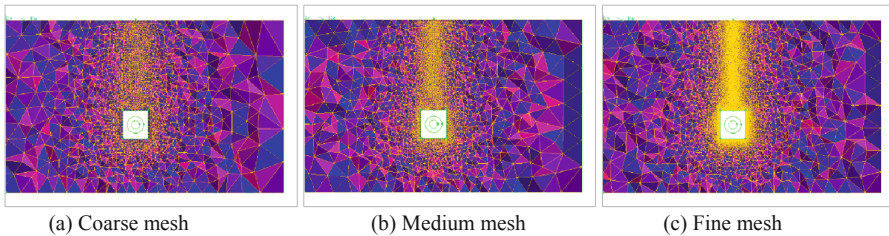


Fig. 3. Close-up views of computational cell (mesh) across the media, showing the tribometer located at distance $r = 250$ mm, depth $z = 200$ mm and $\theta = 0$. Three different types of mesh resolution were initially tested: coarse, medium and fine, shown here in tetrahedral type.

Figure 4 shows selected plots of velocity contours on the horizontal cut plane across the tribometer for three parametric studies. From the colour of the contour plots, the media flow velocity is shown to increase proportional to radial distance r . The flow features show that the tribometer (as a work piece) provides a blockage such that the media particles must go around it as they move. This consequently alters the flow field in the surrounding the tribometer including the formation of a stagnation region. In practice, the media particles that are in contact with the surface of the work piece will erode the surface so as to polish it, which is the main intention of the surface finishing.

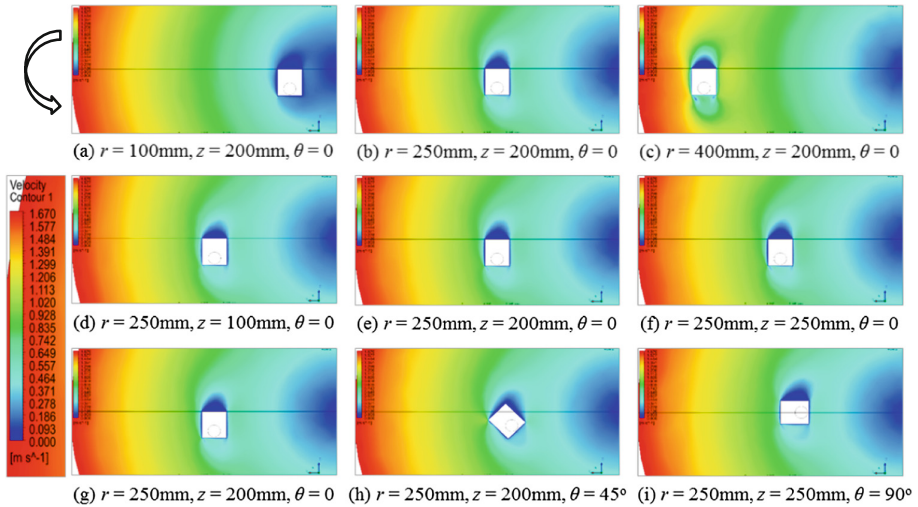


Fig. 4. Top views of the plots of velocity contours around the tribometer on the horizontal cut planes for different scenarios based on radial distance r , depth z from the free surface and glancing angles θ . The drum is rotated at 30 rpm in an anti-clockwise direction.

The comparison shown in Fig. 4(a–c) for the cases of fixed depth $z = 200$ mm and different distances r of 100 mm, 250 mm and 400 mm, indicates that the tribometer is naturally subjected to an increasing velocity regime as distance r increases. As a result, the pressure loading imposed by the media in front of the tribometer rises. The plots of pressure loading measured by the tribometer button in Fig. 5(a) show a good comparison between the simulations (ANSYS Fluent and CFX) and the experiment whereby the pressure increases from just over 25 kPa to nearly 50 kPa in a near linear fashion. The pressure measured in the experiment for the case of $r = 250$ mm and $z = 200$ mm is, however, lower than the one predicted by simulations.

For cases with fixed distance r and different depth z , the plots of velocity contours in Fig. 4(d–f) shows no remarkable differences. The comparison of pressure loading for different depth z in Fig. 5 shows that while the simulations from two CFD solvers matching quite well, the measurement by experiment for $z = 100$ mm is much lower than those of the simulations. For different angle θ , the low velocity region associated with the stagnation point changes (Fig. 4(g–i)). As the angle θ increases, the tribometer button experiences more of shear flow and becomes less stagnated. Consequently, Fig. 5(c) indicated that the pressure loading on this surface decreases. However, the simulation using ANSYS Fluent suggests that the pressure loading imposed on the tribometer is the highest when the glancing angle θ is around 15° .

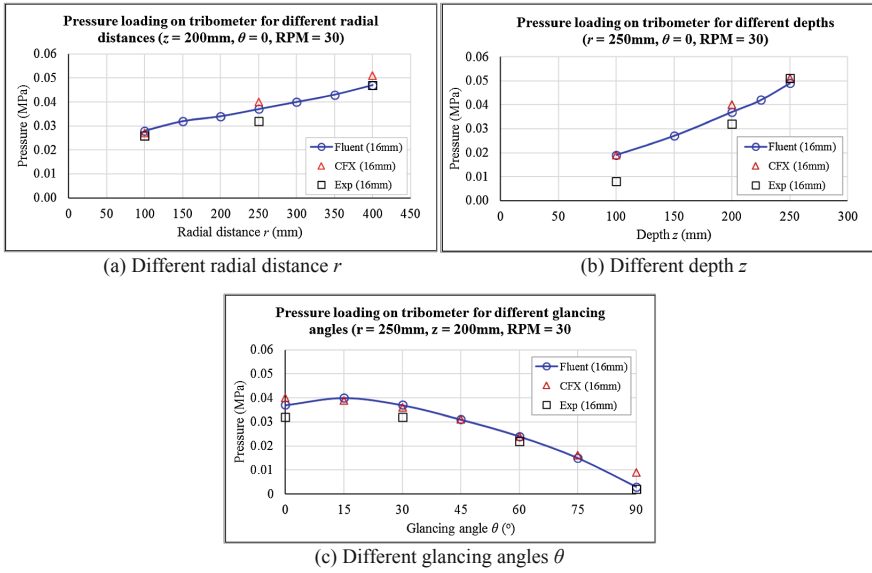


Fig. 5. Plots of pressure loading on the tribometer for different radial distances r , depths z and glancing angles θ . The comparison suggests that the prediction by simulations shows a similar trend as measured in the experiment.

4 Flow Dynamics and Velocity Comparison

A simplified square work piece was submerged in the media particles such that the middle of the work piece was at depth $z = 100$ mm from the free surface. The drum was rotated at 30 rpm in the anti-clockwise direction. The primary aims are: (1) to measure the velocity of the media particles that are in contact with the work piece surface, and (2) to compare the velocity measured in the experiment and that from the CFD simulations in which the rheology model has been incorporated. This work piece was made of glass that is hard enough to withstand the pressure imposed by the media flow, and must be transparent for a small Go-Pro camera to be inserted to record the particle flow.

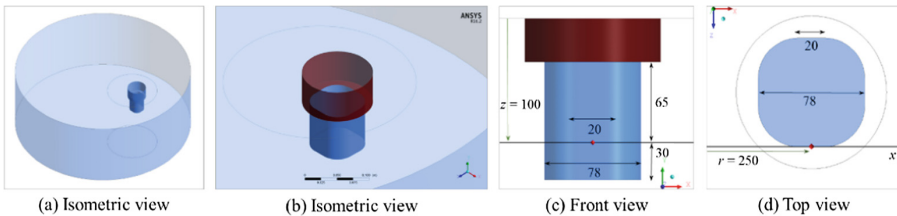


Fig. 6. The schematic of the computational domain of the simple square work piece inside a stream finishing drum showing the isometric, front and top views. Dimensions are in mm.

Figure 6 illustrates the schematic of the case study and the domain for the CFD simulations. Note that the square work piece model is not a perfect square, similar to the one used in the experiment. The width of its flat surface is only about 20 mm but for the present work it was deemed sufficient. For this case, the square work piece was placed at a distance $r = 250$ mm from the centre of the drum. Four cases have been simulated based on the glancing angle θ . To obtain the angle, the front of the work piece was rotated in the anti-clockwise direction with respect to the vertical axis passing through the coordinate point of (250 mm, -100 mm, 0).

We first compared the velocity profile of the media along the radial distance of the drum for 30 rpm speed when subjected to a semi-submerged work piece. Note that in the experiment, the velocity was measured on the free surface. However, in the simulation it was measured at a depth of 100 mm because the free surface was not modelled. Away from the work piece, we found that the velocity profiles from the experiment and simulation agrees well. It follows the $v = r\omega$ relation. However, in the region about 50 mm away from the work piece, the profiles start to deviate. The disparities are associated with the creation of the humps and dips on the free surface in the experiment, which do not occur in the simulation as the evolution of the free surface due to the flow was not modelled.

Figure 7 shows the comparison of velocity contours on the horizontal cut plane for different glancing angles θ . When the media hits the work piece, it creates a stagnation region and the media is directed to flow around the surface. As the work piece is rotated and angle θ increases, the shape of the stagnation region changes slightly. Consequently, the front of the work piece experiences more shear as the flow passes through and the velocity magnitude recorded on this surface increases.

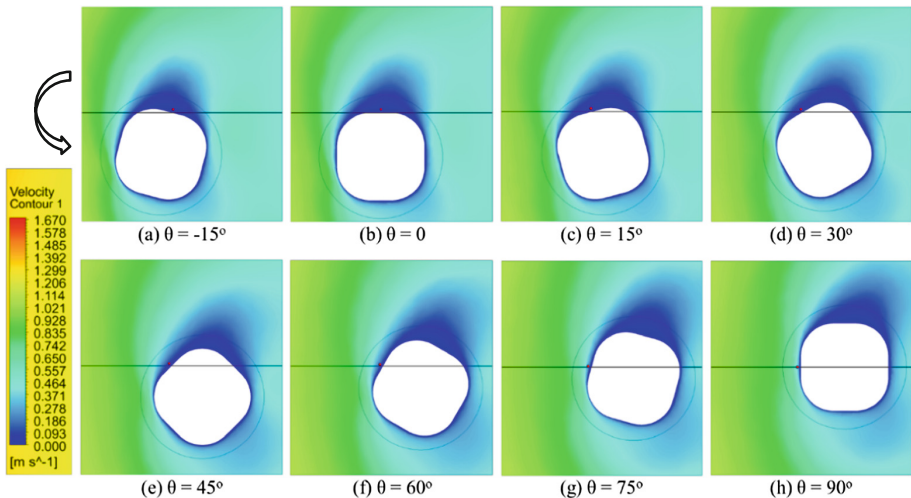


Fig. 7. Close-up (top) views of the velocity contours plotted on the horizontal cut planes for different glancing angles θ of the work piece with $r = 250$ mm, $z = 100$ mm and 30 rpm. The red dots indicate the location where the velocity of particle in front of the work piece is recorded. The horizontal line indicates the positive x axis and the flow direction is indicated by the arrow.

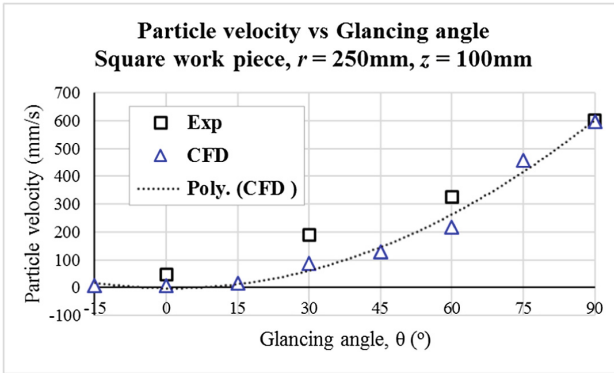


Fig. 8. Plot of particle velocity versus glancing angles of the square work piece with distance $r = 250$ mm, depth $z = 100$ mm and rotational speed of 30 rpm.

In the experiment, owing to the nature of the particles, there are voids between particles that may affect how the particles move. The particles may rotate and tumble while sliding on the surface of the work piece. To take into account the particle shape (blunt conical shape with 6 mm size), their rotations and tumbling, the velocity measurement for the comparison with the experimental results is taken at the distance of 5 mm in front of the surface of the work piece. The velocity versus glancing angle θ is plotted in Fig. 8. Note that a polynomial line of the simulation result is also shown. From the simulations, the velocity appears to increase in a near polynomial fashion, reaching the maximum of about 600 mm/s at around angle $\theta = 90^\circ$. The velocity magnitude is influenced by the shape of the work piece. When we compare the CFD result with that of the experiment, the plots show a similar trend but there is a significant disparity especially at the 30° and 60° glancing angles.

5 Conclusions

We have developed the rheology model on stream finishing, calibrated the rheology model by means of comparison with a tribometer and predicted the flow field of granular flow. For the calibration of the rheology model, three parametric studies were performed. By comparing the pressure imposed by the granular flow on the tribometer, we were able to estimate the constants, i.e. $\mu_1 = 0.35$, $\mu_2 = 0.65$, $I_0 = 0.3$. From the study of the flow around a transparent work piece model (simple square), the granular velocity along the drum centre line is similar to that of experiment for locations away from the work piece to satisfies the $v = r\omega$ relationship (v is velocity, r is radial distance and ω is angular velocity). In the vicinity of the work piece, although CFD simulation generally predicts a correct velocity profile, there exists small disparities compared to the experiment, which may be attributed to the location of the velocity measurement. The plots of velocity versus glancing angle θ show that the velocity


increases in a near polynomial fashion, and the ones predicted by simulations are comparable to those of experiments. The work presented here demonstrates that the rheology model we developed is able to simulate the correct granular flow field and predict its flow variables.

References

1. Cariapa, V., Park, H.J., Kim, J.S., Cheng, C.J., Evaristo, A.: Development of a metal removal model using spherical ceramic media in a centrifugal disk mass finishing machine. *Int. J. Adv. Manuf. Technol.* **39**, 92–106 (2008)
2. Fleischhauer, E., Azimi, F., Tkacik, P., Keanini, R., Mullany, B.: Application of particle image velocimetry (PIV) to vibrational finishing. *J. Mater. Process. Technol.* **229**, 322–328 (2016)
3. Hashimoto, F., Johnson, S.P., Chaudhari, R.G.: Modeling of material removal mechanism in vibratory finishing process. *CIRP Ann.* **65**(1), 325–328 (2016)
4. Ten, J.Y., Wan, S.: Benchmarking study on continuum-based granular flow dynamics models for simulating the drag finishing process on a CFD framework. *Int. J. Abras. Technol.* **6**(3), 214–225 (2014)
5. Wan, S., Fong, W.S., Tay, Z.H.: Process modelling and simulation of vibratory finishing of fixtured components. In: *Proceedings of the 10th European Society for Precision Engineering and Nanotechnology (EUSPEN)*, vol. 2, pp. 269–273 (2010)
6. Wan, S., Liu, Y.C., Woon, K.S., Tnay, G.L.: A material removal and surface roughness evolution model for loose abrasive polishing of free form surfaces. *Int. J. Abras. Technol.* **6**(4), 269–285 (2014)
7. Wan, S., Liu, Y.C., Woon, K.S.: A simple general process model for vibratory finishing. *Int. J. Adv. Manuf. Technol.* **86**(9), 2393–2400 (2016)
8. Jop, P., Fonterre, Y., Pouliquen, O.: A constitutive law for dense granular flow. *Nature* **441**, 727–730 (2006)
9. Daniel, R.C., Poloski, A.P., Saez, A.E.: A continuum constitutive for cohesionless granular flows. *Chem. Eng. Sci.* **62**(5), 1343–1350 (2007)
10. Itoh, S., Ho, J., Turangan, C., Wan, S.: In situ measurement of granular pressure and velocity on component surfaces in stream finishing. *INCASE2019*, Paper ID025 (2019)



Effects of Combined Wear Mechanisms in Internal Surface Finishing Using Controlled Hydrodynamic Cavitation Abrasive Finishing Process

Arun Prasanth Nagalingam^{1,2}  and Swee Hock Yeo^{1,2}

¹ School of Mechanical and Aerospace Engineering, Nanyang Technological University, 50 Nanyang Avenue, Singapore 639798, Singapore

NA0003TH@e.ntu.edu.sg

² Rolls-Royce@NTU Corporate Lab, N3.1-B2a-01, 50 Nanyang Avenue, Singapore 639798, Singapore

Abstract. Controlled hydrodynamic cavitation abrasive finishing (HCAF) process is presented as a new approach for surface finishing the internal surfaces of mechanical components. A recirculating hydrodynamic apparatus is designed and developed to generate controlled cavitation. Experiments are conducted on the internal channels fabricated using electric discharge machining (EDM). Firstly, the surface wear arising from the combined effects of controlled hydrodynamic cavitation and abrasive particles are investigated at (a) non-cavitating condition without abrasive particle, (b) cavitating condition without abrasive particles (c) abrasion condition without cavitation and (d) combined cavitation and abrasion condition. The effect of various operating conditions on the material removal are discussed. Lastly, the improvements in profile surface roughness (R_a) of the internal channels is characterized using optical profilometer. The results obtained ($R_a < 1 \mu\text{m}$) clearly shows that the combined effect of controlled cavitation and abrasive particles has a significant effect on the surface roughness reduction of internal surfaces.

Keywords: Internal surface finishing · Surface modification · Abrasive finishing · Surface polishing · Surface morphology · Surface texture

1 Introduction

Precision surface finish is often required for components used in mechanical industries. In specific, components that have complex internal channels demand a smooth surface finish less than $1 \mu\text{m}$. Achieving precision surface finishing in internal channels by using controlled material removal methods is possible using techniques like abrasive flow machining and its variants, electrochemical polishing and magnetic polishing techniques. However, maintaining the resulting geometric conformance of the components after surface finishing complex internal channels is still a challenge.

Hydrodynamic cavitation abrasive finishing (HCAF) technique is recently proposed as a potential technique for internal surface finishing of additive manufactured

components [1]. Hydrodynamic cavitation in hydraulic equipment's is considered as a destructive mechanism as it imparts damage to valves, pumps and turbine machineries [2, 3]. Micro-cavitation bubbles are generated as the hydrostatic pressure of fluid reaches the vapor pressure at a given temperature [4]. These micro bubbles entrap vapor inside them and grow to a certain size. As the pressure regains above the vapor pressure of the fluid, these vapor bubbles collapse generating high temperature and pressure [5]. It is also well known that cavitation collapse near a solid boundary generates micro-jets and imparts damage on the surface. Damage imparted on the surface is highly dependent on the target material properties [6]. It is understood that cavitation damage on metals occur in stages such as incubation stage, acceleration stage, maximum erosion stage and deceleration stage. During each stage the amount of deformation/damage to the solid surface varies [7].

Damage and erosion created due to cavitation is of high interest to researchers from early ages. Most of the cavitation studies are focused to identify material behavior under cavitation impacts [8]. This is used to select an appropriate material for a functional component that experiences cavitation. Apart from erosion studies cavitation is widely used as a constructive tool in ultrasonic machining [9], cavitation drilling [10], cavitation peening for enhancing machining properties [11]. In all the above applications the surface under exposure to cavitation impacts will be pre-polished/machined up to few microns. Hence cavitation bubble collapse erodes the surface and it is considered as a damage to the material under investigation.

Alternatively, many studies have currently focused to use cavitation effects as a potential tool for surface enhancement (e.g. Surface roughness). Cavitation nucleation on the surfaces is reported to be dependent on the initial surface integrity of the component. Hence, after cavitation erosion most of the irregularities in the surface are removed and a better surface finishing effect is achieved [1]. Another study using hydrodynamic cavitation jet on an external surface has showed that cavitation can be used as a surface finishing tool. Hydrodynamic cavitation jets are widely used as an addition to enhance the material removal rate in applications such as external surface polishing, ultrasonic lapping and ultrasonic cavitation finishing [12].

In most of the studies, abrasive media is used to provide the finishing effect to the target surface. It is also thought that addition of micro-abrasive particles in a hydrodynamic flow will act as cavitation nucleation spots and increase the intensity of cavitation [13]. Cavitation erosion on a surface with large surface roughness values could potentially remove the irregularities present and addition of abrasives would generate a smooth surface finish. Therefore, in this contribution, the combined effects involved in a cavitating flow entrained with abrasive particles will be studied. Internal channels manufactured using electric discharge machining process will be used for surface finishing. The enhancements in mass loss, thickness removal and the percentage improvements in surface finish will be investigated at pure cavitation erosion and with combined cavitation erosion and abrasion conditions.

2 Machine, Method and Materials

2.1 Experimental Setup

The combined effects of cavitation erosion and abrasive wear in internal channels are tested using a newly designed and developed hydrodynamic cavitation abrasive finishing apparatus. The apparatus as shown in Fig. 1 consists of a pump to drive the working fluid in the hydrodynamic loop. The specimens to be tested are secured firmly in the hydrodynamic cavitation abrasive finishing chamber. A cavitation inducer (orifice in this case) is placed in front of the HCAF chamber to generate cavitation effects. The HCAF chamber consists of upstream and downstream pressure control valves to control the pressure conditions prevailing during the finishing process. The apparatus consists of a flow meter, upstream and downstream pressure gauges to monitor the flow conditions. A temperature controller is provided to control the temperature fluctuations within $\pm 2.5^\circ$ during the entire finishing process. A tank with two partitions, one to hold tap water and the other to hold abrasive slurry is used. A stirrer is provided in the slurry partition to maintain homogeneity in the slurry during the finishing process.

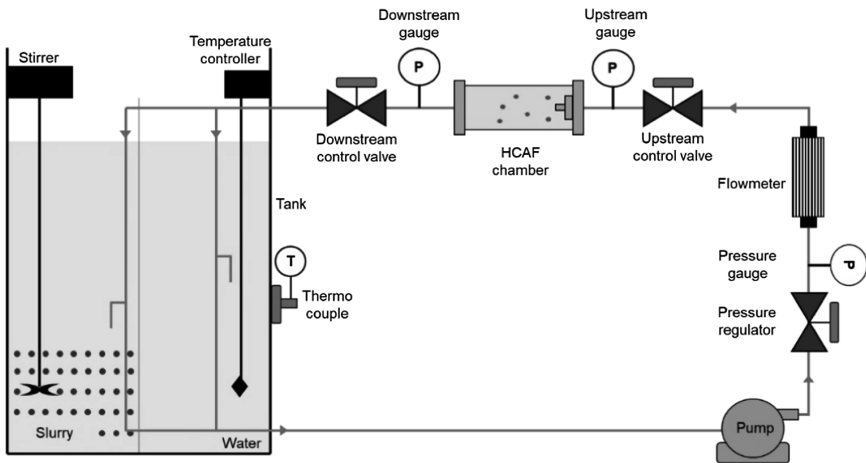


Fig. 1. Hydrodynamic cavitation abrasive finishing setup.

A detailed view of the HCAF chamber is shown in Fig. 2. The HCAF chamber is 200 mm in length and the internal diameter is about 40 mm. A cavitation inducer with a circular opening ($\text{Ø}5$ mm) at the centre is used for generating cavitation. Due to pressure reduction at the cavitation inducer, micro-cavitation bubbles start to nucleate from the cavitation inducer and travel along the flow direction. The internal channels to be surface finished are secured behind the cavitation inducer as shown in Fig. 2. The micro-cavitation bubbles nucleating from the cavitation inducer travel inside the channels and gradually erodes the inner surface upon collapse.

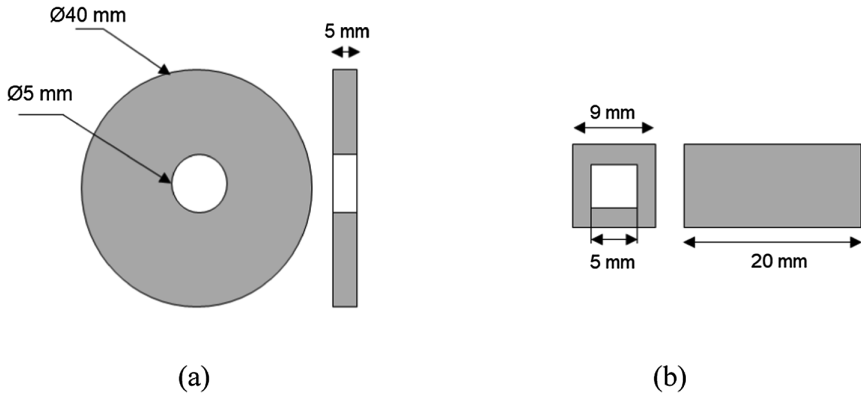


Fig. 2. (a) Cavitation inducer and (b) workpiece dimensions.

2.2 Experimental Procedure

The workpieces to be used for testing were fabricated from electric discharge machining (EDM) process. Al6061-T6 was selected as the work material to identify the combined effects. Al6061 is reported to be less resistant to cavitation erosion [2] as well as abrasion mechanisms, hence the wear effects of combined cavitation erosion and abrasion can be identified within a short duration (processing time). The effective finishing time required to achieve the desired $R_a < 1 \mu\text{m}$ was found to be 150 min from prior experience. Therefore, in this work the combined effects are to be identified within the first 150 min. The combined effects beyond 150 min are not considered as it does not aid in enhancing the surface finish. The workpieces are sliced into two halves and cleaned in an ultrasonic cleaner for 15 min and subjected to surface roughness analysis. Profile surface roughness measurements were taken along the workpiece internal surfaces according to ISO 4288. Lastly, the surface morphology of certain demarcated zones in the surface were examined under a scanning electron microscope (SEM). Such localized surface morphological observations helped realize the process effects better.

To evaluate the combined wear effects in HCAF process, experiments were performed in four different conditions namely at (a) non-cavitating condition without abrasive particle, (b) cavitating condition without abrasive particles (c) abrasion condition without cavitation and (d) combined cavitation and abrasion condition. In order to establish the above conditions, suitable process parameters were selected considering the operating range of HCAF apparatus and are listed in Table 1.

Table 1. Experiment plan.

Processing condition	Parameter level
Liquid impingement (No cavitation + No abrasion)	Pu - 0.2 MPa; Pd - 0.1 MPa; T - 55 ± 2.5 °C; Ac - 0%
Abrasion	Pu - 0.2 MPa; Pd - 0.1 MPa; T - 55 ± 2.5 °C; Ac - 1%
Cavitation erosion	Pu - 0.7 MPa; Pd - 0.1 MPa; T - 55 ± 2.5 °C; Ac - 0%
HCAF (cavitation erosion + abrasion)	Pu - 0.7 MPa; Pd - 0.1 MPa; T - 55 ± 2.5 °C; Ac - 1%

3 Results

3.1 Effect of Combined Wear Mechanisms in Material Removal

The mass loss observed during each finishing conditions at predetermined measurement intervals are shown in Fig. 3. Liquid impingement tests carried out with tap water showed no mass loss throughout the finishing process. This finishing condition is similar to fluid flowing along the pipe. As a next step, the upstream pressure was increased to 0.7 MPa by maintaining downstream pressure at 0.1 MPa. At this condition, due to pressure fluctuations at the cavitation inducer, micro-cavitation bubbles were generated in the flow. A total mass loss of 13.9 mg was recorded. This mass loss was attributed by the micro-jet impact due to cavitation collapse on the workpiece surface. Abrasives particles (silicon carbide, size 10 μm , 1% wt. conc) were then added into the flow. The upstream pressure was reduced to 0.2 MPa to achieve non-cavitation and abrasion condition. At this condition a total mass loss of 3.4 mg was observed. This gradual increase in mass loss as compared to liquid impingement conditions must be attributed by the presence of sharp-edged abrasive particles in the flow. Finally, the upstream pressure was set at 0.7 MPa and downstream pressure to 0.1 MPa to achieve cavitating as well as abrasion conditions. This gives rise to combined hydrodynamic cavitation abrasive finishing conditions. A total mass loss of 40.6 mg that is about 235% more mass loss compared to the total of pure cavitation and pure abrasion conditions. This shows that there is a strong synergistic effect in HCAF process.

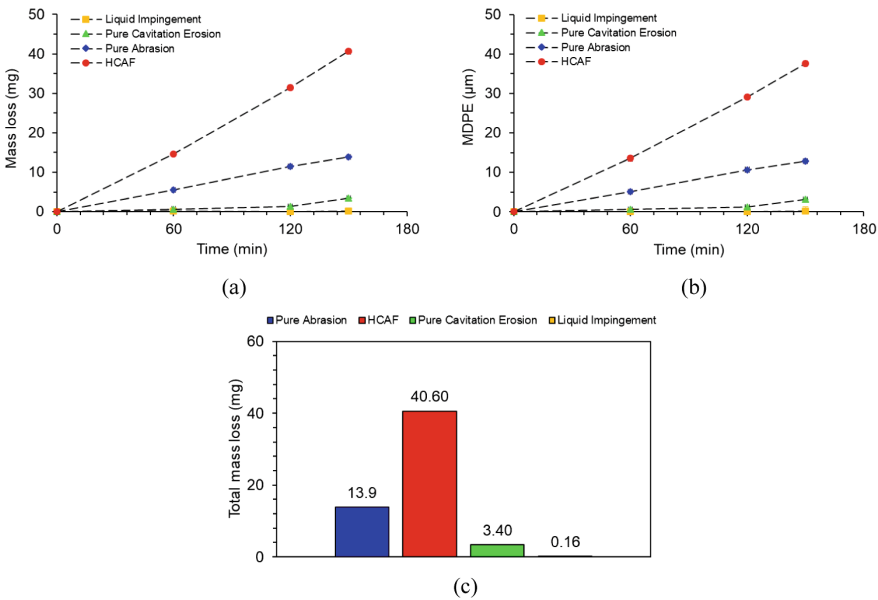


Fig. 3. (a) Mass loss over time (b) mean depth of erosion over time and (c) total mass loss in each finishing mode.

3.2 Effect of Combined Wear Mechanisms in Surface Enhancement

Percentage improvements in each finishing condition over time are shown in Fig. 4. Profile surface texture changes were measured at every 60 min and the percentage improvement is calculated. From Fig. 4, roughness improvements can be seen for all finishing conditions. The percentage change in surface roughness gradually improves with each finishing condition. The large deviations in the percentage change during

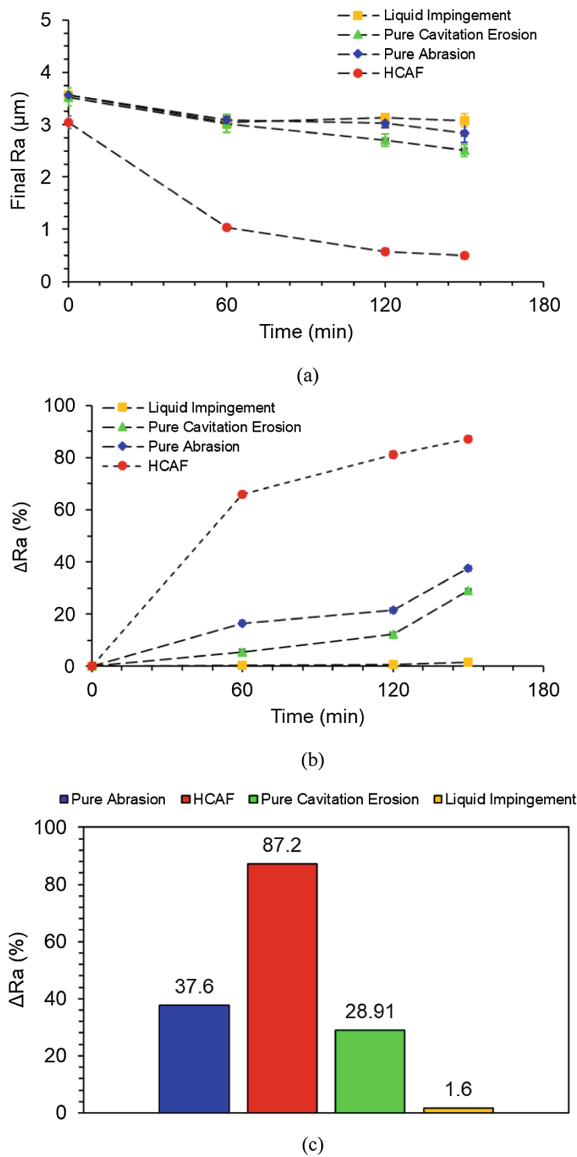


Fig. 4. (a) Percentage change in profile surface texture over time; (b) final Ra over time and (c) overall percentage change.

liquid impingement (no cavitation + no abrasion) is due the error involved in measurements. However, a maximum improvement of 87.2% is seen during HCAF condition. The improvements in surface roughness change during HCAF is 130% higher compared to the sum of pure cavitation and pure abrasion conditions. Relating Figs. 3(c) and 4(c) it is very evident that the change in surface roughness is due to increase in material removal from the internal surfaces of the workpiece.

4 Discussion

To understand the mechanism behind surface finishing in HCAF process, the surface morphological transformations due to cavitation erosion and abrasion must be understood. Figure 5 shows the resulting surface morphology of the specimens after various processing conditions. It can be seen that for the no cavitation and no abrasion condition, the surface morphology after 150 min remains the same as that of EDM surface. Surface morphology after pure abrasion condition contains lot of material fragments. This confirms that the mass loss obtained must be due to material removal by abrasive particles in the non-cavitating flow. It can also be noticed that the surface morphology of the workpiece after pure cavitation erosion contains a unique wavy pattern. These types of undulations arise from erosion due to repeated cavitation collapse. Lastly, the surface after HCAF process with 1% abrasive concentration shows that the surface is smooth without any wavy undulations. This is because the abrasive

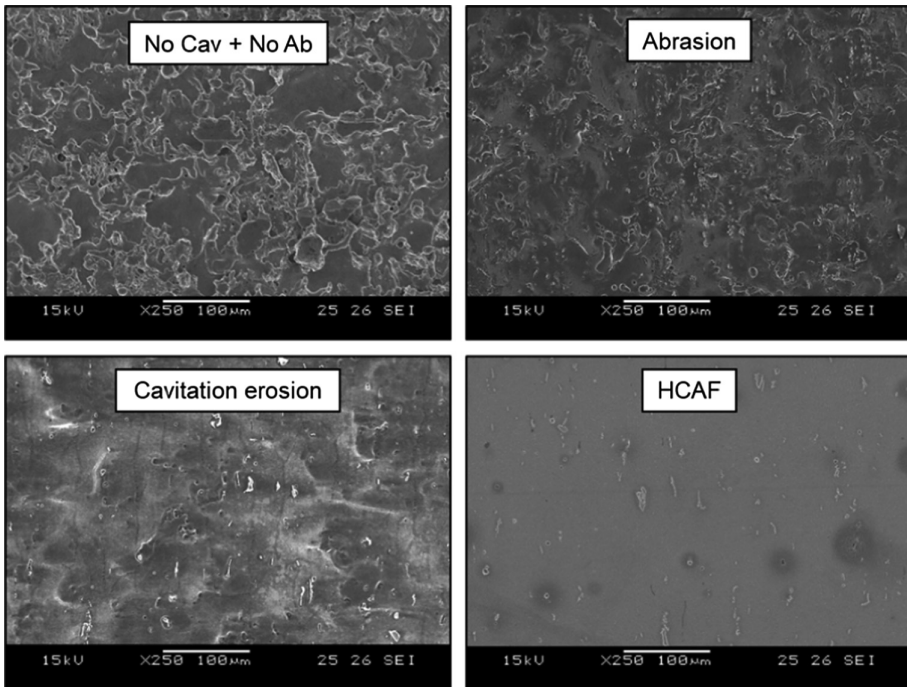


Fig. 5. Surface morphology of internal channels after various processing conditions.

particles would have sheared off any peaks present while flowing past the surface. The calculated mean depth of erosion during HCAF process is found to be $\sim 40 \mu\text{m}$ as seen in Fig. 3(b). Therefore, it can be concluded that the typical recast layer thickness (30 to $50 \mu\text{m}$) arising from EDM process are completely removed after HCAF process.

To further understand the morphology transformations due to cavitation erosion, the surface was viewed under microscope at predetermined intervals. Figure 6 shows the surface morphology changes due to cavitation erosion with respect to time. During the first 60 min it can be observed that the surface experienced minor erosion characteristics. The remains of recast layer still seem to be visible at 60 min partially. At 120 min, the surface can be found free of asperities such as fragments, melt deposits arising due to EDM. However, plastic undulations were noticed across the entire workpiece surface. At 150 min, the surface was found to be eroded severely due to cavitation with the presence of deep cavitation pits and surface cracks with predominant undulations across the surface.

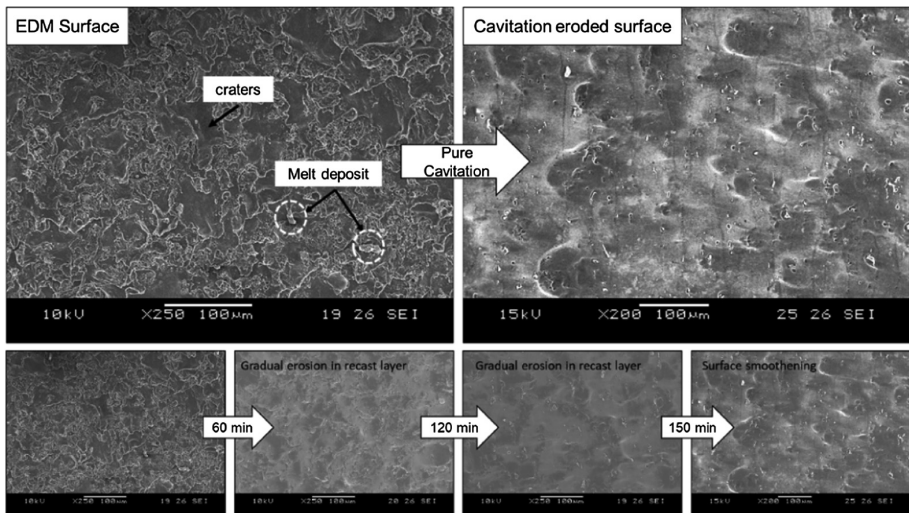


Fig. 6. Surface morphology of internal channels after pure cavitation erosion.

The surface morphology evolution through abrasive-assisted cavitation erosion is shown in Fig. 7. In this condition, a significant smoothing of the workpiece surface was observed in the first 60 min. Almost (87% roughness reduction and $40 \mu\text{m}$ thickness removal) all the EDM irregularities were removed and abrasive shearing has resulted in surface smoothing. In HCAF conditions, wavy undulations and material fragments were not noticed. Due to high-velocity flow, cavitation erosion and abrasive micro-cutting the surface roughness significantly reduced. At higher magnifications abrasive micro-cutting was clearly noticed. This shows that the abrasive micro-cutting mechanism dominates in the process due to high-velocity impact and accelerated abrasive impacts due to shock waves arising from cavitation implosion. Therefore, it is evident that the effects of cavitation combined with abrasive particles accelerated the erosion process and resulted in smooth surface.

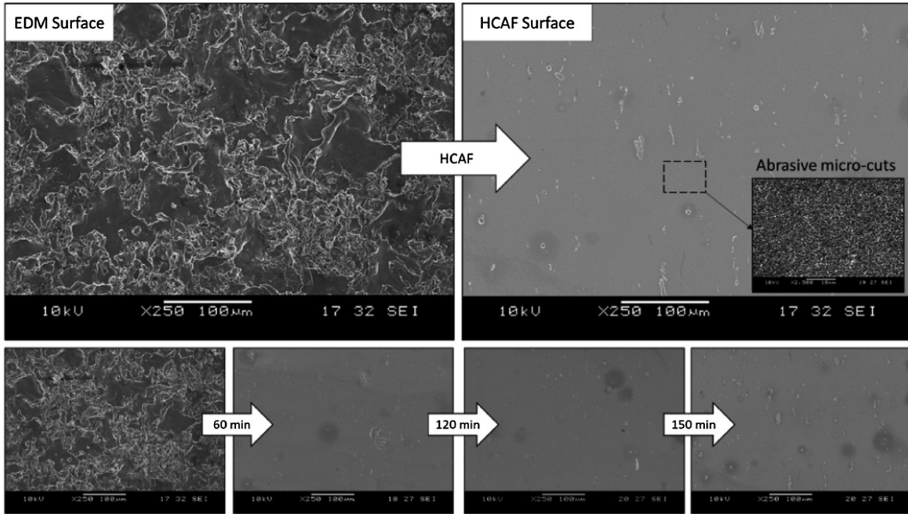


Fig. 7. Surface morphology of internal channels after pure cavitation erosion.

5 Conclusion

The effects of combined wear mechanism involved in hydrodynamic cavitation abrasive finishing process is determined by investigating the material removal and surface morphology characteristics under various conditions such as (a) liquid impingement (no cavitation + no abrasion); (b) pure abrasion; (c) pure cavitation erosion and (d) HCAF (abrasive assisted cavitation erosion). The surface wear arising through combined cavitation and abrasion were found to enhance the material removal by 130% and roughness improvements by 250% compared to pure cavitation and pure abrasion alone. This shows that the addition of micro-abrasives in a cavitating flow has led to increase in cavitation nucleation. In another way, shock waves arising from cavitation implosion have accelerated the abrasive impacts thereby accelerating the wear process enhancing the surface finishing achieved. A consistent and uniform profile surface roughness $R_a < 1 \mu\text{m}$ achieved shows that HCAF process can be potentially used for internal surface finishing applications.




Acknowledgement. This work was conducted within the Rolls-Royce@NTU Corporate Lab with support from the National Research Foundation (NRF) Singapore under the Corp Lab@ University Scheme. The authors would like to thank Dr-Ing Thomas Haubold (Rolls-Royce, Deutschland) and MRP 1.1 team members (Rolls-Royce@NTU Corporate lab, Singapore) for their contributions.

References

1. Nagalingam, A.P., Yeo, S.H.: Controlled hydrodynamic cavitation erosion with abrasive particles for internal surface modification of additive manufactured components. *Wear* **414–415**, 89–100 (2018)
2. Sreedhar, B.K., Albert, S.K., Pandit, A.B.: Cavitation damage: theory and measurements – a review. *Wear* **372–373**, 177–196 (2017)
3. Wu, D., et al.: Experimental study on hydrodynamic performance of a cavitating centrifugal pump during transient operation. *J. Mech. Sci. Technol.* **24**(2), 575–582 (2010)
4. Brennen, C.E.: *Cavitation and Bubble Dynamics*. Oxford University Press, Oxford (1995)
5. Abouel-Kasem, A., Ahmed, S.M.: Cavitation erosion mechanism based on analysis of erosion particles. *J. Tribol.* **130**(3), 031601 (2008)
6. Caccese, V., Light, K.H., Berube, K.A.: Cavitation erosion resistance of various material systems. *Ships Offshore Struct.* **1**(4), 309–322 (2006)
7. Zhu, Y., et al.: A study on surface topography in cavitation erosion tests of AlSi10Mg. *Tribol. Int.* **102**, 419–428 (2016)
8. Laguna-Camacho, J.R., et al.: A study of cavitation erosion on engineering materials. *Wear* **301**(1–2), 467–476 (2013)
9. Thoe, T.B., Aspinwall, D.K., Wise, M.L.H.: Review on ultrasonic machining. *Int. J. Mach. Tools Manuf.* **38**(4), 239–255 (1998)
10. Li, Z.: Criteria for jet cavitation and cavitation jet drilling. *Int. J. Rock Mech. Min. Sci.* **71**, 204–207 (2014)
11. Soyama, H.: Surface mechanics design by cavitation peening. *J. Eng.* **13**, 110–114 (2015)
12. Hutli, E., et al.: The ability of using the cavitation phenomenon as a tool to modify the surface characteristics in micro- and in nano-level. *Tribol. Int.* **101**, 88–97 (2016)
13. Santa, J.F., et al.: Slurry and cavitation erosion resistance of thermal spray coatings. *Wear* **267**(1–4), 160–167 (2009)



Surface Integrity Characteristics of NiTiHf High Temperature Shape Memory Alloys

Yusuf Kaynak¹ , Emre Tascioglu¹ , and Othmane Benafan² 

¹ Department of Mechanical Engineering, Marmara University,
Goztepe Campus, Kadikoy, 34722 Istanbul, Turkey
yusuf.kaynak@marmara.edu.tr

² Materials and Structure Division, NASA Glenn Research Center,
Cleveland, OH 44135, USA

Abstract. This present study focuses on the surface integrity characteristics of the machined NiTiHf high temperature shape memory alloys. The NiTiHf specimens were machined under dry, minimum quantity lubrication (MQL) and cryogenic cooling at two different cutting speeds. Experimental data on microhardness, latent heat and phase transformation temperature is presented and analyzed to evaluate the surface and subsurface characteristics of the machined NiTiHf specimens. It is found that machining process particularly cryogenic machining alters microhardness, latent heat and phase transformation temperature of Ni-rich NiTiHf alloy. This study demonstrates that cryogenic machining process leads to occurring strain hardened layer on the surface and subsurface of machined workpiece. Phase transformation response including transformation temperature and latent heat for transformation of this affected layer shows significant difference comparing with the bulk of the workpiece. This difference is evidently observed from the cryogenically machined specimens than the specimens machined under dry and MQL conditions.

Keywords: Surface integrity · High temperature shape memory alloys · Machining · Phase transformation

1 Introduction

Demand for lightweight and compact actuators in various industries particularly aerospace has increased [1]. Solid-state shape memory alloy (SMA) actuators are promising candidates as replacement for the electrical motor or hydraulic systems in weight and space critical applications since they offer the highest energy density among all known active materials and systems [1, 2]. While NiTi SMAs are the most widely used and commercially available SMAs, they typically have low phase transformation temperature so that they do not meet the high temperature actuators in hot environment [3]. In order to increase transformation temperature for NiTi alloy, the common way is to add ternary alloying elements such as Zr, Pd, Hf, Pt, and Au [4] that creates high temperature shape memory alloys (HTSMAs). They have vast potential in a wide range of applications spanning the aerospace, automotive, and other industries [5].

Ni-rich NiTiHf alloys were found to exhibit superior properties and dimensional stability among all HTSMAs [5]. However, one of the issues impeding greater acceptance of HTSMA technology is the need for improvements in manufacturing and fabrication techniques. The major manufacturing techniques including turning, milling, and drilling are still used for developing bulk actuators [6]. However, shape memory alloys are very sensitive to temperature changes near the transformation regime [7] and it is well established that machining has serious impacts on the final properties of machined components [8]. Considering this fact, it is essential that the machining characteristics of HTSMAs, particularly the effects of machining process on the shape memory behavior and surface integrity characteristics needs to be systematically investigated to establish relationships between the machining process parameters and their shape memory properties, namely to determine the process-microstructure-property relationships machining process [9].

It should be noted that there is a very limited number of studies focusing on machining process of HTSMAs in particular NiTiHf alloy [10]. To the best knowledge of authors, there is no study focusing on machining-induced surface integrity characteristics of NiTiHf alloys. Therefore, this study is aimed at providing a deeper insight into the interrelationship between machining conditions and surface integrity characteristics including microhardness, latent heat and phase transformation.

2 Experimental Details

The material used in this study was a Ni-rich Ni50.3Ti29.7Hf20 (at.%) high temperature SMA. The alloy was produced using a vacuum induction skull melting technique with a heat size of ~ 27 kg (designated as FS#7). The molten metal was poured into steel molds, and the resulting cast ingots were vacuum homogenized for 72 h at 1050 °C and furnace cooled. The material was then canned and extruded at 900 °C through an area reduction ratio of 7:1. The extruded rods were centerless ground to a final diameter of 10 mm, and cut into 35 mm long pieces. A representative micrograph of the NiTiHf alloy is presented in Fig. 1, showing an average grain size of ~ 36 μm , along with some HfO_2 particles (black dots).

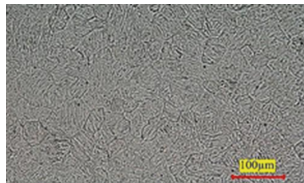


Fig. 1. Optical microscopy image of Ni-rich Ni50.3Ti29.7Hf20 (at.%) [10].

The transformation temperature of specimens was measured by using a Differential Scanning Calorimetry (DSC) at a heating and cooling rate of 5 °C min⁻¹. DSC samples were cut using a slow speed diamond saw from the surface/subsurface region of the

machined samples. The thickness of samples was approximately 300 μm after mechanical polishing. To eliminate the effect of blade cutting, the samples were mechanically polished using 800 grit SiC papers prior to DSC analysis. The NiTiHf alloy was in its martensitic phase at room temperature as determined by Differential Scanning Calorimetry (DSC) where the martensite start (M_s), martensite finish (M_f), austenite start (A_s) and austenite finish (A_f) temperatures are 94 $^\circ\text{C}$, 59 $^\circ\text{C}$, 107 $^\circ\text{C}$ and 134 $^\circ\text{C}$, respectively, as shown in Fig. 2. Microhardness measurements were performed according to ASTM E 384 standard using Future-Tech FM310e.

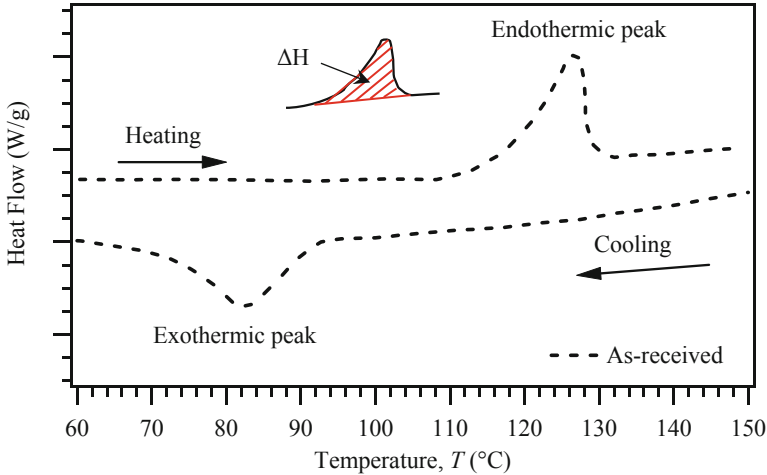


Fig. 2. DSC analysis of as-received NiTiHf alloy.

A N123H1-0500-0002-GE CB20 cutting tool insert with approximately 15 μm edge radius and the QS-LF123H100C16E tool holder with a rake angle of $\alpha = 0^\circ$ was used in the cutting experiments. The cutting experiments were conducted on a Doosan Puma GT2100 lathe CNC machine with 18 kW power and a maximum spindle speed of 4500 rpm. Orthogonal cutting tests were carried out as shown in Fig. 3.

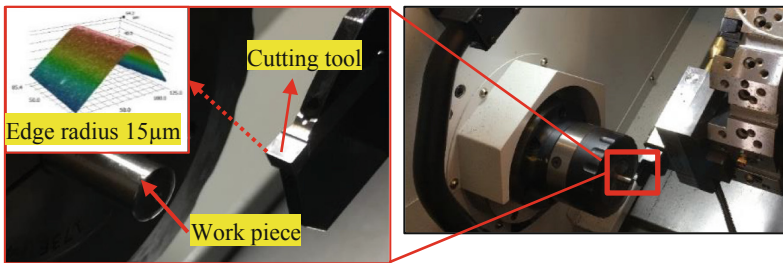


Fig. 3. Experimental setup for orthogonal cutting test.

A constant uncut chip thickness of 0.025 mm, and 7, 14 and 21 m/min cutting speeds were used during the orthogonal cutting tests. Three cutting conditions implemented in cutting tests were dry, cryogenic coolant and minimum quantity lubrication (MQL). The cryogenic coolant was liquid nitrogen (LN_2), applied under 15 bar pressure, and approximately 10 g/s mass flow rate. Liquid nitrogen was delivered to the cutting region through a nozzle with 5 mm diameter. The nozzle was placed at the rake face of the cutting tool as shown in Fig. 4. For minimum quantity lubrication (MQL), metalworking lubricant was used at a flow rate of 21 ml/h, and approximately under 0.4 MPa air pressure. MQL was applied at the rake face of the cutting tool as shown in Fig. 4.

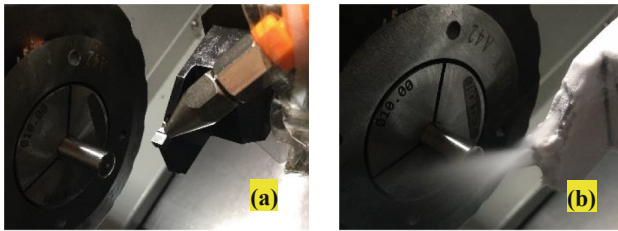


Fig. 4. MQL (a) and LN_2 (b) delivery system.

3 Results and Discussions

Figure 5 shows microhardness variation of the specimen machined under three different conditions at 7, and 21 m/min cutting speed. It is apparent that machining alters the depth 100 μm below the surface of the specimen. It is found that input variables have a profound effect on the surface and subsurface microhardness of the machined specimen. Within this layer, two trends were observed. One is the increased hardness considering the bulk hardness while another is the decreased trend. Increased hardness is attributed to the strain hardening or cold deformation however, decreased hardness can be interpreted as the thermal softening. Cryogenic machining results in increased hardness while dry and MQL conditions leads to softening at the surface and subsurface. Machining process generates high strain and temperature [11] thus the machined surface is subjected to large strains, high strain rates and high temperatures. Once liquid nitrogen is delivered to the cutting region during chip formation process, cutting region becomes very cold. This cold deformation results in large residual stress and hence retain strain due to the increased dislocation density [12]. Consequently, measured hardness is much larger than the as-received specimen. However, in dry machining (without any cooling and lubricant) and MQL machining cutting temperature naturally becomes much higher than cryogenic machining. This high temperature plays an important role to form the final microhardness on the surface and subsurface of the machined specimens. Increased temperature annihilates the residual stress and plastic strain introduced by cutting process and consequently hardness becomes much lower [9]. In addition to the cutting conditions, cutting speed also play a critical role on

the forming the final hardness of the specimen. It is well established that increased cutting speed leads to increased cutting temperature in machining shape memory alloys [7]. This result supports this argument as the lower cutting speeds in all three conditions leads to much higher hardness than the higher cutting speeds, as shown in Fig. 5.

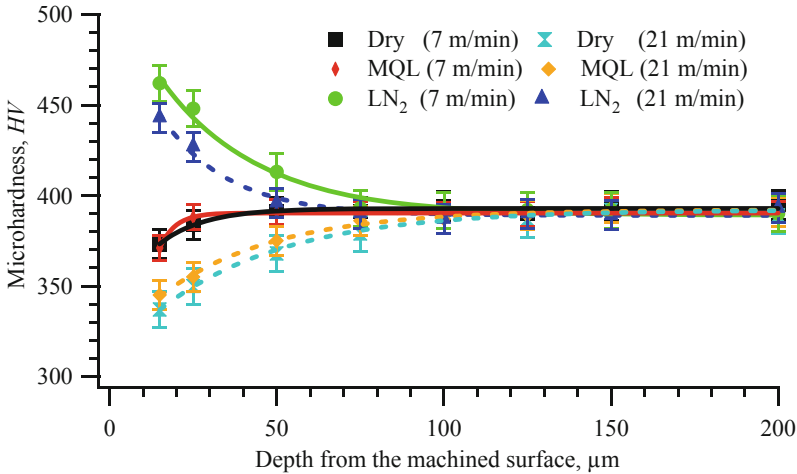


Fig. 5. Microhardness variation of the machined specimens.

DSC is a well-known tool for determining the phase transformation temperature of SMAs. DSC response of the specimens machined under various conditions and resulting phase transformation temperature is discussed in this section. The quantitative results for Austenite start (A_s), austenite finish (A_f), martensite start (M_s) and martensite finish (M_f) temperatures of the machined NiTiHf specimens is shown in Table 1.

Table 1. Phase transformation temperature of the as-received and machined specimens.

	As-received specimen	Machined specimens					
		7 m/min			21 m/min		
		Dry	MQL	LN ₂	Dry	MQL	LN ₂
A_s (°C)	107	112	108	116	112	105	113
A_f (°C)	134	133	133	135	134	131	138
M_s (°C)	94	96	96	98	95	93	99
M_f (°C)	59	66	66	74	63	64	71

Table 1 evidently shows that machined specimens have higher transformation temperature than the as-received specimen. While the A_s of the as-received specimen is 107 °C, the A_s of the specimen machined under dry condition was 112 °C. Similarly the cryogenically machined specimens at 7 and 21 m/min cutting speeds have 116 °C and 113 °C austenite start transformation temperature, respectively. Similar response is

also observed for the M_s of the specimens. While the M_f temperature of the as-received specimen is 59 °C, the M_f temperature of cryogenically machined specimen was measured as 74 °C that indicates 25% increases in the M_f transformation temperature. It should be also noted that cutting speed altered the transformation temperature of the machined specimens. In addition to the increased transformation temperature, peak broadening is also commonly observed in the DSC response of the machined specimens, as shown in Figs. 6 and 7.

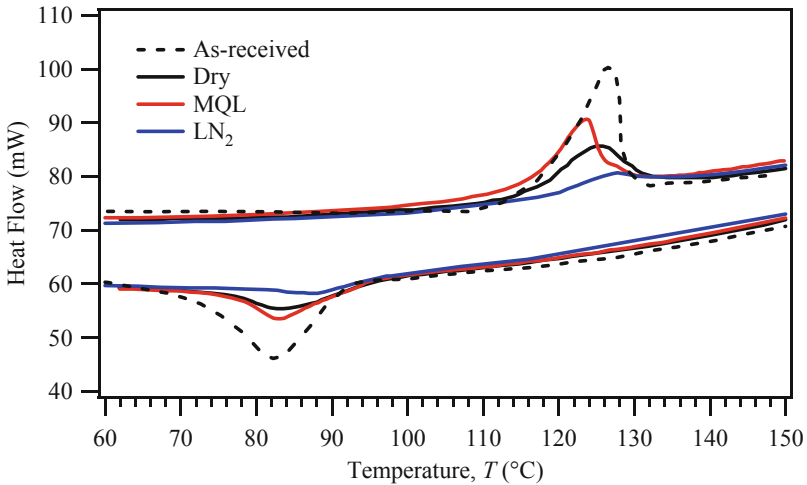


Fig. 6. DSC analysis of as-received and machined specimens (7 m/min).

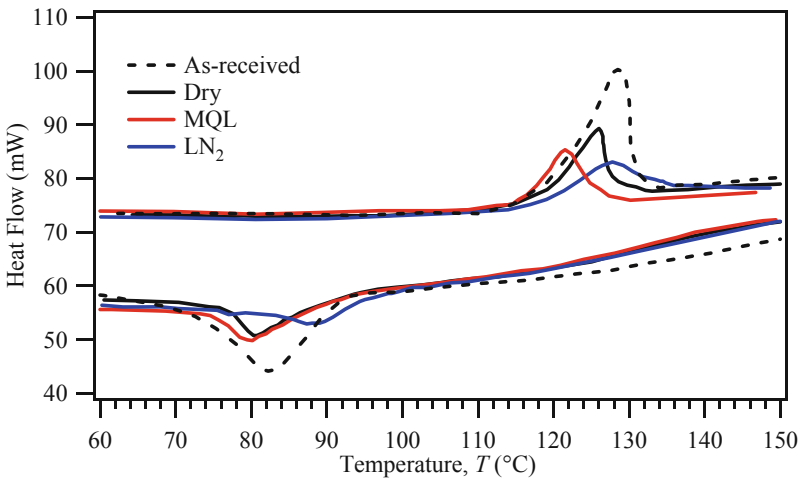


Fig. 7. DSC analysis of as-received and machined specimens (21 m/min).

The cryogenically machined specimens show the largest broadening in all three cutting conditions as depicted in Figs. 6 and 7. The latent heat for the transformation (ΔH) of the deformed layer of the specimens extracted from the DSC curves and illustrated in Figs. 8 and 9. While the latent heat for transformation of the specimens machined under dry and MQL conditions is approximately close to the as-received specimen, the latent heat for transformation of the cryogenically machined specimens for both heating and cooling at lower (7 m/min) and higher (21 m/min) cutting speeds is much lower. For example, while endothermic peak (heating) of the specimen machined under cryogenic cooling at 7 m/min cutting speed needs 4.52 J/g for the transformation, the latent heat of transformation of as received specimen needs 13.3 J/g. This large difference in between cryogenically machined specimen and as-received specimen indicates the influence of machining under cold environment on energy stored on the surface and subsurface of the specimen. It is known that the drop in the ΔH values is attributed to the dislocations inhibiting the amount of material allowed to undergo the phase transformation [13]. In this case, the higher dislocation density resulting from cryogenic machining prevents occurring full transformation. Consequently, the volume fraction of the material that undergoes transformation was much smaller and, in turn, less energy was required.

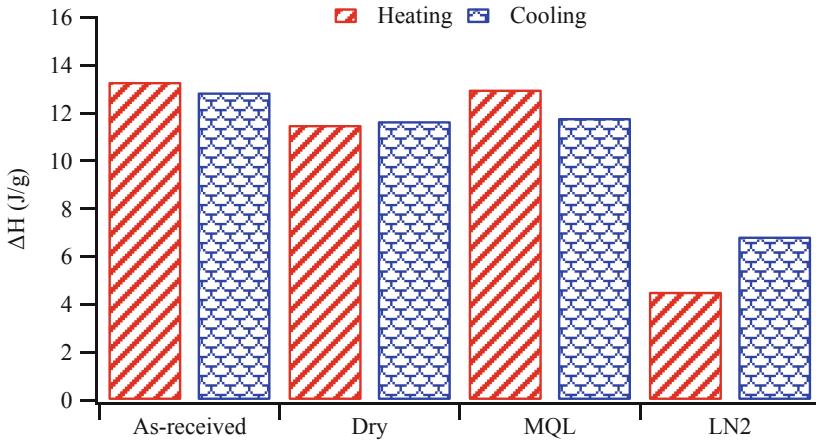


Fig. 8. Latent heat (ΔH) of as-received and machined specimens (7 m/min).

It should be noted that increased cutting speed and resulting increased cutting temperature even in cryogenic machining leads to increasing latent heat. While the latent heat for transformation of the cryogenically machined specimen is 4.52 J/g at 7 m/min cutting speed, it is 8.55 J/g at 21 m/min cutting speed. This evidently indicates the significant role of the cutting temperature for controlling the latent heat for the transformation of the machined specimen. The latent heat for the transformation of the specimens machined under dry and MQL conditions support this argument.

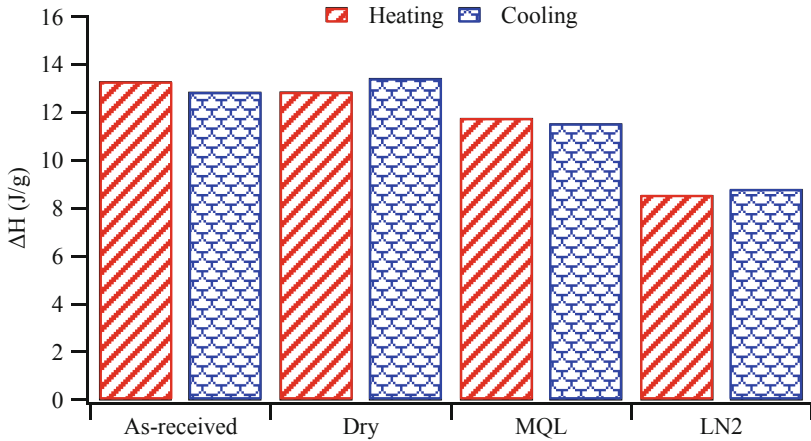


Fig. 9. Latent heat (ΔH) of as-received and machined specimens (21 m/min).

Since the cutting temperature in these two conditions were much higher than cryogenic machining, dry and MQL machining do not make remarkable impact on altering of the latent heat for the transformation of the specimens.

Microhardness variation, the shifted transformation temperature and the latent heat on the surface and subsurface of machined specimens show the consistency and good agreement. While similar responses from dry and MQL machined specimens from these measurements were observed, the response of cryogenically machined specimens showed quite difference.

4 Conclusions

This study presents the effect of machining under dry, MQL, and cryogenic cooling conditions at two different cutting speeds on microhardness, phase transformation temperature, and latent heat of NiTiHf alloy. The results presented in this paper demonstrate that machining process alters the surface and subsurface characteristics of NiTiHf alloy. If the machined NiTiHf alloy has relatively small wall thickness, then heat treatment is evidently needed to eliminate the effect of machining and consequently to generate homogeneous microstructure throughout the entire cross section. Cryogenic cooling is the most effective method that influencing the surface and subsurface characteristics of NiTiHf alloys in all three machining conditions.






Acknowledgments. Financial support from TUBITAK (The scientific and Technological Research Council of Turkey) under Project number 116M346 is greatly acknowledged. OB acknowledges support and funding from the NASA Aeronautics Research Mission Directorate (ARMD) Transformational Tools & Technologies (TTT) project.

References

1. Ma, J., Karaman, I., Noebe, R.D.: High temperature shape memory alloys. *Int. Mater. Rev.* **55**, 257–315 (2010)
2. Jani, J.M., Leary, M., Subic, A., Gibson, M.A.: A review of shape memory alloy research, applications and opportunities. *Mater. Des.* **56**, 1078–1113 (2014)
3. Hayrettin, C., Karakoc, O., Karaman, I., Mabe, J., Santamarta, R., Pons, J.: Two way shape memory effect in NiTiHf high temperature shape memory alloy tubes. *Acta Mater.* **163**, 1–13 (2019)
4. Evirgen, A., Karaman, I., Santamarta, R., Pons, J., Noebe, R.: Microstructural characterization and superelastic response of a Ni₅₀.3Ti₂₉.7Zr₂₀ high-temperature shape memory alloy. *Scr. Mater.* **81**, 12–15 (2014)
5. Benafan, O., Garg, A., Noebe, R., Bigelow, G., Padula li, S., Gaydosch, D., Schell, N., Mabe, J., Vaidyanathan, R.: Mechanical and functional behavior of a Ni-rich Ni 50.3 Ti29.7 Hf20 high temperature shape memory alloy. *Intermetallics* **50**, 94–107 (2014)
6. Benafan, O., Brown, J., Calkins, F.T., Kumar, P., Stebner, A., Turner, T., Vaidyanathan, R., Webster, J., Young, M.L.: Shape memory alloy actuator design: CASMART collaborative best practices. In: *ASME 2011 Conference on Smart Materials*, pp. 18–21 (2011)
7. Kaynak, Y., Karaca, H.E., Noebe, R.D., Jawahir, I.S.: The effect of active phase of the work material on machining performance of a NiTi shape memory alloy. *Metall. Mater. Trans. A* **46**, 2625–2636 (2015)
8. Jawahir, I.S., Brinksmeier, E., M'Saoubi, R., Aspinwall, D.K., Quteiro, J.C., Meyer, D., Umbrello, D., Jayal, A.D.: Surface integrity in material removal processes: Recent advances. *CIRP Ann. Manuf. Technol.* **60**, 603–626 (2011)
9. Kaynak, Y., Karaca, H., Jawahir, I.: Cutting speed dependent microstructure and transformation behavior of NiTi alloy in dry and cryogenic machining. *J. Mater. Eng. Perform.* **24**, 452–460 (2015)
10. Kirmacioglu, K.E., Kaynak, Y., Benafan, O.: Machinability of Ni-rich NiTiHf high temperature shape memory alloy. *Smart Mater. Struct.* **28**, 055008 (2019)
11. Oxley, P.: *Mechanics of Machining*. Ellis Horwood, Chichester (1989)
12. De la Flor, S., Urbina, C., Ferrando, F.: Effect of mechanical cycling on stabilizing the transformation behaviour of NiTi shape memory alloys. *J. Alloy. Compd.* **469**, 343–349 (2009)
13. Miller, D.A., Lagoudas, D.C.: Thermomechanical characterization of NiTiCu and NiTi SMA actuators: influence of plastic strains. *Smart Mater. Struct.* **9**, 640–652 (2000)



The Effect of Finish-Milling Operation on Surface Quality and Wear Resistance of Inconel 625 Produced by Selective Laser Melting Additive Manufacturing

Emre Tascioglu¹ , Yusuf Kaynak¹ , Özgür Poyraz² ,
Akın Orhangül² , and Soner Ören² 

¹ Department of Mechanical Engineering, Marmara University,
Goztepe Campus, Kadikoy, 34722 Istanbul, Turkey
yusuf.kaynak@marmara.edu.tr

² TUSAŞ Engine Industries Inc., 26003 Eskişehir, Turkey

Abstract. Additive Manufacturing (AM) has been recognized as a promising manufacturing technology for the industries including aerospace and biomedical; however, the surface finish requirement for the components used in such industries imposes a severe constraint. Thus, finishing process for any manufacturing operation including additive manufacturing needs to be investigated to provide insights into the finish processing-surface property relationship. In this study, finishing operation in milling process is considered as a post-processing to improve the surface, mechanical and wear properties of the specimens fabricated by selective laser melting (SLM). This study demonstrates that surface and subsurface characteristic such as surface topography, surface roughness, microhardness, and wear resistance is substantially affected from milling parameters. Finish-milling operation with the high feed rate results in 50% reduction in wear rate of the specimen fabricated by SLM process.

Keywords: Additive manufacturing · Inconel 625 · Surface quality · Wear resistance · Finish-milling

1 Introduction

Nickel based alloys are extensively used in aerospace, nuclear reactor, etc., due to high strength and resistance to corrosion in harsh environment [1]. Among all Ni-based alloys, Inconel 625 is a multi-component nickel based super alloy containing several alloying elements with a minimum of 58% nickel content is well suited to manufacture the aerospace components [2]. However, one of the significant drawbacks of Inconel 625 is that due to its high strength, it is very difficult to shape by traditional, subtractive methods [3]. Proper tools and feed rates are essential and material removal rates need to be carefully controlled to limit avoiding work hardening and chatter and machine tools tend to wear quickly [4]. Considering these points, fabricating components with complex geometry made of Inconel 625 by utilizing additive manufacturing (AM) technology particularly selective laser melting (SLM) seems to provide the vital potential.

Although design flexibility is provided by additive manufacturing [5], an extensive research and development stage is required beforehand in order to achieve end-shape parts with the required mechanical properties [6]. Mechanical properties of Inconel 625 fabricated by SLM process has been extensively studied by many researchers [1, 7–10]. The effects of heat treatments including HIP on mechanical and microstructural properties of Inconel 625 have also been reported [10–13]. Although additive manufacturing offers great advantages to produce the complex metal component, surface quality is still seen as an issue due to fact that the additively manufactured metallic parts have generally discontinuous surface characteristics and partially melted powders that substantially increase the surface roughness of the components manufactured. For this main reason, post-processing operations are essential [14]. However, there is a limited study focusing on post-processing-induced surface characteristics of Inconel 625 parts produced by SLM. Witkin et al. [15] investigated the effects of laser polishing on the surface roughness and microstructure of Inconel 625. They reported that although laser polishing improves the surface quality of the parts, it also led to the formation of an oxide film. Brown et al. [16] presented the effect of finish-milling on surface integrity of Inconel 625 parts fabricated by SLM. They also reported that milling process improves the surface quality of the parts. Literature summary illustrates that very limited studies focused on the surface and subsurface aspects of Inconel 625 resulting from post-processing operations. This study present the experimental work focusing on the effects of finish-milling operation on surface topography, roughness, microhardness of Inconel 625 specimens fabricated by SLM process. Obtained results were correlated with the wear resistance of Inconel 625 fabricated by SLM process.

2 Experimental Details

The Inconel 625 powders with the spherical shape and the particle size distribution of 15–45 μm according to ISO 13320 [17] were used to fabricate $20 \times 15 \times 15$ mm rectangular prismatic specimens. It has a chemical composition in according with UNS N06625 [17]. The specimens were built on an EOS 290 machine using 67 J/mm^3 volumetric energy density. The microstructures of the specimen fabricated by SLM are shown in Fig. 1. Finish-milling operation was carried out as a post-processing operation. During finish-milling operation, dry cutting without any cooling and lubricant was used.

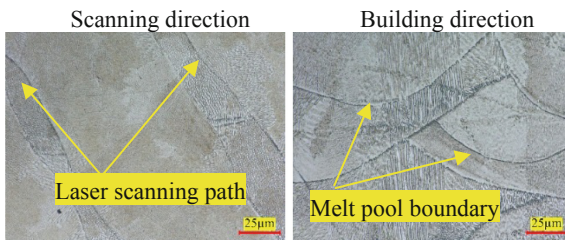


Fig. 1. Microstructure of Inconel 625 fabricated by SLM.

The cutting parameters includes 60 m/min constant cutting speed, three different feed per tooth, 0.05, 0.1, and 0.15 mm, axial depth of cut of 0.3 mm and radial depth of cut of 6 mm. Cutting process is schematically illustrated in Fig. 2. The surface topography, microstructure, and wear morphology images were obtained using 3D Keyence VHX-6000 optical microscope. The Arithmetical average surface roughness (R_a) of the specimens was measured using Mitutoyo SJ210 surface profilometer. The ASTM E 384 standard was followed for the hardness test by using Future-Tech FM310e.

The sliding wear tests were conducted using a reciprocating tribometer as per the ASTM G133 standard. The wear tests were conducted for 40 min under a contact load of 15 N and a stroke length of 6 mm at room temperature in an air atmosphere without any cooling or lubricant. A tungsten carbide ball (WC 94%, CO 6%) with a diameter of 6 mm was used for the reciprocating wear test. To reveal the surface and subsurface layer of Inconel 625 specimens, specimens were cold-mounted in cross-section, ground and polished using conventional techniques, and etched using a solution of 6 ml HCl + 4 ml glycerin + 2 ml HNO₃.

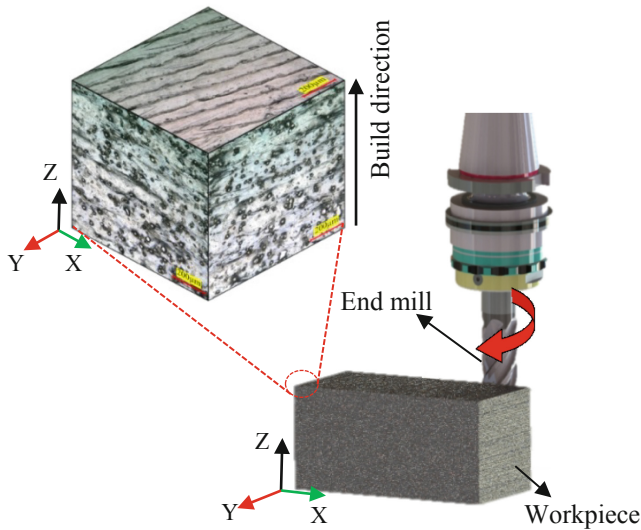


Fig. 2. Schematic representation of Finish-milling process of Inconel 625 produced by SLM.

3 Results and Discussions

3.1 Surface Quality

Surface quality for the functional component is an important requirement for the aerospace industry. It is well-known that machining process has been used as a finishing operation to meet the surface quality for the conventionally fabricated Ni-based alloy. Since machining has been accepted as the fundamental process to give the component the final shape, with chosen an appropriate cutting parameters, finishing operation has not been considered as a challenging process. On the other hand, one of

the challenge needs to be overcome for the components fabricated by additive manufacturing process is still the surface quality [18]. Hence, this section of the present study focuses on the surface quality of the specimen fabricated by SLM process and the contribution of finish-milling to improve it. Figure 3 shows the surface topography of the as-build (building and scanning directions), and post-processed (machined) specimens. It is apparent that the surface on the building direction is much rougher than the surface of scanning direction of the specimens.

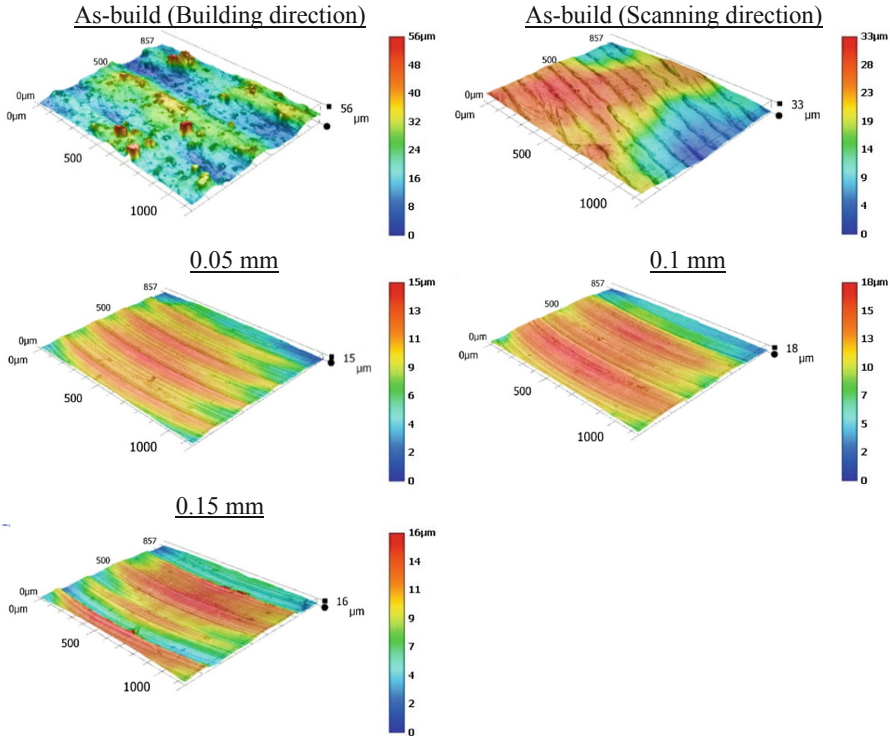


Fig. 3. Surface topography of the as-build (building and scanning directions), and post-processed specimens.

Partially melted powders attached to the outer surface of the specimens results in discontinuous surface. Similar to the building direction, the surface topography of scanning direction is not consistent too. The topography of post-processed specimens evidently shows that with the post-processing, much smoother and consistent topography can be obtained. Measured arithmetical surface roughness values for these surfaces are shown in Fig. 4. Quantitative measurements show good agreement with the topography of as-build and post-processed specimens. While measured average surface roughness was approximately 5.8 μm on the surface of building directions, it was 2.9 μm on the scanning directions. Post-processing decreases the surface roughness of

the specimens. The measured lowest surface roughness with 0.05 mm feed per tooth is approximately 1.28 μm . The obtained results particularly increased surface roughness with an increasing feed rate is also commonly observed response in milling process of conventionally fabricated Ni-based alloy [19].

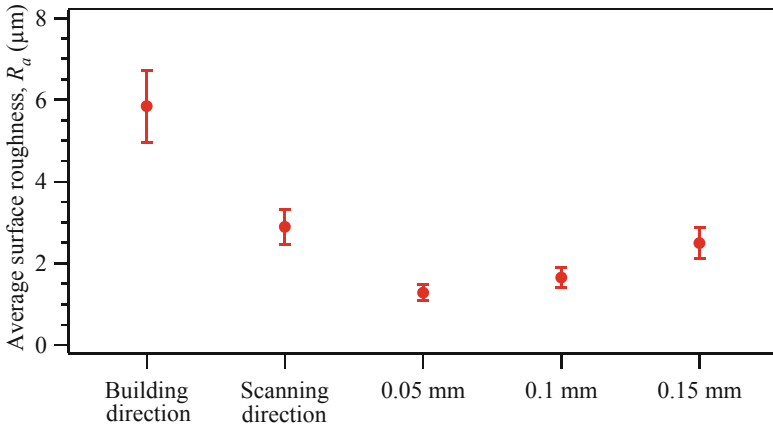


Fig. 4. Surface roughness of the as-build (building and scanning directions), and post-proceeded specimens.

3.2 Microhardness and Wear Performance

Finish-machining process makes a significant improvement on the surface quality of specimens fabricated by SLM process. But the concern is the surface and subsurface mechanical characteristics of the machined specimens. Figure 5 shows the measured microhardness of the as-build, and post-proceeded specimens. The microhardness of the as-build specimen was measured as 319 HV \pm 4. The hardness of post-proceeded specimen makes remarkable difference in comparison with the as-build specimen.

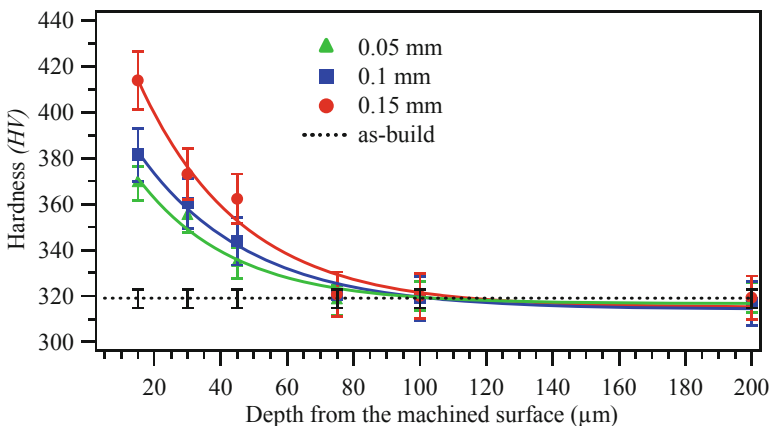


Fig. 5. Microhardness of the as-build and post-proceeded specimens.

The measured hardness at the outer layer of the specimen is approximately 369 HV with the lowest feed per tooth (0.05 mm). The highest hardness measured is 414 HV at the outer layer of the specimen post-proceeded with 0.15 mm feed per tooth. Comparing with the as-build specimen, almost 30% increases is recorded. The surface of the specimen experienced both mechanical and thermal loading, the surface properties depends on the coupling effects of the two loading [20]. As thermal loading in milling operation has the characteristics of discontinuity and short time duration, while mechanical load would be the predominant factor determining the surface's mechanical characteristics [20]. The technical literature reported that this mechanical effect results in compressive residual stress on the surface region of the machined additively manufactured specimens with an increased the density of dislocation [21]. The work hardening and resulting increased hardness on the surface and subsurface is assumed to be caused by residual stress and increased dislocation. Since increasing feed rate results in increased mechanical work and energy during cutting process that eventually causes the increased rate of work hardening on the surface and subsurface of the specimen [20]. This is the main reason of the increased hardness on the surface and subsurface of the specimen when machining them with the higher feed rate.

But it should be underlined that the thickness of the work hardened layer seems to be limited with the first 100 μm depth from the outer surface. There is a good correlation in between microhardness measured on the surface and subsurface vs. wear resistance of specimens. As microhardness varies remarkably depending on the post-processing parameters (feed per tooth), wear track also shows large variation depending on the post processing condition as depicted in Fig. 6. Figure 7 shows 2-D wear track profiles of as-build (building and scanning directions), and post-proceeded specimens. The first finding needs to be noted that there is almost no difference in wear resistance in between building and scanning direction of Inconel 625 alloy fabricated by SLM process. They are almost identical. This is a very good indicator that the roughness does not play a major role to determine the wear resistance of the specimens fabricated by SLM process. The predominant effect on the wear resistance comes from the post-processing. It was already shown that post-processing profoundly increased the hardness of the surface and subsurface of the specimens. Furthermore, the density of porosity on the subsurface and subsurface of the specimens decreases noticeably after post-processing operation [22]. These two parameters played vital role on the wear resistance of the specimens fabricated by SLM. But it is worth to mention that there is a very strong relationship in between the microhardness and wear depth and wear track formation.

The sliding wear rates of the as-build for both scanning and building directions, and post-proceeded specimens are shown in Fig. 8. The wear volume is calculated using Eq. 1, expressed as follows [23]:

$$V = L \left[r^2 \sin^{-1} \left(\frac{w}{2r} \right) - \frac{w}{2} \left(r^2 - \frac{w^2}{4} \right)^{\frac{1}{2}} \right] + \frac{\mu}{3} \left[2r^3 - 2r^2 \left(r^2 - \frac{w^2}{4} \right)^{\frac{1}{2}} - \frac{w^2}{4} \left(r^2 - \frac{w^2}{4} \right)^{1/2} \right] \quad (1)$$

where V , L , w , and r are the wear volume (mm^3), the stroke length (mm), the width of the wear track (mm), and the radius of the carbide ball (mm), respectively.

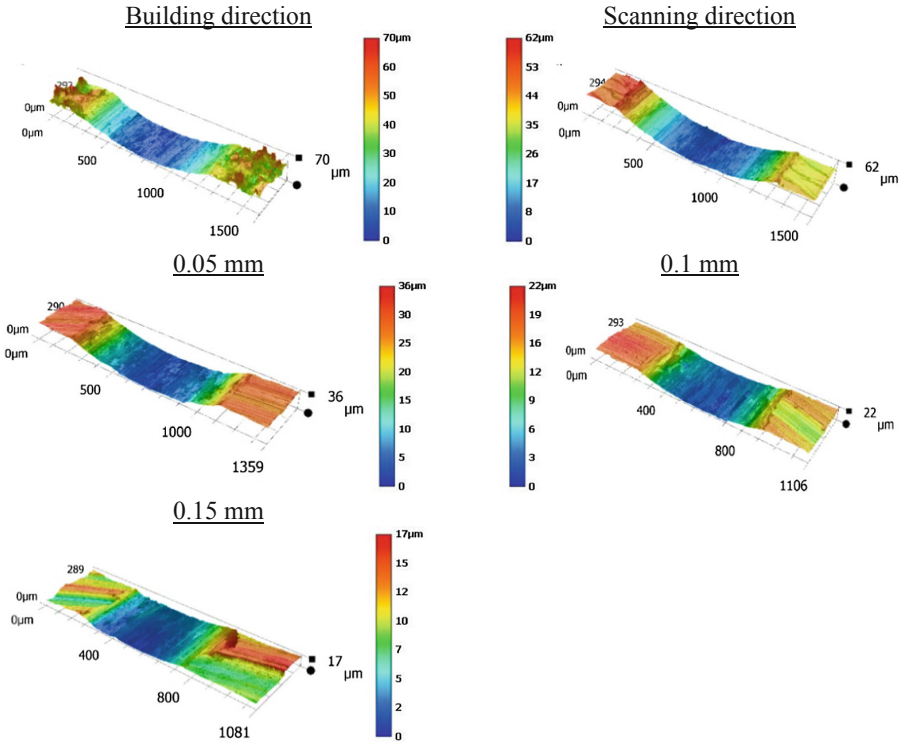


Fig. 6. 3-D wear track profile of the as-build and post-processed specimens.

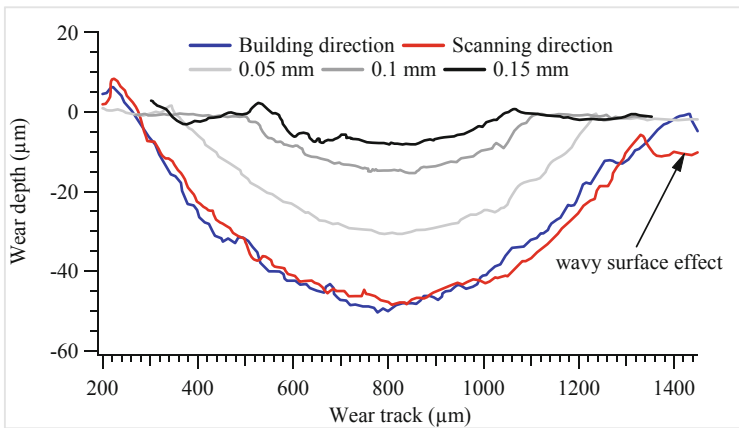


Fig. 7. 2-D wear track profiles of as-build (building and scanning directions) and post-processed specimens.

The wear rate is defined as follows [23]:

$$k = \frac{V}{NxL} \quad (2)$$

where k is the wear rate (mm^3/Nmm) and N is the applied normal force (N). The effect of post-processing on wear rate is profound. It is apparent that wear rate of specimens fabricated by SLM process can be reduced 50% by conducting post-processing operation.

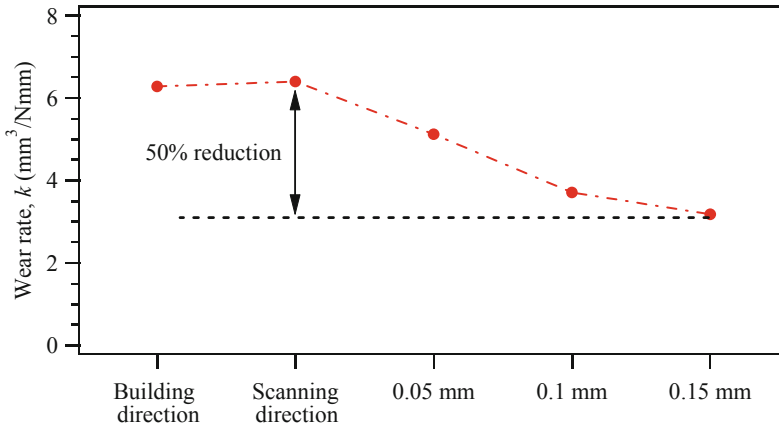


Fig. 8. Wear rate of as-build (building and scanning directions) and post-proceeded specimens.

4 Conclusions

Additive manufacturing is considered as an alternative process to the conventional operations particularly machining process, but the surface quality of parts fabricated by additive manufacturing does not meet the quality requirements for the functional components used in various industries including aerospace and biomedical. This study illustrated that post-processing (finish-machining) operation not only improve surface quality but also profoundly increases wear resistance of the specimens fabricated by additive manufacturing selective laser melting. The current study provides evidence that 50% reduction in wear rate seems to be possible by implementing mechanical post-processing operation. Besides, it is also possible to substantially improve the surface quality of the specimen. Present study demonstrates that both surface quality and wear resistance are evidently induced from the feed rate. Depending on the priorities and requirement for the component fabricated by SLM, it is possible to improve surface quality by reducing feed rate. Moreover, it is possible to notably increase wear performance by chosen the higher feed rate during post-processing operation. As hybrid (Machining and AM) manufacturing concept gains more interest by industries, the contribution of finish-machining to the surface, mechanical and wear properties of Inconel parts fabricated by SLM should be utilized by aerospace industry.

References

1. Pleass, C., Jothi, S.: Influence of powder characteristics and additive manufacturing process parameters on the microstructure and mechanical behaviour of Inconel 625 fabricated by selective laser melting. *Addit. Manuf.* **24**, 419–431 (2018)
2. Ramkumar, K.D., Abraham, W.S., Viyash, V., Arivazhagan, N., Rabel, A.M.: Investigations on the microstructure, tensile strength and high temperature corrosion behaviour of Inconel 625 and Inconel 718 dissimilar joints. *J. Manuf. Process.* **25**, 306–322 (2017)
3. Ezugwu, E.O., Wang, Z.M., Machado, A.R.: The machinability of nickel-based alloys: a review. *J. Mater. Process. Technol.* **86**, 1–16 (1999)
4. Ezugwu, E.O.: Key improvements in the machining of difficult-to-cut aerospace superalloys. *Int. J. Mach. Tools Manuf.* **45**, 1353–1367 (2005)
5. Chen, L., He, Y., Yang, Y., Niu, S., Ren, H.: The research status and development trend of additive manufacturing technology. *Int. J. Adv. Manuf. Technol.* **89**, 3651–3660 (2017)
6. Kundakcioglu, E., Lazoglu, I., Poyraz, Ö., Yasa, E., Cizicioğlu, N.: Thermal and molten pool model in selective laser melting process of Inconel 625. *Int. J. Adv. Manuf. Technol.* **95**, 3977–3984 (2018)
7. Witkin, D.B., Adams, P., Albright, T.: Microstructural evolution and mechanical behavior of nickel-based superalloy 625 made by selective laser melting. In: *Laser 3D Manufacturing II*, p. 93530B. International Society for Optics and Photonics (2015)
8. Leary, M., Mazur, M., Williams, H., Yang, E., Alghamdi, A., Lozanovski, B., Zhang, X., Shidid, D., Farahbod-Sternahl, L., Witt, G.: Inconel 625 lattice structures manufactured by selective laser melting (SLM): mechanical properties, deformation and failure modes. *Mater. Des.* **157**, 179–199 (2018)
9. Gonzalez, J., Mireles, J., Stafford, S., Perez, M., Terrazas, C., Wicker, R.: Characterization of Inconel 625 fabricated using powder-bed-based additive manufacturing technologies. *J. Mater. Process. Technol.* **264**, 200–210 (2019)
10. Marchese, G., Garmendia Colera, X., Calignano, F., Lorusso, M., Biamino, S., Minetola, P., Manfredi, D.: Characterization and comparison of Inconel 625 processed by selective laser melting and laser metal deposition. *Adv. Eng. Mater.* **19**, 1600635 (2017)
11. Fang, X., Li, H., Wang, M., Li, C., Guo, Y.: Characterization of texture and grain boundary character distributions of selective laser melted Inconel 625 alloy. *Mater. Charact.* **143**, 182–190 (2018)
12. Li, C., White, R., Fang, X., Weaver, M., Guo, Y.: Microstructure evolution characteristics of Inconel 625 alloy from selective laser melting to heat treatment. *Mater. Sci. Eng.: A* **705**, 20–31 (2017)
13. Li, C., Guo, Y., Zhao, J.: Interfacial phenomena and characteristics between the deposited material and substrate in selective laser melting Inconel 625. *J. Mater. Process. Technol.* **243**, 269–281 (2017)
14. Bourell, D., Kruth, J.P., Leu, M., Levy, G., Rosen, D., Beese, A.M., Clare, A.: Materials for additive manufacturing. *CIRP Ann.* **66**, 659–681 (2017)
15. Witkin, D., Helvajian, H., Steffeney, L., Hansen, W.: Laser post-processing of Inconel 625 made by selective laser melting. In: *Laser 3D Manufacturing III*, p. 97380W. International Society for Optics and Photonics (2016)
16. Brown, D., Li, C., Liu, Z., Fang, X., Guo, Y.: Surface integrity of Inconel 718 by hybrid selective laser melting and milling. *Virtual Phys. Prototyp.* **13**, 26–31 (2018)
17. ASTM F 3056: Standard specification for additive manufacturing nickel alloy (UNS N06625) with powder bed fusion, ASTM (2014)

18. Moussaoui, K., Rubio, W., Mousseigne, M., Sultan, T., Rezai, F.: Effects of selective laser melting additive manufacturing parameters of Inconel 718 on porosity, microstructure and mechanical properties. *Mater. Sci. Eng.: A* **735**, 182–190 (2018)
19. Akhtar, W., Sun, J., Chen, W.: Effect of machining parameters on surface integrity in high speed milling of super alloy GH4169/Inconel 718. *Mater. Manuf. Process.* **31**, 620–627 (2016)
20. Li, W., Guo, Y., Barkey, M., Jordon, J.: Effect tool wear during end milling on the surface integrity and fatigue life of Inconel 718. *Procedia CIRP* **14**, 546–551 (2014)
21. Brinksmeier, E., Levy, G., Meyer, D., Spierings, A.: Surface integrity of selective-laser-melted components. *CIRP Ann.* **59**, 601–606 (2010)
22. Kaynak, Y., Kitay, O.: Porosity, surface quality, microhardness and microstructure of selective laser melted 316L stainless steel resulting from finish machining. *J. Manuf. Mater. Process.* **2**, 36 (2018)
23. Sharma, S., Sangal, S., Mondal, K.: On the optical microscopic method for the determination of ball-on-flat surface linearly reciprocating sliding wear volume. *Wear* **300**, 82–89 (2013)



Toolpath Generation for Robot Filleting

Srinivasan Lakshminarayanan¹(✉), Omeiy Mohan Manyar^{1,2},
and Domenico Campolo¹

¹ Nanyang Technological University, Singapore, Singapore
srini.gln@ntu.edu.sg

² Rolls-Royce plc, Singapore, Singapore

Abstract. Filleting is a finishing process of rounding off the edge to blunt the sharpness as well as to improve the component's durability by distributing the stress concentration over a larger area, thus enabling the filleted component to last long. Though the filleting process is widespread in manufacturing industry due to its effectiveness, the operation requires subtle changes in position and orientation of the tool when machining the work-piece which is very difficult to capture 'algorithmically' and thus predominantly carried out by skilled manual workers as the generation of the toolpath for the process is a major challenge. In this paper, we propose a novel strategy based on Lissajous curves to generate the required toolpath for filleting. Based on the starting and ending location of the fillet, we conceptualize a Lissajous pattern in 2D space. Through a mathematical relationship between the 2D space and the 3D real-world, a toolpath comprising both position and orientation is determined. Trials on Wooden and Aluminium work coupons using KUKA iiwa R800 robot validate our strategy to obtain the desired geometrical profile.

Keywords: Filleting · Lissajous · Robot toolpath

1 Introduction

Robots are getting increasingly widespread in the Industrial shop floor despite their high initial cost as the manual processes such as Polishing, Filleting, Chamfering are inefficient, time consuming, involves lot of rework and prone to human errors [1]. For these reasons, automation is highly beneficial and is an active research area [1, 2]. Though the usage of the robots is prevalent, programming the robots still remains as a largely cumbersome process which is a big bottleneck. Not only factories require skilled personnel to code the robot for a specific task, even tiny changes in the workpiece geometry requires reprogramming the robots [2–4] which is often the case for Small and medium-sized enterprises (SMEs) that has high mix-low volume production model. Thus, generating the toolpath automatically is an active research problem [2–7] among the robotics researchers. In order to automatically generate toolpath for a process, various different methods are being followed as shown below,

- (1) CAD Based toolpath generation [8, 9]
- (2) Vision based toolpath generation
- (3) Toolpath generation through the Manual teaching (widely used)

Most of the research is focused on incorporating the vision systems to locate the workpiece and automatically generating corresponding toolpath based on required task, in which the quality of the vision systems is paramount to the desired output. The vision-based programming can be further categorized into two types namely,

- (a) Based on active vision system
- (b) Based on passive vision system

In Active vision systems consists of an expensive external light source like LASER [10, 11] are used to illuminate the scene while a passive vision system [12] generally just captures the scene using cheap CMOS or CCD camera. While generating toolpath based on active vision system is very effective for many manufacturing applications, the output accuracy largely depends on quality of the sensors used where the active vision sensors typically produce better quality than passive sensors. Though, it makes sense for large organizations to invest in expensive high-quality active vision sensors to generate the toolpath automatically, it is quite unfeasible for SMEs.

In order to eliminate the bottlenecks of the tedious programming, the SMEs are deploying collaborative robots that can be programmed by teaching a process on compliant mode. The popular collaborative robots include UR Robots, KUKA iiwa etc. The toolpath generation based on the manual teaching alone is very time consuming as the robot has to be taught through trial and error which may take up 6–8 weeks for each path program [2] which is not compatible with high mix- low volume. Thus, in this paper, we present an approach to generate the toolpath easily for Filleting process that is in real-time leveraging the manual teaching and very simple without any trial and errors suitable for SMEs.

In this paper, we propose a mathematical model to generate the toolpath for Filleting process based on the lissajous curves. Though the indirect path generation method based on lissajous for surface polishing is not completely novel [1, 13, 14], the application of the lissajous curves for generating the filleting toolpath in a manual teaching framework for the impedance-controlled robots is not previously carried out as far as we know. Though the Learning from demonstrations (LfD) [15] is an active research area for carrying out various tasks, we believe the trajectory learned from the LfD is not adequate enough to emulate the human performance and often needs numerous iterations with reinforcement learning for adequate performance (roughly more than 60 Iterations) and requires hours of training [16]. Further, such a trial and error approach is not safe for machining operation which is why we believe our framework is highly suitable for finishing operation.

We validated our model using a collaborative robot leveraging the inbuilt impedance model to locate the workpiece in the environment. The paper is organized as follows, in Sect. 2, the setup for the experiments are described, followed by our mathematical contributions in Sect. 3. In Sect. 4, we present our conclusions and discussion points based on the results obtained.

2 Experimental Setup

We use KUKA LBR iiwa 7 R800, a collaborative robot with 7° of Freedom and 7 kg payload. For machining Aluminium, an abrasive belt tool called Dynabrade 11476 dynabelter that is driven by compressed air is attached to the flange of the KUKA robot as shown in Fig. 1a. For machining wood, we attach a grinding head through Dremel 4000 as in Fig. 1b. The KUKA robot has impedance control mode, in which the Cartesian and Joint stiffness of the robot can be varied to carry out collaborative tasks.

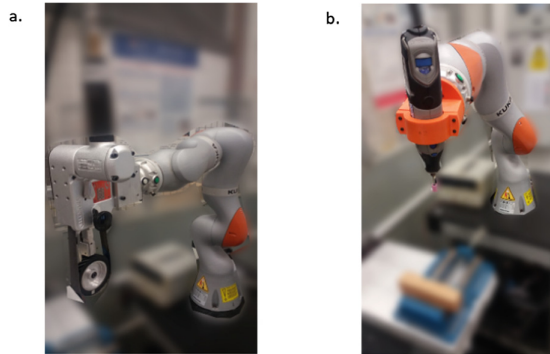


Fig. 1. a. KUKA iiwa with Dynabelter, b. KUKA iiwa with Dremel

The KUKA robot has impedance control mode, in which the Cartesian and Joint stiffness of the robot can be varied to carry out collaborative tasks. The KUKA Robot is programmed with Sunrise Workbench software based on JAVA Programming language using *KUKA RoboticsAPI*. Through a TCP/IP connection, a bi-directional communication link between MATLAB and Sunrise Workbench is established. Further, an in-built mode in Sunrise-Workbench known as *Sunrise.Connectivity Servoing* is used to program one end-destination frame at a time from MATLAB, which is updated in real time to obtain a continuous stream of path. In the KUKA impedance control mode, the operator can manually teach the starting and ending positions on the edge section where the fillet is desired. The positional information is then communicated to MATLAB in real-time to generate the trajectory based on lissajous curves for the filleting operation.

3 Filletting Framework

3.1 Lissajous Curves

Filletting is a manufacturing operation of rounding off an edge with desired fillet radius as shown in the Fig. 2. In order to round off an edge, the operator manually glides the tool in a reciprocating motion along the edge with subtle changes in orientation.

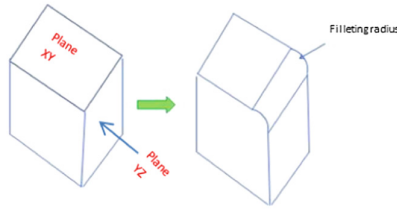


Fig. 2. Filleting operation to round off an edge

Typically, the filleting operation carried out by the manual skilled operators is characterized by two distinct attributes. The reciprocal movement of the tool in the direction along the edge as shown in the Fig. 3a and the changes in the orientation of the tool at different parts of the workpiece as depicted in Fig. 3b.

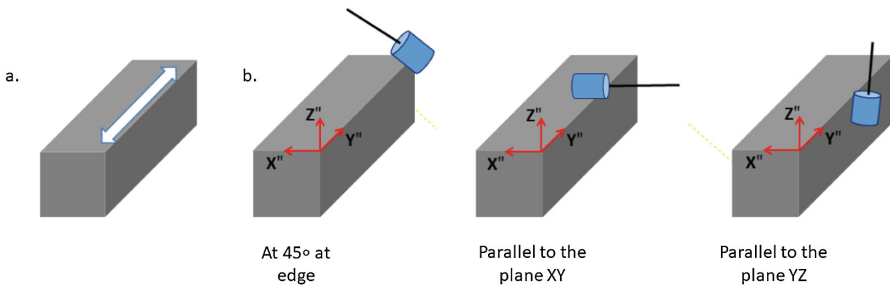


Fig. 3. a. Back and forth movement, b. Changes in orientation to round an edge

Essentially by following the aforementioned two features, the filleting can be construed as a special case of chamfering. The chamfering which is another popular process of blunting the edge by a tool at an exact inclination angle of 45° to the two adjoining right angled faces of an edge. Therefore, Filleting can be modelled as chamfering at different angles in different parts of the workpiece. For example, the tool is inclined at exactly 45° on the edge, which is the intersection of two planes XY and YZ as indicated in Fig. 2. While machining the workpiece along the plane XY, it is held horizontally on the surface parallel to plane XY. Similarly, the tool is held at an upright vertical position on the surface parallel to plane YZ, while machining it. While this convention is followed intuitively by the human operators, it's complicated to make the robot adjust its position and orientation simultaneously to carry out filleting. To emulate a similar filleting strategy to the one used by the human operator, we formulate a mathematical framework based on Lissajous curves. The Lissajous curves are the patterns generated when we plot two sinusoidal waves on both x and y axis as indicated in the equations below. The filleting operation is commenced with the operator teaching the starting $P_1(x_1, y_1, z_1)$ and ending positions $P_2(x_2, y_2, z_2)$ where the fillet is desired. Subsequently we use that positional information (P_1 and P_2) to generate lissajous curves. We added the axes (X'' , Y'' , Z'') to Figs. 3b and 4a & b for

ease of understanding of the framework and it's not the actual origin for the coordinate system (X, Y, Z) we used. In general, the Lissajous curves are of the form,

$$Y' = A \sin(at + \delta) \tag{1}$$

$$\theta = B \sin(bt) \tag{2}$$

Where,

A, B = Amplitude of the functions Y' and θ respectively

a, b = Frequencies of the functions Y' and θ respectively

δ = Phase shift between the functions.

By varying the frequency, amplitude, and phase shift, we can generate wide variety of patterns for disparate application. We use two parameters Y' and θ to carry out filleting based on the following equations,

$$Y' = \frac{(y_2 + y_1)}{2} + \left(\frac{y_2 - y_1}{2}\right) * \sin(2 * t) \tag{3}$$

$$\theta = \frac{\pi}{4} + \left(\frac{\pi}{4}\right) * \sin(0.43 * t) \tag{4}$$

Using Eqs. (3) and (4), we form a 2D Lissajous pattern. To emulate the trajectory followed by humans, we need to transform the 2D parametric space to a 3D trajectory, simultaneously computing the orientation for every frames in that trajectory. This is accomplished using the following Eqs. (5) and (6) that let us establish the relationship between the 2D space and 3D that we derived using the Fig. 4a.

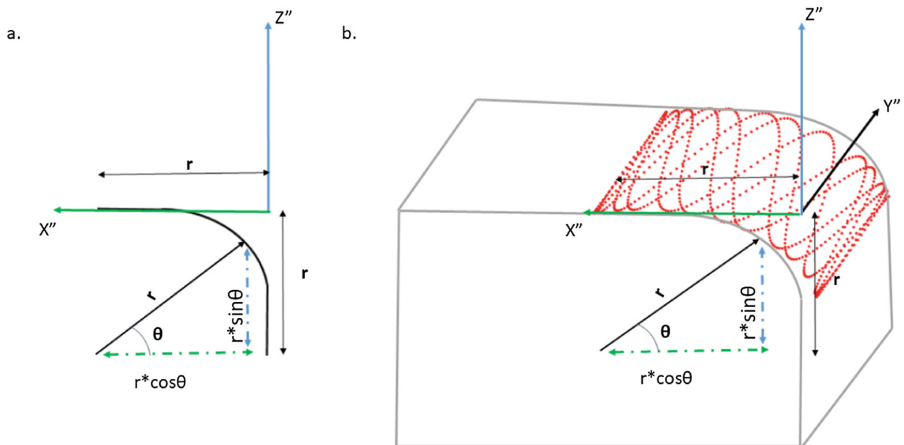


Fig. 4. a. Framework to find 3D Pose, b. Robot reference trajectory for fillet

As the edge is along the Y direction as depicted in the Fig. 4b.

$$P = \begin{bmatrix} r - r \cos \theta \\ Y' \\ -(r - r \sin \theta) \end{bmatrix} \tag{5}$$

$$ROT = \begin{bmatrix} \sin \theta & 0 & -\cos \theta \\ 0 & 1 & 0 \\ \cos \theta & 0 & \sin \theta \end{bmatrix} \tag{6}$$

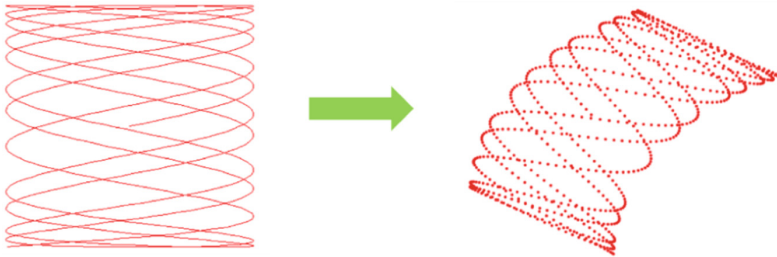


Fig. 5. Transforming from 2D parametric space to 3D

Based on the Eq. (5), the lissajous curve in the parametric space is transformed to the 3D realworld as shown in the Fig. 5. As the orientation obtained through Eq. (6) keep changing from point to point, we found that the tool to be quite unstable for carrying out the filleting as well as prone to tool collisions with environment at extreme angles. Thus, we approximated the filleting orientation by using 8 discrete set of angle θ between 0° – 90° by rounding off the angles and formulated a trajectory that would yield us desired geometrical profile of the edge.

3.2 Experiments

The experiments are carried out in both wooden coupons and aluminium using KUKA iiwa R800 to validate the proposed filleting framework. The reference trajectory with 800 way points obtained using the Eqs. (5) and (6) is shown in the Fig. 6.

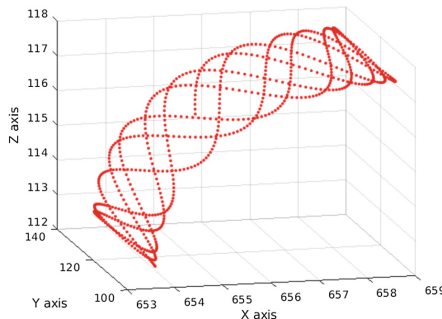


Fig. 6. Reference Trajectory formed from lissajous curves (in mm)

Since the actual path followed by the robot in the Filletting process not always where we command the robot to go, we have incorporated this filletting toolpath into an Iterative learning feedback controller based on positional adaptation and carried out each trial with 5 passes. The required fillet radius is set to be 5 mm and the accuracy for the outputs of the filleted coupons are validated using a non-contact laser profile measurement device (GapGun Pro). As this profile measurement device only measures the radius at a particular point, 3 random points are sampled throughout the filleted part and averaged as shown for a particular trial in Table 1.

Table 1. GapGun measurement of filleted component

S.No	Target filletting radius (in mm)	Actual radius of the output (in mm)	
		Trial in Aluminium	Trial in Wood
1	5	5.53	5.26
2		5.37	4.95
3		5.41	6.12
Average =		5.43	5.44

From the measurements, the filleted radius of the output is 5.43 mm 5.44 mm, on average, for Aluminium and Wood respectively. This result is within ± 1 mm tolerance that we targeted as it is acceptable for filletting.

4 Conclusion

In this paper, we proposed a framework based on lissajous to generate a robot toolpath for filletting process. Experiments are carried out in the various wooden and aluminum workcoupons to determine the feasibility of the approach and outputs are validated using a non-contact laser profile measurement device. The results on the Aluminium and wooden coupons prove that the approach is robust enough to get the fillet profile of desired radius. Though the proposed algorithm is described here assuming the Fillet edge is along the direction of Y axis, it can be adapted to any type of edges with slight modifications to the Eqs. (3), (5) and (6). Tradeoff of our simple approach is that our framework can only handle linear edges owing to the fact that the portion of the edge to be filleted is identified through the manual teaching of the starting and end points by the operator, which is not adequate enough for the complex edges. Generalizing our framework for such complex edges will be the focus of our future works.

Acknowledgment. This project was conducted within the Rolls-Royce@NTU Corporate Lab with support from the National Research Foundation (NRF), Singapore under the CorpLab@University Scheme. This grant was partly supported by the MOE Tier1 grant (RG48/17).




References

1. Tam, H.Y., Lui, O.C.H., Mok, A.C.: Robotic polishing of free-form surfaces using scanning paths. *J. Mater. Process. Technol.* **95**(1–3), 191–200 (1999)
2. Zhang, H., Chen, H., Xi, N., Zhang, G., He, J.: On-line path generation for robotic deburring of cast aluminum wheels. In: 2006 IEEE/RSJ International Conference on Intelligent Robots and Systems, pp. 2400–2405. IEEE, October 2006
3. Malhotra, R., Reddy, N.V., Cao, J.: Automatic 3D spiral toolpath generation for single point incremental forming. *J. Manuf. Sci. Eng.* **132**(6), 061003 (2010)
4. Yang, D.C., Chuang, J.J., OuLee, T.H.: Boundary-conformed toolpath generation for trimmed free-form surfaces. *Comput. Aided Des.* **35**(2), 127–139 (2003)
5. Huang, H., Gong, Z.M., Chen, X.Q., Zhou, L.: Robotic grinding and polishing for turbine-vane overhaul. *J. Mater. Process. Technol.* **127**(2), 140–145 (2002)
6. Bailey-Van Kuren, M.: Flexible robotic demanufacturing using real time tool path generation. *Robot. Comput. Integr. Manuf.* **22**(1), 17–24 (2006)
7. Pandremenos, J., Doukas, C., Stavropoulos, P., Chryssolouris, G.: Machining with robots: a critical review. In: Proceedings of DET2011, pp. 1–9 (2011)
8. Braumann, J., Brell-Cokcan, S.: Parametric robot control: integrated CAD/CAM for architectural design (2011)
9. Ding, D., Shen, C., Pan, Z., Cuiuri, D., Li, H., Larkin, N., van Duin, S.: Towards an automated robotic arc-welding-based additive manufacturing system from CAD to finished part. *Comput. Aided Des.* **73**, 66–75 (2016)
10. Liu, X., Wang, G., Shi, Y.: Image processing of welding seam based on single-stripe laser vision system. In: Sixth International Conference on Intelligent Systems Design and Applications, vol. 2, pp. 463–470. IEEE, October 2006
11. Peiquan, X., Xinhua, T., Fenggui, L., Shun, Y.: An active vision sensing method for welded seams location using “circle–depth relation” algorithm. *Int. J. Adv. Manuf. Technol.* **32**(9–10), 918–926 (2007)
12. Dinham, M., Fang, G.: Autonomous weld seam identification and localisation using eye-in-hand stereo vision for robotic arc welding. *Robot. Comput.-Integr. Manuf.* **29**(5), 288–301 (2013)
13. Lee, M.C., Go, S.J., Jung, J.Y., Lee, M.H.: Development of a user-friendly polishing robot system. In: Proceedings 1999 IEEE/RSJ International Conference on Intelligent Robots and Systems. Human and Environment Friendly Robots with High Intelligence and Emotional Quotients (Cat. No. 99CH36289), vol. 3, pp. 1914–1919. IEEE (1999)
14. Go, S.J., Lee, M.C., Park, M.K.: Fuzzy-sliding mode control of automatic polishing robot system with the self tuning fuzzy inference based on genetic algorithm. In: Proceedings 2001 ICRA. IEEE International Conference on Robotics and Automation (Cat. No. 01CH37164), vol. 3, pp. 2962–2967. IEEE (2001)
15. Argall, B.D., Chernova, S., Veloso, M., Browning, B.: A survey of robot learning from demonstration. *Robot. Auton. Syst.* **57**(5), 469–483 (2009)
16. Mülling, K., Kober, J., Kroemer, O., Peters, J.: Learning to select and generalize striking movements in robot table tennis. *Int. J. Robot Res.* **32**(3), 263–279 (2013)

Laser Processes



Effect of Bubble Radius on Ability of Submerged Laser Peening

Hirotooshi Sasaki¹ , Yuka Iga² , and Hitoshi Soyama¹ 

¹ Department of Finemechanics, Tohoku University, Sendai, Japan
hirotoshi.sasaki.cl@tohoku.ac.jp

² Institute of Fluid Dynamics, Tohoku University, Sendai, Japan

Abstract. In submerged laser peening, it has been experimentally clarified that the collapse impact of the bubble which occurs after laser ablation is stronger than the impact of laser ablation itself. Moreover, the experimental results showed the arc height increased in proportion to the cube of the bubble development time with various material. Here, the arc height shows the processing capacity of peening, and the bubble development time is proportional to the bubble radius. Therefore, it was shown that the processing capacity of peening by the bubble collapse increased in proportion to the cube of the bubble radius. In order to clarify the effect of bubble radius on submerged laser peening capacity, the fluid/material two-way coupled numerical analysis of a hemispherical bubble on the wall surface with changing the bubble radius was performed. From the analysis results, the relationship between the bubble radius and the maximum pressure in the fluid and maximum equivalent stress in the material was clarified. If the ratio of internal and external pressure of a bubble was the same, the bubble radius had little effect on the bubble collapse pressure and the maximum equivalent stress in the material. However, the material volume of which the maximum equivalent stress exceeded the threshold of yield stress of the materials increased in proportional to the cube of bubble radius. Therefore, also in the numerical analysis, it was shown that the effect of bubble collapse on materials is proportion to the cube of bubble radius.

Keywords: Submerged laser peening · Bubble radius · Bubble collapse · Fluid/material coupled method

1 Introduction

It is known that very high pressure occurs when cavitation bubbles collapse [1]. This collapse pressure of cavitation bubbles causes the cavitation erosion by which materials are damaged. However, at the same time, it is also used for cavitation peening [2], which is one of material surface modification techniques. Therefore, many studies have been conducted about cavitation in term of both objects of suppression and efficient use. The cavitation peening is the surface modification method which increases the material strength by introducing a compressive residual stress in the material by using the collapse pressure of cavitation bubbles. Many experimental studies have been conducted on the collapse pressure of cavitation bubbles and these pressure are known to be on the order of 1 GPa [3, 4].

A shot peening [5, 6] and laser peening [7, 8] is included in peening techniques for material surface modification. In submerged laser peening, a pulsed laser with an intensity capable of ablating metal is irradiated to a processed surface of material placed in water. So the plastic deformation is given to the material by a shock wave generated from the plasma occurring on the metal surface. At the time of this laser irradiation, Soyama showed experimentally that the hemispherical cavitation bubbles (laser cavitation) occurred on the surface of the material [9] (Fig. 1) after impact pressure induced by ablation. Moreover, Soyama also showed that this collapse pressure may exceed the impact pressure of ablation in some cases [9] (Fig. 2). If this bubble collapse pressure is effectively utilized, it can be expected that the effects of laser peening and cavitation peening can be obtained at the same time.

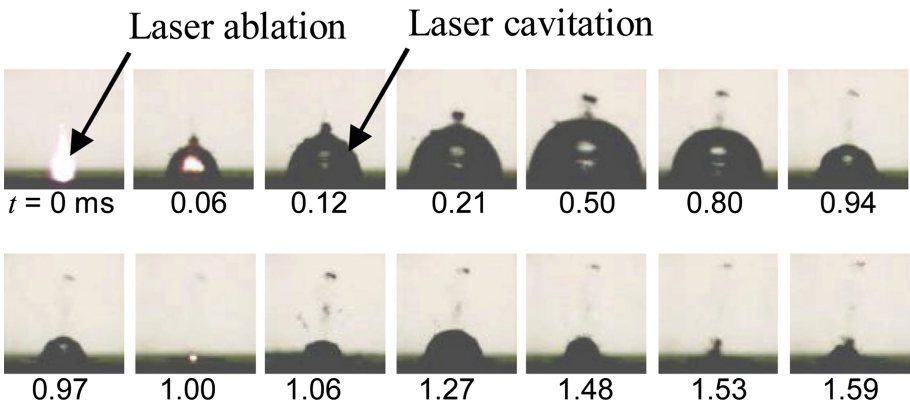


Fig. 1. Aspect of laser cavitation (laser induced bubble) [9].

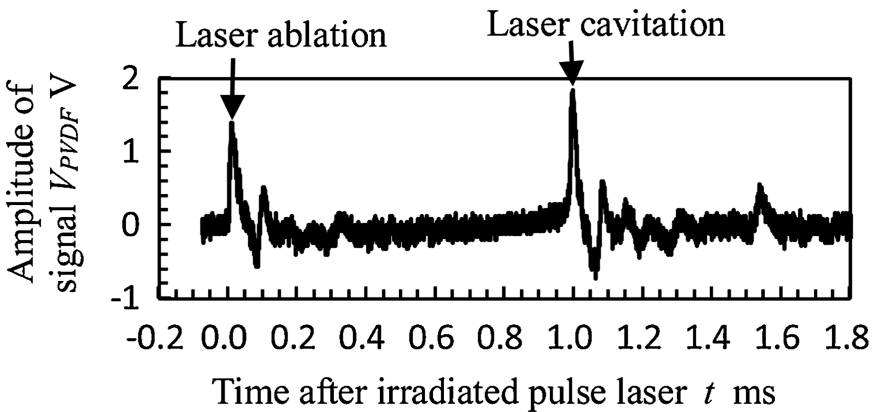


Fig. 2. Noise induced by laser ablation and laser cavitation [9].

In this study, the simulation of the collapse behavior of single hemispherical vapor bubble with different initial bubble radius on the material wall was performed. The present numerical analysis is an in-house fluid/material two-way coupled numerical method which considers reflection and transmission on the fluid/material interface. Therefore, the collapse pressure in the fluid side and equivalent stress in the material side by bubble collapse can be analyzed at the same time. However, this analysis cannot be treated for plastic deformation and residual stress of materials because of elastic body analysis in the material. For this reason, by providing a threshold by the yield stress for the maximum equivalent stress distribution on the material side by bubble collapse, the volume of this distribution is relatively compared and the effect of bubble collapse on materials is evaluated. From these numerical analysis results and the results shown by submerged laser cavitation experiments, the effect of bubble radius on the processing capacity of submerged laser peening is investigated.

2 Numerical Method

2.1 Governing Equation in Fluid

In this study, the locally homogeneous model of compressible gas-liquid two-phase medium [10] is used for the interface capturing method of bubble. The governing equations in fluid are the continuity, the momentum equations, the total energy conservation equation of gas-liquid mixture phase, and the continuity equation of gas phase. The governing equation system is closed by satisfying the following two equations, which are the equation of state of homogeneous medium and the total energy equation of two-phase medium. In the bubble interface, the surface tension is calculated by the CFS model [11] and the phase equilibrium theory of a flat gas-liquid interface [12] extended to homogeneous gas-liquid two phase medium [13] is used for the phase change term. The saturated vapor pressure of water p_v is calculated by the empirical formula given by Sugawara [14]. The pressure propagation in the bubble collapse process can be reproduced by considering the compressibility in both gas phase and liquid phase.

2.2 Governing Equation in Material

For the simulation of stress wave propagation in material, the governing equations composed of the equation of motion and the time-differential constitutive equations of homogeneous isotropic elastic medium are simultaneously solved [15]. The material deformation and density change are neglected.

2.3 Numerical Scheme of Analyzing Method

The cell centered finite volume formulation is used to discretize the governing equations of both the fluid and material. The convective term is estimated AUSM type scheme with interpolation by using the 3rd-order MUSCL-TVD method with a min-mod limiter. The 4th-order Runge-Kutta method is used for the time integration. The

algorithm of two-way coupled method in fluid/material interface [16] is applied as follows: Fluid surface pressure and normal stress of vertical direction on material surface are obtained by considering reflection and transmission of pressure and stress waves with acoustic impedance. Non slip condition is adopted on fluid/material surface, where vertical speed has minimal values which are obtained by considering reflection and transmission, and tangential velocity of fluid has the same minimal velocity of material which is calculated by material analysis.

3 Results and Discussion

3.1 Initial Condition and Calculation Area

In this study, in order to analyze the effect of variation of bubble radius on materials by bubble collapse, the numerical analysis of an in-house fluid/material two-way coupled numerical method of a single bubble collapse was conducted. Figure 3 shows a schematic diagram of the calculation area. In this calculation, though the main calculation area in fluid is $3.0R_0$, the buffer area exists outside of the main calculation area. Therefore, it is assumed that the bubble exist in infinite liquid depth. In addition, since the displacement of material is very small in the occasion of collapse of single bubble, the material area which includes its surface is calculated with fixed mesh system although the displacement velocity is taken into account. In the whole calculation area, due to assuming the phenomenon of plane symmetry, a quarter of all the space is calculated. Assumed as the behavior of bubble of the experiment of the submerged laser peening, the hemispherical vapor bubble generated by laser ablation touches the material surface.

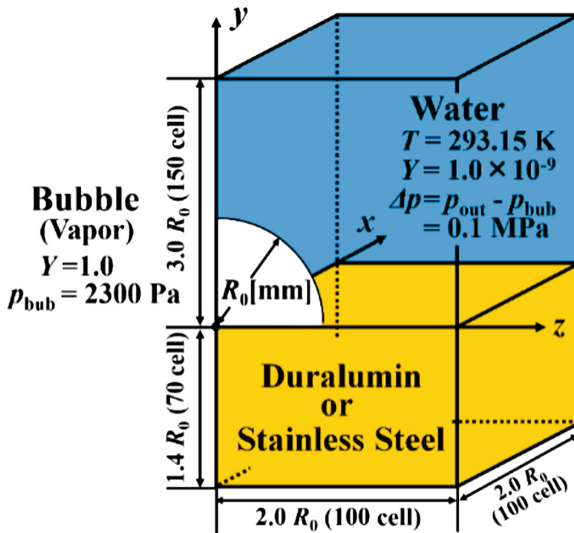


Fig. 3. Calculation area and initial conditions.

In the initial condition, the temperature in fluid is $T = 293.15$ K and the pressure inside this bubble is $p_{\text{bub}} = 2300$ Pa, which is the vapor saturated pressure at $T = 293.15$ K. The pressure difference between inside and outside of the vapor bubble is $\Delta p = 0.1$ MPa due to be a collapse in atmospheric pressure. In addition, this bubble has the mass fraction of gas $Y = 1.0$ and the water around the bubble has the mass fraction of gas phase $Y = 1.0 \times 10^{-9}$. The initial bubble radius is changed with $R_0 = 1.0, 2.0, 3.0, 4.0, 5.0$ mm, and the effect of bubble radius is analyzed. The material is assumed to be two kind of duralumin and stainless steel, in the case of duralumin, the material properties are set as follows: density $\rho_s = 2790$ kg/m³, Young's modulus $E = 69$ GPa and Poisson's ratio $\nu = 0.3$. On the other hand, in the case of stainless steel, the material properties are set as follows: density $\rho_s = 7800$ kg/m³, Young's modulus $E = 200$ GPa and Poisson's ratio $\nu = 0.3$.

3.2 Definition of Stress Effective Volume

In this study, stress effective volume [16] is defined to evaluate the effect of bubble collapse on materials. This indicates a volume above a certain threshold for the distribution of the maximum equivalent stress generated in the material by bubble collapse in this numerical analysis. This volume is used as an index of evaluation of effect on material. As for the threshold value, in general, in shot peening processing, since the material is plastically deformed by striking a shot against the material and the material surface gets work hardened, the yield stress of the material is used. The volume in which the maximum equivalent stress exceeds the yield stress was used as a stress effective volume to evaluate the effect of the material by numerical analysis and compared with the experimental results.

3.3 Relationship Between Maximum Pressure in Fluid, Maximum Equivalent Stress in Material and Bubble Radius

Figure 4 shows the time evolution of pressure and void fraction in fluid and equivalent stress in material, which showed the process of bubble collapse. A hemispherical bubble shrinks and collapses while maintaining a hemispherical shape uniformly with the time evolution. When a bubble collapses, a high collapse pressure exceeding 1 GPa is generated on the fluid side and a high equivalent stress is also generated on the material side accordingly. Figure 5 shows the relation between initial bubble radius R_0 and maximum pressure p_{max} and maximum equivalent stress $(\sigma_{\text{eq}})_{\text{max}}$ with each case of duralumin and stainless steel.

Although the p_{max} is different on each material, the p_{max} is almost constant regardless of bubble radius. As a study to explain this result, there is the Shima and Tomita' analysis result based on the theory of bubble dynamics [17]. They explained that the ratio of initial radius and minimum radius of bubble was expressed by the initial pressure ratio of internal and external bubble and specific heat ratio of gas inside bubble. In addition, they also explained that the relationship between maximum collapse pressure of bubble and ratio of initial radius and minimum radius of bubble. From combining these analysis results, it is shown that the maximum collapse pressure of bubble is expressed by the initial pressure ratio of internal and external bubble and

specific heat ratio of gas inside bubble but is not affected by bubble radius. Therefore, it is considered that this calculation result agrees with Shima and Tomita’s analysis result.

As for the maximum equivalent stress in the material side, it is different with kind of material. However, the maximum equivalent stress is hardly affected by the bubble radius since the maximum pressure in the fluid side does not change significantly depending on the bubble radius.

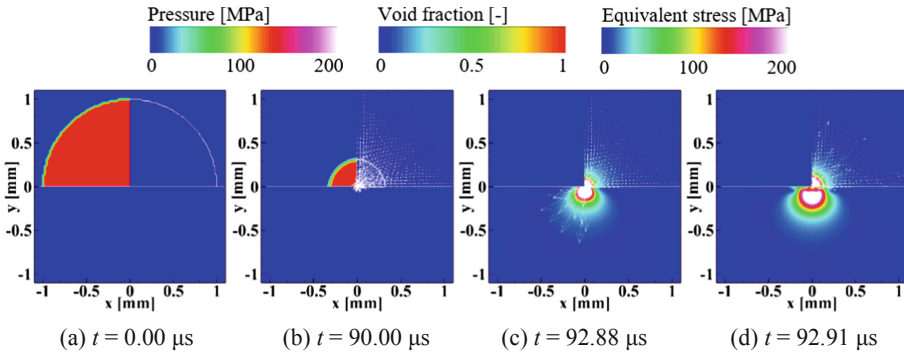


Fig. 4. Time evolution of pressure and void fraction in fluid and equivalent stress in material ($R_0 = 1.0$ mm, Duralumin).

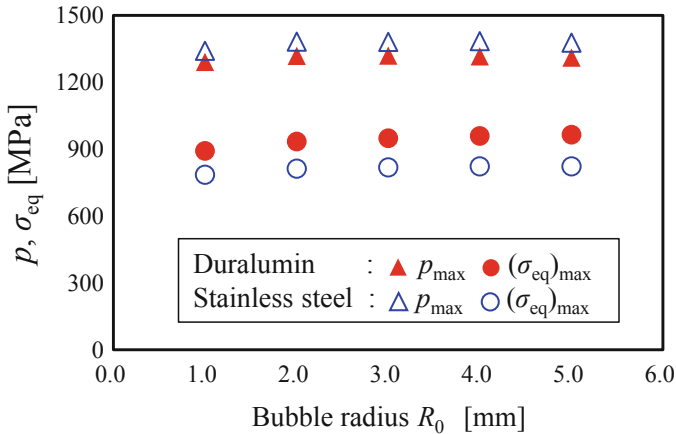


Fig. 5. Relation between bubble radius and maximum pressure and equivalent stress with each case of duralumin and stainless steel.

3.4 Evaluation of Effect of Bubble Radius on Materials by Stress Effective Volume

Figure 6 shows an example of the change in the distribution of stress effective volume in the case of duralumin with each bubble diameter, and Fig. 7 shows the relationship between bubble radius and stress effective volume in both duralumin and stainless steel. When the surrounding conditions of bubble collapse except bubble radius were the same, the maximum equivalent stress distribution shapes generated on the material side became almost the same regardless of the bubble radius. However, the stress effective volume increased in proportion to the cube of the bubble radius in both materials when the yield stress of each material is used as the threshold.

These results show that while the maximum equivalent stress alone cannot show the effect of the bubble radius on the material, the effect of the bubble radius on the material can be shown by using the evaluation of stress effective volume by the present numerical analysis.

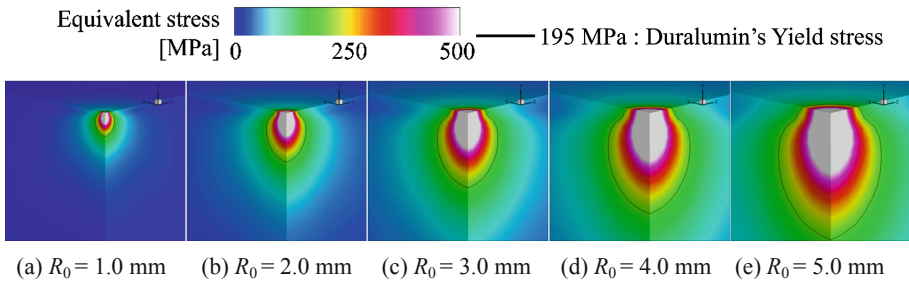


Fig. 6. Comparison of the stress effective volume with each bubble radius (Duralumin).

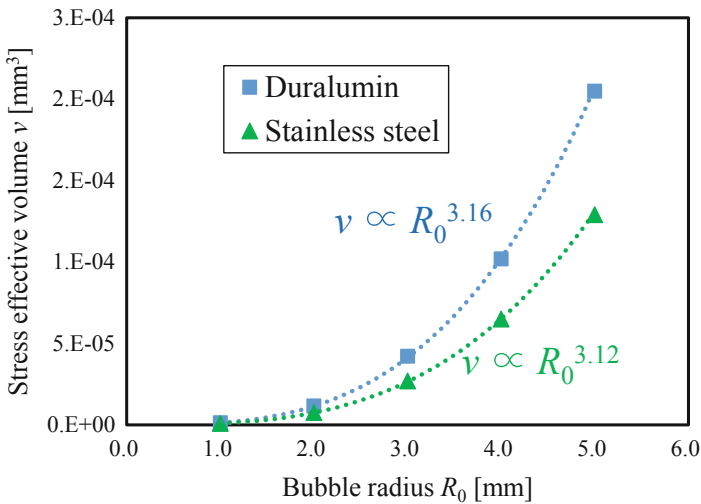


Fig. 7. Comparison of Stress effective volume and bubble radius with each case of duralumin and stainless steel.

Soyama conducted the submerged laser cavitation experiment and investigated the relationship between the developing time of the cavitation bubble and the arc height with several materials [18, 19]. Here, the arc height is used to evaluate the peening strength in shot peening, and it is shown that the larger the arc height, the higher the peening ability. In this experiment, the ability of cavitation peening was evaluated by the arc height. In addition, the developing time of the cavitation bubble is proportional to the bubble radius. Namely, as this time is long, the bubble radius is large. From the experimental result, the arc height increases in proportion to the cube of the developing time of bubble with various materials. Therefore, the processing ability by laser cavitation is considered to increase in proportion to the cube of the bubble radius [18].

From the above two results, the present numerical analysis results are in good agreement with the experimental result. Therefore, it is suggested that the processing ability of submerged laser peening increases in proportion to the cube of bubble radius by both experiment and numerical analysis.

4 Conclusion

In order to investigate the effect of bubble radius on the processing ability of submerged laser peening, the simulation of single hemisphere bubble collapse on the material surface is conducted by using our in-house fluid/material coupled numerical method of which fluid analysis based on compressible gas-liquid two-phase medium model and the material analysis based on elastic dynamics are coupled with boundary conditions considering acoustic impedance. The numerical analysis results are compared with the laser cavitation experiment and the effect of bubble radius on the processing capacity of submerged laser peening is evaluated. The obtained results can be summarized as follows:

- (1) In the numerical analysis of hemisphere bubble collapse, both maximum pressure on the fluid and maximum equivalent stress generated on the material were almost the same value regardless of the bubble radius. As a result, the effect of bubble radius did not appear. However, by using the evaluation of stress effective volume, the stress effective volume increased with the cube of bubble radius. Therefore, it was shown that the material is affected in proportion to the cube of the bubble radius by the present numerical analysis.
- (2) In the submerged laser cavitation experiment, it has been shown that the processing ability of cavitation peening increases in proportion to the cube of the bubble radius for various materials. Therefore, in both the present numerical analysis and the submerged laser cavitation experiment, it was suggested that the processing ability of submerged laser peening increases in proportion to the cube of bubble radius.

Acknowledgments. This work was partly supported by JSPS KAKENHI Grant Number 17H03138 and 18KK0103. The numerical simulations were performed on the Supercomputer system “AFINITY” at the Advanced Fluid Information Research Center, Institute of Fluid Science, Tohoku University.

References

1. Brennen, C.E.: *Cavitation and Bubble Dynamics*. Oxford University Press, New York (1995)
2. Soyama, H.: Key factors and applications of cavitation peening. *Int. J. Peen. Sci. Technol.* **1**, 3–60 (2017)
3. Jones, I.R., Edwards, D.H.: An experimental study of the forces generated by the collapse of transient cavities in water. *J. Fluid Mech.* **7**(4), 596–609 (1960)
4. Fujikawa, S., Akamatsu, T.: Experimental investigations of cavitation bubble collapse by a water shock tube. *Bull. JSME* **21**(152), 223–230 (1978)
5. Wang, S.P., Li, Y.J., Yao, M., et al.: Compressive residual stress introduced by shot peening. *J. Mater. Process. Technol.* **73**, 64–73 (1998)
6. Zhou, J., Retraint, D., Sun, Z., et al.: Comparative study of the effects of surface mechanical attrition treatment and conventional shot peening on low cycle fatigue of a 316L stainless steel. *J. Surf. Coat. Technol.* **349**, 556–566 (2018)
7. Sano, Y., Obata, M., Kubo, T., et al.: Retardation of crack initiation and growth in austenitic stainless steels by laser peening without protective coating. *Mater. Sci. Eng.: A* **417**, 334–340 (2006)
8. Yella, P., Venkateswarlu, P., Buddu, R.K., et al.: Laser shock peening studies on SS316LN plate with various sacrificial layers. *J. Appl. Surf. Sci.* **435**, 271–280 (2018)
9. Soyama, H.: Comparison between the improvements made to the fatigue strength of stainless steel by cavitation peening, water jet peening, shot peening and laser peening. *J. Mater. Process. Technol.* **269**, 65–78 (2019)
10. Okuda, K., Ikohagi, T.: Numerical simulation of collapsing behavior of bubble clouds. *JSME Ser. B* **62**(603), 3792–3797 (1996). (in Japanese)
11. Brackball, J.U., Kothe, D.B., Zemach, C.: A continuum method for modeling surface tension. *J. Comp. Phys.* **100**(2), 335–354 (1992)
12. Fujikawa, S., Akamatsu, T.: Effects of the non-equilibrium condensation of vapour on the pressure wave produced by the collapse of a bubble in a liquid. *J. Fluid Mech.* **97**, 481–512 (1980)
13. Ochiai, N., Iga, Y., Nohmi, M., et al.: Numerical analysis of nonspherical bubble collapse behavior and induced impulsive pressure during first and second collapses near the wall boundary. *J. Fluid. Sci. Technol.* **6**(6), 860–874 (2011)
14. Sugawara, S.: New steam tables. *JSME* **35**(186), 999–1004 (1932). (in Japanese)
15. Takano, Y., Goto, T., Nishino, S.: A finite volume scheme for elastodynamic equations (1st Report, Algorithm for Elastodynamics). *JSME. Ser. A* **64**(626), 2471–2476 (1998). (in Japanese)
16. Sasaki, H., Ochiai, N., Iga, Y.: Numerical study of high speed liquid droplet impingement phenomena by fluid/material coupled numerical method. *Jpn. J. Multiph. Flow* **30**(1), 65–74 (2016). (in Japanese)
17. Shima, A., Yukio, T.: *Turbomachinery* **2**(3), 252–259 (1974). (in Japanese)
18. Soyama, H.: Effect of Laser Energy on Mechanical Surface Treatment Enhanced by Laser Cavitation. In: *The Proceedings of Autumn Conference of Tohoku Branch, JSME*, vol. 2017.53, paper No. 108, pp. 1–2 (2017). (in Japanese)
19. Soyama, H.: Similarity between cavitation bubble produced by pistol shrimp and bubble induced by pulse laser. In: *The Proceedings of Conference of Tohoku Branch, JSME*, vol. 2016.51, pp. 63–64 (2016). (in Japanese)



Crack Retardation of Damage Through Enhanced Crack Closure Effect Induced by Laser Peening

Yongxiang Hu^(✉)  and Han Cheng

State Key Laboratory of Mechanical System and Vibration,
School of Mechanical Engineering, Shanghai Jiao Tong University,
Shanghai 200240, China
huyx@sjtu.edu.cn

Abstract. The effect of laser peening (LP) on damage is of great significance to recover the service life of damaged material. However, it is still unclear for the reason behind to introduce this effect by high-dynamic loading of LP. In this study, experiments are conducted to investigate the retardation of pre-crack growth by LP treatment. Pre-cracks fabricated by cyclic loading are introduced on CT specimens of aluminum alloy 2024-T351 to act as initial fatigue crack damage. LP treatment is performed to cover the specimen surface with pre-crack. Fatigue crack propagation (FCP) experiments are conducted to demonstrate the crack retardation effect following LP treatment. Digital image correlation (DIC) method is also employed to obtain the full field displacement around the crack tip to evaluate the enhancement of crack closure level behind pre-crack tip. The results show that crack arrest and retardation and hence a significant fatigue life promotion are observed for the pre-cracked specimen with LP treatment. It even sustains more loading cycles than the undamaged specimen with LP treatment. DIC analysis reveals that the immediate enhancement of crack closure level is introduced behind the crack tip due to high-dynamic loading of LP treatment. Plastic deformation produced by the high dynamic loading of LP, is possibly dominant to introduce crack retardation behind the pre-crack tip.

Keywords: Damage · Crack retardation · Laser peening · Crack closure · Digital image correlation

1 Introduction

Damages, induced by both different kinds of manufacturing process and fatigue loading, greatly debilitate mechanical properties and service life of metallic components to result in the premature and unexpected fracture failure ultimately. Various approaches, such as laser cladding and mechanical surface treatments, have been developed to heal and repair the existing damage to extend service life of critical components. Mechanical surface treatments are potential and promising approaches for damage repair of metallic components because crack damages generally nucleated from surface layer, is exactly in the range they can take effect.

Laser peening (LP) is well-known to introduce substantial deeper compressive residual stress compared to the traditional methods [1, 2]. Due to its excellent characteristics, LP is widely employed to enhance fatigue resistance of aerospace components, welded joint and so on [3–5]. However, relatively few studies have been reported to utilize LP process on healing or repairing damaged components. Ganesh et al. demonstrated the promotion effect of LP on the high-cycle fatigue life in pre-fatigued 6 mm-thick SAE 9260 spring steel sheets [6]. Liu et al. also performed LP treatment on pre-fatigued and intact copper films [7, 8]. They found that LP treatment results in a more pronounced fatigue life promotion for the damaged specimens than that of without pre-fatigue specimens. However, both work by Ganesh and Liu only provides the improvement of fatigue life. Lack of work concerns the possible damages introduced by pre-fatigue and their behaviors under further cyclic loading. Although additional fatigue life promotion has been reported to demonstrate the possibility of LP to introduce healing effect on pre-fatigue or damaged materials, the reason for the damage healing effect is rarely involved. Crack is recognized as the essence of damage in the majority of cases and its propagation is usually used to investigate the damage development.

Crack closure has been commonly utilized to explain the primary mechanism of crack retardation. Crack closure effect is an important phenomenon in which crack flanks keep contact even when cyclic loading is not equal to its minimum value. Generally, it is recognized as the primary cause of reduction of fatigue crack growth rate (FCGR). LP can introduce high dynamic loading to generate high-strain-rate plastic deformation and compressive residual stress on the surface layer of the material. Therefore, compared with various phenomenon introduced on the crack flanks, it is possible to generate similar crack retardation if LP treatment is conducted on the surface area with pre-crack.

The purpose of present study is to investigate the effect of high-dynamic loading on damage and to clarify the reason for the alteration of crack growth behavior after LP treatment. The pre-crack is fabricated on CT specimens by fatigue loading to act as the initial fatigue crack damage. The crack retardation effect possibly resulting from LP treatment, was demonstrated and quantified by the fatigue crack growth rate (FCGR). The particular characteristics of crack retardation in the pre-cracked specimens with LP treatment are analyzed by full-field displacement versus cyclic loading around pre-crack through the digital image correlation method (DIC). Results are used to quantify the level of crack closure behind pre-crack tip. Furthermore, morphology observation across the thickness section is performed to analyze the behavior of crack flanks behind the pre-crack tip during high dynamic loading of LP treatment.

2 Experiments

Aluminum alloy 2024-T351 with the thickness of 6.5 mm is used as the material for experiments. The specimen geometry for crack propagation test is designed according to ASTM E647-11 standard and is shown in Fig. 1(a). The plate of aluminum alloy 2024-T351 was cut into CT specimens with an initial crack length $a_0 = 10$ mm and the external loading is applied parallel to the rolling direction. To include an initial damage

in material, the pre-crack with the length $a_{pre} = 3.0$ mm as illustrated in Fig. 1(a), was fabricated by applying cyclic loading at room temperature. It was performed at a constant loading ratio $R = 0.1$, the maximum load $F_{max} = 4$ kN and the frequency of 15 Hz. The relationship of crack length versus load cycle in the process of pre-crack preparation was recorded during experiments. LP treatment was applied on the specified area of both sides by using a Q-switched Nd: YAG laser with the pulse energy of 10 J and the duration of 15 ns. The round laser spot was set to be 4 mm in diameter. The scanning path and sequence of the laser spots are illustrated in Fig. 1(b). As shown in Fig. 1(b), laser shocks were applied on a square zone with the size of 14.0×14.0 mm².

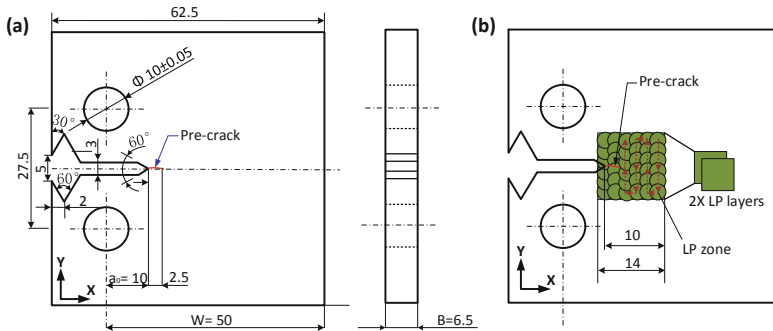


Fig. 1. Schematic of CT specimen with pre-crack for laser peening experiments: (a) specimen geometry and the fabricated pre-crack; (b) laser peening on both sides of specimen.

FCP tests were performed on three typical specimens including as-received specimens, standard specimens with LP treatment, and pre-cracked specimens with LP treatment. The tests were conducted by a servo-hydraulic fatigue test machine at room temperature. The test conditions for all CT specimens, such as loading history and ambient temperature, were kept consistent during experiments. The loading ratio, the loading frequency and the maximum force of the external cyclic loading were 0.1, 15 Hz and 4.0 kN, respectively. These parameters were identical to those for pre-crack fabrication. In order to precisely measure crack length under cyclic loading, CCD camera was employed to capture the transient crack profile. The fatigue crack length was acquired by positioning the crack tip in the image. DIC is utilized in this investigation to capture the presence of crack closure phenomenon and evaluate its level behind crack tip. DIC imaging collection were conducted by utilizing a ring light and a JT-H1080P CCD equipped with a microscope consisting of a $12\times$ zoom lens and a $1\times$ adapter tube. Micro speckle patterns with the mean diameter about $15\ \mu\text{m}$, were sprayed on the polished surface behind the notch of CT specimen. After DIC analysis, the results for full-field displacement around crack tip were obtained. The relative displacement curves of crack flanks versus the external cyclic loading were plotted out from the post-processing to evaluate crack closure level behind the crack tip.

3 Results and Discussion

Results of FCP test are used to analyze the crack retardation behavior of CT specimens with and without LP treatment. Figure 2 shows the development of crack propagation related to the number of loading cycles under different conditions. Stage I shown in Fig. 2 is the period for pre-crack fabrication that the crack propagates from the length of 10 mm (a_0) to 13 mm ($a_0 + a_{pre}$), while Stage II is the period that the crack propagates from the length of 13 mm to be fractured. As shown in Fig. 2, it can be observed from curves that the standard specimen with two layers of LP treatment appears to obtain much longer fatigue life because it requires more cycles for crack to reach the length of 25 mm compared with the as-received specimen. From the curves for FCP test, it can be found that the pre-cracked specimen with LP treatment obtains the most cycles in Stage II to propagate the fatigue crack to the length of 25 mm. The number of cycles in Stage II for the as-received specimens can be used to identify the effect of laser peening on the pre-cracked specimens. Excluding the number of cycles in Stage I, the results are increased by ten times. Laser peening is effective to extend the fatigue life of specimen with crack damages. Furthermore, it can be also observed that the standard specimens with LP treatment are failed with much lower cycles than that for the pre-cracked specimens with LP treatment. Extra extension of fatigue life is observed for the pre-cracked specimen after laser peening compared with the standard specimen with LP treatment. Different from the result for the standard specimen with LP treatment, crack arrest can be observed from in Fig. 2 for the pre-cracked specimen with LP treatment, where the crack stops propagating for a long duration a little less than 70,000 cycles.

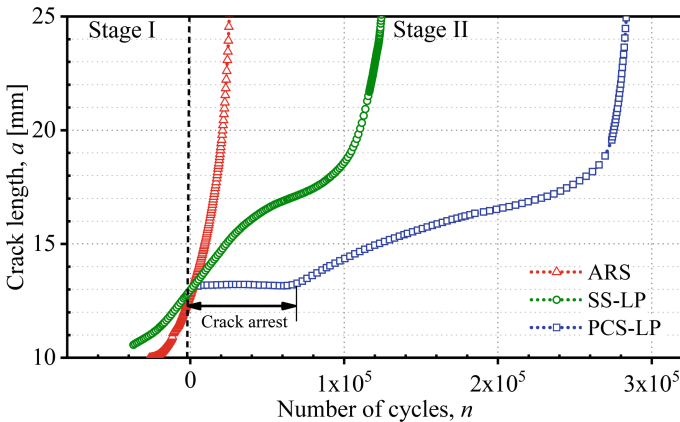


Fig. 2. Crack propagation behaviors under cyclic loading (ARS: as-received specimen; SS-LP: standard specimen with LP; PCS-LP: pre-cracked specimen with LP treatment)

To investigate the transient process of crack opening under uploading, external load versus relative displacement curves of crack flank are plotted in Fig. 3 for different specimens. Figure 3(a) shows the crack opening behavior of the as-received specimen

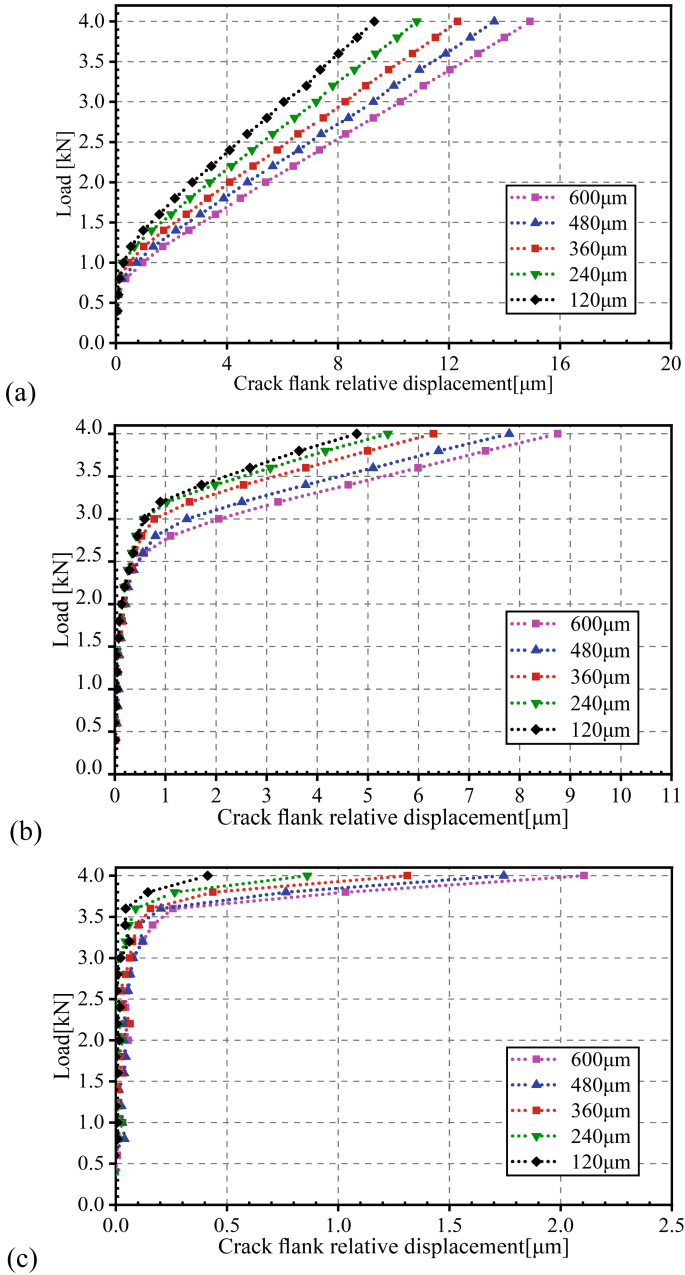


Fig. 3. Relative open displacement about crack flanks versus external load: (a) as-received specimen without LP treatment; (b) standard specimen with LP treatment; and (c) pre-cracked specimen with LP treatment after fatigue loading of 31612 cycles.

when the crack reaches the length of 13 mm, which is identical to the length of the fabricated pre-crack fabrication. It can be found that the crack flanks maintain contact when the load is low. As the load is increased to be 0.8 kN, the crack flanks begin to open at the position with 600 μm behind the tip. And they were separated totally when the applied load reaches the value of 1.0 kN, which is provided by the displacement curve near the tip with the distance of 120 μm in Fig. 3(a). After separation, the relative displacement of crack flanks increases linearly by increasing the external load. Figure 3(b) provides the crack opening process of the standard specimens with LP treatment when the crack reaches the length of 13 mm. It can be found that the separation of crack flanks can't be separated until the external load reaches the value of 1.7 kN. Subsequently, the crack flanks are gradually separated by increasing the load. The opening load of the crack flanks near tip is about 1.9 kN. Compared with the result of as-received specimen as shown in Fig. 3(a), the critical load for the standard specimen with LP treatment is 1.9 times to fully open the crack. Figure 3(c) provides the results for the pre-cracked specimen with LP treatment under 31612 loading cycles. It can be observed that the values of opening loadings are 3.4 kN for the location with 600 μm behind the crack tip. And the results for the location with 120 μm behind the crack tip are 3.8 kN, respectively.

4 Conclusions

This study investigates the effect of laser peening to improve the fatigue life of specimen with initial damage. Laser peening is proved to be an effective method to extend the fatigue life of specimen with crack damages. The pre-cracked specimen with LP treatment can sustain more loading cycles than that of undamaged specimen after LP treatment. Crack arrest and retardation can be induced in the pre-cracked specimen after laser peening, which result in additional increase of fatigue cycles in crack propagation compared with the standard specimen with LP treatment. The transient process of crack opening through DIC validates the observed crack retardation phenomenon induced by laser peening.

Acknowledgements. The present work was supported by National Science and Technology Major Project (grant number 2018ZX04005001). This work is also supported by the State Key Laboratory of Mechanical System and Vibration.

References

1. Pant, B.K., Pavan, A.H.V., Prakash, R.V., et al.: *Int. J. Fatigue* **93**, 38–50 (2016)
2. Gujba, K.A., Medraj, M.: *Materials* **7**, 7925–7974 (2014)
3. Dhakal, B., Swaroop, S.: *J. Manuf. Process.* **32**, 721–733 (2018)
4. Zhang, Y.K., Lu, J.Z., Ren, X.D., et al.: *Mater. Des.* **30**, 1697–1703 (2009)
5. Kalentics, N., Boillat, E., Peyre, P., et al.: *Mater. Des.* **130**, 350–356 (2017)
6. Ganesh, P., Sundar, R., Kumar, H., et al.: *Mater. Des.* **54**, 734–741 (2014)
7. Liu, X.-D., Shang, D.-G., Li, M., et al.: *Int. J. Fatigue* **54**, 127–132 (2013)
8. Liu, X.-D., Shang, D.-G., Zhang, L.-H., et al.: *Int. J. Fatigue* **63**, 145–153 (2014)



Application of Laser Peening for Cold Work Steel

Norihito Shibuya¹(✉), Fumiaki Kumeno¹, Yuki Nakamura²,
and Ryo Yoshinouchi²

¹ SINTOKOGIO, LTD., 180-1, Komaki, Ohgi-cho,
Toyokawa, Aichi 441-1205, Japan
n-shibuya@sinto.co.jp

² National Institute of Technology, Toyota College, 2-1, Eiseicho,
Toyota, Aichi 471-8525, Japan

Abstract. Forming technology using dies is utilized by various industries because of its reasonable price and high productivity. Cold forging technology is used in the automotive industry because it can make high precision products. However, die lifespan is a major concern because dies make up the largest proportion of manufacturing costs in cold forging. To improve die life, one can ensure the die's exact physical properties through fundamental material development, or improve the die's fatigue life through surface reforming. Laser peening technology mainly progressed as a technology for fatigue life improvement of aerospace parts. As a result, there is much literature about special materials (ex. Titanium, Inconel alloy). On the other hand, there is little literature about tool steel, which is used for cold forging and die-casting. In this study, basic research was conducted to determine the possibilities of laser peening as technology to improve the fatigue life of cold forging dies. As a result, fatigue strength improvement of JIS-SKD11 needs post-polishing because of Roughening of surface, besides, irregular position of chromium carbide inner material occur large variation of fatigue life.

Keywords: Laser peening · Cold work tool steel · Fatigue strength · Residual stress · Surface roughness

1 Introduction

Quality demand for metal parts which is supported manufacturing is yearly getting strict. In such a situation, it is required technology development, such as optimal shape design, material development, and surface treatment to respond even more expansion of design margin, life extension, and compact and lightweight. In surface treatment technology, shot peening is used for automobile and airplane market because of low-cost and simple surface modification method comparatively.

Laser peening can get same effect with shot peening. This method can induce peening effect using impact power, made of high pressure plasma laser ablation. It is used for fatigue life improvement of aircraft wing parts which is occurred sand erosion and prevention of nuclear power plant parts which is occurred stress corrosion cracking [1].

In addition, laser peening can severely control laser energy and irradiation procedure so that it can get accurate effect and high repeatability. On the other hand, processing time is very long compare with shot peening because it depends on spot size and irradiation speed of laser. That's why laser peening is now limited for using high added value and parts which can beforehand identify its destruction points.

There is much literature about special materials (ex. Titanium, Inconel alloy) [2]. On the other hand, there is little literature about other material. But study of other material (ex. ceramics) for laser peening is starting because laser technology is daily progressing about processing speed and output energy improvement [3]. This can be predicted that application of laser peening will be expanded in the order from high value product not only in the aircraft and nuclear power plant markets, but also in other market, such as medical and die-casting. Therefore we focused about cold work tool steel of cold forging dies, and investigated for the effect of fatigue life improvement for laser peening.

2 Experimental Method

2.1 Specimens

JIS-SKD11, which is used for cold forging, was used for the specimens. The chemical components are shown in Table 1. The shapes and dimensions of the specimens are shown in Fig. 1. Heat treatment conditions are shown in Fig. 2. The specimens were heat treated after machining, and surface roughness is as machined in this state.

Table 1. Chemical component [wt%].

C	Si	Mn	P	S	Cu	Cr	Mo	V
1.46	0.29	0.34	0.29	0.10	0.07	11.6	0.81	0.21

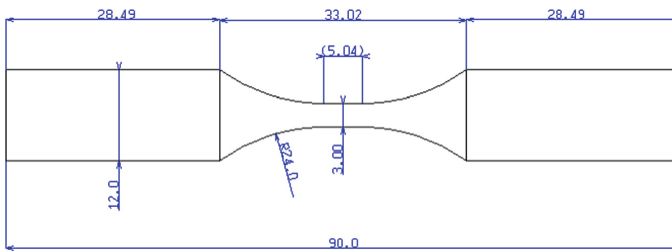


Fig. 1. Shapes and dimensions of specimens.

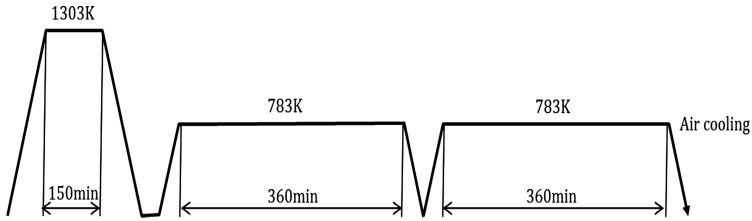


Fig. 2. Heat treatment conditions

Specimen was prepared for fatigue life evaluation. Symbol for each specimen are shown in Table 2. To evaluate presence or absence of melting layer of laser, two type laser peened specimens were prepared. NP and LPP specimen was processed emery paper and buff after machining or laser peening, respectively.

Table 2. Symbols for each specimen.

Symbol	Meaning
○NP	Non-peening, polishing after machining
△LP	As laser peening
□LPP	Polishing after laser peening

2.2 Peening Condition

Laser peening conditions are shown in Table 3. These conditions were optimized in advance.

Table 3. Laser peening condition.

Wave length	Spot size	Power density	Coverage	Coating
532 nm	φ 1.0 mm	13 GW/cm ²	50	Without coating

2.3 Evaluation Method of Fatigue Strength

Rotary bend test was used for evaluation of fatigue strength. Figure 3 shows Ono-style rotary bend machine. This test was evaluated at room temperature and under atmospheric pressure condition, and stress ratio is $R = 1$. Fracture number was counted and repetition number was evaluated under same load stress. Fracture surface after fatigue fracture was observed by using scanning microscope.

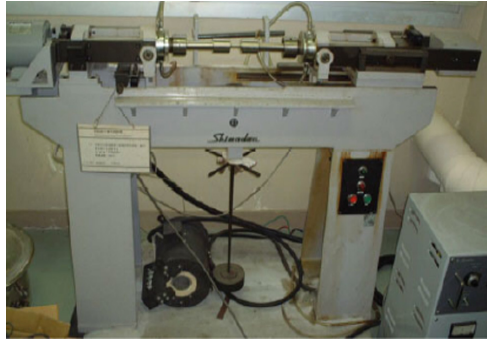


Fig. 3. Ono-style rotary bend machine (SHIMAZU CORPORATION, H5 type).

3 Experimental Result

3.1 Rotary Bend Fatigue Test Result

Figure 4 shows stress endurance diagram of rotary bend fatigue test. LP and LPP were improved fatigue strength compare with NP.

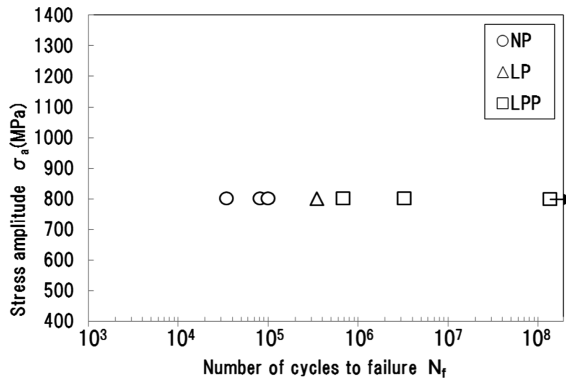


Fig. 4. Stress endurance diagram.

3.2 Fractography Result

Figure 5 shows fractography of each specimen. NP could confirm that starting point of fracture is chromium carbide of near the surface. On the other hand, that for LP specimen was on surface, not chromium carbide [4]. And that for LPP specimen was internal chromium carbide, and it made fish eye.

As a result of fracture surface observation, chromium carbide is identified at fracture surface of all specimens, and that of NP specimen and LPP specimen was starting point of fracture. But that of LP specimen was on surface.

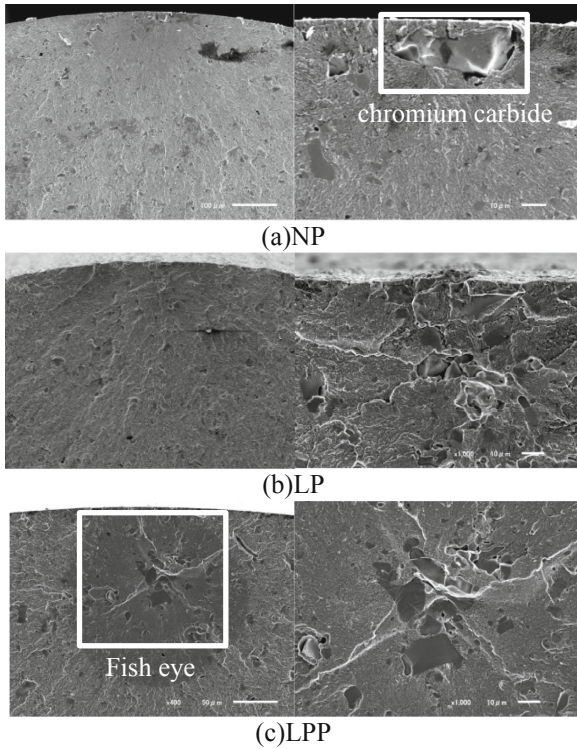


Fig. 5. Fractography result of each specimen.

4 Discussion

4.1 Effect of Surface for Laser Peening

Fatigue characteristic depends on surface roughness. Table 4 shows surface roughness measurement result of each specimen. Surface roughness of NP and LPP specimen is almost same, and that of LP specimen increased.

Table 4. Surface roughness of specimen.

Symbol	NP	LP	LPP
Ra (μm)	0.030	0.8008	0.029

Surface of LP and LPP specimen was observed to evaluate surface characteristics. Figures 6 and 7 is that of LP and LPP, respectively. About surface of LP specimen, there are many cracking and chipping on all of surface. On the other hand, about LPP specimen, there are a little cracking and chipping on surface after polishing. It means that a number of micro cracking was caused of fracture which is occurred by laser ablation to the material, and starting point of fracture is on surface.

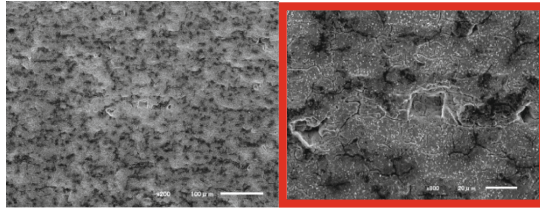


Fig. 6. SEM image of LP specimen.

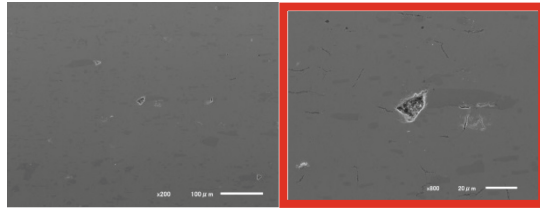


Fig. 7. SEM image of LPP specimen.

4.2 Residual Stress Distribution

X-ray stress measurement was used for evaluate residual stress distribution by laser peening. Algorithm was used $\cos\alpha$ method. Figure 8 shows residual stress distribution compare with NP and LP specimen. Stress value of NP specimen at depth direction doesn't almost change. On the other hand, LP specimen got to maximum compressive residual stress at the depth of 10 μm . It was caused by heat effect layer by laser ablation, and surface is induced tensile stress. As a result, residual stress on surface doesn't maximum compressive residual stress. Compressive residual stress by laser peening can introduce to the depth of 300 μm , so that it is good effect to fatigue life improvement.

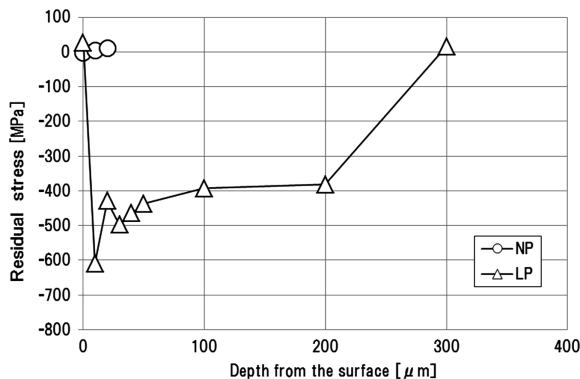


Fig. 8. Residual stress distribution.

5 Conclusion

Effect of rotation bend fatigue characteristic for cold work steel by laser peening was investigated. Also, as a result of fracture surface observation, the below result were confirmed.

- (1) Laser peening process for cold work steel has a good effect to fatigue life improvement. But it is not remarkable effect, we have to investigate about further optimization.
- (2) Fatigue fracture starting point of LP specimen occurs on surface because of surface roughness roughening. To polishing surface after laser peening, it can good effect to improve fatigue strength.
- (3) JIS SKD11 has a lot of chromium carbide internal of material, and position and size of it are random. So it is difficult to indicate the effect of laser peening.

References

1. Sano, Y.: Laser peening for extending service life of components. *J. Surf. Finish. Soc. Jpn.* **60**(11), 698 (2009)
2. Masaki, K., Kameshima, Y., Hisamori, N., Sano, Y., Akita, K., Shobu, T.: Effects of laser peening on rotating bending fatigue properties of Ti-6Al-4V titanium alloy. *J. Soc. Mater. Sci. Jpn.* **62**(5), 297–304 (2013)
3. Saigusa, K., Takahashi, K., Shibuya, N.: Evaluation of mechanical properties of silicon nitride ceramics with laser peening. In: *The Proceedings of the Materials and Mechanics Conference* (2017)
4. Ozaki, K.: Effect of the distribution of primary carbide on fatigue strength of cold work die steels. *DENKI-SEIKO* **76**(4), 249–257 (2005)



Influence of Laser Shock Peening (LSP) on the Material Properties of Additive Manufactured IN718

Ching Kiat Yong¹(✉), Geoff D. West¹, Greg J. Gibbons¹,
and Chow Cher Wong²

¹ Warwick Manufacturing Group (WMG), University of Warwick,
Coventry, UK

ching-kiat.yong@warwick.ac.uk

² Advanced Remanufacturing and Technology Centre (ARTC),
Singapore, Singapore

Abstract. Surface treatments such as laser shock peening (LSP) have been attempted to increase the usability of additive manufactured (AM) IN718. This paper investigates the influence of industrial LSP on IN718 manufactured by both the traditional wrought and AM process. The result of the mechanical properties and microstructure of the produced specimens, directly after the manufacturing process and after AMS 5663 heat treatment are presented. The LSP treated AM component has around 25% less compressive residual stress throughout the depth as compared to its wrought counterpart despite using the same LSP energy densities. Microstructural characterisation technique (EBSD) suggested that the AM IN718 has a higher stored strain energy as compared to the wrought components.

Keywords: Laser shock peening · Additive Manufacturing · Material characterisation

1 Introduction

Additive Manufacturing (AM) is a promising technology for the fabrication of complex geometrical parts with mechanical properties matching those of their wrought counterparts. Laser-Powder Bed Fusion (L-PBF) has a unique position because of its potential to manufacture metal components with complex geometry, which has broadened the application to various industries. The process consists of thin layers of fine powder on a platform which are then fused together with a laser beam. Many metallic materials such as stainless and tool steels, aluminium alloys, titanium and its alloys, and nickel-based alloys can be manufactured by this process [1]. One of the many benefits of AM is that it can provide an economical and flexible method to fabricate high-value aero-engine components e.g. turbine components and blisk blades [2, 3]. Efforts have been made to limit the defects through the use of heat treatment and hot isostatic pressing (HIP-ing), but the results have been mixed [4–7].

Surface treatments, such as shot-peening, deep-rolling and laser shock peening (LSP) are commonly used [8–10] to increase the fatigue life of wrought materials. Several investigations have shown that LSP induces deeper and higher residual stresses than the other two methods mentioned [11–13]. It is an innovative surface treatment technique that applies a pulse laser with high power density onto the surface of metallic component to provide a longer fatigue life [20, 21]. Deeper and higher compressive residual stresses on AM component than on wrought components using LSP has been reported extensively by Kalentic et al. [14].

In this paper, LSP was applied to both AM Inconel 718 (IN718) and its wrought counterpart, where residual stresses and surface quality were investigated.

2 Experimental Procedure

2.1 Materials and Direct Metal Laser Sintering

Table 1. Chemical composition wt % of IN718 specimen.

Ni	Cr	Nb	Mo	Ti	Al	Co	Cu	C	Si	Mn	Fe
50	17	4.70	2.80	0.60	0.20	1	0.30	0.08	0.35	0.35	bal

IN718 were prepared using EOS M290 (EOS GmbH, Germany) with a 400 W fiber laser which was operated in a continuous mode and the chemical composition of the IN718 powder (Progressive Technology Limited, UK) used is given in Table 1. The AM specimens were then heat treated according to Aerospace Material Specifications (AMS) 5663, where it was solution annealed at 980 °C for 1 h and then aged at 720 °C for 8 h. The specimens used in this paper were designed to be 40 × 40 × 10 mm for easy access to the laser peening machine and the area for electron backscatter diffraction (EBSD) measurements is illustrated in Fig. 1. The operating parameters were done accordingly to OEM recommendations and the heat treatment was performed under argon atmosphere. These samples are hereafter referred to as AM samples.

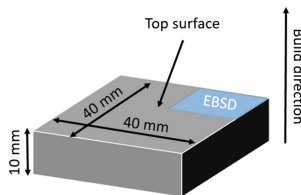


Fig. 1. Geometry of the specimens and the area that was used for EBSD

2.2 Laser Shock Peening Process

An industrial laser shock peening machine (YS120-R200A, Tyrida International Pte Ltd) was used for the experiment. It was conducted at room temperature ($\sim 25\text{ }^{\circ}\text{C}$) using a Q-switched Nd:YAG laser that operated at a wavelength of 1064 nm, pulse repetition rate of 5 Hz and pulse duration of 18 ns. Figure 2(a) shows the schematic diagram of the experimental setup. The specimen was clamped and fixed at the tip of a robot arm which was able to move in a zig-zag direction. A black tape together with water layer with a thickness of a millimetre was applied on the specimen's surface. The treated water will enhance the pressure of plasma, generate the shock waves, and at the same time, displace the ablated particles.

Table 2. LSP condition utilised on IN718 component

	Laser energy [J]	Spot size [mm]	Fluence [J/cm^2]	Power density [GW/cm^2]	Pressure [GPa]
Condition 1	8.0	4.0	63.6	3.5	3.3
Condition 2	9.0	3.0	127.3	7.1	4.7
Condition 3	10.0	2.0	318.3	17.7	7.7

Laser peening was conducted with a variation of spot size and an overlapping rate of 50% for all specimens, shown in Fig. 2(b). Table 2 lists the LSP condition that were employed in this study. Using an empirical equation, pressure (GPa) = $1.75\sqrt{I_o}(\frac{\text{GW}}{\text{cm}^2})$ from Kalentic et al. [13], the pressure created at the surface was formulated for the respective conditions.

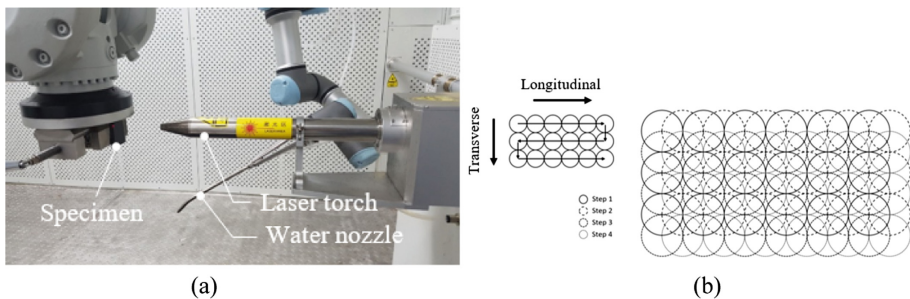


Fig. 2. (a) Experimental setup, (b) Laser path illustrating an overlapping rate of 50%

2.3 Residual Stress Measurements

The surface residual stress was measured using X-ray Diffraction technique (Xstress Robot System, Stresstech) while a laboratory grade equipment (PRISM, Stresstech) was used to measure the residual stresses through the depth based on an advanced hole-drilling system, as shown in Fig. 3. The hole drilling method is a destructive residual

stress measurement where a small drilling rig is used to drill a flat-bottomed hole. The instrument measures changes in the part surface caused by the drilling and determines the previously existing residual stresses. The system measures surface distortion optically using laser light that is diffusely reflected from the sample surface. The hole drilling method was carried out with 1.6 mm drill bits and hole depth increments of 0.050, 0.075, 0.100, 0.200, 0.300, 0.400, 0.500, 0.600, 0.700, 0.800, 0.900, 1.00, 1.10 mm.

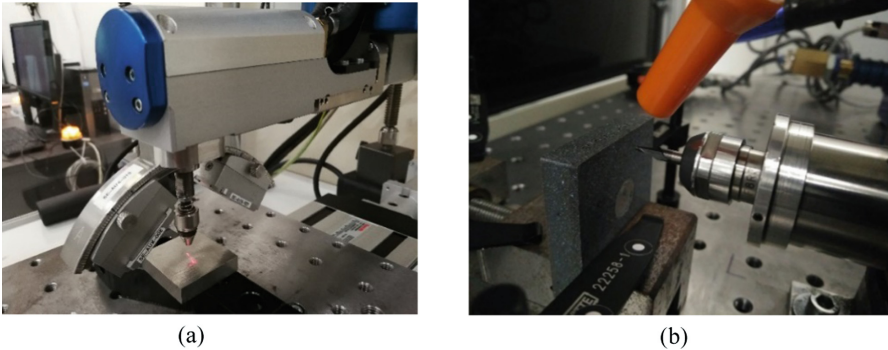


Fig. 3. (a) XRD measurement and (b) residual stress measurement using hole drilling method

2.4 Surface Roughness Measurements

For the surface roughness measurement, a stylus profilometer (PGI 800; Taylor Hobson) was used to determine the arithmetic average of the profile height deviations from the mean line (R_a) in the longitudinal and transverse directions. All roughness measurements were performed three times and the average of these measurements was reported as surface roughness for each direction of the treated surface.

2.5 Microstructure Characterisation Measurements

The grain structure and texture of the specimens were investigated using EBSD in a scanning electron microscope (JSM-7800F, JEOL) at a voltage of 20 kV. The top surface was mechanically polished with P240 grit SiC and subsequently with a series of cloth using 9, 3 and 1 μm diamond suspension. The final polishing was performed with 0.02 μm colloidal silica suspension. Both AM and wrought samples were characterised on the same locations, using a step size of 1 μm . Grain size in the materials was calculated using EBSD maps using CHANNEL 5 software (Oxford Instruments, UK).

3 Results and Discussion

3.1 Residual Stress

In Fig. 4(a), the residual stresses of an AM component in the longitudinal and transverse direction to the plane that has been laser peened with low power density are

compared (Condition 1 in Table 2). The measurements for both directions showed similar results, indicating that the LSP process introduced an equi-biaxial state of stress [15]. Hence, only data from one in-plane component is shown for all the LSP conditions for the rest of the paper.

The residual stress profiles for both wrought and AM specimens that were laser peened with the three power densities are shown in Fig. 4(b) (Condition 1–3 in Table 2). By increasing the power density, there is an increasing trend observed in the residual stresses for both wrought and AM components. Between Condition 2 and 3, there seems to be a certain threshold of the compressive stress that can be induced into the component despite the pressure exerted for Condition 3 was almost twice of that in Condition 2. This phenomenon was verified by Fabbro et al. [16] when LSP power densities exceed more than 10 GW/cm². Pressure saturation occurs at its surface as the water breakdown generated an absorbing plasma instead. The AM specimens after LSP displayed a residual stresses with a maximal value of -813 MPa and an affected depth of up to 1.10 mm for the case of LSP Condition 2.

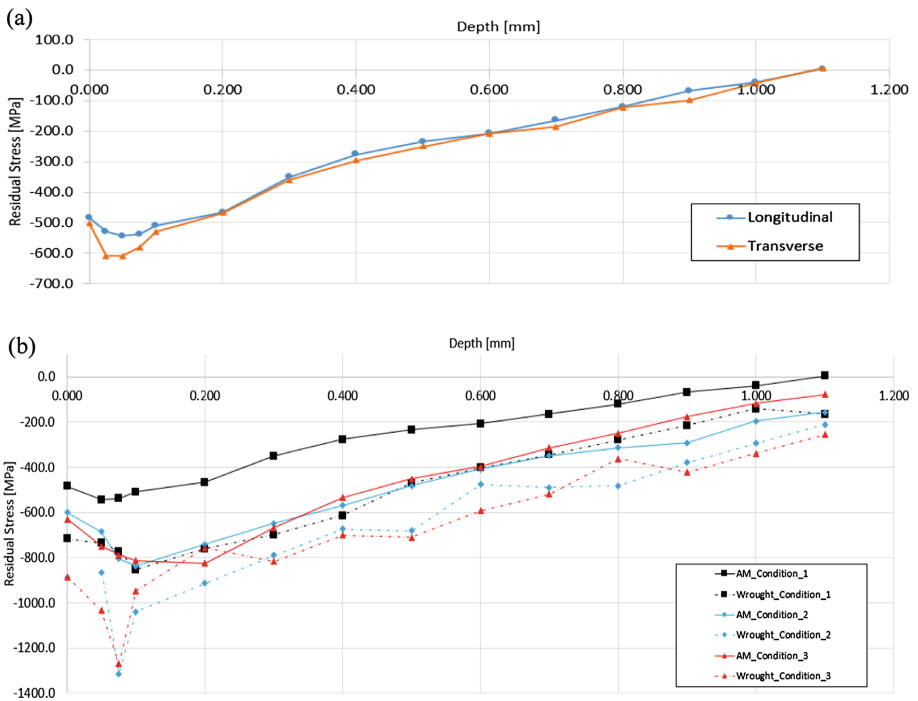


Fig. 4. Residual stress distributions. (a) Comparison of AM coupons through LSP in longitudinal and transverse direction, (b) comparison of wrought and AM components in various peening intensities.

3.2 Surface Roughness

Table 3. Surface roughness values of AM in the longitudinal and transverse directions.

	Longitudinal [μm]	Transverse [μm]
Pre-peening	1.15 ± 0.71	1.05 ± 0.73
Condition 1	1.36 ± 0.59	1.36 ± 0.63
Condition 2	1.33 ± 0.66	1.42 ± 0.89
Condition 3	1.40 ± 0.59	1.29 ± 0.29

The mean surface roughness with three standard deviation values in the longitudinal and transverse directions are shown in Table 3. Based on the measured data and the use of analysis of variance (ANOVA), there is a significant effect of the Ra values before and after LSP. Also, increasing power density do not have a significant effect on the Ra value with a 95% confidence interval. This is synonymous to Cellard [15] study on Ti-17 alloy which show that the surface roughness increase is moderate with increasing power densities on hard materials such as steel and titanium.

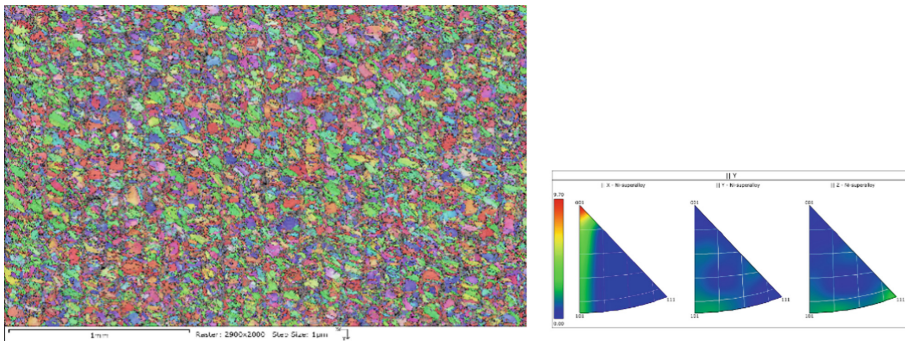


Fig. 5. EBSD inverse pole figure map showing the grain microstructure in the centre of AM samples of IN718 after LSP

3.3 Microstructure

Figure 5 shows the microstructure of AM specimens that have been subjected to LSP Condition 2. Since the analysis was performed at the centre of the sample away from surfaces subjected to the LSP this shows the microstructure of the material after the AM process. The AM samples exhibit a mixture of equiaxed and columnar grains, with grain size ranging from $3.57 \mu\text{m}$ to $129 \mu\text{m}$. In addition, it has an average major axis of $17.9 \mu\text{m}$ and an average minor axis of $8.88 \mu\text{m}$. The IPF map suggest that there is an inclination to $\langle 100 \rangle$ fiber texture along the build direction of the AM samples (refer to Fig. 1), which was also observed by other researchers [17, 19]. On the other hand, grain texture of LSP treated wrought material displayed a typical equiaxed grain structure [17] as shown in Fig. 6.

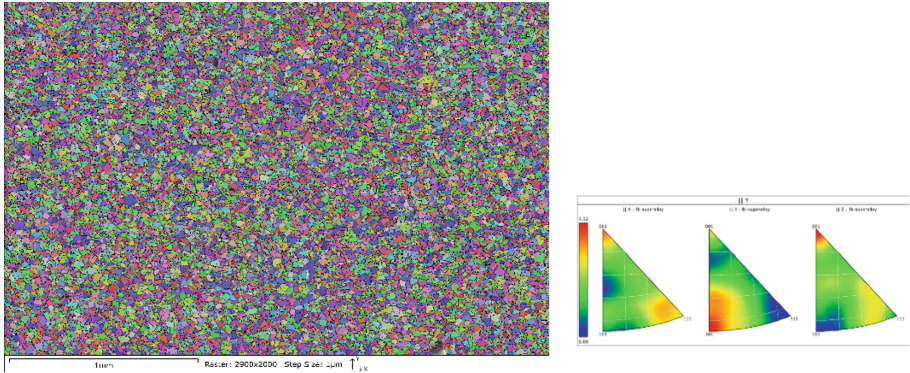


Fig. 6. EBSD maps and inverse pole showing the microstructure of the wrought samples of IN718 after LSP

Figure 7 illustrates the equivalent circle diameter distribution of LSP AM and LSP wrought IN718 that has been superimposed onto one another. The wrought sample display a normal distribution with grain size ranging from 3.57 μm to 102 μm , and a mean diameter of 23.2 μm . In contrast, the AM sample seem to display a bimodal distribution that is skewed to the left which result in a smaller mean diameter of the grain size as compared to the wrought samples. This difference is mainly attributed to how the samples were manufactured. The rapid heating and cooling effect of the L-PBF give rise to this anomaly where a mixture of both equiaxed and columnar grains were promoted. Generally, the temperature gradient and the thermal-gradient at the solid-liquid interface during the build process affects the microstructure dimensions [18].

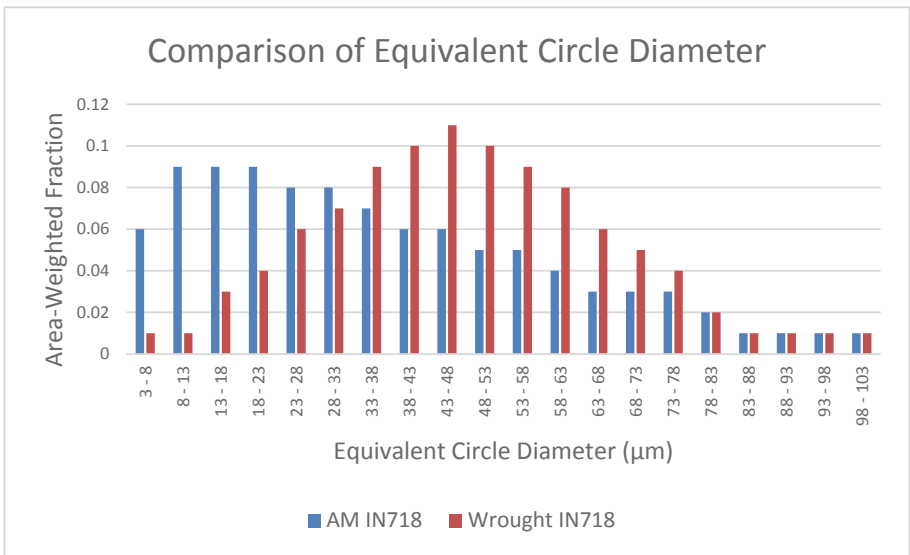


Fig. 7. Comparison of equivalent circle diameter of LSP AM and wrought IN718

The Kernel Average Misorientation (KAM) map of both LSP Condition 2 treated wrought and AM IN718 samples are shown in Fig. 8. KAM is used to represent the average misorientation between a given point and its nearest neighbours which belongs to the same grain. The analysis helps to understand local lattice distortion and could suggest stored strain energy in the grain. Interestingly, the AM sample seems to have a relatively high KAM which may suggest that recrystallisation has taken place during the build process or the inherent characteristic of the AM powder. Further investigations are necessary before any conclusion can be made.

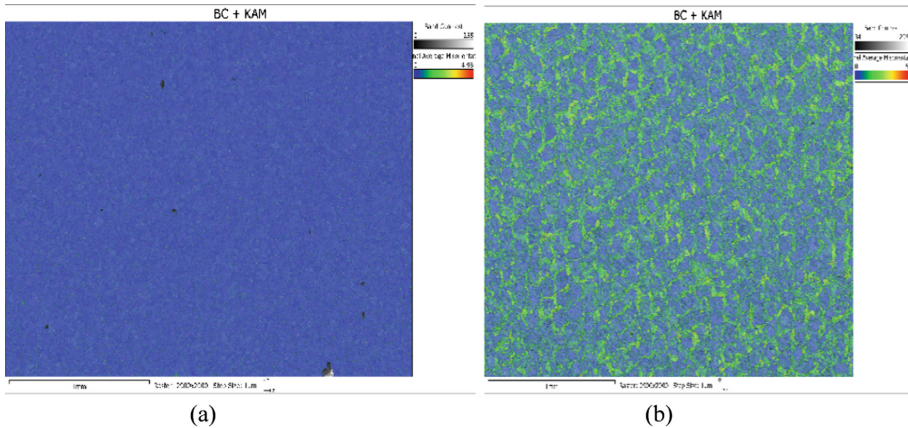


Fig. 8. KAM map of (a) LSP wrought IN718 and (b) LSP AM IN718

4 Conclusions

AM coupons that were laser peened exhibited a lower depth of influence and lower maximum compressive stress as compared to the wrought components. On the surface, AM components that were subjected to Condition 2 displayed a maximal compressive residual stress of around 600 MPa whereas the wrought counterpart was approximately 891 MPa. The differences between these two manufacturing techniques sums up to approximately 25%. Interestingly, the general trend of the stresses throughout the depth were relatively similar and its highest compressive stress act at a depth of 100 μm . Even at its lowest LSP power density, both AM and wrought could have up to 1.1 mm depth of influence. Also, increasing power densities do not necessary translate to a higher compressive stresses due to the occurrence of pressure saturation.





The mean diameter of the grain size of the LSP AM IN718 seem to suggest a bimodal distribution with much smaller grains as compared to its wrought counterpart. The KAM analysis showed that recrystallisation may have happened during AM process for various reasons that was not investigated in this study. Future work will focus on the amount of cold work that was imparted into the specimen to validate the deep compressive stresses that LSP could provide. Also, the fatigue life of these components will be studied to give an overview of the applicability of AM material on critical applications.

References

1. Ngo, T.D., et al.: Additive manufacturing (3D printing): a review of materials, methods, applications and challenges. *Compos. Part B Eng.* **143**, 172–196 (2018)
2. Qi, H., et al.: Studies of standard heat treatment effects on microstructure and mechanical properties of laser net shape manufactured Inconel 718. *Metall. Mater. Trans. A* **40**(10), 2410–2422 (2009)
3. Reed, R.C.: *The Superalloys: Fundamentals and Applications*. C.U. Press, Cambridge (2006)
4. Kreitzberg, A., et al.: Effect of heat treatment and hot isostatic pressing on the microstructure and mechanical properties of Inconel 625 alloy processed by laser powder bed fusion. *Mater. Sci. Eng. A* **689**, 1–10 (2017)
5. Tillmann, W., et al.: Hot isostatic pressing of IN718 components manufactured by selective laser melting. *Addit. Manuf.* **13**, 93–102 (2017)
6. Xu, Z., et al.: Effect of post processing on the creep performance of laser powder bed fused Inconel 718. *Addit. Manuf.* **24**, 486–497 (2018)
7. Zhang, D., et al.: Comparison of microstructures and mechanical properties of Inconel 718 alloy processed by selective laser melting and casting. *Mater. Sci. Eng. A* **724**, 357–367 (2018)
8. Zhuang, W., et al.: Deep surface rolling for fatigue life enhancement of laser clad aircraft aluminium alloy. *Appl. Surf. Sci.* **320**, 558–562 (2014)
9. Kattoura, M., et al.: Effect of laser shock peening on elevated temperature residual stress, microstructure and fatigue behavior of ATI 718Plus alloy. *Int. J. Fatigue* **104**, 366–378 (2017)
10. AlMangour, B., Yang, J.-M.: Improving the surface quality and mechanical properties by shot-peening of 17-4 stainless steel fabricated by additive manufacturing. *Mater. Des.* **110**, 914–924 (2016)
11. Nikitin, I., et al.: High temperature fatigue behaviour and residual stress stability of laser-shock peened and deep rolled austenitic steel AISI 304. *Scr. Mater.* **50**(10), 1345–1350 (2004)
12. Peyre, P., et al.: Laser shock processing of aluminium alloys. Application to high cycle fatigue behaviour. *Mater. Sci. Eng. A* **210**, 102–113 (1996)
13. Kalentics, N., et al.: Laser shock peening: a promising tool for tailoring metallic microstructures in selective laser melting. *J. Mater. Process. Technol.* **266**, 612–618 (2019)
14. Kalentics, N., et al.: Tailoring residual stress profile of selective laser melted parts by laser shock peening. *Addit. Manuf.* **16**, 90–97 (2017)
15. Cellard, C., et al.: Laser shock peening of Ti-17 titanium alloy: influence of process parameters. *Mater. Sci. Eng. A* **532**, 362–372 (2012)
16. Fabbro, R., et al.: Physics and application of laser shock processing of materials. In: *Proceedings of SPIE - The International Society for Optical Engineering* (2000)
17. Gribbin, S., et al.: Role of grain structure, grain boundaries, crystallographic texture, precipitates, and porosity on fatigue behavior of Inconel 718 at room and elevated temperatures. *Mater. Charact.* **149**, 184–197 (2019)
18. Saboori, A., et al.: An overview of additive manufacturing of titanium components by directed energy deposition: microstructure and mechanical properties. *Appl. Sci.* **7**(9), 883 (2017). <https://doi.org/10.3390/app7090883>
19. Smith, D.H., et al.: Microstructure and mechanical behavior of direct metal laser sintered Inconel alloy 718. *Mater. Charact.* **113**, 1–9 (2016)
20. Ganesh, P., et al.: Studies on fatigue life enhancement of pre-fatigued spring steel specimens using laser shock peening. *Mater. Des.* (1980–2015) **54**, 734–741 (2014)
21. Leap, M.J., et al.: Effects of laser peening on fatigue life in an arrestment hook shank application for Naval aircraft. *Int. J. Fatigue* **33**(6), 788–799 (2011)



A Comparison of Surface and Sub-surface Features Induced by Shot Peening vs. Laser Peening on a Duplex Aged Beta Ti Alloy

S. Sudhagara Rajan¹ , Geetha Manivasagam² ,
Sathya Swaroop³ , and Nageswara Rao Muktinutalapati¹ 

¹ School of Mechanical Engineering, Vellore Institute of Technology,
Vellore 632014, Tamil Nadu, India
sudhagar.rajana@gmail.com

² Centre for Biomaterials, Cellular and Molecular Theranostics, Vellore Institute
of Technology, Vellore 632014, Tamil Nadu, India
geethamanivasagam@vit.ac.in

³ Surface Modification Laboratory, School of Advanced Sciences,
Vellore Institute of Technology, Vellore 632014, Tamil Nadu, India

Abstract. The paper presents a study of the surface and subsurface characteristics induced by laser peening without coating (LPwC) and dual shot peening (DSP) on the duplex aged Ti-15 V-3Al-3Cr-3Sn alloy. In 3D-optical topography analysis, DSP resulted in a six-fold enhancement in the surface roughness (S_a). Whereas, LPwC resulted in unaltered surface roughness (S_a) compared to the polished/unpeened sample. In cross-sectional microstructure studies, deformed grains and heat affected zones were observed in the near surface region of shot peened, and laser peened samples respectively. Moreover, compared to bulk hardness, shot peening and laser peening has resulted in maximum increment of $\sim 28\%$ and $\sim 12\%$ in microhardness of the near peened surface region respectively.

Keywords: Shot peening · Laser peening · Beta titanium alloy

1 Introduction

Known for their high strength and ability to attain a broad range of strength through heat treatment, beta titanium alloys hold a leading position in the aerospace industries [1, 2]. A significant portion (15 to 16%) of the weight of Boeing 787 is predominantly contributed by high strength metastable beta titanium alloys [3]. Among the beta titanium alloys, Ti-15-3 alloy is an excellent candidate for airframe application due to its optimum strength-toughness combination when compared with the alpha-beta and alpha alloys [4]. Besides, cold formability of Ti-15-3 makes this alloy an economical choice for thin sheet application in supersonic aircraft [5, 6]. However, the major disadvantage of the Ti-15-3 alloy is its low fatigue life compared to alpha-beta alloys [7] and even with other beta titanium alloys [8]. To overcome this issue, various heat treatment/aging and thermomechanical processing have been carried out to enhance

fatigue life [7, 9, 10]. Other than heat treatment, surface peening (i.e., shot peening and laser peening) is the most promising method utilised for enhancing the fatigue life of titanium alloys [11, 12]. Since 1950s, conventional shot peening is being a promising technique to enhance the fatigue life of metal alloys. Moreover, Shot peening has resulted in the 29% and 27% increment in the fatigue limit of Ti-10V-2Fe-3Al and Ti-5Al-5Mo-5V-1Cr-1Fe alloy respectively [13]. Recently, shot peening induced nanocrystallisation and increase in microhardness were reported in Ti-10 V-2Fe-3Al [14]. However, owing to the capability of imparting deeper residual stress [15], ultimate control in operation and unaltered surface [16], laser peening is being widely explored as a better tool to enhance the fatigue life of titanium alloys. Laser peening without coating (LPwC), a recent technique invented a couple of decades ago and successfully attempted in various materials such as steels, aluminium and titanium alloys [17]. LPwC utilises low energy Nd-YAG laser and considered more economical compared to conventional laser peening. Despite the increased surface roughness caused due to the absence of a sacrificial coating, better fatigue life enhancement was reported for Ti-6Al-4V [18]. In beta titanium LCB (Ti-6.8 Mb-4.5Fe-1.5Al) alloy, LPwC yielded a notable increase in fatigue life [19]. Recently, the effect of LPwC on Ti-15-3 alloy in solution treated and single aged condition was reported [20, 21]. Other than this, the literature on shot peening and LPwC of beta titanium/Ti-15-3 alloys is sparse. Hence, in this present paper, the effect of LPwC and shot peening on the surface and subsurface characteristic of duplex aged Ti-15-3 alloy is studied.

2 Material and Method

Ti-15V-3Al-3Cr-3Sn (Ti-15-3) alloy used in this study was procured in the solution treated condition (850 °C/1 h). Flat strip samples with dimensions of 76 × 13 × 5 mm (lbh) and disc samples with 16 mm dia and 5 mm thick were machined using EDM for the dual shot peening and LPwC respectively. The machined samples were subjected to the duplex aging at 250 °C/24 h/AC + 520 °C/8 h/AC to impart an excellent strength-ductility combination as reported by Santhosh et al. [10]. Prior to the peening process, aged samples were mechanically polished to obtain a surface roughness (Sa) of <0.3 µm. Dual shot peening (DSP) was performed in two stages (i) peening with cast steel shots (S330) (ii) peening with glass beads (AGB 15). Almen intensity of the peening process was 0.38 mm A, and the coverage of 200% was maintained to ensure the uniform peening. Shot peening was performed at Curtis Wright Surface Technologies – Bangalore, India. Laser Peening without Coating (LPwC) was performed on the disc samples using Nd-YAG laser in the author's laboratory. LPwC parameters are given in Table 1.

Table 1. LPwC parameter

Operating wavelength	532 nm
Power density	5 GW/cm ²
Spot diameter	0.8 mm
Overlap	78%
Confinement medium	Water

Surface topography of the peened samples was analysed using Talysurf CCI non-contact 3D roughness profiler. The area examined was 0.8×0.8 mm. Peened samples were cross-sectioned using a low-speed diamond saw and hot mounted in such a way that the cross-sectioned surface is exposed for further examination. After standard metallographic preparation, the microstructure of the subsurface region of the peened samples was observed through an optical microscope. Through depth microhardness profile was measured using MATUZAWA-MMT-X automatic loading and unloading machine with 100 g load and 10 s dwell time.

3 Results and Discussions

3.1 Surface Topography

Fatigue is the most dominating mechanism of failure when it comes to aerospace and automotive components. In most of the cases, fatigue failure originates right from the surface importantly due to the presence of tensile residual stresses induced during various manufacturing processes. Hence, mechanical surface modification technique such as laser peening and shot peening can be more effective in enhancing fatigue properties, in addition to bulk processing techniques such as heat treatment. However, surface peening may also lead to an increase of surface roughness, and this may deteriorate the fatigue life by accelerating crack nucleation during fatigue loading. Hence, in the present study, in addition to the conventional shot peening, peening with glass beads were performed to reduce the surface roughness and also to remove the residues of the previous stage peening. As expected, surface topography analysis reveals a remarkable effect of the second stage peening in reducing ($\sim 45\%$) the surface roughness (Arithmetic mean height - S_a) induced by the first stage of peening. This notable reduction is attributed to the removal of weaker asperities formed during the first stage of peening. Moreover, this reduction in surface roughness could result in a remarkable beneficial effect on fatigue behaviour. Despite this favourable note, compared to the unpeened and LPwC samples, DSP resulted in a rougher surface in terms of both S_a & S_z (Maximum Height). Compared to the unpeened/polished sample ($S_a = 0.22 \mu\text{m}$), the surface roughness (S_a) of the laser peened sample ($S_a = 0.20 \mu\text{m}$) remains almost same. However, in terms of the S_z value, laser peened sample ($S_z = 14.3 \mu\text{m}$) shows more than a three-fold increase compared to the unpeened/polished sample ($S_z = 3.9 \mu\text{m}$). This drastic increase is believed to be contributed by the erratic presence of LPwC induced resolidified droplets and craters. Due to the significant influence on the fatigue behavior, S_a and S_z values were selected among the other roughness parameters (Fig. 1).

3.2 Microstructure

In case of laser peening, when laser pulses were irradiated on the target material surface, the surface gets vaporised due to the direct ablation, and during this process, the temperature at the surface will excite beyond $10,000^\circ\text{C}$ for a shot time (ns) [22]. Due to the absence of protective coating, direct laser-material interaction happened in the LPwC

process and this lead to the formation of the heat affected layers in the near peened surface region as shown in Fig. 2(a). In 6061-T6 aluminium alloy, the undoing effect of such heat affected zone on the near-surface microhardness and residual stress was clearly brought out by Gomez-Rosas et al. [23]. On the other hand, as the temperature involved in the shot peening process is comparatively insignificant. Hence, the shot peened near-surface region is found to be free of the heat affected zone. Deformed and fragmented grains were observed in the near surface region as shown in Fig. 2(b). This deformation is attributed to the severe mechanical distortion caused during the peening process. As a concluding remarks, shot peening has pronounced mechanical effects and laser peening has a pronounced thermal effect in the surface and near surface region.

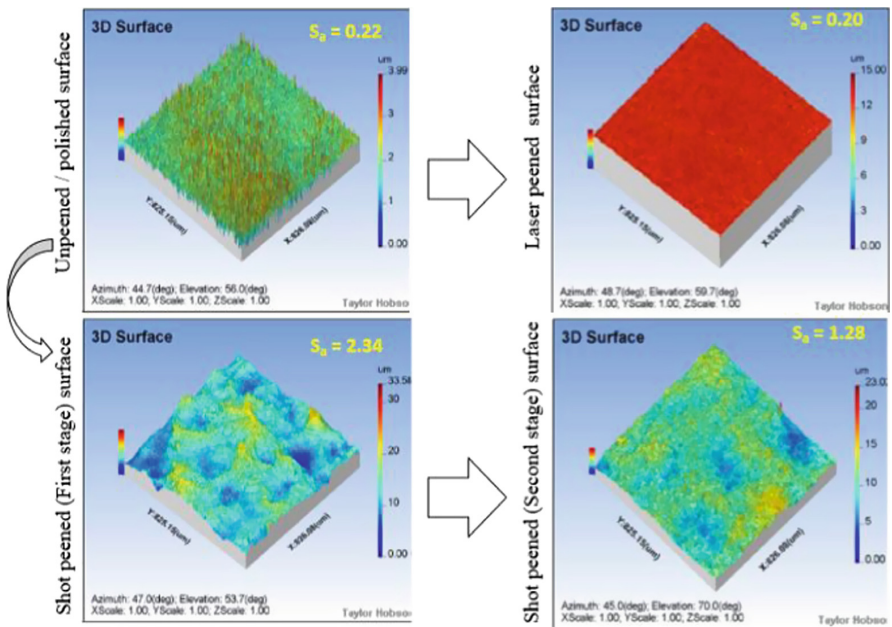


Fig. 1. Surface topography

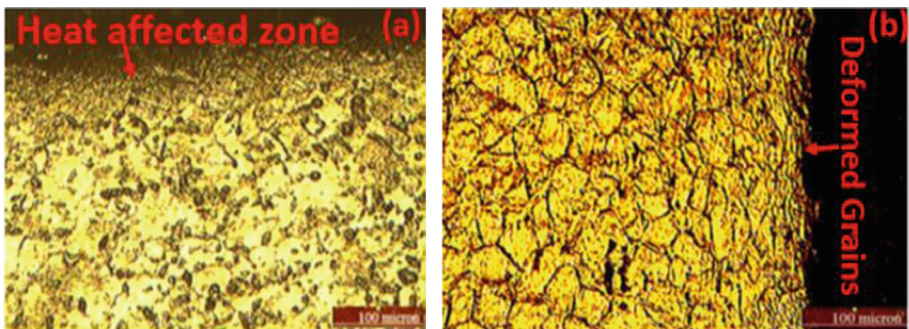


Fig. 2. (a) Laser peened, (b) Shot peened near surface region

3.3 Micro-hardness Profile

The important and common outcome of the peening processes is work hardening effect resulted due to a local plastic deformation. In the present study, shot peening results in a higher magnitude of the hardness ($538 \pm 17 \text{ HV}_{0.1}$) right from the near-surface region ($50 \mu\text{m}$ from the shot peened surface) as shown in Fig. 3. This pronounced effect on enhancing microhardness is attributed to the enhanced microstrain and cold working effect of shot peening compared to laser peening. In line with the present observation, Pant et al. [24] have reported a higher work hardening effect of shot peening compared to laser peening. Moreover, in Ti–10 V–2Fe–3Al alloy, a remarkable increase in surface microhardness ($\sim 37\%$) compared to unpeened surface microhardness is achieved through shot peening [14]. This increased microhardness will be beneficial in retarding the fatigue crack nucleation and hindering the fatigue crack propagation. However, in laser peened sample, the hardness value measured in the near-surface region is slightly lower than the further measurements in the consecutive depths. This observation is attributed to the softening effect due to direct laser-material interaction [25].

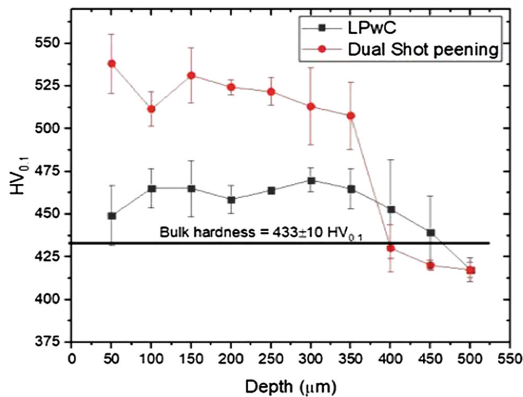


Fig. 3. Through depth microhardness profile

4 Conclusions

- Surface roughness (S_a) induced by the first stage of shot peening was significantly reduced ($\sim 47\%$) by second stage peening.
- Shot peening resulted in the higher surface roughness (S_a & S_z) compared to laser peening without coating (LPwC).
- LPwC resulted in a three-fold increase in maximum height (S_z) value compared to the S_z value of the unpeened/polished sample. However, surface roughness in terms of S_a remains unaltered.

- LPwC induced heat affected layers and shot peening resulted deformation in grains were revealed through subsurface microstructure analysis.
- Shot peening's better work hardening effect, and laser peening's near-surface softening effect was substantiated through the through-depth microhardness profile.

Acknowledgement. We would like to thank Vellore Institute of Technology (VIT)-Vellore for their infrastructure and support for publishing this research article. We also thank Curtis Wright Surface Technologies – Bangalore, India for helping us in shot peening the samples. The Authors would also like to thank Science & Engineering Research Board (SERB) – India for the financial grant (ITS/2019/003713) to attend this conference.

References

1. Boyer, R.R., Briggs, R.D.: The use of beta titanium alloys in the aerospace industry. *J. Mater. Eng. Perform.* **14**, 680–684 (2005)
2. Boyer, R.R.: An overview on the use of titanium in the aerospace industry. *Mater. Sci. Eng. A* **213**, 103–114 (1996)
3. Banerjee, D., Williams, J.C.: Perspectives on titanium science and technology. *Acta Mater.* **61**, 844–879 (2013)
4. Santhosh, R., Geetha, M., Nageswara Rao, M.: Recent developments in heat treatment of beta titanium alloys for aerospace applications. *Trans. Indian Inst. Met.* **70**, 1681–1688 (2016)
5. Kazanjian, S.M., Starke Jr., E.A.: Effects of microstructural modification on fatigue crack growth resistance of Ti-15V-3Al-3Sn-3Cr. *Int. J. Fatigue* **21**, 127–135 (1999)
6. Sudhagara Rajan, S., Jithin, V., Geetha, M., Nageswara Rao, M.: Processing of beta titanium alloys for aerospace and biomedical applications, vol. 2, p. 64. Intech open (2018)
7. Boyer, R.R., Rack, H.J., Venkatesh, V.: The influence of thermomechanical processing on the smooth fatigue properties of Ti-15V-3Cr-3Al-3Sn. *Mater. Sci. Eng. A* **243**, 97–102 (1998)
8. Jha, S.K., Ravichandran, K.S.: High-cycle fatigue resistance in beta-titanium alloys. *JOM* **52**, 30–35 (2000)
9. Santhosh, R., Geetha, M., Saxena, V.K., Nageswara Rao, M.: Studies on single and duplex aging of metastable beta titanium alloy Ti-15V-3Cr-3Al-3Sn. *J. Alloy. Compd.* **605**, 222–229 (2014)
10. Santhosh, R., Geetha, M., Saxena, V.K., Nageswara Rao, M.: Effect of duplex aging on microstructure and mechanical behavior of beta titanium alloy Ti-15V-3Cr-3Al-3Sn under unidirectional and cyclic loading conditions. *Int. J. Fatigue* **73**, 88–97 (2015)
11. Drechsler, A., Dorr, T., Wagner, L.: Mechanical surface treatments on Ti-10V-2Fe-3Al for improved fatigue resistance. *Mater. Sci. Eng. A* **243**, 217–220 (1998)
12. Kiese, J., Zhang, J., Schauerte, O., Wagner, L.: Shot peening to enhance fatigue strength of TIMETAL LCB for application as suspension springs. In: *Shot Peening*, pp. 380–385 (2003)
13. Gao, Y.K.: Influence of shot peening on tension–tension fatigue property of two high strength Ti alloys. *Surf. Eng.* **22**, 299–303 (2006)
14. Zheng, H.Z., Guo, S.-H., Luo, Q.-H., Shu, X.-Y.: Effect of shot peening on microstructure, nanocrystallization and microhardness of Ti-10V-2Fe-3Al alloy surface. *J. Iron Steel Res. Int.* **26**, 52–58 (2019)

15. Gujba, A.K., Medraj, M.: Laser peening process and its impact on materials properties in comparison with shot peening and ultrasonic impact peening. *Materials (Basel)* **7**, 7925–7974 (2014)
16. Anand Kumar, S., Sundar, R., Ganesh Sundara Raman, S., Kumar, H., Kaul, R., Ranganathan, K., Oak, S.M., Kukreja, L.M., Bindra, K.S.: Influence of laser peening on microstructure and fatigue lives of Ti-6Al-4V. *Trans. Nonferrous Met. Soc. China (English Ed.)* **24**, 3111–3117 (2014)
17. Sano, Y., Akita, K., Masaki, K., Ochi, Y., Altenberger, I., Scholtes, B.: Laser peening without coating as a surface enhancement technology. *JLMN-J. Laser Micro/Nanoeng.* **1**, 161–166 (2006)
18. Altenberger, I., Nalla, R.K., Sano, Y., Wagner, L., Ritchie, R.O.: On the effect of deep-rolling and laser-peening on the stress-controlled low- and high-cycle fatigue behavior of Ti-6Al-4V at elevated temperatures up to 550 °C. *Int. J. Fatigue* **44**, 292–302 (2012)
19. Maawad, E., Sano, Y., Wagner, L., Brokmeier, H.G., Genzel, C.: Investigation of laser shock peening effects on residual stress state and fatigue performance of titanium alloys. *Mater. Sci. Eng. A* **536**, 82–91 (2012)
20. Sudhagara Rajan, S., Swaroop, S., Manivasagam, G., Rao, M.N.: Fatigue life enhancement of titanium alloy by the development of nano/micron surface layer using laser peening. *J. Nanosci. Nanotechnol.* **19**, 7064–7073 (2019)
21. Sudhagara Rajan, S., Geetha, M., Ranganathan, M., Swaroop, S.: Influence of laser peening without coating on microstructure and fatigue limit of Ti-15V-3Al-3Cr-3Sn. *Opt. Laser Technol.* **111**, 481–488 (2019)
22. Masse, J.E., Barreau, G.: Laser generation of stress waves in metal. *Surf. Coat. Technol.* **70**, 231–234 (1995)
23. Gomez-Rosas, G., Rubio-Gonzalez, C., Ocaña, J.L., Molpeceres, C., Porro, J.A., Morales, M., Casillas, F.J.: Laser shock processing of 6061-T6 Al alloy with 1064 nm and 532 nm wavelengths. *Appl. Surf. Sci.* **256**, 5828–5831 (2010)
24. Pant, B.K., Pavan, A.H.V., Prakash, R.V., Kamaraj, M.: Effect of laser peening and shot peening on fatigue striations during FCGR study of Ti6Al4V. *Int. J. Fatigue* **93**, 38–50 (2016)
25. Umapathi, A., Swaroop, S.: Residual stress distribution in a laser peened Ti-2.5Cu alloy. *Surf. Coat. Technol.* **307**, 38–46 (2016)



Effect of Laser-Induced Microstructure in Cavitation Erosion Performance of Martensitic Stainless Steel

Niroj Maharjan^(✉) and Dennise Tanoko Ardi

Advanced Remanufacturing and Technology Centre, 3 CleanTech Loop,
CleanTech Two, #01/01, Singapore 637143, Singapore
maharjan_niroj@artc.a-star.edu.sg

Abstract. Cavitation erosion causes material removal from the surface of metal components submerged under swift flowing fluid due to implosions of gas bubbles on their surface. Since erosion is a surface degradation phenomenon, laser surface hardening can be a promising solution to tackle this problem without affecting the bulk properties of material. Laser acts as a localized surface heater which induces rapid non-equilibrium phase transformation and produces hard microstructure near the surface. In this paper, the effect of laser-induced microstructure on cavitation erosion performance of AISI 420 martensitic stainless steel is systematically investigated. Surface hardness as high as 700 HV is recorded after laser hardening and the microstructure consisted of fine carbides and retained austenite in a martensitic matrix. Such microstructure is attributed to result in high cavitation erosion resistance. The cavitation erosion resistance of laser hardened surface was found to be 18 times higher than that of untreated surface. The results indicate the significance of microstructural transformation induced by laser treatment on erosion performance of stainless steels.

Keywords: Cavitation erosion · Laser hardening · Microstructure · Hardness · Martensitic stainless steel

1 Introduction

Machine components submerged under swiftly flowing fluid such as propellers and turbines are prone to damage by cavitation erosion [1]. The erosion occurs by sudden collapse of cavities or bubbles that form due to local fluctuation in pressure inside the fluid [2]. The damage appears as pits due to removal of material by impact of bubbles and can be quite detrimental in some cases, demonstrated by significant mass losses and rough surfaces. Generally, such erosion is prevented by using an erosion resistant material such as austenitic steel with high work hardenability [3] or improving the design of the component to reduce pressure variation [4]. However, the solution can be very costly as it involves using expensive material (like stainless steels and high speed steels) or modifying the design.

An alternative cost effective method to combat cavitation erosion is to perform surface treatment of vulnerable areas in order to increase the life of the component.

Laser surface hardening is a well-established surface modification method which employs laser beam to increase hardness of steels [5]. It generates martensitic phase transformation near the surface due to rapid heating and cooling of the surface without affecting the bulk of the material. The method is widely used in automotive and heavy machinery industries to increase wear resistance of shafts, bearings and gears [6].

The phase transformation induced by laser treatment might have beneficial effect on improving cavitation erosion resistance. Generally, it is reported that the formation of fine-grained microstructure and increase in surface hardness produced by laser hardening contributes to significant improvement in cavitation erosion resistance [7–9]. An excellent review on cavitation erosion behavior of laser treated surfaces has been reported by Kwok et al. [10]. This indicates the potential of using laser surface treatment as a solution to tackle cavitation erosion problem. However, a systematic study investigating the influence of laser-induced microstructural changes in cavitation erosion resistance of stainless steel is still lacking.

In this study, the cavitation erosion performance of laser hardened stainless steel is investigated in detail. Cavitation tests were performed in an ultrasonic test rig which produces high frequency ultrasonic waves in a liquid to induce cavities formation near the surface of specimen. Various characterization studies such as microscopy, hardness testing and X-ray diffraction were performed to understand the effect of microstructure and properties of the hardened surface on cavitation erosion resistance. The study shows the improvement in cavitation erosion resistance after laser hardening compared to that of untreated surface.

2 Materials and Methodology

The material used for the study was AISI 420 martensitic steel, which is a corrosion resistant steel commonly used in pumps and valves that are prone to cavitation erosion. The chemical composition of the steel is shown in Table 1. Each specimen had a dimension of $40 \times 40 \times 10 \text{ mm}^3$ and was subjected to a standard stress relief heat treatment by heating in an air furnace at $650 \text{ }^\circ\text{C}$ for 2 h. This produced an annealed microstructure with a large number of spherical carbides randomly distributed in the matrix (see Fig. 1). The specimens were ground to an average roughness of about $0.7 \text{ }\mu\text{m}$ before performing laser treatment.

Table 1. Elemental composition of AISI 420 martensitic stainless steel

Elements	C	Si	Mn	P	S	Cr	Ni	Mo	V	Cu	Al
wt%	0.41	0.33	0.74	0.025	0.001	12.69	0.16	0.05	0.046	0.05	0.017

The laser hardening trials were performed using LaserTec 65 3D system (DMG Mori) which uses a high power diode laser of 1064 nm wavelength. The laser beam was focused through a focusing lens producing a beam spot diameter of 3 mm at the specimen surface. Different operating parameters were utilized to determine the optimal parameters to achieve hardened surface without any surface melting. Based on the

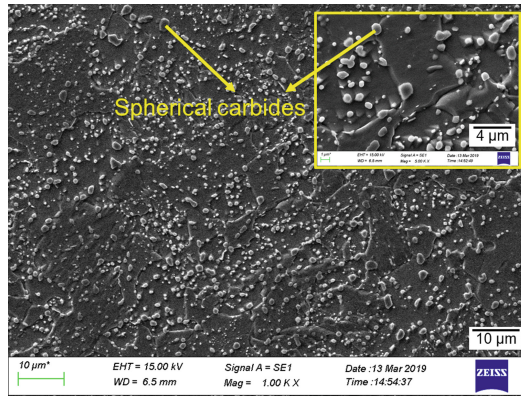


Fig. 1. A typical spheroidized microstructure of as-received steel showing carbides distributed randomly in the matrix

analysis, a laser power of 360 W and a traverse speed of 20 mm/s was chosen which delivered an energy density of about 5 J/mm^2 at the surface. The beam spot was scanned along the surface to perform a single pass laser treatment with an overlap of 60%. All the experiments were carried out in air.

For cavitation testing, an ultrasonic vibratory test setup conforming to ASTM G32-16 standard was utilized. Both as-received as well as laser hardened specimens were tested for comparison. The specimen was held stationary below the vibrating horn at a distance of 0.5 mm. The vibration frequency and peak-to-peak amplitude were 20 kHz and 50 μm respectively. The testing was performed for a total of 15 h with mass loss recorded at 1 h interval. The cavitation medium was distilled water maintained at a constant room temperature of $25 \pm 2^\circ\text{C}$.

The laser hardened surface and the eroded surface were characterized using optical microscope (Zeiss Axioscope A1) and electron microscope (Zeiss Evo HD25). Standard metallographic technique was implemented to study the cross-section microstructure of laser-hardened surface. Hardness measurements were performed using Vickers hardness indenter at 100 gf with 15 s dwell time. Furthermore, X-ray diffraction data were collected using Panalytical Empyrean X-ray diffractometer. The diffractometer used a copper target as a source of X-ray with wavelength $\lambda = 1.5404 \text{ \AA}$ ($\text{Cu K}_{\alpha 1}$). The residual stresses along the depth were measured by electrospackle pattern interferometry (ESPI) with hole drilling method (StressTech PRISM).

3 Results and Discussion

3.1 Characterization of Laser Hardened Surface

Figure 2 shows a typical cross-microstructure of the steel near the surface after laser hardening. The microstructure is clearly distinct from the parent microstructure. It consisted of refined microstructure with numerous δ -ferrite dendrites in martensitic matrix and some retained austenite. The rapid heating by the laser energy results in rapid

austenitization of the surface and produces non-equilibrium microstructure due to rapid cooling as the heat is conducted to the bulk of the material [11]. An affected region of about 660 μm thickness formed with the laser parameter chosen. The microstructure varied gradually along the depth due to decreasing influence of laser heating.

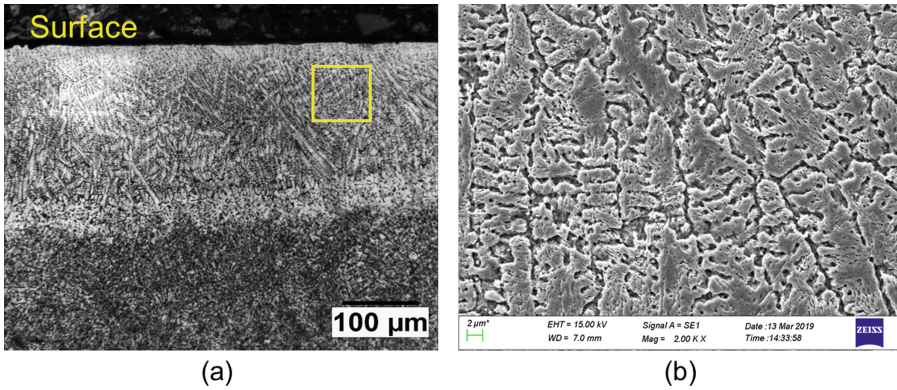


Fig. 2. Cross section microstructure of laser hardened steel showing (a) laser hardened region near the surface, and (b) magnified image of square inset in (a)

X-ray diffraction data was collected to verify the phases formed after laser hardening. Figure 3 compares the XRD diffractograms of as-received and laser hardened specimens. As observed in the micrographs, the as-received specimen consisted of ferrite peaks and laser hardened surface revealed peaks of martensite, austenite, carbides and some oxides.

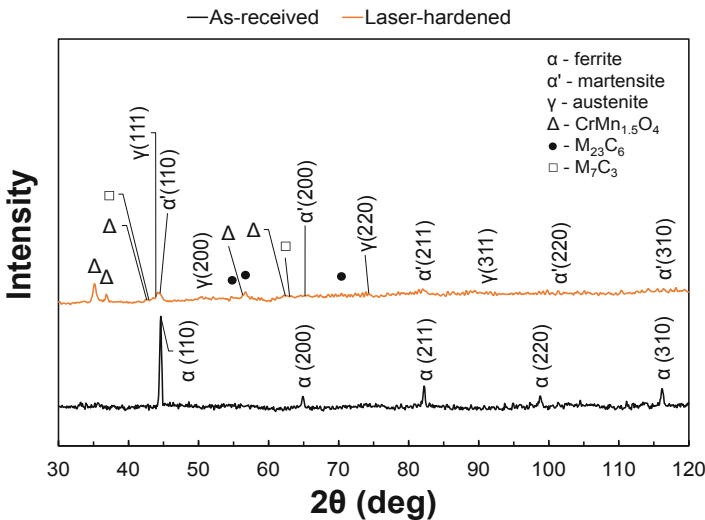


Fig. 3. X-ray diffraction data of as-received and laser hardened surfaces

The hardness measurements also supported the microstructure and phases observed from microscopy and XRD. As seen in Fig. 4, the laser hardened surface had a very high hardness (~ 700 HV) owing to the presence of hard martensite and microstructure refinement. The hardness decreased gradually along the depth. This suggests the decreasing volume fraction of martensite along the depth due to decreasing effect of laser heating [12]. The values reach the base material hardness at about $700 \mu\text{m}$ which matches with the laser-affected region measured by optical microscopy.

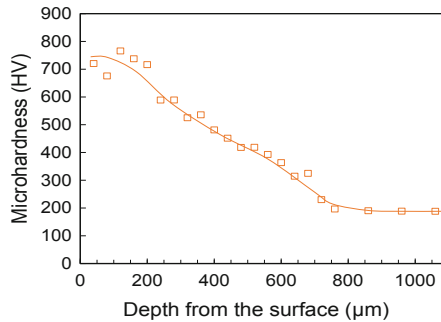


Fig. 4. Variation of microhardness along the depth for laser hardened specimen

Furthermore, the residual stresses induced by laser hardening is shown in Fig. 5. The as-received surface had slightly tensile residual stresses near the surface due to prior machining and polishing of the surface. In case of laser hardened specimen, compressive residual stresses were found near the surface which reached its maximum value of ~ -300 MPa at the depth of about $180 \mu\text{m}$. At higher depths, the stress state changed to tensile and reached very high tensile stresses at around $680 \mu\text{m}$. The residual stresses in laser hardened components arise from combination of volumetric dilatation due to phase transformation and thermal residual stresses [13]. Near the surface, the volume expansion due to martensitic phase transformation suppresses tensile thermal stresses and thus, produces net beneficial compressive residual stresses. At higher depths, however, the thermal effect is dominant and thus results in tensile stresses.

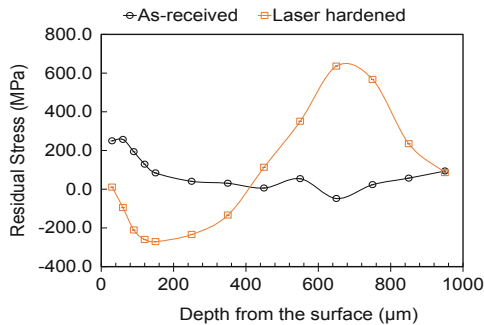


Fig. 5. Distribution of residual stresses along the depth for both as-received and laser hardened specimen

3.2 Cavitation Erosion Performance

The cumulative mass loss during cavitation test of the specimens tested as a function of time are plotted in Fig. 6. The as-received specimen did not show any appreciable mass loss up to 3 h of testing, which suggests the erosion is still in incubation phase. After 3 h, the mass loss increases linearly and reached up to 70 mg after 15 h of testing.

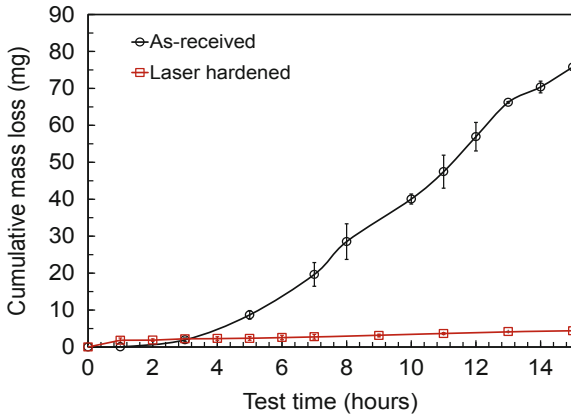


Fig. 6. Graph showing cumulative mass loss of the steel specimen against time during cavitation erosion test

Compared to as-received specimen, laser hardened specimen exhibited very little mass loss. Interestingly, a careful observation of the mass loss at initial stage shows the mass loss starts as early as 1 h of testing for laser hardened specimen. This is probably due to the removal of oxide layers from the surface which formed during laser hardening in air [14]. Nevertheless, the cumulative mass loss still does not increase tremendously as compared to as-received specimen. A mere mass loss of about 9.5 mg was recorded even after 40 h of testing.

Table 2 summarizes the cavitation performance of as-received and laser hardened surfaces after 15 h of testing. It can be seen that the cavitation erosion resistance of laser hardened specimen is about 18 times higher than that of as-received specimen. This shows that laser hardening enhances cavitation erosion resistance of 420 martensitic stainless steel.

Table 2. Comparison of cavitation erosion performance of as-received and laser hardened surfaces after 15 h of cavitation erosion testing

Specimen	Cumulative mass loss (mg)	Mean depth of erosion (μm)	Mean erosion rate ($\mu\text{m}/\text{h}$)	Cavitation erosion resistance (Re) ($\text{h}/\mu\text{m}$)
As-received	75.79	5.73	5.73	0.17
Laser hardened	4.39	0.65	0.33	3.06

Figure 7(a) shows the morphology of eroded surface after 15 h of cavitation testing. Due to extensive plastic deformation, the as-received specimens exhibited deep craters on the surface. The damage occurred due to localized pile up of plastic deformation by impact of micro-jets generated from sudden collapse of cavities [15]. Some work hardening might have occurred on the surface which after exceeding the strength of the material results in nucleation of cracks. The cracks then quickly propagate and coalesce producing brittle surface fracture. The phenomenon is repeated at multiple regions by collapsing of bubbles which finally manifests as pits and severe surface undulations. The damage on the laser hardened surface was superficial and less severe as shown in Fig. 7(b). A closer observation of the specimen showed early stage of cavitation with lots of shallow craters on the surface. This suggests the resistance of the hardened surface prevented formation of deep pits.

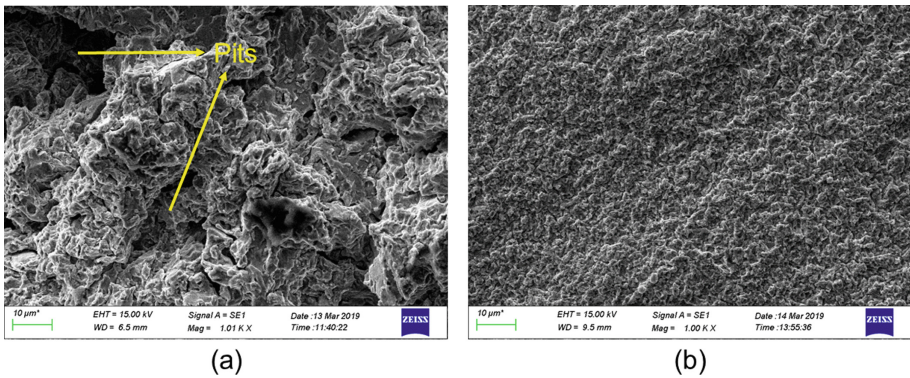


Fig. 7. Surface morphology after 15 h of cavitation erosion testing for (a) as-received surface, and (b) laser hardened surface

The higher cavitation resistance of laser hardened specimen reveals the significance of microstructure evolution in improving cavitation performance. Laser hardening produced martensitic phase transformation. Martensite is considered beneficial as it provides a cushioning effect during collapsing of bubbles by taking up some of the impact energy [16, 17]. In addition, it increases surface hardness which is often attributed to increase in cavitation erosion resistance [18, 19]. Moreover, the presence of retained austenite improves toughness of the material [20]. Furthermore, the compressive stresses are known to attenuate the crack initiation and propagation during loading. However, the influence of residual stresses is difficult to judge from the results as it had very little compressive residual stresses near the surface. Therefore, the results indicate the proper combination of martensite and retained austenite formed by laser hardening has beneficial effect on improving cavitation erosion resistance of AISI 420 martensitic stainless steel.

4 Conclusions

In this study, laser hardening of AISI 420 stainless steel was performed to investigate its effect on cavitation erosion performance and the results are compared with that of untreated steel. It was found that the cavitation erosion resistance of laser hardened steel is ~ 18 times higher than untreated steel after 15 h of cavitation erosion testing. Such improvement in cavitation erosion resistance is attributed to rapid non-equilibrium phase transformation produced by laser induced hardening. The fast heating and cooling by laser beam produces a refined microstructure consisting of martensite, retained austenite and carbides. The surface microstructure resists cavitation damage by virtue of its high hardness and resilience to fracture. Further work is being done to control the microstructure evolution during laser hardening using different processing parameters and evaluate its effect on cavitation erosion resistance.

Acknowledgements. Support for this work was provided by A*STAR Advanced Remanufacturing and Technology Centre (ARTC), Singapore under the In-house Research Project ARTC19_01_DSE. The authors thank Prof. Yeo Swee Hock at Nanyang Technological University, Singapore for assisting in cavitation test rig setup and Mr. Lek Yung Zhen for his help in performing cavitation erosion tests.

References

1. Karimi, A., Martin, J.L.: Cavitation erosion of materials. *Int. Met. Rev.* **31**, 1–26 (1986)
2. Sreedhar, B.K., Albert, S.K., Pandit, A.B.: Cavitation damage: theory and measurements—a review. *Wear* **372**, 177–196 (2017)
3. Liu, W., Zheng, Y.G., Liu, C.S., et al.: Cavitation erosion behavior of Cr–Mn–N stainless steels in comparison with 0Cr13Ni5Mo stainless steel. *Wear* **254**, 713–722 (2003)
4. Schiavello, B., Visser, F.C.: Pump Cavitation: various NPSHR criteria, NPSHA margins, impeller life expectancy. In: *Proceedings of the 25th International Pump Users Symposium*. Texas A&M University. Turbomachinery Laboratories (2009)
5. Maharjan, N.: Laser surface hardening of bearing steels (2019)
6. Nath, A.K., Sarkar, S.: Laser transformation hardening of steel. In: *Advances in Laser Materials Processing*, pp. 257–298. Elsevier (2018)
7. Kwok, C.T., Man, H.C., Cheng, F.T.: Cavitation erosion and pitting corrosion behaviour of laser surface-melted martensitic stainless steel UNS S42000. *Surf. Coat. Technol.* **126**, 238–255 (2000)
8. Lo, K.H., Cheng, F.T., Man, H.C.: Laser transformation hardening of AISI 440C martensitic stainless steel for higher cavitation erosion resistance. *Surf. Coat. Technol.* **173**, 96–104 (2003)
9. Mann, B.S.: Water droplet erosion behavior of high-power diode laser treated 17Cr4Ni PH stainless steel. *J. Mater. Eng. Perform.* **23**, 1861–1869 (2014)
10. Kwok, C.T., Man, H.C., Cheng, F.T., Lo, K.H.: Developments in laser-based surface engineering processes: with particular reference to protection against cavitation erosion. *Surf. Coat. Technol.* **291**, 189–204 (2016)
11. Ashby, M.F., Easterling, K.E.: The transformation hardening of steel surfaces by laser beams—I. Hypo-eutectoid steels. *Acta Metall.* **32**, 1935–1948 (1984)

12. Bojinović, M., Mole, N., Štok, B.: A computer simulation study of the effects of temperature change rate on austenite kinetics in laser hardening. *Surf. Coat. Technol.* **273**, 60–76 (2015). <https://doi.org/10.1016/j.surfcoat.2015.01.075>
13. Bailey, N.S., Tan, W., Shin, Y.C.: Predictive modeling and experimental results for residual stresses in laser hardening of AISI 4140 steel by a high power diode laser. *Surf. Coat. Technol.* **203**, 2003–2012 (2009)
14. Maharjan, N., Zhou, W., Zhou, Y., Wu, N.: Influence of operating parameters on morphology of laser hardened surfaces. In: *High-Power Laser Materials Processing: Applications, Diagnostics, and Systems VII*. International Society for Optics and Photonics (2018)
15. Dular, M., Požar, T., Zevnik, J.: High speed observation of damage created by a collapse of a single cavitation bubble. *Wear* **418**, 13–23 (2019)
16. Park, M.C., Shin, G.S., Yun, J.Y., et al.: Damage mechanism of cavitation erosion in austenite → martensite phase transformable Fe–Cr–C–Mn/Ni alloys. *Wear* **310**, 27–32 (2014)
17. Wang, K.Y., Lo, K.H., Kwok, C.T., et al.: The influences of martensitic transformations on cavitation-erosion damage initiation and pitting resistance of a lean austenitic stainless steel. *Mater. Res.* **19**, 1366–1371 (2016)
18. Espitia, L.A., Dong, H., Li, X.-Y., et al.: Cavitation erosion resistance and wear mechanisms of active screen low temperature plasma nitrided AISI 410 martensitic stainless steel. *Wear* **332**, 1070–1079 (2015)
19. da Severo, F.S., Scheuer, C.J., Cardoso, R.P., Brunatto, S.F.: Cavitation erosion resistance enhancement of martensitic stainless steel via low-temperature plasma carburizing. *Wear* **428**, 162–166 (2019)
20. Wu, R., Li, W., Zhou, S., et al.: Effect of retained austenite on the fracture toughness of quenching and partitioning (Q&P)-treated sheet steels. *Metall. Mater. Trans. A* **45**, 1892–1902 (2014)



Effect of In-Situ Laser Remelting on the Microstructure of SS316L Fabricated by Micro Selective Laser Melting

Balasubramanian Nagarajan¹, Zhiheng Hu¹, Shubo Gao², Xu Song¹,
Rui Huang¹, Matteo Seita², and Jun Wei¹(✉)

¹ Singapore Institute of Manufacturing Technology (SIMTech),
Agency for Science, Technology and Research (A*STAR), Singapore, Singapore
jwei@simtech.a-star.edu.sg

² School of Mechanical and Aerospace Engineering,
Nanyang Technological University, 50 Nanyang Avenue,
Singapore 639798, Singapore

Abstract. Due to the increasing attention on additive manufacturing of micro components, an in-house micro-selective laser melting (SLM) system using a fine laser spot size and a small layer thickness with an ability to handle fine powders has been developed recently. In this research work, in-situ laser remelting effects on the part density and microstructure of the SS316L parts fabricated using micro SLM have been studied. After every layer of micro SLM, laser remelting was performed using the same laser source. Remelting effects have been investigated at different process conditions with varying laser power and scanning speeds. The effects of remelting on the part porosity and microstructure of the micro SLM parts have been studied. Experimental results revealed that in-situ laser remelting significantly influences the part density and microstructure of the 316L micro SLM parts. The study highlights that in addition to the purpose of improving the surface finish, laser remelting can be used to tailor the microstructure and hence mechanical properties of the micro SLM parts.

Keywords: Micro selective laser melting · Laser remelting ·
AM post processing · Microstructure

1 Introduction

In recent times, there has been a growing demand for the fabrication of microcomponents and features using additive manufacturing (AM) due to its ability to realize complex geometries [1]. Microscale selective laser melting (SLM) typically consists of spot size < 40 μm , powder size and layer thickness lesser than 10 μm , has been considered as one of the suitable AM techniques to achieve metallic microfabrication [2]. As micro SLM employs fine laser spot sizes, the melt pool dynamics and subsequent solidification are different from the conventional SLM due to higher energy densities involved. Generally, a reduction in the laser beam diameter improves the surface finish, part density and mechanical properties [3]. Recently, a micro-selective laser melting (SLM) system has been developed with a fine laser spot size and a small

layer thickness with an ability to handle fine powders [4]. Despite a significant improvement in the feature resolution by micro SLM, the achieved surface finish and part density still needs improvement in order to realize defect-free microparts.

In order to improve the surface finish and part density of SLM parts, laser remelting or laser polishing has been successfully exploited by various researchers [5–7]. Remelting of the solidified surface after SLM typically results in the redistribution of surface peaks into the valleys due to the surface tension of the molten pool. Yasa and Kruth [8] reported that the laser remelting after every layer of SLM results in a reduction of pores formed between the melt pool boundaries, finer lamellar structures and microstructure refinement. The remelting parameters including laser power, scanning speed, number of scans and hatch spacing are found to influence the part characteristics.

In this paper, the effects of in-situ laser remelting of parts during micro SLM of SS316L have been investigated. Remelting experiments were conducted with different laser power and scanning speed to study the effect of process variables. After remelting, the part density and microstructure along the build direction are characterized using Optical microscope (OM) and Scanning electron microscope (SEM) to understand the effect of remelting on the micro SLM parts.

2 Experimental Setup

SS316L powders (gas-atomized) with an average diameter of 13 μm was used in the experiments. A self-developed micro SLM system consists of fiber laser (IPG) with a maximum power of 100 W was employed to conduct the trials. Major features of the developed system includes the following: fine laser spot size, precision drives to control the layer thickness to 1 μm and a modular powder-recoating system with the ability to handle fine powders. The laser spot size used for the SLM and remelting was 15 μm . The experiments were conducted in an inert gas environment. The same laser source has been used for both micro SLM and laser remelting experiments. After every layer of micro SLM, remelting has been conducted. The SLM parameters remain consistent for all the remelting trials in order to segregate the effect of remelting. The condition for SLM is as follows: laser power – 50 W, scanning speed – 400 mm/s, hatch spacing – 10 μm , hatch angle – 90°.

Laser remelting has been studied at different process conditions with varying laser power and scanning speed. The experimental condition for remelting trials are illustrated in Table 1. Only one remelting scan was performed for all the experimental conditions.

Table 1. Process parameters for micro SLM and laser remelting experiments

	Micro SLM (no remelting)	Laser remelting	
		First scanning (micro SLM)	Remelting
Laser power (W)	50	50	30, 50, 70
Scanning speed (mm/s)	400, 800, 1200, 1600	400	400, 800, 1200, 1600
Hatch spacing (μm)	10	10	10
Layer thickness (μm)	10	10	10

Test samples were fabricated with a dimension of 13 mm x 5 mm x 5 mm. For characterization, the cross section of the samples were cut in the center in the direction parallel to the hatch angle. After wire-cut, the samples were mounted and polished to characterize the porosity. Optical microscope (Olympus MX51) images were acquired and processed using an image processing software (Image-Pro) to measure the porosity of the samples. In order to reveal the microstructure, samples were etched using the Aqua Regia solution ($\text{HNO}_3:\text{HCl}:\text{H}_2\text{O} = 1:3:4$) for 50–60 s and characterized using Field emission scanning electron microscope (Carl Zeiss Ultra plus).

3 Results and Discussions

3.1 Microstructure of Micro SLM Samples

Figure 1 shows the OM and SEM micrographs of the micro SLM samples without remelting using 50 W laser power and 400 mm/s scanning speed. It can be noted that the microstructure of the micro SLM samples follow the typical characteristics of the conventional SLM. The columnar grains, typical for high cooling rates, can be visible from Fig. 1(a). The mode of heat transfer is found to be predominantly conduction whereas a small proportion of keyhole mode is also observed.

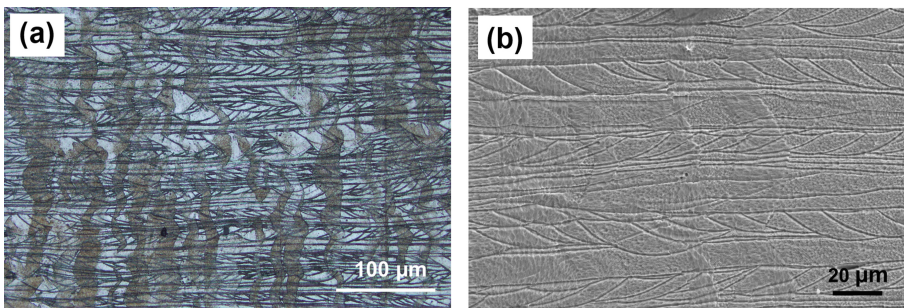


Fig. 1. Microstructure of SS316L parts after micro SLM without remelting (a) OM micrograph (b) SEM micrograph

3.2 Effects of Laser Remelting on Porosity

The porosity of the micro SLM samples before and after laser remelting is compared in Fig. 2. It is obvious that the as-SLM parts (Fig. 2(a)) contain binding defects and gas pores, thereby having high porosity. After laser remelting at 70 W power (Fig. 2(b)), the porosity has drastically reduced, highlighting the effect of laser remelting in improving the relative density of the micro SLM parts.

Figure 3 compares the effect of remelting process parameters on the porosity of the fabricated parts. The highest porosity was observed for the micro SLM parts without remelting at higher scanning speeds (not shown in Fig. 3). For the no remelting condition, an obvious increase in porosity along with the scanning speed was observed,

possibly due to insufficient melting at higher speeds. After remelting, the porosity is found to be reduced for most of the process conditions, except at high scanning speeds. At low scanning speeds of 400 and 800 mm/s, the porosity decreased drastically with an increase in remelting laser power, where the highest part density (99.8%) occurred for remelting at 70 W (as seen in Fig. 2(b)). At higher scanning speeds, an increase in porosity was observed between as-SLM condition and parts remelted at all laser power.

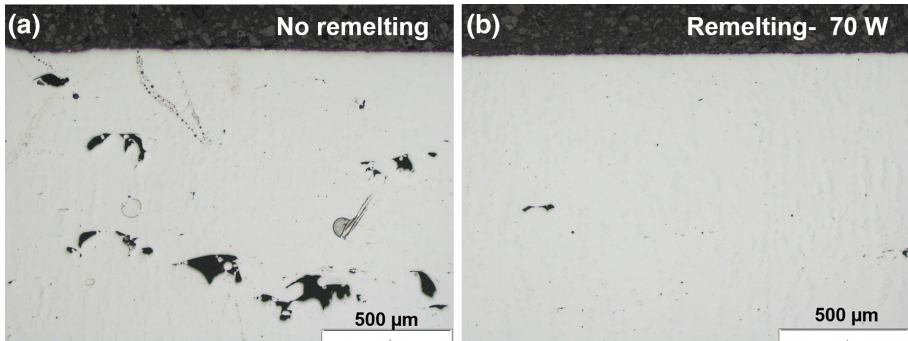


Fig. 2. Optical micrographs of sample cross-section at different conditions (a) As micro SLM (no remelting) (b) Remelting with the laser power of 70 W [Scanning speed – 400 mm/s]

The results highlight that both the laser power and scanning speed of the laser remelting influence the porosity of the resulting parts:

- Lower scanning speed evidently resulted in a higher density, irrespective of the remelting laser power.
- Laser power does not show an obvious trend with respect to the porosity though 50 W laser power (same as the first SLM layer scanning power) resulted in a better density for all the scanning speeds except that of 400 mm/s. It is understood that the remelting laser power has to be optimized to achieve a better part characteristics.

It can be noted that the porosity levels reported in this paper are relatively higher than that of the values typically reported for the conventional SLM. However, the relative part densities as high as 99.8% could be achieved for optimized process conditions.

3.3 Effects of Laser Remelting on Microstructure

Figure 4 illustrates the microstructure of the samples before and after laser remelting at varying laser power and scanning speed of remelting. Figure 5 compares the SEM images of the samples at different laser remelting power for the scanning speed of 400 mm/s. The depth of the melt pool after micro SLM is estimated to be around 20 μm . The remelting depth gradually increased with the increase in laser power from 30 W (Fig. 5(b)) to 70 W (Fig. 5(d)). At higher remelting powers, the remelting depth fully remelts the previous layer fabricated during micro SLM. Typically, laser

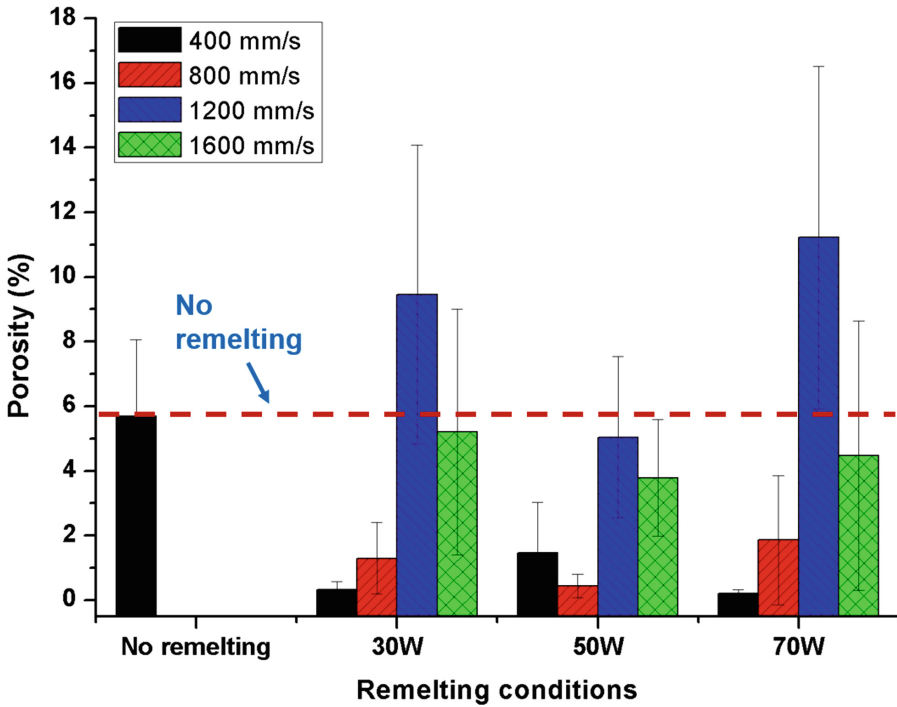


Fig. 3. Effect of in-situ laser remelting on the porosity of micro SLM parts at different remelting laser power and scanning speed

remelting results in a fine lamellar structure with uniform horizontal lines of melt pool boundaries [8]. However, it is noticed from Figs. 4 and 5 that, the melt pool scan tracks are still visible for most of the processing conditions in this study. Despite the occurrence of lamellar structure at lower scanning speed and higher laser power, it was not as prominent as reported in the previous studies. Yasa et al. [8] reported that horizontal lines became coarser with an increase in the hatch spacing (for overlap > 20%). Similarly, during this micro SLM study, the hatch spacing of 10 μm was used (much larger than 20% overlap), which explains the coarser horizontal lines and well formed melt pool scan tracks. In addition, only one remelting passes were conducted, which might be insufficient to significantly modify the melt pool morphology.

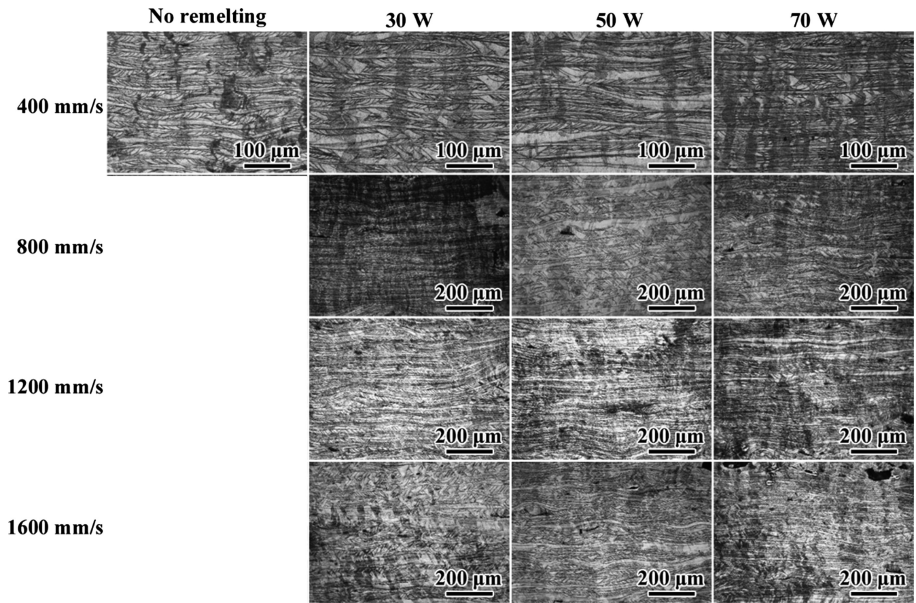


Fig. 4. Effect of remelting on the microstructure of the parts along the building direction for different processing conditions

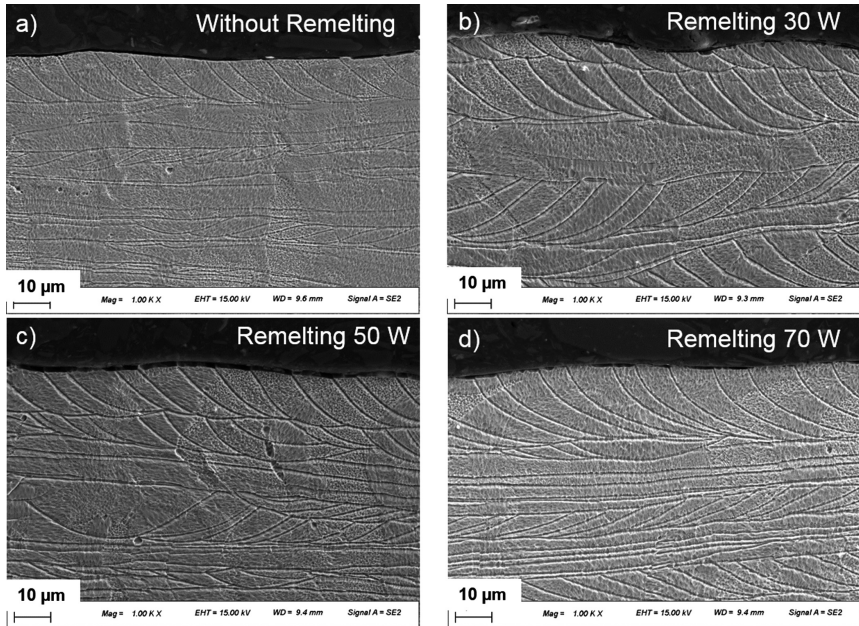


Fig. 5. Effect of in-situ remelting laser power on the microstructure of the micro SLM parts [Scanning speed – 400 mm/s]

4 Conclusions

This paper studied the effect of in-situ laser remelting during micro SLM of 316L powders. The following conclusions can be drawn from the results:

- (a) The porosity of the parts have significantly reduced after laser remelting for optimized process parameters, highlighting the effect of laser remelting in improving the part density of the micro SLM parts.
- (b) Both the laser power and scanning speed of the remelting process have a significant influence on the porosity where lower scanning speeds and an optimized laser power achieved better part densities.
- (c) The remelting depth increases with increasing laser power. In order to achieve a complete remelting of the previous layer fabricated during micro SLM, higher remelting laser powers are required.
- (d) The microstructure after remelting shows evidence of conduction mode heat transfer, overlapped SLM and remelting scan tracks and minor occurrences of lamellar structure.

References

1. Vaezi, M., Seitz, H., Yang, S.: A review on 3D micro-additive manufacturing technologies. *Int. J. Adv. Manuf. Technol.* **67**, 1721–1754 (2013)
2. Fischer, J., Kniepkamp, M., Abele, E.: Micro laser melting: analyses of current potentials and restrictions for the additive manufacturing of micro structures. In: *Proceedings of the 25th Annual International Solid Freeform Fabrication* (2014)
3. Liu, B., Wildman, R., Tuck, C., Ashcroft, I., Hague, R.: Investigaztion the effect of particle size distribution on processing parameters optimisation in selective laser melting process. In: *Solid Freeform Fabrication Symposium* (2011)
4. Hu, Z., Nagarajan, B., Song, X., Huang, R., Zhai, W., Wei, J.: Formation of SS316L single tracks in micro selective laser melting: surface, geometry, and defects. *Adv. Mater. Sci. Eng.* **2019**, 1–9 (2019)
5. Kruth, J.-P., Badrossamay, M., Yasa, E., Deckers, J., Thijs, L., Van Humbeeck, J.: Part and material properties in selective laser melting of metals. In: *Proceedings of the 16th International Symposium on Electromachining* (2010)
6. Marimuthu, S., Triantaphyllou, A., Antar, M., Wimpenny, D., Morton, H., Beard, M.: Laser polishing of selective laser melted components. *Int. J. Mach. Tools Manuf.* **95**, 97–104 (2015)
7. Ma, C.P., Guan, Y.C., Zhou, W.: Laser polishing of additive manufactured Ti alloys. *Opt. Lasers Eng.* **93**, 171–177 (2017)
8. Yasa, E., Kruth, J.-P.: Microstructural investigation of Selective Laser Melting 316L stainless steel parts exposed to laser re-melting. *Procedia Eng.* **19**, 389–395 (2011)



Tailoring Surface Roughness of Micro Selective Laser Melted SS316L by In-Situ Laser Remelting

Zhiheng Hu, Balasubramanian Nagarajan, Xu Song, Rui Huang,
Wei Zhai, and Jun Wei^(✉)

Singapore Institute of Manufacturing Technology (SIMTech),
Agency for Science, Technology and Research (A*STAR),
73 Nanyang Drive, Singapore 637662, Singapore
jwei@simtech.a-star.edu.sg

Abstract. Micro selective laser melting (SLM) has been developed for the fabrication of complex parts with a fine resolution and smooth finish. Although the fine laser spot size, fine powder size and thin layer thickness can result in a relatively smooth surface compared with the conventional SLM, the surface quality still needs to be improved. In this work, in-situ laser remelting was chosen for the improvement of the surface quality. The effects of in-situ laser remelting process parameters on the surface roughness were investigated using various remelting process parameters. The surface roughness of the top and side surfaces of the samples was characterized using an optical surface profiler. Surface morphology of the parts was characterized using scanning electron microscope. It was observed that the surface texture was evidently different after in-situ laser remelting. Overall, the obtained results indicate that tailoring the top surface roughness of the parts fabricated by micro SLM can be achieved through in-situ laser melting.

Keywords: Micro selective laser melting · Stainless steel · Remelting · Surface roughness

1 Introduction

Additive manufacturing (AM) has attracted an increasing attention due to its capability to fabricate complex components [1]. Selective laser melting (SLM), as one of the powder-bed based AM technology, has emerged as a promising technology for the fabrication of pure metals and alloys since 1980s [2]. It utilizes a high intensity laser beam to selectively melt the metallic powders [3]. Due to the ever-growing demand for miniaturization, micro SLM is gaining attention in recent times. Compared with the traditional SLM, micro SLM utilized smaller laser spot size, finer powders, and thinner layer thickness. It enhances the feature resolution of the traditional SLMed parts, which broadens the application of SLM technology.

In SLM, surface roughness is one of the most important characteristics of the parts, which depends upon the physical phenomena occurring during SLM process. There are a number of research works available in the literature on the surface characteristics of

the SLM process. The treatments, such as abrasive blasting [4], abrasive flow machining [5], electrochemical polishing [6] and laser remelting [7], have been evaluated on their capability to surface finish the SLM fabricated parts. Among them, laser remelting holds an edge as it can be used during the SLM process. To improve the surface quality, laser remelting can be divided into two types: surface remelting or interlayer remelting. The surface remelting does not increase the SLM process time vastly and it was proved useful to improve the top surface quality [8]. But interlayer remelting is still attractive as it can reduce the porosity and change the microstructure of the SLMed parts. Yu et al. [9] studied the influence of remelting on the surface roughness of the SLMed AISi10Mg. The results showed that both remelting from the same direction or opposite direction would improve the top surface quality but the side surface was not affected. Wei et al. [10] studied the remelting times effect on the surface roughness of the SLMed Ti-5Al-2.5Sn alloy. The results showed that the top surface quality gradually improved along with the remelting cycle. Similarly, remelting could not improve the side surface quality significantly.

It is understood from literature that the process parameters have a great effect on the surface roughness. However, previous studies on laser remelting were mainly concentrated on the effect of laser rescanning strategies. So this study focuses on effect of the process parameters of the in-situ remelting on both top and side surface roughness. Our results bridge the limited understanding of the interaction between laser remelting and surface roughness of the micro SLM parts.

2 Materials and Methods

Gas atomized spherical 316L stainless steel (SS316L) powders with a mean particle size of 13.32 μm were used in this experiment. The nominal chemical composition (wt%) of the powder was 12.6 Ni, 17.7 Cr, 2.67 Mo, 0.73 Si, 1.64 Mn, 0.027 C, 0.01 P, 0.15 Cu and Fe (balance). The powder was dried for 4 h at 353 K before the experiments.

A self-developed micro SLM machine was used for the experiments. The system consists of a continuous wave IPG fiber laser (wavelength: 1.07 μm , maximum power: 100 W, focused spot size: 15 μm), an automatic powder delivery system, a building platform with the precision of 1 μm , an enclosed process chamber for inert gas environment, and a computer system for the process control [11]. Samples with the size of 5*13*5 mm³ have been fabricated for the experiments. During the process, the building platform was preheated to 353 K. For the samples without laser remelting, the process parameters are listed in Table 1, and the scanning strategy is shown in Fig. 1a. The scanning direction changes by 90° for every layer. For the remelting samples, the process parameters are listed in Table 2, and the scanning strategy is shown in Fig. 1b. The re-scanning paths are exactly the same as the first scanning paths.

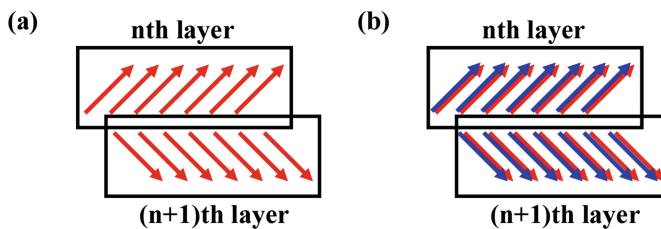
The top and side surface roughness (Sa) was measured by an Alicona optical 3D non-contact metrology system. The top and side surface morphology was captured by a scanning electron microscopy (SEM, JEOL IT300 LV). The mean surface roughness (Sa) of at least three measurements has been reported in this study.

Table 1. Process parameters of the samples without laser remelting

Process parameters	Value
Laser power (P, W)	50
Scanning velocity (v, mm/s)	400, 800, 1200, 1600
Hatch spacing (h, μm)	10
Layer thickness (s, μm)	10

Table 2. Process parameters of the laser remelting samples

Process parameters	First scanning	Re-scanning
Laser power (P, W)	50	30, 50, 70
Scanning velocity (v, mm/s)	400	400, 800, 1200, 1600
Hatch spacing (h, μm)	10	10
Layer thickness (s, μm)	10	10

**Fig. 1.** Scanning strategies of the samples (a) samples without laser remelting (b) laser remelting samples

3 Results and Discussion

3.1 Samples Without Laser Remelting

Figure 2 shows the surface roughness of the top and side surfaces of the samples fabricated at different scanning velocities. The results show that the surface roughness of both the top surface and side surface increases with the increasing scanning velocity. The observed results are found to be different from the results published by Mumtaz et al. [12] for SLM of IN625. They studied the surface roughness of the top and side surfaces of the thin wall parts and observed a similar result with the top surface but a contradicting trend with the side surface. Regarding the top surface, the bulk parts are more complex when compared to the thin wall parts. By comparing with our previous results of the single tracks [11], the top surface roughness of the bulk parts with the same parameters is much higher than that of the single tracks. The behavior can be attributed not only to the molten pool dynamics but also to the overlapping of the adjacent tracks as they have an effect on the top surface quality. With the same hatch spacing, the overlap ratio of the molten pool changes with the change of the molten pool size. The molten pool size decreases with the increasing of the scanning velocity. As a result, the overlap ratio decreases. With a lesser overlap ratio, the roughness

increases. The increasing scanning velocity results in an unstable molten pool, which will also result in a higher roughness. These two behaviours explain the increase in the top surface roughness along with scanning velocity. When it comes to the side surface, Mumtaz et al. [12] reckoned that the low scanning velocity resulted in a larger molten pool and a larger variation in thermal properties across the molten pool, which would cause the molten pool to break off into smaller entities. These entities solidified at the edge and resulted in a poor side surface quality. In addition, the adjacent powders will be dragged to the molten pools due to the Marangoni flow and generate adherent particles on the side surface [10]. The Marangoni flow decreases with the increasing of the scanning velocity [13]. However, the instability of the molten pool should also be considered. These two opposite aspects competed in affecting the side surface quality. In our study, the molten pool instability is considered to be a predominant effect on the side surface quality. So the side surface roughness increases as the scanning velocity increases within the chosen range.

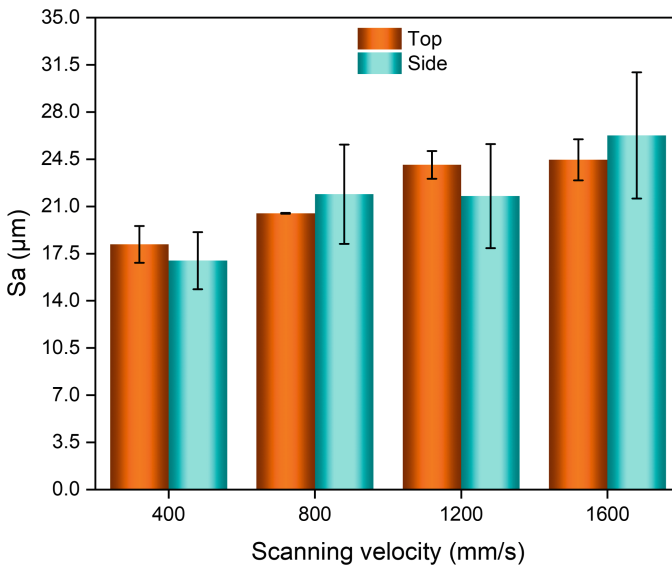


Fig. 2. Surface roughness (S_a) of the top and side plane of the samples fabricated with different scanning velocity

3.2 Laser Remelting Samples

Figure 3a shows the top surface roughness of the remelting samples. In comparison with the samples without remelting, the top surface roughness of the laser remelting samples rescanned at a lower scanning velocity is much lower. The lowest top surface roughness is $7.168 \mu\text{m}$, which decreases by 60.6%. The results indicate that the surface quality can be improved via laser remelting with the proper process parameters. As the remelting scanning velocity increases, the top surface roughness increases. When the

remelting scanning velocity is high, the top surface roughness is even higher than that of the samples without remelting. The effect of the laser remelting power is on the surface roughness is found be correlated to the scanning velocity. When the scanning velocity is relatively low, the top surface roughness decreases as the laser remelting power increases. However, when the scanning velocity is relatively high, the effect of the laser remelting power changes. The excessive high power results in a poor top surface quality. Laser remelting with the optimized process parameters will result in a better molten pool flow behaviour and subsequent spreading, which hence will improve the surface finish.

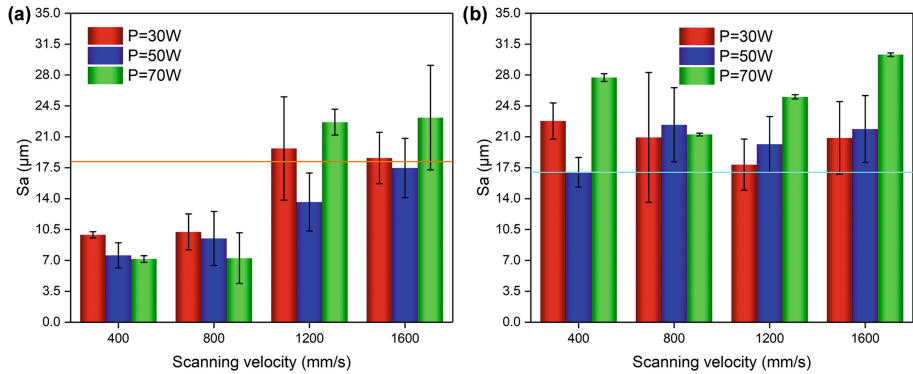


Fig. 3. Surface roughness (S_a) of the top plane (a) and side plane (b) of the laser remelting samples fabricated with different scanning velocities

Figure 3b shows the side surface roughness of the remelting samples. In comparison with the samples without remelting, the side surface roughness becomes larger. A high laser remelting power usually results in a large side surface roughness. Besides, the effect of the remelting scanning velocity is not significant. Therefore, in-situ laser remelting is not helpful in improving the side surface quality.

Figure 4 shows the top surface texture of the samples remelted by different laser power with the scanning velocity of 400 mm/s. It can be seen that the larger power results in a smoother surface due to the prolonged time for the molten pool spreading in addition to the increased fluid flow strength. It is also noticed that some pores have formed during the remelting process (red arrows), which is not desirable. It may be caused by the high energy input during the remelting process.

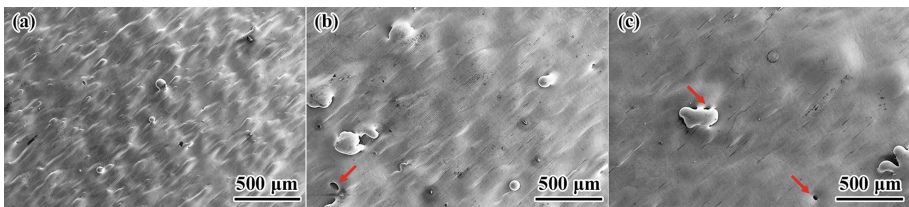


Fig. 4. Top surface morphologies of the samples remelted by different laser power (a) 30 W, (b) 50 W, (c) 70 W

Figure 5 shows the morphology of the side surface remelted at different laser power with scanning velocity of 400 mm/s. The side surface morphologies show the adherent powders increase as the laser remelting power increases. It is obvious from the results that the side surface could not be improved via the laser remelting. For the change in the scanning velocity, there is no obvious trend in the side surface roughness. But it can be seen that the larger laser remelting power usually results in a much worse side surface quality. Although laser remelting can promote the melting of the adhered particles, the molten pool during remelting might drag the adjacent powders causing adherence of new powders [14]. The different responses compete in affecting the side surface quality. The larger laser remelting power results in more new adherent particles, makes the side surface quality worse.

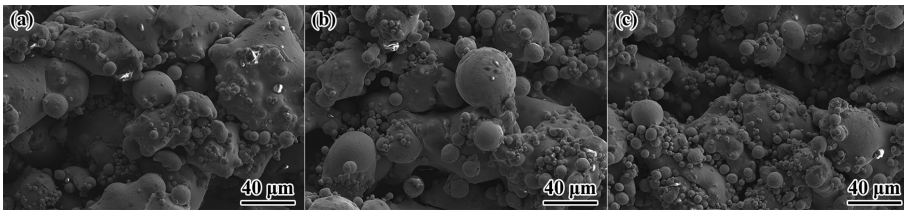


Fig. 5. Side surface morphologies of the samples remelted by different laser power (a) 30 W, (b) 50 W, (c) 70 W

4 Conclusions

In this study, the effects of the in-situ laser remelting process parameter on the top and side surface roughness have been investigated. Following conclusions can be drawn from the results:

- (1) With the optimized process parameters, top surface quality of the micro SLMed samples can be improved. The surface roughness of the improved surface decreases by 60.6% when compared to the samples without laser remelting.
- (2) As the laser remelting scanning velocity increases, the top surface roughness increases. When the scanning velocity is relatively low, the top surface roughness decreases as the laser remelting power increases; when the scanning velocity is relatively high, the excessive high power results in a poor top surface quality.
- (3) The laser remelting could not improve the side surface quality. The remelting of the adhered particles and the new adherent powders compete in affecting the side surface quality. The larger laser remelting power results in more new adherent particles, makes the side surface quality worse.
- (4) Both the top and side surface roughness of the samples without laser remelting increases as the scanning velocity increases. The fluid flow and the overlap of the molten pool affect the top surface while the fluid flow and adherent powders affect the side surface.

References

1. Wang, P., Sin, W.J., Nai, M.L.S., Wei, J.: Effects of processing parameters on surface roughness of additive manufactured Ti-6Al-4V via electron beam melting. *Materials* **10**, 1121 (2017)
2. Yap, C.Y., Chua, C.K., Dong, Z.L., Liu, Z.H., Zhang, D.Q., Loh, L.E., Sing, S.L.: Review of selective laser melting: materials and applications. *Appl. Phys. Rev.* **2**, 041101 (2015)
3. Hu, Z., Zhu, H., Nie, X., Zhang, C., Zhang, H., Zeng, X.: On the role of atmospheric oxygen into mechanical properties and fracture behavior of selective laser melted AlCu5MnCdVA. *Mater. Des.* **150**, 18–27 (2018)
4. de Wild, M., Schumacher, R., Mayer, K., Schkommodau, E., Thoma, D., Bredell, M., Gujer, A.K., Grätz, K.W., Weber, F.E.: Bone regeneration by the osteoconductivity of porous titanium implants manufactured by selective laser melting: a histological and micro computed tomography study in the rabbit. *Tissue Eng. Part A* **19**, 2645–2654 (2013)
5. Wang, X., Li, S., Fu, Y., Gao, H.: Finishing of additively manufactured metal parts by abrasive flow machining. In: 27th International Solid Freeform Fabrication Symposium, pp. 2470–2472 (2016)
6. Zhang, B., Lee, X., Bai, J., Guo, J., Wang, P., Sun, C., Nai, M., Qi, G., Wei, J.: Study of selective laser melting (SLM) Inconel 718 part surface improvement by electrochemical polishing. *Mater. Des.* **116**, 531–537 (2017)
7. Richter, B., Blanke, N., Werner, C., Parab, N.D., Sun, T., Vollertsen, F., Pfefferkorn, F.E.: High-speed X-ray investigation of melt dynamics during continuous-wave laser remelting of selective laser melted Co-Cr alloy. *CIRP Ann.* **68**, 229–232 (2019)
8. Yasa, E., Deckers, J., Kruth, J.P.: The investigation of the influence of laser re-melting on density, surface quality and microstructure of selective laser melting parts. *Rapid Prototyp. J.* **17**, 312–327 (2011)
9. Yu, W., Sing, S.L., Chua, C.K., Tian, X.: Influence of re-melting on surface roughness and porosity of AlSi10Mg parts fabricated by selective laser melting. *J. Alloy. Compd.* **792**, 574–581 (2019)
10. Wei, K., Lv, M., Zeng, X., Xiao, Z., Huang, G., Liu, M., Deng, J.: Effect of laser remelting on deposition quality, residual stress, microstructure, and mechanical property of selective laser melting processed Ti-5Al-2.5Sn alloy. *Mater. Charact.* **150**, 67–77 (2019)
11. Hu, Z., Nagarajan, B., Song, X., Huang, R., Zhai, W., Wei, J.: Formation of SS316L single tracks in micro selective laser melting: surface, geometry, and defects. *Adv. Mater. Sci. Eng.* **2019**, 9 (2019)
12. Mumtaz, K., Hopkinson, N.: Top surface and side roughness of Inconel 625 parts processed using selective laser melting. *Rapid Prototyp. J.* **15**, 96–103 (2009)
13. Hu, Z., Zhu, H., Zhang, C., Zhang, H., Qi, T., Zeng, X.: Contact angle evolution during selective laser melting. *Mater. Des.* **139**, 304–313 (2018)
14. Yadroitsev, I., Gusarov, A., Yadroitsava, I., Smurov, I.: Single track formation in selective laser melting of metal powders. *J. Mater. Process. Technol.* **210**, 1624–1631 (2010)



Surface Structuring of Multilayer Coated Cutting Tool Using Nd: YVO₄ Nanosecond Laser

Ahmed Alghamdi^(✉)  and Paul Mativenga 

School of Mechanical, Aerospace and Civil Engineering,
The University of Manchester, Manchester, UK
ahmed.alghamdi-2@manchester.ac.uk

Abstract. Micro-structuring of cutting tools surfaces using laser technology is an important technology for modifying tool chip contact phenomenon. While lasers are becoming popular for surface structuring and texturing of cutting tool surfaces, the size and the shapes that can be obtained has not been fully explored for multilayer coated cutting tools using Nd: YVO₄ nanosecond laser. In this study, the micromachining of TiCN/Al₂O₃/Cr multilayer coated tungsten carbide tools using Nd: YVO₄ nanosecond laser at 532 nm wavelength and 7 ns pulse width was undertaken. The impact of the variation of laser travel speed, power, and the number of passes on the structured grooves width and depth is described. The study shows that various grooves' cross-section profiles can be produced. The performance of a structured cutting tools was also evaluated using orthogonal cutting of steel AISI4140.

Keywords: Nanosecond laser · Surface structuring · Cutting tools · Multilayer coatings

1 Introduction

The work on surface structuring and texturing of cutting tools is increasing due to the promising results demonstrated by the researchers in the field of metal cutting. The benefits include reduced cutting forces and improved tool life [3, 5, 6, 23, 27–30]. Structuring methods used by researchers included; micro-EDM [13, 17], micro-grinding [32], FIB [2, 25], photolithography [24] and lasers [3–12, 14, 20, 22, 23, 26–31, 33]. However, lasers are the most widely used method for cutting tools structuring and the reason could be attributed to the limitation in other techniques. In micro-EDM the size of the structures is dictated by the electrode or the wire used. Therefore, it is hard to achieve narrow structures bellow 100 μm. In literature structures machined using micro-EDM were either linear structures that are (50 to 100 μm deep and 100 to 110 μm wide) or holes that are (200 to 250 μm diameter and 250 μm deep) [13, 15–17, 34]. Another drawback for micro-EDM is the possibility of developing microcracks in the structured walls, Lee and Li observed such defects that were extending deep into structured walls machined using micro-EDM method [19]. In FIB the drawbacks are mainly the cost and the significant amount of time it can take to structure the tool

surface. Obikawa et al. reported significant amount of time up to 150 min to achieve a 3 μm deep groove using FIB technology [25]. Micro-grinding is like micro-EDM, is limited by the size of the grinding disc used. The lowest reported width achieved was 400 μm grooves by Xie et al. [32]. Photolithography is an expensive, lengthy process and limited to building structures out of coating material on substrate; Obikawa et al. used Photolithography to build structures over the rake face of a cutting tool using the coating material and described a process that is typical to photolithography processes where it required many steps [24]. Thus, only lasers were found to be capable of delivering high precision structures (i.e. from nano to few micron width channels [4, 6, 28, 29]) in easy steps and minimum damage to tool surface compared to other available processes. However, lasers can produce structures of various shapes and sizes that could serve different objectives during metal cutting and other applications. Micro channels or grooves can be used to deliver cutting fluid to the cutting zone and help control the cutting temperature and friction [3, 11, 12, 14, 30]. Micro dimples (holes) had been reported to be useful to store cutting lubricant during metal cutting [13, 18, 20, 23, 24]. However, femtosecond lasers were mostly used to perform cutting tools structuring and texturing [5, 6, 9–12, 30]. Laser operating at nanosecond pulse width were rarely investigated in the context of cutting tools structuring. In fact, there were no research on structuring and texturing using Nd: YVO₄ nanosecond laser. The micro grooves produced using Nd: YAG nanosecond laser by Da Silva et al. operating at 100 ns pulse width on cemented carbide (WC-Co) substrate and multilayer coating of (TiCN/Al₂O₃/Cr) provides a motivation that a reasonable quality can be achieved using a shorter wavelength and pulse duration [3]. The nanosecond lasers performance can be improved when operating at short wavelength due to higher energy absorption [21]. Therefore, in this study the aim is to investigate the use of Nd: YVO₄ nanosecond laser operating at 532 nm wavelength (green) and 7 ns pulse width to structure a multilayer coated carbide tool. Nanosecond lasers are considered more productive when compared to femtosecond or picosecond lasers because they remove material using combined process of material ablation and melting (photothermal ablation) [21]. Nanosecond lasers are economical in terms of cost when compared with ultrashort lasers which makes them more attractive for industrial applications if they can serve the intended objectives. The study will also investigate the cutting performance of the structured cutting tools in comparison to unstructured cutting tools.

2 Experimental Details

The selected Nd: YVO₄ nanosecond laser specifications are shown in Table 1. However, a calibration test revealed that it gives maximum of 3.2 W at 30 kHz. Thus, using the highest average power available at the identified frequency of 30 kHz and then descending by the order of 5% of the pumping power, few trials on the surface intended for structuring were conducted by focusing the laser spot over the surface at low speeds of 10 mm/s. The pilot test showed that the laser was not able to ablate the surface below 2 W average power. Thus, two experiments were conducted using the lowest value identified (2 W) and the maximum available (3.2 W). The laser peak fluence for a Gaussian beam at these values was estimated using Eqs. 1 and 2:

$$E (J) = \frac{Avg.Power (W)}{Repetition Rate (Hz)} \quad (1)$$

Where, E , is the pulse energy, F , is the laser fluence, and, A , is the laser spot area.

$$F (J/cm^2) = \frac{E (J)}{A (cm^2)} \quad (2)$$

Hence the peak fluence was estimated at $3.2 \text{ W} = 9 \text{ J/cm}^2$ and at $2 \text{ W} = 5.6 \text{ J/cm}^2$. In the first experiment, the laser speed was varied over a wide range of speeds [the low range (2, 4, 6, 8, 10, 20, 30, 40, and 50) mm/s, the medium range of (100, 200, 300, 400, and 500) mm/s, and the higher speed range of (1000, 1500, 2000, 2500, 3000, 4000, 8000, 12000, 16000, and 20000) mm/s]. The experiments were done at fixed peak fluence of 9 J/cm^2 and 30 passes. In the second experiment the number of passes were varied between (5, 10, 20, 40, 80, to 120) passes at two different peak fluences of (5.6 and 9 J/cm^2). The speeds were also varied between (5, 10, 20, 40, 80, 160, 320, and 640) mm/s.

Table 1. The Nd: YVO₄ nanosecond laser specifications

Spot size	55 μm
Wavelength	532 nm
Pulse Duration	7 ns
Max. Power	7 W
Repetition rate	10–80 kHz

The cutting tools used for laser experiment and the cutting case study were cemented carbide (WC-Co) tools with a multilayer coating of (TiCN/Al₂O₃/Cr). Figure 1 shows the cross-section SEM image for the multiple layers of coating over the carbide substrate however, it should be noted that the chromium layer thickness was only 1 μm and hence was not clearly visible at this scale. The cutting tool shape and profile are shown in Fig. 2. The rake face was restricted contact type with land size of 0.24 mm and built in chip breaker type, the rake angle of the land and the flank face was 0° and 7° respectively. The structuring for laser tests was performed over the flat surfaces of the tool, however, before that the surfaces were tested for the availability of the coating using the SEM/EDX analysis. The laser structuring for cutting tests were performed over the chip breaker surface using linear structures (microgrooves). Figure 3 show sectional view SEM image for a structured tool.

The characterization of the microstructures was performed using both optical microscope and a 3D laser optical microscope. The SEM/EDX were used to measure the Fe concentration over the rake face for cutting tools after cutting. The cutting was orthogonal cutting using CNC lathe. The workpiece for cutting tests was steel AISI 4140 alloy. The workpiece was cut into tube shape to facilitate the orthogonal cutting. The force measurement was performed using force dynamometer and signal filter.

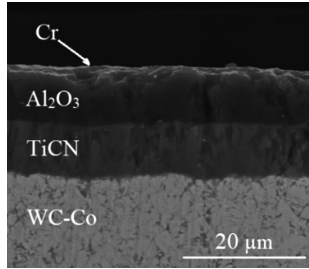


Fig. 1. The SEM image of the cemented carbide (WC-Co) and the multilayer coating of (TiCN/Al₂O₃/Cr).

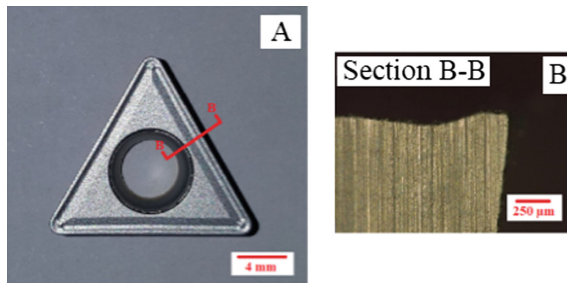


Fig. 2. The cutting tools used for laser work and case study; (A) Top view, and (B) The sectional view B-B illustrates the profile of the tool rake and flank faces.

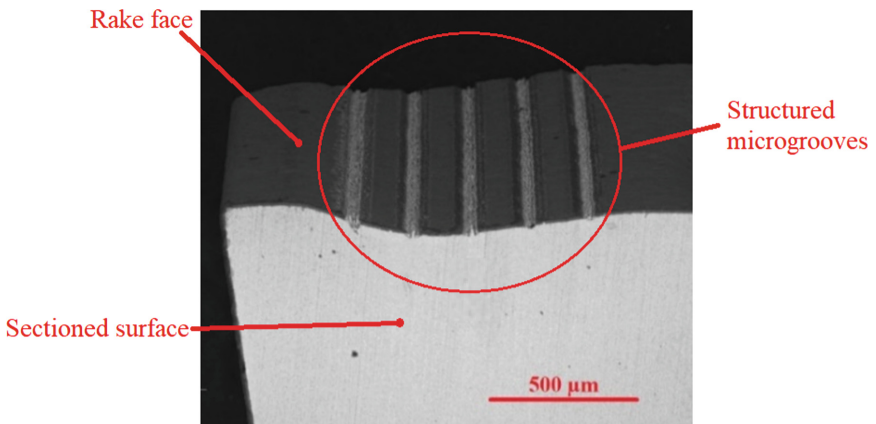


Fig. 3. SEM image of sectional view for a sample structured tool used for the orthogonal cutting tests.

The data were collected and analyzed using software package for force data processing. The cutting velocities were (100, 200, 300, and 400 m/min). The feed rate was fixed at 0.20 mm/rev for all cuts. The depth of cut was the tube thickness of 2.5 mm. The cutting was performed in dry cutting condition and the length of each cut was limited to 5 mm to reduce the impact of tool wear.

3 Results and Discussion

3.1 The Laser Surface Structuring Results

The first laser test results are shown in Fig. 4. They demonstrate the wider process window for the used Nd: YVO₄ nanosecond laser to structures the multilayer coating of the cutting tool surface. The images in Fig. 4 A–C reveals that the laser beam at 9 J/cm² fluence had successfully produced linear structures (microgrooves) while the travel speed of the beam spot over the surface was varied between 5 mm/s to 500 mm/s and the number of passes was fixed at 30 passes. The linear structures width ranged between 0.65 to 0.90 μm. However, Fig. 4 D and E show that the increase in the speed beyond 500 mm/s changed the type of structures to separate periodic structures. The shape of the periodic structures are micro dimples/pits that had diameter ranging between 0.54 to 0.87 μm and depth varied between less than 1 μm up to 2 μm. The depth for the linear structures was not evaluated at this stage as the aim was to identify the wider process window only. However, the distance between the laser periodic structures was characterized in relation to spot overlap for each setting and shown in Fig. 5. the spot overlap was calculated based on Eq. (3):

$$\text{Spot Overlap } \% = \left(1 - \frac{S(\text{mm/s})}{v(\text{Hz}) \times D(\text{mm})} \right) \times 100 \quad (3)$$

Where S is the laser beam spot's surface travel speed in mm/s, v is laser repetition rate (frequency) and D is the spot diameter. The linear structures started to separate at nearly 1000 mm/s and above where the spot overlap was at 39%. Thus, this value can be identified as the threshold value between linear and periodic structures for this type of coating.

The second laser test was designed to identify the various cross-sectional profiles for linear structures for the Nd: YVO₄ nanosecond laser. Figures 6 and 7 show the 3D profile for linear structures produced at fluence rates of 9 and 5.6 J cm², 5 mm/s speed and (5 to 120) passes. The general shape for the linear structures' cross-sectional profile varied from micro-grooves with (V-shape) to micro-channels with (U-shape). The summary of the width and depth of the linear structures are given in Figs. 8, 9, 10 and 11 for both fluence rates tested at different speeds and number of passes. It is noticeable from Fig. 8 that the structures depth at the higher fluence rate of 9 J/cm² was changing in nearly upward trend as the number of passes was changing from 5 to 120 passes. Similarly, the change of the laser beam travel speed from 5 mm/s to 640 mm/s had influenced the values of the depth when comparing the individual lines that represent the laser spot travel speeds. The result show that depths values between 20 to 30 μm at

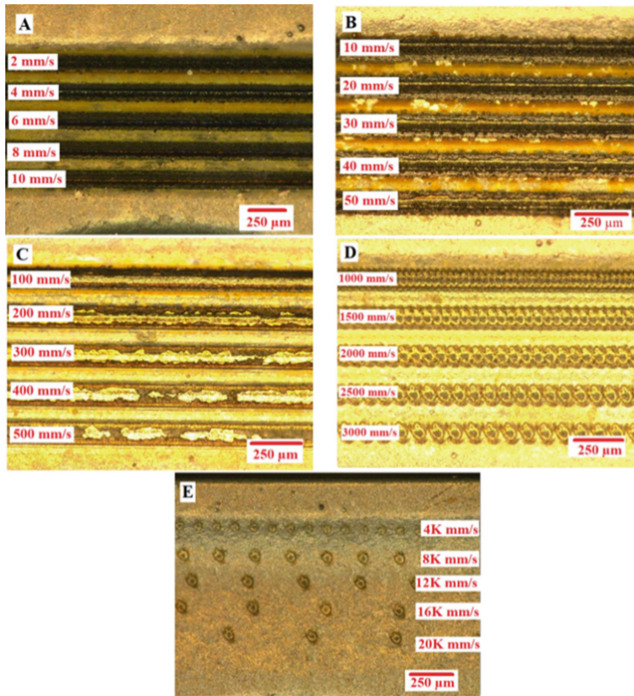


Fig. 4. Structures variation at different speeds and fixed peak fluence of 9 J/cm^2 (A–C) linear structures, (D and E) separate periodic surface structures.

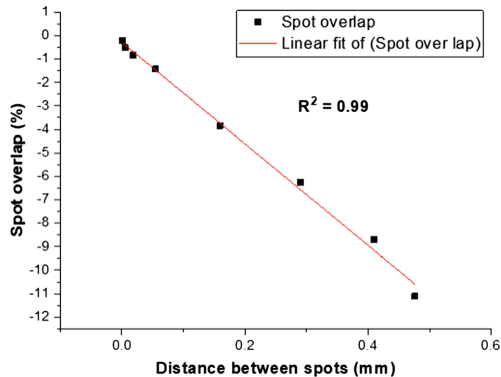


Fig. 5. Relationship between spot overlap and distance between the separate periodic structures

lower speed rate of 5 mm/s were achieved and from 0.6 to $17 \text{ }\mu\text{m}$ for the higher speed rate of 640 mm/s . The cross-sectional profile shape was V-shape at lower speed range and gradually changed to U-shape at higher speeds. The results suggest that the depth and the cross-sectional profile are function of both laser spot travel speed and the

number of passes at the 9 J/cm^2 fluence level. The width of the microstructures in Fig. 9 showed nearly horizontal linear trend as both the spot travel speed and spot overlap were changing, which suggest a weak relationship with both. The linear structures depth results in Fig. 10 for the 5.6 J/cm^2 fluence rate had nearly the same trends in relation to laser spot travel speed and the number of passes. However, the difference was in the range of the values obtained, at this level the depth range was from 1.27 to $1.73 \mu\text{m}$ at 5 mm/s speed and from 0.6 to $1.3 \mu\text{m}$ at speed of 640 mm/s . Other noticeable difference is the shape of the cross-sectional profile obtained; the shape was mostly U shape for all structures. The width of the microstructures also did not show a specific relationship, but it was noticeable that values close to the spot size diameter were obtained (few micrometers larger or less). However, the significant difference between the two values of fluence rates used is the volume of burrs. The higher fluence resulted in higher volume of coating material melting and solidification process. This suggest that the material removal was mostly performed by photothermal ablation process. This was not the case for the lower fluence value, the microscope images show less burrs around the structures which suggest that the material was mostly removed by ablation rather than melting. However, this does not mean that there were no material melting but rather suggest that it was less significant.

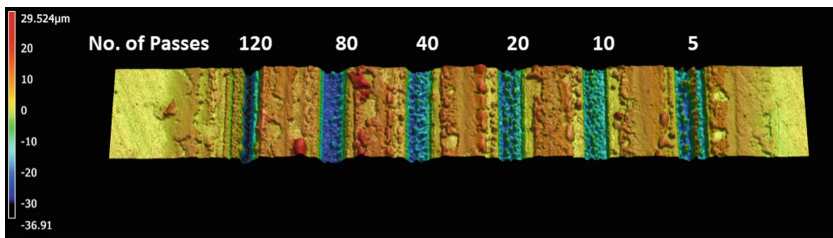


Fig. 6. 3D profile of the linear structures at various number of passes, fixed peak fluence and speed of 9 J/cm^2 and 5 mm/s respectively.

3.2 Discussion on the Laser Structuring

The laser structuring results demonstrate that the Nd: YVO₄ nanosecond laser can produce various linear and periodic structures of various sizes and different cross-sectional profiles. At the higher fluence rate of 9 J/cm^2 the laser was capable of penetrating through all the coating layers of the TiCN/Al₂O₃/Cr and the carbide substrate, Fig. 12 confirms such findings. The issue that arises at the high fluence rate is the excessive burrs resulting from the photothermal ablation and the solidification of the molten material over the surface. This issue was not significant when lower fluence was used. Though the lower fluence resulted in lower depth values, but it remains an option if the objective was to achieve 1 to 2 microns of depths. The cross-sectional shapes varied between U to V-shapes and in few occasions at the lower fluence settings wavy form of W shape was achieved. The main reason for the shape variation with the speed could be attributed to the spot overlap. When the fluence and spot size are kept fixed, the pulse energy does not change, this can be explained by Eqs. 1 and 2. Thus, the only

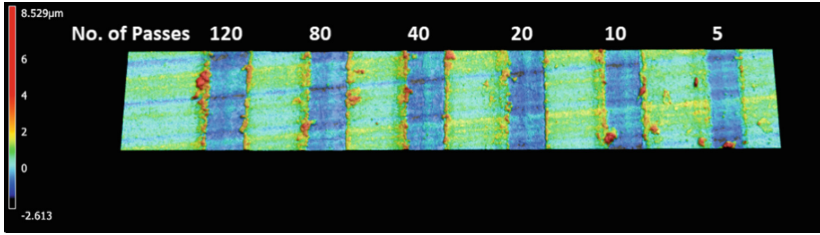


Fig. 7. 3-D profile of the linear structures at various number of passes, fixed peak fluence and speed of 5.6 J/cm^2 and 5 mm/s respectively.

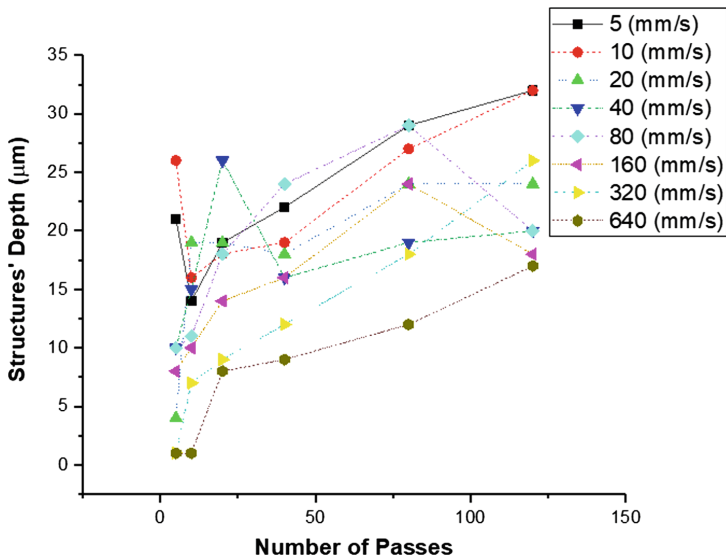


Fig. 8. The change in linear structures' depth in relation to the number of passes and speed at fixed peak fluence of 9 J/cm^2 .

parameter that was changing is the spot overlap which was explained earlier in Eq. 3. The mechanism of how the spot overlap is affecting the depth and shape of the structures is that; when the speed at the lower range between 5 to 160 mm/s , the spot overlap is kept well above 90% , which allows more energy to be applied at the exact same spot at the same rate of frequency setting. This means that the same spot will endure more heat and thus the material is removed by melting and ablation. The thermal process and the ablation cause higher removal rate and allows the laser beam to penetrate deeper through the coating layers. The molten material splashed away with the ablation of the particles from the deep spot of the groove over the side walls and the edges, forming the burrs and causing the shape of the groove to change from U-shape to V-shape. The excessive burrs also make it hard to measure the width accurately. At the medium to high speed range from 340 to 640 mm/s the spot overlap drops from

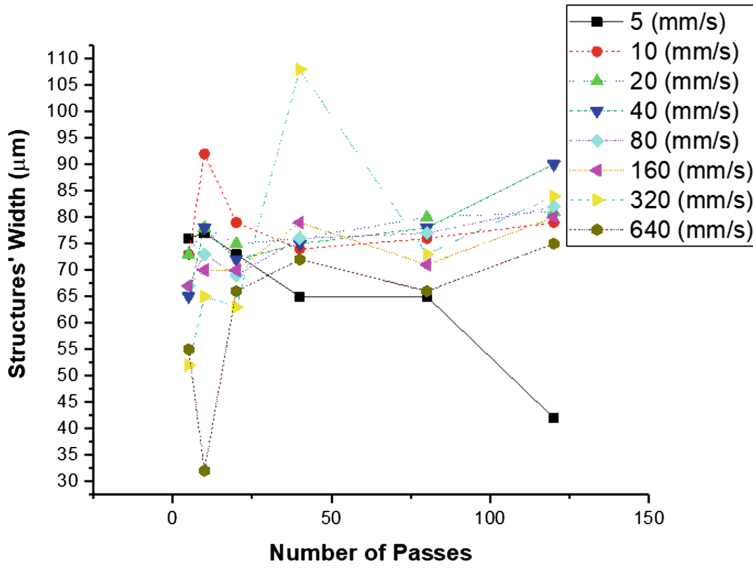


Fig. 9. The change in linear structures' width in relation to the number of passes and speed at fixed peak fluence of 9 J/cm^2 .

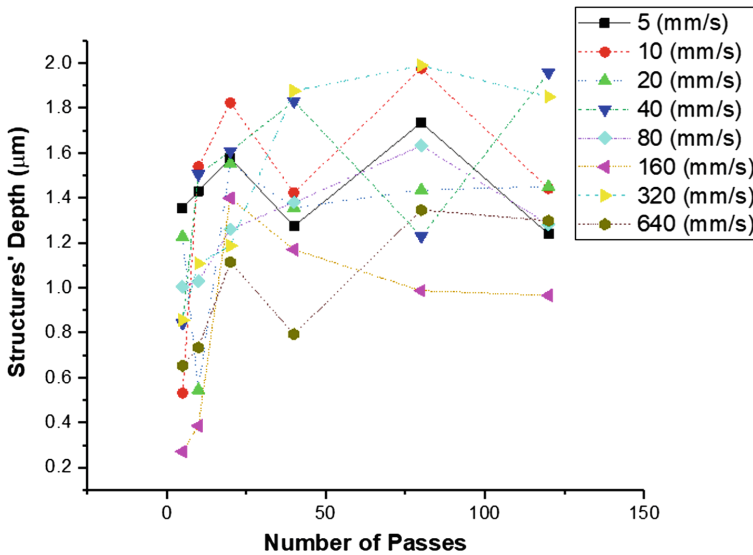


Fig. 10. The change in linear structures' depth in relation to the number of passes and speed at fixed peak fluence of 5.6 J/cm^2 .

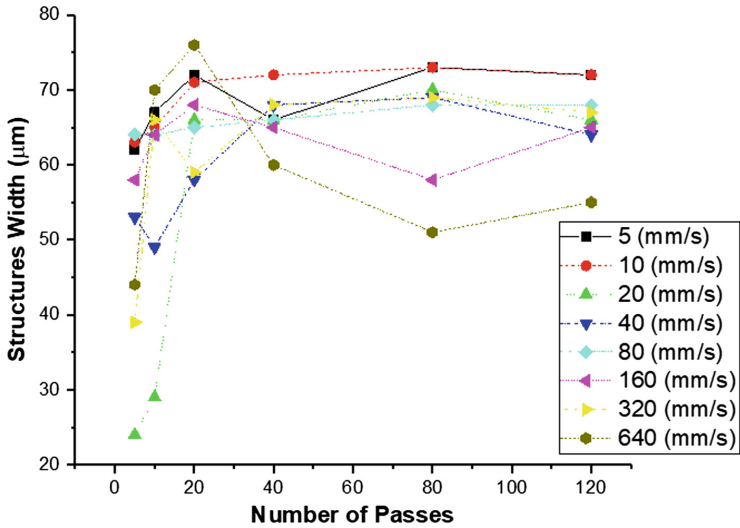


Fig. 11. The change in linear structures' width in relation to the number of passes and speed at fixed peak fluence of 5.6 J/cm^2 .

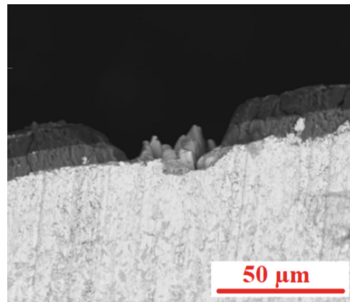


Fig. 12. SEM image for cross-sectional sample for structured surface at 9 J/cm^2

the 90% level to 79 and 61% levels. This means less heat will be absorbed by the material and thus the removal of the material was mainly done by the ablation process which resulted in less burrs and preserved the uniformity of the groove cross-sectional shape.

3.3 Cutting Tests Results and Discussion

The orthogonal cutting tests' results show that the average contact area over the cutting tool rake face had been reduced for structured tools as shown in Fig. 13 by nearly 33%. The reduction in contact area is supported by the EDX analysis which shows a reduction of 27% in iron wt.% over the rake face as shown in Fig. 14. The reduction in the main cutting forces and the frictional forces, shown in Figs. 15 and 16, were only 3.5 and 3.1% respectively. The reason for the low reduction in cutting forces can be

attributed to the use of contact restricted tool and the limiting of the structuring to the chip breaker surface. Contact restricted tools were designed to keep the cutting forces to minimum and thus, further reduction is expected to be limited. The absence of cutting fluids or solid lubricant could be another factor that influenced the limited improvement in cutting forces reduction. The creation of lubrication film and the hydrodynamic lift by the cutting fluids or solid lubricants had been reported to play a role in the reduction of frictional forces [1, 16].

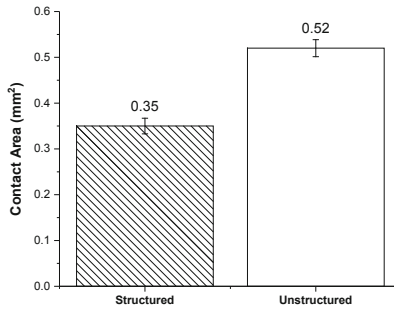


Fig. 13. The tool chip contact area over the rake face for structured and unstructured tools.

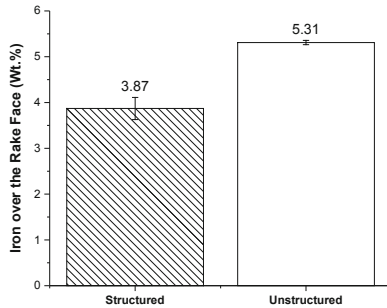


Fig. 14. The Fe wt.% concentration level over the rake face of the cutting tools.

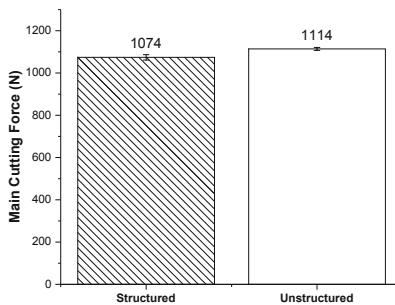


Fig. 15. The main cutting forces.

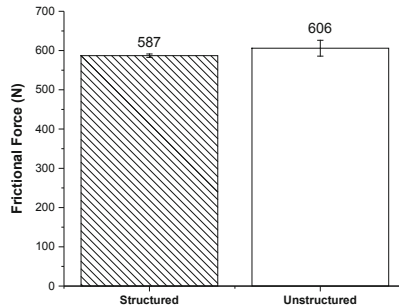


Fig. 16. The frictional forces.

4 Conclusion

Laser technology is important when it comes to cutting tools surface structuring. The need for laser that can deliver more output with reasonable quality and cost is on the rise for both research and industrial application. The Nd: YVO₄ nanosecond laser operating at short wavelength of 532 nm and 7 ns pulse width can be used as an alternative for higher cost and less productive laser system. The conducted experimental work on the Nd: YVO₄ nanosecond showed that;

1. Using one factor at a time method a process window for surface structuring of cemented tungsten carbide coated with multilayer coating of TiCN/Al₂O₃/Cr using nanosecond laser had been identified. The laser operating at short wavelength of 532 nm and 7 ns pulse width, beam spot of 0.055 mm diameter and within range between 5.6 to 9 J/cm² fluence rates, where variation of laser beam spot travel speed between (5, 10, 20, 40, 80, 160, 320, and 640 mm/s) and number of passes between (5, 10, 20, 40, 80, to 120) produced multiple structures that varied in cross-sectional shape and size. Shapes of U, V and wavy form were achievable at sizes that varied between 0.20 to 32.5 μm in depth and 28.7 to 105 μm in width.
2. It was also identified that separate organized structures were achievable as function of the laser spot overlap. The threshold value for the transition from linear structures to separate organized structures was 39%, and to obtain linear structures at straight linear edge the spot overlap required to be kept well above 90%.
3. There is a motivation for laser optimization to achieve higher depths with minimum burrs and better control over the width of the micro channels. The variation of the repetition rate (frequency) might help to reduce the burrs issue.

The orthogonal cutting tests using structured cutting tool reduced the tool chip contact area by nearly 30%. The average reduction of cutting forces didn't exceed 3%. The reason for limited reduction in cutting forces was attributed to the use of contact restricted contact tool and the limiting of structuring to the chip breaker surface. Another reason could be the absence of cutting fluids or solid lubricants. Therefore, further investigation is required to identify the best location for surface structuring of contact restricted tools and the impact of using cutting fluids and/solid lubricants.

References

1. Arslan, A., Masjuki, H.H., Kalam, M.A., Varman, M., Mufti, R., Hossain, M., Leang, S.K., Quazi, M.M.: Surface texture manufacturing techniques and tribological effect of surface texturing on cutting tool performance: a review. *Crit. Rev. Solid State Mater. Sci.* **41**, 447–481 (2016)
2. Chang, W., Sun, J., Luo, X., Ritchie, J.M., Mack, C.: Investigation of microstructured milling tool for deferring tool wear. *Wear* **271**(9), 2433–2437 (2011)
3. Da Silva, W.M., Suarez, M.P., Machado, A.R., Costa, H.L.: Effect of laser surface modification on the micro-abrasive wear resistance of coated cemented carbide tools. *Wear* **302**(1), 1230–1240 (2013)
4. Enomoto, T.: Development of a cutting tool with micro engineering surface. In: Proceedings of Spring Conference of the Japan Society for Precision Engineering (2006)
5. Enomoto, T., Sugihara, T.: Improvement of anti-adhesive properties of cutting tool by nano/micro textures and its mechanism. *Procedia Eng.* **19**, 100–105 (2011)
6. Enomoto, T., Sugihara, T., Yukinaga, S., Hirose, K., Satake, U.: Highly wear-resistant cutting tools with textured surfaces in steel cutting. *CIRP Ann. – Manuf. Technol.* **61**(1), 571–574 (2012)
7. Enomoto, T., Watanabe, T., Aoki, Y., Ohtake, N.: Development of a cutting tool with micro structured surface. *Trans. Jpn. Soc. Mech. Eng. Ser. C* **73**(729), 1560–1565 (2007)
8. Fatima, A., Mativenga, P.T.: Assessment of tool rake surface structure geometry for enhanced contact phenomena. *Int. J. Adv. Manuf. Technol.* **69**(1-4), 771–776 (2013)
9. Fatima, A., Mativenga, P.T.: Performance of flank face structured cutting tools in machining of AISI/SAE 4140 over a range of cutting speeds. *Proc. Inst. Mech. Eng. Part B J. Eng. Manuf.* **230**, 3–18 (2014)
10. Fatima, A., Mativenga, P.T.: A comparative study on cutting performance of rake-flank face structured cutting tool in orthogonal cutting of AISI/SAE 4140. *Int. J. Adv. Manuf. Technol.* **78**(9-12), 2097–2106 (2015)
11. Fatima, A., Mativenga, P.T.: On the comparative cutting performance of nature-inspired structured cutting tool in dry cutting of AISI/SAE 4140. *Proc. Inst. Mech. Eng. Part B J. Eng. Manuf.* **231**(11), 1941–1948 (2017)
12. Fatima, A., Whitehead, D.J., Mativenga, P.T.: Femtosecond laser surface structuring of carbide tooling for modifying contact phenomena. *Proc. Inst. Mech. Eng. Part B J. Eng. Manuf.* **228**(11), 1325–1337 (2014)
13. Jianxin, D., Wenlong, S., Hui, Z.: Design, fabrication and properties of a self-lubricated tool in dry cutting. *Int. J. Mach. Tools Manuf.* **49**(1), 66–72 (2009)
14. Kawasegi, N., Sugimori, H., Morimoto, H., Morita, N., Hori, I.: Development of cutting tools with microscale and nanoscale textures to improve frictional behavior. *Precis. Eng.* **33**(3), 248–254 (2009)
15. Kim, D.M., Bajpai, V., Kim, B.H., Park, H.W.: Finite element modeling of hard turning process via a micro-textured tool. *Int. J. Adv. Manuf. Technol.* **78**(9), 1393–1405 (2015)
16. Kim, D.M., Lee, I., Kim, S.K., Kim, B.H., Park, H.W.: Influence of a micropatterned insert on characteristics of the tool–workpiece interface in a hard turning process. *J. Mater. Process. Technol.* **229**, 160–171 (2016)
17. Koshy, P., Tovey, J.: Performance of electrical discharge textured cutting tools. *CIRP Ann. – Manuf. Technol.* **60**(1), 153–156 (2011)
18. Kuemmel, J., Braun, D., Gibmeier, J., Schneider, J., Greiner, C., Schulze, V., Wanner, A.: Study on micro texturing of uncoated cemented carbide cutting tools for wear improvement and built-up edge stabilisation. *J. Mater. Process. Technol.* **215**, 62–70 (2015)

19. Lee, S.H., Li, X.: Study of the surface integrity of the machined workpiece in the EDM of tungsten carbide. *J. Mater. Process. Technol.* **139**(1), 315–321 (2003)
20. Lei, S., Devarajan, S., Chang, Z.: A study of micropool lubricated cutting tool in machining of mild steel. *J. Mater. Process. Technol.* **209**(3), 1612–1620 (2009)
21. Meijer, J., Du, K., Gillner, A., Hoffmann, D., Kovalenko, V.S., Masuzawa, T., Ostendorf, A., Poprawe, R., Schulz, W.: Laser Machining by short and ultrashort pulses, state of the art and new opportunities in the age of the photons. *CIRP Ann.* **51**(2), 531–550 (2002)
22. Neves, D., Diniz, A.E., de Lima, M.S.F.: Efficiency of the laser texturing on the adhesion of the coated twist drills. *J. Mater. Process. Technol.* **179**(1), 139–145 (2006)
23. Niketh, S., Samuel, G.L.: Surface texturing for tribology enhancement and its application on drill tool for the sustainable machining of titanium alloy. *J. Clean. Prod.* **167**, 253–270 (2017)
24. Obikawa, T., Kamio, A., Takaoka, H., Osada, A.: Micro-texture at the coated tool face for high performance cutting. *Int. J. Mach. Tools Manuf.* **51**(12), 966–972 (2011)
25. Obikawa, T., Kani, B.: Micro ball end milling of titanium alloy using a tool with a microstructured rake face. *J. Adv. Mech. Des. Syst. Manuf.* **6**(7), 1121–1131 (2012)
26. Pfeiffer, M., Engel, A., Weißmantel, S., Scholze, S., Reisse, G.: Microstructuring of steel and hard metal using femtosecond laser pulses. *Phys. Procedia* **12**, 60–66 (2011)
27. Sugihara, T.: Development of a cutting tool with nano-micro textured surface. In: *Proceedings of Spring Conference of Japan Society for Precision Engineering Student Division*, vol. 2008, p. R-11 (2008)
28. Sugihara, T., Enomoto, T.: Development of a cutting tool with a nano/micro-textured surface—Improvement of anti-adhesive effect by considering the texture patterns. *Precis. Eng.* **33**(4), 425–429 (2009)
29. Sugihara, T., Enomoto, T.: Improving anti-adhesion in aluminum alloy cutting by micro stripe texture. *Precis. Eng.* **36**(2), 229–237 (2012)
30. Sugihara, T., Enomoto, T.: Crater and flank wear resistance of cutting tools having micro textured surfaces. *Precis. Eng.* **37**(4), 888–896 (2013)
31. Vasumathy, D., Meena, A., Duraiselvam, M.: Experimental study on evaluating the effect of micro textured tools in turning AISI 316 austenitic stainless steel. *Procedia Eng.* **184**, 50–57 (2017)
32. Xie, J., Luo, M.J., He, J.L., Liu, X.R., Tan, T.W.: Micro-grinding of micro-groove array on tool rake surface for dry cutting of titanium alloy. *Int. J. Precis. Eng. Manuf.* **13**(10), 1845–1852 (2012)
33. Ze, W., Jianxin, D., Yang, C., Youqiang, X., Jun, Z.: Performance of the self-lubricating textured tools in dry cutting of Ti-6Al-4V. *Int. J. Adv. Manuf. Technol.* **62**(9), 943–951 (2012)
34. Zhang, J., Li, Q., Zhang, H., Sui, Y., Yang, H.: Investigation of micro square structure fabrication by applying textured cutting tool in WEDM. *Micromachines* **6**(10), 1427–1434 (2015)

Author Index

A

Ahluwalia, Kunal, 26
Akebono, Hiroyuki, 69
Alghamdi, Ahmed, 344
Aoki, Kan, 190
Arakawa, Jinta, 69
Aramcharoen, Ampara, 26
Ardi, Dennise Tanoko, 182, 321

B

Baak, Nikolas, 198
Beaudonnet, Anne-Laure, 36
Benafan, Othmane, 254
Biermann, Dirk, 198
Billot, Thomas, 3

C

Cabrero, Julien, 36
Campolo, Domenico, 273
Cao, Chenyao, 97
Chang Wei, Kang, 26
Cheng, Fang, 155
Cheng, Han, 292
Chin, Kai Siang, 182

D

Damodara, Reddy Chilla, 133
Dides, Corentin, 3
Ding, Jialuo, 121

E

El Hadrouz, M., 36
Everaerts, J., 144

F

Fu, Shaowei, 155

G

Gao, Shubo, 330
Gao, Yukui, 56
Gibbons, Greg J., 305
Görtan, Mehmet Okan, 173
Groche, Peter, 108
Guillemot, Nicolas, 3
Guo, Junyan, 133

H

Hayashi, Yoshiichirou, 69
Ho, Jeremy, 226, 234
Hohmann, Johannes, 108
Hönnige, Jan, 121
Hu, Yongxiang, 292
Hu, Zhiheng, 330, 337
Huang, Rui, 330, 337

I

Idapalapati, Sridhar, 182
Iga, Yuka, 283
Itoh, Sho, 226, 234

J

Jin, X. Z., 144

K

Kameyama, Yutaka, 46
Kaynak, Yusuf, 254, 263
Kobayashi, Yuji, 190
Korsunsky, A. M., 144
Kumagai, Isao, 19
Kumar, Deepak, 163
Kumeno, Fumiaki, 298
Kuriachen, Basil, 163

L

Lakshminarayanan, Srinivasan, 273
 Levy, Benjamin, 36
 Li, F., 144
 Liu, E. J., 144
 Loi, Qizhong, 133

M

Maharjan, Niroj, 321
 Makino, Yoshiyasu, 190
 Manivasagam, Geetha, 314
 Manyar, Omey Mohan, 273
 Marinescu, I., 144
 Martina, Filomeno, 121
 Mathew, Jose, 163
 Mativenga, Paul, 344
 Mezghani, Sabeur, 36
 Mizuno, Hiroki, 215
 Mohamed, El Mansori, 36
 Msolli, Sabeur, 133
 Muktinutalapati, Nageswara Rao, 314

N

Nagalingam, Arun Prasanth, 244
 Nagarajan, Balasubramanian, 330, 337
 Nakamura, Yuki, 298
 Nambu, Koichiro, 19
 Narayanaswamy, Sridhar, 133
 Neto, Leonor, 121
 Nickel, Jan, 198

O

Ohta, Tatsuya, 46
 Okumiya, Masahiro, 19
 Okura, Yuya, 88
 Ören, Soner, 263
 Orhangül, Akin, 263

P

Pan, Jisheng, 133
 Paradowska, Anna, 182
 Philip, Jibin T., 163
 Poyraz, Özgür, 263

R

Rajan, S. Sudhagara, 314
 Reid, Mark, 182

S

Sasaki, Hirotoshi, 88, 283
 Sasaki, Keita, 46
 Sato, Hideaki, 46

Seita, Matteo, 330
 Seitz, Michael, 10
 Shibuya, Norihito, 298
 Shimpo, Ryokichi, 46
 Shukla, Shashwat, 182
 Song, X., 144, 330, 337
 Soyama, Hitoshi, 76, 88, 283
 Sticht, Peter, 108
 Suesuga, Hiroaki, 215
 Sugeta, Atsushi, 69
 Sümer, Bilsay, 173
 Sun, W., 144
 Swaroop, Sathya, 314

T

Takashima, Kenta, 19
 Tan, Boon Hee, 133
 Tan, W. Y., 144
 Tanaka, Tomohisa, 97
 Tao, Xuefei, 56
 Tascioglu, Emre, 254, 263
 Te, Ba, 26
 Teo, Augustine, 26
 Tjahjowidodo, Tegoeh, 155
 Turangan, Cary, 226
 Turangan, Cary Kenny, 234

V

Van Bo, Nguyen, 26

W

Walther, Frank, 198
 Wan Yee Ming, Stephen, 234
 Wan, Stephen, 226
 Wei, Jun, 330, 337
 Weidenmann, Kay André, 10
 West, Geoff D., 305
 Williams, Stewart, 121
 Wong, Chow Cher, 305

Y

Yeo, Swee Hock, 244
 Yong, Ching Kiat, 305
 Yoshinouchi, Ryo, 298
 Yüksel, Berkay, 173

Z

Zhai, W., 144
 Zhai, Wei, 337
 Zhang, Zheng, 133
 Zhang, Zhi-Qian, 133
 Zhu, Jiang, 97